

Litao Sun
Tao Xu
Ze Zhang *Editors*

In-Situ Transmission Electron Microscopy

 Springer


In-Situ Transmission Electron Microscopy


Litao Sun · Tao Xu · Ze Zhang
Editors

In-Situ Transmission Electron Microscopy

 Springer

Editors

Litao Sun 
School of Electronic Science
and Engineering
Southeast University
Nanjing, Jiangsu, China

Tao Xu 
School of Electronic Science
and Engineering
Southeast University
Nanjing, Jiangsu, China

Ze Zhang
School of Materials Science
and Engineering
Zhejiang University
Hangzhou, Zhejiang, China

ISBN 978-981-19-6844-0

ISBN 978-981-19-6845-7 (eBook)

<https://doi.org/10.1007/978-981-19-6845-7>

© The Editor(s) (if applicable) and The Author(s), under exclusive license to Springer Nature Singapore Pte Ltd. 2023

This work is subject to copyright. All rights are solely and exclusively licensed by the Publisher, whether the whole or part of the material is concerned, specifically the rights of translation, reprinting, reuse of illustrations, recitation, broadcasting, reproduction on microfilms or in any other physical way, and transmission or information storage and retrieval, electronic adaptation, computer software, or by similar or dissimilar methodology now known or hereafter developed.

The use of general descriptive names, registered names, trademarks, service marks, etc. in this publication does not imply, even in the absence of a specific statement, that such names are exempt from the relevant protective laws and regulations and therefore free for general use.

The publisher, the authors, and the editors are safe to assume that the advice and information in this book are believed to be true and accurate at the date of publication. Neither the publisher nor the authors or the editors give a warranty, expressed or implied, with respect to the material contained herein or for any errors or omissions that may have been made. The publisher remains neutral with regard to jurisdictional claims in published maps and institutional affiliations.

This Springer imprint is published by the registered company Springer Nature Singapore Pte Ltd. The registered company address is: 152 Beach Road, #21-01/04 Gateway East, Singapore 189721, Singapore

Foreword

When I started my career in electron microscopy, it was with in situ experiments under direct observation in the transmission electron microscope. The 1970s and the 1980s were the time of the “dinosaurs” in electron microscopy. To the great disappointment not only of electron opticians but also of materials scientists, it had not been possible to correct the optical aberrations of the electromagnetic lenses by then, despite intensive efforts, so that the then generation of electron microscopes with 100 kV accelerating voltage, could not be led to a higher resolution in this way. On the other hand, advances in electronics and accelerator technology had made it possible to go to higher accelerating voltages, with the result that in the late sixties and early seventies electron microscopes were constructed first at 200 kV, then at 650 kV, 1000 kV, and even up to 3000 kV. The latter three, the so-called high-voltage electron microscopes, were “gigantic”, not only in terms of acquisition costs but also in terms of their dimensions. They occupied halls for installation, two stories in height and with the lateral dimensions of a large experimental laboratory.

There were three reasons that led to the rapid growth in the number of high-voltage electron microscope installations worldwide. The first had its origin in Scherzer’s equation for the maximum resolution (smallest object distance that can still be resolved) under phase contrast conditions, which goes with $\lambda^{3/4}$ (λ is the electron wavelength) and thus improves with decreasing electron wavelength, i.e. increasing acceleration voltage. The second reason originated from the Bethe–Bloch relation for inelastic electron scattering, whose effective cross section decreases with the square of the electron velocity in a first approximation. This allows higher sample thicknesses to be transmitted as the voltage increases. There was a third point: as the accelerating voltage increased, to achieve the same optical effect, the dimensions of the objective lens polepieces necessarily became larger. This allowed, as a by-product, the accommodation of miniaturized experimental apparatus within the lens and around the sample position. Although the first physical and chemical experiments had been done earlier with 100 kV microscopes, and Manfred von Ardenne and Ernst Ruska had already observed (at 70 kV) gas reactions in the STEM and CTEM in 1942, this resulted in an actually unexpected first boom of in situ experiments.

As the first major review paper by Paul Butler (E. P. Butler (1979) Rep. on Prog. in Phys. 42(5), 833) shows, almost all of the in situ techniques still in use today were invented and used during this period. Heating stages for temperatures of up to 1000 °C, helium gas cooled stages for temperatures down to below 9 K (the superconductivity transition point of Nb) both for ultrastable operation under double tilt conditions, deformation stages, as well as environmental and gas reaction cells, were constructed in top-entry and side-entry geometry. The often spectacular experimental results were greeted with enthusiasm. In situ experiments developed into a separate branch of electron microscopy, which organized its own conferences and whose results were widely discussed at international meetings. Topics were, among others, solid-state phase transformations, melting, recovery and recrystallization, plastic deformation and creep, chemical reactions, oxidation, and reduction, as well as magnetic investigations and superconductor flux-line studies in Lorentz mode. At last, it was possible to see, study, and measure directly what had previously been inferred indirectly only from static sequences of images and almost never for the same object with respect to dynamics. I remember well the movie Toru Imura and his collaborators produced on the motion of dislocations during plastic deformation. One could see Frank–Read sources in action for the first time. From then on, the film was used as teaching material in material science lectures all over the world, and it was awarded the “Grand Prix of the International Science and Technology Festival 1978.”

There were also lessons to be learned from these experiments. These mainly concerned the special conditions under which they are carried out in the electron microscope, in particular the effects of the thin electron-transparent films and the intense electron irradiation. Quite a few of the results of the measurements made in the initial euphoria, for example, of the dislocation velocity, had to be revised later. It turned out that metallic alloys changed their composition at high temperatures by selective evaporation so that the observed phase transformations were in some cases not typical of bulk behavior. And of course, it was not surprising that such elementary important variables as temperature, pressure, or current chemical composition could either not be determined at all or only with great effort and rarely with the accuracy that was standard in bulk material experiments.

And it became immediately clear that the fact that the experiments are performed under intense electron irradiation requires special attention. A wide range of energies is transmitted in electron–atom collisions, from values above the displacement threshold energy of the atoms, producing interstitial atoms and vacancies in the crystal, to very high rates of lower energies comparable to the diffusion activation energies for atoms and vacancies. The former lead to damage and other effects, e.g., to irradiation-enhanced or accelerated phase transformations, and the latter lead to irradiation-induced diffusion, where the energy for the atomic site changes originates from subthreshold electron–atom collisions. While this type of electron–atom interaction increases with electron energy, the second type of interaction, radiolysis, resulting from interaction of the incident electrons with the electrons involved in chemical bonding in the material, in general decreases with increasing electron

energy. On the one hand, one learned to reduce the irradiation effects by appropriate choice of electron acceleration voltage or, if this was not possible, to take them into account in the interpretation of experimental results. On the other hand, with regard to the development of materials for the construction of new fission and fusion reactors, high-voltage electron microscopes were widely used as a tool for studying the behavior of reactor materials under high irradiation dose rates and at high temperatures.

By comparing the generation of high-voltage electron microscopes with the appearance of dinosaurs in the early geological ages, one implicitly considers that they have become extinct and that the habitat they filled then is now occupied by species better adapted to the requirements of today. The time for the high-voltage electron microscopes had come in the nineties. Ze Zhang, one of the authors of this book, and I were among the last to carry out a plastic deformation experiment in a double-tilt straining stage in a 1000 kV high-voltage electron microscope at 800 °C. Using this experiment, in 1993, after finding dislocations in quasicrystals to our own surprise and that of our colleagues in the quasicrystal community, we were able to show together with our colleagues that these dislocations are mobile at high temperature and that they carry the plastic deformation in these strange materials. Immediately thereafter, the microscope was dismantled and scrapped along with the fantastically working object goniometer, an all-time jewel.

The exact reasons for the disappearance of the high-voltage electron microscopes and with them, except for a few installations in institutes that specialized in them, also of the in situ experiments will have to be investigated one day by the history of science. However, we can already say that, among other causes, the following points played a role. The time when high-voltage electron microscopes disappeared overlapped with the time when it became finally possible to compensate for the optical aberrations of electron lenses by using multiple lenses. This permitted, for the first time on a broad scale, transmission electron microscopy of materials with atomic resolving power. This book appears on the 25th anniversary of the publication, in 1997, in which this was reported in the literature. The new generation of aberration-corrected electron microscopes provided, for much less money, a level of resolving power previously thought scarcely possible. It had been learned by now that for most material problems, reducing the accelerating voltage to a maximum of 300 kV was a good compromise in terms of transmissivity and electron beam damage. This reduced the equipment requirements considerably. This shifted research interest, and modern electron microscopy turned to new, challenging topics.

However, a price had to be paid for the new technology. The lens usually employed today for atomic resolution, the single-field condenser-objective lens after Riecke and Ruska (1965), restricts the space around the specimen to such an extent that object goniometers manufactured using classical technology, not to mention object manipulation devices such as were possible with the large dimensions of the lenses of the high-voltage electron microscopes, can no longer be used.

This, fortunately, did not mean the end of in situ experiments in the electron microscope. In the more than three decades that had passed since the first such

experiments, progress in the sciences and in miniaturization, especially in semiconductor technology, had created a new field, micro- and nanotechnology. In fact, since the early 2000s, we have seen an accelerated increase in the development and commercial production of high-precision goniometers for electron microscopy using MEMS (microelectromechanical systems) technology. These contain object manipulation devices of the type previously used for experiments in the high-voltage electron microscope, with the crucial difference that their dimensions are much smaller and their special design allows the processing of samples in nanodimensions, and often in atomic dimensions. In addition, there are a variety of new ideas, including the production of miniaturized devices that mimic the function of real components during their operation. An interesting example (out of many) is the observation of chemical reactions in a model of a Li-ion battery during charging and discharging. A new term was even introduced for this, the observation “*in operando*”.

The new capabilities of MEMS technology, often combined with the great optical properties of aberration-corrected electron microscopes have brought about a new in situ electron microscopy in the last decades, which now occupies a prominent place in modern electron microscopy. The new in-situ electron microscopy, which is mostly advantageous for observing temporal dynamics, is mainly performed in CTEMs (conventional transmission electron microscopes). However, there is also increasing work employing STEMs (scanning transmission electron microscopes). The user can choose between closed cells and open differentially pumped systems. The type of operation used depends on the problem to be studied. As this preface is being written, it is state of the art for microscope manufacturers, in cooperation with the customer and stage manufacturers, to provide platforms optimized for specific types of experiments. And it is possible to operate the instrument as a dedicated instrument essentially for in situ experiments only, or alternatively in alternating mode for conventional static studies and for dynamic studies.

It is a general principle of nature that the universal experiment, which leaves no questions unanswered, does not exist. On the other hand, experiments performed in the electron microscope under direct observation with a resolution down to the atomic level offer a unique access to understanding the nature of physical and chemical processes and the observation and quantitative measurement of their course and dynamics. In their now 50-odd-year history, we have gained a huge amount of insight that allows us to understand the specific conditions under which these experiments are conducted and how their results can be interpreted and understood.

There is no better way to gain access to a field of research than to look at its type of questions, its type of results and answers, and how these were obtained, using typical examples. In a field as large and constantly growing as that represented by experiments in situ in the electron microscope, it is of elementary importance to make a qualified selection of the work to be discussed for an appropriate overview. This selection has to be made with the target audience in mind and on the background of knowledge of what is being done or has been done in the field as a whole. The same holds for the manner in which the selected topics are discussed. The two editors and co-authors of this book have decades of experience in the field of in situ electron microscopy. The selected contributions to this volume are from research groups that

belong to the top group of the field. The articles follow a common structural scheme that makes them easier to read. They are written for beginners who want to get a first overview as well as for those scientists who have been working in this field for a longer time and are searching for a handy reference or want to extend their knowledge, in case of a planned new experiment or possibly in preparation for the acquisition of a new instrument.

Prof. Dr. Dr. h.c. Knut W. Urban
Senior (Distinguished) Professor of Physics
Jülich-Aachen Research Alliance (JARA)
RWTH Aachen University and Forschungszentrum Jülich GmbH
Ernst Ruska Center for Microscopy and Spectroscopy with Electrons (ER-C)
Jülich, Germany

Preface

It is natural that human beings believe what they see before the object is well understood, which promotes the development of instruments and methodologies to visualize objects with sizes beyond the resolving power of the unaided human eyes. Transmission electron microscopy permits not only real space images revealing morphologies and atomic structures of objects but also chemical analysis, which has become indispensable in the study of materials.

Because of the lack of dynamic observation, conventional transmission electron microscopy cannot meet the growing demand in new application fields such as nanocatalysts, nanoelectronics, and nanomechanics in which structural and/or property responses to external stimuli are key information to learn. Characterization of these complex processes requires the use of advanced in situ methodologies without losing any information about intermediate states.

In situ transmission electron microscopy refers to the experiments where the specimen is changed while it is observed in a transmission electron microscope, which requires that the microscope should be not only an imaging tool but also a miniaturized laboratory where some form of stimulus or/and exotic environment can be applied deliberately to the specimen and corresponding changes can be simultaneously monitored. In fact, the idea of in situ transmission electron microscopy was proposed at the very dawn of electron microscopy, it was just the dramatic advancements achieved in the last 20 years. Nowadays, thermal excitation, mechanical force, electric field, optical excitation, magnetic field, as well as liquid and/or gaseous environment, can be applied directly to the specimen area in a controllable manner by modifications of the microscope, which enable in situ transmission electron microscopy as one of the most powerful approaches for revealing physical and chemical process dynamics at atomic resolution.

In this book, we have attempted to give an overview of in situ transmission electron microscopy including historical background, modern techniques, application achievements, and development trends. This book is intended for advanced undergraduate and graduate students and professional researchers in materials science, chemistry, physics, environmental and energy, electronics, and any subjects that want to explore nanoworld.

This book starts with a brief introduction to in situ transmission electron microscopy in Chap. 1. After that, the book is organized into ten chapters in terms of the conditions and stimuli applied to the specimens. Considering that every specimen is affected by the electron beam for a long-time observation, the physical principles of electron irradiation effects are summarized in Chap. 2. In situ studies of electron irradiation-induced processes are also presented in this chapter. We then move on to Chaps. 3–10 on the following directions: mechanical, thermal, electrical, optical, magnetic, liquid environmental, gaseous environmental, and ultrafast transmission electron microscopy. We hope this book can illustrate the huge variety of experiments possible, and then inspire more people to observe and further understand materials' function and dynamics by using in situ transmission electron microscopy.

Nanjing, China
Nanjing, China
Hangzhou, China

Litao Sun
Tao Xu
Ze Zhang

Contents

1	Introduction to In-Situ Transmission Electron Microscopy	1
	Litao Sun, Tao Xu, and Ze Zhang	
2	Electron Beam Irradiation Effects and In-Situ Irradiation of Nanomaterials	17
	Tao Xu, He Zheng, Jianbo Wang, Florain Banhart, and Litao Sun	
3	In-Situ Nanomechanical TEM	53
	Li Zhong, Lihua Wang, Jiangwei Wang, Yang He, Xiaodong Han, Zhiwei Shan, and Xiuliang Ma	
4	In-Situ Heating TEM	83
	Shijian Zheng and Longbing He	
5	In-Situ Biasing TEM	105
	Liqiang Zhang, Yongfu Tang, Lin Gu, and Jianyu Huang	
6	In-Situ Optical TEM	151
	Peng Wang, Feng Xu, Peng Gao, Songhua Cai, and Xuedong Bai	
7	Magnetism In-Situ TEM	187
	Renchao Che, Yong Peng, and He Tian	
8	In-Situ Liquid Cell TEM	221
	Chao Zhu, Wen Wang, Honggang Liao, and Litao Sun	
9	In-Situ Gas Transmission Electron Microscopy	251
	Ke Fang, Wentao Yuan, Jakob B. Wagner, Ze Zhang, and Yong Wang	
10	4D Ultrafast TEM	327
	Bin Chen, Jianming Cao, and Dongping Zhong	

Chapter 1

Introduction to In-Situ Transmission Electron Microscopy



Litao Sun, Tao Xu, and Ze Zhang

1.1 Definition of In-Situ Transmission Electron Microscopy

It is natural that human beings believe what they see before the object is well understood, which promotes the development of instruments and methodologies to visualize objects with sizes beyond the resolving power of the unaided human eyes (100–200 μm). Generally, the visualization of very small objects can be mediated by light (optical microscopy) or electron beams (electron microscopy) using optical or magnetic lenses, respectively.

The optical microscopy instruments probably developed from the Galilean telescope during the seventeenth century. One of the earliest instruments for seeing very small objects was made by Anton van Leeuwenhoek. With a simple microscope, Leeuwenhoek was able to magnify objects from ten to hundred times, and was the first to classify red blood cells by shape and the first to visualize bacteria [1]. The optical microscope had gained popularity with researchers in the area of microbiology, botany, zoology, geology, and materials science in the eighteenth century. However, the spatial resolution of an ordinary optical microscope (the smallest distance between two points that can be resolved, about 0.2 μm), which is not only limited by the quality of the lens but also by the wavelength of the light used for illumination, had been not competent for seeing small objects in many conditions in late nineteenth century.

L. Sun (✉) · T. Xu

Key Lab of MEMS of Ministry of Education, SEU-FEI Nano-Pico Center, Southeast University, Nanjing 210096, China
e-mail: slt@seu.edu.cn

Z. Zhang

Center of Electron Microscopy and State Key Laboratory of Silicon Materials, School of Materials Science and Engineering, Zhejiang University, Hangzhou 310027, China

© The Author(s), under exclusive license to Springer Nature Singapore Pte Ltd. 2023

L. Sun et al. (eds.), *In-Situ Transmission Electron Microscopy*,
https://doi.org/10.1007/978-981-19-6845-7_1

In the 1920s, Louis de Broglie proposed that accelerated electrons should exhibit wavelike properties with a wavelength substantially shorter than light [2]. Furthermore, it was discovered that electric and magnetic fields could be conceived of as a lens to bend and focus the electron beam, like a glass lens for visible light [3]. Hence, it was feasible to build an instrument that uses electrons to illuminate a specimen and surpass the resolution limit of optical microscope. In the early 1930s, Ernst Ruska at the University of Berlin, along with Max Knoll, developed the idea into a practical reality, the first transmission electron microscope (TEM) was built in Germany [4], for which Ruska received the Nobel Prize in 1986.

Normally, a TEM includes elements analogous to those of a light microscope. The electron beam emerges from the electron gun and transmits through a thin specimen that is in part transparent to electrons and in part scatters them out of the beam. Then the transmitted electrons that carried structural information of the specimen are collected, focused, and projected onto the viewing device. The entire electron trajectory is under vacuum to achieve high resolution. Nowadays, lattice resolution images of crystalline materials are acquired routinely by TEM. Unlike glass lens, the focal length of the electromagnetic lens can be adjusted continuously by changing the excitation current of the lens, which can lead to the change in magnification and the exchange between image mode and diffraction mode. Hence, TEM permits not only real space images revealing morphologies and atomic lattice structures of objects but also electron diffraction patterns revealing structural information in the reciprocal space. Furthermore, the interaction of electron with matter produces a wide range of secondary signals, which can be collected and then used for chemical analysis, such as characteristic X-ray for energy-dispersive X-ray spectroscopy (EDS) and inelastic scattering electrons for electron energy loss spectroscopy (EELS). At present, TEM has become indispensable in the study of individual sub-micron size objects (such as nanomaterials, molecules, biological cells, etc.) and locally deformed structures (strained lattice, dislocations, stacking faults, etc.).

Conventional transmission electron microscopy focuses on stable structures in the electron microscope vacuum and at ambient temperature because of the technical feasibility. The specimen is typically treated outside of a TEM and then moved back into the instrument for observation. From such experiments, only the beginning and ending status of materials can be learned, and what has happened during the middle stage is missed. Misinterpretations, questionable assumptions, and incorrect derivations were not rare in reality because of the lack of dynamical observation, thus, conventional transmission electron microscopy cannot meet the growing demand in new application fields such as nanocatalysts, nanoelectronics, and nanomechanics in which structural and/or property responses to external stimuli are key information to learn. Characterization of these complex processes requires the use of advanced *in situ* methodologies.

“*In situ*” is a Latin phrase that translates to “in position” or “on site”, which means in the same place the phenomenon is occurring without isolating it from other systems or altering the original conditions of the test. Spontaneously, *in situ* transmission electron microscopy refers to the experiments where the specimen is changed while it is observed in a TEM, which requires that the microscope should be not

only an imaging tool but also a miniaturized laboratory where some form of stimulus or/and exotic environment can be applied deliberately to the specimen and corresponding changes can be simultaneously monitored. Obviously, in situ transmission electron microscopy has two important characters, stimulus and real-time observation. Typical stimulus used for in situ transmission electron microscopy includes thermal excitation, mechanical force, electric field, optical excitation, magnetic field, as well as liquid and/or gaseous environment, which can be applied directly to the specimen area in a controllable manner by modifications of the microscope, and in most cases via specially designed specimen holders. In order to give a continuous view of a process, in situ transmission electron microscopy also requires a fast image recording system, such as a camera. At present, most TEM systems are equipped with a charge-coupled device (CCD) or complementary metal oxide semiconductor (CMOS) camera, which is able to operate at rates of tens of frames per second.

It should be noted that electron beam is also a stimulus that affected the specimen through electron–matter interaction; therefore, in a sense, every TEM observation is an in situ experiment because electron–matter interactions are generally unavoidable during TEM imaging. We stress that in situ transmission electron microscopy only includes the experiments where the stimulus is applied to the specimen in a deliberate way and something can be concluded from the dynamical process.

1.2 A Brief History of In-Situ Transmission Electron Microscopy

The invention of the TEM was driven, in part, by the increasing interest in structures with sizes beyond the resolving power of the optical microscope. Although TEMs have an obvious advantage in high spatial resolution, the optical microscope allows looking at specimens in their original states and environments such as in the gaseous environment or in the liquid solution. Naturally, a goal has been to image objects in their live state even since the earliest days of TEM (Fig. 1.1).

However, the strong interaction of the electron beam with matter requires a very low-pressure path to avoid extraneous scatter, which is generally incompatible with a specimen immersed in a liquid, a gas, or both. In 1935, Marton suggested two methods to restrict or control the gaseous or liquid solutions around specimens [5]. One is to construct an open environmental chamber with a pair of small apertures which can limit gas leakage into the column, maintaining the chamber at high pressure, while the rest of the column at a sufficiently low pressure. The idea was realized by Ruska [6] and Ardenne [7], respectively, in 1942, although the specimen volume pressure was limited to a few Torr. On this basis, a complex environment chamber consisted of four apertures and an extra differential pumping was developed in the late 1960s and early 1970s by several groups around the world independently [8–10], which can maintain the specimen volume pressure 10^6 times or larger than the column vacuum. Today, state-of-the-art environmental TEM (ETEM) still utilizes a

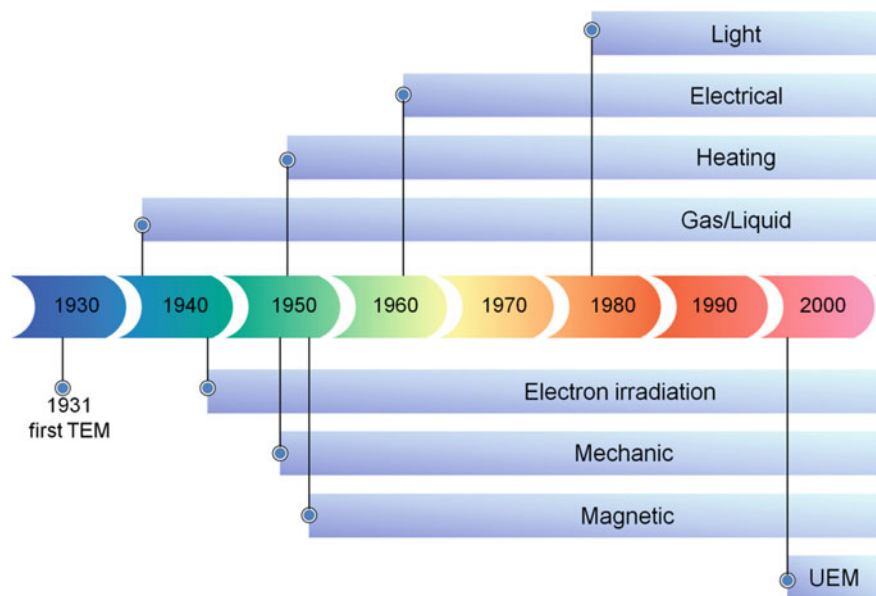


Fig. 1.1 The origination of in situ transmission electron microscopy

differentially pumped vacuum system. The other approach is to enclose and totally isolate the specimen volume from the rest of the microscope column by a cell with electron-transparent windows. Such windows should be sufficiently strong to withstand the pressure differences between cell interior and microscope vacuum, thin enough to transmit the electron beam but robust under electron bombardment. In 1944, Abrams and McBain from Stanford University devised the first closed cell with plastic windows and observed the movement of liquid and bubbling [11]. However, the windows are difficult and time-consuming to manufacture and can rupture during use. Such a closed-cell route didn't meet the expectation for a long time, the spatial resolution achieved, especially in the observation of specimens in liquid solution, was often not much better than what was available through optical microscopy. Until the 2000s, developments in thin-film technology and microfabrication brought new life to closed-cell route [12].

As early as in the late 1940s, electron beam in TEM, as a stimulus, had been intentionally used to trigger structural transformations in ionic crystals [13] and organic pigments [14]. In situ electron irradiation experiments can be carried out in every standard TEM even without technical modifications. With a continuous improvement of spatial resolution, modern TEM has enabled us to study irradiation-induced processes on the atomic scale since the 1980s [15].

External fields can be deliberately applied to the specimen area by modifying specimen holders. As early as 1955, Weichan stretched nylon and rubber ribbons in an electron microscope using a dedicated apparatus consisted of two mounting plates onto which the specimens were glued and a spring mechanism for their operation

[16]. Two years later, the holder designed by Wilsdorf already showed a capability for direct observation of tension, compression, and torsion in a TEM [17]. The basic idea was to make a specimen in a rectangular shape with one end fixed and the other end connected to a movable rod, which could slide along the length of the holder. The deficiency of the early mechanical holders is unable to quantify the force. After decades of development, modern mechanical holders can achieve nanometers per second displacement rate and nanonewtons measurements by mechanical/piezo positioning elements and displacement–force sensors, respectively.

In situ heating can be realized by placing a heating element at the tip of a TEM specimen holder, which normally uses precise Joule heating and temperature dissipation to obtain tunable and stable specimen temperatures. The first in situ heating holder may be traced back to the middle of the twentieth century. In 1956, Takahashi from Yamanashi University reported a specimen holder where an electric furnace heats the specimen up to 1000 °C by thermal radiation, and an embedded thermal couple measures temperature in the furnace cup [18]. The heating zone of furnace-heating holders is relatively huge, and then a few tens of minutes are needed to achieve a stable goal temperature and to seize the specimen drift caused by the thermal expansion effect during which high-resolution TEM imaging is a challenge. In the next decades, many efforts had been made to minimize the heating area, and then specimen drift following temperature change is tolerable; therefore, atomic resolution at elevated temperatures is achievable.

In essence, heating element is a resistance. Naturally, electrical transport measurements can be achieved in microscope when the heating element is replaced by the specimen. In 1967, Blech and Meieran designed a dedicated holder which permitted the passage of electrical current through the specimen and directly observed the electrotransport in thin Al strips by TEM [19]. However, the specimen should be specially designed or be connected to the prefabricated circuitry before inserting into the microscope, which involves a large microfabrication effort and is time-consuming. An alternative approach with movable probe was developed in the 1990s although the original goal was to achieve scanning tunneling microscopy (STM) imaging in a TEM [20]. The basic idea was to use a piezo-driven conductive nanoprobe to contact the specimen fixed on an electrode, which is more straightforward and convenient.

Light illumination system can also be integrated into the holder by inserting a light source in the circuit [21]. Another way to achieve the illumination system is using optical fiber for the introduction of outside light into the microscope, which can be traced back to the 1980s or even earlier [22]. It should be careful to distinguish the changes triggered by light beam and electron beam. In addition, four-dimensional ultrafast TEM (UEM) could be created after the introduction of femtosecond laser pulses into the electron gun and specimen chamber [23].

Besides, magnetization processes and other properties of magnetic materials can also be studied in TEM making use of the Lorentz force experienced by a beam of electrons traversing a magnetic field (Lorentz microscopy), which can date back to the late 1950s [24]. Generally, a vertical magnetic field is generated at the specimen's location and by tilting the specimen the resulting in-plane component of the magnetic field can be used for magnetizing experiments. However, the permanently present

out-of-plane component may affect the reversal behavior. As an alternative approach, dedicated magnetizing holders have been developed to generate a magnetic field at the specimen area since the 2000s [25].

1.3 Modern In-Situ Transmission Electron Microscopy

In the past decades, the lateral resolution of TEMs has already been extended below 0.1 nm due to the wide application of spherical and chromatic aberration correction techniques. At the same time, the development of microscopy is also noticeable for electron guns with better monochromaticity and higher energy resolution, cameras (not only CCD but also CMOS and direct electronic detectors), novel spectrometers (such as large-area multiple EDS detectors), data processing algorithms and software packages, TEM isolations and vibration controls, and many other technologies [26]. All these improvements have their impact on the development of modern in situ transmission electron microscopy, and made it possible to characterize dynamic changes in size, shape, interface structure, electronic state, and chemical composition in specimens at and below the nanoscale [27–29].

In general, specimen and microscope requirements for in situ experiments are not much different from those of conventional operation. The major difference is in the ability of applying external stimuli inducing changes in the specimen. The stimuli are usually introduced into the TEM by modifications of the microscope or the development of dedicated specimen holders. The only exception is electron irradiation. In situ electron irradiation can be carried out in almost every standard TEM without any modifications and the lateral resolution depends on the microscope. Especially the operation of the aberration-corrected microscope promises the visualization of individual atoms under electron irradiation. Many electron irradiation-induced processes such as atom rearrangements and phase transformations have been studied at the atomic scale [30–34], which is beneficial to reveal the physics behind the irradiation effects, explore nonequilibrium states of nanosystems, and extend the technical applicability of electron irradiation. On the other hand, the electron beam in TEMs with an aberration corrector can be focused onto spots of less than 0.1 nm which offers the possibility to fabricate and modify the specimen on the scale of few or even single atoms [35].

A related topic is in situ ion irradiation inside the TEM, which requires extensive modifications on the microscope column. An ion beam is introduced into the column and guided to the specimen area for bombardment. In situ ion irradiation TEMs have been well developed since the 1960s and are normally applied for nuclear materials, space and astronautic engineering materials, and materials for irradiation environments [36]. However, ion irradiation TEMs are not commercially available and only several instruments are still in operation at present. Similarly, laser sources can be integrated into the TEMs by modification of the microscope. Ultrafast TEM introduces two synchronized laser beams with nanosecond or femtosecond pulses into the TEM. The first pulsed laser allows for triggering structural changes in the

specimens, while the second is used to generate electron pulses from photocathodes to probe changes with well-defined time delays relative to the beginning of the triggered changes [23]. Such a technology permits the study of structural phase transitions, mechanical deformations, and the embryonic stages of nucleation and crystallization on a time scale down to 10^{-13} s at present [37–39] and is expected to extend to attosecond scale in future.

In most cases, external stimuli or exotic environments are introduced into the specimen area by specially designed holders. Holder-based in situ TEM technologies are much more widespread because such a technical route does not require modification of the electron optics nor vacuum system and can be conveniently carried out in almost every standard TEM. The spatial resolution depends on the specimen holders, because the application of external stimuli can introduce disturbance such as drift or vibration, which is a major limiting factor for high-resolution dynamic observations. Recent improvements in micro-nano machining and MEMS (micro-electromechanical system) technologies have been achieved to minimize the vibrations or drift during recording images, which makes the resolution close to a specified resolution limit of the microscope. Nowadays, most of the matured in situ TEM technologies are based on specially designed holders, and the dedicated holders are not only homemade but also available commercially. To some extent, modern in situ transmission electron microscopy is about specimen holders.

Depending on what stimulus is to be applied, a corresponding specimen holder can be designed. Heating is normally easier to be realized by placing a heating element at the tip of a TEM specimen holder. Nowadays, there are two typical types of heating holders: furnace-heating holders, and microfabricated holders based on the MEMS process. Furnace-heating holders can accommodate a 3-mm specimen disk and reach 1300 °C. However, the heating zone is huge and involves many components and supporting materials, the total thermal expansion effect causes a severe problem of specimen drift when changing temperature. It has to take tens of minutes to seize the specimen drift; therefore, it is difficult to take high-resolution TEM images in a short period of time. MEMS-based heating holders are composed of a MEMS device suspended on a Si chip, which produce localized resistive heating [40]. Much lower thermal mass results in a small sample drift rate and high-temperature stability, which allows high-resolution imaging at elevated temperatures. Another unique feature of MEMS-based heating holders is ultrafast temperature change rate (the maximum rate reaches 10^5 – 10^6 °C/s), which makes the holder a good choice for thermal cycling experiments [41]. In situ transmission electron microscopy for thermal effects is particularly interesting in melting behaviors, phase transformations, crystallizations, and chemical reactions of nanomaterials [42–45].

In situ biasing TEM means TEM observation and electrical transport measurement of a specimen on which a bias voltage is applied. The specimen as a component should be connected to a circuit where the current–voltage characteristics can be measured. Nowadays, there are generally two types of biasing holders: MEMS-based holders, and STM-TEM holders. The first approach uses prefabricated circuitry developed on Si chips containing thin silicon nitride membranes, the specimen dispersed on electron transparent membrane and connected to the circuitry by directly writing metal

interconnects outside of the TEM. Such a strategy is almost the same as a MEMS-based heating system; therefore, heating and biasing can be integrated on the same holder. According to experiments, heating, biasing or both can be selected to apply to the specimen. The second is more popular, which uses an STM probe to contact the specimen fixed on an electrode. The probe has a very broad variety of movements, ranging from picometers to millimeters, therefore, electrical contacts with nanoscale interfaces can be established with the precise positioning of the piezo-driven probe to a desired location inside the TEM; electrical currents passed through individual specimen can be measured with a precision up to picoamp [21]. Both types of biasing holders are used to study behaviors and structural changes of specimens in an electrical field, as well as electrical transport properties of individual nanostructures and Joule heating effects [46–48]. Specifically, in situ biasing TEM is widely applied to reveal the underlying mechanisms of rechargeable batteries and random access memories [49–52].

The piezo-driven probes can also be utilized for introducing mechanical stress to the specimen; therefore, STM-TEM holders have frequently been applied to study mechanical behaviors [53–55]. Some novel phenomena such as diffusion-assisted liquid-like behaviors in some small-volume metals have been captured at room temperature [53]. However, STM-TEM holders cannot directly measure mechanical parameters. After the integration of mechanical quantity sensors, dedicated mechanical holders (such as AFM-TEM holders and nanoindentation holders) can achieve nanometers per second displacement rate and nanonewtons measurements. Another approach is the use of MEMS-based chips where load is always applied by using a thermal actuator [56]. Mechanical holders are widely used to characterize the mechanical behaviors and corresponding structural changes in micro- and nanostructures [57–59].

In situ illumination can be achieved by embedding a light-emitting diode (LED) inside the biasing holders. Another type of holder utilizes optical fibers or lenses to introduce outside light into the microscope. In some applications, the TEM column should be additionally modified. These techniques have been widely used to study optically driven processes, such as photoluminescence, cathodoluminescence, photocatalysis, and photocurrent [60–62].

The magnetic behavior of small magnetic structures can be studied in situ by varying the local magnetic field in Lorentz TEM. In the microscope, a magnetic field that is perpendicular to the viewing plane is applied to the specimen by changing the current of the objective lens, which is high enough to make most of the magnetic specimens saturated. As an alternative approach, dedicated magnetizing holders can generate horizontal magnetic field which may deflect the electron beam. The applied horizontal field is generally less than 1000 oersted; therefore, this approach is suitable for the study of soft magnetic materials with less coercive force. At present, in situ magnetic TEM is widely used to study skyrmions, ferroelectric or ferromagnetic vortices, and domain switching [29].

The observation of liquid samples in the TEM benefits from the development of liquid cells, which can enclose small volumes of liquid by two electron-transparent windows. At present, the most popular window material is silicon nitride, as it is

robust, and easily manufactured based on standard silicon processing techniques. Silicon nitride cells can reach atomic resolution in some cases and have been widely used to study the growth and assembly of colloidal nanoparticles [63–66]. Additionally, electrodes, heating elements, or flow capability can be incorporated in silicon nitride cells so that electrochemical reactions, electrocatalysis, and solvothermal synthesis can be triggered and followed in situ [67–69]. Very recently, other membranes such as monolayer graphene have been applied in liquid cells [70–72]. On this foundation, some novel phenomena such as ligand-controlled oriented attachments of citrate-stabilized gold nanoparticles have been observed at atomic resolution [71].

Specially designed cells can also be used to introduce gas environments into the region around the specimen, and the pressure in gas cells can be up to 1 atmosphere and above. Similarly, heating elements can also be integrated into gas cells to study transformations under high temperatures and varying gas environments. However, both observation windows and gas layers will limit the obtainable resolution during the imaging. ETEM with an additional differential pumping system is increasingly accessible and gaining popularity although it is much more expensive than conventional TEM. The maximum gas pressure in ETEM is two orders of magnitude lower than that of gas cells but it is in the possibility to obtain atomic resolution images, especially by aberration-corrected ETEM [73]. It is important that ETEM equipped with specially designed specimen holders becomes extremely powerful in observing specimens at high resolution under external stimuli and varying gas environments, which is attractive for the study of vapor growth, catalysis, and alkali metal–oxygen battery [74–76].

1.4 Challenges and Opportunities

Large quantities of in situ experiments have been carried out inside the TEM, and provided significant insights into nanoscale phenomena. However, some difficulties remained a challenge. It is known that electron irradiation damage can restrict the applicability of in situ transmission electron microscopy due to the strong interaction of electrons with matter. Long-time exposure to electron bombardment is certainly to affect the dynamic behaviors of the specimen. How to identify the side effects of electron beam irradiation and to reduce their influences is crucial if irradiation is not the purpose of the study. Considering that irradiation damage is proportional to the electron dose, the key is to minimize the dose on the specimen.

In most cases, in situ experiments are conducted in conventional TEMs equipped with specially designed holders, which supply a desired stimulus to the specimen. Almost all modern in situ holders allow imaging with lattice resolution in vacuum, while environmental cells are normal in observing the morphology dynamics of reactions at the nanometer range. The spatial resolution deteriorates because the electron beam significantly loses coherency in windows, liquid layers or gaseous layers. There is much space to promote the resolution for in situ environmental cell

microscopy, such as the optimization of the design for environmental cells and the use of chromatic aberration correction.

In the past, in situ experiments mainly focus on the dynamical behaviors of specimen response to single stimulus. The attention has gradually moved to observing and measuring the changes of specimen under multiple stimuli, which is limited by the small space in the objective pole piece. This issue may be solved by ongoing developments in the TEM with a higher pole piece gap and aberration corrector. Extra space promises the introduction of multiple stimuli, while the attendant loss of resolution can be mitigated by the correction of the spherical aberration of the objective lens. Another significant benefit resulting from aberration correction is the ability to go to low voltages without extreme loss of resolution. Decreasing the voltage is effective to reduce the influence of electron irradiation in some cases, it is extremely important and attractive. An alternative way to introduce multiple stimuli is to distribute the stimuli to microscope column and specimen holder. Such an approach has been applied in some studies of catalysis, where the gas supply is controlled by differential pumps within the TEM column, while heating is realized by a dedicated heating holder [76].

Most of the in situ experiments focus on the structural and properties evolution under external stimulus, the monitoring of chemical changes is a particular challenge at present. EDS and EELS promise chemical analysis but are few used in time-resolved in situ experiments because of the poor signal-to-noise ratio. Thus, the ongoing improvements in detectors should be promising to examine time-resolved chemical changes at and below the nanoscale. Besides, future developments should also require the capability for quantitative measurements of the applied fields or exotic environments such as temperature, gas pressure, and gas or liquid composition right on TEM specimens, which is important to quantify the influence of stimuli or chemical environments on specimen evolution.

In situ transmission electron microscopy requires the capability of recording what is seen at an adequate time resolution. Higher recording speed is certainly desired but the shortened exposure time for each frame lowers the image quality because the problem of image noise cannot be overcome. At present, the widely used CCD cameras for in situ microscopy are capable to record images with a frame rate of 10–30 frames per second. The state-of-the-art direct electronic detector can reach 1500 frames per second, which opens new phenomena for study. However, the vast data rates from the detectors exacerbate the problems of data collection and analysis, which impose demands for data mining and machine learning approaches to track the transformations.

1.5 Concept of This Book

In this book, we have attempted to give an overview of in situ transmission electron microscopy from the following aspects: historical background, modern techniques, application achievements, and development trends. This book is intended

for advanced undergraduate and graduate students and professional researchers in materials science, chemistry, physics, environmental and energy, electronics, and any subjects that want to explore the nanoworld. We hope this book can illustrate the huge variety of experiments possible, and then inspire more people to observe and further understand materials' function and dynamics by using in situ transmission electron microscopy.

This book starts with a brief introduction to in situ transmission electron microscopy in this chapter. After this, the book is organized into nine chapters in terms of the conditions and stimuli applied to the specimens. Considering that every specimen is affected by the electron beam for a long time observation, the physical principles of electron irradiation effects are summarized in Chap. 2. In situ studies of electron irradiation-induced processes are also presented in this chapter. We then move on to Chaps. 3–10 on the following directions: mechanical, thermal, electrical, optical, magnetic, liquid environmental, gaseous environmental, and ultrafast transmission electron microscopy.

References

1. Porter JR (1976) Antony van Leeuwenhoek: tercentenary of his discovery of bacteria. *Bacteriol Rev* 40(2):260–269. <https://doi.org/10.1128/MMBR.40.2.260-269.1976>
2. De Broglie L (1923) Waves and quanta. *Nature* 112(2815):540–540. <https://doi.org/10.1038/112540a0>
3. Busch H (1927) Über die Wirkungsweise der Konzentrierungsspule bei der Braunschen Röhre. *Archiv für Elektrotechnik* 18(6):583–594. <https://doi.org/10.1007/bf01656203>
4. Knoll M, Ruska E (1932) Das elektronenmikroskop. *Zeitschrift für physik* 78(5–6):318–339. <https://doi.org/10.1007/BF01330526>
5. Marton L (1935) La microscopie electronique des objets biologiques. *Académie Royale de Belgique: Bulletin de la Classe des Sciences* 21:553–564
6. Ruska E (1942) Beitrag zur übermikroskopischen Abbildung bei höheren Drucken. *Kolloid-Zeitschrift* 100(2):212–219. <https://doi.org/10.1007/bf01519549>
7. von Ardenne M (1942) Reaction chamber over microscopism with the universal electron microscope. *Z Phys Chem B-Chem Elem Aufbau Mater* 52(1–2):61–71
8. Hashimoto H, Naiki T, Eto T, Fujiwara K (1968) High temperature gas reaction specimen chamber for an electron microscope. *Jpn J Appl Phys* 7(8):946–952. <https://doi.org/10.1143/jjap.7.946>
9. Moretz RC, Hausner G, Johnson HM, Parsons DF (1969) Design of a wet specimen chamber for investigation of hydrated specimens in electron microscope. *Biophys J* 9:A194
10. Swann P, Tighe N (1971) High voltage microscopy of gas oxide reactions. *Jernkontorets Annaler* 155(8):497–501
11. Abrams IM, McBain JW (1944) A closed cell for electron microscopy. *J Appl Phys* 15(8):607–609. <https://doi.org/10.1063/1.1707475>
12. Williamson MJ, Tromp RM, Vereecken PM, Hull R, Ross FM (2003) Dynamic microscopy of nanoscale cluster growth at the solid-liquid interface. *Nat Mater* 2(8):532–536. <https://doi.org/10.1038/nmat944>
13. Burton E, Sennett R, Ellis S (1947) Specimen changes due to electron bombardment in the electron microscope. *Nature* 160(4069):565–567. <https://doi.org/10.1038/160565b0>
14. Hamm FA, Norman EV (1948) Transformations in organic pigments. *J Appl Phys* 19(12):1097–1109. <https://doi.org/10.1063/1.1715026>

15. Cherns D, Hutchison JL, Jenkins ML, Hirsch PB, White S (1980) Electron irradiation induced vitrification at dislocations in quartz. *Nature* 287(5780):314–316. <https://doi.org/10.1038/287314a0>
16. Weichan C (1955) Electron microscopical study of extension processes by means of a spreading cartridge. *Zeitschrift für wissenschaftliche Mikroskopie und mikroskopische Technik* 62(3):147–151
17. Wilsdorf H (1958) Apparatus for the deformation of foils in an electron microscope. *Rev Sci Instrum* 29(4):323–324. <https://doi.org/10.1063/1.1716192>
18. Takahashi N, Takeyama T, Ito K, Ito T, Mihama K, Watanabe M (1956) High temperature furnace for the electron microscope. *J Electron Microsc* 4(1):16–23. <https://doi.org/10.1093/oxfordjournals.jmicro.a051220>
19. Blech IA, Meieran ES (1967) Direct transmission electron microscope observation of electro-transport in aluminum thin films. *Appl Phys Lett* 11(8):263–266. <https://doi.org/10.1063/1.1755127>
20. Iwatsuki M, Murooka K, Kitamura S-i, Takayanagi K, Harada Y (1991) Scanning Tunneling Microscope (STM) for conventional Transmission Electron Microscope (TEM). *J Electron Microsc* 40(1):48–53. <https://doi.org/10.1093/oxfordjournals.jmicro.a050869>
21. Dong H, Xu T, Sun Z, Zhang Q, Wu X, He L, Xu F, Sun L (2018) Simultaneous atomic-level visualization and high precision photocurrent measurements on photoelectric devices by in situ TEM. *RSC Adv* 8(2):948–953. <https://doi.org/10.1039/c7ra10696c>
22. Suzuki K, Ichihara M, Takeuchi S, Nakagawa K, Maeda K, Iwanaga H (1984) In situ TEM observation of dislocation motion in II–VI compounds. *Philos Mag A* 49(3):451–461. <https://doi.org/10.1080/01418618408233287>
23. Zewail AH (2005) Diffraction, crystallography and microscopy beyond three dimensions: structural dynamics in space and time. *Philos Trans Roy Soc A: Math Phys Eng Sci* 363(1827):315–329. <https://doi.org/10.1098/rsta.2004.1513>
24. Hale ME, Fuller HW, Rubinstein H (1959) Magnetic domain observations by electron microscopy. *J Appl Phys* 30(5):789–791. <https://doi.org/10.1063/1.1735233>
25. Uhlig T, Heumann M, Zweck J (2003) Development of a specimen holder for in situ generation of pure in-plane magnetic fields in a transmission electron microscope. *Ultramicroscopy* 94(3):193–196. [https://doi.org/10.1016/S0304-3991\(02\)00264-4](https://doi.org/10.1016/S0304-3991(02)00264-4)
26. Zhang C, Firestein KL, Fernando JFS, Siriwardena D, von Treilfeldt JE, Golberg D (2020) Recent progress of in situ transmission electron microscopy for energy materials. *Adv Mater* 32(18):1904094. <https://doi.org/10.1002/adma.201904094>
27. Xu T, Sun L (2016) Investigation on material behavior in liquid by in situ TEM. *Superlattices Microstruct* 99:24–34. <https://doi.org/10.1016/j.spmi.2016.06.021>
28. Xu T, Sun L (2015) Dynamic in-situ experimentation on nanomaterials at the atomic scale. *Small* 11(27):3247–3262. <https://doi.org/10.1002/smll.201403236>
29. Zheng H, Zhu Y (2017) Perspectives on in situ electron microscopy. *Ultramicroscopy* 180:188–196. <https://doi.org/10.1016/j.ultramicro.2017.03.022>
30. Xu T, Shen Y, Yin K, Sun L (2019) Precisely monitoring and tailoring 2D nanostructures at the atomic scale. *APL Mater* 7(5):050901. <https://doi.org/10.1063/1.5096584>
31. Liu X, Xu T, Wu X, Zhang Z, Yu J, Qiu H, Hong J-H, Jin C-H, Li J-X, Wang X-R, Sun L-T, Guo W (2013) Top-down fabrication of sub-nanometre semiconducting nanoribbons derived from molybdenum disulfide sheets. *Nat Commun* 4:1776. <https://doi.org/10.1038/ncomms2803>
32. Shen Y, Xu T, Tan X, He L, Yin K, Wan N, Sun L (2018) In Situ Repair of 2D Chalcogenides under Electron Beam Irradiation. *Adv Mater* 30(14):1705954. <https://doi.org/10.1002/adma.201705954>
33. Krashennnikov AV, Nordlund K (2010) Ion and electron irradiation-induced effects in nanostructured materials. *J Appl Phys* 107(7):071301. <https://doi.org/10.1063/1.3318261>
34. Xu T, Zhou Y, Tan X, Yin K, He L, Banhart F, Sun L (2017) Creating the smallest BN nanotube from Bilayer h-BN. *Adv Func Mater* 27(19):1603897. <https://doi.org/10.1002/adfm.201603897>

35. Tripathi M, Mittelberger A, Pike NA, Mangler C, Meyer JC, Verstraete MJ, Kotakoski J, Susi T (2018) Electron-beam manipulation of silicon dopants in graphene. *Nano Lett* 18(8):5319–5323. <https://doi.org/10.1021/acs.nanolett.8b02406>
36. Hinks JA (2009) A review of transmission electron microscopes with in situ ion irradiation. *Nucl Instrum Methods Phys Res, Sect B* 267(23):3652–3662. <https://doi.org/10.1016/j.nimb.2009.09.014>
37. Barwick B, Park HS, Kwon O-H, Baskin JS, Zewail AH (2008) 4D imaging of transient structures and morphologies in ultrafast electron microscopy. *Science* 322(5905):1227. <https://doi.org/10.1126/science.1164000>
38. Fu X, Chen B, Tang J, Hassan MT, Zewail AH (2017) Imaging rotational dynamics of nanoparticles in liquid by 4D electron microscopy. *Science* 355(6324):494. <https://doi.org/10.1126/science.aah3582>
39. Yoo B-K, Kwon O-H, Liu H, Tang J, Zewail AH (2015) Observing in space and time the ephemeral nucleation of liquid-to-crystal phase transitions. *Nat Commun* 6(1):8639. <https://doi.org/10.1038/ncomms9639>
40. Zhang M, Olson E, Twesten R, Wen J, Allen L, Robertson I, Petrov I (2005) In situ transmission electron microscopy studies enabled by microelectromechanical system technology. *J Mater Res* 20(7):1802–1807. <https://doi.org/10.1557/JMR.2005.0225>
41. Allard LF, Bigelow WC, Jose-Yacamán M, Nackashi DP, Damiano J, Mick SE (2009) A new MEMS-based system for ultra-high-resolution imaging at elevated temperatures. *Microsc Res Tech* 72(3):208–215. <https://doi.org/10.1002/jemt.20673>
42. Yu K, Zhao W, Wu X, Zhuang J, Hu X, Zhang Q, Sun J, Xu T, Chai Y, Ding F, Sun L (2018) In situ atomic-scale observation of monolayer graphene growth from SiC. *Nano Res* 11(5):2809–2820. <https://doi.org/10.1007/s12274-017-1911-x>
43. He L-B, Zhang L, Tan X-D, Tang L-P, Xu T, Zhou Y-L, Ren Z-Y, Wang Y, Teng C-Y, Sun L-T, Nie J-F (2017) Surface energy and surface stability of Ag nanocrystals at elevated temperatures and their dominance in sublimation-induced shape evolution. *Small* 13(27):1700743. <https://doi.org/10.1002/smll.201700743>
44. Lian R, Yu H, He L, Zhang L, Zhou Y, Bu X, Xu T, Sun L (2016) Sublimation of Ag nanocrystals and their wetting behaviors with graphene and carbon nanotubes. *Carbon* 101:368–376. <https://doi.org/10.1016/j.carbon.2016.01.105>
45. He X, Xu T, Xu X, Zeng Y, Xu J, Sun L, Wang C, Xing H, Wu B, Lu A, Liu D, Chen X, Chu J (2014) In situ atom scale visualization of domain wall dynamics in VO₂ insulator-metal phase transition. *Sci Rep* 4:6544. <https://doi.org/10.1038/srep06544>
46. Zhang Q, Yin K, Dong H, Zhou Y, Tan X, Yu K, Hu X, Xu T, Zhu C, Xia W, Xu F, Zheng H, Sun L (2017) Electrically driven cation exchange for in situ fabrication of individual nanostructures. *Nat Commun* 8:14889. <https://doi.org/10.1038/ncomms14889>
47. Wan N, Perriat P, Sun L, Huang Q, Sun J, Xu T (2012) Fullerene as electrical hinge. *Appl Phys Lett* 100(19):193111. <https://doi.org/10.1063/1.4714682>
48. Wan N, Sun L, Ding S, Xu T, Hu X, Sun J, Bi H (2013) Synthesis of graphene–CNT hybrids via joule heating: structural characterization and electrical transport. *Carbon* 53:260–268. <https://doi.org/10.1016/j.carbon.2012.10.057>
49. Huang JY, Zhong L, Wang CM, Sullivan JP, Xu W, Zhang LQ, Mao SX, Hudak NS, Liu XH, Subramanian A, Fan H, Qi L, Kushima A, Li J (2010) In situ observation of the electrochemical lithiation of a single SnO₂ nanowire electrode. *Science* 330(6010):1515–1520. <https://doi.org/10.1126/science.1195628>
50. Xu F, Wu L, Meng Q, Kaltak M, Huang J, Durham JL, Fernandez-Serra M, Sun L, Marschilok AC, Takeuchi ES, Takeuchi KJ, Hybertsen MS, Zhu Y (2017) Visualization of lithium-ion transport and phase evolution within and between manganese oxide nanorods. *Nat Commun* 8(1):15400. <https://doi.org/10.1038/ncomms15400>
51. Wu X, Yu K, Cha D, Bosman M, Raghavan N, Zhang X, Li K, Liu Q, Sun L, Pey K (2018) Atomic scale modulation of self-rectifying resistive switching by interfacial defects. *Adv Sci* 5(6):1800096. <https://doi.org/10.1002/advs.201800096>

52. Liu Q, Sun J, Lv H, Long S, Yin K, Wan N, Li Y, Sun L, Liu M (2012) Real-time observation on dynamic growth/dissolution of conductive filaments in oxide-electrolyte-based ReRAM. *Adv Mater* 24(14):1844–1849. <https://doi.org/10.1002/adma.201104104>
53. Sun J, He L, Lo Y-C, Xu T, Bi H, Sun L, Zhang Z, Mao SX, Li J (2014) Liquid-like pseudoelasticity of sub-10-nm crystalline silver particles. *Nat Mater* 13(11):1007–1012. <https://doi.org/10.1038/nmat4105>
54. Zhong L, Sansoz F, He Y, Wang C, Zhang Z, Mao SX (2017) Slip-activated surface creep with room-temperature super-elongation in metallic nanocrystals. *Nat Mater* 16(4):439–445. <https://doi.org/10.1038/nmat4813>
55. Zheng H, Cao A, Weinberger CR, Huang JY, Du K, Wang J, Ma Y, Xia Y, Mao SX (2010) Discrete plasticity in sub-10-nm-sized gold crystals. *Nat Commun* 1(1):144. <https://doi.org/10.1038/ncomms1149>
56. Zhu Y, Espinosa HD (2005) An electromechanical material testing system for in situ electron microscopy and applications. *Proc Natl Acad Sci* 102(41):14503–14508. <https://doi.org/10.1073/pnas.0506544102>
57. Wang X, Zhong L, Mao SX (2018) Advances in understanding atomic-scale deformation of small-sized face-centered cubic metals with in situ transmission electron microscopy. *Mater Today Nano* 2:58–69. <https://doi.org/10.1016/j.mtnano.2018.09.002>
58. Yu Q, Legros M, Minor A (2015) In situ TEM nanomechanics. *MRS Bull* 40(1):62–70. <https://doi.org/10.1557/mrs.2014.306>
59. Spiecker E, Oh SH, Shan Z-W, Ikuhara Y, Mao SX (2019) Insights into fundamental deformation processes from advanced in situ transmission electron microscopy. *MRS Bull* 44(6):443–449. <https://doi.org/10.1557/mrs.2019.129>
60. Fernando JFS, Zhang C, Firestein KL, Golberg D (2017) Optical and optoelectronic property analysis of nanomaterials inside transmission electron microscope. *Small* 13(45):1701564. <https://doi.org/10.1002/smll.201701564>
61. Yang S, Wang L, Tian X, Xu Z, Wang W, Bai X, Wang E (2012) The piezotronic effect of zinc oxide nanowires studied by in situ TEM. *Adv Mater* 24(34):4676–4682. <https://doi.org/10.1002/adma.201104420>
62. Dong H, Xu F, Sun Z, Wu X, Zhang Q, Zhai Y, Tan XD, He L, Xu T, Zhang Z, Duan X, Sun L (2019) In situ interface engineering for probing the limit of quantum dot photovoltaic devices. *Nat Nanotechnol* 14(10):950–956. <https://doi.org/10.1038/s41565-019-0526-7>
63. Zheng H, Smith RK, Jun Y-w, Kisielowski C, Dahmen U, Alivisatos AP (2009) Observation of single colloidal platinum nanocrystal growth trajectories. *Science* 324(5932):1309–1312. <https://doi.org/10.1126/science.1172104>
64. Liao H-G, Zherebetskyy D, Xin H, Czarnik C, Ercius P, Elmlund H, Pan M, Wang L-W, Zheng H (2014) Facet development during platinum nanocube growth. *Science* 345(6199):916–919. <https://doi.org/10.1126/science.1253149>
65. Liao H-G, Cui L, Whitelam S, Zheng H (2012) Real-time imaging of Pt₃Fe nanorod growth in solution. *Science* 336(6084):1011–1014
66. Zhou Y, Powers AS, Zhang X, Xu T, Bustillo K, Sun L, Zheng H (2017) Growth and assembly of cobalt oxide nanoparticle rings at liquid nanodroplets with solid junction. *Nanoscale* 9(37):13915–13921. <https://doi.org/10.1039/c7nr04554a>
67. Zeng Z, Zhang X, Bustillo K, Niu K, Gammer C, Xu J, Zheng H (2015) In situ study of lithiation and delithiation of MoS₂ nanosheets using electrochemical liquid cell transmission electron microscopy. *Nano Lett* 15(8):5214–5220. <https://doi.org/10.1021/acs.nanolett.5b02483>
68. Niu K-Y, Park J, Zheng H, Alivisatos AP (2013) Revealing bismuth oxide hollow nanoparticle formation by the kirkendall effect. *Nano Lett* 13(11):5715–5719. <https://doi.org/10.1021/nl4035362>
69. Leenheer AJ, Sullivan JP, Shaw MJ, Harris CT (2015) A sealed liquid cell for in situ transmission electron microscopy of controlled electrochemical processes. *J Microelectromech Syst* 24(4):1061–1068. <https://doi.org/10.1109/jmems.2014.2380771>
70. Ye X, Jones MR, Frechette LB, Chen Q, Powers AS, Ercius P, Dunn G, Rotskoff GM, Nguyen SC, Adiga VP, Zettl A, Rabani E, Geissler PL, Alivisatos AP (2016) Single-particle mapping of

- nonequilibrium nanocrystal transformations. *Science* 354(6314):874. <https://doi.org/10.1126/science.aah4434>
71. Zhu C, Liang S, Song E, Zhou Y, Wang W, Shan F, Shi Y, Hao C, Yin K, Zhang T, Liu J, Zheng H, Sun L (2018) In-situ liquid cell transmission electron microscopy investigation on oriented attachment of gold nanoparticles. *Nat Commun* 9(1):421. <https://doi.org/10.1038/s41467-018-02925-6>
 72. Yuk JM, Park J, Ercius P, Kim K, Hellebusch DJ, Crommie MF, Lee JY, Zettl A, Alivisatos AP (2012) High-resolution EM of colloidal nanocrystal growth using graphene liquid cells. *Science* 336(6077):61–64. <https://doi.org/10.1126/science.1217654>
 73. Gai PL, Boyes ED (2009) Advances in atomic resolution in situ environmental transmission electron microscopy and 1 Å aberration corrected in situ electron microscopy. *Microsc Res Tech* 72(3):153–164. <https://doi.org/10.1002/jemt.20668>
 74. Luo L, Liu B, Song S, Xu W, Zhang J-G, Wang C (2017) Revealing the reaction mechanisms of Li–O₂ batteries using environmental transmission electron microscopy. *Nat Nanotechnol* 12(6):535–539. <https://doi.org/10.1038/nnano.2017.27>
 75. Crozier PA, Hansen TW (2015) In situ and operando transmission electron microscopy of catalytic materials. *MRS Bull* 40(1):38–45. <https://doi.org/10.1557/mrs.2014.304>
 76. Yuan W, Zhu B, Li X-Y, Hansen TW, Ou Y, Fang K, Yang H, Zhang Z, Wagner JB, Gao Y, Wang Y (2020) Visualizing H₂O molecules reacting at TiO₂ active sites with transmission electron microscopy. *Science* 367(6476):428. <https://doi.org/10.1126/science.aay2474>

Chapter 2

Electron Beam Irradiation Effects and In-Situ Irradiation of Nanomaterials



Tao Xu, He Zheng, Jianbo Wang, Florain Banhart, and Litao Sun

2.1 A Brief History of In-Situ Electron Irradiation

The transmission electron microscope (TEM) is capable of directly imaging the atomic structure of the specimen, which has become an indispensable tool to obtain atomic-level information and establish the relationship between structure and properties [1]. It is well known that the formation of an image in the TEM requires the elastic interaction of the object with an energetic electron beam (typically 60–300 keV, in a few instruments up to 1–3 MeV), raising a natural problem of electron irradiation. In fact, the interaction of the incident electrons with atomic nuclei or electrons surrounding the nuclei can cause temporary or permanent changes in the structure and/or the chemistry of the specimen, which is often referred to as electron irradiation damage [2]. Such damage has already been perceived in the early days of TEM [3] and is usually undesirable in TEM studies because radiation artifacts may appear in the images. Still today, radiation damage remains a fundamental difficulty and limits the applicability of TEM in the study of certain materials. Considering that the amount of radiation damage is proportional to the accumulated electron dose [2], beam-induced changes is more obvious in *in situ* experiments, where the specimen is inevitably exposed to electron bombardment for an extended period to allow the

T. Xu · L. Sun (✉)

Key Lab of MEMS of Ministry of Education, SEU-FEI Nano-Pico Center, Southeast University, Nanjing 210096, P. R. China
e-mail: slt@seu.edu.cn

H. Zheng · J. Wang

School of Physics and Technology, Center for Electron Microscopy, MOE Key Laboratory of Artificial Micro- and Nano-Structures, and Institute for Advanced Studies, Wuhan University, Wuhan 430072, P. R. China

F. Banhart

Institut de Physique Et Chimie Des Matériaux, UMR 7504, CNRS, Université de Strasbourg, 67000 Strasbourg, France

recording of transformations in time [4–6]. Separating electron irradiation effects from the analysis of the desired observations requires a detailed understanding of fundamental damage mechanisms.

Although radiation damage in the TEM is known since the 1940s [3], electron irradiation effects haven't become a subject of intense research until the 1960s, when electron irradiation in the TEM was widely used to simulate particle irradiation in nuclear fission or fusion reactor materials [7–9]. The particular advantage of *in situ* irradiation experiments is that the evolution of radiation defects can be observed directly in real time. It should be noticed that the electrons causing structural alterations and the electrons for imaging are usually not the same. But they stem from the same beam that can be used for both at the same time. With a continuous improvement of spatial resolution, TEM has enabled us to study radiation effects on the atomic scale since the 1980s [10]. Nowadays, aberration-corrected instruments promise further advance in this direction as the rearrangement of individual atoms in two-dimensional (2D) sheets of monoatomic thickness becomes visible without any overlap of other atom layers and projection artifacts in the image [11–13]. A large number of different radiation phenomena have been experimentally identified, ranging from atom displacements to electronic excitations. The main effects can be categorized into electron–nucleus scattering (atom displacement and sputtering) and electron–electron scattering events (electrostatic charging, radiolysis, or electron beam heating).

It is known that different damage mechanisms can be correlated with each other and depend on the material. Generally, inelastic electron–electron scattering can cause severe difficulties in the studies of insulators, ionic crystals, and organic materials [14–16] but is unimportant for metallic materials due to the presence of conduction electrons. Elastic electron–nucleus scattering can sometimes be neglected in insulating or organic specimens when the displacement cross section is lower than the excitation or ionization cross section. By contrast, electronic effects are quenched in conducting specimens where radiation damage is essentially restricted to atom displacements [17].

It is important to point out that electron irradiation is not only damaging specimens but also beneficial in *in situ* experiments to explore thermal nonequilibrium phenomena and the dynamic behavior of atomic defects, reveal the physics behind novel phenomena at the atom scale, and extend the applicability of electron irradiation. This chapter focuses on the variety of electron irradiation-induced processes where the electron beam triggers and drives the dynamic behavior of materials while in several cases some other excitations (such as heating) may be applied to the specimen at the same time.

As early as the late 1940s, electron beams in TEM had been intentionally used to trigger structural transformations in ionic crystals [18] and organic pigments [19], followed by the study of electron irradiation-induced decompositions in the early 1950s [20]. Due to the low spatial resolution in this period, electron diffraction always had to be used to confirm the formation of irradiation-induced phases. Over the same period, electron beam-induced deposition of carbonaceous residue of hydrocarbons

or other organic molecules has shown the capability to fix the specimen and partly protect the specimen from chemical attacks or electron bombardment [21].

Driven by the needs of nuclear power industry, electron irradiation in the TEM was widely applied to the study of structural stability of reactor materials under electron bombardment in the 1960s and 1970s [22], enabling the development of materials that are robust under neutron irradiation in the reactor. However, electron irradiation-induced point defects were not visible in the TEM at that time except they appeared in agglomerates or secondary defects such as dislocation loops, voids, and precipitates or induced observable structural changes of other defects. Consequently, electron irradiation-induced nucleation, growth or migration of dislocations [23], crystalline-amorphous transformations [24], and precipitation [25] begun to attract increasing attention. At the same time, electron beam flashing became a well-established technique to prepare thin crystal specimens with clean surfaces [26].

Electron irradiation-induced deposition became also of interest when gaseous precursors could have continuously flowed into the specimen chamber without considerable loss of spatial resolution [27]. Gas molecules may be ionized by the electron beam, making the molecules more reactive to interact or etch solid materials. Even without gas precursors, adatoms generated by electron irradiation can migrate and deposit within some areas of the object, resulting in the formation of novel structures [28]. Since the 1970s, computer-controlled electron beam-induced deposition and etching performed inside the TEM has become a productive technique to fabricate nanostructures [29].

Almost all subjects mentioned above have been studied again with atomic resolution since the 1980s when the spatial resolution of modern TEMs was promoted to the scale of 0.1 nm or even below. Many unexpected phenomena and novel effects were discovered in nanomaterials under electron irradiation [30]. For instance, spherical carbon particles showed self-compression under electron beam irradiation at high temperature, resulting in the nucleation and growth of diamond crystals [31]. The electron beam in TEMs with an aberration corrector can be focused onto spots of less than 0.1 nm which offer the possibility to fabricate and modify the specimen on the scale of few or even single atoms [32]. Besides, environmental specimen stages with liquid cells are used intensively in the last 15 years, and the interaction between the electron beam and the solution may induce reactions and produce species which play an important role in the observed nucleation and growth behaviors of nanocrystals in solution [33].

2.2 Fundamental Electron Irradiation Effects

In an electron microscope, the specimen is exposed to energetic electron bombardment during observation. As a low-mass particle, the electron can easily be deflected by the Coulomb interactions with the atomic nucleus or/and electrons in the specimen. The electron scattering can be categorized into elastic events without energy

loss and inelastic events with energy loss of the electrons. Elastic scattering represents electrostatic deflection by the Coulomb field of each atomic nucleus, which gives rise to electron diffraction patterns and to contrast in TEM images; inelastic scattering represents Coulomb interaction with the electrons surrounding the nucleus, which can generate several types of excitations in the specimen, and these signals can be used for elemental analysis in TEM [34]. However, these processes can also cause temporary or permanent changes in the structure and/or the chemistry of the specimen. For instance, electron–nucleus scattering can lead to atom displacements in the bulk of the specimen or sputtering of atoms from its surface, while electron–electron scattering can result in ionization, electrostatic charging, radiolysis, heating, and deposition [2]. Generally, displacement damage increases, whereas ionization damage decreases with increasing incident electron energy. An optimum accelerating voltage should be chosen to minimize the combined radiation damage depending on the materials to study.

2.2.1 Atom Displacements

A displacement event occurs by the direct transfer of the kinetic energy of the electrons to atoms in the solid via electron–nucleus collisions, knocking them out of their atomic sites and thereby degrading the crystalline perfection. It is the primary radiation damage mechanism in specimens with conduction electrons. Taking into account the energy and momentum conservation, only little energy E can be transferred from the incident electron to the nucleus, and the energy depends on the deflection angle θ :

$$E = E_{\max} \sin^2\left(\frac{\theta}{2}\right), \quad (2.1)$$

where E_{\max} is the maximum energy transferred by a head-on collision ($\theta = 180^\circ$). It is a function of the incident-electron energy E_0 :

$$E_{\max} = \frac{2E_0(E_0 + 2m_e c^2)}{M c^2}, \quad (2.2)$$

where m_e is the electron mass, M is the mass of the nucleus, and c is the speed of light. It is intuitively clear that head-on collisions are less likely than high-angle scattering [35].

If E exceeds displacement threshold energy E_d , the atom can be displaced to an interstitial position so that a vacancy–interstitial pair is created which does not spontaneously recombine. The migration of existing vacancies and interstitials can be promoted by electron irradiation even if the transferred energy is below E_d . Such a radiation-induced diffusion has qualitatively the same effect as thermal diffusion [35]. Generally, E_d (the energy of the displaced atom) is above 10 eV for atoms

in most bulk crystals and is characteristic of the material depending on its chemical composition and crystal structure. For instance, E_d of carbon in diamond is obviously larger than that in graphite, and the value along the hexagonal axis is evidently smaller than along the basal plane in graphite; atoms at grain boundaries or other structural defects are also displaced more easily because of their lower binding energy [35].

The displacement rate p , which states how often each atom is displaced per second, is given by

$$p = \sigma J, \quad (2.3)$$

where σ is the displacement cross section and J is the beam current density which typically ranges between 10 A/cm² in high-resolution imaging in a typical TEM and 10⁴ A/cm² with the fully focused electron beam on the specimen. For light elements, σ can be an approximation calculated by the McKinley–Feshbach formalism [36]:

$$\begin{aligned} \sigma = & \frac{4Z^2 E_R^2}{m_e^2 c^4} \left(\frac{E_{\max}}{E_d} \right) \pi a_0^2 \left(\frac{1 - \beta^2}{\beta^4} \right) \left\{ 1 + 2\pi\alpha\beta \left(\frac{E_d}{E_{\max}} \right)^{1/2} \right. \\ & \left. - \frac{E_d}{E_{\max}} \left[1 + 2\pi\alpha\beta + (\beta^2 + \pi\alpha\beta) \ln \left(\frac{E_{\max}}{E_d} \right) \right] \right\} \end{aligned} \quad (2.4)$$

where Z is the atomic number of the displaced atom, E_R is the Rydberg energy, a_0 is the Bohr radius of the hydrogen atom, $\beta = v/c$, and $\alpha = Z/137$. It should be noticed that this equation is suitable to evaluate the total displacement cross section for static atoms. If the effect of atomic vibrations is taken into account, the maximum transferred energy E_{\max} has to be replaced by a function containing the atom vibration and incident electron energy E_0 [37]. Such a modification just smoothens the cross section at the onset without changing the trend.

Normally, the cross section increases rapidly above the threshold E_{thr} (value of E_0 above which displacement occurs, which can be obtained by setting $E_{\max} = E_d$ in Eq. 2.2, normally larger than tens of keV), and reaches its maximum value at about twice the threshold and decreases again at higher energy due to relativistic effects [35]. Assuming the atoms are hard spheres, the displaced atoms may cause further displacements when $E_{\max} \geq 2E_d$. Such displacement cascades are of importance in larger objects where the total cross section may increase with the electron energy even at high electron energy [35].

The only way to avoid atom displacements is to use an electron energy below E_{thr} for microscopy. If the energy cannot be achieved experimentally, lowering the beam current and shortening the illumination time as much as possible should be considered to reduce displacement damage.

2.2.2 Surface Sputtering

If high-angle elastic scattering occurs at a surface atom, the atom can easily leave the specimen due to the open space above the surface, which is known as sputtering. It is obvious that sputtering primarily occurs on the beam-exit surface because the momentum transfer in a high-angle scattering is mainly along the incident direction [2].

Equations 2.1–2.4 remain valid but the sputtering threshold energy E_s for surface atoms is much lower as they are less tightly bound than bulk atoms [34], as shown in Table 2.1. E_s is often taken as the sublimation energy E_{sub} as well as the values between E_{sub} and $2E_{sub}$ [38]. Almost all low- Z and medium- Z atoms can be knocked away from the surface by 300 keV electrons, which means that the morphology of the specimen can be modified in a controllable manner in this way. Similar to displacement damage, the strategy for avoiding sputtering is to use a low electron energy and to limit the accumulated radiation dose. Besides, coating a thin layer of carbon onto the specimen surface may prevent sputtering damage.

It is a remarkable fact that most displaced atoms at the surface diffuse on the surface as adatoms and do not leave the specimen immediately. These atoms are weakly bound to the surface by physisorption or/and chemisorption and can be further sputtered if the transferred energy exceeds the adsorption energy E_{ad} . Surface diffusion is facilitated because the activation energy E_{sd} is typically lower than E_{ad} by a factor of 3 or more [39]. In this perspective, it is understandable that sputtering-induced rough surfaces tend to anneal under electron beam irradiation if the beam-induced surface migration is sufficient to fill the vacant sites. However, it is hard to quantify adatom motion because the structure of the surface is often unknown. Atomic steps, water molecules, or hydrocarbon contamination on the surface can affect adatom diffusion [39].

Table 2.1 Comparison of the maximum transferred energy E_{max} at 300 keV with displacement threshold energies E_d and sputtering threshold energies E_s [34]

Element	E_{max} (eV)	E_d (eV)	E_s (eV)	Element	E_{max} (eV)	E_d (eV)	E_s (eV)
Al	31.6	16	4–8	Ti	17.8	15	4–8
V	16.72	29	7–14	Cr	16.38	22	5–11
Fe	15.25	16	4–8	Co	14.45	23	5–12
Ni	14.5	22	6–11	Cu	13.4	18	4–9
Zn	13.03	16	4–8	Nb	9.17	24	6–12
Mo	8.88	27	7–14	Ag	7.90	28	7–14
Cd	7.58	20	5–10	Ta	4.71	33	8–16
Pt	4.37	33	8–16	Au	4.32	36	9–18

2.2.3 *Electrostatic Charging*

Electrostatic charging occurs primarily in electrically insulating specimens due to the lack of conductivity to neutralize the local charge. Under normal conditions, the irradiated area charges positively due to the emission of secondary and Auger electrons. The net charge accumulated by the specimen per second depends both on the backscattering coefficient η and the yield for secondary electrons δ . For thin TEM specimens, the steady-state condition represents an equilibrium between the electrical currents [2]:

$$I - I_t + V_s/R_s = I\eta + I\delta(V_s), \quad (2.5)$$

where I is the incident electron current, I_t is the transmitted electron current, V_s is the surface potential developed in the beam, and R_s is the effective electrical resistance between the irradiated and the surrounding regions of specimen. The terms on the left-hand side represent currents entering the irradiated area, while the right-hand side represents the loss of current by backscattering and by secondary emission. In view of the fact that very few electrons from the beam are absorbed in a thin specimen, I_t approaches I , causing V_s to be positive, especially at high E_0 . In addition, electrostatic charging can also occur via the Knotek–Feibelman (K–F) mechanism in which Auger electrons lead to a positive charge buildup [2].

At high current density, V_s may be dozens of volts [40]. This voltage can lead to an ultra-high electrical field of up to 10^{10} V/m at the edge of the illuminated area, which may cause an electrical breakdown in the insulating specimen and ion migration in the lateral direction [41]. In addition, electrostatic charging can also produce a mechanical force, which may even cause rupture of thin films [2].

Good conductive contacts between the specimen and the support or specimen holder can reduce charging, therefore reducing electron beam irradiation-induced charging effects.

2.2.4 *Radiolysis*

Radiolysis is the beam-induced ionization of atoms or breaking of chemical bonds by electron–electron scattering which may lead to a locally modified chemistry of the sample under the beam. Radiolysis is of significance in insulators (such as halides, oxides, hydroxides, sulfides, silicates, and so on) where inelastic scattering can cause local irreversible bond breaking and even mass loss. For alkali halides, which are a class of radiation-sensitive inorganic materials, the decay of exciton states leads to the formation of double-halogen ions and anion vacancies. Then the vacancies aggregate to form voids, while the halogen ions may condense to create dislocation loops and diffuse to the surface, eventually followed by halogen loss.

In the case of transition metal oxides, radiolysis may involve considerable electrostatic charging. The Auger decay of the inner-shell vacancy states in the metal atoms leads to positively charged O atoms, which can be ejected from the surface due to the electrostatic repulsion of the surrounding metal ions, thus leaving a metal-rich surface [42]. Such a process does not stop till the specimen surface becomes sufficiently conductive to screen the positive charge.

Radiation damage in organic solids is generally more extensive. Amorphous polymers or molecular crystals consist of strong covalent bonds and weak non-covalent bonds. Non-covalent bonds are easily broken followed by structural changes and displacements of molecules, resulting in crystallinity degradation and even mass loss [43]. Normally, aromatic compounds are much stable than aliphatic compounds due to their ring structures with π electrons which allows the deposited energy to be dissipated within the π electron pool without bond breakage [44].

The radiolysis of liquid solutions had attracted growing attentions, especially with the development of liquid cell TEM [33]. Considering that most solutions used in liquid cell TEM experiments have low concentrations of solutes, inelastic scattering in the liquid causes primarily radiolysis of the solvent. Radiolysis in both aqueous and organic solvents is applied to establish oxidizing or reducing environments, which is the basis for studying nucleation, growth, and degradation [45]. When water molecules interact with incident electrons, they decompose into strongly reducing solvated electrons e_h^- , hydrogen radicals H^\bullet , and oxidizing hydroxyl radicals OH^\bullet . Then these initial products diffuse and participate in further reactions to yield reactive products, including H_2 , O_2 , H_2O_2 , H_3O^+ , HO_2^\bullet , and so on [33]. These radicals will change the chemical environment but their concentration reaches an equilibrium within a very short time; furthermore, the radiolysis of water may alter the solution's PH because of the presence of H_3O^+ ions, which influences diverse processes such as aggregation [33]. Radiolysis of organic solvents is more complex, and results in a mixture of solvated electrons, molecular hydrogen, organic radical species, and even large polymeric molecules [45].

2.2.5 Electron Beam Heating

A local temperature rise under electron irradiation is expected when the transferred energy is dissipated in the form of heat with or without damage. Heating is dominated by inelastic electron–electron scattering while the transferred energy in elastic electron–nucleus collisions is much lower.

Supposing the specimen is bounded by a circular heat conductor of infinite conductivity held at a fixed temperature and the irradiation intensity is symmetrical within the circle, the temperature in the specimen is determined by 2D heat conduction, and the maximum temperature rise is given approximately by [46]

$$\Delta T = \frac{I}{4\pi\kappa} \frac{\Delta E}{t} \left(\gamma + 2\ln \frac{R}{r} \right), \quad (2.6)$$

where R and r are the radii of the specimen and the beam, respectively, κ is the thermal conductivity of the specimen, γ is Euler's constant, and ΔE is the average energy loss in a specimen of thickness t . The average energy loss for relativistic electrons can be estimated by [46]

$$\frac{\Delta E}{t} = \frac{2\pi e^4 N Z}{m v^2} \left\{ \ln \left[\frac{E_0 (E_0 + m_e c^2)^2 \beta^2}{2 E_{ex}^2 m_e c^2} \right] + (1 - \beta^2) - (1 - \sqrt{1 - \beta^2} + \beta^2) \ln 2 + \frac{1}{8} (1 - \sqrt{1 - \beta^2})^2 \right\} \quad (2.7)$$

where N is Loschmidt's number and E_{ex} is the excitation energy which is almost proportional to the atomic number Z . As a result, the temperature rise is independent of specimen thickness and proportional to the average density of the specimen. It can also be seen that the temperature rise is proportional to the beam current I and inversely proportional to the thermal conductivity. Generally, the temperature rise in TEM specimens during imaging is insignificant, provided the specimen is thin enough (order of magnitude 10 nm), as it is the case for typical lattice-resolution TEM studies. However, beam heating may be a serious problem at high incident currents, and it is detrimental for the specimen with quite low thermal conductivities.

Generally, heating is less if the electron energy is high, which seems quite counter-intuitive, but is due to the decreasing cross section for inelastic scattering towards higher energies. It is therefore preferable to use high acceleration voltages if the specimens are thermally unstable. However, possible damage by atom displacements has to be taken into account. On the other hand, good conductive contacts between specimen and support or specimen holder can enhance thermal dissipation, therefore reducing the beam-induced temperature rise of the specimen.

2.2.6 Electron Beam-Induced Deposition

Electron beam-induced deposition occurs when the irradiation is carried out in the presence of either volatile species in an atmosphere around the specimen or when mobile species are attached to the specimen surface. These species dissociated into volatile and nonvolatile components under the electron beam. The former disappears into the vacuum, while the latter adheres to the substrate, resulting in a local increase in thickness. Conversely, if the beam-activated molecules react with the specimen so that volatile species form, the substrate might be etched. Both deposition and etching occur only locally at or around the irradiated area.

In TEM, the most common deposition results from residual hydrocarbon, which is known as hydrocarbon contamination, especially in the STEM mode. Normally, hydrocarbon contamination is dominant around room temperature, whereas at high or low specimen temperatures it is negligible. At low specimen temperature, the mobility of hydrocarbon molecules on the specimen surface is too low to reach the

irradiated surface and, at high temperature, hydrocarbons evaporate from the specimen before being cracked by the electron beam. For hydrocarbon contamination, the precursors consist of the gaseous hydrocarbons in the vacuum (e.g., oil from the pumping system) and the adsorbed hydrocarbons on specimen surface (impurities by adhesion of molecules during specimen preparation or from the air). The deposition process is complex, consisting of specimen–hydrocarbon interaction, electron–specimen interaction, and electron–hydrocarbon interaction. The most important mechanism is governed by highly mobile hydrocarbon molecules that diffuse rapidly over the specimen surface. Once the molecules diffuse into the irradiated area, they are cracked so that immobile amorphous carbon is left on the specimen. Such a carbon deposit can be removed by plasma treatment, which is normally done *ex situ*. Intuitively, there are many factors involved in hydrocarbon contamination, such as beam current density, dissociation cross section, the residence time of hydrocarbons on specimen surface, specimen geometry, and the orientation of hydrocarbons with respect to the deposition location [47]. Some of the factors are almost impossible to control during the experiments, but it is certain that the diffusion of hydrocarbons along the specimen surface provides the major source because the contamination seriously occurs at the edge of the irradiated area as a ring in TEM imaging [48]. If the electron beam is focused onto spots with diameters smaller than several nanometers, a dot rather than a ring is formed. A line and even more complicated shapes can be formed by deflecting the beam.

Although this effect can be applied for lithography [49] and the fabrication of three-dimensional (3D) structures [50], it should generally be avoided for *in situ* experiments because the deposited layer might alter the behavior of the specimen [51]. Beam shower (short-time pre-illumination with a strong electron beam flux) is frequently employed to suppress hydrocarbon contamination. Heating may also reduce the hydrocarbon contamination rate by a factor of 10–30, depending on the temperature [52].

2.3 Electron Irradiation-Induced Processes in Nanomaterials

In situ electron irradiation experiments can be carried out in every standard TEM, even without technical modifications. Considering that the specimen temperature has a major influence on the evolution of radiation defects, a dedicated heating specimen stage is generally of advantage. On this basis, many irradiation phenomena in nanostructured materials were observed accidentally. This section presents some examples of electron irradiation-induced processes on the atomic scale in five main categories: (1) structural dynamics of defects, (2) phase transformations, (3) nucleation and growth of nanostructures, (4) generation and modification of novel structures, and (5) mechanical deformation.

2.3.1 The Dynamics of Defects Under Electron Beam Irradiation

The rise of 2D materials with atomic thickness such as graphene has opened a new window for the TEM observation of individual point defects such as vacancies or interstitials. As the atom positions in atomically thin 2D sheets can be intuitively identified from high-resolution image series, a detailed picture of the rearrangement of individual atoms under irradiation becomes visible without any imaging artifacts due to overlapping atoms or projection effects. Therefore, we focus on the electron irradiation-induced defect dynamics observed in 2D materials at the level of single atoms.

Typically, 2D materials are more sensitive to electron irradiation than 3D materials due to the fact that almost every atom is a surface atom. Displacement and ionization damage are the most relevant electron beam-induced processes. As shown in Table 2.2, the incident threshold electron energy for displacing C atoms in a graphene sheet is 86 keV at room temperature [12], which means that pristine graphene remains stable at a TEM voltage of 80 kV. But when contamination is adsorbed on the surface, atomic defects can be created at contamination sites in graphene even if the incident electron energy is much lower than the threshold energy [37]. As shown in Fig. 2.1a monovacancy forms at an adatom site under an 80 keV electron beam, which is attributed to a beam-induced chemical reaction of an adatom with the graphene substrate. Similarly, anion vacancies can be generated in pristine transition metal dichalcogenides (TMDC, such as MoS₂, MoSe₂, WS₂, etc.) sheets even if the incident electron energy is lower than the threshold energy for displacements [53], which probably results from the ionization effects.

The atomic defect continues growing so that holes are formed because atoms with unsaturated bonds around the vacancy are removed more easily than atoms within the sheet without dangling bonds [54]. In the case of graphene, Meyer et al. found that the growth of extended holes is not dominated by displacements because the growth rate of holes only weakly depends on the beam energy within a wide range of 20–100 keV [37]. Holes can form and grow in graphene even under a 20 keV electron beam, which is not expected from displacement effects because the threshold energy for displacing edge C atoms is assumed to be close to 50 keV. The observation that the growth rate of the holes is related to the vacuum level in the column further confirms that hole growth may be predominantly beam-induced etching by residual water or oxygen in the system [37]. It is worth noting that the shape of as-formed

Table 2.2 Displacement threshold energy E_d and corresponding energy of the beam electrons E_{thr} for typical 2D materials [12]

Materials	Graphene	<i>h</i> -BN		MoS ₂		MoSe ₂	WS ₂
		B	N	S	Mo	Se	S
E_d (eV)	16	16	14	6.1	13.9	5.6	6.3
E_{thr} (keV)	86	74	84	83	430	175	86

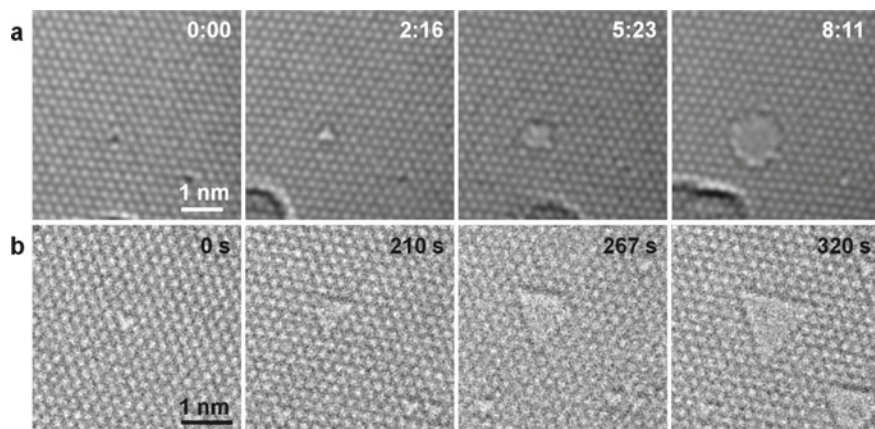


Fig. 2.1 Formation of holes starting from atomic defects under 80 keV electron beam irradiation. **a** Circular hole in graphene. Irradiation intensity is 700 A/cm^2 . **b** Triangular-shaped hole in a monolayer of *h*-BN. Irradiation intensity is 480 A/cm^2

holes usually depends on the crystal structure of 2D substrate. As shown in Fig. 2.1, the monovacancy prefers to evolve into a circular hole in graphene; however, a triangular-shaped hole with N-terminated zigzag edges forms in monolayer *h*-BN at room temperature under 80 keV electron beam irradiation. Besides, the specimen temperature is expected to affect the shape of the hole. Rhomb-shaped and hexagonal holes with both B- and N-terminated edges become prominent in monolayer *h*-BN if the sheet is heated to above $700 \text{ }^\circ\text{C}$ during electron beam irradiation [55].

The atomic defects can also migrate over a long distance and agglomerate with other atomic defects under electron irradiation, resulting in the formation of more extended defects. It is obvious that defect migration is more frequently observed than their formation because the migration barrier is generally far less than the displacement threshold. Taking graphene as an example, prolonged electron beam irradiation will make isolated vacancies agglomerate into large multivacancies consisting of rotated hexagons and other polygons, but the multivacancies tend to reorganize into a dislocation dipole terminated by two-edge dislocations if the number of sputtered C-atoms is larger than 10 [56]. In the case of MoS_2 , the diffusion of S-vacancies under the 80 keV electron beam is significantly fast and accelerated as the local vacancy concentration increases; therefore, S-vacancies are prone to agglomerate to form two typical straight-line defects [57]. It should be noted that the line defects do not only grow but also migrate occasionally under electron beam irradiation. In BN monolayers, Cretu et al. found that square-octagon line defects, involving less favorable B–B and N–N bonds, can migrate within monolayer *h*-BN at a temperature above 700°C through the glide of one or two atomic rows along the armchair direction [58].

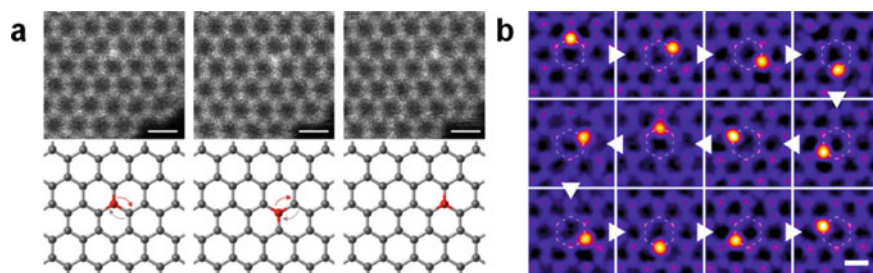


Fig. 2.2 Migration of foreign atoms in graphene under the electron beam. **a** Structural dynamics of a graphitic-N substitution via C–N bond inversion. Scale bar is 2.5 Å (reproduced with permission from Ref. [60], Copyright 2015, American Chemical Society). **b** Electron beam-controlled migration of Si substitution around a single hexagon. Scale bar is 2 Å (reproduced with permission from Ref. [32], Copyright 2018, American Chemical Society)

On the other hand, structural defects in 2D sheets can act as a trapping site for adatoms. However, the trapped atoms may still be mobile under electron beam irradiation. For example, Robertson et al. observed that Fe substitutions occupying a monovacancy or divacancy in graphene can move to adjacent lattice positions and reversibly switch their bonding between four and three nearest neighbors under the electron beam [59]. Other impurity atoms in graphene also show similar behavior under irradiation. Lin et al. found that pyridinic-N substitution can jump forth and back repeatedly between equivalent bonding sites across a monovacancy, while a graphitic-N substitution can migrate in the graphene plane via C–N bond inversions [60], as shown in Fig. 2.2a. Similarly, Si substitutions can also migrate via out-of-plane C–Si bond inversions [61], and Si trimer can rotate in a multivacancy [62]. Those movements can be well controlled by directing the electron beam onto the desired position which is possible with atomic precision. As shown in Fig. 2.2b, an Si atom can be precisely moved around a single hexagon by parking the electron beam on the C neighbor in the direction the Si should move [32].

In addition, electron beam-induced bond rotation can also lead to the formation, migration, and reconstruction of structural defects by keeping the atom number constant. A typical example is the formation and annihilation of a Stone–Wales (SW) defect in pristine graphene [63], as shown in Fig. 2.3a. An SW defect is considered to be formed by an in-plane 90° rotation of a C–C bond (SW rotation), and the kinetic barrier is 9–10 eV [64]. The maximum energy transferred from even 60 keV electrons is below the displacement threshold energy but sufficient to form multiple SW defects. Another typical example is the formation and annihilation of closed-loop “flower defects” [65]. Such a flower-like defect can be created via six consecutive bond rotations and relax into a less disordered state or even turn back to the pristine lattice by C–C bond rotations. Some other novel defects have also been created in 2D sheets through bond rotations. Lin et al. found a new threefold symmetric trefoil-like defect in monolayer TMDCs created via 60° rotations of metal–chalcogen bonds in the trigonal prismatic lattice [66]. The defect can expand through sequential

bond rotations and eventually evolve into larger linear defects consisting of aligned 8–5–5–8 membered rings.

Bond rotations can lead to structural transformations between several different configurations. As shown in Fig. 2.3b, the 5–8–5 (two pentagons separated by one octagon) divacancy can convert to a 5555–6–7777 defect (one hexagon surrounded by four pentagon–heptagon pairs) by means of a 555–777 (three circularly arranged pentagon–heptagon pairs) configuration [67], which releases the strain and reduces the influence of the divacancy onto the surrounding hexagonal lattice [68]. Bond rotation-mediated structural transformations also take place between various configurations of a tetravacancy [69]. Nevertheless, the most frequently observed tetravacancies are extended linear structures during the transformation, although they do not have the lowest formation energy. However, they are in a metastable state with

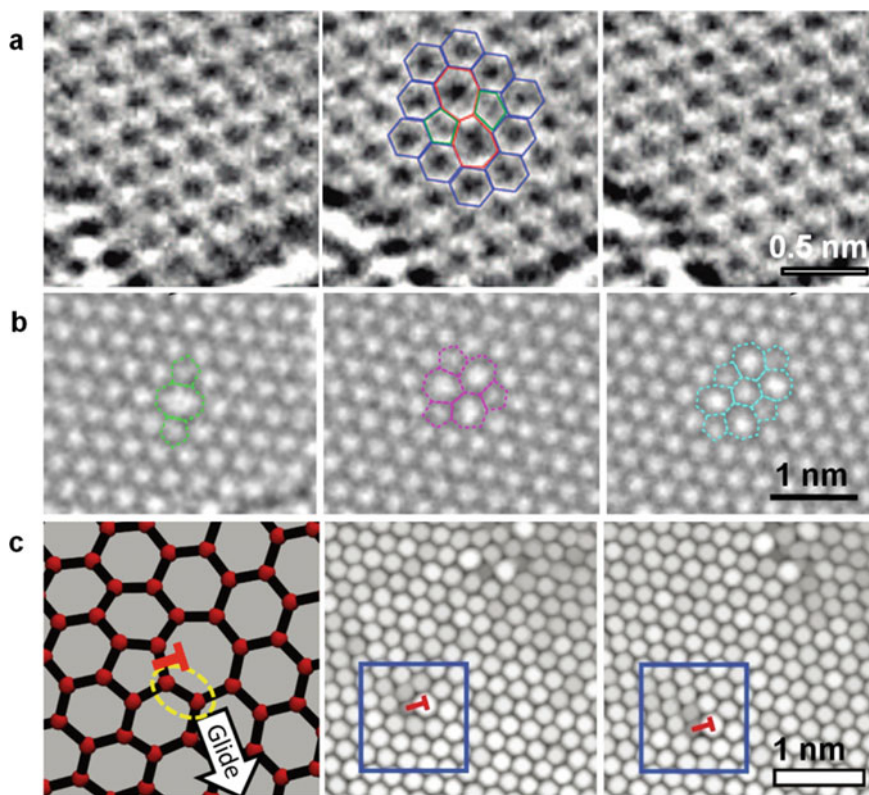


Fig. 2.3 Bond rotation-induced structural evolutions in graphene under 80 keV electron beam irradiation. **a** Formation and annihilation of a Stone–Wales defect (reproduced with permission from Ref. [63], Copyright 2008, American Chemical Society). **b** Transformation of a divacancy between different configurations (reproduced with permission from Ref. [67], Copyright 2011, American Physical Society). **c** Gliding of an edge dislocation via bond rotation (reproduced with permission from Ref. [56], Copyright 2013, Springer Nature)

a local energy minimum in the overall energy landscape. It is known that electron irradiation generally drives the system away from thermal equilibrium.

Bond rotations can also lead to the migration of structural defects, such as a random walk of divacancies [67] and dislocation glide in graphene [56]. As shown in Fig. 2.3c, the dislocation core consisting of a pentagon–heptagon pair can glide along the zigzag direction in graphene with a step of 0.25 nm via bond rotations [56]. Grain boundaries in 2D sheets can also migrate under electron beam irradiation. Kurasch et al. found that grain boundaries in graphene can migrate under electron beam irradiation via bond rotation, and the driving force depends only on the in-plane curvature of grain boundaries rather than on the detailed atomic arrangements [65]. The grain boundary with low curvature undergoes configuration changes without a preferred direction of migration. In contrast, the grain boundary with high curvature is expected to migrate towards the center of curvature, thereby shrinking the grain located on the same side of the boundary. The closed grain boundary can even unwind and restore towards the pristine lattice [65].

2.3.2 *Irradiation-Induced Phase Transformations*

It is known for a long time that electron beam irradiation-induced structural changes can lead to phase transformations in the irradiated specimen area. Such transformations can be classified into two categories, namely (1) changes in morphology or crystal structure and (2) changes in composition.

Electron beam irradiation-induced changes in morphology or crystal structure have been observed in many different materials systems. An example is beam-induced complete disordering of a stable crystalline structure and transformation into a metastable amorphous phase. Conversely, the crystallization of metastable amorphous materials has also been observed frequently under the electron beam. In the case of carbon, electron irradiation can transform graphene sheets into a quasi-amorphous 2D membrane with a random arrangement of polygons when the incident beam energy is just above the threshold energy for displacements [67]. On the other hand, the graphitization of amorphous carbon can also be achieved by electron irradiation. Börmert et al. found that freestanding amorphous carbon converted into graphitic carbon onions, while amorphous carbon supported on flat 2D sheets graphitized in a planar structure parallel to the support sheet due to van der Waals interactions with the underlying support [70]. With respect to the case of an amorphous carbon cluster on a 2D sheet, heat dissipation either through the underlying substrate or by radiative process is negligible, thus the cluster can potentially heat up significantly as the cluster volume decreases [70].

The transformation between different crystalline phases can also be achieved by electron irradiation. In carbon nanocrystals, for example, flat graphene flakes can curl up by steric stress due to pentagonal rings which are introduced by electron beam-induced sputtering of edge C atoms, until it is able to zip up its open edges to form a completely closed fullerene [71]. Similarly, the formation of spherical onion-like

graphitic particles by electron irradiation of flat graphitic precursors is predictable [72]. When such carbon onions are exposed to sustained electron irradiation at high temperature, the gradual loss of C atoms from the surface induces a shrinkage and self-compression of the onions. This leads to high pressure in the interior of the particles [72]. The pressure in the center is hydrostatic and may reach values higher than 40 GPa [73], which may be far inside the stability regime of diamond. The extreme curvature of the innermost shells may trigger changes in the hybridization of C atoms from sp^2 to sp^3 , leading eventually to the formation of a diamond crystal in the center. Conversely, the transformation of diamond nanoparticles into carbon onions is also feasible under irradiation. However, the transformation may depend on the initial size of the diamond particles. Hiraki et al. found that 5 nm diamond particles can change into onions by 300 keV electron beam irradiation, while 20 nm particles don't transform into carbon cages but to a graphite layer on the surface of the diamonds [74].

A real phase transformation in carbon can also occur under electron irradiation at high temperature. The transformation of graphite to diamond has been observed experimentally, which is surprising, given the fact that graphite is thermodynamically the more stable phase of carbon at low pressure [75]. As shown in Fig. 2.4, irradiation at high temperature leads to the growth of a diamond crystal at the interface between graphite and diamond [75]. When C atoms at the interface are displaced, they can aggregate to either of the two phases but the lifetime of the interfacial atoms is higher when they are bound in the diamond phase (diamond has a higher radiation hardness than graphite). It is known that atoms in graphite are easier to be displaced due to the lower mass density and van der Waals stacking with much space between the basal planes.

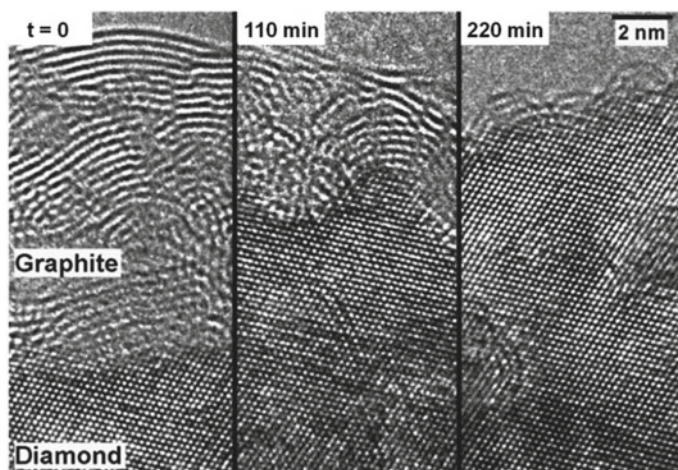


Fig. 2.4 Electron beam irradiation-induced transformation of graphite to diamond at a temperature of 700 °C and a beam current density of 100 A/cm² (reproduced with permission from Ref. [75], Copyright 1999, AIP Publishing)

Dynamic studies of phase transformation in transition metal chalcogenide under electron beam irradiation have also been shown by several groups. In Cu_2S , the transformation temperature is relatively close to room temperature and the Cu_2S nanocrystal can be heated above its phase-transition temperature by controlled electron irradiation. Zheng et al. directly observed the structural fluctuations between the low- and high-chalcocite phases of Cu_2S nanorods in the TEM [76], which provided insight into the understanding of microscopic pathways of structural fluctuations. Another example is the transformation of semi-conducting 2H- MoS_2 to metallic 1T- MoS_2 via lattice-plane gliding which is triggered by electron irradiation [77]. As shown in Fig. 2.5, the transformation starts with the formation of the α -phase precursor with three or four constricted zigzag chains, followed by local strain-caused S-plane or Mo-S atoms gliding if two non-parallel α -phases are in contact. Consequently, a triangular nucleus of the 1T phase forms and further expands via migration of a β -boundary [77]. Such a transformation only occurs in the irradiated region so that this can be easily controlled in STEM mode of the microscope.

Irradiation-induced changes in composition are also frequently observed in compounds consisting of two or more elements. It is natural that the element ratio will change if the rate of loss for different elements does not match the initial stoichiometry of the specimen. Consequently, the transformation between phases with different stoichiometry is feasible under irradiation [78–81]. Taking layered tin dichalcogenides as an example, the progressive removal of chalcogen atoms can be achieved by irradiation in a controllable manner, which first results in the formation of a mixed mono- and dichalcogenide and is followed by complete conversion to highly anisotropic orthorhombic monochalcogenides [82]. Figure 2.6a presents, as an example, the transformation from rhombohedral SnS_2 to highly anisotropic orthorhombic SnS . Another example is the transformation of bilayer PdSe_2 to monolayer Pd_2Se_3 by creating Se vacancies using electron irradiation [83]. The undercoordinated Pd atoms tend to bond with the nearest Se atoms in the adjacent layer, which creates a quantum force that pulls two layers towards each other. As the concentration of Se vacancies increases, the interlayer distance decreases to the length of a typical Pd–Se bond, resulting in the merging of the two layers and eventually the formation of the new Pd_2Se_3 2D phase [83]. Figure 2.6b presents the formation of monolayer Pd_2Se_3 which has a misoriented angle relative to the parent bilayer PdSe_2 .

Eventually, some elements may be totally lost under the electron beam, resulting in the decomposition of the specimen [84]. For instance, under electron beam irradiation, the hexagonal γ - CaSO_4 will transform into a transient orthorhombic β - CaSO_4 and eventually CaO phase, accompanied with the complete loss of S element [85]. Another common example is the decomposition of radiation-sensitive crystals, e.g., organic–inorganic hybrid perovskites [86]. Chen et al. found that single-crystalline $\text{CH}_3\text{NH}_3\text{PbI}_3$ rapidly decomposes into hexagonal PbI_2 through the loss of iodine ions and subsequent collapse of the perovskite structure [86].

The change in composition as mentioned above is attributed to partial loss of components. Conversely, a phase transition by adding a new component to the specimen is feasible if both the specimen and the feedstock for new components are exposed together to electron bombardment. For instance, electron beam-induced

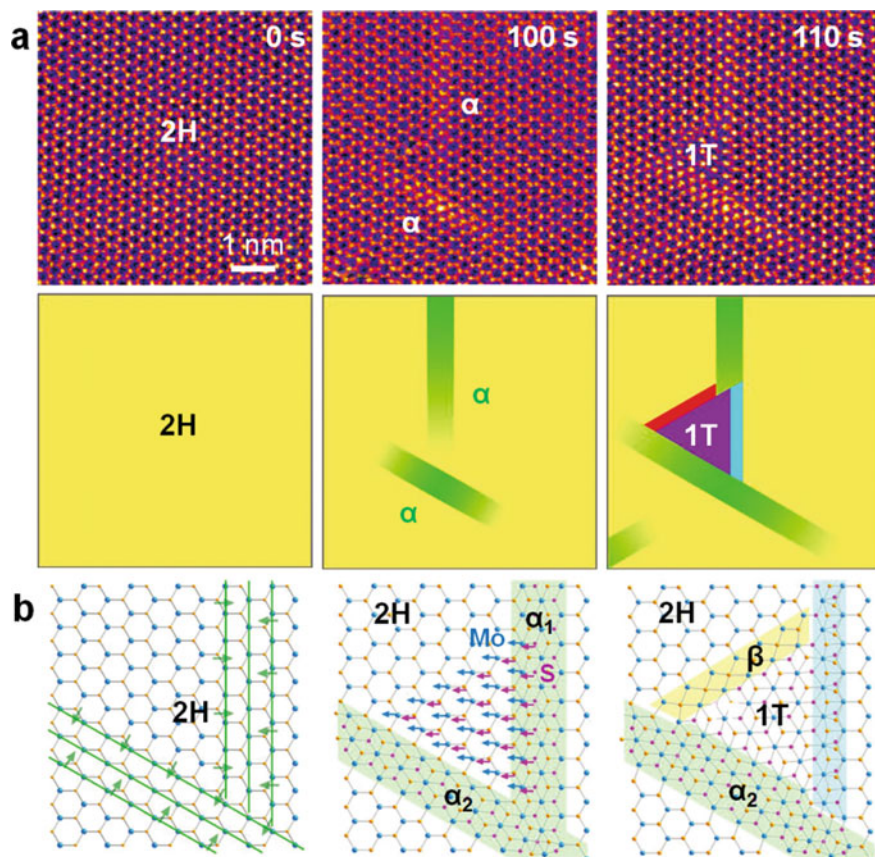


Fig. 2.5 Transformation between different crystalline phases in monolayer MoS₂ at 600 °C (reproduced with permission from Ref. [77], Copyright 2014, Springer Nature). **a** STEM image series and corresponding models showing the step-by-step progress of the phase transformation. **b** Model of atomic movements in the phase transformation

substitutional C doping can gradually transform *h*-BN sheets and tubes into hybrid ternary B–C–N honeycomb structures when a BN network with adsorbed hydrocarbon molecules is exposed to the electron beam [87]. It is understandable that B and N vacancies generated by electron irradiation are healed by C atoms that stem from decomposed hydrocarbon molecules. Another example is the formation of a metal carbide when graphitic onions encapsulating metals are subjected to electron irradiation in the TEM [88]. Such a transformation is induced by ballistic displacements of interface atoms and by the high pressure that the graphite shells exert onto the encapsulated metal particle.

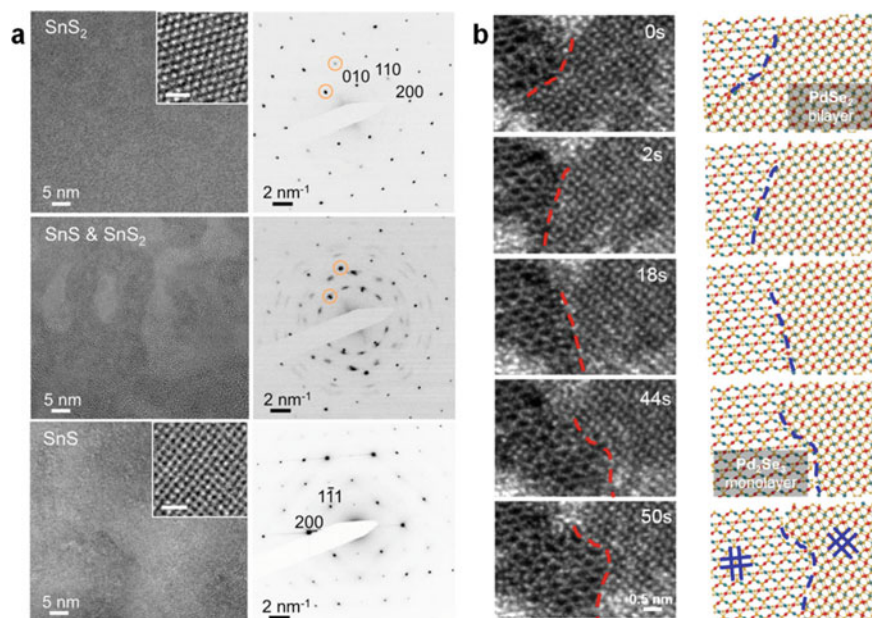


Fig. 2.6 Phase transformation between structures with different stoichiometry under electron irradiation. **a** The transformation from SnS_2 to SnS (reproduced with permission from Ref. [82], Copyright 2016, American Chemical Society). **b** The transformation from bilayer PdSe_2 to monolayer Pd_2Se_3 (reproduced with permission from Ref. [83], Copyright 2017, American Physical Society)

2.3.3 Nucleation and Growth of Nanostructures Under Irradiation

It has been shown that electron irradiation can trigger the nucleation and growth of nanostructures. Real-time observation of nucleation and growth has, for a long time, been carried out under vacuum condition in conventional TEMs, whereas new environmental specimen stages allow using gaseous and liquid precursors (see details in other chapters). Here, we focus on the nucleation and growth of nano-objects under vacuum conditions during which electron irradiation plays an essential role.

The key to study nucleation and growth inside a conventional TEM is to choose appropriate precursors which can be introduced into the specimen chamber and released in sufficient quantities to lead to the growth of the desired structures. Gas residues in the column and surface adsorbate on specimens or specimen grids are possible feedstocks, which provide small amounts of C and O atoms for growth. A simple experiment is the controlled growth of a metal oxide under electron beam irradiation. For instance, pure Ag can be locally oxidized as signified by the nucleation and growth of Ag_2O islands on its surface (Fig. 2.7) [89]. Interestingly, the Ag_2O structures only nucleate in the irradiated area under a low beam current density ($\sim 10^2 \text{ A/cm}^2$). Although Ag is resistant to oxidation by molecular oxygen at room

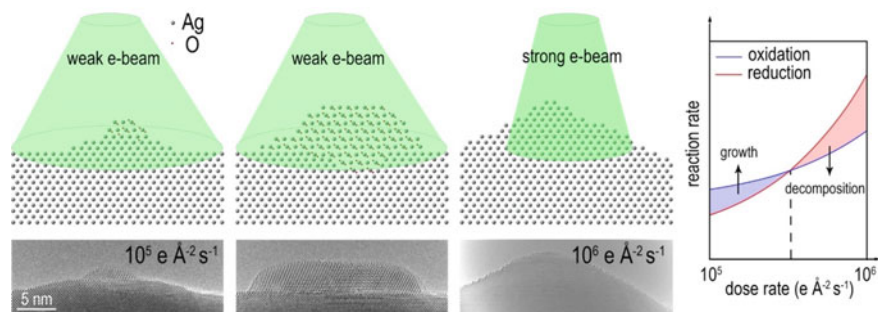


Fig. 2.7 Beam density-dependent nucleation and decomposition of the Ag_2O island on the Ag substrate (reproduced with permission from Ref. [89], Copyright 2019, Royal Society of Chemistry)

temperature, O_2 molecules adsorbed on the surface can be split into active radicals by electron irradiation and then react with the Ag substrate. It should be noticed that the Ag_2O islands can be fully reduced back to elemental Ag with an increase in the beam density ($\sim 10^3 \text{ A/cm}^2$). The controllable oxidation and reduction at different beam densities imply that electron beam may play a complex role in TEM studies of metal structures, especially when the metal is easily oxidized in air ambient, such as Mg [90, 91] or Fe [92]. Another example is the formation of In_2O_3 nanoparticles on the surface of In_2S_3 polycrystalline sheets [93]. The dangling bonds, resulting from electron beam-induced bond distortion, react with residual traces of O and water vapor in the TEM column, thus forming In_2O_3 nanoparticles.

For an efficient deposition, the precursor materials (substrates) should be highly unstable and easy to manipulate with the electron beam. When tiny amounts of an explosive precursor are irradiated by electron beam with sufficient beam density, the explosive decomposition happens due to heating or electrical charging. Consequently, a large number of nanoparticles are ejected outwards and caught by support membrane. Such a beam-induced fragmentation is mostly used for the production of metallic nanoparticles consisting of a single element [94].

If the precursor is decomposable under irradiation, the nucleation and growth may follow the beam-induced decomposition of the substrate and atomic rearrangements in the domain that is previously chemically modified. In many cases, amorphous films are used for the nucleation and growth of crystalline nanoparticles inside the amorphous matrix. For instance, crystalline Si nanoparticles can be formed within an amorphous SiO_2 film through either amorphous Si film [95] or amorphous SiO_x ($x < 2$) nanoparticles [96]. The substrates can also be polymers or metal–organic frameworks filled with the desired precursor [94]. At times, one-dimensional (1D) nanostructures can also grow with the help of a catalyst. Gonzalez-Martinez et al. demonstrated a straightforward route to grow amorphous core–shell B/BO $_x$ nanowires and BO $_x$ nanotubes by irradiating a composite made of Au nanoparticles embedded within an amorphous BO $_x$ matrix [97]. The Au nanoparticles were initially guided toward the composite surface by the condensed electron beam and then catalyzed the growth of a 1D structure in the presence of oxygen species. The B^+ ions generated within

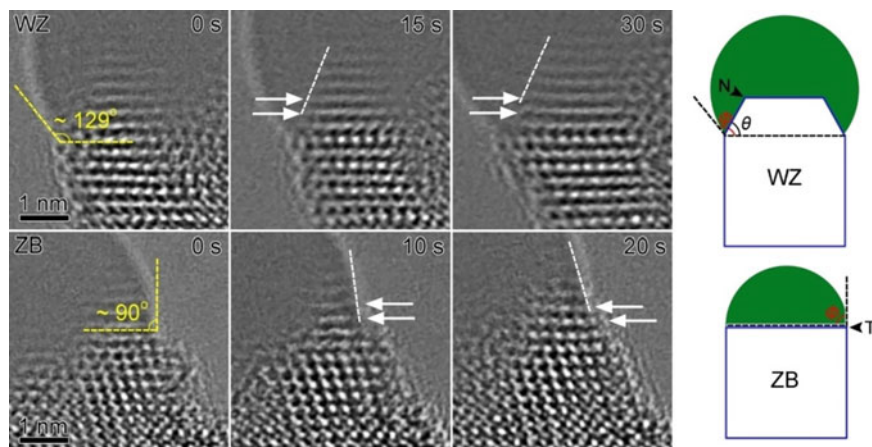


Fig. 2.8 The growth kinetics of wurtzite and zinc blende ZnO nanowires under 200 keV electron beam (reproduced with permission from Ref. [98], Copyright 2018, American Chemical Society)

the irradiated volume through charging and a Knotek–Feibelman mechanism could diffuse to the reaction sites in the Au nanoparticles due to electrostatic repulsion. The growth of coaxial B/BO_x nanowires continued as long as enough B species were supplied, and the catalytic process could use B from the core of a coaxial nanowire, forming eventually a BO_x nanotube if the quantity of the B species was insufficient [97]. Another example is Sn-catalyzed growth of ZnO nanowires by electron beam irradiation of Zn₂SnO₄ (Fig. 2.8) [98]. Sn became liquid droplet under electron irradiation due to low melting point (~505 K), and diffused onto the surface of Zn₂SnO₄, catalyzing the growth of wurtzite or zinc blende nanowires. Even without a catalyst, 1D structures can grow rooted at their base to the precursor materials and be extruded by a beam-induced field gradient within the substrates [99].

If the precursor is easily damaged, nucleation and growth phenomena are frequently observed. An example is the growth of a carbon nanotube from a metal (e.g., Fe, Co, Ni, or Fe/Co alloy) encapsulated partially by a host nanotube when subjected to electron beam irradiation at high temperature [100], as shown in Fig. 2.9. Carbon atoms from the shells are ejected into the encapsulated FeCo crystal and precipitate at the uncovered metal as an extended array of C filaments after a short time, because the solubility of C in these metals is low but the diffusion is fast. Ordering of the filament eventually leads to the growth of another carbon nanotube inside the host tube. In such an experiment, the host carbon nanotube is utilized both as a feedstock material and as a local template.

Another example is the aggregation and rearrangement of beam-introduced adatoms on the surface or at the defect sites, which manifests itself as epitaxial growth or healing [101–103]. As mentioned above, most displaced atoms at the surface are weakly bonded and able to diffuse over the surface under the electron

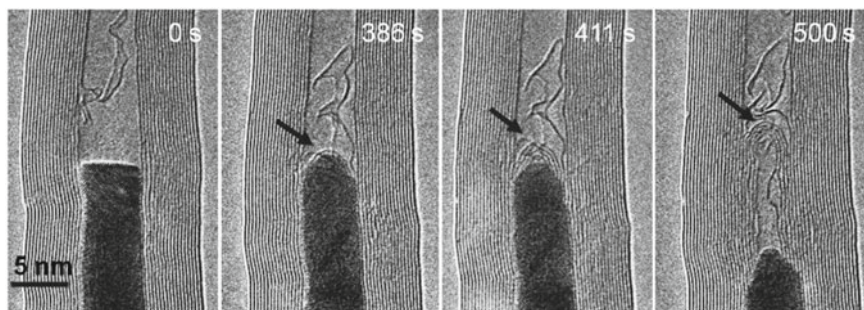


Fig. 2.9 Growth of a new nanotube from a FeCo crystal inside the host carbon nanotube. Temperature is 600 °C and irradiation density is 100 A/cm² (reproduced with permission from Ref. [100], Copyright 2007, Springer Nature)

beam, which provides the source for epitaxial growth or annealing. This has been observed for the healing of holes in MoS₂ and Bi₂Te₃ and is shown in Fig. 2.10 [103].

2D structures may also form from clusters if the transferred energy is sufficient to trigger the reconstruction. Zhao et al. found that Fe residues were able to entirely fill small perforations in graphene and thus form free-standing crystalline single-atom Fe layers [104]. The lattice constant for such Fe membranes was larger than bulk Fe and increased towards the center of the membranes due to the strain resulting from the lattice mismatch between graphene and the suspended Fe sheet. However, the largest stable Fe monolayer is only 10–12 atoms wide [104]. Similarly, metal oxide monolayers can form both on graphene substrates and inside graphene nanopores. This has been observed for crystalline single-atom CuO membranes on graphene substrates and is shown in Fig. 2.11 [105].

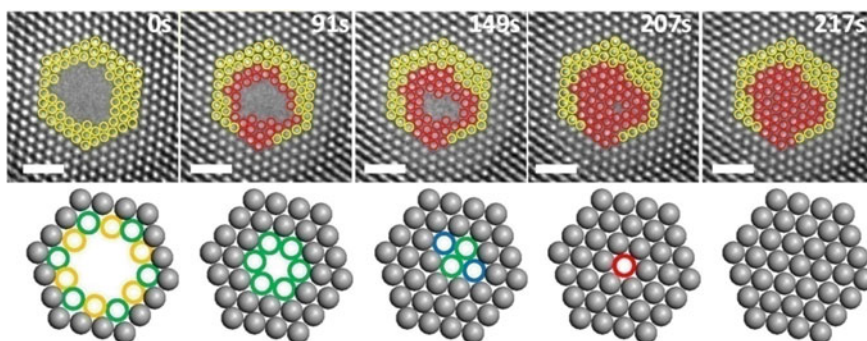


Fig. 2.10 Healing of a nanohole in Bi₂Te₃ under a 300 keV electron beam. Irradiation density is 16 A/cm², scale bar is 1 nm (reproduced with permission from Ref. [103], Copyright 2018, John Wiley and Sons)

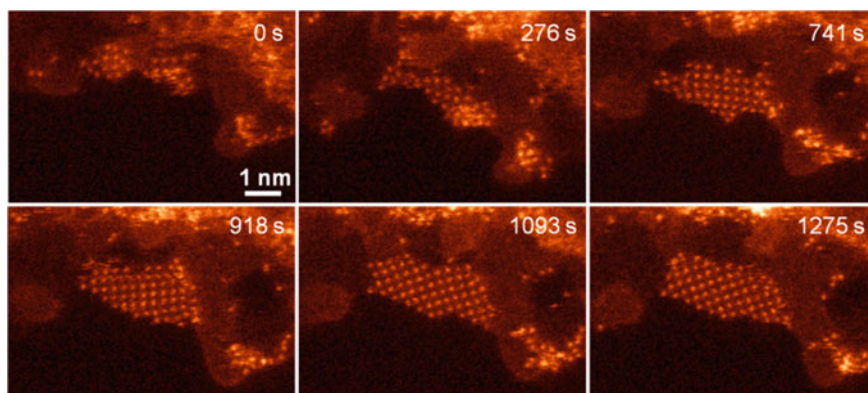


Fig. 2.11 Growth of a CuO membrane of monoatomic thickness on a graphene substrate (reproduced with permission from Ref. [105], Copyright 2017, IOP Publishing)

2.3.4 Fabrication of New Structures Under Irradiation

Although the fabrication of nanodevices via electron irradiation inside an electron microscope remains a challenge due to the lack of operational flexibility, the creation of new structures with atomic precision as building blocks for devices is nevertheless of interest. Sub-nanometer 1D structures are among the most promising building blocks for future electronic devices. Hence, we focus on the fabrication of ultrathin 1D structures, such as atomic chains, nanowires, and nanotubes in this section.

A large number of experimental studies have shown that electron irradiation provides a top-down strategy to fabricate novel structures [106–111]. Normally, ultrathin quasi-1D structures can be created when holes are first drilled in thin films using a focused electron beam so that the size of the hole is given by the dimensions of the beam profile. A low-dimensional ribbon spans between two adjacent holes so that the initial size of the ribbons depends on the irradiated regions. Subsequently, extremely narrow ribbons and even atomic chains eventually form after further thinning.

As early as the late 1990s, Kondo et al. proposed that stable Au nanowires could be prepared by electron beam irradiation in a 3 nm-thick Au film through the formation of Au bridges between two neighboring holes and further thinning of the Au bridge [112]. The as-formed nanowires were 0.8–3 nm in diameter but remained stable due to surface reconstruction, leading to a hexagonal prism consisting of a hexagonal-close-packed surface layer and a face-centered-cubic core [112] or a coaxial tube with helical atom rows coiled round its axis [113]. Soon afterwards, Ugarte et al. reported that such an experimental procedure can be extended to atomic Au chains [114] and other ultrathin metal nanowires [115–117].

In the late 2000s, the technique was applied to sculpt natural 2D planes. As shown in Fig. 2.12a, linear C chains were made by further removing edge atoms from graphene ribbons [118]. Interestingly, the arrangement of C bonds in the chain seems to be affected by temperature and local strain. The as-formed 1D structure is

interpreted as a polyynane chain with alternating single and triple bonds if it is under strain, and a cumulene chain with uniform double bonds if it is unstrained [119]. These two distinct arrangements coexist at low or ambient temperature, while an unexpectedly high polyene ratio is observed in carbon chains fabricated at elevated temperatures [120]. Such a top-down method is also suitable for other 2D systems. Atomic chains with alternating B and N atoms have been created in *h*-BN sheets [121]; phosphorus chains with zigzag configurations have been created in phosphorene and their stability is enhanced if the chains are supported by a substrate [122].

Unlike atomic chains formed in graphene, *h*-BN, or phosphorene, extremely narrow wires can be constructed from TMDCs. As shown in Fig. 2.12b, ultra-narrow wires can be derived from monolayer MoS₂ by further thinning the ribbons between two adjacent holes [123]. Interestingly, the wire is robust under electron irradiation and its atomic structure is obviously different from the initial MoS₂. Similar structures can be created in other TMDC sheets, and the as-formed wires have been experimentally proven to be metallic [124]. On this basis, complex junctions of nanowires can form from narrow constrictions, and alloyed nanowires such as MoS_xSe_{1-x} can be fabricated by sculpting their alloyed monolayer counterpart or corresponding van der Waals heterostructures [125].

Similarly, bilayer nanoribbons can form between two adjacent pores in bilayer sheets. Sometimes, the dangling bonds at the edges can be saturated with interlayer

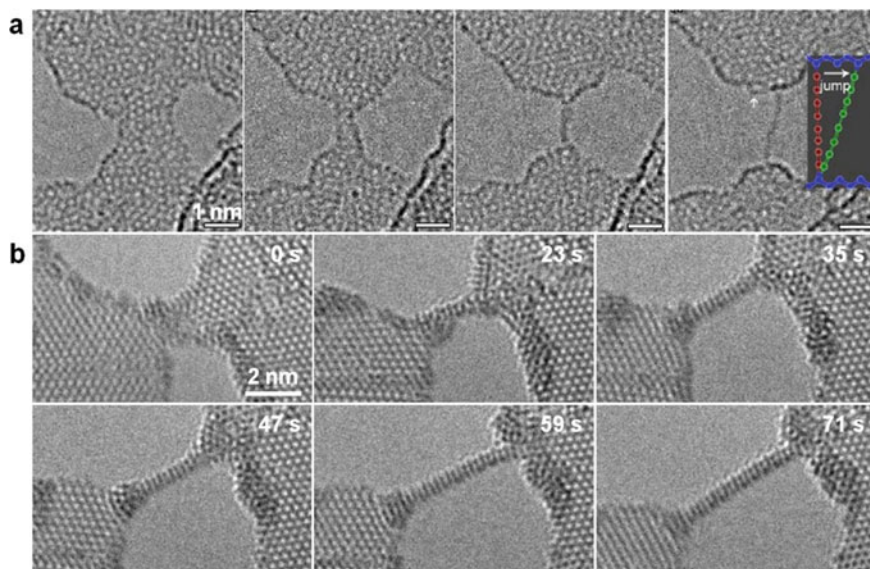


Fig. 2.12 Atomic wires sculpted from 2D sheets. **a** Formation of a free-standing C chain in graphene under a 120 keV electron beam. Irradiation intensity is 4 A/cm² (reproduced with permission from Ref. [118], Copyright 2009, American Physical Society). **b** Formation of a suspended wire in a MoS₂ sheet under an 80 keV electron beam. Irradiation intensity is 10 A/cm² (reproduced with permission from Ref. [123], Copyright 2013, Springer Nature)

bonds, resulting in a structural transformation from bilayer ribbons with open edges to single-walled tubular structures. For example, single-walled tubular structures can be fabricated in AA' stacked bilayer *h*-BN at predefined positions by controlling the location of pores, and then thinned by removing atomic rows one by one under sustained irradiation [126].

2.3.5 Deformation of Nanostructures Under Electron Irradiation

As pointed out above, intense electron irradiation can cause the shrinkage of graphitic shells when spherical carbon onions or cylindrical nanotubes encapsulating other crystals are subjected to electron bombardment at high temperatures. The self-contraction of the outer shells, which is due to the reconstruction of vacancies in the shells after the sputtering-induced loss of carbon atoms, can exert an enormous pressure on the encapsulated crystals, resulting in heavy deformation or extrusion effects. Generally, these experiments need a defined strategy to study in situ the deformation of individual nanometer-sized crystals at the atomic scale.

It is known that the polyhedral graphitic particles synthesized by arc discharge generally transform into a perfectly spherical “onion” under the electron beam. The process is facilitated at specimen temperatures above 300–400°C where the graphitic shells reconstruct after the creation of radiation defects. During the morphological transformation, the encapsulated crystal is subjected to compressive forces and eventually deformation which manifests itself, besides visible shape changes, in a decrease in lattice spacing [73], or the formation of twins or grain boundaries [127]. The process is accessible to direct observation at atomic resolution. This has been observed for W and Mo crystals inside graphitic shells and is shown in Fig. 2.13a [127]. It should be noted that the crystals inside the onions have no freedom to evade the pressure (if the shells are closed); ultimately the atoms of the crystal may gradually diffuse through the graphite shells towards the surface [128]. If the shells have an opening, the crystal is squeezed out through the opening where particularly high stress appears to prevail [127]. Carbon onions that have been punctured with a focus electron beam allow to use them as extrusion cells to study the deformation of nanocrystals in detail under continuous load [129]. The plastic deformation of individual Au, Pt, Mo, and W crystals has been observed inside carbon onions which is shown in Fig. 2.13b [129]. Similarly, controlled irradiation of carbon nanotubes can cause large pressure buildup to the order of 40 GPa within the nanotubes. Therefore, carbon nanotubes can be used as robust jigs for deforming and extruding even hard materials such as iron carbide along the tube axis as shown in Fig. 2.13c [130].

In addition, as mentioned above, a large number of studies have demonstrated that electron irradiation provides a top-down strategy to fabricate nanowires. Interestingly, the as-formed nanowires have a tendency to elongate and even break under the electron beam mainly due to the existence of tensile strain, which results from the

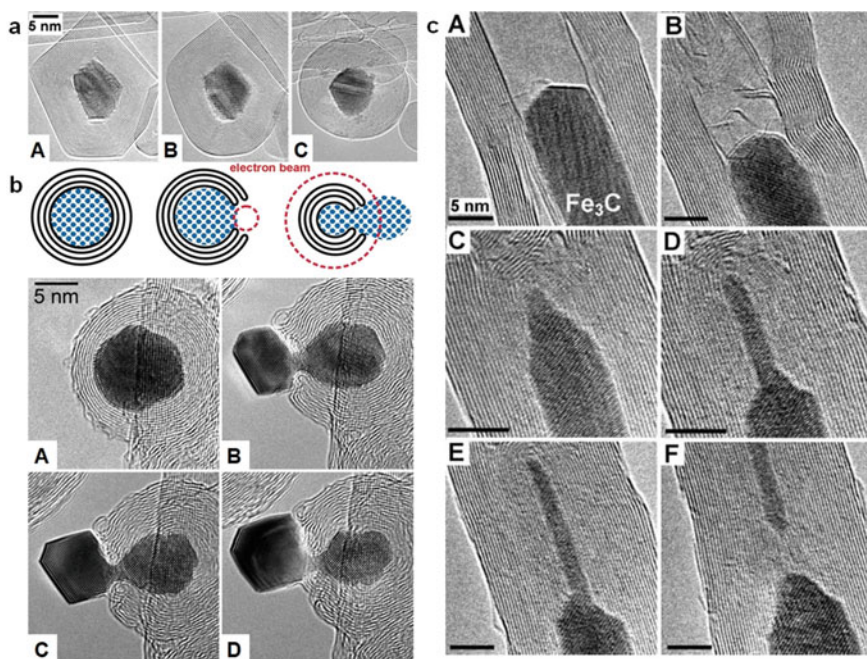


Fig. 2.13 Deformation of nanocrystals encapsulated inside graphitic shells under electron irradiation. **a** Deformation of a Mo crystal inside a carbon onion at 600 °C (reproduced with permission from Ref. [127], Copyright 2005, John Wiley and Sons). **b** Extrusion of an Au crystal from punctured onion at 300 °C (reproduced with permission from Ref. [129], Copyright 2008, American Physical Society). **c** Extrusion of a Fe_3C crystal inside a collapsing carbon nanotube along the tube axis at 600 °C (reproduced with permission from Ref. [130], Copyright 2006, AAAS)

relative displacement and/or rotation of the nanowire apices, probably due to thermal deformation of the whole substrate. These experiments thus provide a method for the *in situ* study of structural changes under tensile strain. Several phenomena have been observed. Lagos et al. reported the spontaneous formation of the smallest possible hollow metal wires with a square cross-section during the elongation of Ag junctions and interpreted this configuration as a minimization of surface energy and generation of a soft structure, capable of absorbing a huge tensile deformation when high stress is applied [131]. Strain-mediated reversible phase transformations from the wurtzite structure to an intermediate body-centered tetragonal and *h*-MgO structure in quantum-confined ZnO nanowires (with a diameter less than 2 nm) have been observed using a similar approach (Fig. 2.14) [132]. Both *in situ* observation and theoretical calculations demonstrate that tensile stress plays a pivotal role in mediating the phase transformation.

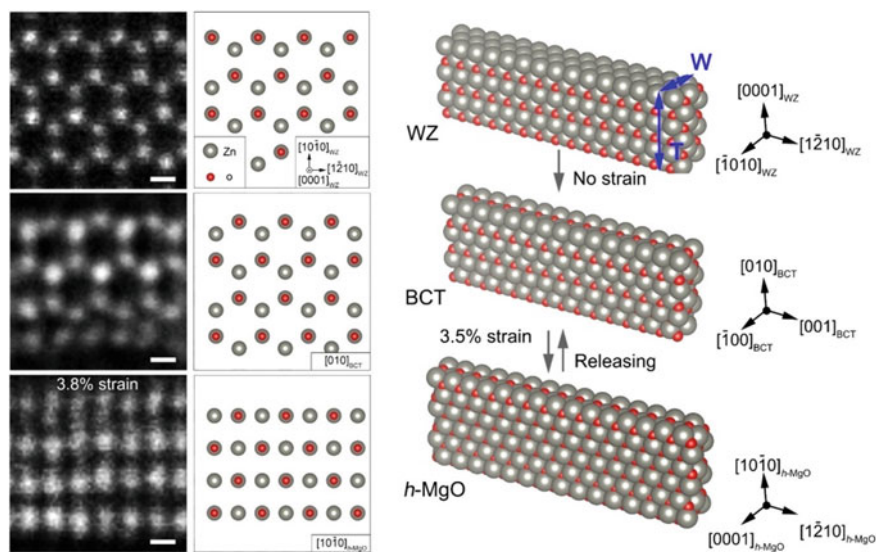


Fig. 2.14 The reversible phase transformation of a sub-2-nm ZnO nanowire. Scale bar is 2 Å (reproduced with permission from Ref. [132], Copyright 2019, American Physical Society)

2.4 Conclusions and Outlook

Although radiation damage is normally an unwelcome artifact, the electron beam can be intentionally used to trigger structural evolutions in a controllable way, while the structural changes can be monitored at the same time with the same beam. The ability to both generate and investigate structural transformations simultaneously made it possible that electron irradiation became an important direction of *in situ* microscopy.

In situ irradiation of nanomaterials has shown many phenomena of fundamental importance. Beam-induced structural transformations serve as models to understand the dynamic behavior of nanocrystals at the atomic scale and even the migration of individual atoms. The formation of secondary phases by electron irradiation, especially non-equilibrium phases, is expected to become a key experiment to develop and understand new nanostructured materials. However, there are still many technical challenges and opportunities, especially in the observation of dynamic phenomena at the atomic scale in beam-sensitive materials. Normally, the live observation requires instantaneous exposure of the material to the beam; however, the maximum electron dose for most beam-sensitive materials is low, which restricts the image resolution due to the poor signal-to-noise ratio at short exposure times. Some technological and methodological strategies, such as an electron detector coupled with direct-detection and electron counting techniques, low-dose imaging through compressive sensing, or pulsed laser-triggered ultrafast electron microscopy, have been proposed to improve

and extend the imaging capabilities [133], which is expected to expand our knowledge on radiation phenomena in beam-sensitive materials in the future. Besides, irradiation of composite systems may give the opportunity to study the response of one component to the stimulation arising from the radiation-induced evolution of the other component.

References

1. Xu T, Sun L (2015) Dynamic In-Situ experimentation on nanomaterials at the atomic scale. *Small* 11(27):3247–3262. <https://doi.org/10.1002/sml.201403236>
2. Egerton RF, Li P, Malac M (2004) Radiation damage in the TEM and SEM. *Micron* 35(6):399–409. <https://doi.org/10.1016/j.micron.2004.02.003>
3. Lembke A, Ruska H (1940) Vergleichende Mikroskopische und Übermikroskopische Beobachtungen an den Erregern der Tuberkulose. *J Mol Med* 19(10):217–220
4. Sheng H, Zheng H, Cao F, Wu S, Li L, Liu C, Zhao D, Wang J (2015) Anelasticity of twinned CuO nanowires. *Nano Res* 8(11):3687–3693. <https://doi.org/10.1007/s12274-015-0868-x>
5. Zheng H, Liu Y, Mao SX, Wang J, Huang JY (2012) Beam-assisted large elongation of in situ formed Li₂O nanowires. *Sci Rep* 2(1):542. <https://doi.org/10.1038/srep00542>
6. Sun J, He L, Lo Y-C, Xu T, Bi H, Sun L, Zhang Z, Mao SX, Li J (2014) Liquid-like pseudoelectroelasticity of sub-10-nm crystalline silver particles. *Nat Mater* 13(11):1007–1012. <https://doi.org/10.1038/nmat4105>
7. Silk ECH, Barnes RS (1959) Examination of fission fragment tracks with an electron microscope. *Phil Mag* 4(44):970–972. <https://doi.org/10.1080/14786435908238273>
8. Cowley J (1966) Irradiation effects in beryllia and zinc oxide. *Acta Crystallogr A* 21(2):192–196. <https://doi.org/10.1107/S0365110X66002603>
9. Makin M (1968) Electron displacement damage in copper and aluminium in a high voltage electron microscope. *Phil Mag* 18(153):637–653. <https://doi.org/10.1080/14786436808227466>
10. Bursill L, Thomas J, Rao K-J (1981) Stability of zeolites under electron irradiation and imaging of heavy cations in silicates. *Nature* 289(5794):157–158. <https://doi.org/10.1038/289157a0>
11. Sun L, Banhart F, Warner J (2015) Two-dimensional materials under electron irradiation. *MRS Bull* 40(01):29–37. <https://doi.org/10.1557/mrs.2014.303>
12. Xu T, Yin K, Sun L (2017) In-situ study of electron irradiation on two-dimensional layered materials. *Chin Sci Bull* 62(25):2919–2930. <https://doi.org/10.1360/N972016-01031>
13. Xu T, Shen Y, Yin K, Sun L (2019) Precisely monitoring and tailoring 2D nanostructures at the atomic scale. *APL Mater* 7(5):050901. <https://doi.org/10.1063/1.5096584>
14. Stenn K, Bahr GF (1970) Specimen damage caused by the beam of the transmission electron microscope, a correlative reconsideration. *J Ultrastruct Res* 31(5):526–550. [https://doi.org/10.1016/S0022-5320\(70\)90167-X](https://doi.org/10.1016/S0022-5320(70)90167-X)
15. Thomas L, Humphreys C, Duff W, Grubb D (1970) Radiation damage of polymers in the million volt electron microscope. *Radiat Eff* 3(1):89–91. <https://doi.org/10.1080/00337577008235620>
16. Hobbs LW (1987) Electron-beam sensitivity in inorganic specimens. *Ultramicroscopy* 23(3):339–344. [https://doi.org/10.1016/0304-3991\(87\)90244-0](https://doi.org/10.1016/0304-3991(87)90244-0)
17. Urban K (1979) Radiation-induced processes in experiments carried out in-situ in the high-voltage electron microscope. *Phys Status Solidi A* 56(1):157–168. <https://doi.org/10.1002/pssa.2210560116>
18. Burton E, Sennett R, Ellis S (1947) Specimen changes due to electron bombardment in the electron microscope. *Nature* 160(4069):565–567. <https://doi.org/10.1038/160565b0>

19. Hamm FA, Norman EV (1948) Transformations in Organic Pigments. *J Appl Phys* 19(12):1097–1109. <https://doi.org/10.1063/1.1715026>
20. Fischer RB (1954) Decompositions of Inorganic Specimens During Observation in the Electron Microscope. *J Appl Phys* 25(7):894–896. <https://doi.org/10.1063/1.1721764>
21. Hillier J, Mudd S, Smith AG, Beutner EH (1950) The “Fixation” of electron microscopic specimens by the electron beam. *J Bacteriol* 60(5):641–654
22. Wilkes P (1979) Phase stability under irradiation—a review of theory and experiment. *J Nucl Mater* 83(1):166–175. [https://doi.org/10.1016/0022-3115\(79\)90602-0](https://doi.org/10.1016/0022-3115(79)90602-0)
23. Saka H, Noda K, Matsumoto K, Imura T (1975) Effect of electron irradiation on dislocation behavior in Ni during in-situ deformation experiment in HVEM. *Scr Metall* 9(5):499–504. [https://doi.org/10.1016/0036-9748\(75\)90340-3](https://doi.org/10.1016/0036-9748(75)90340-3)
24. Cherns D, Hutchison JL, Jenkins ML, Hirsch PB, White S (1980) Electron irradiation induced vitrification at dislocations in quartz. *Nature* 287(5780):314–316. <https://doi.org/10.1038/287314a0>
25. Fisher SB, Williams KR (1972) Irradiation enhanced precipitation in stainless steel. *Phil Mag* 25(2):371–380. <https://doi.org/10.1080/14786437208226811>
26. Yagi K, Honjo G (1964) Transmission electron microscopy of sodium chloride films prepared by electron beam flashing thinning technique. *J Phys Soc Jpn* 19(10):1892–1905. <https://doi.org/10.1143/jpsj.19.1892>
27. Matsui S, Ichihashi T (1988) In situ observation on electron-beam-induced chemical vapor deposition by transmission electron microscopy. *Appl Phys Lett* 53(10):842–844. <https://doi.org/10.1063/1.100089>
28. Golberg D, Bando Y, Stéphan O, Kurashima K (1998) Octahedral boron nitride fullerenes formed by electron beam irradiation. *Appl Phys Lett* 73(17):2441–2443. <https://doi.org/10.1063/1.122475>
29. Furuya K (2008) Nanofabrication by advanced electron microscopy using intense and focused beam. *Sci Technol Adv Mater* 9(1):014110. <https://doi.org/10.1088/1468-6996/9/1/014110>
30. Krasheninnikov AV, Nordlund K (2010) Ion and electron irradiation-induced effects in nanostructured materials. *J Appl Phys* 107(7):071301. <https://doi.org/10.1063/1.3318261>
31. Banhart F, Ajayan PM (1996) Carbon onions as nanoscopic pressure cells for diamond formation. *Nature* 382(6590):433–435. <https://doi.org/10.1038/382433a0>
32. Tripathi M, Mittelberger A, Pike NA, Mangler C, Meyer JC, Verstraete MJ, Kotakoski J, Susi T (2018) Electron-Beam manipulation of silicon dopants in graphene. *Nano Lett* 18(8):5319–5323. <https://doi.org/10.1021/acs.nanolett.8b02406>
33. Schneider NM, Norton MM, Mendel BJ, Grogan JM, Ross FM, Bau HH (2014) Electron–water interactions and implications for liquid cell electron microscopy. *The Journal of Physical Chemistry C* 118(38):22373–22382. <https://doi.org/10.1021/jp507400n>
34. Williams DB, Carter CB (2009) *Transmission Electron Microscopy*, 2nd edn. Springer, New York
35. Banhart F (1999) Irradiation effects in carbon nanostructures. *Rep Prog Phys* 62(8):1181–1221. <https://doi.org/10.1088/0034-4885/62/8/201>
36. McKinley WA, Feshbach H (1948) The Coulomb scattering of relativistic electrons by nuclei. *Phys Rev* 74(12):1759. <https://doi.org/10.1103/PhysRev.74.1759>
37. Meyer JC, Eder F, Kurasch S, Skakalova V, Kotakoski J, Park HJ, Roth S, Chuvilin A, Eychens S, Benner G, Krasheninnikov AV, Kaiser U (2012) Accurate measurement of electron beam induced displacement cross sections for single-layer graphene. *Phys Rev Lett* 108(19):196102. <https://doi.org/10.1103/PhysRevLett.108.196102>
38. Egerton RF, McLeod R, Wang F, Malac M (2010) Basic questions related to electron-induced sputtering in the TEM. *Ultramicroscopy* 110(8):991–997. <https://doi.org/10.1016/j.ultramic.2009.11.003>
39. Egerton RF (2013) Beam-Induced motion of adatoms in the transmission electron microscope. *Microsc Microanal* 19(02):479–486. <https://doi.org/10.1017/S1431927612014274>
40. Cazaux J (1995) Correlations between ionization radiation damage and charging effects in transmission electron microscopy. *Ultramicroscopy* 60(3):411–425. [https://doi.org/10.1016/0304-3991\(95\)00077-1](https://doi.org/10.1016/0304-3991(95)00077-1)

41. Hobbs LW (1990) Murphy's law and the uncertainty of electron probes. *Scanning Microsc Suppl* 4:171–183
42. McCartney MR, Crozier PA, Weiss JK, Smith DJ (1991) Electron-beam-induced reactions at transition-metal oxide surfaces. *Vacuum* 42(4):301–308. [https://doi.org/10.1016/0042-207X\(91\)90042-H](https://doi.org/10.1016/0042-207X(91)90042-H)
43. Henderson R, Glaeser RM (1985) Quantitative analysis of image contrast in electron micrographs of beam-sensitive crystals. *Ultramicroscopy* 16(2):139–150. [https://doi.org/10.1016/0304-3991\(85\)90069-5](https://doi.org/10.1016/0304-3991(85)90069-5)
44. Isaacson M, Johnson D, Crewe A (1973) Electron beam excitation and damage of biological molecules; its implications for specimen damage in electron microscopy. *Radiat Res* 55(2):205–224. <https://doi.org/10.2307/3573678>
45. Woehl T, Abellan P (2017) Defining the radiation chemistry during liquid cell electron microscopy to enable visualization of nanomaterial growth and degradation dynamics. *J Microsc* 265(2):135–147. <https://doi.org/10.1111/jmi.12508>
46. Fisher S (1970) On the temperature rise in electron irradiated foils. *Radiat Eff* 5(2):239–243. <https://doi.org/10.1080/00337577008235027>
47. van Dorp WF, Hagen CW (2008) A critical literature review of focused electron beam induced deposition. *J Appl Phys* 104(8):081301. <https://doi.org/10.1063/1.2977587>
48. Xu T, Xie X, Yin K, Sun J, He L, Sun L (2014) Controllable atomic-scale sculpting and deposition of carbon nanostructures on graphene. *Small* 10(9):1724–1728. <https://doi.org/10.1002/sml.201303377>
49. Meyer JC, Girit CO, Crommie MF, Zettl A (2008) Hydrocarbon lithography on graphene membranes. *Appl Phys Lett* 92(12):123110–123113. <https://doi.org/10.1063/1.2901147>
50. He L, Xu T, Sun J, Yin K, Xie X, Ding L, Xiu H, Sun L (2012) Investment casting of carbon tubular structures. *Carbon* 50(8):2845–2852. <https://doi.org/10.1016/j.carbon.2012.02.051>
51. He L-B, Zhang L, Tan X-D, Tang L-P, Xu T, Zhou Y-L, Ren Z-Y, Wang Y, Teng C-Y, Sun L-T, Nie J-F (2017) Surface energy and surface stability of ag nanocrystals at elevated temperatures and their dominance in sublimation-induced shape evolution. *Small* 13(27):1700743. <https://doi.org/10.1002/sml.201700743>
52. Pashley DW, Stowell MJ, Jacobs MH, Law TJ (1964) The growth and structure of gold and silver deposits formed by evaporation inside an electron microscope. *Phil Mag* 10(103):127–158. <https://doi.org/10.1080/14786436408224212>
53. Komsa H-P, Kotakoski J, Kurasch S, Lehtinen O, Kaiser U, Krashennnikov AV (2012) Two-dimensional transition metal dichalcogenides under electron irradiation: defect production and doping. *Phys Rev Lett* 109(3):035503. <https://doi.org/10.1103/PhysRevLett.109.035503>
54. Russo CJ, Golovchenko JA (2012) Atom-by-atom nucleation and growth of graphene nanopores. *Proc Natl Acad Sci USA* 109(16):5953–5957. <https://doi.org/10.1073/pnas.1119827109>
55. Pham T, Gibb AL, Li Z, Gilbert SM, Song C, Louie SG, Zettl A (2016) Formation and dynamics of electron-irradiation-induced defects in hexagonal boron nitride at elevated temperatures. *Nano Lett* 16(11):7142–7147. <https://doi.org/10.1021/acs.nanolett.6b03442>
56. Lehtinen O, Kurasch S, Krashennnikov AV, Kaiser U (2013) Atomic scale study of the life cycle of a dislocation in graphene from birth to annihilation. *Nat Commun* 4:2098. <https://doi.org/10.1038/ncomms3098>
57. Komsa H-P, Kurasch S, Lehtinen O, Kaiser U, Krashennnikov AV (2013) From point to extended defects in two-dimensional MoS₂: Evolution of atomic structure under electron irradiation. *Phys Rev B* 88(3):035301. <https://doi.org/10.1103/PhysRevB.88.035301>
58. Cretu O, Lin Y-C, Suenaga K (2014) Evidence for active atomic defects in monolayer hexagonal boron nitride—a new mechanism of plasticity in 2D materials. *Nano Lett* 14(2):1064–1068. <https://doi.org/10.1021/nl404735w>
59. Robertson AW, Montanari B, He K, Kim J, Allen CS, Wu YA, Olivier J, Neethling J, Harrison N, Kirkland AI, Warner JH (2013) Dynamics of single fe atoms in graphene vacancies. *Nano Lett* 13(4):1468–1475. <https://doi.org/10.1021/nl304495v>

60. Lin Y-C, Teng P-Y, Yeh C-H, Koshino M, Chiu P-W, Suenaga K (2015) Structural and chemical dynamics of pyridinic-nitrogen defects in graphene. *Nano Lett* 15(11):7408–7413. <https://doi.org/10.1021/acs.nanolett.5b02831>
61. Susi T, Kotakoski J, Kepaptsoglou D, Mangler C, Lovejoy TC, Krivanek OL, Zan R, Bangert U, Ayala P, Meyer JC, Ramasse Q (2014) Silicon-Carbon bond inversions driven by 60-keV electrons in graphene. *Phys Rev Lett* 113(11):115501. <https://doi.org/10.1103/PhysRevLett.113.115501>
62. Yang Z, Yin L, Lee J, Ren W, Cheng H-M, Ye H, Pantelides ST, Pennycook SJ, Chisholm MF (2014) Direct observation of atomic dynamics and silicon doping at a topological defect in graphene. *Angew Chem Int Ed* 53(34):8908–8912. <https://doi.org/10.1002/anie.201403382>
63. Meyer JC, Kisielowski C, Erni R, Rossell MD, Crommie MF, Zettl A (2008) Direct imaging of lattice atoms and topological defects in graphene membranes. *Nano Lett* 8(11):3582–3586. <https://doi.org/10.1021/nl801386m>
64. Li L, Reich S, Robertson J (2005) Defect energies of graphite: Density-functional calculations. *Phys Rev B* 72(18):184109. <https://doi.org/10.1103/PhysRevB.72.184109>
65. Kurasch S, Kotakoski J, Lehtinen O, Skákalová V, Smet J, Krill CE, Krashennnikov AV, Kaiser U (2012) Atom-by-Atom observation of grain boundary migration in graphene. *Nano Lett* 12(6):3168–3173. <https://doi.org/10.1021/nl301141g>
66. Lin Y-C, Björkman T, Komsa H-P, Teng P-Y, Yeh C-H, Huang F-S, Lin K-H, Jadcak J, Huang Y-S, Chiu P-W (2015) Three-fold rotational defects in two-dimensional transition metal dichalcogenides. *Nat Commun* 6:6736. <https://doi.org/10.1038/ncomms7736>
67. Kotakoski J, Krashennnikov A, Kaiser U, Meyer J (2011) From point defects in graphene to two-dimensional amorphous carbon. *Phys Rev Lett* 106(10):105505. <https://doi.org/10.1103/PhysRevLett.106.105505>
68. Chen Q, Robertson AW, He K, Gong C, Yoon E, Lee G-D, Warner JH (2015) Atomic level distributed strain within graphene divacancies from bond rotations. *ACS Nano* 9(8):8599–8608. <https://doi.org/10.1021/acs.nano.5b03801>
69. Robertson AW, Lee G-D, He K, Yoon E, Kirkland AI, Warner JH (2014) Stability and dynamics of the tetravacancy in graphene. *Nano Lett* 14(3):1634–1642. <https://doi.org/10.1021/nl500119p>
70. Börrnert F, Avdoshenko SM, Bachmatyuk A, Ibrahim I, Büchner B, Cuniberti G, Rummeli MH (2012) Amorphous carbon under 80 kV electron irradiation: a means to make or break Graphene. *Adv Mater* 24(41):5630–5635. <https://doi.org/10.1002/adma.201202173>
71. Chuvilin A, Kaiser U, Bichoutskaia E, Besley NA, Khlobystov AN (2010) Direct transformation of graphene to fullerene. *Nat Chem* 2(6):450–453. <https://doi.org/10.1038/nchem.644>
72. Banhart F, Füller T, Redlich P, Ajayan PM (1997) The formation, annealing and self-compression of carbon onions under electron irradiation. *Chem Phys Lett* 269(3):349–355. [https://doi.org/10.1016/S0009-2614\(97\)00269-8](https://doi.org/10.1016/S0009-2614(97)00269-8)
73. Sun L, Rodriguez-Manzo J, Banhart F (2006) Elastic deformation of nanometer-sized metal crystals in graphitic shells. *Appl Phys Lett* 89(26):263104. <https://doi.org/10.1063/1.2403898>
74. Hiraki J, Mori H, Taguchi E, Yasuda H, Kinoshita H, Ohmae N (2005) Transformation of diamond nanoparticles into onion-like carbon by electron irradiation studied directly inside an ultrahigh-vacuum transmission electron microscope. *Appl Phys Lett* 86(22):223101. <https://doi.org/10.1063/1.1935047>
75. Lyutovich Y, Banhart F (1999) Low-pressure transformation of graphite to diamond under irradiation. *Appl Phys Lett* 74(5):659–660. <https://doi.org/10.1063/1.122978>
76. Zheng H, Rivest JB, Miller TA, Sadtler B, Lindenberg A, Toney MF, Wang L-W, Kisielowski C, Alivisatos AP (2011) Observation of transient structural-transformation dynamics in a Cu₂S nanorod. *Science* 333(6039):206–209. <https://doi.org/10.1126/science.1204713>
77. Lin Y-C, Dumcenco DO, Huang Y-S, Suenaga K (2014) Atomic mechanism of the semiconducting-to-metallic phase transition in single-layered MoS₂. *Nat Nanotechnol* 9(5):391–396. <https://doi.org/10.1038/nnano.2014.64>

78. Peng H, Meng W, Zheng H, Wei Y, Sheng H, Liu H, Li L, Wen G, Jia S, Li L, Wang J (2019) Probing the crystal and electronic structures of molybdenum oxide in redox process: implications for energy applications. *ACS Appl Energy Mater* 2(10):7709–7716. <https://doi.org/10.1021/acsaem.9b01747>
79. Zhao P, Cao F, Jia S, Zheng H, Wang J, Zhao D (2017) Phase transition of MoO₃ nanobelts under external fields. *J Chin Electron Microsc Soc* 36(5):429–435. <https://doi.org/10.3969/j.issn.1000-6281.2017.05.002>
80. Wang Y, Wen G, Li L, Liu H, Peng H, Jiang R, Zhuang Y, Jia S, Zheng H, Wang J (2019) Electron-beam-induced Growth and Reduction of WO_{2.72} Single Crystal. *J Chin Electron Microsc Soc* 38(6):600–607. <https://doi.org/10.3969/j.issn.1000-6281.2019.06.004>
81. Jia S, Li L, Zhao L, Zheng H, Zhao P, Guan X, Chen G, Wu J, Zhou S, Wang J (2018) Surface-dependent formation of Zn clusters in ZnO single crystals by electron irradiation. *Physical Review Materials* 2(6):060402. <https://doi.org/10.1103/PhysRevMaterials.2.060402>
82. Sutter E, Huang Y, Komsa HP, Ghorbani-Asl M, Krasheninnikov AV, Sutter P (2016) Electron-Beam induced transformations of layered Tin Dichalcogenides. *Nano Lett* 16(7):4410–4416. <https://doi.org/10.1021/acs.nanolett.6b01541>
83. Lin J, Zuluaga S, Yu P, Liu Z, Pantelides ST, Suenaga K (2017) Novel Pd₂Se₃ Two-Dimensional phase driven by interlayer fusion in layered PdSe₂. *Phys Rev Lett* 119(1):016101. <https://doi.org/10.1103/PhysRevLett.119.016101>
84. Zhang H, Wang W, Xu T, Xu F, Sun L (2020) Phase transformation at controlled locations in nanowires by in situ electron irradiation. *Nano Res* 13(7):1912–1919. <https://doi.org/10.1007/s12274-020-2711-2>
85. Cao F, Zheng H, Jia S, Bai X, Li L, Sheng H, Wu S, Han W, Li M, Wen G, Yu J, Wang J (2015) Atomistic observation of phase transitions in calcium sulfates under electron irradiation. *The Journal of Physical Chemistry C* 119(38):22244–22248. <https://doi.org/10.1021/acs.jpcc.5b07508>
86. Chen S, Zhang X, Zhao J, Zhang Y, Kong G, Li Q, Li N, Yu Y, Xu N, Zhang J, Liu K, Zhao Q, Cao J, Feng J, Li X, Qi J, Yu D, Li J, Gao P (2018) Atomic scale insights into structure instability and decomposition pathway of methylammonium lead iodide perovskite. *Nat Commun* 9(1):4807. <https://doi.org/10.1038/s41467-018-07177-y>
87. Wei X, Wang M-S, Bando Y, Golberg D (2011) Electron-Beam-Induced substitutional carbon doping of boron nitride nanosheets, nanoribbons, and nanotubes. *ACS Nano* 5(4):2916–2922. <https://doi.org/10.1021/nn103548r>
88. Sun L, Banhart F (2006) Graphitic onions as reaction cells on the nanoscale. *Appl Phys Lett* 88(19):193121. <https://doi.org/10.1063/1.2202106>
89. Sheng H, Zheng H, Jia S, Chan MK, Rajh T, Wang J, Wen J (2019) Atomistic manipulation of reversible oxidation and reduction in Ag with an electron beam. *Nanoscale* 11(22):10756–10762. <https://doi.org/10.1039/C8NR09525F>
90. Zheng H, Wu S, Sheng H, Liu C, Liu Y, Cao F, Zhou Z, Zhao X, Zhao D, Wang J (2014) Direct atomic-scale observation of layer-by-layer oxide growth during magnesium oxidation. *Appl Phys Lett* 104(14):141906. <https://doi.org/10.1063/1.4870832>
91. Cao F, Zheng H, Jia S, Liu H, Li L, Chen B, Liu X, Wu S, Sheng H, Xing R (2016) Atomistic observation of structural evolution during magnesium oxide growth. *J Phys Chem C* 120(47):26873–26878. <https://doi.org/10.1021/acs.jpcc.6b08833>
92. Meng S, Wu J, Zhao L, Zheng H, Jia S, Hu S, Meng W, Pu S, Zhao D, Wang J (2018) Atomistic insight into the redox reactions in Fe/Oxide Core-Shell nanoparticles. *Chem Mater* 30(20):7306–7312. <https://doi.org/10.1021/acs.chemmater.8b03679>
93. Su Q, Du G, Xu B (2014) In situ growth of In₂O₃ nanocrystals by electron irradiation in transmission electron microscope. *Mater Lett* 120:208–211. <https://doi.org/10.1016/j.matlet.2014.01.068>
94. Gonzalez-Martinez I, Bachmatiuk A, Bezugly V, Kunstmann J, Gemming T, Liu Z, Cuniberti G, Rummeli M (2016) Electron-beam induced synthesis of nanostructures: a review. *Nanoscale* 8(22):11340–11362. <https://doi.org/10.1039/C6NR01941B>

95. Du X-w, Takeguchi M, Tanaka M, Furuya K (2003) Formation of crystalline Si nanodots in SiO₂ films by electron irradiation. *Appl Phys Lett* 82(7):1108–1110. <https://doi.org/10.1063/1.1555691>
96. Yu K, Xu T, Wu X, Wang W, Zhang H, Zhang Q, Tang L, Sun L (2019) In Situ Observation of Crystalline Silicon Growth from SiO₂ at Atomic Scale. *Research* 2019:3289247. <https://doi.org/10.34133/2019/3289247>
97. Gonzalez-Martinez IG, Gorantla SM, Bachmatiuk A, Bezugly V, Zhao J, Gemming T, Kunstmann J, Jr E, Cuniberti G, Rummeli MH (2014) Room temperature in situ growth of B/BO x nanowires and BO x nanotubes. *Nano Lett* 14(2):799–805. <https://doi.org/10.1021/nl404147r>
98. Jia S, Hu S, Zheng H, Wei Y, Meng S, Sheng H, Liu H, Zhou S, Zhao D, Wang J (2018) Atomistic interface dynamics in Sn-Catalyzed growth of Wurtzite and Zinc-Blende ZnO nanowires. *Nano Lett* 18(7):4095–4099. <https://doi.org/10.1021/acs.nanolett.8b00420>
99. Edmondson MJ, Zhou W, Sieber S, Jones I, Gameson I, Anderson P, Edwards P (2001) Electron-Beam induced growth of bare silver nanowires from zeolite crystallites. *Adv Mater* 13(21):1608–1611. [https://doi.org/10.1002/1521-4095\(200111\)13:21%3C1608::AID-ADMA1608%3E3.0.CO;2-S](https://doi.org/10.1002/1521-4095(200111)13:21%3C1608::AID-ADMA1608%3E3.0.CO;2-S)
100. Rodríguez-Manzo JA, Terrones M, Terrones H, Kroto HW, Sun L, Banhart F (2007) In situ nucleation of carbon nanotubes by the injection of carbon atoms into metal particles. *Nat Nanotechnol* 2(5):307–311. <https://doi.org/10.1038/nnano.2007.107>
101. Sang X, Xie Y, Yilmaz DE, Lotfi R, Alhabeib M, Ostadhossein A, Anasori B, Sun W, Li X, Xiao K, Kent PRC, van Duin ACT, Gogotsi Y, Unocic RR (2018) In situ atomistic insight into the growth mechanisms of single layer 2D transition metal carbides. *Nat Commun* 9(1):2266. <https://doi.org/10.1038/s41467-018-04610-0>
102. Zheng H, Liu Y, Cao F, Wu S, Jia S, Cao A, Zhao D, Wang J (2013) Electron beam-assisted healing of nanopores in magnesium alloys. *Sci Rep* 3(1):1920. <https://doi.org/10.1038/srep01920>
103. Shen Y, Xu T, Tan X, He L, Yin K, Wan N, Sun L (2018) In Situ Repair of 2D chalcogenides under electron beam irradiation. *Adv Mater* 30(14):1705954. <https://doi.org/10.1002/adma.201705954>
104. Zhao J, Deng Q, Bachmatiuk A, Sandeep G, Popov A, Eckert J, Rummeli MH (2014) Free-Standing Single-Atom-Thick Iron membranes suspended in graphene pores. *Science* 343(6176):1228–1232. <https://doi.org/10.1126/science.1245273>
105. Yin K, Zhang YY, Zhou Y, Sun L, Chisholm MF, Pantelides ST, Zhou W (2017) Unsupported single-atom-thick copper oxide monolayers. *2D Materials* 4(1):011001. <https://doi.org/10.1088/2053-1583/4/1/011001>
106. Wan N, Xu J, Xu T, Matteo M, Sun L, Sun J, Zhou Y (2013) Surface energy guided sub-10 nm hierarchy structures fabrication by direct e-beam etching. *RSC Adv* 3(39):17860–17865. <https://doi.org/10.1039/c3ra42370k>
107. Shen Y, Xu T, Tan X, Sun J, He L, Yin K, Zhou Y, Banhart F, Sun L (2017) Electron beam etching of CaO crystals observed atom by atom. *Nano Lett* 17(8):5119–5125. <https://doi.org/10.1021/acs.nanolett.7b02498>
108. Tang L, He L, Zhang L, Yu K, Xu T, Zhang Q, Dong H, Zhu C, Sun L (2018) A novel domain-confined growth strategy for in situ controllable fabrication of individual hollow nanostructures. *Advanced Science* 5(5):1700213. <https://doi.org/10.1002/advs.201700213>
109. Wu S, Zheng H, Jia S, Sheng H, Cao F, Li L, Hu S, Zhao P, Zhao D, Wang J (2016) Three-dimensional structures of magnesium nanopores. *Nanotechnology* 27(12):125603. <https://doi.org/10.1088/0957-4484/27/12/125603>
110. Wu S, Cao F, Zheng H, Sheng H, Liu C, Liu Y, Zhao D, Wang J (2013) Fabrication of faceted nanopores in magnesium. *Appl Phys Lett* 103(24):243101. <https://doi.org/10.1063/1.4841515>
111. Xu T, Yin K, Xie X, He L, Wang B, Sun L (2012) Size-dependent evolution of graphene nanopores under thermal excitation. *Small* 8(22):3422–3426. <https://doi.org/10.1002/smll.201200979>
112. Kondo Y, Takayanagi K (1997) Gold nanobridge stabilized by surface structure. *Phys Rev Lett* 79(18):3455. <https://doi.org/10.1103/PhysRevLett.79.3455>

113. Kondo Y, Takayanagi K (2000) Synthesis and characterization of helical multi-shell gold nanowires. *Science* 289(5479):606–608. <https://doi.org/10.1126/science.289.5479.606>
114. Rodrigues V, Fuhrer T, Ugarte D (2000) Signature of atomic structure in the quantum conductance of gold nanowires. *Phys Rev Lett* 85(19):4124. <https://doi.org/10.1103/PhysRevLett.85.4124>
115. Rodrigues V, Bettini J, Rocha A, Rego LG, Ugarte D (2002) Quantum conductance in silver nanowires: Correlation between atomic structure and transport properties. *Phys Rev B* 65(15):153402. <https://doi.org/10.1103/PhysRevB.65.153402>
116. González JC, Rodrigues V, Bettini J, Rego LG, Rocha AR, Coura PZ, Dantas SO, Sato F, Galvão DS, Ugarte D (2004) Indication of unusual pentagonal structures in atomic-size Cu nanowires. *Phys Rev Lett* 93(12):126103. <https://doi.org/10.1103/PhysRevLett.93.126103>
117. Rodrigues V, Sato F, Galvão DS, Ugarte D (2007) Size limit of defect formation in pyramidal Pt nanocontacts. *Phys Rev Lett* 99(25):255501. <https://doi.org/10.1103/PhysRevLett.99.255501>
118. Jin C, Lan H, Peng L, Suenaga K, Iijima S (2009) Deriving carbon atomic chains from graphene. *Phys Rev Lett* 102(20):205501. <https://doi.org/10.1103/PhysRevLett.102.205501>
119. La Torre A, Botello-Mendez A, Baaziz W, Charlier JC, Banhart F (2015) Strain-induced metal–semiconductor transition observed in atomic carbon chains. *Nat Commun* 6:6636. <https://doi.org/10.1038/ncomms7636>
120. Lin Y-C, Morishita S, Koshino M, Yeh C-H, Teng P-Y, Chiu P-W, Sawada H, Suenaga K (2017) Unexpected huge dimerization ratio in one-dimensional carbon atomic chains. *Nano Lett* 17(1):494–500. <https://doi.org/10.1021/acs.nanolett.6b04534>
121. Cretu O, Komsa H-P, Lehtinen O, Algara-Siller G, Kaiser U, Suenaga K, Krasheninnikov AV (2014) Experimental observation of boron nitride chains. *ACS Nano* 8(12):11950–11957. <https://doi.org/10.1021/nn5046147>
122. Xiao Z, Qiao J, Lu W, Ye G, Chen X, Zhang Z, Ji W, Li J, Jin C (2017) Deriving phosphorus atomic chains from few-layer black phosphorus. *Nano Res* 10(7):2519–2526. <https://doi.org/10.1007/s12274-017-1456-z>
123. Liu X, Xu T, Wu X, Zhang Z, Yu J, Qiu H, Hong J-H, Jin C-H, Li J-X, Wang X-R, Sun L-T, Guo W (2013) Top-down fabrication of sub-nanometre semiconducting nanoribbons derived from molybdenum disulfide sheets. *Nat Commun* 4:1776. <https://doi.org/10.1038/ncomms2803>
124. Lin J, Cretu O, Zhou W, Suenaga K, Prasai D, Bolotin KI, Cuong NT, Otani M, Okada S, Lupini AR (2014) Flexible metallic nanowires with self-adaptive contacts to semiconducting transition-metal dichalcogenide monolayers. *Nat Nanotechnol* 9(6):436–442. <https://doi.org/10.1038/nnano.2014.81>
125. Lin J, Zhang Y, Zhou W, Pantelides ST (2016) Structural flexibility and alloying in ultrathin transition-metal chalcogenide nanowires. *ACS Nano* 10(2):2782–2790. <https://doi.org/10.1021/acsnano.5b07888>
126. Xu T, Zhou Y, Tan X, Yin K, He L, Banhart F, Sun L (2017) Creating the smallest BN nanotube from bilayer h-BN. *Adv Func Mater* 27(19):1603897. <https://doi.org/10.1002/adfm.201603897>
127. Li J, Banhart F (2005) The deformation of single, nanometer-sized metal crystals in graphitic shells. *Adv Mater* 17(12):1539–1542. <https://doi.org/10.1002/adma.200401917>
128. Banhart F, Charlier J-C, Ajayan P (2000) Dynamic behavior of nickel atoms in graphitic networks. *Phys Rev Lett* 84(4):686. <https://doi.org/10.1103/PhysRevLett.84.686>
129. Sun L, Krasheninnikov AV, Ahlgren T, Nordlund K, Banhart F (2008) Plastic deformation of single nanometer-sized crystals. *Phys Rev Lett* 101(15):156101. <https://doi.org/10.1103/PhysRevLett.101.156101>
130. Sun L, Banhart F, Krasheninnikov A, Rodriguez-Manzo J, Terrones M, Ajayan P (2006) Carbon nanotubes as high-pressure cylinders and nanoextruders. *Science* 312(5777):1199–1202. <https://doi.org/10.1126/science.1124594>
131. Lagos M, Sato F, Bettini J, Rodrigues V, Galvão DS, Ugarte D (2009) Observation of the smallest metal nanotube with a square cross-section. *Nat Nanotechnol* 4(3):149–152. <https://doi.org/10.1038/NNANO.2008.414>

132. Zhao P, Guan X, Zheng H, Jia S, Li L, Liu H, Zhao L, Sheng H, Meng W, Zhuang Y (2019) Surface-and strain-mediated reversible phase transformation in quantum-confined ZnO nanowires. *Phys Rev Lett* 123(21):216101. <https://doi.org/10.1103/PhysRevLett.123.216101>
133. Chen Q, Dwyer C, Sheng G, Zhu C, Li X, Zheng C, Zhu Y (2020) Imaging Beam-Sensitive materials by electron microscopy. *Adv Mater* 32:1907619. <https://doi.org/10.1002/adma.201907619>

Chapter 3

In-Situ Nanomechanical TEM



Li Zhong, Lihua Wang, Jiangwei Wang, Yang He, Xiaodong Han, Zhiwei Shan, and Xiuliang Ma

3.1 A Brief History of In Situ Nanomechanical TEM

Plastic deformation of materials usually proceeds via the nucleation, growth, and migration of various lattice defects. As the structure continuously evolves during deformation, conventional post-mortem TEM structural characterization only provides a glimpse on the structure after completion of deformation where critical intermediate structural insights concerning the deformation process are missing. The fast dynamics and short life span of some defects such as dislocations may not be observed via post-mortem TEM. In addition, possible structural artifacts [1]

L. Zhong

Key Laboratory of MEMS of Ministry of Education, SEU-FEI Nano-Pico Center, Southeast University, Nanjing 210096, China

L. Wang · X. Han (✉)

Beijing Key Lab of Microstructure and Properties of Advanced Materials, Beijing University of Technology, Beijing 100022, China
e-mail: xdhan@bjut.edu.cn

J. Wang

Center of Electron Microscopy and State Key Laboratory of Silicon Materials, School of Materials Science and Engineering, Zhejiang University, Hangzhou 310027, China

Y. He

Beijing Advanced Innovation Center for Materials Genome Engineering, Department of Materials Science and Engineering, University of Science and Technology, Beijing, Beijing 100083, China

Z. Shan

Center for Advancing Materials Performance From the Nanoscale (CAMP-Nano) & Hysitron Applied Research Center in China (HARCC), State Key Laboratory for Mechanical Behavior of Materials, Xi'an Jiaotong University, Xi'an 710049, China

X. Ma

Shenyang National Laboratory for Materials Science, Institute of Metal Research, Chinese Academy of Sciences, Shenyang 110016, China

(e.g. changes in dislocation structures and local structural relaxations) introduced during specimen preparation, such as the grinding/polishing process, may complicate structural characterization and shroud the intrinsic deformation mechanisms. As a result, interpretation of detailed deformation mechanisms has been heavily relying on theoretical studies such as molecular dynamics (MD) simulations [2, 3]. Although informative, MD simulations could suffer from validity issues arising from the inherent extremely high strain rates (10^7 – 10^9 /s) and the lack of inter-atomic potentials accuracy, and caution should be made when directly extrapolating MD simulation predictions to laboratory conditions. A fundamental understanding on the deformation mechanisms and the structure–property relationships relies on 1) direct evidence on the microstructural evolution (e.g. lattice defect dynamics) during deformation, and 2) quantitative measurements of mechanical properties, necessitating in situ mechanical characterization methods with exceptional spatial and good temporal resolutions that are beyond the capabilities of most characterization techniques. The rapidly developing in situ TEM, with the ability to resolve the atomic-scale structure and to operate on a time scale within a fraction of one second [4–10], opens up great opportunities to overcome the technical challenges.

The advent of in situ nanomechanical TEM can be dated back to the late 1950s and early 1960s [11, 12]. The classic tensile holders originate from the principle of straining-induced stretching of thin film samples actuated by an electric motor located at the end of the holder outside the TEM (to be discussed in detail in the next section). Despite the extreme versatility of this classic in situ TEM tensile straining technique, the tensile displacement resolution actuated by the electric motor is comparatively insufficient for dynamic observations at the atomic-scale. Recently, Zeptool Co. has substituted the conventional electric motor with a piezo-controlled actuator, which is expected to achieve much higher displacement resolution for revealing atomistic dynamics in nanomechanical testing.

To further resolve the atomistic dynamics during the tensile straining of materials, X. Han et al., developed several novel in situ nanomechanical approaches, as exemplified in Fig. 3.1 (to be discussed in detail in the following section). Figure 3.1a shows the Ni nanowires scattered on the colloidal thin film, which could be stretched or bent controllably by expansion or contraction of the film under the electron beam irradiation [13]. Figure 3.1b shows another example of a home-made tensile straining device compatible with a heating holder, which incorporates a pair of Cu-Ti bimetallic-strips onto the grid [14]. When the grid was slightly heated (~ 40 °C), the different apparent thermal expansions of Cu and Ti strips lead to an evident bending towards the Ti side, which readily induces a tensile straining in the sample attached between the bimetallic strips. It is noted that these two approaches well retain the double-tilt function of either the conventional holder or the heating holder, which benefits the high-resolution TEM observation of the deformation dynamics and the investigation of deformation behaviors at the atomic-scale [14].

In addition to different types of tensile straining methodologies, in situ TEM nanoindentation or compression technique has seen rapid development as well. The in situ TEM nanoindentation technique was first proposed in 1995 and first adopted in the investigation of deformation behaviors in Si single crystal in 1998

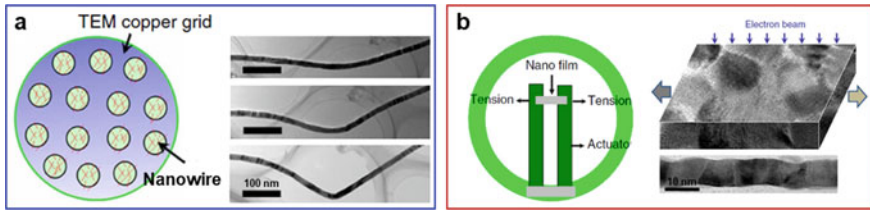


Fig. 3.1 **a** In situ straining of nanowires induced by colloidal thin film under electron beam irradiation (reproduced with permission from Ref. [13], Copyright 2013, Springer Nature). **b** Home-made testing device used for tensile testing of metallic thin film in TEM (reproduced with permission from Ref. [14], Copyright 2014, Springer Nature)

[15]. Figure 3.2a shows a commercialized in situ TEM nanoindentation holder PI-95 produced by Hysitron[®]. Taking advantage of the development in sample preparation via focused ion beam (FIB), more flexible designs of samples have been successfully incorporated into the in situ nanoindentation experiments. A. Minor and Z. Shan et al. have accomplished a series of pioneer works on the fabrication and in situ compression of nanopillars with controlled orientations [16–18], as exemplified in Fig. 3.2b, c. Different from the classic tensile holders, the nanoindenter is commonly equipped with a load sensor, which can supplement real-time load–displacement curves to structural evolutions (Fig. 3.2d), providing more quantitative data for in situ experiments and analysis. Furthermore, the researchers have developed a number of novel sample preparation methodologies that can transform the nanoindentation into tensile straining, while recording the real-time stress history. For example, the FIB-fabricated dog-bone samples combined with the reverse displacement of the diamond indenter can directly realize in situ tensile straining [19, 20]; in addition, several push-to-pull devices have been developed [21], which can transform the indentation into tensile straining via a built-in spring (Fig. 3.2e). When further coupled with environmental TEM (ETEM), this FIB fabrication-nanomechanical testing approach can be extended with in situ sample treatment under different gas environments (e.g., H₂, O₂ or CO₂) and/or temperature [22], which can be applied to explore the novel behaviors of materials under multi-field effects.

Following the emerging designs of preliminary micro-devices for in situ TEM holders, microelectromechanical system (MEMS) with more precise built-in actuators and load sensors has been introduced into in situ nanomechanical testing. Y. Zhu and H. Espinosa were among the first to develop the MEMS platform for in situ nanomechanical testing [23], and have been devoted to quantitative mechanical testing of a wide range of metallic nanowires [24, 25]. Recently, the thermal field has been successfully coupled to MEMS stage, realizing in situ nano-thermomechanical testing of metallic or semiconductor nanowires inside TEM [26, 27]. However, the current temperature level during the MEMS-nanomechanical testing is comparatively low (below 500 °C); meanwhile, other factors such as thermal gradient and inhomogeneous thermal expansion at higher temperatures in MEMS imposes further challenges to the observations of deformation dynamics at the atomic-scale. Yet, a

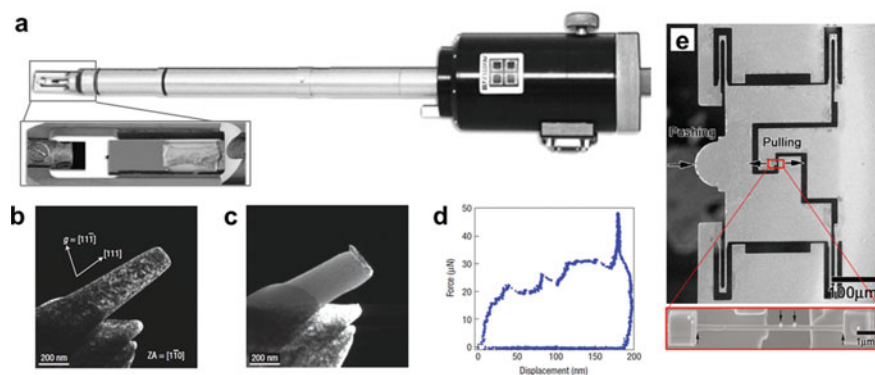


Fig. 3.2 **a** PI-95 indentation holder manufactured by Hysitron[®]. **b, c** A sub-micron Ni pillar fabricated by FIB and after in situ compression. **d** Real-time force–displacement feedback during the in situ test. (reproduced with permission from Ref. [18], Copyright 2007, Springer Nature) **e** Commercialized push-to-pull device (reproduced with permission from Ref. [21], Copyright 2011, American Chemical Society)

fundamental understanding of the atomistic behaviors of materials under high load and elevated temperature is vital for the development of superior structural materials for harsh service conditions. Recently, a team led by Z. Zhang and X. Han et al. have overcome a range of challenges (including those mentioned above) and successfully developed a novel MEMS-based high-temperature mechanical testing stage (Fig. 3.3, will also be introduced in detail in the next section), which allows in situ thermomechanical testing to be performed under temperatures approaching 1560 K and loads as high as 1 N [28]. This MEMS-based thermomechanical testing technique has been integrated into a commercialized TEM holder manufactured by BestronST Co., LTD.

To further incorporate nanomanipulation capabilities during the in situ TEM testing, a novel scanning tunneling microscopy (STM)-TEM holder has been developed (Fig. 3.4a), which consists of a static side for sample accommodation and a precisely-controlled probe for multifunctional nanomanipulation. The three-dimensional degree of freedom of the probe enables more flexible mechanical testing inside TEM. Using this type of in situ holder, A. Merkle et al. from Northwestern University reported direct observations of friction behaviors between tungsten tip and graphite/Au (110) film [29, 30], where a substantial amount of the sample can be directly transferred to the probe after friction. Meanwhile, this STM holder is compatible with other external stimuli such as an electric bias or pulse, which enables the investigation of deformation mechanisms under more complex environments. For example, J. Huang et al. took advantage of the piezo-controlled probe displacement and electric bias of this STM system, and reported the superplastic deformation of single-walled carbon nanotubes with a tensile elongation of $\sim 280\%$ at high temperatures [31]. For nanosized samples, this electric bias or pulse has also been used as an in situ approach for sample preparation, such as the vitrification of elemental metals

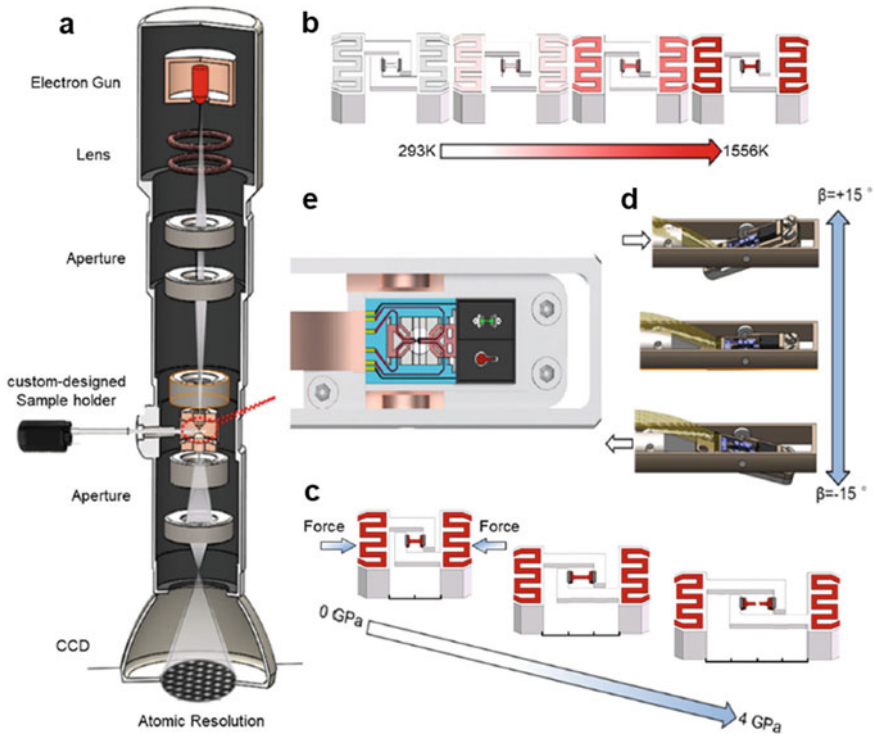


Fig. 3.3 MEMS for atomic-resolved high-temperature mechanical testing. **a** Specially designed thermomechanical test device inside the TEM column. **b** The temperature control module. **c** The in situ deformation module. **d** Custom-designed double-tilt sample holder containing the MEMS for high-temperature mechanical testing. **e** Details of the head of the sample holder (reproduced with permission from Ref. [28], Copyright 2021, Springer Nature)

or the growth of nanocrystals with specific orientations (to be discussed in detail in the following section). Recently, MEMS has even been introduced to the STM-TEM system (Fig. 3.4b), which could enable the in situ nanomechanical testing under a multi-field environment, such as coupled temperature and/or electric field.

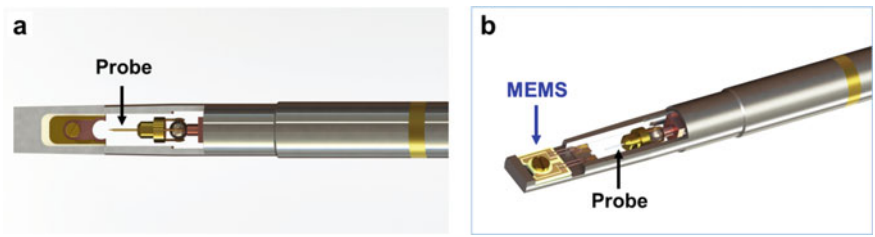


Fig. 3.4 **a** STM-TEM holder. **b** MEMS-STM-TEM holder

3.2 Current In Situ TEM-based Mechanical Testing Techniques

3.2.1 Thin Film Straining Technique

Figure 3.5a shows the most widely used tensile holder produced by Gatan Inc. In addition to in situ straining at room temperature, heating or cooling conditions can be attached to this type of holder as well, which are commonly realized by a built-in miniaturized furnace or an affiliated liquid N₂ reservoir outside the TEM, respectively. Custom-designed electron-transparent samples compatible with the in situ tensile holder (Fig. 3.5b) are glued to the substrate, which was then fixed to the holder by a pair of screws [32]. Figure 3.5c, d respectively provide typical examples of dislocation motion in CrMnFeCoNi high-entropy alloy (HEA) and grain growth ahead of the crack in Al film during the in situ TEM tensile tests [33, 34]. These dynamic findings significantly improved the understanding of plastic deformation mechanisms at the nanoscale, holding important implications to establishing the structure–property relations in materials.

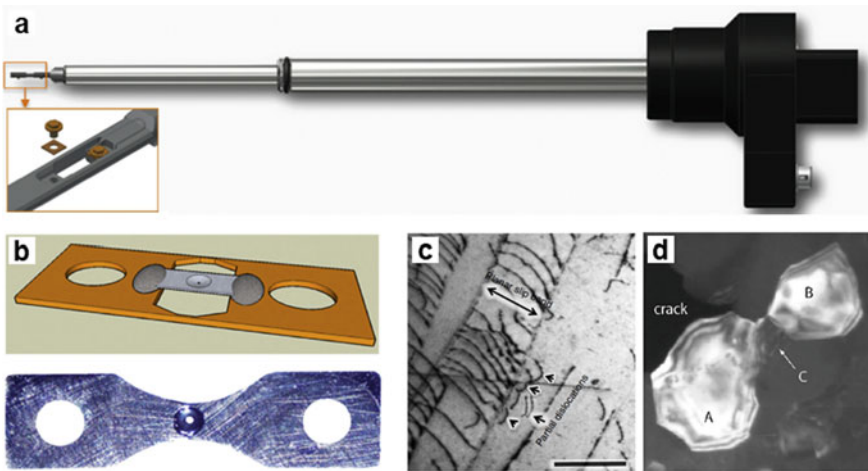


Fig. 3.5 **a** A classic tensile holder manufactured by Gatan[®] (model 654). **b** Schematic and image of custom-designed samples compatible with the tensile holder. (reproduced from Ref. [32], Copyright 2014, Elsevier Masson SAS) **c** Dislocation motion in CrMnFeCoNi HEA. (reproduced with permission from Ref. [33], Copyright 2015, Springer Nature) **d** Grain growth ahead of the crack in Al film (reproduced with permission from Ref. [34], Copyright 2008, Elsevier)

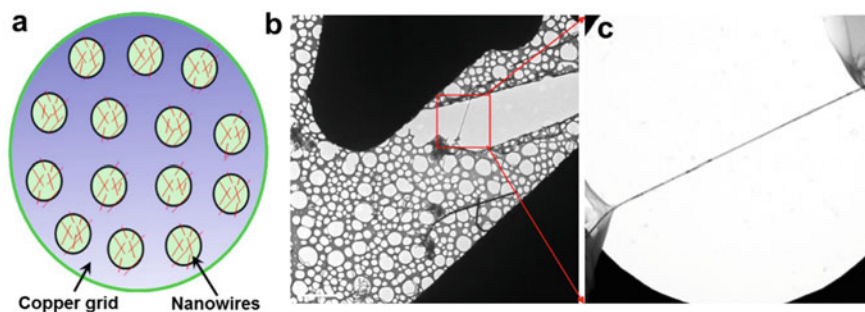


Fig. 3.6 **a** A schematic view shows that the Ni NWs were scattered on the previously broken TEM grid, which was covered by colloidal thin films. **b** An example shows that a single NW could then be deformed by tensile stress induced by the colloidal thin films under electron beam irradiation. **c** Enlarged TEM image taken from the red framed region of (b) (reproduced with permission from Ref. [13], Copyright 2013, Springer Nature)

3.2.2 TEM Grid Technique

Han et al. developed an alternative TEM grid technique [35–42] that can conduct bend or axial tensile experiments on individual nanowires (NWs). As shown in Fig. 3.6a, the NWs were scattered on a previously broken TEM grid, which was covered by colloidal thin films (CTF). Then, these NWs were randomly bridged on the prior broken collodion supporting film. With the heating/irradiating of electron beam, the collodion thin film was curved, which drives bending or tensile deformation of the NWs at relatively low strain rates of $\sim 10^{-4}$ /s (Fig. 3.6b, c). The advantage of this method is that no special TEM specimen holder or special mechanical tensile attachments are required, thus allowing large tilting angles along two orthogonal directions ($\pm 20^\circ$). This is extremely helpful for finding optional viewing directions, so that structure evolution of NWs during deformation can be revealed at atomic-scale resolution.

3.2.3 Thermal-Bimetallic-Based Technique

Based on the thermal bimetallic technique [43], Han et al. developed a novel in situ controllable tensile testing device for TEM. This technique can slowly and gently deform the testing samples while retaining the double-tilt capability for in situ atomic-scale observations [14, 39, 44]. This method can also study regular TEM samples prepared by FIB fabrication [45–48]. The in situ deformation device was fabricated by bimetallic-strips. The bimetallic strip is made of two materials with a large discrepancy in their thermal expansion coefficients, so that a significant deflection at relatively low operation temperatures can be achieved. As shown in Fig. 3.7a, c, operated under optical microscope, the thin films can be attached on the surface of the

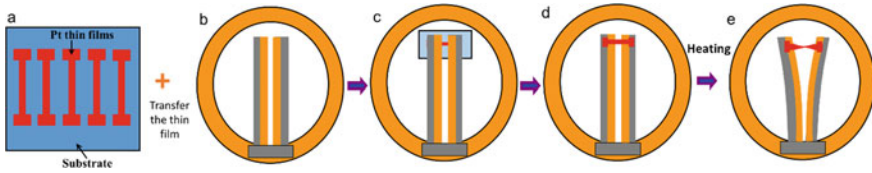


Fig. 3.7 **a** Nanocrystalline thin films were sputtering deposited using magnetron sputtering techniques. **b** and **c**, make the axial direction of the bimetallic-strips perpendicular to the axial direction of the thin film strip, then using epoxy-resin attached on the surface of the extensor. **d** Etching away the substrate in the water, free standing bimetallic-strips together with nanomaterials samples are released from the NaCl substrate. **e** A significant deflection can be achieved under heating conditions

bimetallic extensor (using epoxy-resin) in an almost ideal geometrical configuration. Etching away substrate, free standing bimetallic-strips together with thin film tensile samples are released (Fig. 3.7d). Then, the bimetallic-strips with the attached thin films, together with Heating TEM specimen holders were loaded in the TEM. The in situ uniaxial tensile deformation can be realized by increasing the temperature of the TEM heat stage (Fig. 3.7e). With this device, the specimen could be tilted along two orthogonal directions by large angles ($\pm 20^\circ$), which is essential for atomically resolved imaging. Unlike the case in the grid technique, the strain rate here is controllable in the range from 10^{-2} to 10^{-5} /s. Because the bimetallic were fixed on the Cu-ring grid with superglue, the operation temperature was usually below $\sim 200^\circ\text{C}$ in order to avoid superglue evaporation. Thus, this method is only suitable for low temperature in situ deformation.

3.2.4 MEMS-Based Techniques

MEMS-based platforms have been widely used in nanomechanical testing, owing to their capabilities to precisely control the deformation process and quantitative measurements of the displacement and forces. In specific, the input electrical power drives the thermal actuator, which serves to apply a stress on nanowire samples; meanwhile, the change in capacitance directly returns a real-time feedback of displacement or strain [23]. In addition, multi-fields such as electric and thermal fields can be readily integrated into the MEMS platform, opening up opportunities for a more comprehensive understanding on the mechanical properties. Recently, Han's group developed a method that enables in situ observation of the atomic-scale deformation process of nanomaterials at high-temperature [28]. The advantage is that this method allows in situ observation of the atomic-scale deformation process of nanomaterials from low to high temperatures (300 K–1500 K). Figure 3.8a shows the custom-designed in situ thermomechanical TEM sample holder. This device contains two essential units, one for temperature control and the other for applying deformation. Heating of the sample was achieved using a built-in micro-heater controlled by a MEMS chip. The deformation was driven by a lead zirconate titanate (PZT) actuator under

displacement control. The MEMS heating chip and the miniature PZT actuator were built on a miniature stage to form a thermomechanical integrated stage (TMIS), as shown in Fig. 3.8b. The TMIS was fixed on a double-tilt sample holder. Figure 3.8c and 3.8d show an SEM image of the MEMS heating chip. The stretched sample is lift-out from a bulk sample with predetermined crystal orientation and accurately transferred to the push-to-pull unit (the two “L” shaped sample mounting arms) in FIB. Then, these units were loaded in the double-tilt sample. This holder can tilt the sample about the x and y axes for up to $\pm 15^\circ$. This capability is essential to allow good atomic-scale resolution, which requires precise alignment of the electron beam to a low index zone axis of the sample during thermomechanical testing. After the sample is loaded, the displacement was applied using a miniature PZT actuator. The displacement was controlled (but not measured) by controlling the applied voltage to the actuator based on a calibration. The PZT actuator was able to provide a full displacement range of $4 \mu\text{m}$ with a step size of 0.1 nm (corresponding to a strain resolution of $\sim 10^{-4}$ relative to the sample size used), a maximum load on the order of 1 N (corresponding to a maximum stress of $\sim 4 \text{ GPa}$ for the sample size used) with a 1 nN resolution. The accuracy of displacement control by the PZT actuator is 0.1 nm , for a length of 1000 nm of the sample, the corresponding strain accuracy can be about 0.01% .

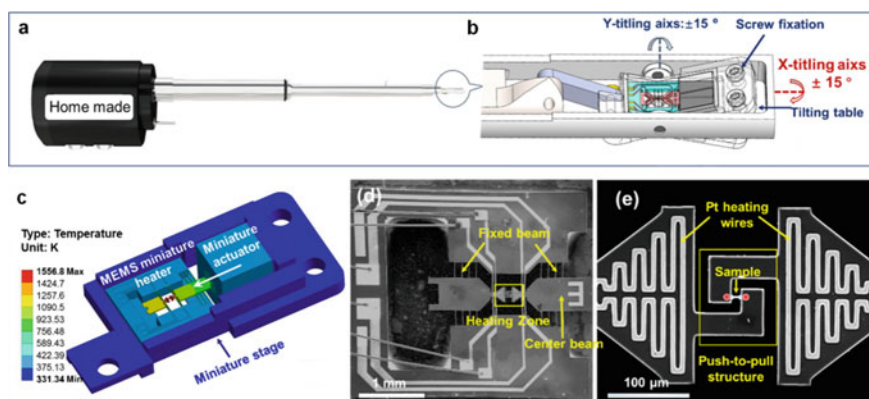


Fig. 3.8 A custom-designed in situ thermomechanical TEM sample holder. **a** The custom-designed in situ thermomechanical TEM sample holder. **b** Schematic diagram of the front end of the sample holder. The thermomechanical integrated stage (TMIS) is fixed on the tilting table of the sample holder. The TMIS allows the miniature actuator and the MEMS miniature heater to tilt with the sample at the same time. **c** ANSYS simulation of temperature distribution in the TMIS at 1556 K . **d** SEM image of the MEMS miniature heater. **e** SEM image of heating zone and push-to-pull structure of the MEMS chip (reproduced with permission from Ref. [28], Copyright 2021, Springer Nature)

3.2.5 Sequential Fabrication-Testing Technique

Based on the STM-TEM holder, a sequential in situ fabrication and nanomechanical testing methodology has been developed, providing an ideal platform for atomistic insights into the deformation behaviors. The experimental setup for in situ nanofabrication is shown in Fig. 3.9a. In a typical experiment, two metal rods (with a diameter of approximately 0.25 mm) were fractured to obtain a fresh surface with numerous nanoscale tips (Fig. 3.9b), which were loaded onto the static and probe sides of the holder, respectively. Then, the metal rod on the probe side was actuated to contact with the rod on the static side of the holder (Fig. 3.9c). Upon contact, the nanoscale metal tips (e.g., Au) can be cold welded together via mechanically assisted surface atom diffusion [49]. To further enhance the weldability, a voltage potential of approximately -1.5 V can be pre-applied on the nanoscale tip on the probe side before nanowelding [50, 51], producing a metallic nanocrystal or nanowire with designed orientations inside TEM (see an example in Fig. 3.9d). In addition to single crystals, nanoscale bicrystals containing different grain boundary (GB) structures can be produced as well (Fig. 3.9e), taking advantage of the misorientations between nanoscale tips on both sides [52]. After the nanowelding process, in situ nanomechanical testing including tension/compression, shear or cyclic loading, can be instantly carried out via the precise displacement control of the probe.

Besides a pre-applied electric bias, an electric pulse can also be introduced into the nanofabrication process via a pulse generator integrated with the STM-TEM system. Due to the higher energy density associated with the electric pulse, a melting zone at the nanotip contact can be created, followed by ultrafast quenching (with an unprecedentedly high liquid quenching rate of $\sim 10^{14}$ K·s⁻¹) via rapid heat dissipation through the bulk substrates. Using this experimental approach, L. Zhong et al. [53] reported the in situ vitrification of monatomic metallic liquids, where the melts of pure refractory body-centered cubic (BCC) metals, such as liquid Ta and V, were successfully vitrified to form metallic glasses suitable for property interrogations

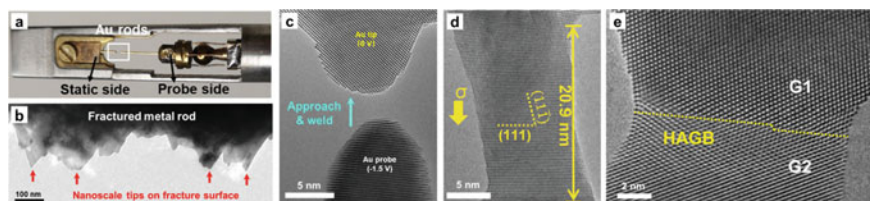


Fig. 3.9 **a** Set-up for nanofabrication. **b** Numerous nanoscale tips at the fracture surface of the metal rod. **c** The probe with an electrical bias was propelled by a piezo-controlled actuator to approach the Au tip on the static side. **d** Nanoscale single crystal with controlled orientation. **e** Nanoscale bicrystal containing a HAGB. **a**, **c** and **e**, reproduced with permission from Ref. [52], Copyright 2019, Springer Nature; **d**, reproduced with permission from Ref. [51], Copyright 2018, John Wiley and Sons

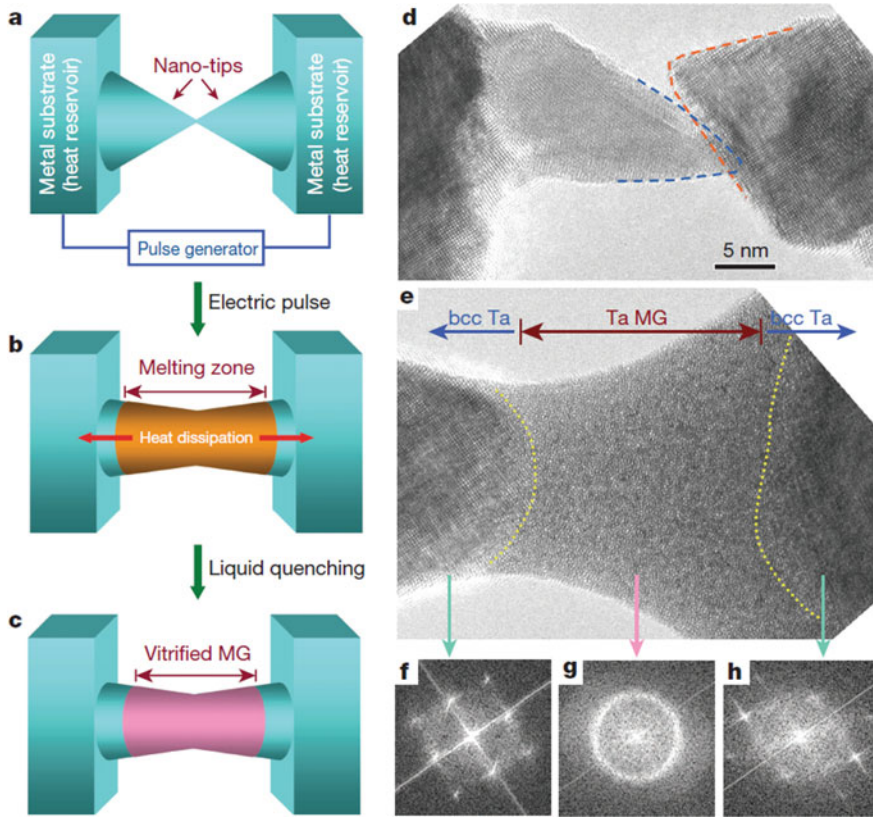


Fig. 3.10 a, c Illustration of in situ ultrafast liquid quenching inside TEM. d High-resolution TEM images showing two contacting Ta nano-tips. e Ta MG formed after the application of a 0.8 V, 3.6 ns electric pulse. f, h Fast Fourier transform patterns confirming a fully vitrified region bounded by two crystalline substrates (reproduced with permission from Ref. [53], Copyright 2014, SpringerNature)

(Fig. 3.10). The above-mentioned sequential fabrication-testing technique can minimize possible surface contamination of the testing specimen. Given the significant specific surface areas associated with nanoscale samples, this advantage can improve the accuracy of the nanomechanical testing results.

3.3 Typical Applications

Nanostructured materials [54–60] can usually sustain larger elastic strains than conventional materials, indicating their fundamental dislocation processes that initiate plastic flow is different from their conventional bulk counterparts. Revealing the atomic-scale deformation mechanisms of nanomaterials used to be a formidable

task due to technical difficulties. Fortunately, by taking advantage of the development of in situ nanomechanical testing techniques, significant achievements have been made in understanding the deformation mechanisms of various nanostructured materials.

3.3.1 *Deformation of Metallic Nanowires*

One dimensional nanomaterials resemble miniaturized standard mechanical testing samples, and are thus ideal for performing nanomechanical testing, wherein many unique and novel deformation mechanisms have been unveiled. Using the in situ nanowelding methodology via an electric bias or pulse, nanoscale metals including face-centered cubic (FCC), BCC and hexagonal close packed (HCP) crystal structures with specific orientations can be produced; subsequent in situ tensile testing enabled by the STM-TEM holder unambiguously revealed a range of the atomistic deformation behaviors in nanoscale metals, which exhibits marked discrepancies compared with bulk counterparts. Taking nanoscale Au crystals as an example, Zheng et al. [50] have clarified the surface-dominated plastic deformation in nanosized Au crystals (Fig. 3.11a, b), which is in sharp contrast to the conventional dislocation multiplication from Frank-Read sources in bulk materials. Due to this surface-dominated heterogeneous (partial) dislocation nucleation mechanism, a new kind of stacking fault tetrahedra formed via the interaction and cross-slip of partial dislocations has been reported (Fig. 3.11c, d), which differs from the classic vacancy-originated formation mechanism [61]. Further in situ experiments have demonstrated that the crystal slips can in turn activate surface diffusional creep in Ag nanocrystals at room temperature (Fig. 3.11e), leading to super-elongation [62]. This surface diffusion-mediated plasticity is consistent with the liquid-like Coble pseudoelasticity of sub-10 nm Ag nanoparticles in tension–compression loading cycles at room temperature [63]. However, when the Ag nanowire diameter is further reduced to sub-5 nm, the combined slip and surface diffusion tend to accelerate the reduction of nanowire diameter under tensile straining, leading to fracture with relatively small homogeneous elongation [64]. In fact, such surface diffusion-mediated plastic deformation is not limited to nanocrystals, which readily changes the crack growth dynamics in nanocrystalline metals, leading to either void formation ahead of the crack or substantial crack blunt [65, 66].

In addition to nanoscale single crystals, in situ STM nanomechanical testing provides an ideal platform for systematic investigation of the deformation behaviors of nanotwinned metals, where a near-ideal theoretical strength has been revealed in nanotwinned Au nanowires with ultrahigh twin density (twin boundary (TB) spacing < 2.8 nm) [67]. When the twin thickness is smaller than 4 atom layers, the transverse dislocation slip intersecting the TB abruptly changes from dislocation transmission on conventional {111} slip planes to an unusual (100) slip inside the twin lamella [68].

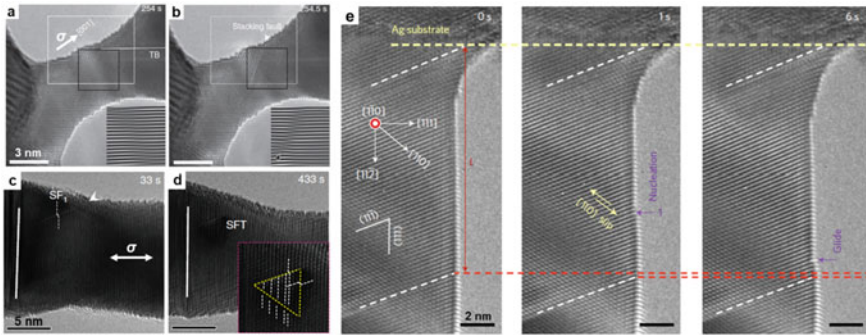


Fig. 3.11 Atomistic deformation mechanisms in FCC metallic nanocrystals. **a, b** A partial dislocation nucleated from the surface of Au nanocrystal (reproduced with permission from Ref. [50], Copyright 2010, Springer Nature). **c, d** Formation of a stacking fault tetrahedra via the interaction and cross-slip of partial dislocations in Au nanocrystal (reproduced with permission from Ref. [61], Copyright 2013, Springer Nature). **e** Slip-activated surface diffusional creep in Ag nanocrystals at room temperature (reproduced with permission from Ref. [62], Copyright 2015, Springer Nature)

Compared with FCC metals, the deformation mechanism in BCC metals, especially twinning, has long been controversial, due to the lack of mechanical testing with precisely-controlled crystallographic orientations and the incompatible stress states compared with theoretical predictions. These challenges can be readily overcome by the in situ nanomechanical testing with STM-TEM holder. For example, Wang et al. reported the first direct observation of deformation twinning in W nanocrystals with diameters below 20 nm during in situ compression along the $\langle 110 \rangle$ direction (Fig. 3.12a), which nucleate from either the free surface or GB [69]. Statistical investigations further revealed an evident orientation and size dependence of the competition between deformation twinning and dislocation-dominated plasticity, in which twinning is favored in smaller samples under maximum Schmid factor. Geometric analysis further suggests an anti-twinning mechanism under the reversed loading, e.g., uniaxial tensile straining along the $\langle 110 \rangle$ direction, where a unit slip on the (112) plane with a Burgers vector of $1/3[1\bar{1}1]$, instead of $1/6[\bar{1}11]$, is required. Apparently, a much higher resistance is associated with this anti-twinning route, which has been deemed impossible. By conducting in situ TEM nanomechanical testing, such unexpected anti-twinning mechanism has been unambiguously resolved in W nanowire with a diameter below 20 nm (Fig. 3.12b), due to the ultrahigh stress in these nanosized crystals [70]. In Nb nanowires, however, consecutively nucleated multiple reorientation processes have been reported [71], which proceeded sequentially via stress-activated phase transformation (BCC–FCC–BCC), deformation twinning and slip-induced crystal rotation, leading to a remarkable superplastic elongation of more than 269% (Fig. 3.12c).

The TEM grid technique has been used for different metallic NWs [13, 41, 42, 48, 72]. Figure 3.13 shows the atomic-scale structure evolution process in a bent strained Ni NW [13]. The atomic-scale image shows that the inter-planar angle (α)

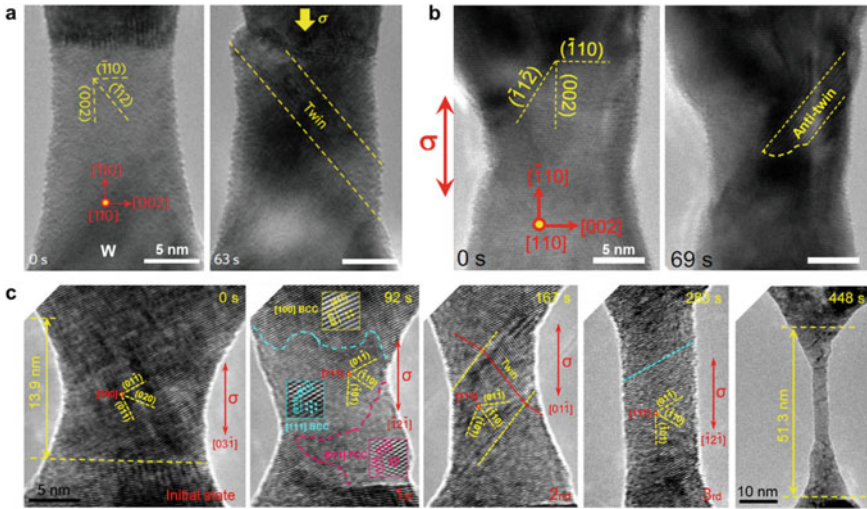


Fig. 3.12 Mechanistic insight into the deformation mechanism of BCC metallic nanocrystals. **a** Deformation twinning in W nanocrystal under compressive loading (reproduced with permission from Ref. [69], Copyright 2015, Springer Nature) **b** Anti-twinning in W under tensile loading. (reproduced with permission from Ref. [70], Copyright 2020, The American Association for the Advancement of Science) **c** Superplastic elongation of Nb nanowire via sequential phase transformation, twinning and slip-induced crystal rotation (reproduced with permission from Ref. [71], Copyright 2018, The American Association for the Advancement of Science)

of the $\{111\}$ planes continuously increased from the normal 70.5° (projected along the $[110]$ direction of the FCC lattice) to exceed 90° and approached the theoretical lattice shearing limit ($\sim 109^\circ$). Figure 3.13a is a typical atomic-scale image of the initial atomic structure of the Ni NW. Figure 3.13b is an atomic image showing that the dislocation-free lattice shear gives rise to a gradual increase in α from $\sim 70.5^\circ$ to $\sim 90^\circ$ and then to $\sim 109^\circ$ (Fig. 3.13c), which corresponds to a continuous increase in the lattice shear strain from 0% to 17.3% and further to 34.6%. This large shear strain arises from the continuous lattice changes from the original FCC through orthogonal path, to the tetragonal lattice and finally, to a re-oriented FCC lattice. Interestingly, the ultra-large lattice shear is fully reversible. When further straining was imposed, the continuous lattice shearing was terminated by dislocations/small angle boundaries. As shown in Fig. 3.13d, the lattices return to their original parallelogram shape, with $\alpha \sim 70.5^\circ$ corresponding to the original FCC lattice, indicating that the 34.6% strain is reversible. This large shear strain is approximately four times that of the theoretical elastic strain limit for unconstrained loading. Figure 3.13e is a schematic drawing of the projected atomic configurations to show the FCC structure with the shear strains of 0, 17.3% and 34.6%, respectively.

Compared with the TEM grid technique, the bimetallic technique is more controllable and is usually used for the metallic nanocrystals and nanocrystalline materials [45, 46, 64, 73–76]. With this method, dislocation dynamics can be atomically

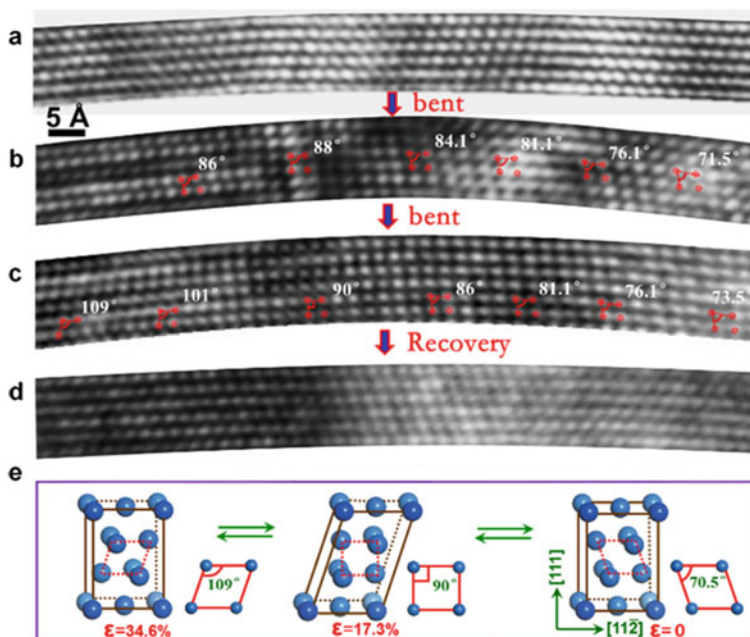


Fig. 3.13 Continuous and reversible lattice strain far beyond the elastic limit. **a, b** HRTEM images of a Ni nanowire captured before and after applying a bending strain of $\sim 1.9\%$. **c** Enlarged atomic-scale image shows the continuous increase in α from 71° to approximately 109° . The simulated HREM images are inserted accordingly. **d** HRTEM image captured after the bending strain was released. No square lattice and other type sheared lattices were observed, indicating the 34.6% lattice shear strain was fully recovered. Atomic configurations that correspond to (c) show the ultra-large continuous lattice shear from 0 to 34.6% more clearly. **e** Schematic 3D structures and corresponding side views show the shear and recover process of the FCC lattice (reproduced with permission from Ref. [13], Copyright 2013, Springer Nature)

resolved at real-time [73]. Plastic deformation of the nanosized single crystalline Pt commenced with dislocation “appreciation” at first, and followed by a dislocation “saturation” phenomenon. Figure 3.14a is an HRTEM image captured under the earlier stage of tensile loading. Two full dislocations were revealed (marked by arrows), indicating a dislocation density of $\sim 5 \times 10^{15} \text{ m}^{-2}$. Interestingly, the dislocation underwent “appreciation” stage, in which the dislocation nucleation rate was faster than its escape rate (Fig. 3.14a–c), leading to an increased density of dislocations. With further tensile loading, Fig. 3.14d demonstrates the increase of the dislocation density (estimated at $\sim 4.4 \times 10^{16} \text{ m}^{-2}$) to a level one order higher compared to the initial value. Under further tensile loading, however, the dislocation density becomes stationary (Fig. 3.14d–f) although individual dislocations continually nucleated and escaped, suggesting a balanced dislocation nucleation rate versus escape rate. Several dislocation types, such as Lomer dislocation (LD) locks and Lomer–Cottrell (L-C) locks, and their formations and destructions were also observed. The in situ observation shows that the magnitude of strain plays a key

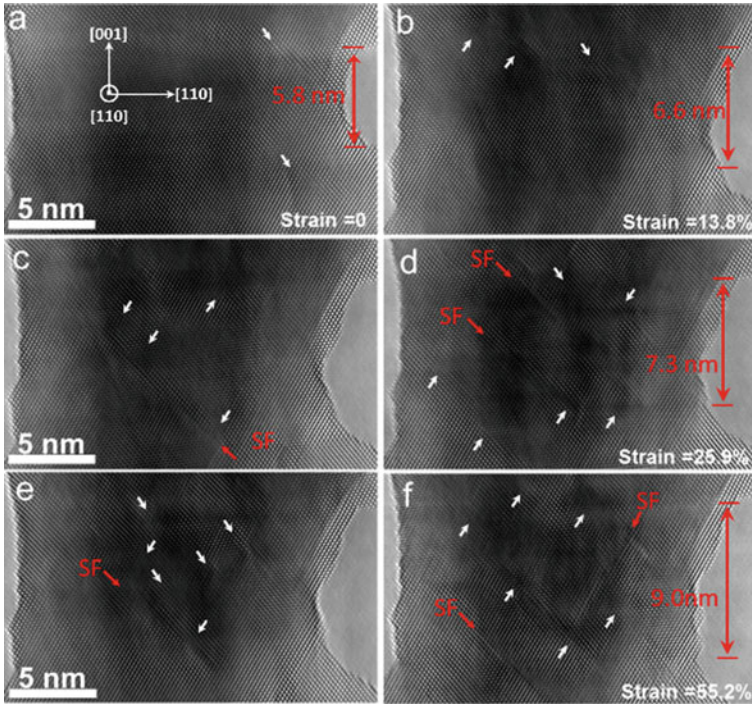


Fig. 3.14 A series of HRTEM images show the tensile process of the Pt nanocrystal. During tensile loading, the dislocation density increased. Dislocation activities are different at different deformation stages (reproduced with permission from Ref. [73], Copyright 2017, American Chemical Society)

role in dislocation behaviors. At the earlier to intermediate stage of deformation, the plastic deformation was controlled by the full dislocation activities accompanied with the formation of LD locks from the reaction of full dislocations. When the strain increased to a significant level, stacking faults and extended dislocations as well as L-C locks appeared. The L-C locks can unlock through transferring into LD locks first, and then LD locks were destructed under high stresses.

3.3.2 Deformation of Nanocrystalline Metals

The atomic-scale deformation mechanisms of nanocrystalline metals were investigated by using the bimetallic, MEMS, or thin film straining techniques. Through in situ observation on the deformation process of Pt nanocrystalline thin film, a strong grain size effect on the deformation mechanism was clearly revealed [14, 77]. With decreasing grain sizes, the deformation mechanism switches from full dislocations to partial dislocations inside the grains, and eventually to GB dislocation

mediated grain rotation [78, 79]. In larger grains ($d > \sim 10$ nm), movements and interactions of cross-grain dislocations were frequently observed. Figure 3.15a, b provide a typical in situ HRTEM observation of full dislocation (marked with “T”) nucleation and motion in a ~ 11 nm sized grain, with a Burgers vector of $a/2[011]$. Sometimes, the interaction of two non-dissociated full dislocations on two intersecting slip planes will lead to the LD formation. Figure 3.15c is a typical HRTEM image of a LD that is formed by full dislocations interaction; extra half planes are observed on both the (-111) and the (1-11) planes, which represents a LD. For grain sizes between 6 and 10 nm, the amount of full dislocations reduces, while that of the stacking faults (SFs) resulting from the passage of partial dislocations increases. For example, Fig. 3.15d, e successfully captured nucleation of partial dislocations (marked with arrows) in a ~ 8 nm sized grain. A statistical study demonstrates that there is a clear trend with decreasing grain size: The prevailing plastic deformation carrier changes from full to partial dislocations and twinning inside the grains. When the grain size decreases below 6 nm, the grain rotation mediated by the climb and absorption/generation of GB dislocations dominates the plasticity. Figure 3.15g demonstrates a typical example of in situ observation of grain rotation, both G1 and G2 show clear [110] zone axis HREM images and the GB angles are 8.3° and 6.4° for G1-2 and G1-3, respectively. As the strain increases, the number of the dislocations at G1-2 increases and the average spacing of the GB dislocations decreases from 3.1 to 1.2 nm during straining. This increased number of GB dislocations leads to the increased misorientation angle of G1-2, from 8.3° to 13.5° , as well as that of G1-3, from 6.4° to 10.6° .

The relatively high tendency toward deformation twinning in nanocrystalline materials provides a good opportunity for twinning mechanism investigation. In classic twinning theory for FCC metals, a deformation twin is nucleated through layer-by-layer movement of partial dislocations on consecutive close-packed atomic planes layer-by-layer without interruption. However, through in situ atomic-scale observation, Han et al. showed that deformation twinning nucleation in Pt nanograins initiates with the formation of two stacking faults separated by a single atomic layer (Fig. 3.16b), and then proceeds with the emission of a partial dislocation in between (Fig. 3.16c), forming a three-layer twin embryo [80]. This process of twin nucleation is intrinsically different from the previous twinning models in which a twin embryo forms through the successive emission of partial dislocations on consecutive (111) planes. Based on in situ observation, the energy landscape underlying the new twinning route was evaluated using ab initio density functional theory (DFT) calculations. As shown in Fig. 3.16d, path A represents the classical layer-by-layer twinning mechanism, and path B represents the new twinning route revealed by their observations. It can be seen that the energy barriers for path B are much lower than that of path A. These findings explained why deformation twins are frequently observed in experiments but are highly unfavorable in theory for FCC metals such as Al and Pt.

The deformation mechanism of twinned nanocrystalline metals is found to be both grain size and twin thickness dependent [77]. Figure 3.17 shows the statistical results of plasticity events for different twins/matrixes and grains obtained from

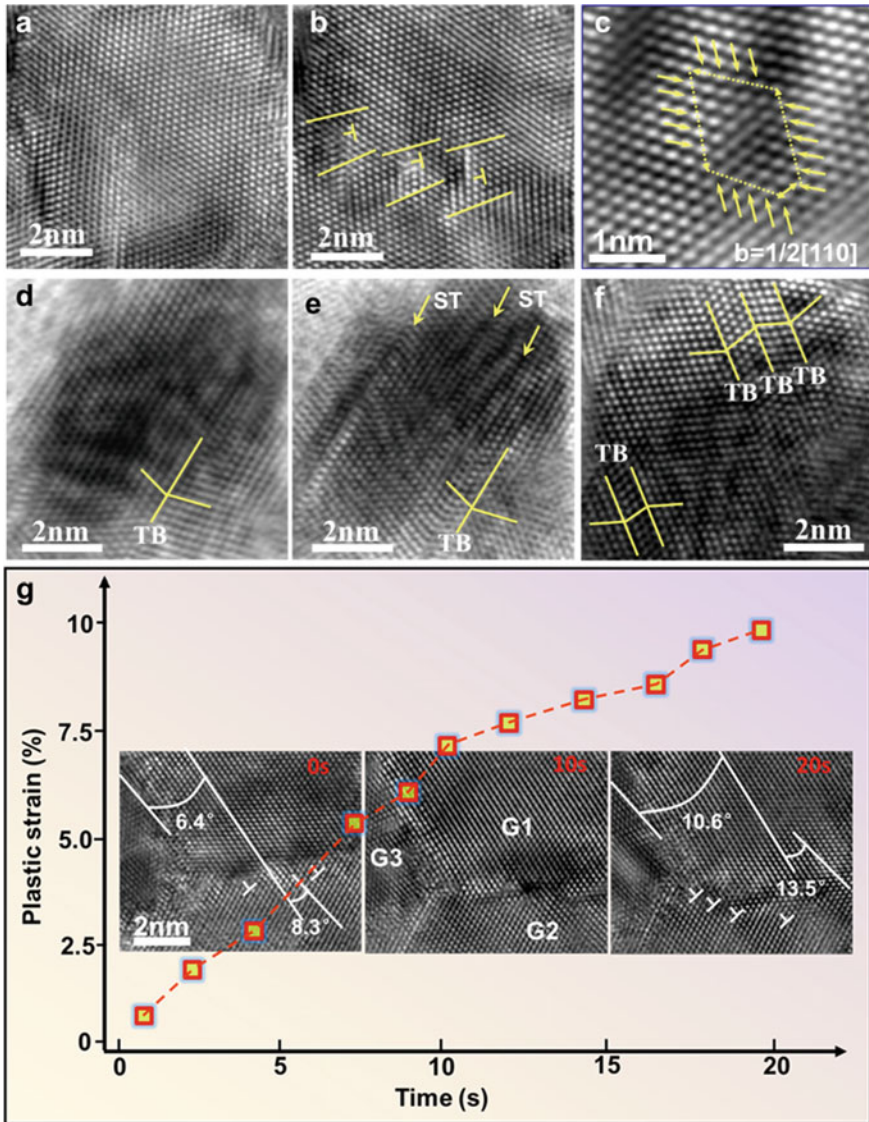


Fig. 3.15 The cross-over plasticity mechanisms in nanocrystalline metals. **a, b** In situ HRTEM observation of full dislocation (marked with “T”) nucleation and motion in a ~ 11 nm sized grain. **c** A typical HRTEM image of a Lomer dislocation that is formed by full dislocation interaction. **d, e** In situ HRTEM observation of partial dislocation (marked with arrows) nucleation in a ~ 8 nm sized grain. **f** the deformation twins were also observed in a ~ 7 nm sized grain. **g** In situ atomic-scale observation of grain rotation through GB dislocation climb (reproduced with permission from Ref. [78], Copyright 2015, Elsevier)

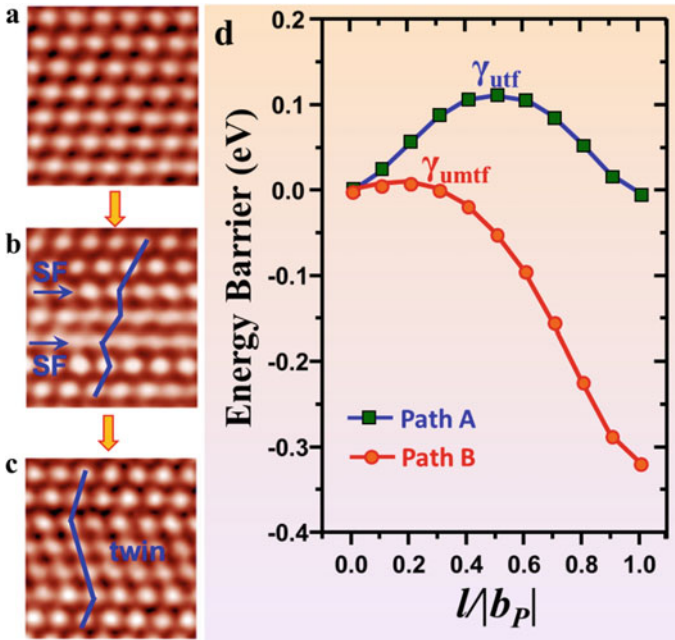


Fig. 3.16 **a** A region of a Pt nano-grain with no defects observed initially. **b** Two SFs separated by one atomic layer were observed during straining. **c** A three-layer twin was formed through the nucleation of a partial dislocation between the two previously formed SFs. **d** Density functional theory calculations of twinning energy landscape (reproduced with permission from Ref. [80], Copyright 2017, Springer Nature)

in situ and ex situ HRTEM observations. Based on the results, twin-structured grains can be divided into 3 different categories. (1) For grain sizes above 10 nm, there exists a transition in the deformation mechanisms that occurs at a critical twin thickness; at this point, plastic deformation switches from nucleation and gliding of full dislocations intersecting the TBs to partial dislocations that are parallel with TBs. Interestingly, the critical twin thickness value changes with different grain sizes: The smaller the grain size, the smaller the critical value. (2) For grain sizes in 6–9 nm, the dominant deformation mode becomes partial dislocations nucleation and gliding on crystal planes parallel with the TBs. (3) For grain sizes below 6 nm, plastic deformation converts from lattice dislocation to GB-mediated plasticity, i.e., GB migration. These results indicate that for large-size twin-structured grains (above ~10 nm), the deformation mode is affected by both the grain size and twin thickness, while in small-size twin-structured grains (below ~10 nm), the deformation mode only depends on grain size.

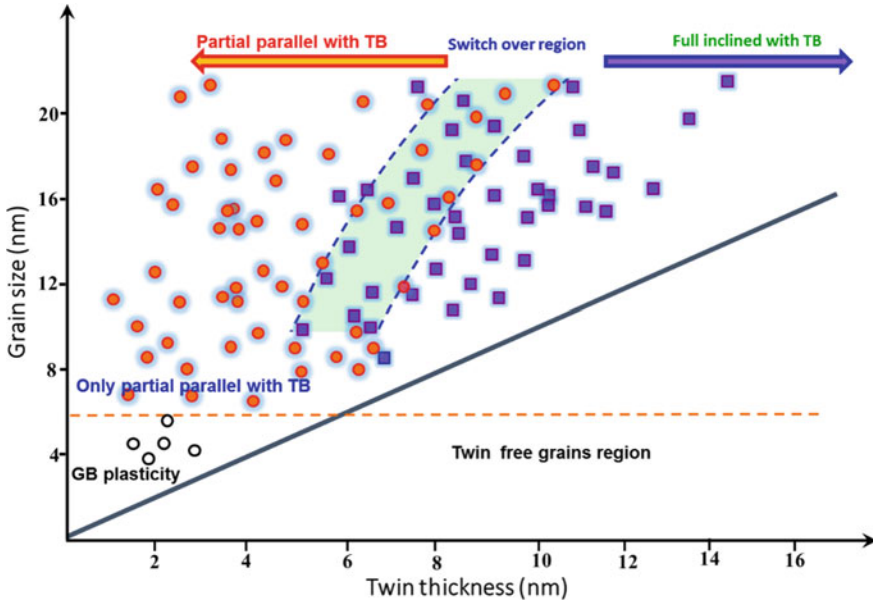


Fig. 3.17 Statistical results of the plasticity for twin-structured nanocrystalline and twin free nanocrystalline metals. For $d > \sim 10$ nm, there is a transition from full dislocation intersecting with the TB to partial dislocation migration parallel with TBs, and the critical twin thickness for the deformation transition is grain size dependent. For $d = 6\text{--}9$ nm, partial dislocation parallel with the TBs dominates. For $d < \sim 6$ nm, there is a transition from dislocation-controlled plasticity to GB-mediated plasticity. The black circles correspond to statistical results of plasticity events in twin free nanocrystalline metals (reproduced with permission from Ref. [77], Copyright 2020, Springer Nature)

3.3.3 Deformation at Grain Boundaries

Taking advantage of the misorientation between opposite nanocrystals on both sides of the STM-TEM holder, nanoscale bicrystals with designable GBs can be produced via the nanowelding process (Fig. 3.18a), inspiring more systematic research of the atomistic mechanisms of GB-dominated plastic deformation. In situ shear testing of nanoscale Au bicrystals unambiguously demonstrated the continuous migration of $\Sigma 11(113)$ GB (a typical high angle tilt GB with low energy) mediated by the nucleation and motion of GB disconnections (interfacial defects with both Burgers vector and step character) [52], as shown in Fig. 3.18b. Specifically, both single-atom-layer disconnections ($\mathbf{b} = 1/22 \langle 471 \rangle$) and double-atom-layer disconnections ($\mathbf{b} = 1/22 \langle 332 \rangle$) were nucleated consecutively from the surface at room temperature, which exhibited frequent dynamic interactions (e.g., composition or decomposition) between each other throughout the GB migration process. These dynamic atomistic observations provide clear evidence for the theory of GB-dominated deformation and advance the understanding of GB-dominated plasticity in the community. Further

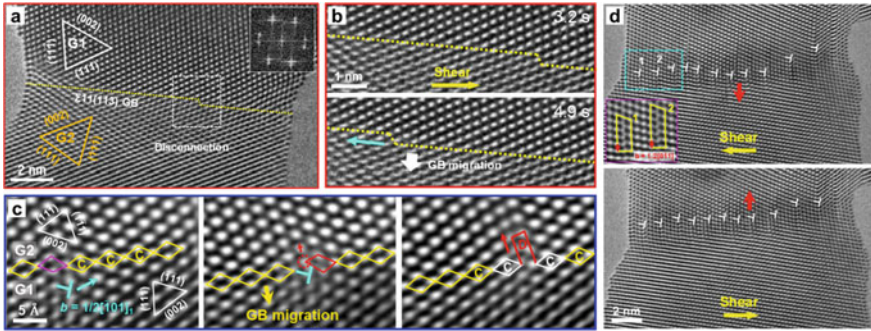


Fig. 3.18 Atomistic mechanism of GB-dominated plastic deformation. **a** An Au bicrystal containing a $\Sigma 11(113)$ GB. **b** Disconnection-mediated GB migration coupled to shear loading. (reproduced with permission from Ref. [52], Copyright 2019, Springer Nature) **c** Disconnection-dominated GB migration subjected to the intersection of a lattice dislocation (reproduced with permission from Ref. [81], Copyright 2020, Elsevier) **d** Reversible migration of a $13.5^\circ \langle 110 \rangle$ GB in shear loading cycles via the conservative motion of dissociated dislocations (reproduced with permission from Ref. [82], Copyright 2020, Springer Nature)

in situ experiments show that the disconnection-mediated dynamics of $\Sigma 11(113)$ GB generally retains under the intersection of common lattice defects inside the grains such as dislocation, stacking fault and nanotwins (Fig. 3.18c), and the lattice defect configurations evolve in coordination with GB migration [81]. Moreover, these GB-lattice defect interactions can facilitate the formation of GB disconnections, serving as additional nucleation sites for intrinsic GB defects. When the GB misorientation is further reduced to low angle regime, the GBs typically consist of geometrically necessary dislocations and the GB migration generally proceeds via the conservative motion of GB dislocations. Such GB dislocations are prone to dissociation in FCC metals with low stacking fault energies (SFEs) [82], which increases the slip continuity across the GB, benefiting the cyclic shear deformability of metallic nanocrystals via reversible GB migration (Fig. 3.18d). In polycrystalline and nanocrystalline materials, the triple junctions tend to serve as important nucleation sites of GB defects and the coordinated motions among neighboring GBs become dominant. For example, the synergistic climb of GB dislocations surrounding the grain can lead to grain rotation and merging in nanocrystalline Pt thin film [14]. In addition, the atomistic mechanisms of grain shrinkage or grain growth via coordinated GB migration have been widely reported in FCC metals [77, 83].

3.3.4 Deformation Under Elevated Temperature

Nanomechanical tests under high-temperature require concurrent application of both mechanical and thermal stimuli on the nanoscale specimen, which is technically

demanding. Hence most nanomechanical tests were performed at ambient temperature. With recent advances in high-temperature in situ nanomechanical testing techniques, the atomic-scale deformation process of metals was captured at extremely high temperatures [28]. Figure 3.19 shows the deformation process of BCC W at a temperature of 973 K. Under tensile loading, a crack was nucleated in a nanosized W crystal (Fig. 3.19a). Atomically resolved images of the crack tip were successfully captured at such an elevated temperature, where both BCC and FCC lattices were identified. The basic lattice vectors in Region I are perpendicular, conforming to the $\{110\}$ planes in the $[100]_{\text{BCC}}$ zone axis, while those in Region II show an angle of 70.5° , in good agreement with the $\{111\}$ planes when viewed along the $[110]_{\text{FCC}}$ zone axis. The $(011)_{\text{BCC}}$ d -spacing in Region I was determined to be 2.250 \AA , corresponding to a local lattice strain of 1.58%. While the $(\bar{1}11)_{\text{FCC}}$ d -spacing in Region II was determined to be 2.457 \AA , corresponding to a local lattice strain of 3.58%. After continuous stretching, a small portion of the BCC structure in Region I transformed into an intermediate structure (Region III) (Fig. 3.19c), which evolved into a $[110]_{\text{FCC}}$ structure and merged into Region II (Fig. 3.19d), providing new insights into the $[100]_{\text{BCC}} \rightarrow [110]_{\text{FCC}}$ transformation path.

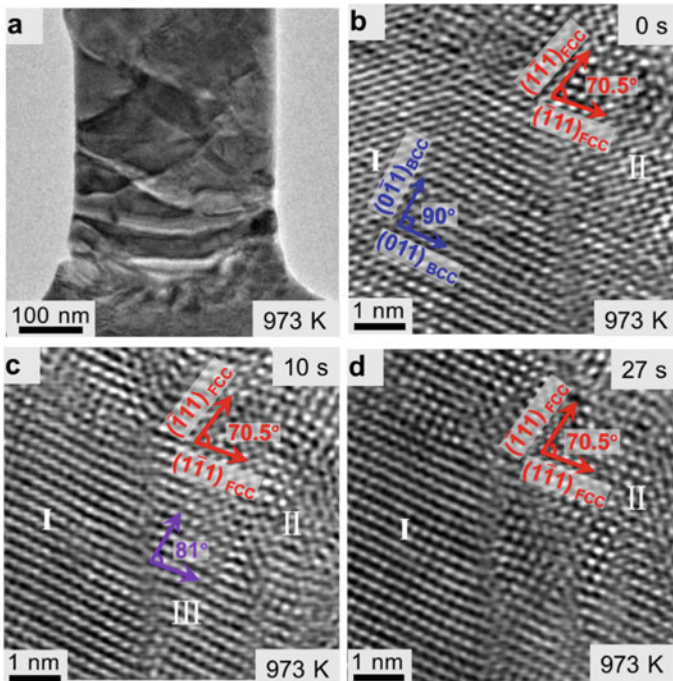


Fig. 3.19 a TEM image of the W nanocrystal. b–d In situ atomic-scale observation BCC–FCC transition at crack tip during tension (reproduced with permission from Ref. [28], Copyright 2021, Springer Nature)

3.3.5 Deformation of “Brittle” Materials

The mechanical properties of materials are dramatically affected by specimen size. Materials that are known to be brittle in the bulk form could show a decent amount of plasticity in the nanometer size regime. Many studies have revealed that small-sized semiconductor and ceramic materials can exhibit ductile features at room temperature [84–91], in stark contrast to their bulk counterparts. For example, an unusually large bending strain was observed in ceramic SiC NWs close to RT via the TEM grid technique [36]. In situ atomic-scale observation revealed that the plasticity of the SiC NWs was accompanied by a process of increased dislocation density during the early stages, followed by an obvious lattice distortion and then amorphization in the most strained region of the NW. Room temperature plasticity was also observed in Si and SiO₂ NWs by conducting axial tensile [35] and bending tests [37] inside the TEM. Figure 3.20a–d show a typical example of a SiO₂ NW exhibiting large plasticity under tensile loading. Similar to the case for SiC NWs, crystalline-amorphous(*c-a*) transition was also observed in Si NWs through dislocation reaction in ultra-large strained (up to 14%) region (Fig. 3.20e–h). Direct atomic-scale observation (Fig. 3.20i–l) revealed that partial and full dislocation nucleation, motion and interaction, and the *c-a* transition was responsible for absorbing the ultra-large strain in bending Si NWs. An atomically resolved view at the bending section reveals that a Lomer dislocation (Fig. 3.20k) was formed by a reaction of full dislocations (Fig. 3.20j), and eventually induced the *c-a* transition during subsequent straining (Fig. 3.20l). These results provide a direct explanation for the ultra-large straining ability and the *c-a* transition mechanism for those semiconductor and ceramic nanostructures [92–94].

3.4 Outlook

During the past decades, in situ TEM based nanomechanical investigations have provided abundant and invaluable insights into the deformation mechanisms of nanostructured materials. As demonstrated by recent in situ TEM studies [62, 95], fundamental understandings on the deformation modes of materials can provide guidelines for achieving excellent mechanical properties. However, these atomic deformation mechanisms and superior mechanical properties were obtained in the laboratory, where testing conditions may deviate significantly from the practical working conditions in terms of materials composition, working environments, loading conditions etc. As such, future in situ TEM nanomechanical investigations are to be carried out under conditions comparable to practical service environments, so that results obtained by laboratory efforts can provide good implications for practical applications. To this end, several desirable future research directions are discussed below.

First, most in situ TEM nanomechanical studies targeted on simple material systems that consist of very few elements and phases. While structural materials

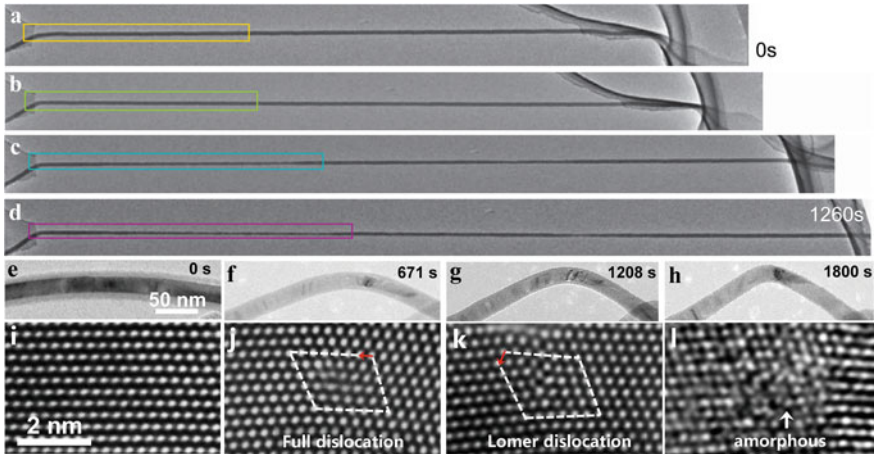


Fig. 3.20 a–d A series of TEM images show the tensile process of the SiO₂ NW. (reproduced with permission from Ref. [38], Copyright 2010, Springer Nature) e–h In situ observation of the bending process of Si NW. During tensile loading, the dislocation density increased. i–l In situ observation of dislocation activities and crystalline-amorphous transition through a dislocation reaction (reproduced with permission from Ref. [91], Copyright 2011, American Chemical Society)

adopted in practical applications usually take advantage of a combination of multiple elements (e.g. alloys) and complex microstructures such as multiple phases and hierarchical structures. The evolutions in element distribution could lead to phase segregation and changes in the stability of defects, thus dramatically altering the deformation mechanisms and mechanical properties of materials. Tracking the evolutions of local composition and microstructures in these complex material systems is critical but technically demanding, which necessitates optimum characterization conditions. However, current in situ nanomechanical testing platforms consisting of force/displacement control and measurement units tend to introduce issues such as specimen drift and vibration, which degrades the imaging condition and brings significant challenges in in situ TEM characterization of complex material systems. As such, efforts could be made to minimize the compromise in resolution caused by in situ TEM deformation platforms.

Second, nanomechanical studies are usually carried out under ideal loading conditions such as uniaxial loading and pure bending. Deformation mechanisms and mechanical performances obtained in the laboratory may not be necessarily applicable to materials in practical applications where complex loading conditions exist, e.g. multiaxial stress conditions and shocking loading. In addition, many materials may serve in environments far from those in laboratory, such as under elevated temperature, electric field and specific gaseous environments. Recent hydrogen embrittlement studies based on environmental TEM [96–98] successfully demonstrated the strength and potential of in situ nanomechanical study. The development of advanced nanomechanical testing techniques capable of investigating the mechanical

behaviors of materials under their working conditions warrants significant research effort in the future.

Third, facilitated by the rapid development in fast camera technology, the temporal resolution associated with in situ TEM characterization could be dramatically improved in the future. As a result, in situ nanomechanical studies may be performed at a time scale on par with that of dislocation activities (e.g. milliseconds), which is critical for tracking dislocation dynamics during deformation. In the meantime, however, fast frame rates also lead to a massive amount of experimental data and increasing difficulties in data analysis. It is thus foreseeable that advanced data analysis and image processing strategies will be indispensable for future in situ nanomechanical studies.

References

1. Butler EP (1979) In situ experiments in the transmission electron microscope. *Rep Prog Phys* 42(5):833–895. <https://doi.org/10.1088/0034-4885/42/5/002>
2. Yamakov V, Wolf D, Phillpot SR, Mukherjee AK, Gleiter H (2002) Dislocation processes in the deformation of nanocrystalline aluminium by molecular-dynamics simulation. *Nat Mater* 1(1):45–49. <https://doi.org/10.1038/nmat700>
3. Yamakov V, Wolf D, Phillpot SR, Mukherjee AK, Gleiter H (2004) Deformation-mechanism map for nanocrystalline metals by molecular-dynamics simulation. *Nat Mater* 3(1):43–47. <https://doi.org/10.1038/nmat1035>
4. Zhang H, Gilbert B, Huang F, Banfield JF (2003) Water-driven structure transformation in nanoparticles at room temperature. *Nature* 424(6952):1025–1029. <https://doi.org/10.1038/nature01845>
5. Oh SH, Kauffmann Y, Scheu C, Kaplan WD, Rühle M (2005) Ordered liquid aluminum at the interface with sapphire. *Science* 310(5748):661–663. <https://doi.org/10.1126/science.1118611>
6. Kim Judy S, LaGrange T, Reed Bryan W, Taheri Mitra L, Armstrong Michael R, King Wayne E, Browning Nigel D, Campbell Geoffrey H (2008) Imaging of transient structures using nanosecond in situ TEM. *Science* 321(5895):1472–1475. <https://doi.org/10.1126/science.1161517>
7. Fujita T, Guan P, McKenna K, Lang X, Hirata A, Zhang L, Tokunaga T, Arai S, Yamamoto Y, Tanaka N, Ishikawa Y, Asao N, Yamamoto Y, Erlebacher J, Chen M (2012) Atomic origins of the high catalytic activity of nanoporous gold. *Nat Mater* 11(9):775–780. <https://doi.org/10.1038/nmat3391>
8. Boston R, Schnepf Z, Nemoto Y, Sakka Y, Hall Simon R (2014) In situ TEM observation of a microcrucible mechanism of nanowire growth. *Science* 344(6184):623–626. <https://doi.org/10.1126/science.1251594>
9. Liao H-G, Zherebetskyy D, Xin H, Czarnik C, Ercius P, Elmlund H, Pan M, Wang L-W, Zheng H (2014) Facet development during platinum nanocube growth. *Science* 345(6199):916–919. <https://doi.org/10.1126/science.1253149>
10. Liao H-G, Cui L, Whitelam S, Zheng H (2012) Real-time imaging of Pt₃Fe nanorod growth in solution. *Science* 336(6084):1011–1014. <https://doi.org/10.1126/science.1219185>
11. Boswell FW (1958) Symposium on advances in electron metallography. *ASTM Spec Tech Publ* 245:31–42. <https://doi.org/10.1520/STP245-EB>
12. Berghezan A, Fourdeux A (1959) Transmission electron microscopy studies of the mechanism of plastic deformation. *J Appl Phys* 30(12):1913–1922. <https://doi.org/10.1063/1.1735089>
13. Wang L, Liu P, Guan P, Yang M, Sun J, Cheng Y, Hirata A, Zhang Z, Ma E, Chen M, Han X (2013) In situ atomic-scale observation of continuous and reversible lattice deformation beyond the elastic limit. *Nat Commun* 4(1):2413. <https://doi.org/10.1038/ncomms3413>

14. Wang L, Teng J, Liu P, Hirata A, Ma E, Zhang Z, Chen M, Han X (2014) Grain rotation mediated by grain boundary dislocations in nanocrystalline platinum. *Nat Commun* 5(1):4402. <https://doi.org/10.1038/ncomms5402>
15. Wall MA, Dahmen U (1998) An in situ nanoindentation specimen holder for a high voltage transmission electron microscope. *Microsc Res Tech* 42(4):248–254. [https://doi.org/10.1002/\(SICI\)1097-0029\(19980915\)42:4%3c248::AID-JEMT3%3e3.0.CO;2-M](https://doi.org/10.1002/(SICI)1097-0029(19980915)42:4%3c248::AID-JEMT3%3e3.0.CO;2-M)
16. Yu Q, Qi L, Tsuru T, Traylor R, Rugg D, Morris JW, Asta M, Chrzan DC, Minor Andrew M (2015) Origin of dramatic oxygen solute strengthening effect in titanium. *Science* 347(6222):635–639. <https://doi.org/10.1126/science.1260485>
17. Liu B-Y, Liu F, Yang N, Zhai X-B, Zhang L, Yang Y, Li B, Li J, Ma E, Nie J-F, Shan Z-W (2019) Large plasticity in magnesium mediated by pyramidal dislocations. *Science* 365(6448):73–75. <https://doi.org/10.1126/science.aaw2843>
18. Shan ZW, Mishra RK, Syed Asif SA, Warren OL, Minor AM (2008) Mechanical annealing and source-limited deformation in submicrometre-diameter Ni crystals. *Nat Mater* 7(2):115–119. <https://doi.org/10.1038/nmat2085>
19. Dang C, Chou J-P, Dai B, Chou C-T, Yang Y, Fan R, Lin W, Meng F, Hu A, Zhu J, Han J, Minor Andrew M, Li J, Lu Y (2021) Achieving large uniform tensile elasticity in microfabricated diamond. *Science* 371(6524):76–78. <https://doi.org/10.1126/science.abc4174>
20. Wang Y, Ding J, Fan Z, Tian L, Li M, Lu H, Zhang Y, Ma E, Li J, Shan Z (2021) Tension–compression asymmetry in amorphous silicon. *Nat Mater* 20(10):1371–1377. <https://doi.org/10.1038/s41563-021-01017-z>
21. Guo H, Chen K, Oh Y, Wang K, Dejoie C, Syed Asif SA, Warren OL, Shan ZW, Wu J, Minor AM (2011) Mechanics and dynamics of the strain-induced M1–M2 structural phase transition in individual VO₂ Nanowires. *Nano Lett* 11(8):3207–3213. <https://doi.org/10.1021/nl201460v>
22. Wang Y, Liu B, Xia Z, Zhang X, Miao Y, Yang N, Yang B, Zhang L, Kuang W, Li J, Ma E, Shan Z (2018) Turning a native or corroded Mg alloy surface into an anti-corrosion coating in excited CO₂. *Nat Commun* 9(1):4058. <https://doi.org/10.1038/s41467-018-06433-5>
23. Zhu Y, Espinosa HD (2005) An electromechanical material testing system for in situ electron microscopy and applications. *Proc Natl Acad Sci USA* 102(41):14503. <https://doi.org/10.1073/pnas.0506544102>
24. Qin Q, Yin S, Cheng G, Li X, Chang T-H, Richter G, Zhu Y, Gao H (2015) Recoverable plasticity in penta-twinned metallic nanowires governed by dislocation nucleation and retraction. *Nat Commun* 6(1):5983. <https://doi.org/10.1038/ncomms6983>
25. Cheng G, Yin S, Li C, Chang T-H, Richter G, Gao H, Zhu Y (2020) In-situ TEM study of dislocation interaction with twin boundary and retraction in twinned metallic nanowires. *Acta Mater* 196:304–312. <https://doi.org/10.1016/j.actamat.2020.06.055>
26. Chen LY, He M-r, Shin J, Richter G, Gianola DS (2015) Measuring surface dislocation nucleation in defect-scarce nanostructures. *Nat Mater* 14(7):707–713. <https://doi.org/10.1038/nmat4288>
27. Cheng G, Zhang Y, Chang T-H, Liu Q, Chen L, Lu WD, Zhu T, Zhu Y (2019) In situ nano-thermomechanical experiment reveals brittle to ductile transition in silicon nanowires. *Nano Lett* 19(8):5327–5334. <https://doi.org/10.1021/acs.nanolett.9b01789>
28. Zhang J, Li Y, Li X, Zhai Y, Zhang Q, Ma D, Mao S, Deng Q, Li Z, Li X, Wang X, Liu Y, Zhang Z, Han X (2021) Timely and atomic-resolved high-temperature mechanical investigation of ductile fracture and atomistic mechanisms of tungsten. *Nat Commun* 12(1):2218. <https://doi.org/10.1038/s41467-021-22447-y>
29. Merkle AP, Marks LD (2007) Friction in full view. *Appl Phys Lett* 90(6):064101. <https://doi.org/10.1063/1.2456192>
30. Merkle AP, Marks LD (2008) Liquid-like tribology of gold studied by in situ TEM. *Wear* 265(11):1864–1869. <https://doi.org/10.1016/j.wear.2008.04.032>
31. Huang JY, Chen S, Wang ZQ, Kempa K, Wang YM, Jo SH, Chen G, Dresselhaus MS, Ren ZF (2006) Superplastic carbon nanotubes. *Nature* 439(7074):281–281. <https://doi.org/10.1038/439281a>

32. Legros M (2014) In situ mechanical TEM: Seeing and measuring under stress with electrons. *C R Phys* 15(2):224–240. <https://doi.org/10.1016/j.crhy.2014.02.002>
33. Zhang Z, Mao MM, Wang J, Gludovatz B, Zhang Z, Mao SX, George EP, Yu Q, Ritchie RO (2015) Nanoscale origins of the damage tolerance of the high-entropy alloy CrMnFeCoNi. *Nat Commun* 6(1):10143. <https://doi.org/10.1038/ncomms10143>
34. Legros M, Gianola DS, Hemker KJ (2008) In situ TEM observations of fast grain-boundary motion in stressed nanocrystalline aluminum films. *Acta Mater* 56(14):3380–3393. <https://doi.org/10.1016/j.actamat.2008.03.032>
35. Han XD, Zheng K, Zhang YF, Zhang XN, Zhang Z, Wang ZL (2007) Low-temperature in situ large-strain plasticity of silicon nanowires. *Adv Mater* 19(16):2112–2118. <https://doi.org/10.1002/adma.200602705>
36. Han XD, Zhang YF, Zheng K, Zhang XN, Zhang Z, Hao YJ, Guo XY, Yuan J, Wang ZL (2007) Low-temperature in situ large strain plasticity of ceramic SiC nanowires and its atomic-scale mechanism. *Nano Lett* 7(2):452–457. <https://doi.org/10.1021/nl0627689>
37. Zheng K, Han X, Wang L, Zhang Y, Yue Y, Qin Y, Zhang X, Zhang Z (2009) Atomic mechanisms governing the elastic limit and the incipient plasticity of bending Si nanowires. *Nano Lett* 9(6):2471–2476. <https://doi.org/10.1021/nl9012425>
38. Zheng K, Wang C, Cheng Y-Q, Yue Y, Han X, Zhang Z, Shan Z, Mao SX, Ye M, Yin Y, Ma E (2010) Electron-beam-assisted superplastic shaping of nanoscale amorphous silica. *Nat Commun* 1(1):24. <https://doi.org/10.1038/ncomms1021>
39. Han XD, Wang LH, Liu P, Yue YH, Yang MJ, Sun JL, Zhang Z (2010) Dynamic atomic mechanisms of plasticity of Ni nanowires and nano crystalline ultra-thin films. *Mater Sci Forum* 654–656:2293–2296. <https://doi.org/10.4028/www.scientific.net/MSF.654-656.2293>
40. Wang L, Sun T, Wei R, Guan P, Liu P, Chen M, Zhang Z, Han X (2019) Bent strain values affect the plastic deformation behaviours of twinned Ni NWs. *Scripta Mater* 167:1–5. <https://doi.org/10.1016/j.scriptamat.2019.03.020>
41. Li Q, Wang L, Teng J, Pang X, Han X, Zou J (2020) In-situ observation of cooperative grain boundary sliding and migration in the nano-twinned nanocrystalline-Au thin-films. *Scripta Mater* 180:97–102. <https://doi.org/10.1016/j.scriptamat.2020.01.025>
42. Wang L, Lu Y, Kong D, Xiao L, Sha X, Sun J, Zhang Z, Han X (2015) Dynamic and atomic-scale understanding of the twin thickness effect on dislocation nucleation and propagation activities by in situ bending of Ni nanowires. *Acta Mater* 90:194–203. <https://doi.org/10.1016/j.actamat.2015.02.002>
43. Zhang Y, Han X, Zheng K, Zhang Z, Zhang X, Fu J, Ji Y, Hao Y, Guo X, Wang ZL (2007) Direct observation of super-plasticity of Beta-SiC nanowires at low temperature. *Adv Func Mater* 17(17):3435–3440. <https://doi.org/10.1002/adfm.200700162>
44. Wang L, Han X, Liu P, Yue Y, Zhang Z, Ma E (2010) In Situ observation of dislocation behavior in nanometer grains. *Phys Rev Lett* 105(13):135501. <https://doi.org/10.1103/PhysRevLett.105.135501>
45. Shao D, Wang C, Wang L, Guo X, Guo J, Zhang S, Lu Y (2021) A N-doped Cobalt@graphitized carbon material derived from ZIF-67 assisted polyvinylidene fluoride hollow fiber membrane for supercapacitors. *J Alloy Compd* 863:158682. <https://doi.org/10.1016/j.jallcom.2021.158682>
46. Lu Y, Sun S, Zeng Y, Deng Q, Chen Y, Li Y, Li X, Wang L, Han X (2020) Atomistic mechanism of nucleation and growth of a face-centered orthogonal phase in small-sized single-crystalline Mo. *Materials Research Letters* 8(9):348–355. <https://doi.org/10.1080/21663831.2020.1764122>
47. Yue Y, Liu P, Zhang Z, Han X, Ma E (2011) Approaching the theoretical elastic strain limit in copper nanowires. *Nano Lett* 11(8):3151–3155. <https://doi.org/10.1021/nl201233u>
48. Yue Y, Liu P, Deng Q, Ma E, Zhang Z, Han X (2012) Quantitative evidence of crossover toward partial dislocation mediated plasticity in copper single crystalline nanowires. *Nano Lett* 12(8):4045–4049. <https://doi.org/10.1021/nl301413z>
49. Lu Y, Huang JY, Wang C, Sun S, Lou J (2010) Cold welding of ultrathin gold nanowires. *Nat Nanotechnol* 5(3):218–224. <https://doi.org/10.1038/nnano.2010.4>

50. Zheng H, Cao A, Weinberger CR, Huang JY, Du K, Wang J, Ma Y, Xia Y, Mao SX (2010) Discrete plasticity in sub-10-nm-sized gold crystals. *Nat Commun* 1(1):144. <https://doi.org/10.1038/ncomms1149>
51. Cao G, Wang J, Du K, Wang X, Li J, Zhang Z, Mao SX (2018) Superplasticity in gold nanowires through the operation of multiple slip systems. *Adv Func Mater* 28(51):1805258. <https://doi.org/10.1002/adfm.201805258>
52. Zhu Q, Cao G, Wang J, Deng C, Li J, Zhang Z, Mao SX (2019) In situ atomistic observation of disconnection-mediated grain boundary migration. *Nat Commun* 10(1):156. <https://doi.org/10.1038/s41467-018-08031-x>
53. Zhong L, Wang J, Sheng H, Zhang Z, Mao SX (2014) Formation of monatomic metallic glasses through ultrafast liquid quenching. *Nature* 512(7513):177–180. <https://doi.org/10.1038/nature13617>
54. Wong Eric W, Sheehan Paul E, Lieber Charles M (1997) Nanobeam mechanics: elasticity, strength, and toughness of nanorods and nanotubes. *Science* 277(5334):1971–1975. <https://doi.org/10.1126/science.277.5334.1971>
55. Wu B, Heidelberg A, Boland JJ (2005) Mechanical properties of ultrahigh-strength gold nanowires. *Nat Mater* 4(7):525–529. <https://doi.org/10.1038/nmat1403>
56. Yu M-F, Lourie O, Dyer Mark J, Moloni K, Kelly Thomas F, Ruoff Rodney S (2000) Strength and breaking mechanism of multiwalled carbon nanotubes under tensile load. *Science* 287(5453):637–640. <https://doi.org/10.1126/science.287.5453.637>
57. Shan ZW, Adesso G, Cabot A, Sherburne MP, Syed Asif SA, Warren OL, Chrzan DC, Minor AM, Alivisatos AP (2008) Ultrahigh stress and strain in hierarchically structured hollow nanoparticles. *Nat Mater* 7(12):947–952. <https://doi.org/10.1038/nmat2295>
58. Uchic Michael D, Dimiduk Dennis M, Florando Jeffrey N, Nix William D (2004) Sample dimensions influence strength and crystal plasticity. *Science* 305(5686):986–989. <https://doi.org/10.1126/science.1098993>
59. Kiener D, Minor AM (2011) Source truncation and exhaustion: insights from quantitative in situ TEM tensile testing. *Nano Lett* 11(9):3816–3820. <https://doi.org/10.1021/nl201890s>
60. Kumar KS, Van Swygenhoven H, Suresh S (2003) Mechanical behavior of nanocrystalline metals and alloys. *Acta Materialia* 51(19):5743–5774. <https://doi.org/10.1016/j.actamat.2003.08.032>
61. Wang JW, Narayanan S, Huang JY, Zhang Z, Zhu T, Mao SX (2013) Atomic-scale dynamic process of deformation-induced stacking fault tetrahedra in gold nanocrystals. *Nat Commun* 4(1):2340. <https://doi.org/10.1038/ncomms3340>
62. Zhong L, Sansoz F, He Y, Wang C, Zhang Z, Mao SX (2017) Slip-activated surface creep with room-temperature super-elongation in metallic nanocrystals. *Nat Mater* 16(4):439–445. <https://doi.org/10.1038/nmat4813>
63. Sun J, He L, Lo Y-C, Xu T, Bi H, Sun L, Zhang Z, Mao SX, Li J (2014) Liquid-like pseudoelasticity of sub-10-nm crystalline silver particles. *Nat Mater* 13(11):1007–1012. <https://doi.org/10.1038/nmat4105>
64. Sun S, Kong D, Li D, Liao X, Liu D, Mao S, Zhang Z, Wang L, Han X (2019) Atomistic mechanism of stress-induced combined slip and diffusion in sub-5 nanometer-sized Ag nanowires. *ACS Nano* 13(8):8708–8716. <https://doi.org/10.1021/acsnano.9b00474>
65. Zhang Y, Wang F, Zang P, Wang J, Mao S, Zhang X, Lu J (2014) In-situ observation of crack propagation through the nucleation of nanoscale voids in ultra-thin, freestanding Ag films. *Mater Sci Eng, A* 618:614–620. <https://doi.org/10.1016/j.msea.2014.09.056>
66. Lu J, Zhu Q, Wang J, Wei H, Wang J, Zhang Y, Zhang Z (2021) Diffusive crack-grain interplay in freestanding nanocrystalline silver thin film. *Materialia* 17:101116. <https://doi.org/10.1016/j.mtla.2021.101116>
67. Wang J, Sansoz F, Huang J, Liu Y, Sun S, Zhang Z, Mao SX (2013) Near-ideal theoretical strength in gold nanowires containing angstrom scale twins. *Nat Commun* 4(1):1742. <https://doi.org/10.1038/ncomms2768>
68. Wang J, Cao G, Zhang Z, Sansoz F (2019) Size-dependent dislocation–twin interactions. *Nanoscale* 11(26):12672–12679. <https://doi.org/10.1039/c9nr03637g>

69. Wang J, Zeng Z, Weinberger CR, Zhang Z, Zhu T, Mao SX (2015) In situ atomic-scale observation of twinning-dominated deformation in nanoscale body-centred cubic tungsten. *Nat Mater* 14(6):594–600. <https://doi.org/10.1038/nmat4228>
70. Wang J, Zeng Z, Wen M, Wang Q, Chen D, Zhang Y, Wang P, Wang H, Zhang Z, Mao Scott X, Zhu T (2020) Anti-twinning in nanoscale tungsten. *Science Advances* 6 (23):eaay2792. <https://doi.org/10.1126/sciadv.aay2792>
71. Wang Q, Wang J, Li J, Zhang Z, Mao Scott X (2018) Consecutive crystallographic reorientations and superplasticity in body-centered cubic niobium nanowires. *Science Advances* 4(7):eaas8850. <https://doi.org/10.1126/sciadv.aas8850>
72. Wang L, Kong D, Zhang Y, Xiao L, Lu Y, Chen Z, Zhang Z, Zou J, Zhu T, Han X (2017) Mechanically driven grain boundary formation in nickel nanowires. *ACS Nano* 11(12):12500–12508. <https://doi.org/10.1021/acsnano.7b06605>
73. Wang L, Teng J, Sha X, Zou J, Zhang Z, Han X (2017) Plastic deformation through dislocation saturation in ultrasmall Pt nanocrystals and its in situ atomistic mechanisms. *Nano Lett* 17(8):4733–4739. <https://doi.org/10.1021/acs.nanolett.7b01416>
74. Wang L, Xin T, Kong D, Shu X, Chen Y, Zhou H, Teng J, Zhang Z, Zou J, Han X (2017) In situ observation of stress induced grain boundary migration in nanocrystalline gold. *Scripta Mater* 134:95–99. <https://doi.org/10.1016/j.scriptamat.2017.03.003>
75. Wang L, Teng J, Kong D, Yu G, Zou J, Zhang Z, Han X (2018) In situ atomistic deformation mechanisms of twin-structured nanocrystal Pt. *Scripta Mater* 147:103–107. <https://doi.org/10.1016/j.scriptamat.2018.01.012>
76. Kong D, Xin T, Sun S, Lu Y, Shu X, Long H, Chen Y, Teng J, Zhang Z, Wang L, Han X (2019) Surface energy driven liquid-drop-like pseudoelastic behaviors and in situ atomistic mechanisms of small-sized face-centered cubic metals. *Nano Lett* 19(1):292–298. <https://doi.org/10.1021/acs.nanolett.8b03916>
77. Wang L, Du K, Yang C, Teng J, Fu L, Guo Y, Zhang Z, Han X (2020) In situ atomic-scale observation of grain size and twin thickness effect limit in twin-structural nanocrystalline platinum. *Nat Commun* 11(1):1167. <https://doi.org/10.1038/s41467-020-14876-y>
78. Han X, Wang L, Yue Y, Zhang Z (2015) In situ atomic scale mechanical microscopy discovering the atomistic mechanisms of plasticity in nano-single crystals and grain rotation in polycrystalline metals. *Ultramicroscopy* 151:94–100. <https://doi.org/10.1016/j.ultramic.2014.11.035>
79. Wang L, Teng J, Wu Y, Sha X, Xiang S, Mao S, Yu G, Zhang Z, Zou J, Han X (2018) In situ atomic scale mechanisms of strain-induced twin boundary shear to high angle grain boundary in nanocrystalline Pt. *Ultramicroscopy* 195:69–73. <https://doi.org/10.1016/j.ultramic.2018.08.022>
80. Wang L, Guan P, Teng J, Liu P, Chen D, Xie W, Kong D, Zhang S, Zhu T, Zhang Z, Ma E, Chen M, Han X (2017) New twinning route in face-centered cubic nanocrystalline metals. *Nat Commun* 8(1):2142. <https://doi.org/10.1038/s41467-017-02393-4>
81. Zhu Q, Zhao SC, Deng C, An XH, Song KX, Mao SX, Wang JW (2020) In situ atomistic observation of grain boundary migration subjected to defect interaction. *Acta Mater* 199:42–52. <https://doi.org/10.1016/j.actamat.2020.08.021>
82. Zhu Q, Huang Q, Guang C, An X, Mao SX, Yang W, Zhang Z, Gao H, Zhou H, Wang J (2020) Metallic nanocrystals with low angle grain boundary for controllable plastic reversibility. *Nat Commun* 11(1):3100. <https://doi.org/10.1038/s41467-020-16869-3>
83. Chen Y, Huang Q, Zhu Q, Song K, Zhou Y, Zhou H, Wang J (2021) Coordinated grain boundary deformation governed nanograin annihilation in shear cycling. *J Mater Sci Technol* 86:180–191. <https://doi.org/10.1016/j.jmst.2021.01.032>
84. Zhu T, Li J (2010) Ultra-strength materials. *Prog Mater Sci* 55(7):710–757. <https://doi.org/10.1016/j.pmatsci.2010.04.001>
85. Deneen J, Mook WM, Minor A, Gerberich WW, Barry Carter C (2006) In situ deformation of silicon nanospheres. *J Mater Sci* 41(14):4477–4483. <https://doi.org/10.1007/s10853-006-0085-9>

86. Michler J, Wasmer K, Meier S, Östlund F, Leifer K (2007) Plastic deformation of gallium arsenide micropillars under uniaxial compression at room temperature. *Appl Phys Lett* 90(4):043123. <https://doi.org/10.1063/1.2432277>
87. He Y, Zhong L, Fan F, Wang C, Zhu T, Mao SX (2016) In situ observation of shear-driven amorphization in silicon crystals. *Nat Nanotechnol* 11(10):866–871. <https://doi.org/10.1038/nnano.2016.166>
88. Banerjee A, Bernoulli D, Zhang H, Yuen M-F, Liu J, Dong J, Ding F, Lu J, Dao M, Zhang W, Lu Y, Suresh S (2018) Ultralarge elastic deformation of nanoscale diamond. *Science* 360(6386):300–302. <https://doi.org/10.1126/science.aar4165>
89. Nie A, Bu Y, Li P, Zhang Y, Jin T, Liu J, Su Z, Wang Y, He J, Liu Z, Wang H, Tian Y, Yang W (2019) Approaching diamond's theoretical elasticity and strength limits. *Nat Commun* 10(1):5533. <https://doi.org/10.1038/s41467-019-13378-w>
90. Nie A, Bu Y, Huang J, Shao Y, Zhang Y, Hu W, Liu J, Wang Y, Xu B, Liu Z, Wang H, Yang W, Tian Y (2020) Direct observation of room-temperature dislocation plasticity in diamond. *Matter* 2(5):1222–1232. <https://doi.org/10.1016/j.matt.2020.02.011>
91. Wang L, Zheng K, Zhang Z, Han X (2011) Direct atomic-scale imaging about the mechanisms of ultralarge bent straining in Si nanowires. *Nano Lett* 11(6):2382–2385. <https://doi.org/10.1021/nl200735p>
92. Smith DA, Holmberg VC, Korgel BA (2010) Flexible germanium nanowires: ideal strength, room temperature plasticity, and bendable semiconductor fabric. *ACS Nano* 4(4):2356–2362. <https://doi.org/10.1021/nn1003088>
93. Asthana A, Momeni K, Prasad A, Yap YK, Yassar RS (2011) In situ observation of size-scale effects on the mechanical properties of ZnO nanowires. *Nanotechnology* 22(26):265712. <https://doi.org/10.1088/0957-4484/22/26/265712>
94. Tang D-M, Ren C-L, Wang M-S, Wei X, Kawamoto N, Liu C, Bando Y, Mitome M, Fukata N, Golberg D (2012) Mechanical properties of Si nanowires as revealed by in situ transmission electron microscopy and molecular dynamics simulations. *Nano Lett* 12(4):1898–1904. <https://doi.org/10.1021/nl204282y>
95. Zhang Z, Sheng H, Wang Z, Gludovatz B, Zhang Z, George EP, Yu Q, Mao SX, Ritchie RO (2017) Dislocation mechanisms and 3D twin architectures generate exceptional strength-ductility-toughness combination in CrCoNi medium-entropy alloy. *Nat Commun* 8(1):14390. <https://doi.org/10.1038/ncomms14390>
96. Xie D-G, Wang Z-J, Sun J, Li J, Ma E, Shan Z-W (2015) In situ study of the initiation of hydrogen bubbles at the aluminium metal/oxide interface. *Nat Mater* 14(9):899–903. <https://doi.org/10.1038/nmat4336>
97. Xie D, Li S, Li M, Wang Z, Gumbsch P, Sun J, Ma E, Li J, Shan Z (2016) Hydrogenated vacancies lock dislocations in aluminium. *Nat Commun* 7(1):13341. <https://doi.org/10.1038/ncomms13341>
98. Xie D-G, Wan L, Shan Z-W (2021) Hydrogen enhanced cracking via dynamic formation of grain boundary inside aluminium crystal. *Corros Sci* 183:109307. <https://doi.org/10.1016/j.corros.2021.109307>

Chapter 4

In-Situ Heating TEM



Shijian Zheng and Longbing He

4.1 A Brief History of In-Situ Heating TEM

In the past, people could only obtain static information from the sample, but advancing science and technology make it possible to apply in-situ stimuli and observe the real-time response. Microheaters allow samples to be thermally stimulated and research on dynamic properties (such as phase transitions, materials growth, sublimation, and catalysis) to rise.

The first likely dynamic STEM observation of the motion of atoms on the surface of thin substrates was reported by Crewe in 1979 [1]. The movement of clusters/atoms and the nucleation process have been observed over periods of several hours. This phenomenon was ascribed to thermal effects and inspired further development of technology to improve the contrast and resolution. Soon after, the first in-situ HRTEM imaging of dislocation formation, motion, interaction, and annihilation in gold due to electron beam irradiation was carried out using a TV system by Hashimoto et al. [2]. A more convincing example of atomic movement caused by heating from an incident electron beam was reported by Sinclair et al. [3]. They captured moving species within the crystal structure of the parent material (CdTe) rather than single atomic jumps and the motion rate became higher with longer exposure (Fig. 4.1). When the beam current density was reduced, the response of the motion rate was slow, which implied that this motion did not result from direct electron-atom collisions or

S. Zheng

Tianjin Key Laboratory of Materials Laminating Fabrication and Interface Control Technology, School of Materials Science and Engineering, Hebei University of Technology, Tianjin 300130, China

e-mail: sjzheng@hebut.edu.cn

L. He (✉)

Key Lab of MEMS of Ministry of Education, SEU-FEI Nano-Pico Center, Southeast University, Nanjing 210096, China

e-mail: helongbing@seu.edu.cn

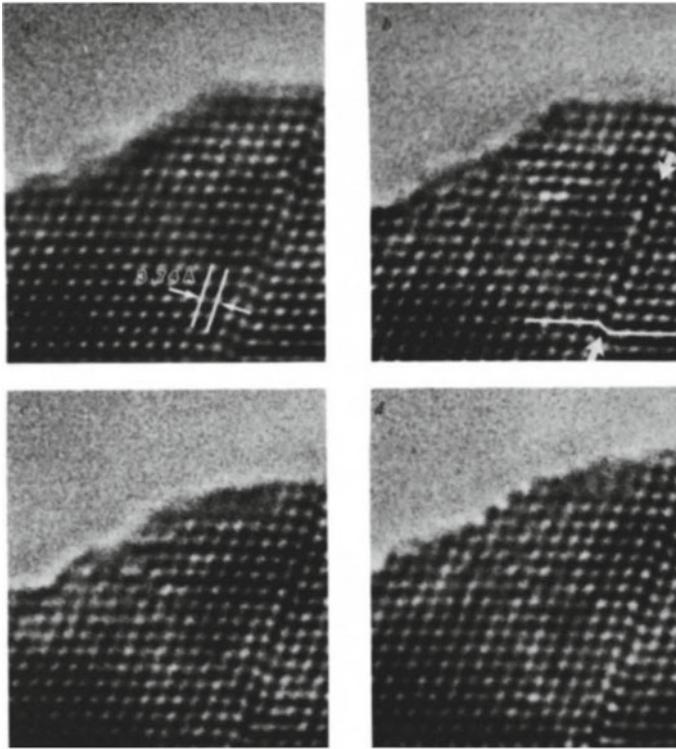


Fig. 4.1 Atomic motion induced by electron beam heating. Four panels are images captured several minutes apart (reproduced with permission from Ref. [3], Copyright 1981, Springer Nature)

ionization effects but presumably arose due to heating dissipation from the active area.

Increasing demand for controllable elevated temperatures during in-situ observation in TEM stimulated Parker's introduction of commercial heating holders in 1986 [4]. The holders exhibited acceptable mechanical and thermal stability to allow high-resolution imaging during the heating process. Besides, a video-rate recording was also realized to follow the dynamic behavior over long periods of time. To demonstrate the technique, Parker et al. observed silicon re-growth at temperatures between 500 and 800 °C. A silicon thin film with a thickness of 300 nm had been deposited on a sapphire substrate and treated by dual ion-implant and annealing. The corresponding TEM specimens were made using a standard cross-section technique. Heating was implemented with a commercial holder (model number PW 6592), where a platinum pad was heated by an electrical feed-through thus the 3-mm disk sample on it was thermally stimulated. There was a thermocouple attached to the pad to measure the temperature and the reading should be fairly close to the actual temperature due to the high thermal conductivities of sapphire and silicon. Reproducible imaging conditions were carefully controlled to keep any beam heating or other effects at a systematic

error level. In their study, they have found that crystallization and defect reactions in silicon are analogous to their predictions that atoms would rearrange at around 600 °C and this phenomenon is similar to that observed in CdTe by electron beam heating [3]. At this point, it is reasonable to expect an atomic-level investigation of structural transformation in many materials during in-situ heating using a similar strategy.

4.2 Current In-Situ Heating TEM Technologies

4.2.1 Operation Mode

TEM can provide extraordinary imaging capability (sub-angstrom spatial resolution) and acquire diffraction and spectroscopy. It generally operates under either TEM mode or STEM mode. TEM mode corresponds to the application of a parallel electron beam while STEM mode uses a focused, small probe scanning over the sample. In TEM mode, HRTEM images are formed by interference between transmitted and diffracted electron beams (phase contrast), but owing to lens aberrations and sample thickness effects, the interpretation of HRTEM images is complicated. In comparison, the interpretation of the image contrast at STEM mode with a high-angle annular dark-field (HAADF) detector is more straightforward, because it is nearly proportional to Z^2 where Z stands for the atomic number. Z-contrast of HAADF-STEM allows visualization of cation mixing at the atomic scale. Furthermore, the combination of STEM and energy-dispersive x-ray spectroscopy (EDX) or electron energy loss spectroscopy (EELS) can obtain chemical information, such as elemental distribution and oxidation state of the materials simultaneously with capture images [5–7]. However, since the low scanning rates may limit the acquisition of instant change of materials, the majority of in-situ observation during heating is operated under TEM mode rather than STEM mode [8].

4.2.2 Type of Heating Holders

The temperature of the specimen can be elevated by using two kinds of heating holders (Fig. 4.2): a furnace-type heating holder (left) that is designed to use standard TEM grids, or a microfabricated-heater-based holder where a localized area is heated through Joule heating [9]. The furnace-based heating holder has long been commercialized and it enables the sample to be heated up to 1300 °C [10, 11]. Unlike the in-situ mechanical experiments in TEM, achieving the sample heating inside a TEM is much easier. For example, Luo et al. investigated the thermal stability of Ni-based superalloy [12], and Liu et al. successfully attached monodisperse Cu nanoparticles onto carbon nanotubes during in-situ heating in a TEM equipped with

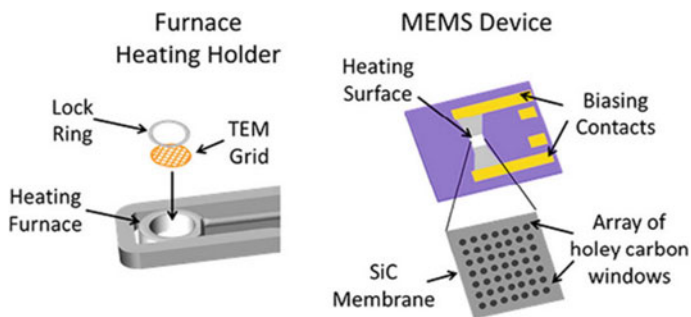


Fig. 4.2 Schematics show two types of heating devices: Furnace heating (left) and MEMS device (right) (reproduced with permission from Ref. [9], Copyright 2018, American Chemical Society)

a Gatan 652 double-tilt heating holder [13]. Nevertheless, the thermal expansion of the stage leads to a non-ignorable image shift during an increase in temperature so it is hard to realize the atomic resolution observation while heating. Especially at temperatures higher than 500 °C, the use of recirculating cooling water to protect the heating unit may also bring vibrations and thereby reduce the imaging stability and resolution. It is challenging to do tests on low-dimensional materials because their morphologies and structures are more sensitive to thermal stimulation. In contrast, the recently developed MEMS-based heating holders only go through negligible mechanical vibrations since heating is localized in a specific small area in the chip and thus allow atomic resolution imaging [14, 15]. For instance, Janish et al. studied nucleation in Ta and captured high-resolution images of nucleating crystallites [16]. In general, the advantage of using furnace-type of holders is that sample preparation is much easier, but the microchip-based holders have better performance regarding temperature control and mitigation of sample drift.

4.2.3 Microheaters

Microheaters are the core of heating holders. The heating zone is usually the region of interest and is placed at the center of the heater since the temperature there is relatively homogeneous. Generally, a microheater includes a silicon substrate or sometimes gallium arsenide and thermally insulating dielectric thin film layers on top [17]. There is an electrically conducting thin film between the substrate and the top insulating layer, where heat is produced by passing electric current provided by the voltage of the current source (This process is called Joule heating). The electrically conducting film can be metal, ceramic or doped polysilicon. Metal is the most frequently used material in microheaters. There are three main reasons. First, since metal has excellent ductility and conductivity, it enables flexible geometrical design and fast response to exerted voltages. Second, due to the near-linear relationship between temperature and resistance, precise temperature control through

resistance measurements can be achieved through a four-point probe. Third, the biggest drawback of metal (i.e. high reaction activity in the environment) can be simply overcome by covering a passivation layer. Ceramic is chemically inert and has high-temperature resistance hence it can be used in tough environments. Doped polysilicon can be easily integrated into standard CMOS processes since it does not limit the following steps as is the issue with metallization [18, 19].

The performance of a microheater is evaluated based on parameters falling into two categories. First, mechanical robustness and stability include mechanical stress, thermal stress, stress distribution, and spatial sample drift. Second, temperature and heat include range and lifetime, homogeneity, accuracy, stability, power consumption, and response time [19].

4.2.4 Synergy with Heating

In addition to single thermal excitation, a combination of heating and other stimuli has shown great potential for research on the dynamic properties of materials in a complicated environment. For example, Karki et al. investigated thermal degradation of overcharged $\text{Li}_{0.1}\text{NCA}$ in different atmospheres using an environmental TEM (ETEM) [20]. Oxidizing, neutral, or reducing environments were created by injecting O_2 , He and H_2 gas into the sample area inside the ETEM. They found that surface oxygen loss and structural evolution were inhibited with the oxidizing environment while greatly enhanced under reductive conditions. Moreover, the understanding thermo-electrical performance of materials is also critical to better manipulate and optimize them for practical applications. For instance, it is crucial to monitor structural changes of ReRAM materials while both heating and biasing are applied to improve their stability for the fabrication of future non-volatile memory devices. Hence, Garza et al. [21] present the design of a system for in-situ biasing and heating called Lightning System as shown in Fig. 4.3. The left panel shows the structure of the nanochips for heating and biasing at the same time. There are eight electrical contacts and half of them are used for heating while the other four are used for biasing. This design ensures 4-point probe measurements for accurate control of the temperature and voltage/current which further guarantees a reproducible response. Then, this nanochip is attached to a customized holder (Right panel in Fig. 4.3), where contact needles are used to provide stimuli from outside of the holder. The system can supply voltage up to 100 V and temperature up to 800 °C while it also enables double-tilt during observation. In-situ simultaneous biasing and heating can carve a new path for a comprehensive understanding of materials and advance the development of nano-electronics. Another typical example has been reported by Wang et al., who utilizes the mechanical tests system during increasing the temperature aiming to select the appropriate alloys for aero-engines [22]. Their work also implies that the cooperation among microscopists, physicists, chemists, and engineers is essential for developing next-generation smart materials.

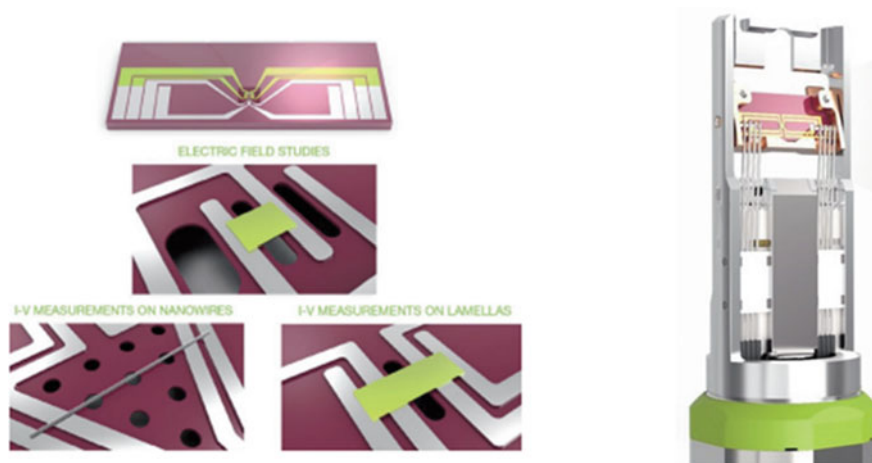


Fig. 4.3 Configuration of nanochip (left) and customized holder with mounted nanochip (right) (reproduced with permission from Ref. [21], Copyright 2016, John Wiley and Sons)

4.3 Research Based on In-Situ Heating TEM

4.3.1 Material Growth

Controllable growth of functional nanomaterials is the starting point for their application in multitudinous devices. Therefore, to explore optimal crystal structures and morphologies, it is necessary to develop methods that can help deeply understand the actual mechanisms behind their growth. The growth of one-dimensional (1D) nanostructures is usually elucidated via a vapor–liquid–solid (VLS) theory. According to the VLS process, the liquid phase dissolves atoms from a solid matrix. When it is supersaturated, growth arises at the surface of the droplet [23]. As the nanostructure is extremely small, a method with a high spatial resolution is crucial to systematically investigate the growth process. The conventional ex-situ observations using microscopy can only analyze the static nanoscale structural information, however, they are incapable of following their forming process [24–26]. By comparison, the in-situ methods enable direct observation of structural transformation occurring at the nanoscale or even atomic scale [27]. For instance, by equipping a heating component, modern TEM can be employed not only for improving resolution but also for making it possible to track dynamic processes during nanowire growth [28, 29], as shown in Fig. 4.4a. During crystal growth, especially in a VLS process, the motion of a semiconductor–metal molten zone is generally motivated by a temperature gradient. Yet, the temperature gradient fields have not been completely understood in earlier ex-situ characterization [30, 31]. Hence, the real-time evidence acquired via in-situ methods provides an opportunity to accurately track liquid zone motion inside the solid [32–34].

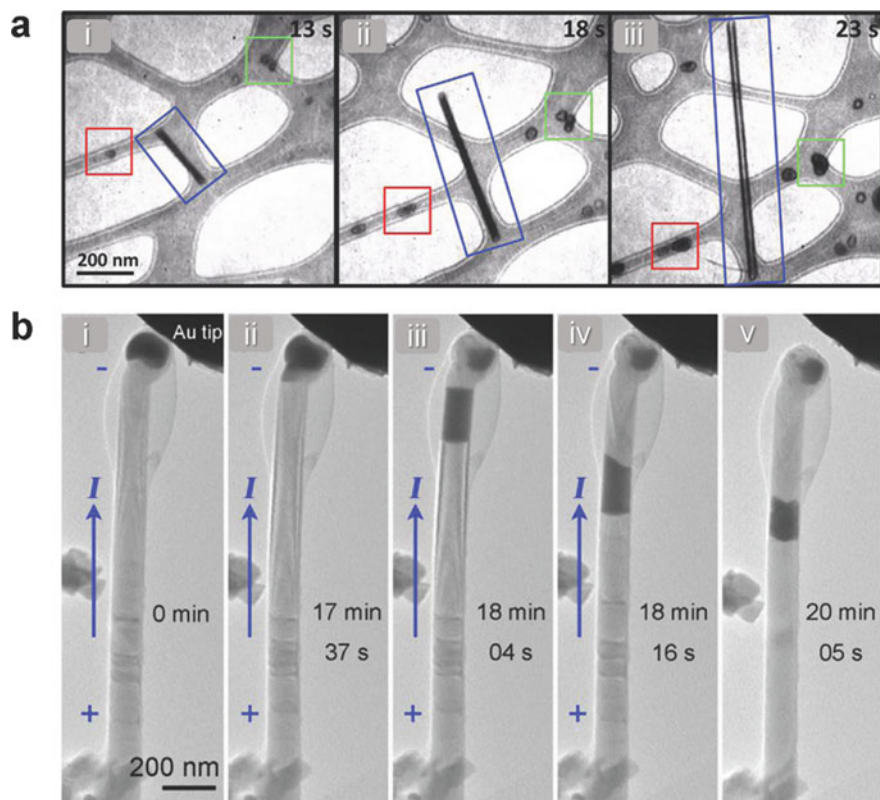


Fig. 4.4 **a** TEM images showing the growth of Cu nanowires during heating (reproduced with permission from Ref. [29], Copyright 2018, American Chemical Society) **b** TEM images exhibiting the motion of Au/Ge alloy during heating (reproduced with permission from Ref. [35], Copyright 2015, American Chemical Society)

Figure 4.4b illustrates an Au particle initially liquifies at the Ge nanowire tip, then creating an Au/Ge alloy liquid area which subsequently moves inside the Ge nanowire [35]. It should be clear that the motion direction and position of the Au/Ge liquid can be manipulated by the applied bias; upon removal of the bias, the Ge nanowire is detached from the Au tip and the liquid Au/Ge alloy quickly hardens. These results resolve the growth kinetics of nanowires, and also inspire more explorations of the growth process of nanoparticles and nanosheets. However, sample handling of them is more complicated. It is expected that a deep investigation of physical and chemical evolutions during material growth at such high resolutions would drive the development of surface and interface engineering.

Later, Cheng et al. found that the growth processes of PbSe nanocrystals (NCs) can be controlled by changing temperature [36]. The NCs begin to grow under the oriented attachment growth mode by attaching dot-shaped NCs along a certain crystal orientation, and sequentially switch to growth with grain-boundary migration

by absorption of smaller NCs by neighboring larger ones through interfacial atom reconstruction.

4.3.2 *Sublimation and Surface Energy*

Besides crystal growth, sublimation is another important phase transition during which the chemical bonds within the solids break-down resulting in gasification. The in-situ experiment in TEM is a direct technique to investigate the sublimation mode at the atomic scale and it should also shed light on a better understanding of the inverted growth process. Additionally, sublimation is strongly linked to material stability, and the research on sublimation of NCs would reveal the critical factors influencing the stability. For example, though the surface free energies of the major crystal planes follow $(111) < (100) < (110)$ in face-centered cubic (FCC) structures [37, 38], the thermally stable surface of FCC metals at elevated temperatures has been under debate for a long period because high-temperature-induced relaxation of crystal planes strongly depends on crystal index [39–41]. Hence the observation of the stable facets of FCC metals at high temperatures has significant importance for clarifying this debate. Ding et al. [42] and He et al. [43] studied the sublimation scenarios of Ag NCs via in-situ heating TEM. The featured shapes and surfaces during sublimation provide direct information for revealing the close linkage between surface free energy and stability (Fig. 4.5). Benefiting from the low drift of the microchip during heating, the dynamic sublimation process of the Ag NC at the very initial can be effectively captured, showing an overwhelming superiority comparing with the furnace-type heating holder.

Aside from this temperature-related surface stability, in fact, the surface energy of a NC itself is still under fierce debate when taking into account the size effect. Theories and simulations from the thermodynamic view suggest a decreasing trend of surface energy with decreasing particle size [44–46], while another view which considers the size-dependent lattice parameters proposes a rather contrary conclusion [47, 48]. On this issue, the in-situ heating TEM becomes the only effective tool for performing investigations from the experimental end. Sambles et al. probed into the surface energies of Au and Ag NCs by fitting the sublimation curves with Kelvin equation [49, 50]. Later, investigations using similar in-situ heating approach achieved more results for understanding the size effect in surface energy [51]. Although the current in-situ heating TEM still cannot clarify all the inconsistencies remained, the development of more delicate microchips with high controllability and accuracy can provide opportunities for modifying/calibrating the physical parameters of nanomaterials.

In addition to the surface energy, the particle size and defects are also of great importance, which further affects the stability of the nanostructure. Cheng et al. discussed the sublimation process of PbSe nanocrystals at the atomic scale and corresponding size, surface, and interface effects [52]. Because of the interplay between the electron beam and surface organic ligands, the sizes of nanocrystals

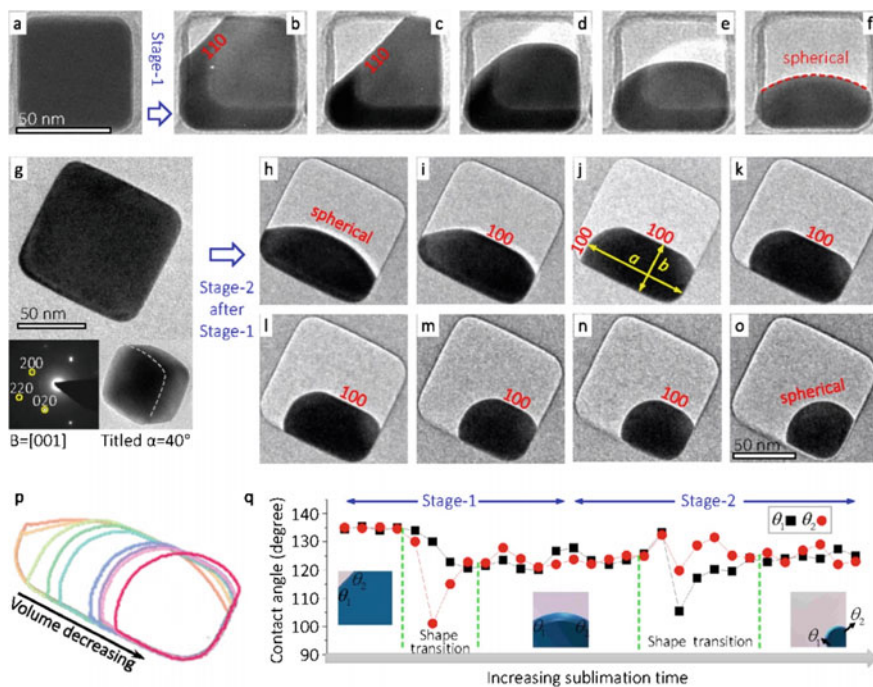


Fig. 4.5 TEM image sequences showing the surface evolution of a cubic Ag NC with a carbon shell (reproduced with permission from Ref. [43], Copyright 2017, John Wiley and Sons)

are successfully manipulated via the introduction of the electron beam at different growth periods, which allows real-time observation of the size dependence of sublimation. As shown in Fig. 4.6, the nanoparticles with a size less than 10 nm exhibit directional orientational sublimation, and those of larger size sublimate uniformly.

4.3.3 Failure Analysis

In in-situ heating TEM, Joule heating is not only used to create a heating region serving as the substrate, but also it is frequently exerted directly in the sample to create synergistic effects. The combination of heat and electromagnetic field frequently leads to unique behaviors in nanomaterials [53]. For example, by controlling the stimulus of atom migration with an appropriate current (i.e. to create a certain temperature and electron-wind force), the mass transport of nano-objects can be implemented at the atomic scale [54–57]. This provides a fantastic method to modulate the nanostructures to enable diverse nanodevices and applications including mass sensors and resonators [58, 59], archival memory [60], oscillators [61], and nano-welding [62]. Aside from these electromigration-based mass transportation phenomena, the

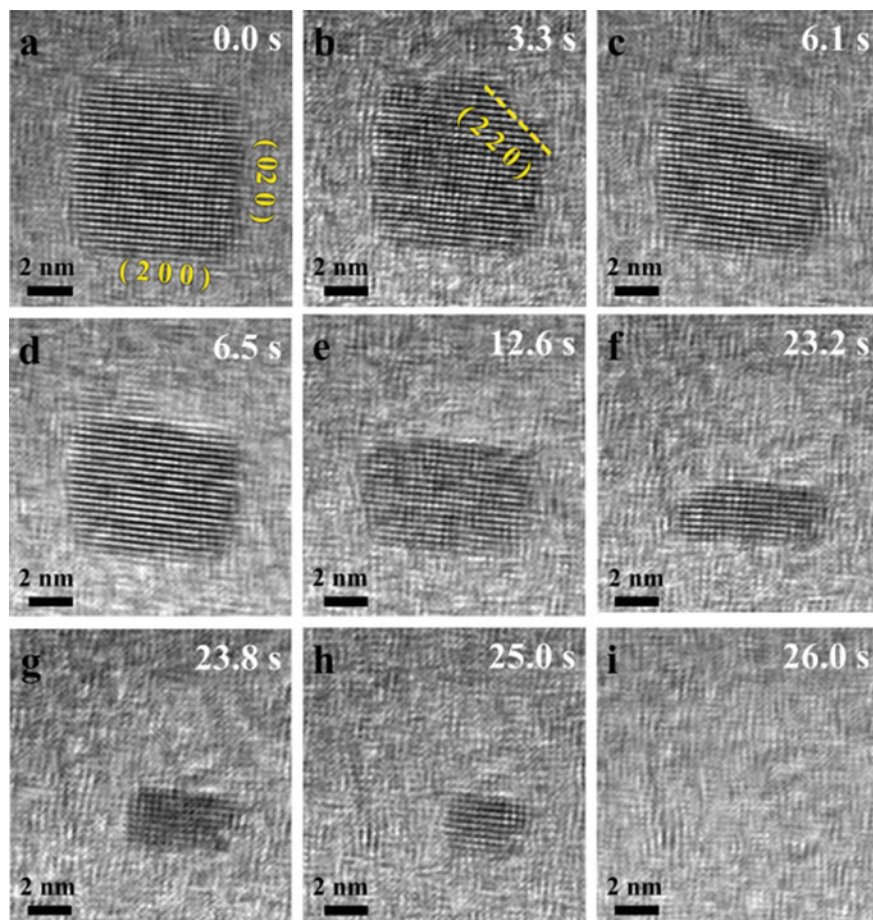


Fig. 4.6 Series of TEM images showing sublimation of a small PbSe nanocube is controlled by its facets (reproduced with permission from Ref. [52], Copyright 2020, Elsevier)

combination of thermal heating with electrical stimuli can also enable ion transport [63–66] and solid-state reactions [67–71]. Mei et al. [72] investigated the solid state reaction/alloying process between nanometer-sized Cu and Al metallic tips. It was found that hetero-joining could be implemented by the coupling of heating and electromigration.

Group III–V nanowires prepared by metal-catalyzed chemical vapor deposition have recently attracted an explosion of interest [73], driven by the inspiring opto-electronic properties, the high crystallinity, and the potential of integrating them with silicon. Recent research on Si nanowires suggests that when the nanowire diameter is below around 150 nm, the thermal conductivity is weakened because of phonon surface scattering [74]. Thermal breakdown in Joule-heated GaN nanowires is studied by in-situ TEM experiment [75]. The thermal conductivity of the nanowires

is reckoned to be below the bulk GaN value. Breakdown in a single nanowire is observed to happen at a maximum temperature of about 1000 K, and nanowire morphology adjacent to the breakdown region suggests that failure happens via thermal decomposition, which is proved by in-situ TEM images captured at the failure stage.

4.3.4 Annealing and Phase Transitions

In-situ annealing provides more dynamic information of sample's structure evolution than the ex-situ approaches. This enables an easy combination between the treating temperatures and the intermediate structures. For example, the FeCrAl alloys are thought to be promising materials of fuel claddings in nuclear reactors. To deeply understand the transformation of helium bubbles and dislocation loops during the annealing process, He⁺-irradiated TEM specimens were annealed and characterized by in-situ TEM [76]. The dislocation density reduced with the rise of temperature, but the loop size presented a different behavior. When the temperature was raised to 1072 K, the bubbles grew quickly while the density reduced. Moreover, in-situ thermal annealing of PtCu₃/C in TEM has also been studied, which reveals essential transformations for achieving highly-active oxygen reduction [77].

Phase transitions are a well-known temperature-dependent process in materials, in-situ techniques in TEM allow direct observation of these processes [78]. For example, polymorphs of Ga₂O₃ [79] are potential candidates for ultra-wide bandgap semiconductors and are widely studied because of the newly developed growth technologies. The temperature-dependent phase transformation of κ -Ga₂O₃ layers grown on sapphire was investigated by high-resolution TEM [80]. Annealing procedures up to 1000 °C were performed in situ in TEM. This enabled the reveal of the mechanisms of κ -to- β phase transition and corresponding atomic rearrangement.

Likewise, the complex phase diagram of Pr_{1-x}Ca_xMnO₃ (PCMO) leads to possibilities of tuning the physical properties for various applications. Significantly, as a result of strong correlation effects, electronic and lattice degrees of freedom are strongly coupled. Therefore, it is arguable whether the bulk phase diagrams can be directly transferred to strained thin films. Beche et al. explored phase transitions at high temperatures in PCMO ($x = 0.1$) deposited as a 400 nm film on a SrTiO₃ (STO) substrate [81]. Combination with TEM, individual domains of the nano-twinned films can be resolved compared with macroscopic X-ray or neutron diffraction studies [82].

Recently, Tang et al. [83] investigated the phase evolution of CuAg alloy NCs by in-situ heating TEM. They found that the transition from a solid solution phase to a Janus-type separated phase leads to the formation of different interfaces related to nanoparticle size. Small nanoparticles tend to form a Cu(100)/Ag(100) interface, while the large ones tend to form a Cu(111)/Ag(111) interface. Ni et al. [84] demonstrates that in-situ annealing also helps fine-tune the phase of Au-Ag nanorods to optimize their plasmonic properties. It is interesting that the microchip can also be used as a calibrator to estimate the beam heating effect inside the TEM. In this way,

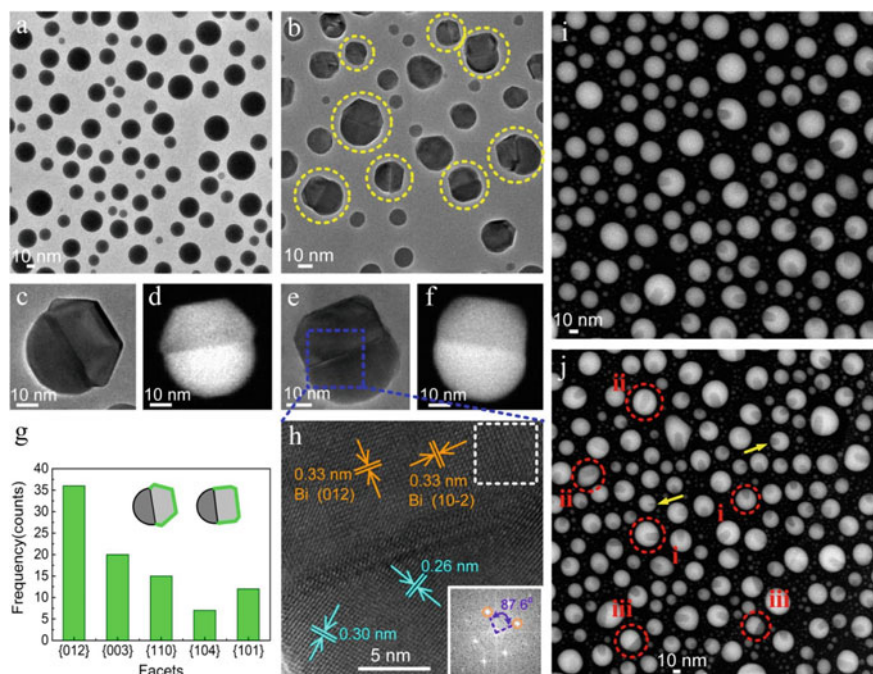


Fig. 4.7 Different morphologies, structures, and phases of PbBi nanoparticles during evolution under in-situ heating treatments (reproduced with permission from Ref. [85] Copyright 2022, American Chemical Society)

the electron beam can be used as an ultra-fast heating source to explore those transient phases that are hardly revealed by conventional methods. Shi et al. [85] used this technique approach to probe into the phase segregation process of PbBi nano-alloy. They have uncovered several metastable phases which haven't been reported before (Fig. 4.7).

4.3.5 Catalysis and Battery

Ordered intermetallic nanoparticles have shown electrocatalysis with improved activity and durability for the oxygen reduction reaction (ORR) [86–88]. Using in-situ heating electron microscopy, morphological evolution and the creation of fully and partially ordered nanocrystals have been observed at the atomic scale [89]. This comprehensive study will have a long-lasting influence on the development of ordered intermetallic electrocatalysts for real-world applications.

Temperature is one of the key factors limiting the application of batteries, thus in-situ heating can be employed to investigate the structural and chemical transformation of battery materials at elevated temperatures. Determining the rational working

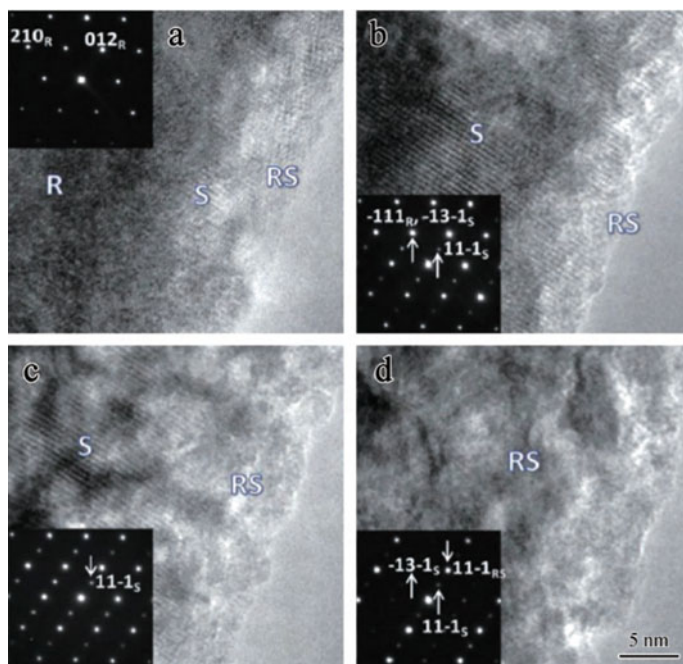


Fig. 4.8 HRTEM images of overcharged nanoparticles: **a** before heating **b** heating at 100 °C **c** heating at 200 °C and **d** heating at 300 °C (reproduced with permission from Ref. [93], Copyright 2013, John Wiley and Sons)

temperature ranges of certain battery materials is critical for developing high-performance batteries to be used in extreme conditions [90–92]. Thermal stability of anode materials may lead to safety issues, so different approaches are demanded to prevent thermal runaway and burning. Nam et al. [93] employed in-situ technologies in TEM to study the thermal stability of overcharged cathode materials, as illustrated in Fig. 4.8. Their work is practically significant since the working temperature is usually changeable rather than constant.

4.3.6 Solid-State Amorphization and Crystallization

One of the most fascinating findings in the 1980s is the formation of amorphous phases by the interplay of two metals at their interfaces [94]. As semiconductor–metal interfaces are vital structures in integrated circuits, Holloway et al. focused on Ti–Si multilayers and discovered that there is also a solid-state amorphization reaction between the interfaces [95]. Additionally, during the early periods of silicidation, an amorphous barrier is formed at the crystalline interface, leading to a high Schottky barrier height [96].

In contrast to amorphization, there is unexpected crystallization observed in some eutectic systems (Al–Si or Ag–Si). In-situ high-resolution TEM reveals that rather than a metastable phase or liquid formation, the initial amorphous phase could be crystallized during adjusting the temperature [97]. Further investigation showed that this crystallization occurred by semiconductor elements diffusing into the metal, then precipitation of the semiconductor would happen after supersaturation [98]. A more thorough research of crystallization in a promising high-k dielectric tantalum oxide enabled a typical Avrami (Kolmogorov–Johnson–Mehl–Avrami) examination of the in-situ experiment. During the observation, the reaction was all the way tracked, thus the nucleation and the growth stages were simply separated for detailed analysis [99].

4.3.7 Degradation of Perovskite Solar Cells

One of the most serious problems limiting the practical application of perovskite solar cells is the lack of thermal stability. Different possible degradation pathways exist in this material system, especially hybrid composites. Therefore, it is inevitable to examine the response of perovskite materials at elevated temperatures. Divitini et al. monitored morphology, structural and chemical changes when heating the prototypes of perovskite solar cells. They present element diffusion and structure break-down and discovered distinct degradation modes in vacuum or air [15].

4.4 Conclusions and Outlook

In summary, in-situ heating TEM plays an increasingly important role in advancing the development of materials for precise structural design and accurate performance control to adapt them to practical applications. In-situ heating offers unique direct information that is not available by other ex-situ methods [100, 101]. In-situ experiments are usually carried out in “TEM mode” to achieve both high spatial resolution and fast recording while “STEM mode” allows more detailed analysis of chemical and electronic information of materials when combined with spectroscopic methods.

However, there are still some issues about in-situ heating in TEM. First, whether the observations are representative of the corresponding bulk materials. Second, the recording rate may still limit the capture of thermally activated processes. Third, data storage and processing capability may affect the in-depth analysis. Fourth, temperature measurement at the microscale remains challenging. Five, it still lacks research on complicated or composite systems, and current studies mainly focus on simple model material systems and reactions.

In the future, in-situ heating TEM should get the following items improved.

Measurement of electron beam effects and their mitigation. High energy electron beam possibly causes destructive changes to the TEM sample and leaves artifacts affecting the objective analysis. Therefore, electron dose, the energy of electrons, vacuum conditions, and nature of materials that determine interaction with the electron beam should be paid careful attention to [102].

High spatial resolution and temporal resolution. Based on more electron-sensitive complementary metal oxide semiconductor, higher spatial and temporal resolution can be realized, which is crucial for revealing the ultra-fast physical and chemical changes and also for investigating the e-beam irradiation sensitive materials [103]. Scanning rates of probe aberration-corrected STEMs are becoming much faster, so HAADF-STEM in-situ observation is expected to play increasingly vital roles in tracking temperature-dependent processes at the atomic scale. Together with EELS and EDS analysis, local changes in chemical composition and valence states of the elements can be monitored during the increasing/decreasing of the temperature [104].

Rapid data recording and processing. Recently developed faster-recording devices will promote the rate/speed at which changes induced by temperature elevation can be tracked, which will result in an enormous increase in data accumulation. The in-situ experiments at nano-second rates by laser pulsing the electron source will also demand much higher data processing power and artificial intelligence should be one of the feasible solutions [105].

Precise temperature measurement down to microscale or even nanoscale. Although estimation of temperature has been achieved via resistivity measurements [106], more accurate local temperature readouts remain challenging.

Multifunctional holders for simultaneous application of different stimuli. Advancement of versatile in-situ TEM approaches that can offer coupled external stimuli. The structural transformation under multiple external stimuli such as mechanical loading, thermal activation, and electric field, or even in a gas atmosphere [107], liquid environments [108], laser illumination [109, 110], magnetic fields [111, 112] etc., have also been observed nowadays. It is expected that future TEM technologies could incorporate multiple fields that simulate the real working environments for the materials.

Expanding material systems where in-situ heating is employed. It is expected that in-situ heating TEM would continue motivating intriguing discoveries in materials science and further promote industrial development. With the development of advanced unique heating holders combined with the ongoing improvement of the transmission electron microscope, the scope of corresponding in-situ heating studies is only limited by the imagination and innovation of the researcher. It should be believed that much fundamental understanding of material properties will be obtained with an increased resolution both spatially and temporally.

References

1. Crewe AV (1979) Direct imaging of single atoms and molecules using the STEM. *Chem Scr* 14:17–20
2. Hashimoto H, Takai Y, Yokota Y, Endoh H, Fukada E (1980) Direct observations of the arrangement of atoms around stacking faults and twins in gold crystals and the movement of atoms accompanying their formation and disappearance. *Jpn J Appl Phys* 19(1):L1–L4. <https://doi.org/10.1143/jjap.19.11>
3. Sinclair R, Yamashita T, Ponce FA (1981) Atomic motion on the surface of a cadmium telluride single crystal. *Nature* 290(5805):386–388. <https://doi.org/10.1038/290386a0>
4. Sinclair R, Parker MA (1986) High-resolution transmission electron microscopy of silicon re-growth at controlled elevated temperatures. *Nature* 322(6079):531–533. <https://doi.org/10.1038/322531a0>
5. Lin F, Markus IM, Nordlund D, Weng T-C, Asta MD, Xin HL, Doeff MM (2014) Surface reconstruction and chemical evolution of stoichiometric layered cathode materials for lithium-ion batteries. *Nat Commun* 5(1):3529. <https://doi.org/10.1038/ncomms4529>
6. Gu M, Belharouak I, Genc A, Wang Z, Wang D, Amine K, Gao F, Zhou G, Thevuthasan S, Baer DR, Zhang J-G, Browning ND, Liu J, Wang C (2012) Conflicting roles of nickel in controlling cathode performance in lithium ion batteries. *Nano Lett* 12(10):5186–5191. <https://doi.org/10.1021/nl302249v>
7. Kim H, Kim MG, Jeong HY, Nam H, Cho J (2015) A new coating method for alleviating surface degradation of $\text{LiNi}_{0.6}\text{Co}_{0.2}\text{Mn}_{0.2}\text{O}_2$ cathode material: nanoscale surface treatment of primary particles. *Nano Lett* 15(3):2111–2119. <https://doi.org/10.1021/acs.nanolett.5b00045>
8. Contarato D, Denes P, Doering D, Joseph J, Krieger B (2012) High speed, radiation hard cmos pixel sensors for transmission electron microscopy. *Phys Procedia* 37:1504–1510. <https://doi.org/10.1016/j.phpro.2012.04.103>
9. Veghte DP, China S, Weis J, Lin P, Hinks ML, Kovarik L, Nizkorodov SA, Gilles MK, Laskin A (2018) Heating-induced transformations of atmospheric particles: environmental transmission electron microscopy study. *Anal Chem* 90(16):9761–9768. <https://doi.org/10.1021/acs.analchem.8b01410>
10. Aradi E, Lewis-Fell J, Harrison RW, Greaves G, Mir AH, Donnelly SE, Hinks JA (2018) Enhanced radiation tolerance of tungsten nanoparticles to He ion irradiation. *Nanomaterials* 8(12). <https://doi.org/10.3390/nano8121052>
11. Ipatova I, Harrison RW, Terentyev D, Donnelly SE, Jimenez-Melero E (2017) Thermal evolution of the proton irradiated structure in tungsten–5 wt% tantalum. *J Fusion Energy* 36(6):234–239. <https://doi.org/10.1007/s10894-017-0145-y>
12. Sihai L, Xiangfan N, Liucheng Z, Xi Y, Weifeng H, Yinghong L (2017) Thermal stability of surface nanostructure produced by laser shock peening in a Ni-based superalloy. *Surf Coat Technol* 311:337–343. <https://doi.org/10.1016/j.surfcoat.2017.01.031>
13. Liu C, Wu S, Zheng H, Cao F, Sheng H, Zhao D, Wang J (2015) Size-controllable fabrication of Cu nanoparticles on carbon nanotubes by simple heating. *Mater Res Bull* 61:270–274. <https://doi.org/10.1016/j.materresbull.2014.10.019>
14. Zhang Q, Chang Y, Gu L, Luo Y, Ge B (2017) Study of microstructure of nickel-based superalloys at high temperatures. *Scripta Mater* 126:55–57. <https://doi.org/10.1016/j.scriptamat.2016.08.013>
15. Divitini G, Cacovich S, Matteocci F, Cinà L, Di Carlo A, Ducati C (2016) In situ observation of heat-induced degradation of perovskite solar cells. *Nat Energy* 1(2):15012. <https://doi.org/10.1038/nenergy.2015.12>
16. Janish MT, Mook WM, Carter CB (2015) Nucleation of fcc Ta when heating thin films. *Scripta Mater* 96:21–24. <https://doi.org/10.1016/j.scriptamat.2014.10.010>
17. Hotovy I, Rehacek V, Mika F, Lalinsky T, Hascik S, Vanko J, Drzik M (2008) Gallium arsenide suspended microheater for MEMS sensor arrays. *Microsyst Technol* 14(4–5):629–635. <https://doi.org/10.1007/s00542-007-0470-6>

18. Franssila S (2010) Introduction to microfabrication, 2 edn. John Wiley & Sons
19. Spruit RG, Ommen JTV, Ghatkesar MK, Garza (2017) A review on development and optimization of microheaters for high-temperature *in situ* studies. *J Microelectromech Syst* 26(6):1165–1182. <https://doi.org/10.1109/jmems.2017.2757402>
20. Karki K, Huang Y, Hwang S, Gamalski AD, Whittingham MS, Zhou G, Stach EA (2016) Tuning the Activity of Oxygen in $\text{LiNi}_{0.8}\text{Co}_{0.15}\text{Al}_{0.05}\text{O}_2$ battery electrodes. *ACS Appl Mater Interfaces* 8 (41):27762–27771. <https://doi.org/10.1021/acsami.6b09585>
21. Pérez Garza HH, Zuo K, Pivak Y, Morsink D, Zakhosheva M, Pen M, van Weperen S, Xu Q MEMS-based system for in-situ biasing and heating solutions inside the TEM. In: European microscopy congress, pp 237–238 (2016). <https://doi.org/10.1002/9783527808465.EMC2016.6710>
22. Wang J, Lu J, You X, Ullah R, Sang L, Chang L, Zhang Y, Zhang Z (2019) In-situ comparison of deformation behavior at 23 °C and 650 °C of laser direct melting deposited Ti-6Al-4V alloy. *Mater Sci Eng, A* 749:48–55. <https://doi.org/10.1016/j.msea.2019.01.111>
23. Joyce HJ, Gao Q, Tan HH, Jagadish C, Kim Y, Fickenscher MA, Perera S, Hoang TB, Smith LM, Jackson HE, Yarrison-Rice JM, Zhang X, Zou J (2009) Unexpected benefits of rapid growth rate for III–V nanowires. *Nano Lett* 9(2):695–701. <https://doi.org/10.1021/nl803182c>
24. Jung CS, Kim HS, Im HS, Park K, Park J, Ahn J-P, Yoo SJ, Kim J-G, Kim JN, Shim JH (2015) In situ temperature-dependent transmission electron microscopy studies of pseudobinary $\text{mGeTe-Bi}_2\text{Te}_3$ ($m = 3-8$) nanowires and first-principles calculations. *Nano Lett* 15(6):3923–3930. <https://doi.org/10.1021/acs.nanolett.5b00755>
25. Behafarid F, Pandey S, Diaz RE, Stach EA, Cuenya BR (2014) An in situ transmission electron microscopy study of sintering and redispersion phenomena over size-selected metal nanoparticles: environmental effects. *Phys Chem Chem Phys* 16(34):18176–18184. <https://doi.org/10.1039/c4cp02574a>
26. Zhu G, Jiang Y, Lin F, Zhang H, Jin C, Yuan J, Yang D, Zhang Z (2014) In situ study of the growth of two-dimensional palladium dendritic nanostructures using liquid-cell electron microscopy. *Chem Commun* 50(67):9447–9450. <https://doi.org/10.1039/c4cc03500c>
27. Zhang Q, Li H, Gan L, Ma Y, Golberg D, Zhai T (2016) In situ fabrication and investigation of nanostructures and nanodevices with a microscope. *Chem Soc Rev* 45(9):2694–2713. <https://doi.org/10.1039/c6cs00161k>
28. Boston R, Schnepp Z, Nemoto Y, Sakka Y, Hall Simon R (2014) In situ TEM observation of a microcrucible mechanism of nanowire growth. *Science* 344(6184):623–626. <https://doi.org/10.1126/science.1251594>
29. Lin T-Y, Chen Y-L, Chang C-F, Huang G-M, Huang C-W, Hsieh C-Y, Lo Y-C, Lu K-C, Wu W-W, Chen L-J (2018) In situ investigation of defect-free copper nanowire growth. *Nano Lett* 18(2):778–784. <https://doi.org/10.1021/acs.nanolett.7b03992>
30. Berg A, Mergenthaler K, Ek M, Pistol M-E, Reine Wallenberg L, Borgström MT (2014) In situ etching for control over axial and radial III–V nanowire growth rates using HBr. *Nanotechnology* 25(50):505601. <https://doi.org/10.1088/0957-4484/25/50/505601>
31. Aslam Z, Nicholls R, Koós A, Nicolosi V, Grobert N (2011) Current-induced restructuring and chemical modification of N-doped multi-walled carbon nanotubes. *Adv Func Mater* 21(20):3933–3937. <https://doi.org/10.1002/adfm.201101036>
32. Ortega Y, Jäger W, Piqueras J, Häußler D, Fernández P (2013) In situ TEM and analytical STEM studies of ZnO nanotubes with Sn cores and Sn nanodrops. *J Phys D Appl Phys* 46(39):395301. <https://doi.org/10.1088/0022-3727/46/39/395301>
33. Wang C-M, Genc A, Cheng H, Pullan L, Baer DR, Bruemmer SM (2014) In-Situ TEM visualization of vacancy injection and chemical partition during oxidation of Ni–Cr nanoparticles. *Sci Rep* 4(1):3683. <https://doi.org/10.1038/srep03683>
34. Wu J, Gao W, Wen J, Miller DJ, Lu P, Zuo J-M, Yang H (2015) Growth of Au on Pt icosahedral nanoparticles revealed by low-dose in situ TEM. *Nano Lett* 15(4):2711–2715. <https://doi.org/10.1021/acs.nanolett.5b00414>
35. Liu Q, Zou R, Wu J, Xu K, Lu A, Bando Y, Golberg D, Hu J (2015) Molten Au/Ge alloy migration in Ge nanowires. *Nano Lett* 15(5):2809–2816. <https://doi.org/10.1021/acs.nanolett.5b01144>

36. Cheng F, Lian L, Li L, Rao J, Li C, Qi T, Zhang Z, Zhang J, Gao Y (2019) Hybrid growth modes of PbSe nanocrystals with oriented attachment and grain boundary migration. *Adv Sci* 6(9):1802202. <https://doi.org/10.1002/advs.201802202>
37. Wang ZL (2000) Transmission electron microscopy of shape-controlled nanocrystals and their assemblies. *J Phys Chem B* 104(6):1153–1175. <https://doi.org/10.1021/jp993593c>
38. Vitos L, Ruban AV, Skriver HL, Kollár J (1998) The surface energy of metals. *Surf Sci* 411(1):186–202. [https://doi.org/10.1016/S0039-6028\(98\)00363-X](https://doi.org/10.1016/S0039-6028(98)00363-X)
39. Stensgaard I, Feidenhans'l R, Sørensen J (1983) Surface relaxation of Cu (110): an ion scattering investigation. *Surf Sci* 128(2–3):281–293. [https://doi.org/10.1016/S0039-6028\(83\)80032-6](https://doi.org/10.1016/S0039-6028(83)80032-6)
40. Jayanthi CS, Tosatti E, Fasolino A, Pietronero L (1985) Multilayer relaxation and melting of a metal surface. *Surf Sci* 152–153:155–161. [https://doi.org/10.1016/0039-6028\(85\)90139-6](https://doi.org/10.1016/0039-6028(85)90139-6)
41. Stairis P, Lu HC, Gustafsson T (1994) Temperature dependent sign reversal of the surface contraction of Ag(111). *Phys Rev Lett* 72(22):3574–3577. <https://doi.org/10.1103/PhysRevLett.72.3574>
42. Ding Y, Fan F, Tian Z, Wang ZL (2009) Sublimation-induced shape evolution of silver cubes. *Small* 5(24):2812–2815. <https://doi.org/10.1002/sml.200901189>
43. He L-B, Zhang L, Tan X-D, Tang L-P, Xu T, Zhou Y-L, Ren Z-Y, Wang Y, Teng C-Y, Sun L-T, Nie J-F (2017) Surface energy and surface stability of Ag nanocrystals at elevated temperatures and their dominance in sublimation-induced shape evolution. *Small* 13(27):1700743. <https://doi.org/10.1002/sml.201700743>
44. Tolman RC (1949) The effect of droplet size on surface tension. *J Chem Phys* 17(3):333–337. <https://doi.org/10.1063/1.1747247>
45. Lu HM, Jiang Q (2004) Size-dependent surface energies of nanocrystals. *J Phys Chem B* 108(18):5617–5619. <https://doi.org/10.1021/jp0366264>
46. Xiong S, Qi W, Cheng Y, Huang B, Wang M, Li Y (2011) Modeling size effects on the surface free energy of metallic nanoparticles and nanocavities. *Phys Chem Chem Phys* 13(22):10648–10651. <https://doi.org/10.1039/c0cp02102d>
47. Medasani B, Park YH, Vasiliev I (2007) Theoretical study of the surface energy, stress, and lattice contraction of silver nanoparticles. *Phys Rev B* 75(23):235436. <https://doi.org/10.1103/PhysRevB.75.235436>
48. Yao Y, Wei Y, Chen S (2015) Size effect of the surface energy density of nanoparticles. *Surf Sci* 636:19–24. <https://doi.org/10.1016/j.susc.2015.01.016>
49. Sambles JR, Skinner LM, Lisgarten ND, Blackman M (1970) An electron microscope study of evaporating small particles: the Kelvin equation for liquid lead and the mean surface energy of solid silver. *Proceed Roy Soc Lond A Math Phys Sci* 318(1535):507–522. <https://doi.org/10.1098/rspa.1970.0157>
50. Blackman M, Sambles J (1970) Melting of very small particles during evaporation at constant temperature. *Nature* 226(5249):938–938. <https://doi.org/10.1038/226938a0>
51. He L-B, Zhang L, Tang L-P, Sun J, Zhang Q-B, Sun L-T (2018) Novel behaviors/properties of nanometals induced by surface effects. *Materials Today Nano* 1:8–21. <https://doi.org/10.1016/j.mtnano.2018.04.006>
52. Cheng F, Lian L, Li L, Rao J, Li C, Qi T, Cheng Y, Zhang Z, Zhang J, Wang J, Gao Y (2020) Sublimation and related thermal stability of PbSe nanocrystals with effective size control evidenced by in situ transmission electron microscopy. *Nano Energy* 75:104816. <https://doi.org/10.1016/j.nanoen.2020.104816>
53. Golberg D, Costa PMFJ, Wang M-S, Wei X, Tang D-M, Xu Z, Huang Y, Gautam UK, Liu B, Zeng H, Kawamoto N, Zhi C, Mitome M, Bando Y (2012) Nanomaterial engineering and property studies in a transmission electron microscope. *Adv Mater* 24(2):177–194. <https://doi.org/10.1002/adma.201102579>
54. Regan B, Aloni S, Ritchie R, Dahmen U, Zettl A (2004) Carbon nanotubes as nanoscale mass conveyors. *Nature* 428(6986):924–927. <https://doi.org/10.1038/nature02496>
55. Svensson K, Olin H, Olsson E (2004) Nanopipettes for metal transport. *Phys Rev Lett* 93(14):145901. <https://doi.org/10.1103/PhysRevLett.93.145901>

56. Golberg D, Costa PM, Mitome M, Hampel S, Haase D, Mueller C, Leonhardt A, Bando Y (2007) Copper-filled carbon nanotubes: Rheostatlike behavior and femtogram copper mass transport. *Adv Mater* 19(15):1937–1942. <https://doi.org/10.1002/adma.200700126>
57. Huang JY, Lo Y-C, Niu JJ, Kushima A, Qian X, Zhong L, Mao SX, Li J (2013) Nanowire liquid pumps. *Nat Nanotechnol* 8(4):277–281. <https://doi.org/10.1038/nnano.2013.41>
58. Kim K, Jensen K, Zettl A (2009) Tuning nanoelectromechanical resonators with mass migration. *Nano Lett* 9(9):3209–3213. <https://doi.org/10.1021/nl901449w>
59. Jensen K, Kim K, Zettl A (2008) An atomic-resolution nanomechanical mass sensor. *Nat Nanotechnol* 3(9):533–537. <https://doi.org/10.1038/nnano.2008.200>
60. Begtrup GE, Gannett W, Yuzvinsky TD, Crespi VH, Zettl A (2009) Nanoscale reversible mass transport for archival memory. *Nano Lett* 9(5):1835–1838. <https://doi.org/10.1021/nl803800c>
61. Regan BC, Aloni S, Jensen K, Zettl A (2005) Surface-tension-driven nanoelectromechanical relaxation oscillator. *Appl Phys Lett* 86(12):123119. <https://doi.org/10.1063/1.1887827>
62. Dong T, Zhang L, Zhang NBJ (2007) Nanorobotic spot welding: controlled metal deposition with attogram precision from copper-filled carbon nanotubes. *Nano Lett* 7(1):58–63. <https://doi.org/10.1021/nl061980+>
63. Park G-S, Kim YB, Park SY, Li XS, Heo S, Lee M-J, Chang M, Kwon JH, Kim M, Chung U-I (2013) In situ observation of filamentary conducting channels in an asymmetric Ta₂O_{5-x}/TaO_{2-x} bilayer structure. *Nat Commun* 4(1):1–9. <https://doi.org/10.1038/ncomms3382>
64. Huang JY, Zhong L, Wang CM, Sullivan JP, Xu W, Zhang LQ, Mao SX, Hudak NS, Liu XH, Subramanian A, Fan H, Qi L, Kushima A, Li J (2010) In situ observation of the electrochemical lithiation of a single SnO₂ nanowire electrode. *Science* 330(6010):1515–1520. <https://doi.org/10.1126/science.1195628>
65. Celano U, Goux L, Belmonte A, Opsomer K, Franquet A, Schulze A, Detavernier C, Richard O, Bender H, Jurczak M, Vandervorst W (2014) Three-dimensional observation of the conductive filament in nanoscaled resistive memory devices. *Nano Lett* 14(5):2401–2406. <https://doi.org/10.1021/nl500049g>
66. Zhang Q, Yin K, Dong H, Zhou Y, Tan X, Yu K, Hu X, Xu T, Zhu C, Xia W (2017) Electrically driven cation exchange for in situ fabrication of individual nanostructures. *Nat Commun* 8(1):1–7. <https://doi.org/10.1038/ncomms14889>
67. Sagel A, Wanderka N, Wunderlich RK, Schubert-Bischoff P, Fecht HJ (1997) Early stages of solid-state amorphization reaction during mechanical alloying of a multicomponent Zr-powder mixture. *Scripta Mater* 38(1):163–169. [https://doi.org/10.1016/S1359-6462\(97\)00408-9](https://doi.org/10.1016/S1359-6462(97)00408-9)
68. Lucadamo G, Barmak K, Carpenter DT, Rickman JM (2001) Microstructure evolution during solid state reactions of Nb/Al multilayers. *Acta Mater* 49(14):2813–2826. [https://doi.org/10.1016/S1359-6454\(01\)00176-8](https://doi.org/10.1016/S1359-6454(01)00176-8)
69. Wang L, Qin XY (2003) The effect of mechanical milling on the formation of nanocrystalline Mg₂Si through solid-state reaction. *Scr Mater* 49(3):243–248. [https://doi.org/10.1016/S1359-6462\(03\)00241-0](https://doi.org/10.1016/S1359-6462(03)00241-0)
70. Fashandi H, Lai CC, Dahlqvist M, Lu J, Rosen J, Hultman L, Greczynski G, Andersson M, Lloyd Spetz A, Eklund P (2017) Ti₂Au₂C and Ti₃Au₂C₂ formed by solid state reaction of gold with Ti₂AlC and Ti₃AlC₂. *Chem Commun* 53(69):9554–9557. <https://doi.org/10.1039/c7cc04701k>
71. Kim G, Lee H, Kim J, Roh JW, Lyo I, Kim B-W, Lee KH, Lee W (2017) Up-scaled solid state reaction for synthesis of doped Mg₂Si. *Scr Mater* 128:53–56. <https://doi.org/10.1016/j.scriptamat.2016.10.010>
72. Mei S, He L, Wu X, Sun J, Wang B, Xiong X, Sun L (2014) Dynamic investigation of interface atom migration during heterostructure nanojoining. *Nanoscale* 6(1):405–411. <https://doi.org/10.1039/c3nr03911k>
73. Qian F, Gradečak S, Li Y, Wen C-Y, Lieber CM (2005) Core/multishell nanowire heterostructures as multicolor, high-efficiency light-emitting diodes. *Nano Lett* 5(11):2287–2291. <https://doi.org/10.1021/nl051689e>

74. Liang LH, Li B (2006) Size-dependent thermal conductivity of nanoscale semiconducting systems. *Phys Rev B* 73(15):153303. <https://doi.org/10.1103/PhysRevB.73.153303>
75. Westover T, Jones R, Huang JY, Wang G, Lai E, Talin AA (2009) Photoluminescence, thermal transport, and breakdown in Joule-Heated GaN nanowires. *Nano Lett* 9(1):257–263. <https://doi.org/10.1021/nl802840w>
76. Chen Y, Li Y, Ran G, Wu L, Ye C, Han Q, Wang H, Du H (2020) In-situ TEM observation of the evolution of dislocation loops and helium bubbles in a pre helium irradiated FeCrAl alloy during annealing. *Prog Nucl Energy* 129:103502. <https://doi.org/10.1016/j.pnucene.2020.103502>
77. Gatalo M, Ruiz-Zepeda F, Hodnik N, Dražić G, Bele M, Gaberšček M (2019) Insights into thermal annealing of highly-active PtCu₃/C oxygen reduction reaction electrocatalyst: an in-situ heating transmission electron microscopy study. *Nano Energy* 63:103892. <https://doi.org/10.1016/j.nanoen.2019.103892>
78. Meng S, Wu J, Zhao L, Zheng H, Jia S, Hu S, Meng W, Pu S, Zhao D, Wang J (2018) Atomistic Insight into the Redox Reactions in Fe/Oxide core-shell nanoparticles. *Chem Mater* 30(20):7306–7312. <https://doi.org/10.1021/acs.chemmater.8b03679>
79. Roy R, Hill VG, Osborn EF (1952) Polymorphism of Ga₂O₃ and the system Ga₂O₃–H₂O. *J Am Chem Soc* 74(3):719–722. <https://doi.org/10.1021/ja01123a039>
80. Cora I, Fogarassy Z, Fornari R, Bosi M, Rečnik A, Pécz B (2020) In situ TEM study of $\kappa \rightarrow \beta$ and $\kappa \rightarrow \gamma$ phase transformations in Ga₂O₃. *Acta Mater* 183:216–227. <https://doi.org/10.1016/j.actamat.2019.11.019>
81. Béché A, Rouvière JL, Clément L, Hartmann JM (2009) Improved precision in strain measurement using nanobeam electron diffraction. *Appl Phys Lett* 95(12):123114. <https://doi.org/10.1063/1.3224886>
82. Meyer T, Kressdorf B, Roddatis V, Hoffmann J, Jooss C, Seibt M (2021) Phase Transitions in a perovskite thin film studied by environmental in situ heating nano-beam electron diffraction. *Small Methods* 5(9):2100464. <https://doi.org/10.1002/smt.202100464>
83. Tang L, Wu W, He L, Yu K, Xu T, Zhang Q, Zhang L, Sun L (2019) Novel interface in CuAg nanostructure induced by size effect. *J Phys Chem Lett* 10(8):1973–1980. <https://doi.org/10.1021/acs.jpcclett.9b00484>
84. Ni Y, Kan C, He L, Zhu X, Jiang M, Shi D (2019) Alloyed Au-Ag nanorods with desired plasmonic properties and stability in harsh environments. *Photon Res* 7(5):558–565. <https://doi.org/10.1364/prj.7.000558>
85. Shi L, He L, Shangguan L, Zhou Y, Wang B, Zhang L, Yang Y, Teng C, Sun L (2022) Revealing the phase segregation and evolution dynamics in binary nanoalloys via electron beam-assisted ultrafast heating and cooling. *ACS Nano* 16(1):921–929. <https://doi.org/10.1021/acsnano.1c08500>
86. Yan Y, Du JS, Gilroy KD, Yang D, Xia Y, Zhang H (2017) Intermetallic nanocrystals: syntheses and catalytic applications. *Adv Mater* 29(14):1605997. <https://doi.org/10.1002/adma.201605997>
87. Chung DY, Jun SW, Yoon G, Kwon SG, Shin DY, Seo P, Yoo JM, Shin H, Chung Y-H, Kim H, Mun BS, Lee K-S, Lee N-S, Yoo SJ, Lim D-H, Kang K, Sung Y-E, Hyeon T (2015) Highly durable and active PtFe nanocatalyst for electrochemical oxygen reduction reaction. *J Am Chem Soc* 137(49):15478–15485. <https://doi.org/10.1021/jacs.5b09653>
88. Kuttiyiel KA, Sasaki K, Su D, Wu L, Zhu Y, Adzic RR (2014) Gold-promoted structurally ordered intermetallic palladium cobalt nanoparticles for the oxygen reduction reaction. *Nat Commun* 5(1):5185. <https://doi.org/10.1038/ncomms6185>
89. Xiong Y, Yang Y, Jores H, Padgett E, Gupta U, Yarlagadda V, Agyeman-Budu DN, Huang X, Moylan TE, Zeng R, Kongkanand A, Escobedo FA, Brock JD, DiSalvo FJ, Muller DA, Abruña HD (2019) Revealing the atomic ordering of binary intermetallics using in situ heating techniques at multilength scales. *Proc Natl Acad Sci* 116(6):1974. <https://doi.org/10.1073/pnas.1815643116>
90. Sun Y, Liu Y, Truong TT, Ren Y (2012) Thermal transformation of δ -MnO₂ nanoflowers studied by in-situ TEM. *Sci China Chem* 55(11):2346–2352. <https://doi.org/10.1007/s11426-012-4688-5>

91. Zhang L, Feng Q, Nie A, Liu J, Wang H, Fang Y (2014) *In situ* study of thermal stability of copper oxide nanowires at anaerobic environment. *J Nanomater* 2014:91. <https://doi.org/10.1155/2014/670849>
92. Wu J, Liu X, Bi H, Song Y, Wang C, Cao Q, Liu Z, Wang M, Che R (2016) Microwave sintering and in-situ transmission electron microscopy heating study of $\text{Li}_{1.2}(\text{Mn}_{0.53}\text{Co}_{0.27})\text{O}_2$ with improved electrochemical performance. *J Power Sources* 326:104–111. <https://doi.org/10.1016/j.jpowsour.2016.06.102>
93. Nam K-W, Bak S-M, Hu E, Yu X, Zhou Y, Wang X, Wu L, Zhu Y, Chung K-Y, Yang X-Q (2013) Combining in situ synchrotron x-ray diffraction and absorption techniques with transmission electron microscopy to study the origin of thermal instability in overcharged cathode materials for lithium-ion batteries. *Adv Func Mater* 23(8):1047–1063. <https://doi.org/10.1002/adfm.201200693>
94. Schwarz RB, Johnson WL (1983) Formation of an amorphous alloy by solid-state reaction of the pure polycrystalline metals. *Phys Rev Lett* 51(5):415–418. <https://doi.org/10.1103/PhysRevLett.51.415>
95. Holloway K, Sinclair R (1987) Amorphous Ti–Si alloy formed by interdiffusion of amorphous Si and crystalline Ti multilayers. *J Appl Phys* 61(4):1359–1364. <https://doi.org/10.1063/1.338114>
96. Si O, Kouzaki T, Yoshida T, Sinclair R (1991) Interface microstructure of titanium thin-film/silicon single-crystal substrate correlated with electrical barrier heights. *J Appl Phys* 70(2):827–832. <https://doi.org/10.1063/1.349641>
97. Konno TJ, Sinclair R (1992) Crystallization of silicon in aluminium/amorphous-silicon multilayers. *Philos Mag B* 66(6):749–765. <https://doi.org/10.1080/13642819208220126>
98. Konno TJ, Sinclair R (1995) Metal-mediated crystallization of amorphous silicon in silicon-siliver layered systems. *Philos Mag B* 71(2):163–178. <https://doi.org/10.1080/01418639508240304>
99. Min KH, Sinclair R, Park IS, Kim ST, Chung UI (2005) Crystallization behaviour of ALD-Ta₂O₅ thin films: the application of in-situ TEM. *Phil Mag* 85(18):2049–2063. <https://doi.org/10.1080/14786430500036546>
100. Danev R, Yanagisawa H, Kikkawa M (2019) Cryo-electron microscopy methodology: current aspects and future directions. *Trends Biochem Sci* 44(10):837–848. <https://doi.org/10.1016/j.tibs.2019.04.008>
101. Wang L, Han X, Liu P, Yue Y, Zhang Z, Ma E (2010) In situ observation of dislocation behavior in nanometer grains. *Phys Rev Lett* 105(13):135501. <https://doi.org/10.1103/PhysRevLett.105.135501>
102. Taheri ML, Stach EA, Arslan I, Crozier PA, Kabius BC, LaGrange T, Minor AM, Takeda S, Tanase M, Wagner JB, Sharma R (2016) Current status and future directions for in situ transmission electron microscopy. *Ultramicroscopy* 170:86–95. <https://doi.org/10.1016/j.ultramicro.2016.08.007>
103. Miller B, Pakzad A, Mick S (2019) Real-time electron counting for continuous TEM imaging of sensitive samples. *Microsc Microanal* 25(S2):1718–1719. <https://doi.org/10.1017/s1431927619009322>
104. Idrobo JC, Zhou W (2017) A short story of imaging and spectroscopy of two-dimensional materials by scanning transmission electron microscopy. *Ultramicroscopy* 180:156–162. <https://doi.org/10.1016/j.ultramicro.2017.02.002>
105. Zhang B, Wang J, Wu B, Guo XW, Wang YJ, Chen D, Zhang YC, Du K, Oguzie EE, Ma XL (2018) Unmasking chloride attack on the passive film of metals. *Nat Commun* 9(1):2559. <https://doi.org/10.1038/s41467-018-04942-x>
106. Winterstein JP, Lin PA, Sharma R (2015) Temperature calibration for in situ environmental transmission electron microscopy experiments. *Microsc Microanal* 21(6):1622–1628. <https://doi.org/10.1017/s1431927615015196>
107. Jiang Y, Zhang Z, Yuan W, Zhang X, Wang Y, Zhang Z (2018) Recent advances in gas-involved in situ studies via transmission electron microscopy. *Nano Res* 11(1):42–67. <https://doi.org/10.1007/s12274-017-1645-9>

108. Liao H-G, Zheng H (2016) Liquid cell transmission electron microscopy. *Annu Rev Phys Chem* 67(1):719–747. <https://doi.org/10.1146/annurev-physchem-040215-112501>
109. Fernando JFS, Zhang C, Firestein KL, Golberg D (2017) Optical and optoelectronic property analysis of nanomaterials inside transmission electron microscope. *Small* 13(45):1701564. <https://doi.org/10.1002/sml.201701564>
110. Song C, Yang S, Li X, Li X, Feng J, Pan A, Wang W, Xu Z, Bai X (2019) Optically manipulated nanomechanics of semiconductor nanowires. *Chin Phys B* 28(5):054204. <https://doi.org/10.1088/1674-1056/28/5/054204>
111. Zhu S, Fu J, Li H, Zhu L, Hu Y, Xia W, Zhang X, Peng Y, Zhang J (2018) Direct observation of magnetocrystalline anisotropy tuning magnetization configurations in uniaxial magnetic nanomaterials. *ACS Nano* 12(4):3442–3448. <https://doi.org/10.1021/acsnano.8b00058>
112. Du H, Zhao X, Rybakov FN, Borisov AB, Wang S, Tang J, Jin C, Wang C, Wei W, Kiselev NS, Zhang Y, Che R, Blügel S, Tian M (2018) Interaction of individual skyrmions in a nanostructured cubic chiral magnet. *Phys Rev Lett* 120(19):197203. <https://doi.org/10.1103/PhysRevLett.120.197203>

Chapter 5

In-Situ Biasing TEM



Liqiang Zhang, Yongfu Tang, Lin Gu, and Jianyu Huang

5.1 Introduction

As the scale of microelectronics continues to shrink, understanding the electron transport through essentially one-dimensional nanowires [1, 2] or quantum wires [3] and carbon nanotubes (CNTs) becomes essential in miniaturizing electronic devices [4, 5]. These nanostructures demonstrate different electronic transport properties from their bulk counterparts and are the future of high-performance electronic devices [3, 5, 6]. The transport properties of nanomaterials strongly depend on their microstructure; however, there exists a gap between the structure and property studies of nanostructured materials, i.e., studying the structure without knowing the property, or vice versa. Therefore, there is an urgent need to bridge this gap by conducting simultaneous structure and property studies of individual nanostructures. This can be accomplished by developing microelectromechanical system (MEMS) devices with electron transparent windows or using a transmission electron microscopy-scanning probe microscopy (TEM-SPM) platform. TEM combined with MEMS devices and TEM-SPM are powerful tools for in situ investigation of structure, physical, chemical/electrochemical, electronic, mechanical properties, and interactions at atomic scale.

L. Zhang · Y. Tang · J. Huang (✉)
State Key Laboratory of Metastable Materials Science and Technology, Clean Nano Energy
Center, Yanshan University, Qinhuangdao 066004, China
e-mail: jyhuang8@hotmail.com

L. Zhang
e-mail: lqzhang@ysu.edu.cn

L. Gu
Beijing National Laboratory for Condensed Matter Physics, Institute of Physics, Chinese
Academy of Sciences, Beijing 100190, China
e-mail: l.gu@iphy.ac.cn

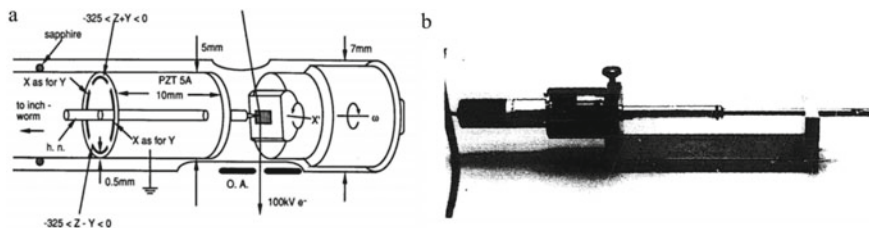


Fig. 5.1 **a** The STM-REM instrument. Tilt of the sample about the axis normal to the tube axis may be preset as shown at X' . Here, O. A. is the objective aperture, h.n. is the hypodermic needle used to hold the tip; **b** Photograph of the completed STM side-entry holder mounted in its external support. The inchworm is at left, the PZT is the dark region inside the opening in the holder at the right (reproduced with permission from Ref. [7], Copyright 1988, Elsevier)

Spence [7, 8] is the first to integrate a scanning tunneling microscopy (STM) into a TEM (Philips EM 400 T), and his intention was to use reflection electron microscopy (REM) to image the working principle of an STM (Fig. 5.1). He obtained REM images of a sample area while the STM was operating.

The TEM-STM instrument consists of a piezoelectric transducer displacing a sharp probe (tip) along three axis. The tip extends to reach the sample with sub-Å precision in XYZ. The coarse motion is realized by the inertial slider motor and the fine motion is accomplished by extension of the piezo-tube itself. Displacement of the probe ranges from millimeter to sub-nanometer scale. Micrometer to nanometer to even atomic chain are easily accessible to the probe. Manual and feedback-regulated control of the motion permits dedicated contacts or tunneling between the tip and the sample. Electrical measurements such as current–voltage (I – V) and current–distance can be acquired.

Wall and Dahmen [9] were the first to design, construct, and test a nanoindentation holder in a high-voltage TEM, which was later commercialized as the Hysitron PI 95 TEM holder. By using a conducting diamond tip or replacing the diamond indenter tip with a conducting probe, the electrical property changes during nanoindentation can be monitored. In situ nanoindentation of Si [9], Al thin film was successfully conducted [10]. The PI 95 holder uses a different coarse motion mechanism from the inertial sliding in the TEM-SPM, i.e., it uses a micrometer screw at the end of the sample holder to manually advance or retract the piezo inside the TEM holder.

Performing STM imaging in a TEM seems not to be the best configuration; instead, the TEM-STM platform is mostly used for in situ biasing experiments. Several companies have commercialized various types of in situ biasing TEM holders [11–14]. Some representative in situ biasing holders are shown in Fig. 5.2.

In addition to the STM holder, MEMS chips are also widely used method for applying bias. The advantage of this technology is that the sample can be transferred and placed at any position of the MEMS electrodes through Focused Ion Beam (FIB), and then the two ends of the sample can be welded together with the electrode through Au/Pt plating to ensure its low contact resistance. The accuracy and stability of this method is much better than the STM method. However, the sample preparation cost

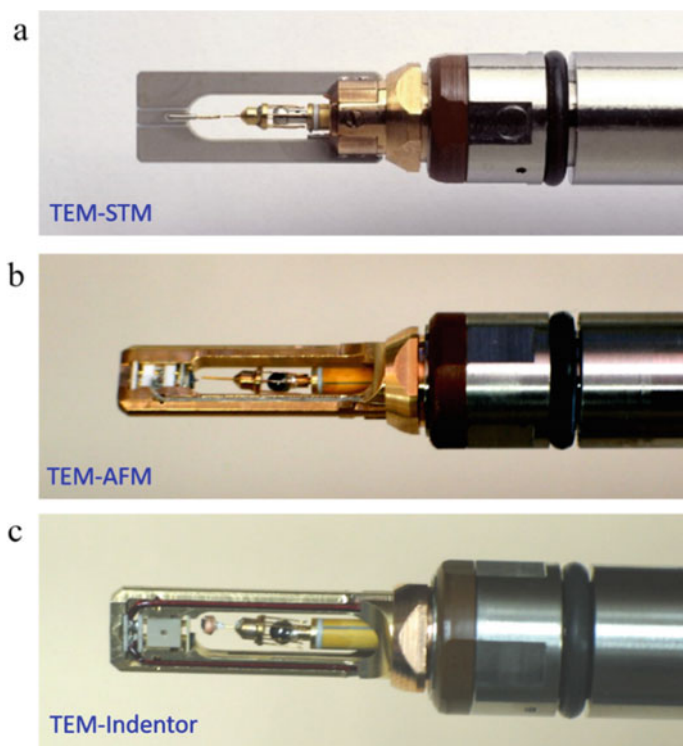


Fig. 5.2 Various types of commercialized in situ biasing TEM holders. **a** TEM-STM; **b** TEM-AFM; **c** TEM-indentor

is relatively high, as the chip needs to be replaced every time. Meanwhile, the sample preparation time is much longer than using the STM holder.

Combining TEM-SPM with various MEMS devices, it is now routine to perform in situ field emission, electric/ion transport, electrical mechanical coupling, electrochemomechanics, electrochemistry, and even thermal studies of various nanomaterials.

5.2 Electrical Measurements

5.2.1 *Field Emission of Carbon Nanotubes and Nanowires*

One of the most promising applications employs carbon nanotubes as electron emitters in the field-emission devices, such as flat panel displays, X-ray tubes, and microwave power amplifiers [15–17]. However, further improvements are necessary to decisively outperform the existing technologies. Most experiments were conducted

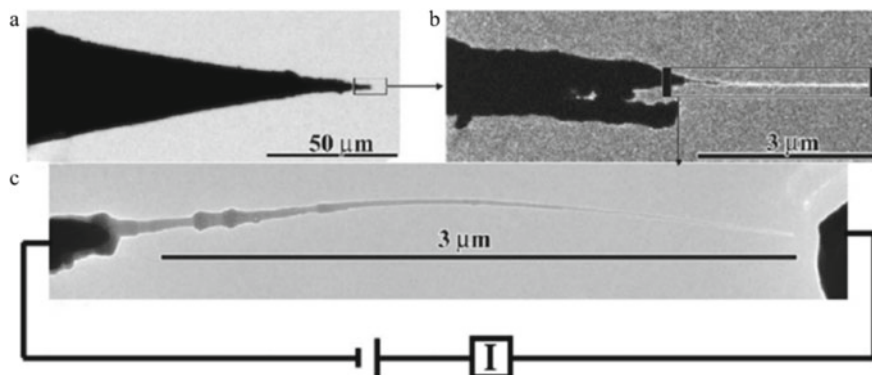


Fig. 5.3 Multistage geometry of a nanotube attached to a conical Au rod. **a–b** are the low and medium magnification images, respectively; **c** is the TEM micrograph of the nanotube and a schematic drawing showing the field-emission setup (reproduced with permission from Ref. [18], Copyright 2005, AIP Publishing)

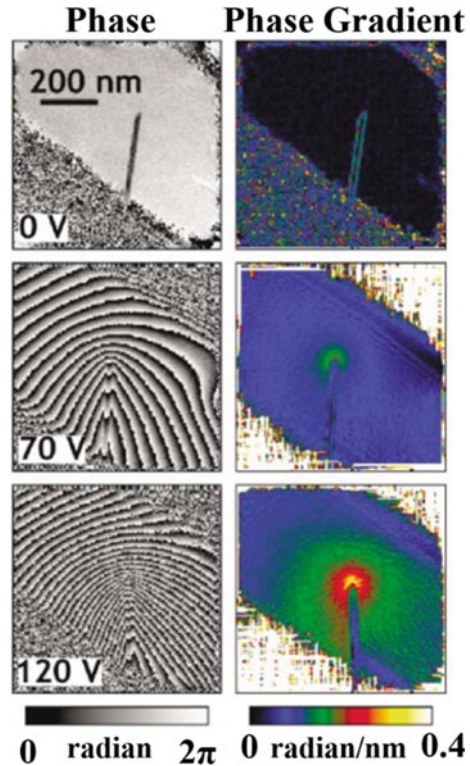
with large area emitters, in which a variety of nanotubes participates in the emission. This randomness obscures the basic mechanisms of the field emission, understanding of which is crucial for applications. Using a TEM-STM platform, Huang et al. [18] conducted field-emission studies to individual CNTs (Fig. 5.3). They reveal a multistage structure of some of the nanotubes, characterized by an order of magnitude smaller nanotubes branching off the tips of bigger nanotubes or carbon fibers. The multistage structure causes a macroscopic enhancement of the electric field, which can match that of a single macroscopically long nanotube with length equal to the combined length of all stages, and the tip radius equal to that of the thinnest nanotube in the structure. This not only explains the observed giant field enhancement, but also provides important clues for the design of nanotube emitters for electronic applications [19]. Field emission properties of boron nitride and carbon nanotubes were also measured in situ by Zettl groups [20].

Electron holography of field-emitting carbon nanotubes had been performed in situ by Zettl groups [21]. It can give information about inner electric fields of materials. Measurements of the phase shift and phase gradient maps show that the electric field is concentrated precisely at the end of nanotubes and not at other nanotube defects such as sidewall imperfections (Fig. 5.4).

5.2.2 *Quantum Conductance of Au Atomic Chain and MWCNT*

As early as in 1967, Blech and Meieran [22] designed a special electrical chip that can be fitted into a TEM sample holder. Thin Al strip was deposited onto the chip which has electrical feed through to the exterior end of the sample holder. They observed

Fig. 5.4 Phase shift and phase gradient maps extracted from holograms of the same nanotube at bias voltages $V_b = 0, 70,$ and 120 V. The phase gradient indicates where the electric field is the strongest; note the concentration of the electric field at the nanotube tip for $V_b = 70$ and 120 V (reproduced with permission from Ref. [21], Copyright 2002, American Physical Society)



void formation in Al strip when electrical current passes through the Al strip. Ertz et al. [23] measured the conductance of Au point contacts with width ranging from 20 nm down to a single atom. The conductance of the Au contacts is a function of the radius, which is comparable with the predictions by Maxwell, Sharvin, and Wexler. In the 1990s, Iwatsuki et al. [24] developed an STM in a TEM operating in an REM mode, and he obtained simultaneously STM and REM images from the same sample area. Using the same apparatus, they observed quantum conductance of Au atomic chains [3]. The conductance and HRTEM images on metal quantum point contacts were acquired simultaneously using a TEM-STM platform, which allows direct observation of the relation between electron transport and structure. As shown in Fig. 5.5, the observed strands of gold atoms are about one nanometer long and one single chain of gold atoms suspended between the electrodes. They verify that the conductance of a single strand of atoms is $2e^2/h$ (e is the electron charge and h is Planck's constant) and that the conductance of a double strand is twice as large, showing that equipartition holds for electron transport in these quantum systems.

The conductance of multiwalled CNTs (MWCNTs) was found to be quantized. The experimental method involved measuring the conductance of nanotubes by replacing the tip of an STM with a nanotube fiber, which could be lowered into a liquid metal to establish an electrical contact with a nanotube at the tip of the fiber.

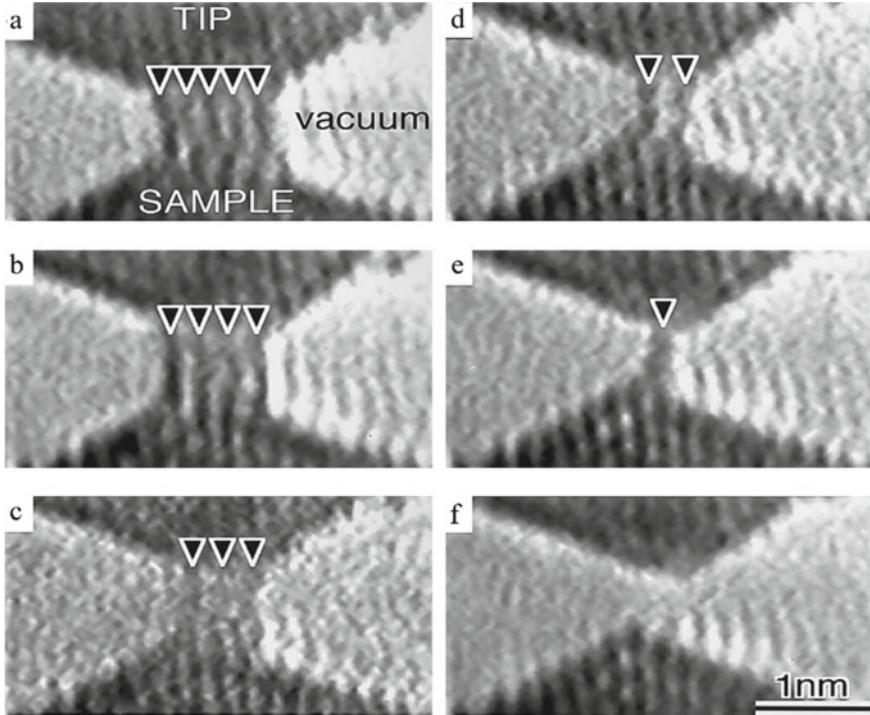


Fig. 5.5 Electron microscope images of a contact while withdrawing the tip. A gold bridge formed between the gold tip (top) and gold substrate (bottom), thinned from (a) to (e), and ruptured at (f), with observation times of 0, 0.47, 1.23, 1.33, 1.80, and 2.17 s, respectively. Dark lines indicated by arrowheads are rows of gold atoms. The faint fringe outside each bridge and remaining in (f) is a ghost due to interference of the imaging electrons. The conductance of the contact is 0 at (f) and $\sim 2 \times 13 \text{ K}\Omega$ at (e). $V_b = -10 \text{ mV}$ and $\text{RF} = 10 \text{ K}\Omega$ (reproduced with permission from Ref. [3], Copyright 1998, Springer Nature)

The conductance of arc-produced MWCNTs is one unit of the quantum conductance $2e^2/h = (12.9 \text{ K}\Omega)^{-1}$. The nanotubes conduct current ballistically and do not dissipate heat [25].

5.2.3 Electrical and Mechanical Coupling

The platform enables microstructure observation with the measurement of force after the introduction of an atomic force microscope (AFM) into the platform, permitting nanoscale mechanical property measurements [26]. Using a home-made TEM-AFM platform, atomic-scale microstructure observation with simultaneous mechanical force and electrical conductance measurements were achieved in Au nanocontacts [27]. Using a similar in situ holder, the conductance of Au atomic chains with length

up to 2.6 nm was measured. It was found that metal–insulator transition occurred in the atomic chains [28].

In 1999, using a home-made electrical biasing holder, static and dynamic mechanical deflections were electrically induced in cantilevered MWCNTs in a TEM by Poncharal et al. [29]. The nanotubes were resonantly excited at the fundamental frequency and higher harmonics as revealed by their deflected contours, which correspond closely to those determined for cantilevered elastic beams (Fig. 5.6). The elastic bending modulus as a function of diameter was found to decrease sharply (from about 1 to 0.1 TPa) with increasing diameter (from 8 to 40 nm), which indicates a crossover from a uniform elastic mode to an elastic mode that involves wave-like distortions in the nanotube. The methods developed have been applied to a nanobalance for nanoscopic particles and also to a Kelvin probe based on nanotubes [29]. Using the same instruments, the bending modulus of MWCNT was measured. The bending modulus of nanotubes with point defects was 30 GPa and that of nanotubes with volume defect was 2–3 GPa [30]. A femtogram nanobalance was demonstrated based on nanotube resonance; it has the potential for measuring the mass of chain-structured large molecules. The in situ TEM provides a powerful approach toward nanomechanics of fiber-like nanomaterials with well-characterized defect structures. Using a similar electrical biasing holder, the work function at the tips of individual MWCNTs has been measured. The tip work function shows no significant dependence on the diameter of the nanotubes in the range of 14–55 nm. Majority of the nanotubes have a work function of 4.6–4.8 eV at the tips, which is 0.2–0.4 eV lower than that of carbon [31].

By integrating a TEM–STM with a AFM, Lu et al. [32] conducted cold welding of Au nanowires (Fig. 5.7). The welding of metals at the nanoscale is likely to have an important role in the bottom-up fabrication of electrical and mechanical nanodevices. Existing welding techniques use local heating, requiring precise control of the heating mechanism and introducing the possibility of damage. The welding of metals without heating (or cold welding) has been demonstrated, but only at macroscopic length scales and under large applied pressures. Lu et al. demonstrate that single-crystalline gold nanowires with diameters between 3 and 10 nm can be cold-welded together within seconds by mechanical contact alone, and under relatively low applied pressures. HRTEM and in situ measurements reveal that the welds are nearly perfect, with the same crystal orientation, strength, and electrical conductivity as the rest of the nanowire. The high quality of the welds is attributed to the nanoscale sample dimensions, oriented-attachment mechanisms, and mechanically assisted fast surface-atom diffusion. Welds are also demonstrated between gold and silver, and silver and silver, indicating that the technique may be generally applicable.

5.2.4 *Ferroelectric Domain Switching*

Electrical- and mechanical-coupling-induced domain switching was observed in ferroelectric devices. In thin film ferroelectric devices, switching of ferroelastic

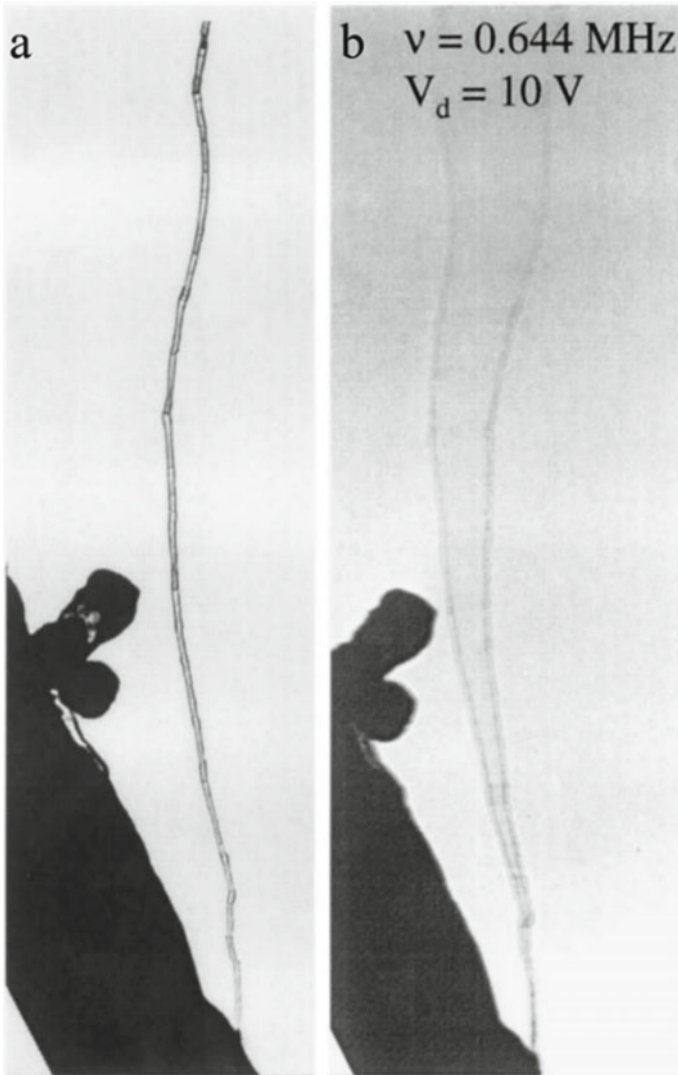


Fig. 5.6 A carbon nanotube at **a** the stationary and **b** the first resonance mode (reproduced with permission from Ref. [30], Copyright 2000, American Physical Society)

domains can significantly enhance electromechanical response. Switching behavior strongly depends on specific microstructures in ferroelectric systems. The switching dynamics of individual ferroelastic domains in thin $\text{Pb}(\text{Zr}_{0.2}, \text{Ti}_{0.8})\text{O}_3$ films under electrical and mechanical stimulation were revealed by using a TEM-STM platform [33], as shown in Fig. 5.8. It is found that ferroelastic domains are effectively and permanently stabilized by dislocations at the substrate interface while

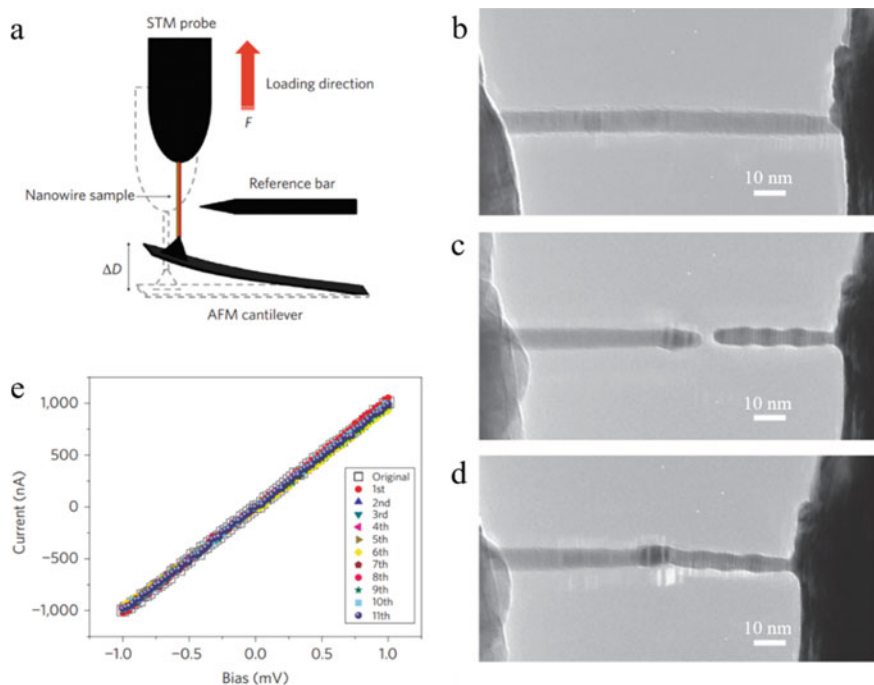


Fig. 5.7 **a** Schematic showing how the AFM cantilever acts as a force sensor (by measuring the deflection of the cantilever, ΔD) and the STM probe acts as an actuator while the attached nanowire sample is under tensile loading. **b–d** Gold nanowire (length, 130 nm; diameter, 7 nm) bridged between gold probes in initial (**a**), broken (**b**), and welding (**c**) states. **e** Comparison of the averaged I–V curves of the original and as-welded gold nanowires. Cold welding was successfully performed 11 times for the same sample by repeated breaking and re-welding of the nanowire (reproduced with permission from Ref. [32], Copyright 2010, Springer Nature)

similar domains at free surfaces without pinning dislocations can be removed by either electric or stress fields. For both electrical and mechanical switching, ferroelastic switching is found to occur most readily at the highly active needle points in ferroelastic domains. The studies provide new insights into the understanding of polarization switching dynamics as well as the engineering of ferroelectric devices.

5.2.5 Resistive Switching

Resistance switching in metal oxides could form the basis for next-generation non-volatile memory. It has been argued that the current in the high-conductivity state of several technologically relevant oxide materials flows through localized filaments, but these filaments have been characterized only indirectly. Kwon et al. [34] probed directly the nanofilaments formation in a Pt/TiO₂/Pt system during resistive switching

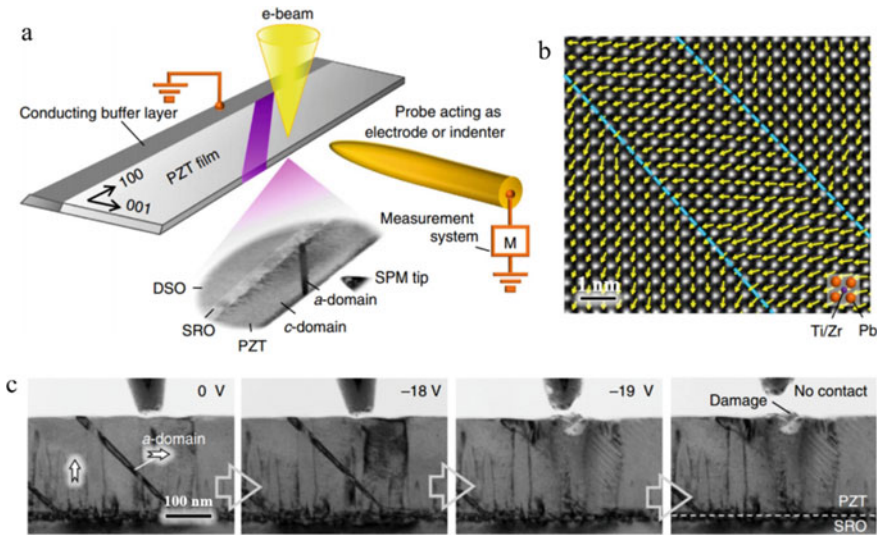


Fig. 5.8 Ferroelastic domain switching via in situ TEM. **a** Schematic and TEM image of experiment setup: a thin cross-sectional $\text{Pb}(\text{Zr}_{0.2}\text{Ti}_{0.8})\text{O}_3$ film with a concentration of ferroelastic 90° domain (α -domains) was grown on $\text{SRO}/\text{DyScO}_3$ and $\text{SRO}/\text{SrTiO}_3$. A mobile tungsten tip acts as one electrode for electrical switching with the SRO layer being grounded, whereas a diamond indenter is used for mechanical switching. **b** High-resolution HAADF STEM image of $c/a/c$ -domains overlaid with vectors describing the head-to-tail polarization arrangement. **c** Image sequence showing a clamped 90° domain is stable at applied negative voltages from $0 \rightarrow (-18 \text{ V})$. At -19 V , the domain is eventually erased and, simultaneously, damage to the film occurs due to the high strength of the electric field (reproduced with permission from Ref. [33], Copyright 2014, Springer Nature)

using a TEM-STM platform (Fig. 5.9). In situ current–voltage and low-temperature (130 K) conductivity measurements confirm that switching occurs by the formation and disruption of $\text{Ti}_n\text{O}_{2n-1}$ (or so-called Magnéli phase) filaments. Similar filament formation was observed in a $\text{Ag}/a\text{-Si}/\text{W}$ memory device [35]. Knowledge of the composition, structure, and dimensions of these filaments will provide a foundation for unraveling the full mechanism of resistance switching in oxide thin films, and help guide research into the stability and scalability of such films for applications.

5.3 Electrothermal Behaviors and Measurements

The thermal properties of nanomaterials can differ greatly from their bulk counterparts, impacting such diverse applications as lasers, transistors, sensors, and thermoelectric energy conversion [36]. For example, due to increased phonon scattering at the surfaces, the thermal conductivity of a silicon nanowire may be reduced by a factor of 100 or more compared to bulk silicon [37]. No fundamental understanding exists regarding the relationships between crystalline structures and the

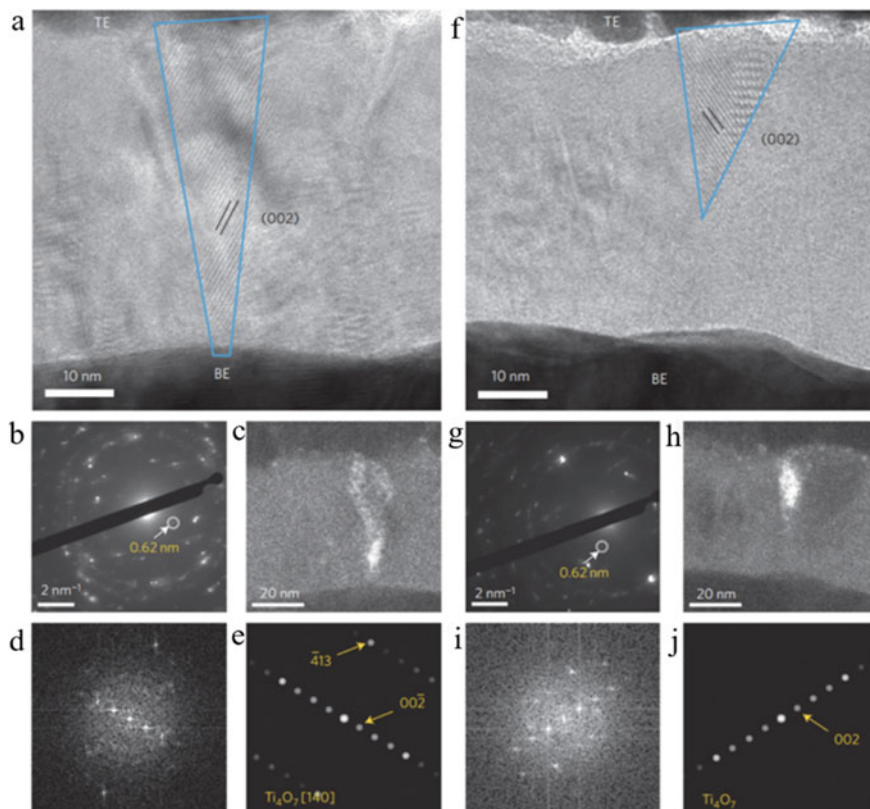


Fig. 5.9 Magnéli structures in the SET sample. **a–e** High-resolution TEM image of a Ti_4O_7 nanofilament (**a**), selected-area diffraction pattern of the film (**b**), dark-field image obtained from the diffraction spot marked as a circle in the diffraction pattern (**c**), a fast Fourier transformed micrograph of the high-resolution image of Ti_4O_7 (**d**), and the corresponding simulated diffraction pattern (**e**). The Bloch-wave method was used to simulate the diffraction patterns. **f–j** Disconnected Ti_4O_7 structure in the conical shape. The images are presented in the same manner as for the connected filament in (**a–e**) (reproduced with permission from Ref. [34], Copyright 2010, Springer Nature)

corresponding thermal properties, thus hindering both cooling and power-conversion applications. In situ biasing TEM provides an effective way to investigate thermal properties of nanomaterials.

5.3.1 Thermal Parameter Measurements

Dames et al. [36] developed a hot-wire probe inside a TEM to measure the thermal resistance of individual nanowires, nanotubes, and their contacts. As shown in Fig. 5.10, an STM probe inside the TEM was used to select a particular nanowire or

nanotube for measurement, and contacts were made with liquid metal droplets or by electron-beam-induced deposition. Detailed thermal analysis shows that the thermal resistance of the hot-wire probe was four times that of the sample. The range of detectable sample thermal resistances spans from approximately 10^3 to 10^9 K W^{-1} . The probe can also be adapted for measurements of the electrical conductance and Seebeck coefficient of the same sample. The probe was used to study a MWCNT with liquid Ga contacts. The measured thermal resistance was about 3.3×10^7 K W^{-1} . For a MWCNT with a length of 2 μm and a diameter of 20 nm, the thermal conductivity is ~ 200 W m^{-1} K $^{-1}$.

Pettes and Shi [38] fabricated an MEMS device that permits simultaneously microstructure and thermal property measurements of individual CNTs (Fig. 5.11). They measured the thermal conductivity of individual carbon nanotubes (CNTs) grown using thermal chemical vapor deposition between two suspended microthermometers. The crystal structure of the measured CNT samples was characterized in detail using TEM. The obtained intrinsic thermal conductivity of approximately 42–48, 178–336, and 269–343 W m^{-1} K $^{-1}$ at room temperature for three MWCNT samples correlates well with TEM-observed defects spaced approximately 13, 20, and 29 nm apart, respectively; whereas the effective thermal conductivity is found to be limited by the thermal contact resistance to be about 600 W m^{-1} K $^{-1}$ at room

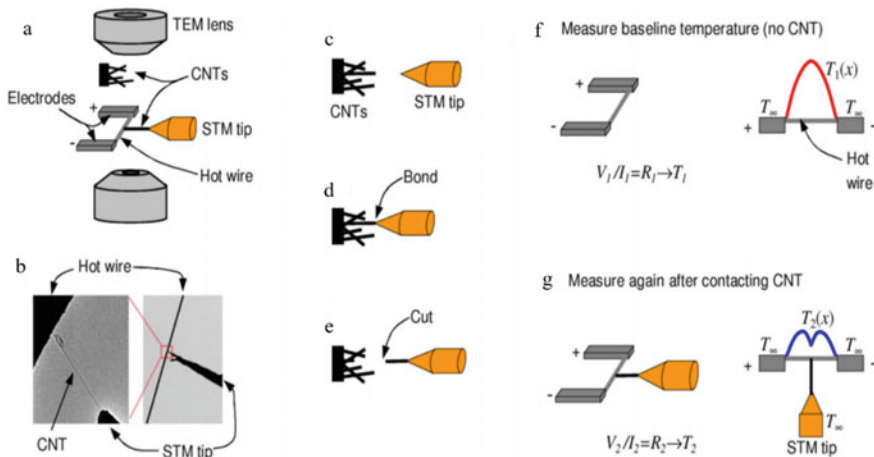


Fig. 5.10 A hot-wire probe for thermal measurements of nanowires and nanotubes. **a** A hot-wire probe mounted inside a TEM. **b** TEM images of the hot wire, STM tip, and a CNT. **c–e** Using the STM tip to remove a particular CNT from a large sample. The bond between the CNT and the STM tip is improved by using liquid metal droplets or by electron-beam-induced deposition. **f** Baseline thermal measurement of the average temperature of the hot wire for a given amount of joule heating. The hot wire is used as both a heat source and a resistance thermometer. **g** After contacting the CNT + STM assembly to the midpoint of the hot wire, for the same amount of joule heating the average temperature of the hot wire is reduced, which is related to the heat conducted through the CNT (reproduced with permission from Ref. [36], Copyright 2007, AIP Publishing)

temperature for the as-grown DWCNT and SWCNT samples without the contact deposition.

Harris et al. [39] developed a microfabricated, chip-based characterization platform that enables both TEM of the atomic structure and defects as well as measurement of the thermal transport properties of individual nanostructures (Fig. 5.12). The platform features a suspended heater line that physically contacts the center of a suspended nanostructure/nanowire that was placed using in situ scanning electron

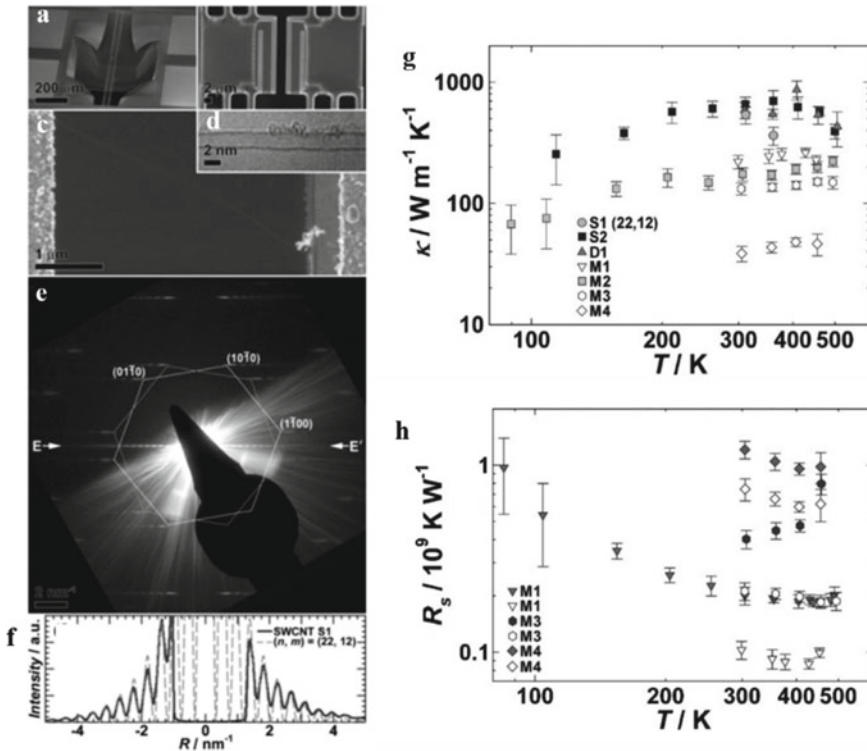


Fig. 5.11 **a** Scanning electron microscopy (SEM) image of the suspended microdevice for thermal conductance measurements of CNTs. **b** SEM image of the two central membranes of the microdevice. **c** SEM and **d** TEM image of SWCNT bridging the two membranes. **e** Diffraction pattern using a 350 nm coherent electron beam. The two hexagons are added to highlight the {1010} layer lines from the top and bottom of the nanotube. The diameter and chiral angle are determined to be 2.33 ± 0.02 nm and $20.44 \pm 0.2^\circ$, respectively. **f** Equatorial oscillations (solid line) along E E' in **e** and calculation (dashed line) for a (22,12) SWCNT are in good agreement. **g** As-measured effective thermal conductivity (κ) versus temperature (T) for the two SWCNT, one DWCNT, and four MWCNT samples in this work. Filled symbols and unfilled symbols are results measured before and after Pt-C deposited at the contacts, respectively. **h** Measured thermal resistance (R_s) versus temperature (T) for three MWCNT samples before (filled symbols) and after (unfilled symbols) Pt-C was deposited at the contacts (reproduced with permission from Ref. [38], Copyright 2009, John Wiley and Sons)

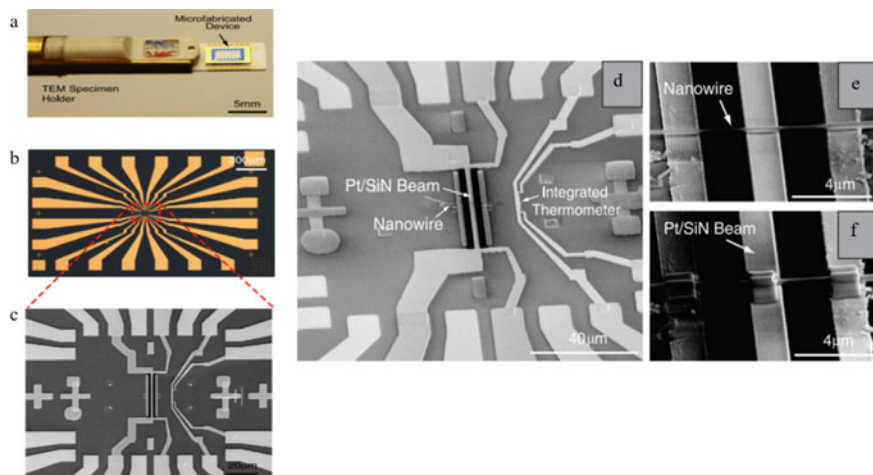


Fig. 5.12 Images of the microfabricated device at various magnifications. **a** An optical image of the microfabricated device mounted onto a TEM specimen holder. An optical image showing the device's gold electrodes and contact pads is shown in **(b)**, and a micrograph showing the Pt/SiNx suspended heater/thermometer, which resides at the very center of the device, is given in **(c)** the black region in the micrograph surrounding the Pt/SiNx composite beam is free space. A microfabricated measurement platform with a GaN nanowire placed on the suspended heater/thermometer. A micrograph taken at a relatively low magnification is given in **(d)**, which shows the nanowire placed perpendicularly to the suspended heater. Also shown are the heater's current and voltage leads and an auxiliary, integrated thermometer (compare with **(e)**). **e** A higher magnification image showing the nanowire immediately after its placement onto the heater. **f** The nanowire after the patterning of electron-beam-induced deposition (EBID) Pt-C contacts (reproduced with permission from Ref. [39], Copyright 2011, IOP Publishing)

microscope nanomanipulators. Suspension of the nanostructure across a through-hole enables TEM characterization of the atomic and defect structure (dislocations, stacking faults, etc.) of the test sample. The thermal conductivities of two GaN nanowires with diameters of 215 and 295 nm were measured to be 24 and $25.7 \text{ W m}^{-1} \text{ K}^{-1}$, which is much lower than that of bulk GaN ($120 \text{ W m}^{-1} \text{ K}^{-1}$) [40].

5.3.2 Joule Heating of Nanocarbon

By passing a high current through a suspended carbon nanotube in a high vacuum, a temperature higher than $2000 \text{ }^\circ\text{C}$ can be reached in the center of the nanotube, suggesting that carbon nanotube can be adopted as a high-temperature heater [41–52].

The tubule formation process from amorphous carbon nanowires under high-bias Joule heating was observed in real time (Fig. 5.13). The temperature rise from Joule heating can be over $2000 \text{ }^\circ\text{C}$, thus inducing crystallization of amorphous carbon [42]. The Joule-heating-induced high temperature can also trigger self-templated growth

of carbon nanotube walls [43], sublimation of graphene [48] and giant fullerene [44], plumbing of carbon nanotubes [50], and even melting diamond nanocrystals encapsulated in a carbon onion.

Sublimation of suspended few-layer graphene was induced by in situ Joule-heating inside a TEM. The graphene sublimation fronts consist of mostly {1100} zigzag edges. Under appropriate conditions, a fractal-like “coastline” morphology was observed (Fig. 5.14). Extensive multiple-layer reconstructions at the graphene edges led to the formation of unique carbon nanostructures, such as sp²-bonded

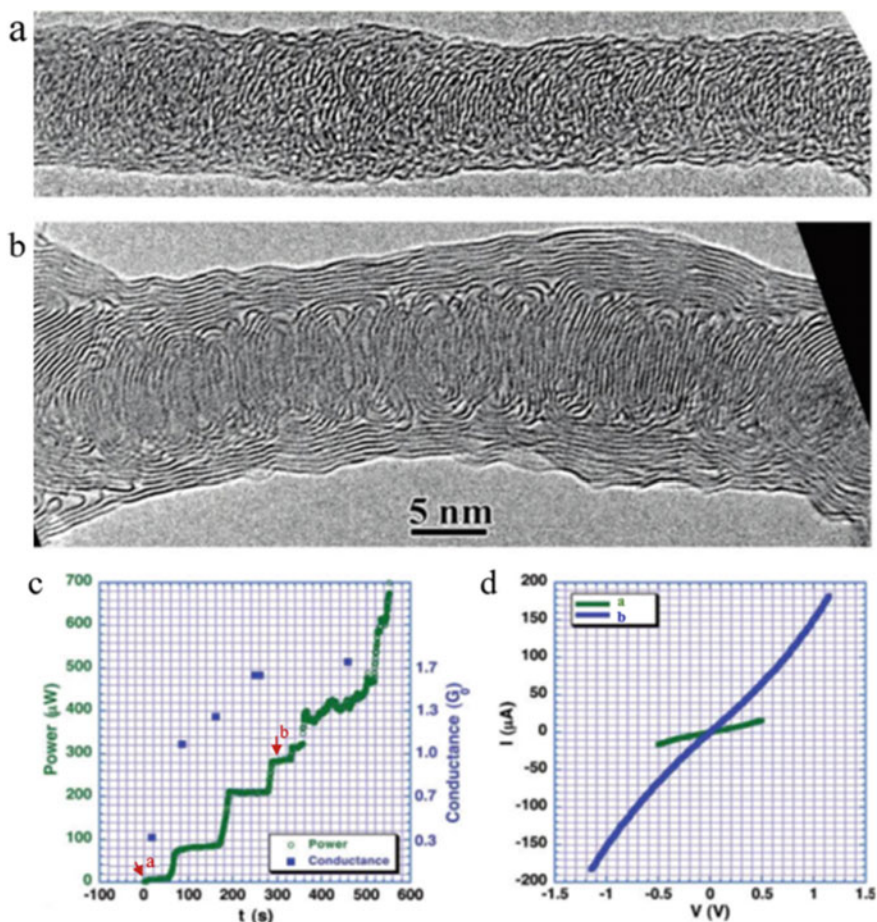


Fig. 5.13 Crystallization of an a-C nanowire into a tubular structure. **a** The initial nanowire produced by electron-beam deposition. The length of the nanowire is about 90 nm. **b** Crystallized tubular structure at a power of 280 μW . **c** Input power, conductance versus time plot. **d** I–V curves labeled correspond to the nanowire (**a**) and the tubular structure (**b**), respectively. The low-bias conductance are $0.3G_0$ and $1.6G_0$ for the nanowire (**a**) and the tubular structure (**b**), respectively (reproduced with permission from Ref. [41], Copyright 2006, American Chemical Society)

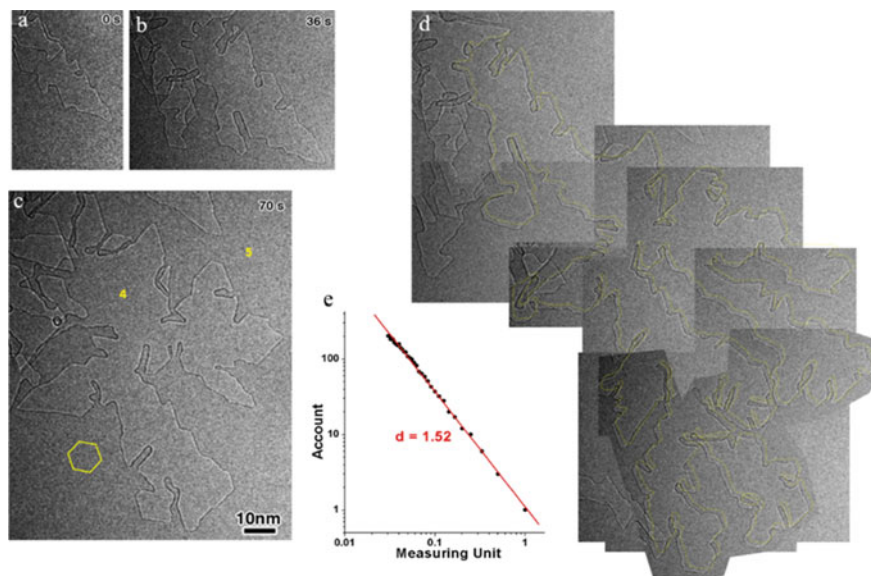


Fig. 5.14 Fractal sublimation of graphene. **a–c** Sequential HRTEM images showing a fractal sublimation pattern of graphene. The numbers 4 and 5 indicate the layer thicknesses are 4 and 5 bilayers, respectively. The hexagon in **c** marks the 6 sets of equivalent $\{1100\}$ zigzag planes. The bias voltage applied to the graphene was 2.5 V. **d** An overlay of sequential images of the propagating void fronts with the void edges highlighted in yellow-dotted lines. **e** A fractal dimension estimation of the yellow-dotted fractal pattern (reproduced with permission from Ref. [48], Copyright 2009, National Academy of Sciences, U.S.A.)

bilayer edges (BLEs) and nanotubes connected to BLEs. Flat fullerenes/nanorods and nanotubes tunneling multiple layers of graphene sheets were also observed. Remarkably, >99% of the graphene edges observed during sublimation are BLEs rather than monolayer edges, indicating that BLEs are the stable edges in graphene at high temperatures [41].

Joule heating also causes electromigration [45–47], and can be used as a heater to trigger phase transformation in nanowires (Fig. 5.15). In situ HRTEM revealed the precipitation of the zinc-blende (ZB) structure InAs at the liquid/solid interface or liquid/solid/amorphous carbon triple point at high temperature induced by Joule heating [49]. Solid-to-solid wurtzite (WZ) to ZB phase transition through gliding of sharp steps with Shockley partial dislocations was observed.

Joule heating can also cause carbon nanotube breakdown (Fig. 5.16). Three distinct breakdown sequences were observed, namely, from the outermost wall inward, from the innermost wall outward, and alternatively between the innermost and the outmost walls. Remarkably, a significant amount of current drop was observed when an innermost wall is broken, proving unambiguously that every wall is conducting. Moreover, the breakdown of each wall in any sequence initiates in the

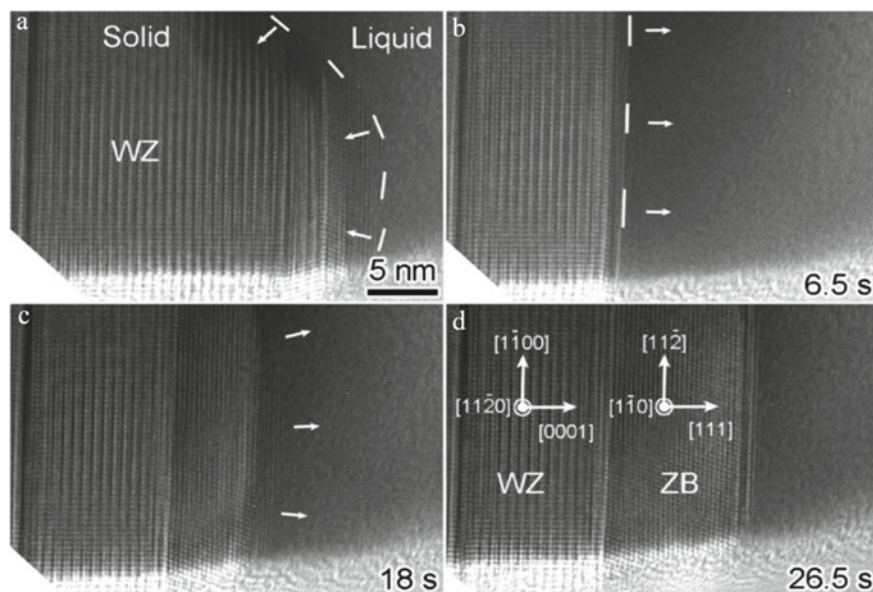


Fig. 5.15 Time-lapsed TEM images showing the dynamic process of the ZB phase precipitation. **a** Initial structure, **b** the liquid particle dissolves one portion of the InAs NW with original WZ structure, **c** after the liquid retracted back, the ZB-structure InAs partially precipitated out at the vicinity of the liquid/solid interface, and **d** the ZB-structure InAs fully precipitated out at the vicinity of the liquid/solid interface. The dashed line depicts the liquid/solid interface. The arrows point out the moving direction of liquid/solid interface (reproduced with permission from Ref. [49], Copyright 2013, American Chemical Society)

middle of the nanotube, not at the contact, proving that the transport is not ballistic [51].

Joule heating and associated electro-migration effects can be used to connect two carbon nanotubes that have the same (or similar) diameters (Fig. 5.17). It should be noted that the highest temperature that a commercial heating TEM holder can reach is within 1200 °C. However, by using CNT as a nanoscale heater, temperatures ~2000 °C are easily achievable, thus enabling high-temperature experiments that have not been possible before. For example, by Joule heating CNT to a temperature of about ~2000 °C and conducting in situ tensile experiments, superplastic deformation of CNT was discovered (Fig. 5.18). The theoretical maximum tensile strain, that is, elongation of a single-walled carbon nanotube is almost 20% [53], but in practice only 6% is achieved [54]. However, at high temperatures, individual single-walled carbon nanotubes can undergo superplastic deformation, becoming nearly 280% longer and 15 times narrower before breaking. This superplastic deformation is the result of the nucleation and motion of kinks in the structure and could prove useful in helping to strengthen and toughen ceramics and other nanocomposites at high temperatures. Another advantage of Joule heating nanoheater is that the heating and cooling rate can be very fast. For example, Zhong et al. claimed that by Joule heating

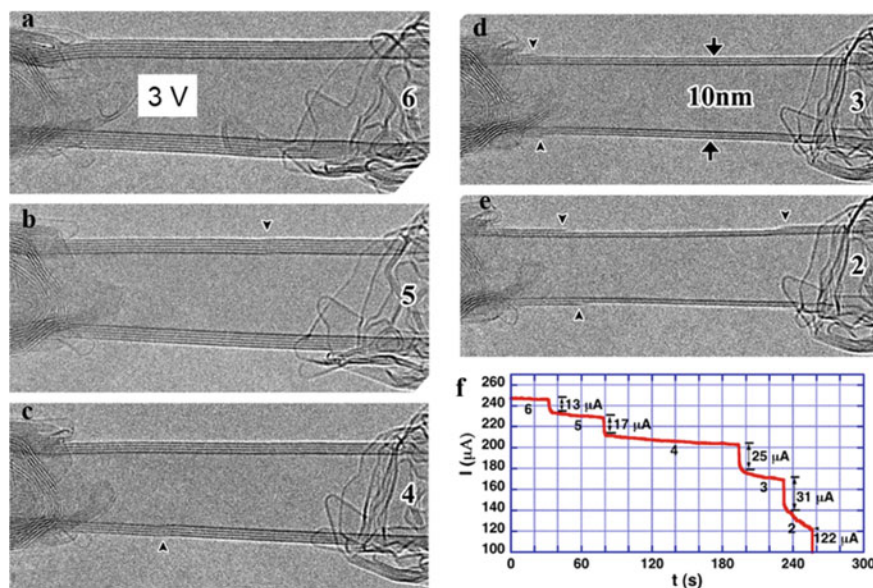


Fig. 5.16 Sequential HRTEM images showing that the six-wall nanotube is removed wall-by-wall from the outermost wall (a) to the innermost wall (e). The numbers indicate the total number of walls. The arrows mark kinks. The arrowheads denote the residue of the fourth and the third walls after breakdown. **f** The current–time (I – t) curve of the breakdown of the MWNT. The numbers below the plateau indicate the total wall number (reproduced with permission from Ref. [51], Copyright 2005, American Physical Society)

nanocontacts of high melting temperature metals, an unprecedentedly high liquid-quenching rate of 10^{14} K s^{-1} was achieved. Under such a high cooling rate, melts of pure refractory body-centered cubic (bcc) metals, such as liquid tantalum and vanadium, are successfully vitrified to form metallic glasses suitable for property interrogations [55].

5.4 In Situ TEM Nanoelectrochemistry

In situ TEM is a very powerful tool for structures and properties correlation of nanostructured materials. However, the applications of in situ TEM in energy storage materials have been limited. This is mainly due to the incompatibility of liquid electrolyte used in batteries with the high vacuum of a TEM. A battery has three main components, that is, the cathode, anode, and electrolyte. The incompatibility of liquid electrolyte with the high vacuum of TEM has been a roadblock for the application of in situ TEM in batteries. Nevertheless, in situ TEM is particularly important in examining mechanisms of charge storage or degradation at atomic level, as

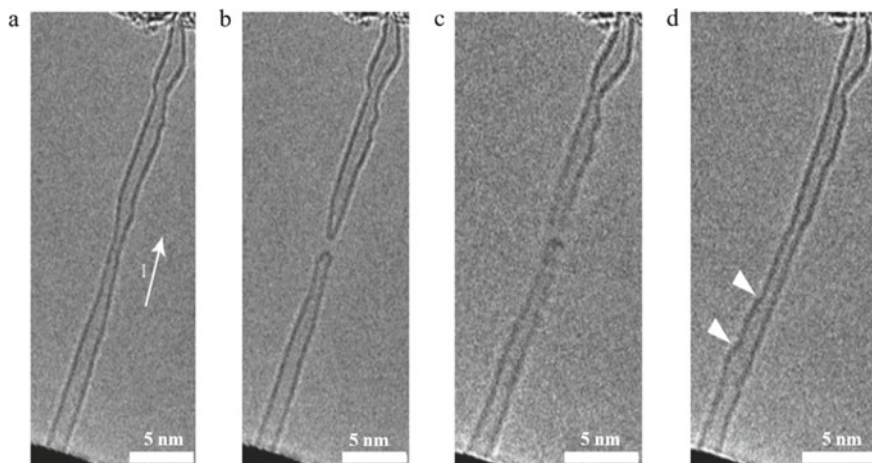


Fig. 5.17 Successful and unsuccessful joining attempts on two different types of SWNTs. **a–d** Successful joining of an SWNT split into two separate SWNTs by applying a large voltage (**a**, **b**), where the arrow in **a** indicates the direction of the current. The two SWNTs re-contact each other (**c**) and a new SWNT forms (**d**), showing some local protrusions appearing (arrowheads) (reproduced with permission from Ref. [50], Copyright 2007, Springer Nature)

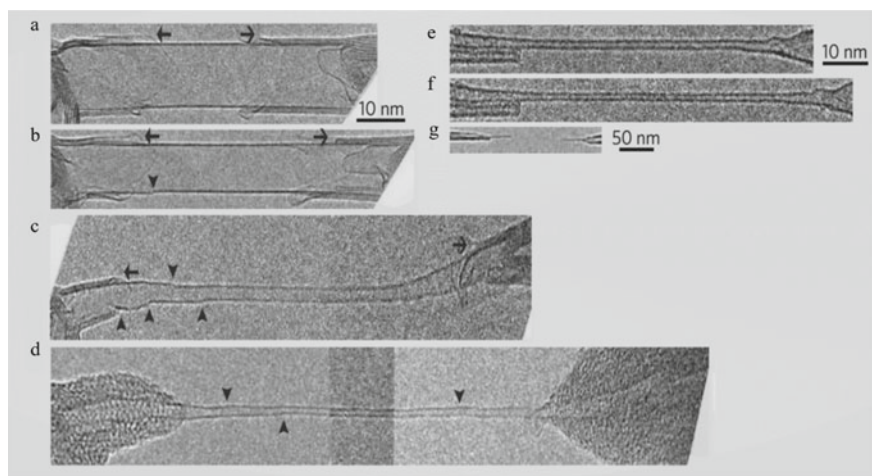


Fig. 5.18 In situ tensile elongation of individual single-walled carbon nanotubes viewed in a high-resolution transmission electron microscope. **a–d** Tensile elongation of a single-walled carbon nanotube (SWCNT) under a constant bias of 2.3 V (images are all scaled to the same magnification). Arrowheads mark kinks; arrows indicate features at the ends of the nanotube that are almost unchanged during elongation. **e–g** Tensile elongation of an SWCNT at room temperature without bias (images **e** and **f** are scaled to the same magnification). Initial length is 75 nm (**e**); length after elongation (**f**) and at the breaking point (**g**) is 84 nm; **g** low-magnification image of the SWCNT breaking in the middle (reproduced with permission from Ref. [52], Copyright 2006, Springer Nature)

opposed to averaging over an ensemble of particles. While traditional electrochemical tests, such as charge–discharge cycling, cyclic voltammetry, or electrochemical impedance spectroscopy, are routinely performed for characterizing battery performance, these tests do not provide insight into mechanisms at the atomic to nanoscale. The development of new characterization tools is an area of need in battery research. For example, in the comprehensive review of LIBs by Tarascon and Armand [56], he specifically cites this need in his summary statements, “The principal challenge for Li-based rechargeable batteries, or indeed for any battery, lies in gaining better understanding and control of the electrode–electrolyte interface in the hope of designing new solid–solid or solid–liquid interfaces. Efforts aimed at developing new characterization tools must be vigorously pursued ...”. Developing new characterization approaches with atomic-to-nano-scale spatial resolution may generate new insights into the mechanisms of storage and degradation in LIBs.

In this context, Huang et al. created the first nanobattery inside the high vacuum of a TEM, enabling real-time simultaneously atomic-scale microstructure evolution and electrochemical measurement [57–60]. The nanobattery consists of a single nanowire anode, an ionic liquid (IL) or Li_2O electrolyte, and Li or LiCoO_2 counterelectrode. The in situ nanobattery technique opens a new field of in situ TEM nanoelectrochemistry, and has been broadly used in battery research. In the following, we shall provide an overview of the progress has been made toward understanding of nanoelectrochemistry via in situ TEM. The progress in the in situ methods will also be provided. Since the inception of the first paper on nanobattery, significant progress has been made in understanding the electrochemistry and degradation of batteries, it is impossible to include all the progress in one chapter. We therefore shall choose only representative work here. Interested readers are referred to several comprehensive reviews for a full picture of the progress in this highly evolving field [59–70].

5.4.1 *IL Cell*

The major technical difficulty for conducting an in situ electrochemical experiment in a TEM is to introduce a liquid electrolyte into the TEM column with a typical vacuum level of 10^{-5} Pa (10^{-7} Torr). The vapor pressures at room temperature of the most widely used solvents, such as ethylene carbonate (EC), propylene carbonate (PC), dimethyl carbonate (DMC), and diethyl carbonate (DEC), are 5–8 orders of magnitude higher than the TEM column pressure [59, 60]. Therefore, it is impossible to place a liquid directly into the high vacuum of a TEM. Ionic liquid, which consists of only positive and negatively charged ions, has very low vapor pressure [59, 71, 72]. Huang et al. [72] discovered that IL can be directly placed into the high vacuum of a TEM and it still behaves as a liquid, flowing a long nanowires and pumping IL from one end of the nanowire to the other end. The discovery breaks up the bottleneck that prevents the application of in situ TEM in batteries and thus sets up the stage for an IL-based nanobattery.

Table 5.1 Physical properties of P₁₄TFSI [59]

Property	Value
Glass transition temperature	-87 °C
Melting point	-18 °C
Fluid density	1.41 g ml ⁻¹ (20 °C)
Fluid conductivity	0.22 S m ⁻¹ (25 °C)
Fluid viscosity	0.085 Pa s (25 °C)
Electrochemical window	>5.5 V (25 °C)

Set-up of IL cell

The IL electrolyte (ILE) was made by dissolving the lithium salt, lithium bis (trifluoromethylsulfonyl) imide (LiTFSI), in a solvent of 1-butyl-1-methylpyrrolidinium bis(trifluoromethylsulfonyl) imide (P₁₄TFSI) at the concentration of 10 wt% LiTFSI. Table 5.1 lists the main physical properties of the solvent, P₁₄TFSI. In a typical experiment, one drop of the ILE was placed on the top surface of the LiCoO₂ bulk, which was glued to an Al rod. On the other side, nanowires were glued to another Al rod with conductive epoxy (Fig. 5.19). For different materials, the exact device structure may be modified to ensure the best performance.

The IL cell is truly a miniaturized LIB with the major components, which shows an interesting phenomenon of liquid beads flowing along nanowires, demonstrating the

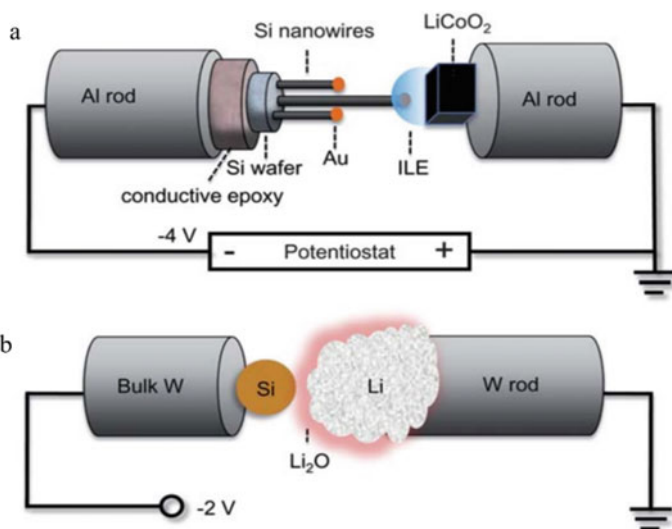


Fig. 5.19 Schematic illustrations of the open cell nanobattery setup inside a TEM, enabling in situ TEM electrochemical experiments. One electrode of the two-terminal devices is connected to a piezo-positioner. **a** Using ILE as liquid electrolyte, **b** using Li₂O as solid electrolyte (reproduced with permission from Ref. [59], Copyright 2011, Royal Society of Chemistry)

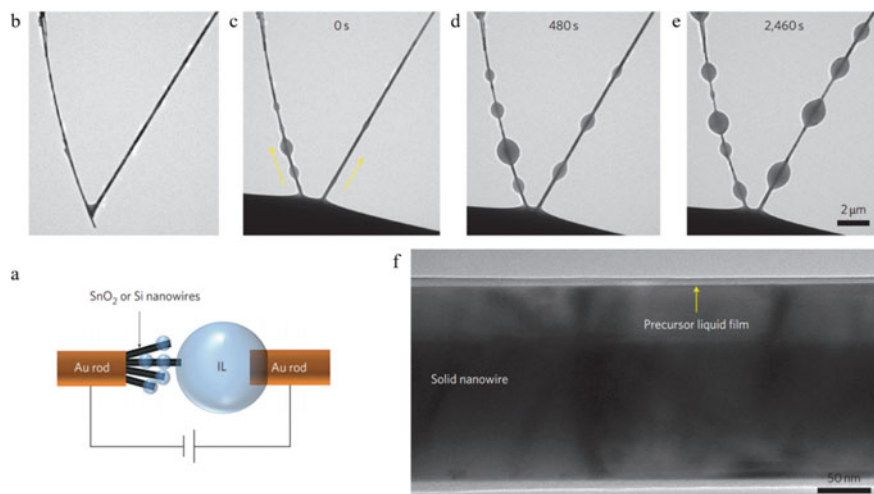


Fig. 5.20 Ionic liquid beads and flat precursor film. **a** Experimental setup. SnO_2 nanowire powders or silicon nanowires grown on a silicon wafer are glued to a gold rod (diameter, $\sim 280 \mu\text{m}$) using conducting silver epoxy (left). The whole nanowire assembly is used as one electrode. The other electrode is a gold STM probe (right). A drop of ionic liquid (IL, middle) is placed on the STM tip. One of the electrodes is attached to a three-dimensional piezo-manipulator to enable it to approach the opposite electrode. **b–e** Time-lapse TEM images showing ionic liquid flowing along two SnO_2 nanowires. The diameters of the nanowires on the left and right are 120 nm and 190 nm, respectively. The arrows in **c** show the bead flow direction. The SnO_2 nanowires were biased at -4 V versus the reference electrode. The growth of beads is seen clearly. **f** A liquid precursor film with a thickness of $\sim 10 \text{ nm}$ wets and flows on a SnO_2 nanowire (reproduced with permission from Ref. [72], Copyright 2013, Springer Nature)

high fluidity of the electrolyte in the vacuum environment (Fig. 5.20). Figure 5.20f shows a typical image of the ILE layer wetted nanowire. Due to the high fluidity and surface tension force of IL, long objects, such as nanowires/nanorods with high aspect ratio, are more suitable for this liquid-cell setup.

Discharge experiments were successfully conducted on a SnO_2 nanowire IL cell in a TEM by MacFarlane et al. [73]. As shown in Fig. 5.21, the initial SnO_2 nanowire was straight with a smooth surface morphology. After contact with the ILE, the ILE wicked up the nanowire, forming a meniscus. Potential was then applied to the SnO_2 nanowire at -3.5 V with respect to the LiCoO_2 counterelectrode. This initiated an electrochemical reaction at the point of contact between the SnO_2 nanowire and the IL where reduction of the SnO_2 was observed. This solid-state reaction front propagated along the longitudinal direction of the nanowire away from the electrolyte. As the reaction front propagated, the diameter and length of the nanowire increased, and the TEM image contrast changed from typical crystalline diffraction contrast to a gray, mostly featureless contrast typical of amorphous materials. After charging, this nanowire had elongated $\sim 60\%$, the diameter expanded $\sim 45\%$, and the total volume expanded about 240% [57]. It is noted that in these experiments, one end of the

nanowire is in contact with the electrolyte (hereafter referred to as an “end contact”) [57]. Therefore, lithiation is featured by a single reaction front advancing in the axial direction [73]. However, in a real battery, the nanowires were immersed entirely in the electrolyte in a flooding geometry hereafter interchangeably referred to as “flooding” or “side contact”. One fundamental question that needs to be addressed is, does the same lithiation mechanism operating in the end contact also operate in a flooding geometry? It is speculated that the previously observed large elongation during charging of SnO₂ nanowires might be related to the end-contact geometry, as it is expected that in an end-contact geometry the reaction interface is perpendicular to the nanowire axis, and the elongation should occur in a direction that is perpendicular to the reaction interface, thus the observed super elongation [73]. In a similar vein, when the nanowire is flooded in the electrolyte, it is expected to swell rather than elongate [74, 75]. To clarify the above argument, further experiments were conducted under both the end-contact and the side-contact (flooding) geometries.

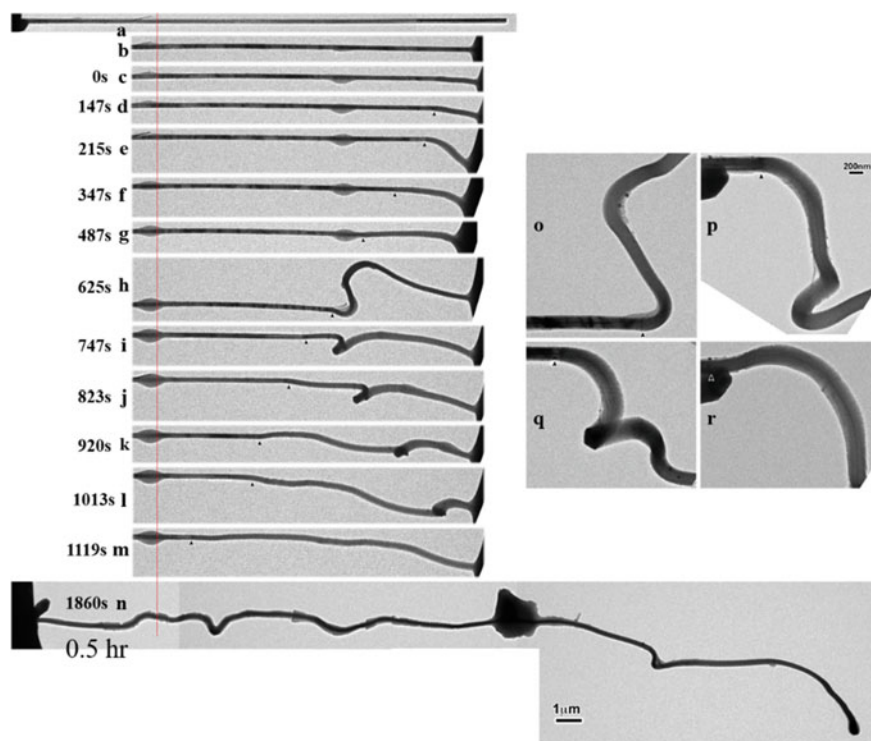


Fig. 5.21 The initially straight nanowire (a, b) became significantly twisted and bent after reaction (c–r). o–r Are sequential high magnification images showing the progressive migration of the reaction front. n The big dark particle is a polymerized ILE (reproduced with permission from Ref. [57], Copyright 2010, The American Association for the Advancement of Science)

Figure 5.21 shows morphology and structure evolution of a SnO_2 nanowire anode during the lithiation process in a partially flooded geometry. The initial single-crystalline nanowire was $45\ \mu\text{m}$ long and $220\ \text{nm}$ thick. About one-third of the nanowire was immersed into the ILE, and the rest of the nanowire was out of the ILE. A $-3.5\ \text{V}$ bias was then applied to the anode with respect to the LiCoO_2 cathode, which initiated an electrochemical charge in the nanowire. Surprisingly, the flooded segment showed similar morphology to the nonflooded segment with elongation, spiral, buckling, and twist after the ILE was retracted (Fig. 5.21n). Similar morphology changes in the flooded and nonflooded segments after lithiation were observed, both undergoing similar elongation and swelling, and exhibiting a typical amorphous gray contrast. It is concluded that the phase transformation mechanisms and the volume changes in the IL cell are independent on the contacting mode, but a reflection of the intrinsic electrochemical properties of the cell. Subtle difference may indeed exist, for example, a multiple-stripe multiple-reaction front lithiation mechanism was observed in the flooding geometry but in the end contact [76], suggesting different reaction kinetics under different contact.

Quantitative nanoelectrochemistry in IL cell

One of the conventional electrochemical measurement approaches is to perform chronopotentiometric sweeps under constant applied current, commonly called charge–discharge cycling. Most of the in situ nanobattery work was performed under a voltage control. By using special instrumentation such as a battery-powered Jaisle IMP 83 Pstat/Gstat with a $1\ \text{fA}$ noise floor sourcing current, it is possible to perform quantitative charge–discharge electrochemical measurements during in situ TEM. This is demonstrated in a nanobattery using a Si nanowire (NW) anode immersed in an IL electrolyte with respect to a LiFePO_4 (LFP) cathode [76].

Quantitative nanoelectrochemistry is also demonstrated in a hollow CNT-IL wet electrochemical cell that permits real-time imaging of polysulfide evolutions in Li–S batteries in a Cs corrected ETEM while measuring the electrochemical parameters (Fig. 5.22) [77]. Upon discharge, sulfur was electrochemically reduced to long-chain polysulfides, which dissolved into the electrolyte instantly and were stabilized by Py_{14}^+ cation solvation. The formation of polysulfides was directly observed by in situ TEM and was correlated with the concurrent cyclic voltammetry measurements from the same CNT-IL cell. The CNT wet electrochemical cell proves to be a universal platform for in situ probing electrochemistry of various batteries.

5.4.2 Solid Cell

In the solid cell, Li metal is the lithium source, and the native Li_2O layer formed on the metal surface acts as a solid electrolyte permitting Li^+ transport but not electron transport [71]. Lithium is extremely reactive and its surface is always covered with a thin Li_2O layer. Moreover, Li_2O is naturally formed on the fresh Li metal that is briefly exposed to the air when the holder is inserted into TEM. Structural analysis

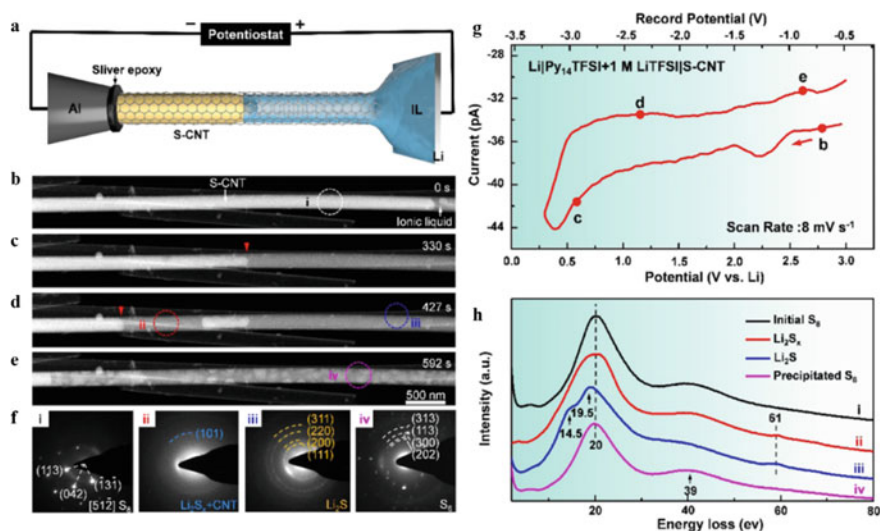


Fig. 5.22 In situ TEM studies of $\text{Li}|\text{Py}_{14}\text{TFSI}+1\text{ M LiTFSI}|\text{S-CNT}$ nanobatteries. **a** Schematic of the experimental setup. A tip-flattened aluminum (Al) rod attached with S-CNT nanowire, a Li metal, and a $\text{Py}_{14}\text{TFSI}$ with or without 1 M LiTFSI were used as the cathode, anode, and electrolyte, respectively. **b–e** Time-lapse structure evolution of the S-CNT cathode in a $\text{Li}|\text{Py}_{14}\text{TFSI}+1\text{ M LiTFSI}|\text{S-CNT}$ nanobattery. The red arrows point to the IL/S interface. **b–d** During the discharge reaction, sulfur reacted with Li to form polysulfides, which dissolved into the electrolyte instantaneously. **e** When the voltage was swept from 0.3 V to open-circuit voltage (OCV) (vs. Li), some semicircular particles precipitated out on the inner wall of the CNT. **f** EDPs from: (i) the pristine S-CNT, acquired from a white-circled region in (b); (ii) polysulfide, acquired from a red-circled region in (d); (iii) Li_2S , acquired from a blue-circled region in (d); (iv) S_8 , acquired from a purple-circled region in (e). **g** Cyclic voltammetry (CV) scan of a single S-CNT nanowire Li–S nanobattery as shown in (a) at a scan rate of 8 mV s^{-1} . The letters in the CV curve correspond to the TEM images labeled as “b”, “c”, “d”, and “e”. **h** Low-loss EELS from the pristine S-CNT nanowire (black), discharge product (red and blue), and precipitated particles (purple) (reproduced with permission from Ref. [77], Copyright 2020, American Chemical Society)

has revealed a typical thickness of $\sim 700\text{--}1000\text{ nm}$ of the Li_2O layer [58]. Due to its large bandgap of $\sim 8\text{ eV}$, Li_2O_2 and Li_2O is electrically insulating. To promote the Li^+ ion transport through this layer, sufficient potential of $\sim -2\text{ V}$ is necessary to initiate the Li^+ diffusion. Although Li_2O is seldom used as an electrolyte in conventional LIBs, it is a common component of the SEI layer. Furthermore, our previous results show that Li_2O is indeed a Li^+ conductor with a potential barrier of only 0.4 eV, and the diffusivity of Li^+ in Li_2O is about $10^{-10}\text{ cm}^2\text{ s}^{-1}$. Our experimental results have indicated sufficient Li^+ transport capability of nanoscale Li_2O [57, 58]. Many of our experiments have demonstrated that the Li_2O layer is indeed a good Li^+ conductor but not electron conducting, thus charging and discharging experiments were successfully conducted in many anode materials [57, 58]. The ionic conductivity of Li_2O is about 10^{-7} s cm^{-1} at $\sim 470\text{ K}$, which is even lower at room temperature [78]. A solid cell is beneficial for fundamental studies of the lithiation behavior of a nanoobject for

two reasons. First, the entire object is visible in the entire electrochemical process. Second, small objects such as nanoparticles with size down to a few nanometers can be cycled and imaged in real time, which is not possible in a liquid cell because the ILE will cover the entire particle due to surface tension of the IL, making it impossible to image the electrochemical reactions. Although differing more from a real battery than the liquid cell, the solid cell offers complete structural information from the very beginning of lithiation. Extensive in situ experiments have been conducted using the solid cells. The materials studied include: chalcogenides (sulfur/selenium/oxygen), sulfides, fluorides, and oxides. Comprehensive review can be found in the review articles [61–70]. In the following, representative results obtained from solid cell nanobattery are presented.

Size-dependent fracture of Si nanoparticles

Si has the highest specific capacity of the anode materials (3579 mAh/g for $\text{Li}_{15}\text{Si}_4$ at room temperature) [79–82] about 10 times larger than that of the carbonaceous anodes (372 mAh/g for LiC_6) used in commercial LIBs. However, Si undergoes 280% volumetric expansion when alloying with Li to form the $\text{Li}_{15}\text{Si}_4$ phase at room temperature [58, 81]. Pulverization and the resultant loss of electrical contact have been recognized as one of the major causes of rapid capacity fading in Si-based electrodes, hindering application of such alloying anodes in LIBs [79, 83–86].

The electro-chemo-mechanical failure mechanism of Si is unclear. In this context, lithiation of individual silicon nanoparticles can be studied in real time with in situ biasing TEM [87]. As shown in Fig. 5.23, the unexpected surface cracking arose owing to the buildup of large tensile hoop stress, which reversed the initial compression, in the surface layer. The stress reversal was attributed to the unique mechanism of lithiation in crystalline Si, taking place by movement of a two-phase boundary between the inner core of pristine Si and the outer shell of amorphous Li–Si alloy. While the resulting hoop tension tended to initiate surface cracks, the small-sized nanoparticles nevertheless averted fracture. This is because the stored strain energy from electrochemical reactions was insufficient to drive crack propagation, as dictated by the interplay between the two length scales, that is, particle diameter and crack size, that control the fracture. These results are diametrically opposite to those obtained previously from single-phase modeling, which predicted only compressive hoop stress in the surface layer and thus crack initiation from the center in lithiated Si particles and wires. The experiment provides direct evidence of the mechanical robustness of small Si nanoparticles for applications in lithium-ion batteries.

Atomic-scale imaging of phase boundary migration in Si

The electrochemical reaction between the electrodes and lithium in LIBs is a critical process that controls the capacity, cyclability, and reliability of the battery. Despite intensive study, the atomistic mechanism of the electrochemical reactions occurring in these solid-state electrodes remains unclear. Liu et al. [88] achieved in situ imaging the dynamic lithiation process of single-crystal silicon with atomic resolution. A sharp interface (1 nm thick) between the crystalline silicon and an amorphous Li_xSi alloy was observed (Fig. 5.24a). The lithiation kinetics are controlled by the

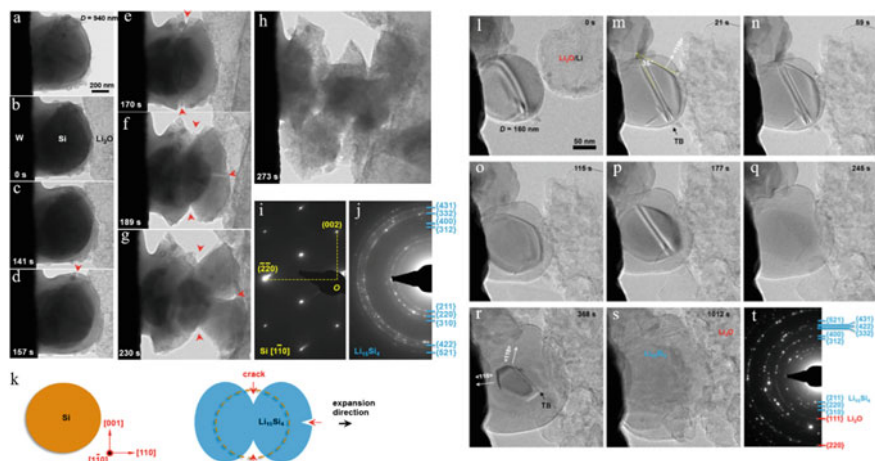


Fig. 5.23 Surface cracking and fracture of a large silicon nanoparticle (SiNP) during electrochemical lithiation. **a** Pristine SiNP with a diameter of 940 nm. **b–h** Crack nucleation and fracture of the SiNP in the lithiation process. After the $\text{Li}_2\text{O}/\text{Li}$ electrode contacted the SiNP sitting on the W electrode, a potential of 2 V was applied to the W electrode with respect to the Li metal (**b**). The lithiation occurred on the particle surface and proceeded inward as the gray-contrasted Li_xSi shell was thickened. When the shell thickness reached 150 nm, the first crack emerged near the surface, as marked by the red arrowhead (**d**). More cracks nucleated and propagated along different directions upon further lithiation (**e–g**), and finally the particle exploded into many tiny pieces (**h**). **i–j** Electron diffraction patterns (EDPs) showing the phase transformation from single-crystalline Si (**i**) to polycrystalline $\text{Li}_{15}\text{Si}_4$ after lithiation (**j**). **k** Schematic illustration showing the crystallography, expansion, and crack formation. The swelling was along Si $\langle 110 \rangle$ directions. Electrochemical lithiation of a small SiNP around the critical size showing no fracture. **l** Pristine SiNP with a diameter of about 160 nm. **m–s** Steady lithiation stage without cracking. There was a twin boundary (TB) in the center of the SiNP. Fast swelling along $\langle 110 \rangle$ resulted in a bump on the flat (110) plane, which formed a 35 angle with the TB (**m**). Anisotropic lithiation led to formation of the faceted Si core during the lithiation process (**r**). **s** Morphology of the fully lithiated particle. The electron beam was blanked during the lithiation process except for a short exposure for imaging. **t** EDP from the fully lithiated particle confirming the formation of polycrystalline $\text{Li}_{15}\text{Si}_4$ phase (blue lines and indices). The Li_2O phase showing up in the EDP was from the adjacent Li_2O layer (red dashed arcs and indices) (reproduced with permission from Ref. [87], Copyright 2012, American Chemical Society)

migration of the interface, which occurs through a ledge mechanism involving the lateral movement of ledges on the close-packed $\{111\}$ atomic planes. Such ledge-flow processes produce the amorphous Li_xSi alloy through layer-by-layer peeling of the $\{111\}$ atomic facets, resulting in the orientation-dependent mobility of the interfaces (Fig. 5.24b–f).

Conversion reaction

Using a modified version of the Li_2O solid cell, Wang et al. [89] conducted in situ experiments to track lithium transport and conversion in FeF_2 nanoparticles by nanoscale imaging, diffraction, and spectroscopy (Fig. 5.25). They found that lithium

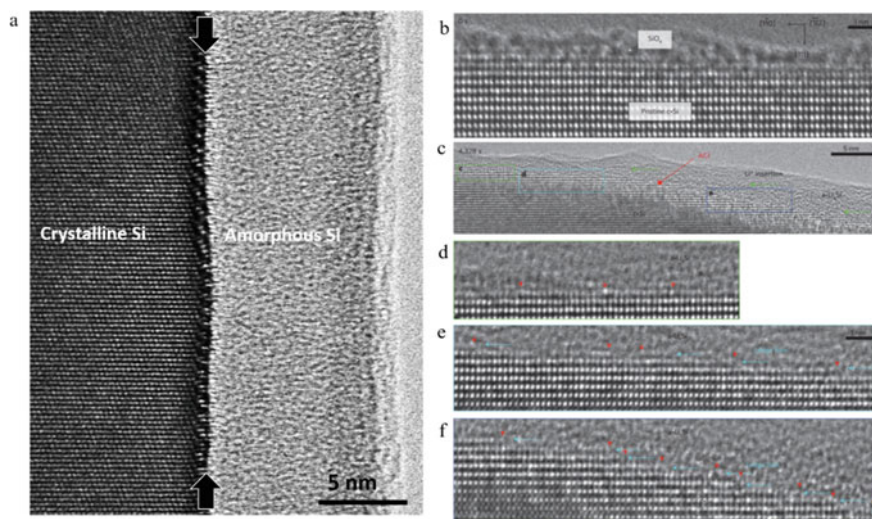


Fig. 5.24 Ledge mechanism observed in **a** $\langle 110 \rangle$ -oriented silicon nanowire during lithiation. **b** High-resolution image of the pristine silicon nanowire with a flat (111) surface and 1-nm-thick SiO_x layer. **c** Morphology of the partially lithiated silicon nanowire. With fast Li^+ transport via surface diffusion, lithiation proceeds along $\langle 110 \rangle$ from top to bottom (that is, from surface to core) and via ledge flow along $\langle 110 \rangle$ from right to left (marked by green arrows). **d–f** Enlarged zones showing vertical etching of the flat {111} plane, formation of ledges, and ledge-flow-dominated lithiation, respectively. Red arrows indicate ledges and cyan arrows ledge-flow directions. These images represent different stages of lithiation, and the ACI was gradually tilted toward $\langle 110 \rangle$ (reproduced with permission from Ref. [88], Copyright 2012, Springer Nature)

conversion was initiated at the surface, sweeping rapidly across the FeF_2 particles, followed by a gradual phase transformation in the bulk, resulting in 1–3 nm iron crystallites mixed with amorphous LiF . The real-time imaging revealed a surprisingly fast conversion process in individual particles (complete in a few minutes), with a morphological evolution resembling spinodal decomposition. This work provides new insights into the inter- and intra-particle lithium transport and kinetics of lithium conversion reactions, and may help to pave the way to develop high energy conversion electrodes for lithium-ion batteries.

All solid-state battery (SSB) cell

Yamamoto et al. used FIB milling to prepare an all SSB inside a biasing TEM holder, and they have succeeded in directly observing changes of electric potential in an all SSB during charge–discharge cycles (Fig. 5.26) [90]. Electron holography has been used to successfully quantify the 2D potential distribution resulting from movement of lithium ions near the positive-electrode/electrolyte interface. The result was confirmed using EELS analysis, which showed that lithium extraction from the positive electrode during charging results in oxidation of cobalt from Co^{3+} to Co^{4+} . Their results shed light on the sources of reaction resistance in all SSBs, which

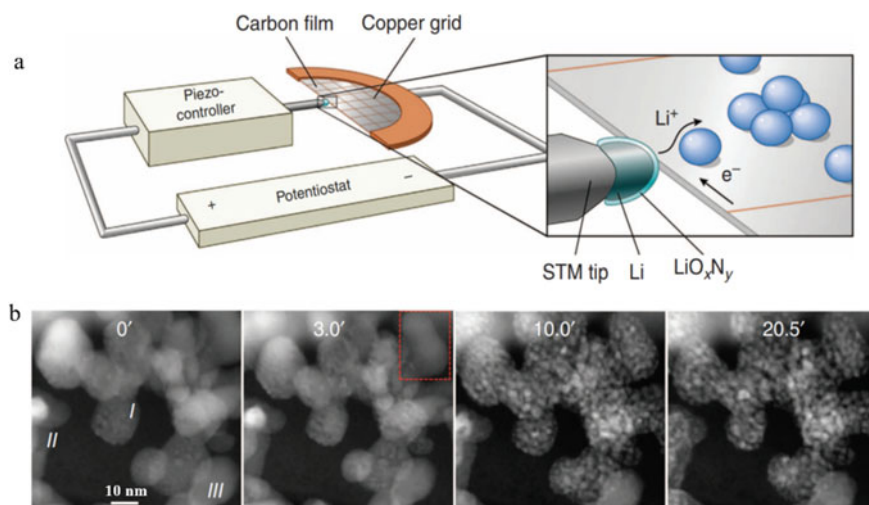


Fig. 5.25 **a** Schematic of the electrochemical cell used for in situ TEM measurements. **b** Time-lapse images from a collection of particles that react with lithium coming from the lower right. The reaction proceeds immediately in region (I), but is delayed and absent in regions (II) and (III), respectively (reproduced with permission from Ref. [89], Copyright 2012, Springer Nature)

is a bottle neck issue in the development of SSBs. Electron holography combined with EELS is a powerful technique for characterizing not only LIBs but also electric double layer capacitors, fuel cell batteries, and other electrochemical devices.

Therefore, Gong et al. [91, 92] combined focused ion beam and chip-based in situ setup to explore atomic-scale structural evolution of the electrode in all-solid-state lithium-ion battery (Fig. 5.27). They used focused ion beam etching to assemble a micro-scale all-solid-state battery on the MEMS chip, and successfully acquired a working battery. The combination of FIB and chip-based in situ sample stage achieves precise control of orientation tilt and high stability in an electric field environment and realizes the observation of lithium-ion migration and its effects in LiCoO_2 cathode under atomic scale with in situ electrochemical control [91]. Comparing with the traditional in situ electrochemical electron microscopy experiment, this methodology has increased the resolution of lithium-ion migration to the atomic scale. Traditional electron microscopy characterization results are two-dimensional projection images, while real materials all have three-dimensional structure information. The two-dimensional characterization results often mean the lack of one-dimensional structure information. On the basis of the above work, Gong et al. [92] continue to improve the atomic-scale in situ electron microscopy methodology, observe the structure evolution of the ordered phase spinel $\text{LiNi}_{0.5}\text{Mn}_{1.5}\text{O}_4$ cathode material in the all-solid-state battery from multiple crystal orientations, building the evolution of its three-dimensional atomic-scale structure and electronic structure, and supplementing the research of this material. From a three-dimensional perspective, they

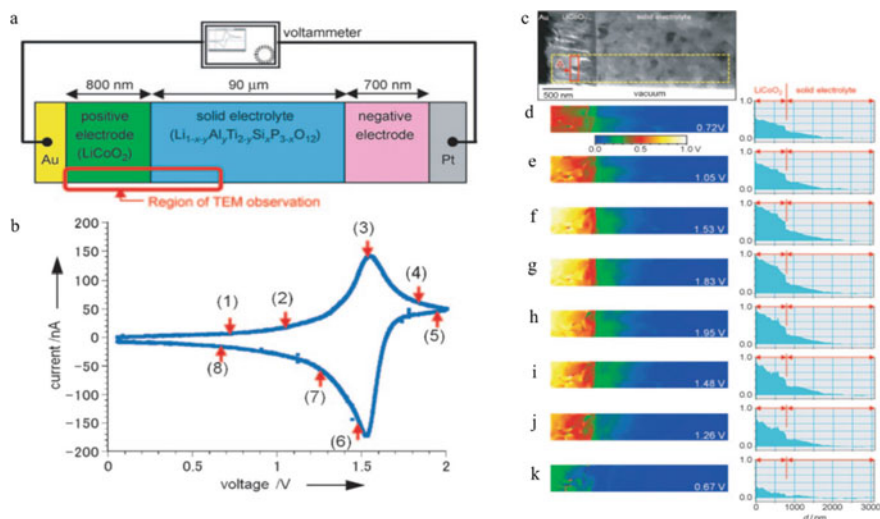


Fig. 5.26 **a** The all-solid-state LIB sample. The red-boxed region was thinned by a focused ion beam and observed by electron holography. **b** Cyclic voltammogram measured in a TEM with a voltage sweep rate of 40 mV min^{-1} . EH images were taken at points (1)–(8) and are given in (d–k), respectively. Electric potential distribution around the $\text{LiCoO}_2/\text{electrolyte}$ interface during the charge–discharge process. **c** Bright-field TEM image of the region near the interface. **d–k** 2D potential images (left) and line profiles (right) for the region bounded by the dashed line in (c) and obtained at voltages corresponding to points (1)–(8) in (b). Potential (V) is given on the y-axis (reproduced with permission from Ref. [90], Copyright 2010, John Wiley and Sons)

discovered a new inhomogeneous structural evolution phenomenon hidden behind the observation of the two-dimensional structure.

Electrochemomechanics of lithium

Lithium metal is considered the ultimate anode material for future rechargeable batteries [56, 93], but the development of Li-metal-based rechargeable batteries has achieved only limited success due to uncontrollable Li dendrite growth [94–98]. In a broad class of all SSBs, one approach to suppress Li dendrite growth has been the use of mechanically stiff solid electrolytes [99, 100]. However, Li dendrites still grow through them [101, 102]. Resolving this issue requires a fundamental understanding of the growth and associated electro-chemo-mechanical behavior of Li dendrites. By using a home-made TEM-AFM platform, Zhang et al. [103] report in situ growth observation and stress measurement of individual Li whiskers, the primary Li dendrite morphologies (Fig. 5.28). At room temperature, a submicrometric whisker grows under an applied voltage (overpotential) against the AFM tip, generating a growth stress up to 130 MPa; this value is substantially higher than the stresses previously reported for bulk ($\sim 1 \text{ MPa}$) and micrometer-sized Li ($\sim 100 \text{ MPa}$) [104]. The measured yield strength of Li whiskers under pure mechanical loading reaches as high as 244 MPa. Similar size effect was also observed in Na dendrite [105]. These results

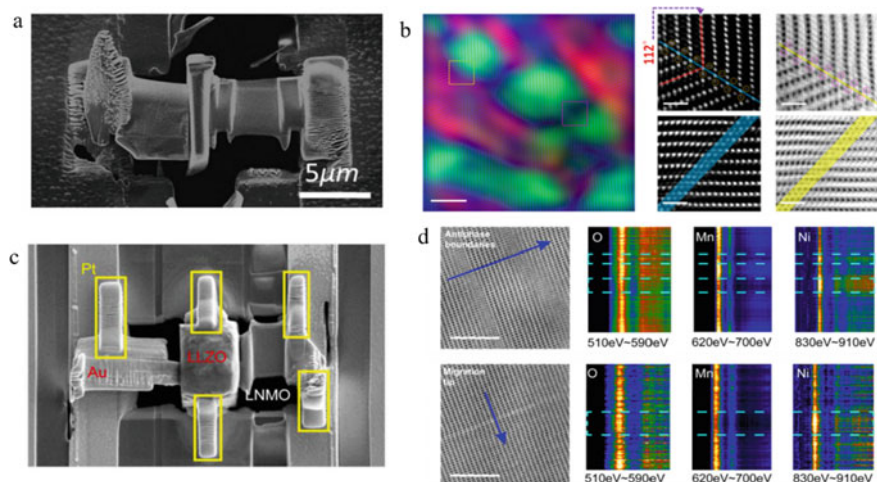


Fig. 5.27 In situ STEM study of the arbitrary combined micro-scale all-solid-state battery. **a** FIB assembled micro-scale all-solid-state battery. **b** Nanocrystalline formed after in situ delithiation in LiCoO₂ cathode (reproduced with permission from Ref. [91], Copyright 2017, American Chemical Society). **c** Improved FIB assembled micro-scale all-solid-state battery. **d** Inhomogeneous atomic structure and electronic structure evolution in LiNi_{0.5}Mn_{1.5}O₄ cathode (reproduced with permission from Ref. [92], Copyright 2018, Springer Nature)

provide quantitative benchmarks for the design of Li/Na dendrite growth suppression strategies in all SSBs.

Li/Na/K-O₂/CO₂ batteries

Vehicle electrification and grid energy storage demands large-scale energy storage devices with much higher energy density than current lithium-ion battery technology. Li/Na/K-O₂/CO₂ batteries are potential “beyond lithium” technology for large-scale energy storage applications. However, the fundamental electrochemistry of the Li/Na-O₂ is still unclear. With the advent of aberration-corrected environmental TEM (ETEM), it is now possible to probe the fundamental electrochemistry of the Li/Na/K-O₂/CO₂ batteries.

Metal-air batteries have much higher theoretical energy density than metal ion batteries; however, their application is hampered by the sluggish oxygen reduction reaction (ORR) and the oxygen evolution reaction (OER). As such, electrocatalysis is employed to facilitate the ORR and OER. Despite enormous efforts, real-time imaging of the electrocatalysis during the ORR and OER processes remains elusive. Furthermore, it is controversial whether or not electrocatalysis is necessary in the Na-O₂ battery. Liu et al. [106] show the first in situ imaging of the operation of the electrocatalysis in a Na-O₂ battery in an advanced aberration-corrected ETEM (Fig. 5.29). In the Au-coated MnO₂ nanowire air cathode, the ORR is characterized by the formation of NaO₂ nanobubbles nucleated from the Au catalysts, causing an 18 times volume increase on the surface of the MnO₂ nanowires; the NaO₂ quickly

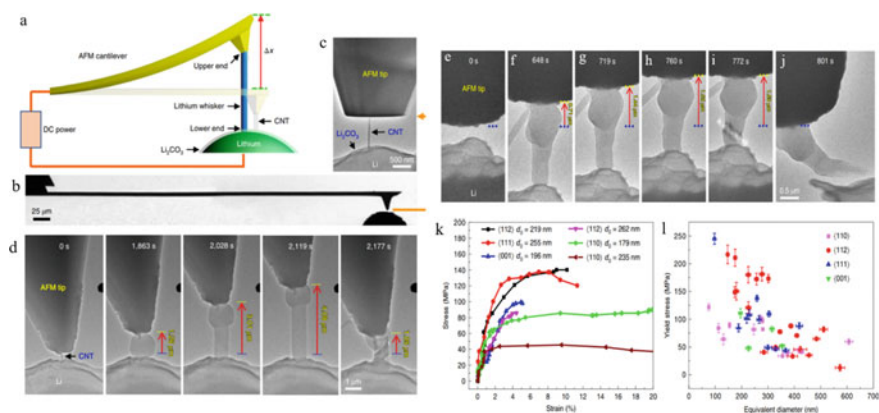


Fig. 5.28 In situ AFM–ETEM characterization of stress generation during Li whisker growth. **a** Schematic of the AFM–ETEM setup used for observation and measurement of Li whisker growth. An arc-discharged CNT was attached to a conducting AFM tip by electron-beam deposition of carbonaceous materials, and this assembly was used as a cathode; the scratched Li metal on the top of a sharp tungsten needle was used as an anode; and the naturally formed Li_2CO_3 on the Li surface was used as a solid electrolyte. The measured displacement of the cantilever tip is denoted as Δx . **b** TEM image showing an AFM cantilever approaching the counterelectrode of Li metal. **c** TEM image showing a CNT attached to a flattened AFM tip. **d** Time-lapse TEM images of Li whisker growth. **e** In situ compression testing of as-grown Li whiskers. Metal Li was manipulated to approach the AFM tip; **f–i** a growing Li whisker pushed up against the AFM tip ($k = 6 \text{ N m}^{-1}$); **j** and this whisker collapsed after extensive compression. The blue dotted line indicates a fixed reference position, and the red arrow indicates the upward displacement of the AFM tip. **k** Compressive stress–strain curves of six whiskers with different growth directions and diameters d_0 . **l** Yield stress versus equivalent diameter measured for Li whiskers with different growth directions (reproduced with permission from Ref. [103], Copyright 2020, Springer Nature)

disproportionated to Na_2O_2 and O_2 , causing collapse of the NaO_2 nanobubbles. In contrast, no ORR took place in the bare MnO_2 nanowire cathode; instead, the MnO_2 nanowires only swelled 217% as a result of the Na^+ intercalation. The results provide not only new insight into the Au-catalyzed oxygen chemistry in the Na– O_2 battery, but also an atom-level characterization technique to evaluate the electrocatalysis in the metal–air batteries. Mechanistic studies in Li– O_2 , Li– CO_2 , Na– O_2/CO_2 , Na– CO_2 , and K– CO_2 battery systems. These studies provide important understanding to the fundamental electrochemistry of metal–gas batteries.

5.4.3 In Situ Liquid Cell

The IL cell and the Li_2O solid cells can be categorized as open cells, since all the electrodes and electrolyte are exposed to the high vacuum of TEM. Although the open cell has produced fruitful results in nanoelectrochemistry, the experimental conditions in open cells are far from the practical LIBs using liquid electrolyte. To

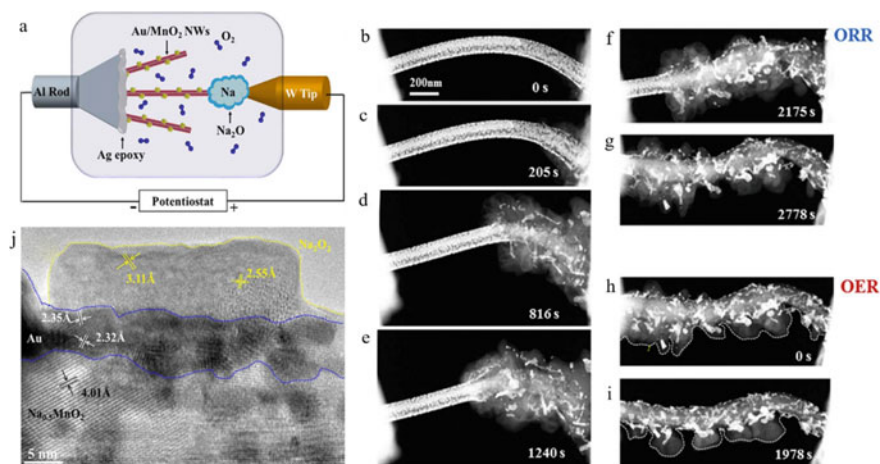


Fig. 5.29 In situ imaging the Au-catalyzed ORR in a Na–O₂ nanobattery. **a** Schematic of the experimental setup. The SOB consists of a Au/MnO₂ NW and O₂ cathode, a Na₂O electrolyte and a Na anode. **b–g** Structure evolution of the NaO₂ discharge product during ORR. Upon applying a negative potential to the Au/MnO₂ NW, bubble-like NaO₂ nucleated on the right contact where the Au/MnO₂ NW and Na₂O intersect (b–c), which then propagated along the NW, causing an 18 times volume increase (d–e). The discharge product shrank as a result of the disproportionation of NaO₂ to Na₂O₂ and O₂ (f–g). **h–i** Charge process of the Au/MnO₂ NW. The Au nanoparticles, which aggregated to larger size after discharge/charge, exhibit much brighter contrast than that of the MnO₂ NW and the discharge products in the ADF images shown in (b–i). **j** HRTEM image of the residue discharge products after the charging process. The residual Na₂O₂ located on the aggregated Au nanoparticles after charging was isolated from the Na⁺ ions, thus the OER ceased. Au nanoparticles resided in between the dashed lines (reproduced with permission from Ref. [106], Copyright 2019, Elsevier)

make the experimental conditions more close to the practical LIBs, particularly in liquid-electrolyte-based LIBs, a liquid cell is therefore preferred [107–113].

Cell Development

One of the greatest challenges in performing liquid electrochemistry inside a TEM is introducing volatile electrolytes into the high vacuum of the TEM sample chamber, typically 10⁻⁵ Torr or better [59]. One approach is to seal the liquid inside a narrow channel that is thin enough to permit electron transmission. One of the first TEM liquid cells was created by Williamson, et al., for the study of Cu electrodeposition during TEM imaging [113]. This platform used two silicon chips with thin silicon nitride membranes assembled face to face, sealing in an aqueous electrolyte. Several other designs based on this flip-chip approach have been pursued by other investigators using membranes of silicon nitride, silicon dioxide, or polymer and for studies ranging from imaging of cells in solution to nanoparticle synthesis [107, 109, 111, 112].

With a focus on developing a versatile electrochemical cell that is TEM-compatible and that permits high-resolution imaging, Sullivan et al. have used MEMS

fabrication processes to create a platform with multiple electrical and insulating layers [108]. Their design utilizes ultrathin silicon nitride windows that are less than 40 nm thick in order to reduce electron absorption during TEM imaging. This approach requires small diameter nitride windows (approximately 20 microns to less than 5 microns across). The top and bottom chips are sealed by a low-viscosity epoxy that wicks along the raised seal ring.

The liquid cell has produced numerous interesting results, such as the successful observation dendrite and SEI formation under liquid electrolyte environments. Some representative results in the studies of batteries are present in the following.

Dendrite and SEI formation in liquid cell

Zheng's group [114] report direct visualization of electrochemical lithiation and delithiation of Au anodes in a commercial $\text{LiPF}_6/\text{EC}/\text{DEC}$ electrolyte for LIBs using TEM (Fig. 5.30a–c). The inhomogeneous lithiation, lithium metal dendritic growth, electrolyte decomposition, and SEI formation were observed in situ. These results shed lights on strategies of improving electrode design for reducing short-circuit failure and improving the performance of LIBs.

Gu et al. did excellent comparison experiments on Si NW using liquid cell and open cell. The liquid-cell nanobattery approach provides indispensable complementary information to the widely applied open-cell approach. The complete electrochemical process can be more fully understood by combining open-cell and liquid-cell battery TEM techniques (Fig. 5.30d–f). The open-cell approach provides important information regarding the composition, phase transformation, and atomic resolution structural changes of the electrode itself, allowing high-resolution microscopy to be obtained. On the other hand, the liquid cell allows the usage of any form of liquid electrolyte that is relevant to real battery and full emersion of the electrodes. Therefore, the liquid cell has tremendous potential for the study of the electrolyte–electrode interaction: the SEI formation and growth kinetics [115].

Regan's group [116] reported in situ STEM observations of the electrodeposition and stripping of lead on polycrystalline gold electrodes from a 1.5 M aqueous solution of lead nitrate (Fig. 5.31). Lead can be induced to deposit in a compact coating or as dendrites, with the latter morphology being more likely with abrupt potential changes. Individual dendrites are crystalline and grow from their tips most commonly along a $\langle 100 \rangle$ crystal axis. With its ability to provide real-time, high-resolution images of both the reactants and the products in electrochemical processes, in situ fluid cell STEM promises to become a powerful tool for solving dendrite formation problems in energy storage devices.

Mehdi et al. [117] studied lithium electrodeposition on a Pt working electrode using the LiPF_6/PC electrolyte in a commercial liquid cell through scanning transmission electron microscopy (EC-S/TEM). They found that a smooth lithium deposition occurred in the first cycle, followed by an uneven deposition in consecutive charge/discharge (plating/stripping) cycles (Fig. 5.32). This occurred due to the presence of dead lithium at the end of each cycle, including from the first stripping process. As the cycle progressed, the amount of dead lithium increased. After the fifth cycle, they observed the SEI formation on the Pt surface. Simultaneously, the

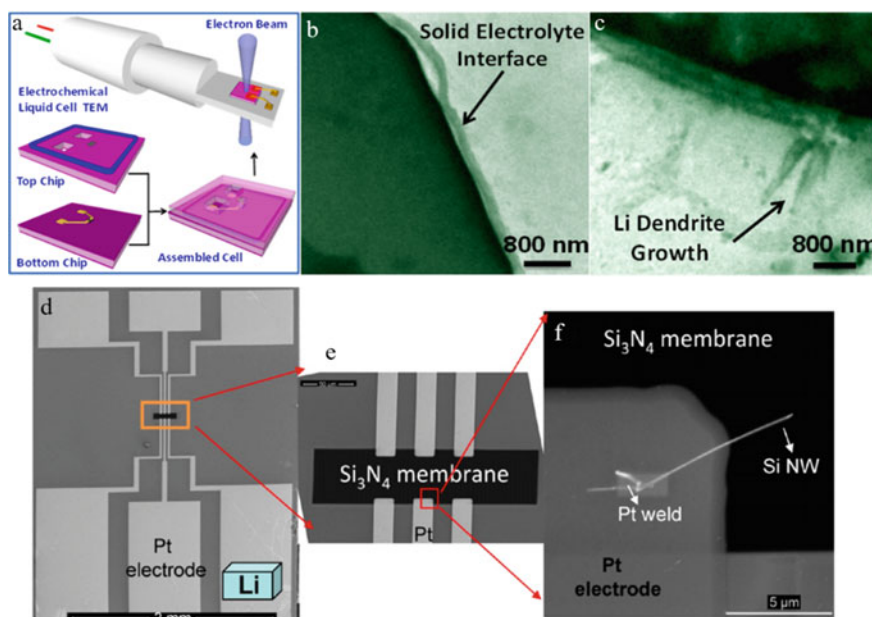


Fig. 5.30 **a** A top microchip patterned with 150-nm-thick metallic indium was covered and stuck onto bottom microchip with 120-nm-thick gold electrode deposited on it, which is the assembled liquid cell for TEM visualization when embedded in a TEM holder. **b** A gas bubble emerged between the gold electrode and the SEI film; **c** the growth and dissolution of lithium dendrite (reproduced with permission from Ref. [114], Copyright 2014, American Chemical Society) **d** SEM image of the inner side of the biasing chip; **e** magnified view of the region labeled by the orange rectangle; **f** SEM image showing the welded Si NW electrode onto the Pt contact. Note that the Li location is labeled by the light blue color object in panel (d) (reproduced with permission from Ref. [115], Copyright 2013, American Chemical Society)

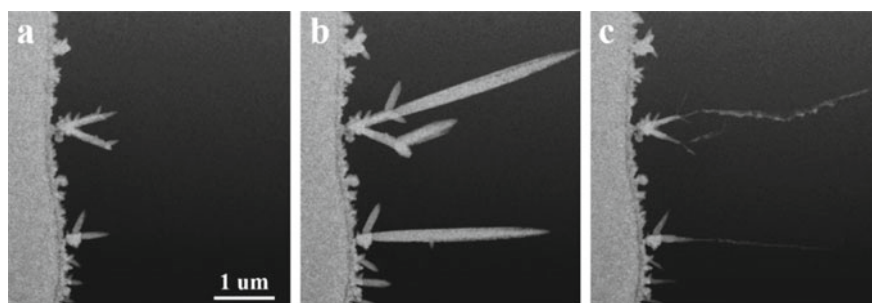


Fig. 5.31 The dendrite growth and collapse (reproduced with permission from Ref. [116], Copyright 2012, American Chemical Society)

edges of the Pt electrode started protruding with the accumulated dead lithium in the form of dendrites from beneath the SEI and with increasing number of cycles these dendrites grew. They also observed reversible volume expansion in the Pt electrode and suggested that Pt is not suitable for electrochemical studies of lithium.

It should be noted that lithium dendrite growth was also observed in IL cell [118–120]. Liu et al. [118] found that Li fibers with length up to 35 μm grew on nanowire tip after charging a $\text{SnO}_2/\text{IL}/\text{LiCoO}_2$ cell. The Li fiber growth was highly directional, i.e., nucleating from the nanowire tip, and extending along the nanowire axis, which was attributed to the strong electric field enhancement effect induced by the sharp nanowire tip. The study reveals a potential safety concern of short-circuit failure for LIBs using nanowire anodes.

Quantitative nanoelectrochemistry in liquid cell

By appropriate passivation of the electrode, Leenheer et al. [121] demonstrate that it is possible to perform quantitative electrochemical measurement and correlate it with the microstructure evolution. They show that by sourcing pA current to a liquid-cell electrode, the changing of voltage to the working electrode is recorded, which is correlated with the lithium deposition and stripping morphology changes (Fig. 5.33). They also observed that the electron beam exposure clearly changed the

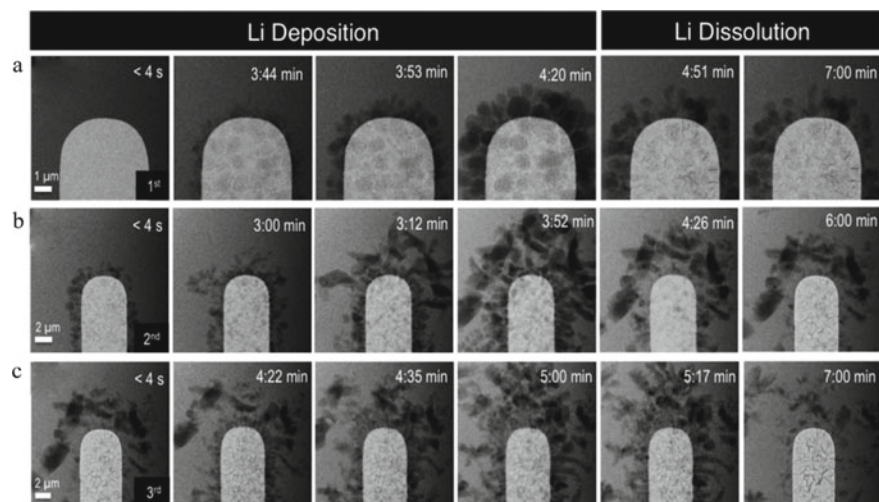


Fig. 5.32 High-angle annular dark-field (HAADF) images of Li deposition and dissolution at the interface between the Pt working electrode and the LiPF_6/PC electrolyte during the **a** first, **b** second, and **c** third charge/discharge cycles of the operando cell. The formation of the SEI layer (ring of contrast around the electrode), alloy formation due to Li^+ ion insertion, and the presence of “dead Li” detached from the electrode can all be seen in the images at the end of the cycle, thereby demonstrating the degree of irreversibility associated with this process (reproduced with permission from Ref. [117], Copyright 2015, American Chemical Society)

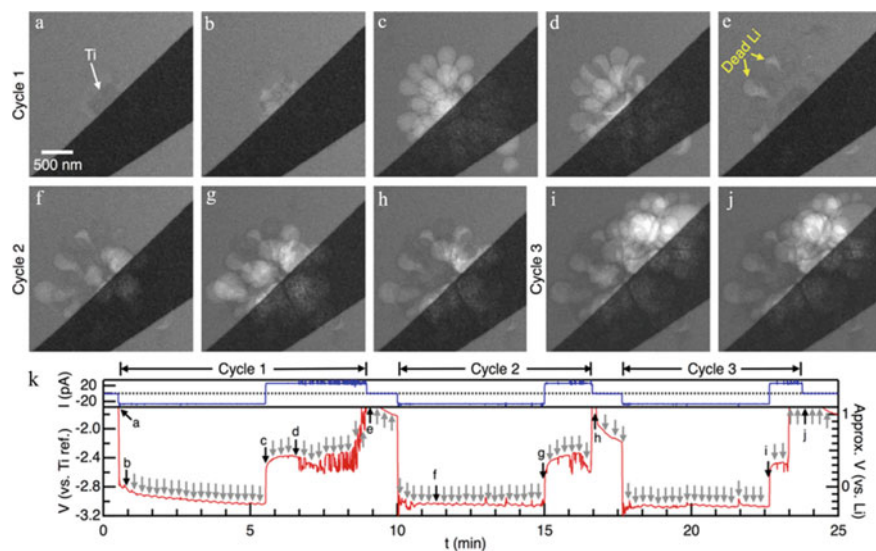


Fig. 5.33 Li cycling at $|j| = 10 \text{ mA/cm}^2$ while imaging every 15 s. **a** BF STEM image before deposition, **b–c** near beginning and end of deposition cycle 1, **d–e** near beginning and end of stripping cycle 1 where disconnected “dead” Li is evident after stripping finished, **f–g** during second deposition, **h** after second stripping, **i** after third deposition, **j** after third stripping, and **k** chronopotentiometry during cycling with the voltage measured versus Ti and inferred versus Li; an STEM image was taken at every arrow (reproduced with permission from Ref. [121], Copyright 2015, American Chemical Society)

deposition morphology and kinetics of lithium to some extent. Without beam exposure, deposited lithium grains show faceting and needle-like morphology, but after exposure to the beam, the growth of any given grain becomes more uniform with a presumably spherical geometry. Furthermore, the beam also causes the nucleation of new grains that may disrupt the growth of the initial grains by electrical disconnection [121]. The quantitative electrochemical measurement opens new avenue to correlate state of charge with the microstructure evolution, and thus has great potential for quantitative nanoelectrochemistry.

5.5 Perspective

In situ biasing TEM has made great contributions in the fields of electronics, nanomechanics, electrochemistry, and electromechanical coupling. With the advent of more advanced instrumentation such as more sophisticated in situ holders and aberration-corrected ETEM, we believe that in situ biasing TEM has great potential to reveal the physics, chemistry, and mechanics of nanomaterials in operando or conditions closer to working environment of practical devices. Challenges and opportunities co-exist.

1. In the in situ biasing liquid cell, the resolution is still limited due to the thick liquid that scatter electrons and the use of thick SiN membrane. Furthermore, the electron beam and liquid interaction complicates the data interpretation. Indeed, beam and sample interaction does alter reaction kinetics in electrochemical cells. Therefore, special precautions need to be taken when conducting in situ biasing experiments and data analysis. It is still challenging to conduct chemical analysis in a liquid-cell configuration, although progress has been made by optimizing the cell design.
2. Quantitative nanoelectrochemistry is still challenging in almost all in situ electrochemical experiments. The main reason is reaction volume in the in situ experiments is usually very small, resulting in weak electrochemical signal. For example, the charging current of a single nanowire is within pA scale, most of the current source meter cannot source such a small current. This is further complicated by the noise level in the experimental environment, which usually exceeds the pA level. Better instrumentation and shielding are required for true quantitative nanoelectrochemistry.
3. In situ electrochemical experiments in intercalation and cathode materials are still scarce due to the challenges in detecting subtle changes in these materials. With advent of new imaging technologies such as aberration-corrected STEM-ABF or iDPC, imaging the light elements such as H, Li, Na is now routine, however imaging the evolution of light elements such as the alkali metals during nanobattery operation is still challenging, because the imaging conditions of ABF and iDPC are very dedicated and time-consuming, thus lacking the temple resolution that is required by in situ electrochemical experiments.
4. In situ imaging under simultaneous multiple external stimuli such as pressures, temperatures, and gaseous environmental are still challenging. Nevertheless, these are usually the working environments of practical materials. Therefore, developing technologies that permit in situ TEM studies under multiple external stimulus are urgently needed.
5. Fuel cells which are electrochemical devices that convert the chemical energy of a fuel (often hydrogen) and an oxidizing agent (often oxygen) into electricity through a pair of redox reactions. Fuel cells can produce electricity continuously for as long as fuel and oxygen are supplied. Fuel cell is an important device to power electrical vehicles. However, the use of rare earth metals such as Pt and Ru rendering it very expensive. Searching for cheap catalysts for is a grand challenge for fuel cell technology. In situ TEM of fuel cell has not been realized due to technique difficult to construct a miniaturized fuel cell device that is operative inside the limited space of a TEM sample chamber; nevertheless, this is a very important field that has not been explored.

References

1. Xiang J, Lu W, Hu Y, Wu Y, Yan H, Lieber CM (2006) Ge/Si nanowire heterostructures as high-performance field-effect transistors. *Nature* 441(7092):489–493. <https://doi.org/10.1038/nature04796>

2. Li Y, Qian F, Xiang J, Lieber CM (2006) Nanowire electronic and optoelectronic devices. *Mater Today* 9(10):18–27. [https://doi.org/10.1016/S1369-7021\(06\)71650-9](https://doi.org/10.1016/S1369-7021(06)71650-9)
3. Ohnishi H, Kondo Y, Takayanagi K (1998) Quantized conductance through individual rows of suspended gold atoms. *Nature* 395(6704):780–783. <https://doi.org/10.1038/27399>
4. Iijima S (1991) Helical microtubules of graphitic carbon. *Nature* 354(6348):56–58. <https://doi.org/10.1038/354056a0>
5. Bockrath M, Cobden DH, McEuen PL, Chopra NG, Zettl A, Thess A, Smalley RE (1997) Single-electron transport in ropes of carbon nanotubes. *Science* 275(5308):1922–1925. <https://doi.org/10.1126/science.275.5308.1922>
6. Pascual JI, Méndez J, Gómez-Herrero J, Baró AM, Garcia N, Landman U, Luedtke WD, Bogachek EN, Cheng HP (1995) Properties of metallic nanowires: from conductance quantization to localization. *Science* 267(5205):1793–1795. <https://doi.org/10.1126/science.267.5205.1793>
7. Spence JCH (1988) A scanning tunneling microscope in a side-entry holder for reflection electron microscopy in the Philips EM400. *Ultramicroscopy* 25(2):165–169. [https://doi.org/10.1016/0304-3991\(88\)90224-0](https://doi.org/10.1016/0304-3991(88)90224-0)
8. Kuwabara M, Lo W, Spence JCH (1989) Reflection electron microscope imaging of an operating scanning tunneling microscope. *J Vac Sci Technol, A* 7(4):2745–2751. <https://doi.org/10.1116/1.575785>
9. Wall MA, Dahmen U (1998) An in situ nanoindentation specimen holder for a high voltage transmission electron microscope. *Microsc Res Tech* 42(4):248–254. [https://doi.org/10.1002/\(SICI\)1097-0029\(19980915\)42:4%3c248::AID-JEMT3%3e3.0.CO;2-M](https://doi.org/10.1002/(SICI)1097-0029(19980915)42:4%3c248::AID-JEMT3%3e3.0.CO;2-M)
10. Minor A, Stach E, Morris J (2001) Quantitative in-situ nanoindentation of thin films in a transmission electron microscope. *Microsc Microanal* 7:912–913. <https://doi.org/10.1017/S1431927600030634>
11. <http://www.zeptools.com>
12. Erts D, Lohmus A, Holmes JD, Olin H (2007) Probing of nanocontacts inside a transmission electron microscope. In: *Fundamentals of friction and wear*. Springer, pp 73–100
13. <https://hummingbirdscientific.com>
14. <https://www.bruker.com/>
15. Dresselhaus MS, Dresselhaus G, Eklund PC, Rao AM (2000) Carbon nanotubes. In: Andreoni W (ed) *The physics of fullerene-based and fullerene-related materials*. Springer Netherlands, Dordrecht, pp 331–379. https://doi.org/10.1007/978-94-011-4038-6_9
16. Rinzler AG, Hafner JH, Nikolaev P, Nordlander P, Colbert DT, Smalley RE, Lou L, Kim SG, Tománek D (1995) Unraveling nanotubes: field emission from an atomic wire. *Science* 269(5230):1550–1553. <https://doi.org/10.1126/science.269.5230.1550>
17. de Heer WA, Châtelain A, Ugarte D (1995) A carbon nanotube field-emission electron source. *Science* 270(5239):1179–1180. <https://doi.org/10.1126/science.270.5239.1179>
18. Huang JY, Kempa K, Jo SH, Chen S, Ren ZF (2005) Giant field enhancement at carbon nanotube tips induced by multistage effect. *Appl Phys Lett* 87(5):053110. <https://doi.org/10.1063/1.2008363>
19. Jo SH, Wang DZ, Huang JY, Li WZ, Kempa K, Ren ZF (2004) Field emission of carbon nanotubes grown on carbon cloth. *Appl Phys Lett* 85(5):810–812. <https://doi.org/10.1063/1.1776330>
20. Cumings J, Zettl A (2004) Field emission and current-voltage properties of boron nitride nanotubes. *Solid State Commun* 129(10):661–664. <https://doi.org/10.1016/j.ssc.2003.11.026>
21. Cumings J, Zettl A, McCartney MR, Spence JCH (2002) Electron holography of field-emitting carbon nanotubes. *Phys Rev Lett* 88(5):056804. <https://doi.org/10.1103/PhysRevLett.88.056804>
22. Blech IA, Meieran ES (1967) Direct transmission electron microscope observation of electrotransport in aluminum thin films. *Appl Phys Lett* 11(8):263–266. <https://doi.org/10.1063/1.1755127>
23. Erts D, Olin H, Ryen L, Olsson E, Thölen A (2000) Maxwell and Sharvin conductance in gold point contacts investigated using TEM-STM. *Phys Rev B* 61(19):12725–12727. <https://doi.org/10.1103/PhysRevB.61.12725>

24. Iwatsuki M, Murooka K, Kitamura S-I, Takayanagi K, Harada Y (1991) Scanning tunneling microscope (STM) for conventional transmission electron microscope (TEM). *J Electron Microscop* 40(1):48–53. <https://doi.org/10.1093/oxfordjournals.jmicro.a050869>
25. Frank S, Poncharal P, Wang ZL, Heer Walt Ad (1998) Carbon nanotube quantum resistors. *Science* 280(5370):1744–1746. <https://doi.org/10.1126/science.280.5370.1744>
26. Erts D, Löhmus A, Löhmus R, Olin H (2001) Instrumentation of STM and AFM combined with transmission electron microscope. *Appl Phys A* 72(1):S71–S74. <https://doi.org/10.1007/s003390100636>
27. Kizuka T, Ohmi H, Sumi T, Kumazawa K, Deguchi S, Naruse M, Fujisawa S, Sasaki S, Yabe A, Enomoto Y (2001) Simultaneous observation of millisecond dynamics in atomistic structure, force and conductance on the basis of transmission electron microscopy. *Japan J Appl Phys* 40(Part 2, No. 2B):L170–L173. <https://doi.org/10.1143/jjap.40.1170>
28. Kizuka T, Umehara S, Fujisawa S (2001) Metal-insulator transition in stable one-dimensional arrangements of single gold atoms. *Japan J Appl Phys* 40(Part 2, No. 1A/B):L71–L74. <https://doi.org/10.1143/jjap.40.171>
29. Poncharal P, Wang ZL, Ugarte D, de Heer WA (1999) Electrostatic deflections and electromechanical resonances of carbon nanotubes. *Science* 283(5407):1513–1516. <https://doi.org/10.1126/science.283.5407.1513>
30. Gao R, Wang ZL, Bai Z, de Heer WA, Dai L, Gao M (2000) Nanomechanics of individual carbon nanotubes from pyrolytically grown arrays. *Phys Rev Lett* 85(3):622–625. <https://doi.org/10.1103/PhysRevLett.85.622>
31. Gao R, Pan Z, Wang ZL (2001) Work function at the tips of multiwalled carbon nanotubes. *Appl Phys Lett* 78(12):1757–1759. <https://doi.org/10.1063/1.1356442>
32. Lu Y, Huang JY, Wang C, Sun S, Lou J (2010) Cold welding of ultrathin gold nanowires. *Nat Nanotechnol* 5(3):218–224. <https://doi.org/10.1038/nnano.2010.4>
33. Gao P, Britson J, Nelson CT, Jokisaari JR, Duan C, Trassin M, Baek S-H, Guo H, Li L, Wang Y, Chu Y-H, Minor AM, Eom C-B, Ramesh R, Chen L-Q, Pan X (2014) Ferroelastic domain switching dynamics under electrical and mechanical excitations. *Nat Commun* 5(1):3801. <https://doi.org/10.1038/ncomms4801>
34. Kwon D-H, Kim KM, Jang JH, Jeon JM, Lee MH, Kim GH, Li X-S, Park G-S, Lee B, Han S, Kim M, Hwang CS (2010) Atomic structure of conducting nanofilaments in TiO₂ resistive switching memory. *Nat Nanotechnol* 5(2):148–153. <https://doi.org/10.1038/nnano.2009.456>
35. Yang Y, Gao P, Gaba S, Chang T, Pan X, Lu W (2012) Observation of conducting filament growth in nanoscale resistive memories. *Nat Commun* 3(1):732. <https://doi.org/10.1038/ncomms1737>
36. Dames C, Chen S, Harris CT, Huang JY, Ren ZF, Dresselhaus MS, Chen G (2007) A hot-wire probe for thermal measurements of nanowires and nanotubes inside a transmission electron microscope. *Rev Sci Instrum* 78(10):104903. <https://doi.org/10.1063/1.2785848>
37. Li D, Wu Y, Kim P, Shi L, Yang P, Majumdar A (2003) Thermal conductivity of individual silicon nanowires. *Appl Phys Lett* 83(14):2934–2936. <https://doi.org/10.1063/1.1616981>
38. Pettes MT, Shi L (2009) Thermal and structural characterizations of individual single-, double-, and multi-walled carbon nanotubes. *Adv Func Mater* 19(24):3918–3925. <https://doi.org/10.1002/adfm.200900932>
39. Harris CT, Martinez JA, Shaner EA, Huang JY, Swartzentruber BS, Sullivan JP, Chen G (2011) Fabrication of a nanostructure thermal property measurement platform. *Nanotechnology* 22(27):275308. <https://doi.org/10.1088/0957-4484/22/27/275308>
40. Sichel EK, Pankove JI (1977) Thermal conductivity of GaN, 25–360 K. *J Phys Chem Solids* 38(3):330. [https://doi.org/10.1016/0022-3697\(77\)90112-3](https://doi.org/10.1016/0022-3697(77)90112-3)
41. Huang JY, Chen S, Ren ZF, Chen G, Dresselhaus MS (2006) Real-time observation of tubule formation from amorphous carbon nanowires under high-bias Joule heating. *Nano Lett* 6(8):1699–1705. <https://doi.org/10.1021/nl0609910>
42. Chen S, Huang JY, Wang Z, Kempa K, Chen G, Ren ZF (2005) High-bias-induced structure and the corresponding electronic property changes in carbon nanotubes. *Appl Phys Lett* 87(26):263107. <https://doi.org/10.1063/1.2155116>

43. Huang J-Y, Ding F, Jiao K, Yakobson BI (2007) Self-templated growth of carbon-nanotube walls at high temperatures. *Small* 3(10):1735–1739. <https://doi.org/10.1002/sml.200700105>
44. Huang JY, Ding F, Jiao K, Yakobson BI (2007) Real time microscopy, kinetics, and mechanism of giant fullerene evaporation. *Phys Rev Lett* 99(17):175503. <https://doi.org/10.1103/PhysRevLett.99.175503>
45. Svensson K, Olin H, Olsson E (2004) Nanopipettes for metal transport. *Phys Rev Lett* 93(14):145901. <https://doi.org/10.1103/PhysRevLett.93.145901>
46. Regan BC, Aloni S, Ritchie RO, Dahmen U, Zettl A (2004) Carbon nanotubes as nanoscale mass conveyors. *Nature* 428(6986):924–927. <https://doi.org/10.1038/nature02496>
47. Regan BC, Aloni S, Jensen K, Ritchie RO, Zettl A (2005) Nanocrystal-powered nanomotor. *Nano Lett* 5(9):1730–1733. <https://doi.org/10.1021/nl0510659>
48. Huang JY, Ding F, Yakobson BI, Lu P, Qi L, Li J (2009) In situ observation of graphene sublimation and multi-layer edge reconstructions. *Proc Natl Acad Sci* 106(25):10103. <https://doi.org/10.1073/pnas.0905193106>
49. Zheng H, Wang J, Huang JY, Wang J, Zhang Z, Mao SX (2013) Dynamic process of phase transition from wurtzite to zinc blende structure in InAs nanowires. *Nano Lett* 13(12):6023–6027. <https://doi.org/10.1021/nl403240r>
50. Jin C, Suenaga K, Iijima S (2008) Plumbing carbon nanotubes. *Nat Nanotechnol* 3(1):17–21. <https://doi.org/10.1038/nnano.2007.406>
51. Huang JY, Chen S, Jo SH, Wang Z, Han DX, Chen G, Dresselhaus MS, Ren ZF (2005) Atomic-scale imaging of wall-by-wall breakdown and concurrent transport measurements in multiwall carbon nanotubes. *Phys Rev Lett* 94(23):236802. <https://doi.org/10.1103/PhysRevLett.94.236802>
52. Huang JY, Chen S, Wang ZQ, Kempa K, Wang YM, Jo SH, Chen G, Dresselhaus MS, Ren ZF (2006) Superplastic carbon nanotubes. *Nature* 439(7074):281. <https://doi.org/10.1038/439281a>
53. Nardelli MB, Yakobson BI, Bernholc J (1998) Brittle and ductile behavior in carbon nanotubes. *Phys Rev Lett* 81(21):4656–4659. <https://doi.org/10.1103/PhysRevLett.81.4656>
54. Yu M-F, Files BS, Arepalli S, Ruoff RS (2000) Tensile loading of ropes of single wall carbon nanotubes and their mechanical properties. *Phys Rev Lett* 84(24):5552–5555. <https://doi.org/10.1103/PhysRevLett.84.5552>
55. Zhong L, Wang J, Sheng H, Zhang Z, Mao SX (2014) Formation of monatomic metallic glasses through ultrafast liquid quenching. *Nature* 512(7513):177–180. <https://doi.org/10.1038/nature13617>
56. Tarascon JM, Armand M (2010) Issues and challenges facing rechargeable lithium batteries. In: *Materials for sustainable energy*. Co-Published with Macmillan Publishers Ltd., UK, pp 171–179. https://doi.org/10.1142/9789814317665_0024
57. Huang JY, Zhong L, Wang CM, Sullivan JP, Xu W, Zhang LQ, Mao SX, Hudak NS, Liu XH, Subramanian A, Fan H, Qi L, Kushima A, Li J (2010) In situ observation of the electrochemical lithiation of a single SnO₂ nanowire electrode. *Science* 330(6010):1515–1520. <https://doi.org/10.1126/science.1195628>
58. Liu XH, Zheng H, Zhong L, Huang S, Karki K, Zhang LQ, Liu Y, Kushima A, Liang WT, Wang JW, Cho J-H, Epstein E, Dayeh SA, Picraux ST, Zhu T, Li J, Sullivan JP, Cumings J, Wang C, Mao SX, Ye ZZ, Zhang S, Huang JY (2011) Anisotropic swelling and fracture of silicon nanowires during lithiation. *Nano Lett* 11(8):3312–3318. <https://doi.org/10.1021/nl201684d>
59. Liu XH, Huang JY (2011) In situ TEM electrochemistry of anode materials in lithium ion batteries. *Energy Environ Sci* 4(10):3844–3860. <https://doi.org/10.1039/c1ee01918j>
60. Liu XH, Liu Y, Kushima A, Zhang S, Zhu T, Li J, Huang JY (2012) In situ TEM experiments of electrochemical lithiation and delithiation of individual nanostructures. *Adv Energy Mater* 2(7):722–741. <https://doi.org/10.1002/aenm.201200024>
61. Harks PPRML, Mulder FM, Notten PHL (2015) In situ methods for Li-ion battery research: a review of recent developments. *J Power Sources* 288:92–105. <https://doi.org/10.1016/j.jpowsour.2015.04.084>

62. Wu F, Yao N (2015) Advances in sealed liquid cells for in-situ TEM electrochemical investigation of lithium-ion battery. *Nano Energy* 11:196–210. <https://doi.org/10.1016/j.nanoen.2014.11.004>
63. Wang C-M (2015) In situ transmission electron microscopy and spectroscopy studies of rechargeable batteries under dynamic operating conditions: a retrospective and perspective view. *J Mater Res* 30(3):326–339. <https://doi.org/10.1557/jmr.2014.281>
64. Ma X, Luo W, Yan M, He L, Mai L (2016) In situ characterization of electrochemical processes in one dimensional nanomaterials for energy storages devices. *Nano Energy* 24:165–188. <https://doi.org/10.1016/j.nanoen.2016.03.023>
65. Yuan Y, Amine K, Lu J, Shahbazian-Yassar R (2017) Understanding materials challenges for rechargeable ion batteries with in situ transmission electron microscopy. *Nat Commun* 8(1):15806. <https://doi.org/10.1038/ncomms15806>
66. Lu J, Wu T, Amine K (2017) State-of-the-art characterization techniques for advanced lithium-ion batteries. *Nat Energy* 2(3):17011. <https://doi.org/10.1038/nenergy.2017.11>
67. Xie Z-H, Jiang Z, Zhang X (2017) Review—promises and challenges of in situ transmission electron microscopy electrochemical techniques in the studies of lithium ion batteries. *J Electrochem Soc* 164(9):A2110–A2123. <https://doi.org/10.1149/2.1451709jes>
68. Pan Y, Lin R, Chen Y, Liu S, Zhu W, Cao X, Chen W, Wu K, Cheong W-C, Wang Y, Zheng L, Luo J, Lin Y, Liu Y, Liu C, Li J, Lu Q, Chen X, Wang D, Peng Q, Chen C, Li Y (2018) Design of single-atom Co–N₅ catalytic site: a robust electrocatalyst for CO₂ reduction with nearly 100% CO selectivity and remarkable stability. *J Am Chem Soc* 140(12):4218–4221. <https://doi.org/10.1021/jacs.8b00814>
69. Fan Z, Zhang L, Baumann D, Mei L, Yao Y, Duan X, Shi Y, Huang J, Huang Y, Duan X (2019) In situ transmission electron microscopy for energy materials and devices. *Adv Mater* 31(33):1900608. <https://doi.org/10.1002/adma.201900608>
70. Cheng Y, Zhang L, Zhang Q, Li J, Tang Y, Delmas C, Zhu T, Winter M, Wang M-S, Huang J (2021) Understanding all solid-state lithium batteries through in situ transmission electron microscopy. *Mater Today* 42:137–161. <https://doi.org/10.1016/j.mattod.2020.09.003>
71. Galiński M, Lewandowski A, Stępniański I (2006) Ionic liquids as electrolytes. *Electrochim Acta* 51(26):5567–5580. <https://doi.org/10.1016/j.electacta.2006.03.016>
72. Huang JY, Lo Y-C, Niu JJ, Kushima A, Qian X, Zhong L, Mao SX, Li J (2013) Nanowire liquid pumps. *Nat Nanotechnol* 8(4):277–281. <https://doi.org/10.1038/nnano.2013.41>
73. MacFarlane DR, Meakin P, Sun J, Amini N, Forsyth M (1999) Pyrrolidinium imides: a new family of molten salts and conductive plastic crystal phases. *J Phys Chem B* 103(20):4164–4170. <https://doi.org/10.1021/jp984145s>
74. Chiang Y-M (2010) Building a better battery. *Science* 330(6010):1485–1486. <https://doi.org/10.1126/science.1198591>
75. Song T, Xia J, Lee J-H, Lee DH, Kwon M-S, Choi J-M, Wu J, Doo SK, Chang H, Park WI, Zang DS, Kim H, Huang Y, Hwang K-C, Rogers JA, Paik U (2010) Arrays of sealed silicon nanotubes as anodes for lithium ion batteries. *Nano Lett* 10(5):1710–1716. <https://doi.org/10.1021/nl100086e>
76. Zhong L, Liu XH, Wang GF, Mao SX, Huang JY (2011) Multiple-stripe lithiation mechanism of individual SnO₂ nanowires in a flooding geometry. *Phys Rev Lett* 106(24):248302. <https://doi.org/10.1103/PhysRevLett.106.248302>
77. Wang Z, Tang Y, Fu X, Wang J, Peng Z, Zhang L, Huang J (2020) In situ imaging polysulfides electrochemistry of Li-S batteries in a hollow carbon nanotubule wet electrochemical cell. *ACS Appl Mater Interfaces* 12(50):55971–55981. <https://doi.org/10.1021/acsami.0c17058>
78. Strange JH, Rageb SM, Chadwick AV, Flack KW, Harding JH (1990) Conductivity and NMR study of ionic mobility in lithium oxide. *J Chem Soc Faraday Trans* 86(8):1239–1241. <https://doi.org/10.1039/ft9908601239>
79. Kasavajjula U, Wang C, Appleby AJ (2007) Nano- and bulk-silicon-based insertion anodes for lithium-ion secondary cells. *J Power Sources* 163(2):1003–1039. <https://doi.org/10.1016/j.jpowsour.2006.09.084>

80. Obrovac MN, Christensen L (2004) Structural changes in silicon anodes during lithium insertion/extraction. *Electrochem Solid-State Lett* 7(5):A93. <https://doi.org/10.1149/1.1652421>
81. Obrovac MN, Krause LJ (2007) Reversible cycling of crystalline silicon powder. *J Electrochem Soc* 154(2):A103. <https://doi.org/10.1149/1.2402112>
82. Liu XH, Zhang LQ, Zhong L, Liu Y, Zheng H, Wang JW, Cho J-H, Dayeh SA, Picraux ST, Sullivan JP, Mao SX, Ye ZZ, Huang JY (2011) Ultrafast electrochemical lithiation of individual Si nanowire anodes. *Nano Lett* 11(6):2251–2258. <https://doi.org/10.1021/nl200412p>
83. Beaulieu LY, Eberman KW, Turner RL, Krause LJ, Dahn JR (2001) Colossal reversible volume changes in lithium alloys. *Electrochem Solid-State Lett* 4(9):A137. <https://doi.org/10.1149/1.1388178>
84. Beaulieu LY, Hatchard TD, Bonakdarpour A, Fleischauer MD, Dahn JR (2003) Reaction of Li with alloy thin films studied by in situ AFM. *J Electrochem Soc* 150(11):A1457. <https://doi.org/10.1149/1.1613668>
85. Hertzberg B, Alexeev A, Yushin G (2010) Deformations in Si–Li anodes upon electrochemical alloying in nano-confined space. *J Am Chem Soc* 132(25):8548–8549. <https://doi.org/10.1021/ja1031997>
86. Graetz J, Ahn CC, Yazami R, Fultz B (2003) Highly reversible lithium storage in nanostructured silicon. *Electrochem Solid-State Lett* 6(9):A194. <https://doi.org/10.1149/1.1596917>
87. Liu XH, Zhong L, Huang S, Mao SX, Zhu T, Huang JY (2012) Size-dependent fracture of silicon nanoparticles during lithiation. *ACS Nano* 6(2):1522–1531. <https://doi.org/10.1021/nn204476h>
88. Liu XH, Wang JW, Huang S, Fan F, Huang X, Liu Y, Krylyuk S, Yoo J, Dayeh SA, Davydov AV, Mao SX, Picraux ST, Zhang S, Li J, Zhu T, Huang JY (2012) In situ atomic-scale imaging of electrochemical lithiation in silicon. *Nat Nanotechnol* 7(11):749–756. <https://doi.org/10.1038/nnano.2012.170>
89. Wang F, Yu H-C, Chen M-H, Wu L, Pereira N, Thornton K, Van der Ven A, Zhu Y, Amatuucci GG, Graetz J (2012) Tracking lithium transport and electrochemical reactions in nanoparticles. *Nat Commun* 3(1):1201. <https://doi.org/10.1038/ncomms2185>
90. Yamamoto K, Iriyama Y, Asaka T, Hirayama T, Fujita H, Fisher CAJ, Nonaka K, Sugita Y, Ogumi Z (2010) Dynamic visualization of the electric potential in an all-solid-state rechargeable lithium battery. *Angew Chem Int Ed* 49(26):4414–4417. <https://doi.org/10.1002/anie.200907319>
91. Gong Y, Zhang J, Jiang L, Shi J-A, Zhang Q, Yang Z, Zou D, Wang J, Yu X, Xiao R, Hu Y-S, Gu L, Li H, Chen L (2017) In situ atomic-scale observation of electrochemical delithiation induced structure evolution of LiCoO₂ cathode in a working all-solid-state battery. *J Am Chem Soc* 139(12):4274–4277. <https://doi.org/10.1021/jacs.6b13344>
92. Gong Y, Chen Y, Zhang Q, Meng F, Shi J-A, Liu X, Liu X, Zhang J, Wang H, Wang J, Yu Q, Zhang Z, Xu Q, Xiao R, Hu Y-S, Gu L, Li H, Huang X, Chen L (2018) Three-dimensional atomic-scale observation of structural evolution of cathode material in a working all-solid-state battery. *Nat Commun* 9(1):3341. <https://doi.org/10.1038/s41467-018-05833-x>
93. Xu W, Wang J, Ding F, Chen X, Nasybulin E, Zhang Y, Zhang J-G (2014) Lithium metal anodes for rechargeable batteries. *Energy Environ Sci* 7(2):513–537. <https://doi.org/10.1039/c3ee40795k>
94. Kushima A, So KP, Su C, Bai P, Kuriyama N, Maebashi T, Fujiwara Y, Bazant MZ, Li J (2017) Liquid cell transmission electron microscopy observation of lithium metal growth and dissolution: root growth, dead lithium and lithium flotsams. *Nano Energy* 32:271–279. <https://doi.org/10.1016/j.nanoen.2016.12.001>
95. Lin D, Liu Y, Cui Y (2017) Reviving the lithium metal anode for high-energy batteries. *Nat Nanotechnol* 12(3):194–206. <https://doi.org/10.1038/nnano.2017.16>
96. Guo Y, Li H, Zhai T (2017) Reviving lithium-metal anodes for next-generation high-energy batteries. *Adv Mater* 29(29):1700007. <https://doi.org/10.1002/adma.201700007>

97. Wang X, Zeng W, Hong L, Xu W, Yang H, Wang F, Duan H, Tang M, Jiang H (2018) Stress-driven lithium dendrite growth mechanism and dendrite mitigation by electroplating on soft substrates. *Nat Energy* 3(3):227–235. <https://doi.org/10.1038/s41560-018-0104-5>
98. Li L, Basu S, Wang Y, Chen Z, Hundekar P, Wang B, Shi J, Shi Y, Narayanan S, Koratkar N (2018) Self-heating-induced healing of lithium dendrites. *Science* 359(6383):1513–1516. <https://doi.org/10.1126/science.aap8787>
99. Liu Y, Liu Q, Xin L, Liu Y, Yang F, Stach EA, Xie J (2017) Making Li-metal electrodes rechargeable by controlling the dendrite growth direction. *Nat Energy* 2(7):17083. <https://doi.org/10.1038/nenergy.2017.83>
100. Monroe C, Newman J (2005) The impact of elastic deformation on deposition kinetics at lithium/polymer interfaces. *J Electrochem Soc* 152(2):A396. <https://doi.org/10.1149/1.1850854>
101. Ren Y, Shen Y, Lin Y, Nan C-W (2015) Direct observation of lithium dendrites inside garnet-type lithium-ion solid electrolyte. *Electrochem Commun* 57:27–30. <https://doi.org/10.1016/j.elecom.2015.05.001>
102. Suzuki Y, Kami K, Watanabe K, Watanabe A, Saito N, Ohnishi T, Takada K, Sudo R, Imanishi N (2015) Transparent cubic garnet-type solid electrolyte of Al₂O₃-doped Li₇La₃Zr₂O₁₂. *Solid State Ionics* 278:172–176. <https://doi.org/10.1016/j.ssi.2015.06.009>
103. Zhang L, Yang T, Du C, Liu Q, Tang Y, Zhao J, Wang B, Chen T, Sun Y, Jia P, Li H, Geng L, Chen J, Ye H, Wang Z, Li Y, Sun H, Li X, Dai Q, Tang Y, Peng Q, Shen T, Zhang S, Zhu T, Huang J (2020) Lithium whisker growth and stress generation in an in situ atomic force microscope–environmental transmission electron microscope set-up. *Nat Nanotechnol* 15(2):94–98. <https://doi.org/10.1038/s41565-019-0604-x>
104. Xu C, Ahmad Z, Aryanfar A, Viswanathan V, Greer JR (2017) Enhanced strength and temperature dependence of mechanical properties of Li at small scales and its implications for Li metal anodes. *Proc Natl Acad Sci* 114(1):57. <https://doi.org/10.1073/pnas.1615733114>
105. Liu Q, Zhang L, Sun H, Geng L, Li Y, Tang Y, Jia P, Wang Z, Dai Q, Shen T, Tang Y, Zhu T, Huang J (2020) In situ observation of sodium dendrite growth and concurrent mechanical property measurements using an environmental transmission electron microscopy-atomic force microscopy (ETEM-AFM) platform. *ACS Energy Lett* 5(8):2546–2559. <https://doi.org/10.1021/acsenerylett.0c01214>
106. Liu Q, Geng L, Yang T, Tang Y, Jia P, Li Y, Li H, Shen T, Zhang L, Huang J (2019) In-situ imaging electrocatalysis in a Na-O₂ battery with Au-coated MnO₂ nanowires air cathode. *Energy Storage Mater* 19:48–55. <https://doi.org/10.1016/j.ensm.2018.08.026>
107. Jonge Nd, Peckys DB, Kremers GJ, Piston DW (2009) Electron microscopy of whole cells in liquid with nanometer resolution. *Proc Natl Acad Sci* 106(7):2159. <https://doi.org/10.1073/pnas.0809567106>
108. Sullivan JP, Huang J, Shaw MJ, Subramanian A, Hudak N, Zhan Y, Lou J (2010) Understanding Li-ion battery processes at the atomic- to nano-scale. In: *Proceedings of SPIE*. <https://doi.org/10.1117/12.849530>
109. Zheng H, Smith Rachel K, Jun Y-W, Kisielowski C, Dahmen U, Alivisatos AP (2009) Observation of single colloidal platinum nanocrystal growth trajectories. *Science* 324(5932):1309–1312. <https://doi.org/10.1126/science.1172104>
110. Ross FM (2000) Growth processes and phase transformations studied in situ transmission electron microscopy. *IBM J Res Dev* 44(4):489–501. <https://doi.org/10.1147/rd.444.0489>
111. Thiberge S, Nechushtan A, Sprinzak D, Gileadi O, Behar V, Zik O, Chowers Y, Michaeli S, Schlessinger J, Moses E (2004) Scanning electron microscopy of cells and tissues under fully hydrated conditions. *Proc Natl Acad Sci USA* 101(10):3346. <https://doi.org/10.1073/pnas.0400088101>
112. Liu K-L, Wu C-C, Huang Y-J, Peng H-L, Chang H-Y, Chang P, Hsu L, Yew T-R (2008) Novel microchip for in situ TEM imaging of living organisms and bio-reactions in aqueous conditions. *Lab Chip* 8(11):1915–1921. <https://doi.org/10.1039/b804986f>
113. Williamson MJ, Tromp RM, Vereecken PM, Hull R, Ross FM (2003) Dynamic microscopy of nanoscale cluster growth at the solid–liquid interface. *Nat Mater* 2(8):532–536. <https://doi.org/10.1038/nmat944>

114. Zeng Z, Liang W-I, Liao H-G, Xin HL, Chu Y-H, Zheng H (2014) Visualization of electrode-electrolyte interfaces in LiPF₆/EC/DEC electrolyte for lithium ion batteries via in situ TEM. *Nano Lett* 14(4):1745–1750. <https://doi.org/10.1021/nl403922u>
115. Gu M, Parent LR, Mehdi BL, Unocic RR, McDowell MT, Sacci RL, Xu W, Connell JG, Xu P, Abellan P, Chen X, Zhang Y, Perea DE, Evans JE, Lauhon LJ, Zhang J-G, Liu J, Browning ND, Cui Y, Arslan I, Wang C-M (2013) Demonstration of an electrochemical liquid cell for operando transmission electron microscopy observation of the lithiation/delithiation behavior of Si nanowire battery anodes. *Nano Lett* 13(12):6106–6112. <https://doi.org/10.1021/nl403402q>
116. White ER, Singer SB, Augustyn V, Hubbard WA, Mecklenburg M, Dunn B, Regan BC (2012) In situ transmission electron microscopy of lead dendrites and lead ions in aqueous solution. *ACS Nano* 6(7):6308–6317. <https://doi.org/10.1021/nm3017469>
117. Mehdi BL, Qian J, Nasybulin E, Park C, Welch DA, Faller R, Mehta H, Henderson WA, Xu W, Wang CM, Evans JE, Liu J, Zhang JG, Mueller KT, Browning ND (2015) Observation and quantification of nanoscale processes in lithium batteries by operando electrochemical (S)TEM. *Nano Lett* 15(3):2168–2173. <https://doi.org/10.1021/acs.nanolett.5b00175>
118. Liu XH, Zhong L, Zhang LQ, Kushima A, Mao SX, Li J, Ye ZZ, Sullivan JP, Huang JY (2011) Lithium fiber growth on the anode in a nanowire lithium ion battery during charging. *Appl Phys Lett* 98(18):183107. <https://doi.org/10.1063/1.3585655>
119. Ghassemi H, Au M, Chen N, Heiden PA, Yassar RS (2011) Real-time observation of lithium fibers growth inside a nanoscale lithium-ion battery. *Appl Phys Lett* 99(12):123113. <https://doi.org/10.1063/1.3643035>
120. Foroozan T, Sharifi-Asl S, Shahbazian-Yassar R (2020) Mechanistic understanding of li dendrites growth by in-situ/operando imaging techniques. *J Power Sources* 461:228135. <https://doi.org/10.1016/j.jpowsour.2020.228135>
121. Leenheer AJ, Jungjohann KL, Zavadil KR, Sullivan JP, Harris CT (2015) Lithium electrodeposition dynamics in aprotic electrolyte observed in situ via transmission electron microscopy. *ACS Nano* 9(4):4379–4389. <https://doi.org/10.1021/acs.nano.5b00876>

Chapter 6

In-Situ Optical TEM



Peng Wang, Feng Xu, Peng Gao, Songhua Cai, and Xuedong Bai

6.1 Introduction

Nanomaterials and devices with diverse response mechanisms to light, including photocatalytic, photoemissive, photoconductive, and photovoltaic effects at the atomic or molecular level, have attracted special attention in recent years [1, 2]. These functional materials play an irreplaceable role in several key fields including pollution disposal [3], clean energy [4], and optoelectronic devices [5].

Transmission electron microscopy (TEM) is one of the most powerful characterization tools for studying nanostructures. In recent decades, the rapid development of aberration correctors has made it possible for conventional TEM to characterize the structure, composition, and spectroscopy of samples at the subatomic scale [6, 7], so as to better understand the principle of material performance, which greatly

P. Wang (✉)

National Laboratory of Solid State Microstructures, Jiangsu Key Laboratory of Artificial Functional Materials, College of Engineering and Applied Sciences and Collaborative Innovation Center of Advanced Microstructures, Nanjing University, Nanjing 210093, China
e-mail: wangpeng@nju.edu.cn

F. Xu

SEU-FEI Nano-Pico Center, Key Laboratory of MEMS of Ministry of Education, Southeast University, Nanjing 210096, China

P. Gao

International Center for Quantum Materials, and Electron Microscopy Laboratory, School of Physics, Peking University, Beijing 100871, China

S. Cai

Department of Applied Physics, The Hong Kong Polytechnic University, Hung Hom, Kowloon, Hong Kong 999077, China

X. Bai

Beijing National Laboratory for Condensed Matter Physics, Institute of Physics, Chinese Academy of Sciences, Beijing 100190, China

promotes the development of nanomaterials [8–11] and devices [12–15]. However, this characterization only observes the static states of materials, that is, obtaining *ex situ* information. With the rising experimental requirements of advanced optical functional materials and devices, it is of great importance to introduce illumination into the TEM to realize *in situ* measurements for the determination of correlations between optical properties and microstructures [16].

Due to the confined geometry inside the TEM chamber, early research usually introduced the light stimuli generated by the external light source into the microscope through light-paths composed of optical fibers and mirrors. The first reported *in situ* illumination TEM experiment was carried out over three decades ago by K. Suzuki et al. [17]. They managed to insert an optical fiber into the specimen chamber and studied the dislocation motion in IIB-VIB compounds with direct illumination. From then on, several groups upgraded the TEM column for modification. Y. Ohno et al. designed an opto-TEM system by fixing mirrors and optical fibers into the JEOL JEM 2000-EX microscope to obtain TEM data, photoluminescence (PL), and cathodoluminescence (CL) spectra simultaneously [18–21]. M. Picher et al. replaced the objective aperture holder with a rod-mirror assembly to deliver the laser and collect CL and Raman spectroscopic signals [22]. B. K. Miller et al. developed an optical fiber system for *in situ* ultraviolet (UV)-visible illumination to study nanostructured photocatalysts [23]. Apart from direct modifications to the TEM column, customizing versatile TEM holders are also considered low risk, easy ways to introduce light-paths into the TEM. Tanabe et al. developed a new type of TEM holder for collecting CL light [24]. D. Shindo et al. developed an opto-TEM holder with a laser irradiation port combined with a piezo-driven probe [25]. F. Cavalca et al. developed both a lens-based and a fiber-based opto-TEM holder [26]. Gatan Inc. eventually developed this method into the commercial Gatan sample holders.

The major advantage of introducing external light stimulus through the light-path is broadband and reversibility. A light-path can introduce illumination from several external light sources and collect optical signals emitted from the sample simultaneously, which enables the detection of PL, CL, and other spectra. Besides, lenses in a light-path have high power transmission efficiency, as well as the capability of focusing light to produce a tiny probe with high intensity [26].

Although the introduction of *in situ* illumination can be achieved by the light-path method, the complex optical connection, and large-scale modifications of TEM and holders may lead to a decrease in reliability and general use. In addition, it is difficult to carry out a joint test of various *in situ* methods, such as electrical and mechanical, in the micro-region of the sample due to the occupation of the space by the light-path components. This problem can be solved by the method based on TEM-STM holders. P. Gao et al. first employed a light-emitting diode (LED) chip inside the *in situ* TEM-STM holder to determine the photoconducting response on the bending of ZnO nanowires [27]. The same setup was then used by S. Yang et al. to study the coupling of the piezoelectric effect and the electrical, optoelectronic, and electromechanical properties of ZnO nanowires [28]. Later, H. Dong et al. upgraded their setup with simultaneous picoampere precision and high stability for atomic resolution imaging [29]. They managed to build a single nanowire quantum dot

heterojunction solar cell (QDHSC) on the holder and achieve a nearly ideal quantum efficiency via precise interfacial tuning [30].

While the TEM-scanning tunneling microscope (STM) holder provides a superior platform for multi-functional in situ micro-area testing, the stability and miniaturization of modification can be further improved by the solution based on in situ microelectromechanical system (MEMS) chips. Due to the recent development of MEMS technology, increasing functional devices can be integrated into a micro-chip to build a lab-on-chip, which makes it a hot spot to apply in situ MEMS chips instead of traditional devices for in situ research [31–33]. Under the reference of mature and widely used commercial products, S. Cai et al. provided a practicable method to realize in situ optoelectrical experiments by designing a MEMS chip with a LED mounted on it [34]. Unlike traditional large size light sources such as lamps and lasers, LEDs with smaller sizes are appropriate for in situ illumination in the front of the TEM holders, thus minimizing modifications to the in situ TEM holders.

These different technical solutions all have preponderant applications in specific material systems and research interests. For the best experimental results, a careful selection of techniques and facilities is important. Different from some existing reviews of in situ optical fields [35], in order to let readers better understand the implementation details and application fields of different technical routes, in the next session, we will first describe the implementation details of the three major technical routes in detail. In the third section, we will describe three typical application fields of photocatalysis, PL/CL, and photocurrent according to different application fields. Finally, we will look into the future of in situ opto-TEM technology in the fourth section.

6.2 Three Typical Technical Routes for in Situ Optical Experimental Setups

6.2.1 *Based on Light-Path*

Techniques based on mirrors and/or fibers inside a TEM chamber for illumination and detection are summarized below. Mirrors fixed inside a TEM chamber can be used to collect and focus the emitted light from the specimen. With the combination of optical fibers, mirrors, and optical lens, the light-path designed for meeting specific research demands can be achieved with a broadband of light sources and reversible path.

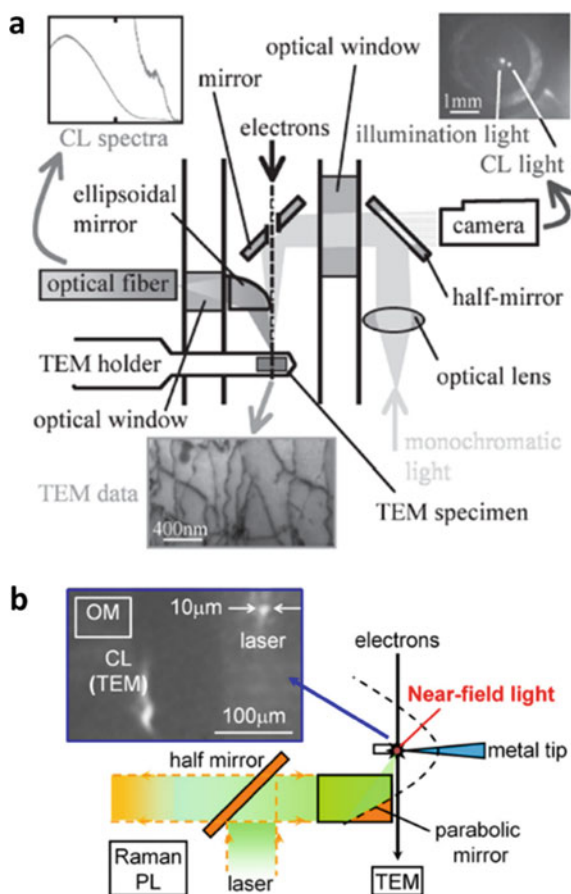
Methods

The in situ opto-TEM observation apparatus developed by Y. Ohno et al. combined mirrors and an optical lens to introduce a monochromatic light onto the specimen in the TEM [19]. As shown in Fig. 6.1a, the monochromatic light beam was first collimated by an optical lens outside the TEM. Then, the light beam was reflected by

a half mirror and introduced into the TEM through an optical window attached on the side of the TEM column. It was reflected to the sample by a reflection mirror in the column, which was located above the objective lens and on the axis of an electron beam. The reflection mirror just below the electron source had a small opening to pass through the electron beam. The horizontal displacement of the optical lens would change the position of the light spot on the specimen surface, which is on the order of $100\ \mu\text{m}$ diameter. For collecting luminescent light from the sample, an ellipsoidal mirror was inserted inside the gap of the pole pieces of the objective lens to focus the emitted PL and CL light to an optical fiber. The optical fiber then transmits the light into a monochromator.

Y. Ohno et al. further improved the system to reach a smaller sized light probe with a near-field light (shown in Fig. 6.1b) [21]. In this apparatus, the laser beam from an optical fiber was first paralleled with the optical lens and then introduced into the microscope by a half mirror. The introduced light was parallel to the revolution axis of the parabolic mirror and could be converged on the focus of it. Most of the

Fig. 6.1 Schematic view of an in situ opto-TEM apparatus for **a** illumination, and **b** micro- and near-field photo-excitation. An image of the CL signal and a laser spot is shown in the inset of **b** (a Reproduced with permission from Ref. [19], Copyright 2009, John Wiley and Sons; b reproduced with permission from Ref. [21], Copyright 2014, Elsevier)

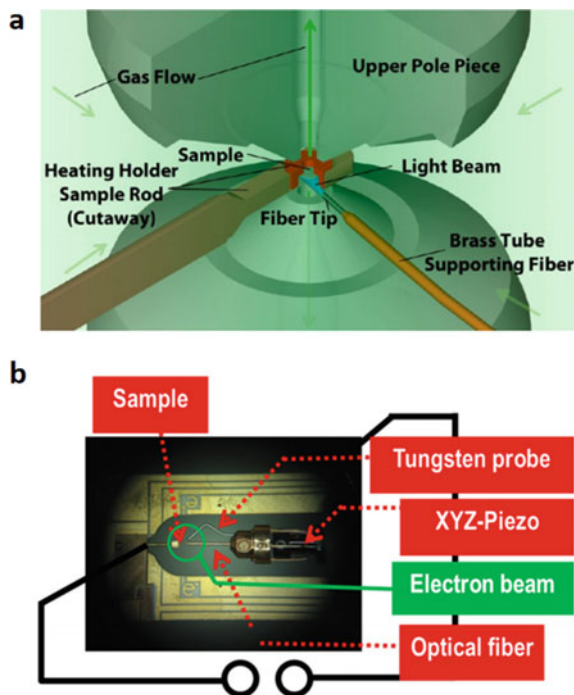


laser light was transmitted to the focus, forming an intense far-field light probe of $10\ \mu\text{m}$ in diameter. A $514.5\ \text{nm}$ laser light was used to illuminate the tip and the power density was on the order of $2 \times 10^3\ \text{W/m}^2$. A tungsten tip was then fixed close to the specimen for the purpose of the near-field light. Due to the tip-enhanced effect, a near-field light was induced adjacent to the tip. In this case, the path of the emitted light was identical to that of the introduced light.

The apparatus improved by Y. Ohno et al. could achieve a smaller beam spot and near-field light excitation. Nevertheless, the achievable functions by these means are still relatively limited. To realize the characterization of multiple materials and phenomena, P. Crozier et al. designed an opto-environmental transmission electron microscope (ETEM) setup for UV–visible illumination of specimens in photocatalytic experiments (Fig. 6.2a) [36]. The optical fiber fixed inside a brass tube could provide light illumination, and the fiber tip could lead the light onto the specimen. Besides, a piezo-driven optical holder which contains a multimode fiber to provide illumination could attain greater flexibility and microzone illumination (Fig. 6.2b) [37]. On this basis, Gatan developed commercial sample holders with more functions by combining fibers and mirrors into holders.

Figure 6.3a shows a Gatan Vulcan™ CL detector which consists of a sample holder with the sample elliptical aluminium mirrors that are positioned above and below the specimen. The emitted light could be converged by the collecting mirrors into the optical fibers and then directed into the detector [38]. Although the light signal

Fig. 6.2 Schematic view of **a** an opto-ETEM apparatus (reproduced with permission from Ref. [36], Copyright 2013, American Chemical Society) and **b** a piezo-driven optical holder (reproduced with permission from Ref. [37], Copyright 2015, IOP Publishing)



emitted from the specimen under illumination could be gathered from anywhere as a result of the fixation of collecting mirrors above and below the specimen, the most efficient region for collection is the focal point with a size of $\sim 100 \mu\text{m}^2$ of the collecting mirrors. The range of dispersion of this Gatan Vulcan™ CL detector is from 5 to 30 meV. Figure 6.3b shows a cryo-CL holder in ETEM designed by M. Vadai et al. and Gatan, Inc. [39]. The parabolic mirrors are able to focus the light and the electron beam can pass the wide aperture with $500 \mu\text{m}$ in diameter of the adjacent mirrors above the sample. The temperature could be precisely controlled with an error of ± 0.1 K. Compared to the modifications to the TEM chamber, the holder integrated with mirrors and fibers is more flexible, adaptable, positionally accurate, and sharable for different TEMs.

Functions

The functions based on the method of light-path are broadband light and reversibility of the optical path.

First, optical fibers, as a kind of flexible light source, can provide control of light illumination through connecting to laser diodes with different wavelengths of light, which is a distinct advantage in contrast to the light source with a single wavelength (Fig. 6.4a) [37].

Secondly, for the method developed by Y. Ohno et al., the laser light from an optical fiber was directed into the TEM column by a half mirror. Then, PL, CL, and Raman signals generated by the laser beam could be gathered by the parabolic mirror. Via the same light-path, these emitted lights were collimated into parallel lights, exported into a 140 mm spectrometer, and finally collected by a CCD detector (Fig. 6.4b) [20]. Thus, the path of introduced light is the same as that of emitted light. By means of this method, the optical spectra data and the TEM data could be obtained simultaneously, and the optical properties of an extended defect could be analyzed with a typical spatial resolution of about 200 nm and a spectral resolution about 1 meV in the spectral range of 1.9–3.3 eV [19]. Besides, the modified in situ opto-TEM observation apparatus is applicable for in situ photo-excitation measurements (Fig. 6.5) [21]. Far-field collimated light transmitted into the TEM can form an

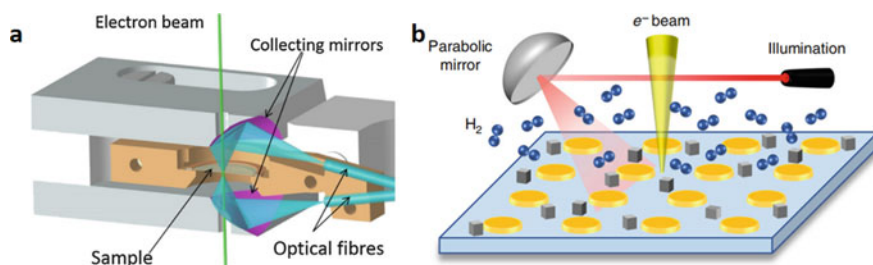


Fig. 6.3 The schematic view of **a** a Gatan Vulcan™ CL detector (reproduced with permission from Ref. [38], Copyright 2017, Elsevier) and **b** a cryo-CL holder in ETEM (reproduced with permission from Ref. [39], Copyright 2018, Springer Nature)

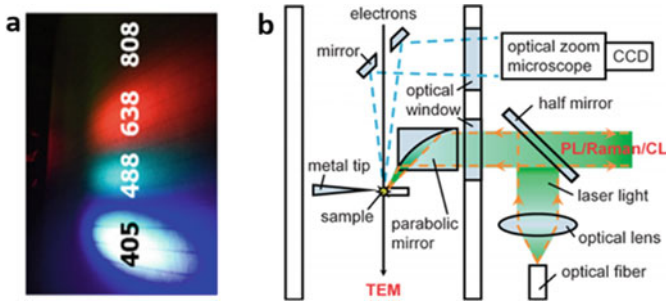
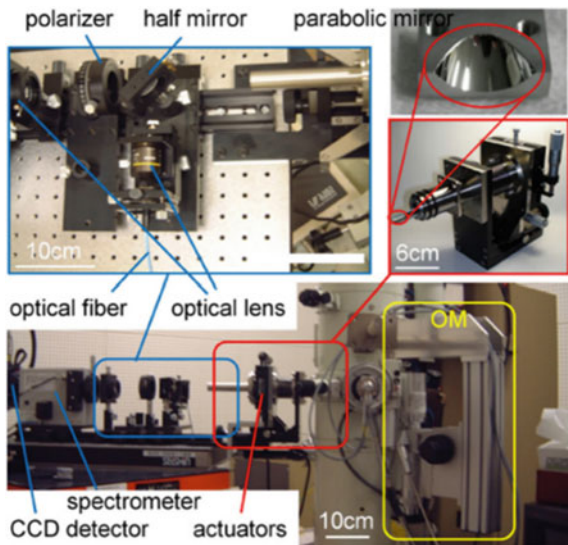


Fig. 6.4 The schematic view of **a** optical fibers connected to different laser diodes (reproduced with permission from Ref. [37], Copyright 2015, IOP Publishing) and **b** an in situ opto-TEM apparatus (reproduced with permission from Ref. [20], Copyright 2012, The Japan Society of Applied Physics)

intense light probe of 10 μm in diameter, which induces an intense near-field light adjacent to the metal tip apex.

Meanwhile, light illumination and optical detection could be achieved by inserting optical fibers into a sample holder. The Gatan CL holder, which was developed by this method, could achieve CL detection for STEM samples. The mirrors around the sample can collect the emitted light signal, which was simultaneously induced by the electron beam [38], and achieve a reversible light-path. Also, the emitted light signal from the specimen could be collected from anywhere in the sample disk, and thus highly efficient collection could be accomplished.

Fig. 6.5 An external view of an in situ opto-TEM apparatus for micro- and near-field photo-excitation (reproduced with permission from Ref. [21], Copyright 2014, Elsevier)



6.2.2 Based on the TEM-STM Holder

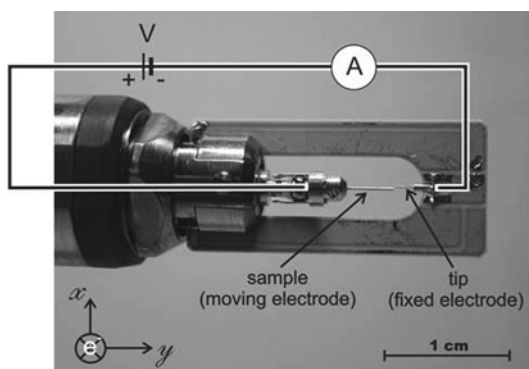
As shown in Sect. 6.2.1, the techniques based on mirrors and/or fibers inside a TEM chamber for illumination and detection have an obvious limitation on the capabilities of in situ electrical and mechanical TEM observation. However, the high-performance TEM-STM sample holder is shown in Fig. 6.6, which allows the direct visualization of the operation of nanoscale devices mounted on it, and can be employed to elucidate the charge transfer and microstructural evolution during the operation of lithium-ion batteries [40] and resistive memories [41, 42] and study the liquid-like deformation mechanism of sub-10-nm crystalline silver particles [43]. As electronic packaging technology develops, the common surface-mounted LED is nearly $3 \times 1.5 \times 0.5$ mm in size. Besides, TEM-STM holders have electrodes with moderate distances fabricated on the sample side, which can provide voltage for LED lighting. Furthermore, considering that the piezo-part takes up most of the space in TEM-STM holders brings complexities on methods of using lens and fibers, thus using LEDs as light sources has more simplicity and better air tightness for no reformation on the TEM. By combining the LEDs with the TEM-STM holders, in situ optoelectrical studies of these energy devices can offer valuable insights on the fundamental understanding of the critical factors for further enhancing device performances.

Methods

P. Gao et al. reported electrical transport coupled with optical and piezoelectric properties of individual ZnO nanowires by introducing ultraviolet illumination during TEM imaging, which can be recognized as a typical case of combining LED with TEM-STM holder [27]. The experimental setup is designed as schematically shown in Fig. 6.7.

Based on that, H. Dong et al. developed an in situ photoelectric system shown in Fig. 6.8, which combines a custom-designed photoelectric TEM holder reformed on a commercially available Nanofactory TEM-STM holder with an external electric measurement system [29, 30]. As shown, the homemade in situ photoelectric setup

Fig. 6.6 Schematic diagram of one kind of TEM-STM sample holder (reproduced with permission from Ref. [44], Copyright 2007, Springer Nature)



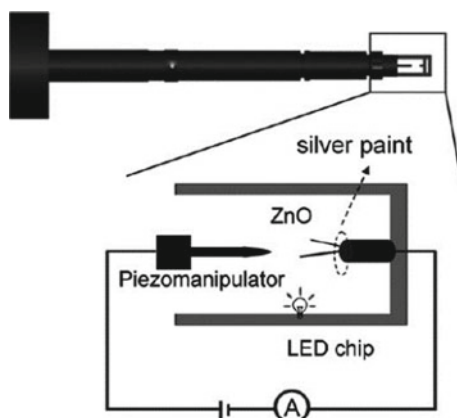


Fig. 6.7 Setup for in situ TEM photoelectric measurements (reproduced with permission from Ref. [27], Copyright 2009, Royal Society of Chemistry)

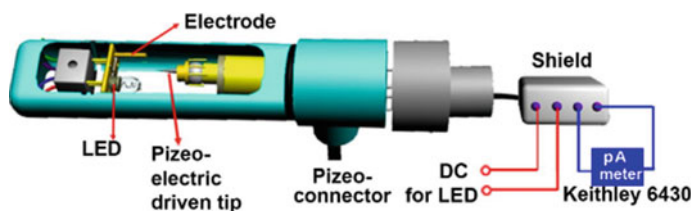


Fig. 6.8 Schematic diagram of the in-house-designed photoelectric sample holder (reproduced with permission from Ref. [29], Copyright 2018, Royal Society of Chemistry)

replaces the original electrical measuring system, which was previously inserted into the slot of the TEM-STM holder. Besides, the shielding system connected with a picoampere meter is designed to measure ultra-small currents.

Sapphire (Al_2O_3) was selected as the substrate and serves as a support for both the LED and electrode. Due to its high resistivity ($>10^{11} \Omega\cdot\text{cm}$), the sapphire support can reduce current interference during imaging. The preparation procedure of the photoelectric measurement system is shown in Fig. 6.9. First, the sapphire substrate is cut into pieces of size $4.0 \times 2.4 \text{ mm}$. Small holes with diameter of 0.3 mm are then drilled to affix the Cu grid. Next, an appropriately sized shadow mask was placed on the sapphire substrate; after which, a gold film was deposited by planar magnetron sputtering to make the selected area conductive. Subsequently, the LED is placed on the substrate using conductive silver adhesives. Finally, the LED is activated to emit light using the indigenous power system.

By implanting different kinds of LEDs on the sapphire substrate, lights of different wavelengths can be emitted inside the TEM as Fig. 6.10 depicts. In addition, different LEDs can be simultaneously implanted on the holder and the intensity of the light

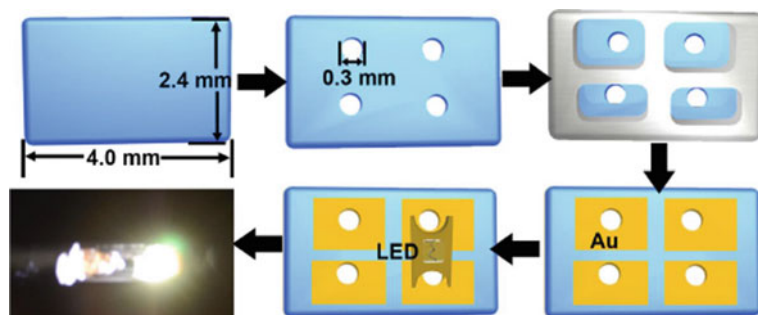


Fig. 6.9 Preparation of the photoelectric block and a photograph of the lighted LED emitting white light (reproduced with permission from Ref. [29], Copyright 2018, Royal Society of Chemistry)

can be controlled by adjusting the output voltage of the homemade power supply system (Fig. 6.11).

The quality of the TEM image was deteriorated when using the DC-regulated power supply or the battery, originates from the unstable output voltage. To circumvent this problem, a stable DC output voltage system was designed and composed

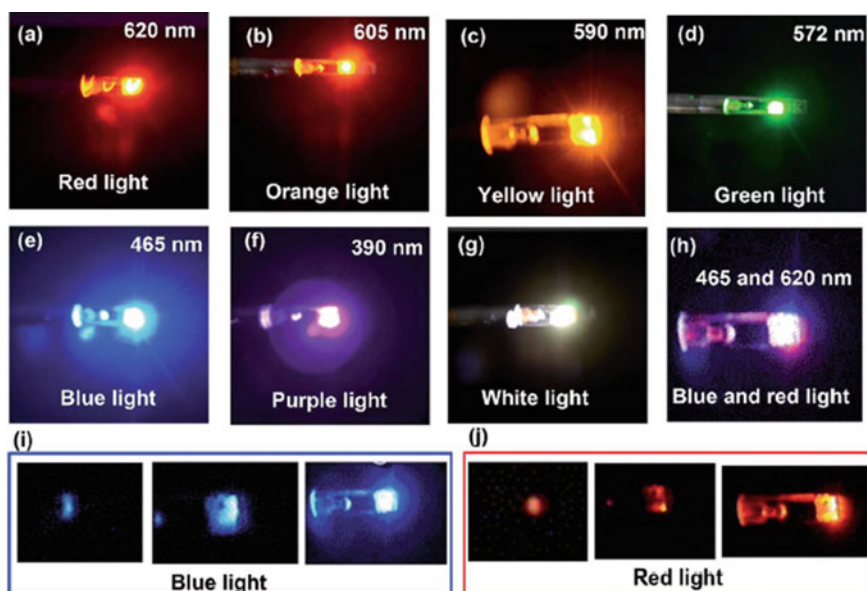
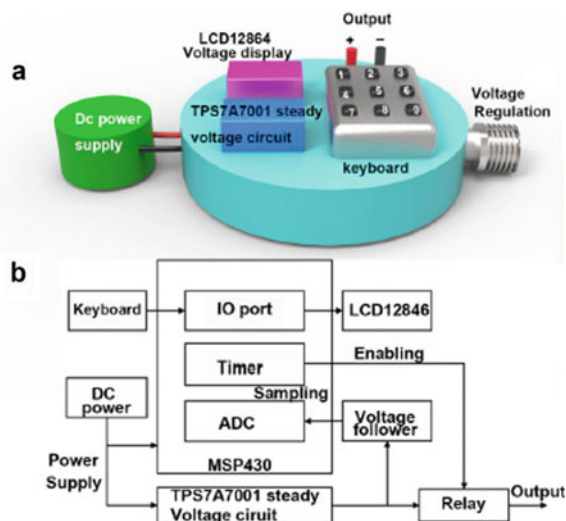


Fig. 6.10 Visible light emission of different wavelengths from LEDs implanted on the holder inside the TEM. **a–g** show red, orange, yellow, green, blue, purple, and white emissions, respectively. **h** Both red and blue light can be switched on simultaneously. The intensity adjustment of blue (**i**) and red light (**j**). (reproduced with permission from Ref. [29], Copyright 2018, Royal Society of Chemistry)

Fig. 6.11 **a** Schematic diagram of our power supply for the LED. The precision of the voltage controller can be increased to measure voltages of 0.01 V. **b** System layout diagram (reproduced with permission from Ref. [29], Copyright 2018, Royal Society of Chemistry)



of five parts: a commercial DC power supply that functioned as the power source, an ultra-low-dropout chip TPS7A7001 for steady voltage, a keyboard for voltage output time setting, an LCD12864 display module to display the voltage values, and a regulator to adjust the voltage as displayed in Fig. 6.11a. The working principle of this system is demonstrated in Fig. 6.11b. This design allows for an ultrahigh steady voltage output of a certain magnitude while converting commercial direct current into ultra-steady direct current output. Thus, high-resolution and stable TEM images at atomic level can be achieved when irradiated by light from the LED. Besides, it is worth noting that when LED being switched on and off, it would induce significant drift which would break the contact of tip onto the sample. Therefore, the actual operating procedures should follow the sequential steps: TEM imaging—LED on—waiting for stabilization—contact tip—close column valves—electrical measurement.

Functions

It is worth noting that by precisely controlling the movement of the Pt tip of the TEM-STM holder, the custom-designed photoelectric TEM holder can achieve in situ dynamic observation under multiple stimuli, such as stress and voltage load. In combination with the LED fixed on the TEM-STM holder, P. Gao et al. investigated the piezoelectric effects of ZnO nanowires under UV illumination [27]. As shown in Fig. 6.12, with increased bending of ZnO nanowire by applying stress, the photocurrent shows an obviously decreasing trend at a bias of 5 V. After turning off the LED, the photocurrent undergoes a decay time which shortens with increased bending [27]. This example clearly displays the typical functions of the photoelectric system.

The accuracy of a photocurrent measurement can be further improved when adding a designed shielding system in the circuit [27]. The detail of the shielding

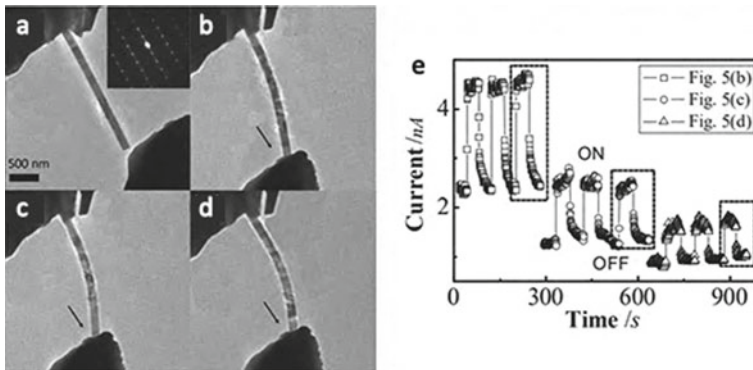


Fig. 6.12 **a** TEM image of the initial ZnO nanowire. **b–d** TEM images of bending ZnO nanowire. **e** Corresponding photocurrent and dark current and response of the ZnO nanowire for three different bending cases (reproduced with permission from Ref. [27], Copyright 2009, Royal Society of Chemistry)

system is shown in Fig. 6.13a. In the Keithley Model 6430 Sub-Femtoamp Remote SourceMeter, the triax connector includes a central conductor with a connector (High), an outer shell (Low) for electrical measurement, and an inner shell (Guard) of DC shielding to reduce noise in the measurement. In the DC shielding, the guard port is connected to the inner port to enable its potential as the same as the high port and prevent current leakage from the sample. External electrostatic shielding is to eliminate the influence of ambient electric and magnetic fields. As depicted in Fig. 6.13b, after multiple measurements and while the LED is being switched on and off, the shielding system can achieve a current test accuracy within 0.5 pA. Thus, the designed shielding system is suitable for measuring ultra-small current and providing a method for precise explaining the relationship between crystal structure and device performance.

6.2.3 Based on in Situ MEMS Chips

While the application of in situ TEM-STM holders provides an efficient method for in situ experiments, the mechanical contact between movable tips and samples often leads to stability reductions, which can hardly meet the requirements of high-resolution in situ characterization.

With the recent developments of MEMS technology, the combination of an in situ holder and specially functionalized MEMS chips has been recognized as a superior route for performing in situ investigations. The MEMS chip serves as a functional sample carrier that can provide localized physical or chemical stimuli for in situ measurements without modification of the TEM or holder. The functional devices on the chips are micro- or even nanoscale, which can be directly set at the position

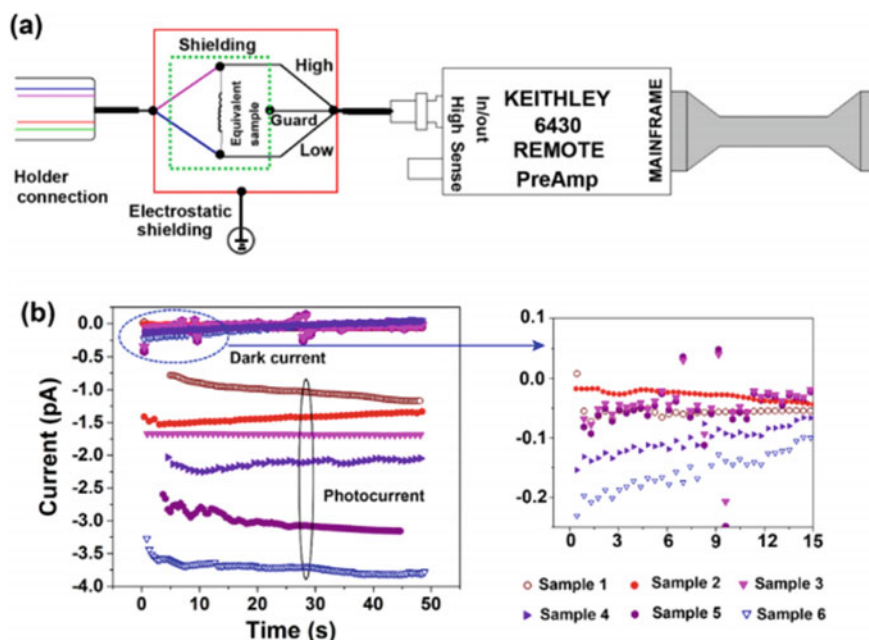


Fig. 6.13 **a** Schematic of the shielding system in current measurement. **b** Current–time curves in the dark and under light exposure (reproduced with permission from Ref. [29], Copyright 2018, Royal Society of Chemistry)

of the sample and thus accurately apply various stimuli to the micro-area where the samples located.

With the advantages such as high working efficiency, high sample stability, and easy operation, a variety of in situ MEMS chips used in thermal [45], electrical [32, 46], mechanical [32], and liquid/gas environmental [47] in situ tests have been developed; however, MEMS chips with photoelectric functions have not attracted widespread attention. Through a combination of an LED and MEMS chip, not only highly stable in situ illumination conditions can be achieved, but also the joint in situ testing of various environmental conditions and device conditions can be expanded in the future. In addition, the light components on the MEMS chips can be further upgraded to micro-fibers, lenses, or even laser diodes.

Method

Figure 6.14 is a schematic diagram of the optoelectrical MEMS chip developed by S. Cai et al. [34]. This optoelectrical MEMS chip is specially designed to adapt commercialized in situ TEM heating systems, which usually consist of a controlling computer, power supply, TEM holder, and heating chips. Typical products such as DENS solution DH30 [48] or Protochips Thermal E-chips [49] usually have four needles (Fig. 6.14c) for electrical connection with MEMS chips, which can be adapted for optical and electrical functions.

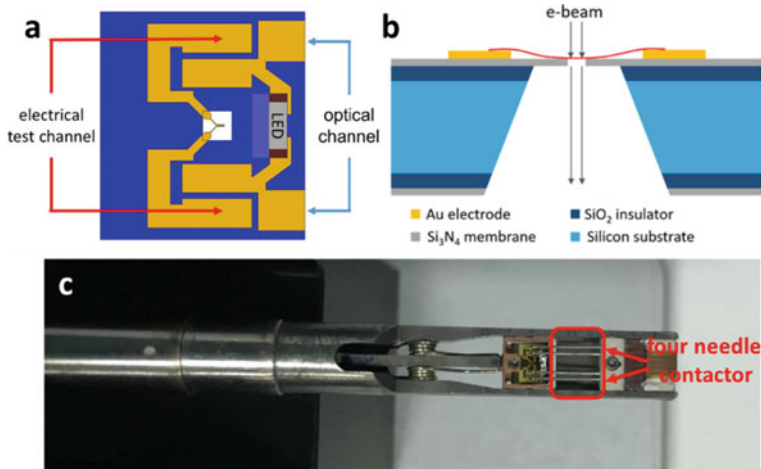


Fig. 6.14 **a** Plane-view and **b** cross-sectional structure of an in situ MEMS chip. The yellow area represents the four gold electrodes on the chip surface, and the LED is connected to the middle two electrodes, facing the sample area. The outer two electrodes are connected to two micro-electrodes in the sample area. **c** Top views of the tip of the DENS solution DH30 holder, showing the four needle contactors for electrical connections (reproduced with permission from Ref. [34], Copyright 2018, Elsevier)

As shown in Fig. 6.14a, gold electrodes deposited on the chip surface serve as electrical and optical channels. The outer two electrodes are connected to two micro-electrodes in the centers of the chips, where a window is opened for passing through the electron beam and covered by the suspending Si_3N_4 membrane with tiny holes to support the transferred samples. For low-dimensional samples such as nanowires and 2D materials, it is possible to directly transfer them onto the micro-electrodes, whereas cross-sectional samples prefer deposited Pt welding for electrical connections using focused ion beam (FIB) systems.

The side-emission LED is connected to the middle two electrodes, facing the sample area to provide in situ illumination. Appropriate LEDs should meet these requirements: (i) the compatibility of the holder with an additional LED chip, (ii) direct light illumination over the sample area, and (iii) no magnetic components to avoid imaging distortion. By adopting the proper commercial LEDs with different wavelengths as shown in Fig. 6.15, this in situ MEMS chip can produce a variety of in situ illumination conditions inside the TEM chamber.

To utilize both electrical and optical channels for illumination control and high accuracy detection of the electrical signal from the sample, a Keithley dual-channel source measure unit (SMU) was used as the power supply and signal detector. A user-friendly custom control system was programmed in LabVIEW software to achieve remote control of this MEMS-chip-based in situ optical system. The interface of the control program is shown in Fig. 6.16. With basic functions such as changing working modes, adjusting working parameters, presetting input waveforms, and showing I/O

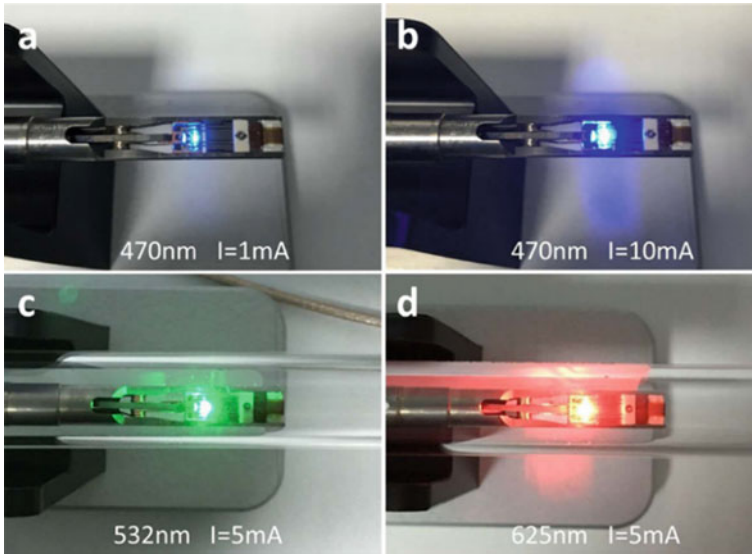


Fig. 6.15 Commercial LEDs with different wavelengths are implanted on the in situ MEMS chips and operate under real working conditions (reproduced with permission from Ref. [34], Copyright 2018, Elsevier)

status, one can freely adjust the light intensity and obtain electrical data automatically, with all signal curves displayed in real time.

Functions

The use of the in situ optoelectrical MEMS-chip-based system ensures that in situ illumination can be simultaneously applied with electrical measurements to the sample inside the TEM chamber with minimum modifications. This in situ system can achieve a variety of lighting conditions with the selection of commercial LEDs with different wavelengths. In addition, its favorable stability under working conditions makes it possible to be combined with advanced TEM techniques such as aberration-corrected S/TEM, electron energy loss spectroscopy (EELS), and energy dispersive spectroscopy (EDS) to achieve atomically resolved in situ observation and spectroscopic measurements.

The intensity of light illumination can be quantified by numerical simulation. This simulation was carried out based on an accurate optical model of the entire sample system. The maximum incident light intensity in the sample area reaches 150 W/m^2 under a forward current of 5 mA for the blue LED (470-nm working wavelength), which can be accurately adjusted by controlling the input current. The electrical Joule heating generated by circuits may lead to decreased sample stability. However, this thermal drift quickly reaches a steady state within approximately 2 min. As shown in Fig. 6.17, the drifting test using an FIB-prepared cross-sectional sample with the LED in a working state suggests that the drifting rate soon decreased to less than 1 nm/min

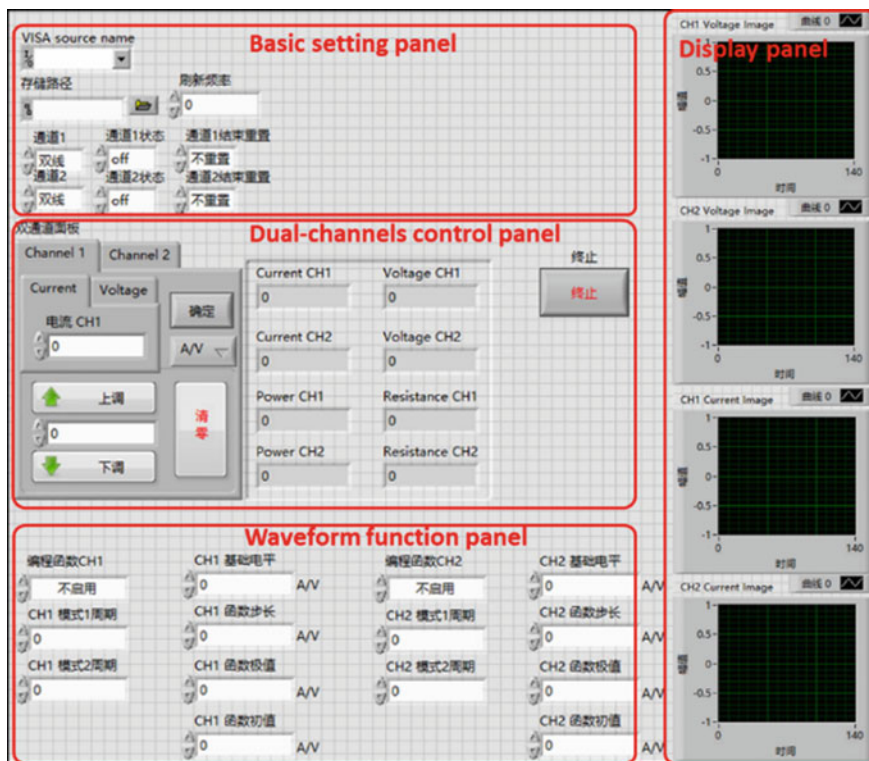


Fig. 6.16 The control interface of an in situ optoelectrical system programmed with LabVIEW

after reaching a steady state. This level of stability meets the requirements for atomic resolution HRTEM and HRSTEM imaging, as well as spectroscopic analyses such as EDS and EELS.

6.3 Applications

Since the first in situ opto-TEM work from 1984, this technique has already gone through several generations with the development of both in situ facilities and TEM hardware. From modification of the TEM chamber to specified in situ holders and MEMS chips, in situ optical measurements have become more available and user friendly. However, the combination with new types of TEMs like ETEMs has effectively extended the characterization range and understanding of functional materials working for pollutant disposal, semiconductors, and clean energy. For typical research contents focused on different physical mechanisms, such as photocatalysis,

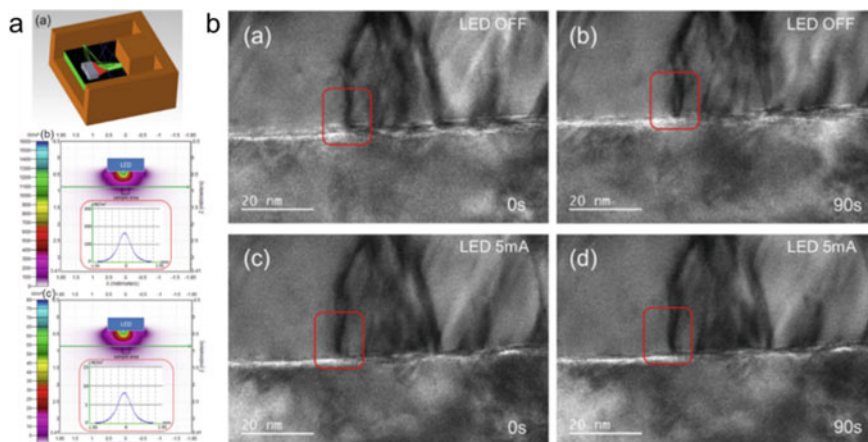


Fig. 6.17 Quantification of light intensity and evaluation of sample drifting rate. **a** Simulation result of light intensity distribution, the maximum incident power density at sample region is 150 W/m^2 . **b** TEM images taken with the LED off and on at 0 s and after 90 s, respectively. The sample drift rate was less than 1 nm/min, suggesting that any additional thermal drift induced by the LED illumination to the sample was small (reproduced with permission from Ref. [34], Copyright 2018, Elsevier)

PL/CL, and photocurrents, in situ illumination/analysis of photosignals plays an irreplaceable role for structure–property exploration. Also different in situ optical techniques have respective application advantages, and the selection should be based on the sample status and photoresponse properties to be studied. Three application topics for in situ optical measurements on physical mechanisms of photocatalysts, PL/CL, and photocurrents will be reviewed in this section, which may provide available references for researchers to design and conduct in situ optical experiments.

6.3.1 Photocatalyst

Due to diminishing fossil fuel reserves, a promising solution that generates clean carbon energy from renewable resources, such as sunlight, has attracted much attention [50]. However, the petrochemical industry and fuel consumption have induced serious atmospheric pollution, which also makes pollutant disposal a critical task. Photocatalysts provide a possible solution for the recombination of chemical bonds in a much simpler way, which may be widely used in the future environmental protection industry [3]. For further understanding of underlying fundamental reaction mechanisms and structure–property relationships of photocatalysts, it is necessary to characterize their behaviors under real working conditions using in situ investigations.

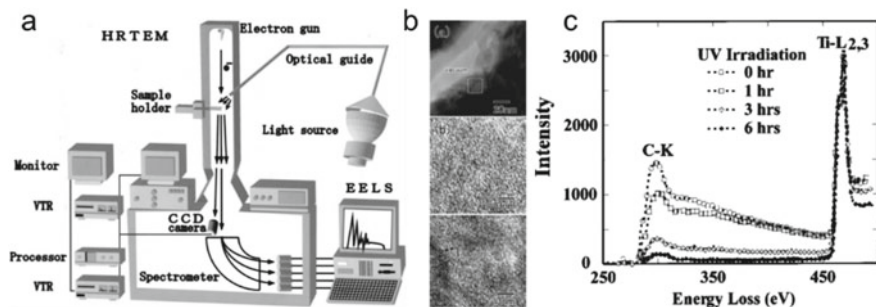


Fig. 6.18 **a** Schematic diagram of an in situ TEM observation system for photochemical reaction. Ultraviolet light is introduced into a 200 kV high-resolution electron microscope through an optical guide. **b** Electron micrograph of a hydrocarbon/TiO₂ sample which had been illuminated for 3 h. **c** EELS spectra with ultraviolet irradiation. The peak of the carbon-K edge, which shows the existence of organic materials, has decreased with increasing ultraviolet irradiation (reproduced with permission from Ref. [51], Copyright 2004, AIP Publishing)

K. Yoshida et al. constructed an in situ TEM system which introduced optical guides directly into the TEM chamber for observation of the photoreactions (Fig. 6.18a) [51]. This system can provide a light intensity up to 10 mW/cm² at a sample plane with a light wavelength of 360 nm, applicable for stimulating photocatalytic reactions of hydrocarbons on TiO₂ films. HRTEM images reveal a clearer lattice structure of TiO₂ after irradiation than before (Fig. 6.18b), which suggests a decomposition of the organic material covered on TiO₂. An EELS spectrum also shows an obvious decrease of carbon-K edge ($E = 283.8$ eV) occurring after long time UV irradiation, further demonstrating the photocatalyzed organic decomposition phenomenon (Fig. 6.18c). Further studies on oxygen release and structural changes in TiO₂ films during photocatalytic oxidation have also been carried out using the same in situ setup [52].

L. Zhang et al. employed atomic resolution ETEM to study the structural evolution of anatase nanoparticles under 1 Torr of water vapor and broadband light illumination with a total intensity of 1430 mW/cm² [36]. An in situ heating holder was also used to provide a temperature of 150 °C to simulate the vapor-phase water splitting (Fig. 6.19a). During this in situ reaction procedure triggered by light illumination, an amorphous phase with a thickness of about one to two monolayers occurs in the initially crystalline surface (Fig. 6.19b). Further, EELS and X-ray photoelectron spectroscopy (XPS) characterization both reveal that the oxidation state of titanium in the surface amorphous layer is +3, while in the bulk is +4 (Fig. 6.19c, d). The amorphous layer remained stable with no thickness increase over time. This study is the first atomic resolution study on the surface evolution of anatase nanocrystals under photocatalytic splitting of water. This system was also utilized for in situ characterization of other photocatalysts under different environmental conditions [53, 54].

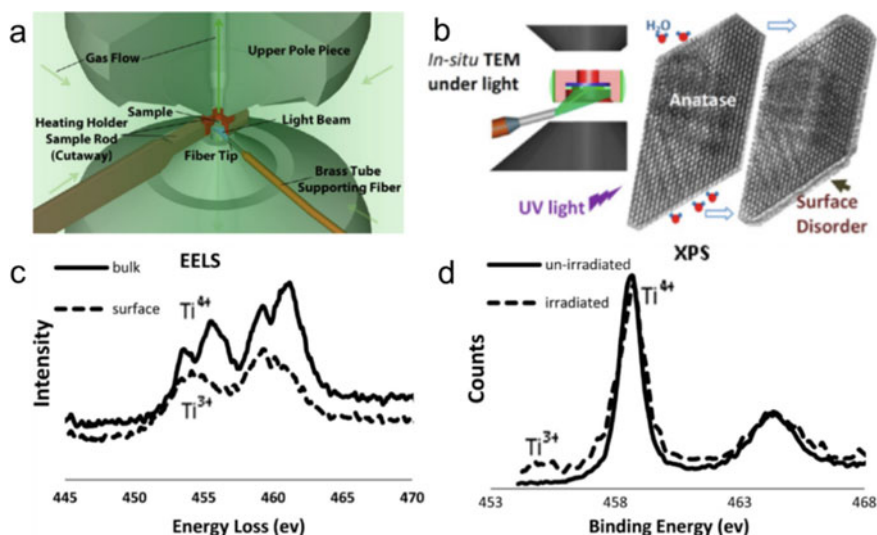


Fig. 6.19 **a** Schematic diagram of an in situ TEM showing gases flowing into the sample chamber, an in situ heating holder for temperature control, and an optical fiber supported by a brass tube perpendicular to the sample rod for light illumination. **b** Surface disorder occurs in TiO₂ anatase nanocrystals under in situ UV light illumination and H₂O gas environment when photocatalytic splitting of water occurs. **c** EELS spectra from the surface and bulk of the irradiated anatase samples. **d** XPS spectra of the irradiated and unirradiated anatase samples (reproduced with permission from Ref. [36], Copyright 2013, American Chemical Society)

F. Cavalca et al. developed two kinds of in situ TEM holders for realization of the photocatalytic reaction inside an ETEM [26]. One used a laser diode casing and a two-lens optical system that can guide light emitted from the laser diode onto the sample position. The other used fibers as light-paths to introduce light from external light sources. An in situ observation of photodeposition of Pt nanoparticles was carried out using this in situ TEM holder combined with ETEM (Fig. 6.20). The H₂PtCl₆ vapor reacted on the surface of the GaN:ZnO particle, which is a highly active photocatalyst for water splitting under visible light exposure. After 4-h illumination with 405 nm wavelength and an intensity of 6 W cm⁻², Pt nanoparticles appeared homogeneously on the surface of the GaN:ZnO with the disappearance of the amorphous layer. Similar work on photodeposition of Au nanoparticles on TiO₂ under UV light was also reported using a specimen chamber with an introduced optical fiber [55].

With the in situ TEM holder developed to contain fibers for light illumination, F. Cavalca et al. then carried out in situ observation of the photoreduction of Cu₂O to metallic Cu under water vapor and illumination with 405 nm light at 6 W/cm² inside the ETEM [56]. The shape and morphology changes were obvious during the reaction, which was directly revealed by TEM-BF images (Fig. 6.21a–f). Selection area electron diffraction (SAED) was also used for structural analysis. As shown in Figs. 6.21g–l, a new (111) reflection of individual Cu grains gradually appeared with increased extent of reaction until exposed to UV light and water vapor for 75 min.

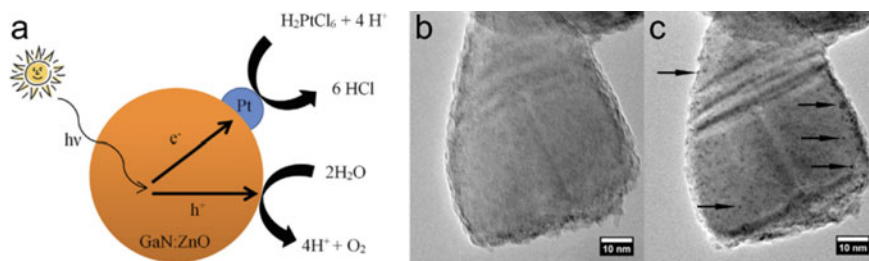


Fig. 6.20 **a** Schematic sketch of the Pt photodeposition process. Light generates an electron–hole pair in the GaN:ZnO photocatalyst. Electrons and holes migrate to the surface and activate reactions with the surrounding chemical species. The electrons are responsible for the Pt precursor decomposition, while the holes drive the water oxidation reaction. **b, c** Bright-field TEM images of a GaN:ZnO particle **b** before and **c** after reaction in 5 mbar H₂O and with 6 W cm⁻² light at a wavelength of 405 nm. The two images were acquired in vacuum, and the reaction was carried out in the absence of the electron beam. The arrows in **c** show some of the deposited Pt nanoparticles (reproduced with permission from Ref. [26], Copyright 2012, IOP Publishing)

This study provides a time-resolved systematic analysis of the light-activated reaction which demonstrates the reduction process of Cu₂O into Cu, as well as giving further insight into the photoreduction reaction mechanisms.

6.3.2 PL and CL

Semiconducting materials, such as ZnO, AlN, and GaN, have been widely studied due to their unique optical and electronic properties for fabricating various optoelectronic devices including field effect transistors, LEDs, photodetectors, etc. [19, 57–59] TEM combined with in situ illumination/detection can provide us with immediate experimental evidence and profound understanding by correlating the microstructure (morphology, crystal orientation, atomic structure, etc.) with the optical and electronic properties of lattice defects in semiconducting materials by measuring the PL and CL [20, 60]. Besides, EELS, which is used to study optical properties such as light extinction and scattering, can be simultaneously available and thus provide complementary information with respect to CL during in situ studies [61–63]. Therefore, we could establish a direct correlation between structural properties and functional optical properties of semiconducting materials by means of in situ TEM optical analysis.

The selective photo-excitation of a single dislocation can be demonstrated by the use of the near-field light probe [20, 21]. For a diamond film (Fig. 6.22a), the PL, CL, and Raman spectra can be acquired from the same specific region as shown in Fig. 6.22. From Fig. 6.22c, d, the observed Raman spectrum with a peak at 1332 cm⁻¹ and a zero-phonon PL spectrum with a peak at 2.156 eV, as well as its phonon replicas, are correlated with nitrogen impurities and vacancies because of the variation of

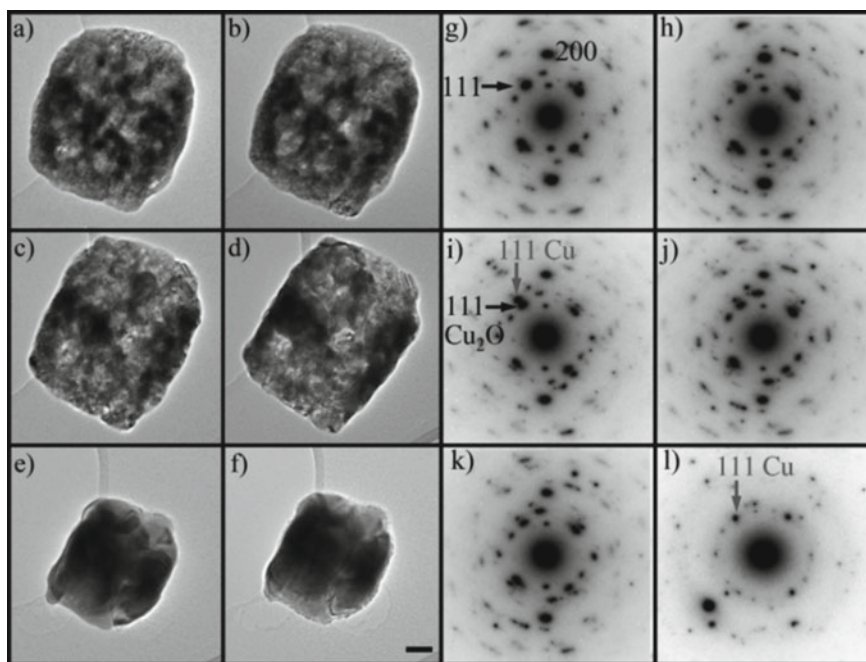


Fig. 6.21 a–f TEM-BF images and g–l corresponding SAED patterns of Cu_2O particles inside in situ ETEM before and during the photocatalytic reaction (every 15 min from 0 to 75 min). Obvious changes can be found on the shape and morphology of particles. New reflections for metallic Cu also appeared in SAED patterns. Scale bar is 50 nm (reproduced with permission from Ref. [56], Copyright 2013, John Wiley and Sons)

the zero-phonon lines obtained at different strains and the absence of local mode structures. The CL spectrum acquired from the same region (Fig. 6.22e) shows similar features to the PL, which should also be associated to the nitrogen impurities and vacancies. However, the signal-to-noise ratio of the CL spectrum is better than that of the PL spectrum.

The newly developed parallel-detection-mode CL-STEM by S. Lim et al. (Fig. 6.23a), which can minimize the impact of electron beam irradiation damage, can also correlate optical properties with the microstructures of GaN/AlGaN nanowires [60]. Figure 6.23b shows the observed CL spectrum with a peak at 365 nm corresponding to the near-band-edge (NBE) emission of GaN at room temperature. Its intensity gradually diminished as the specimen was cooled. The new peak at 378 nm (110 K) could be considered as donor–acceptor pair (DAP) emission as well as LO-phonon replicas, which is related to the acceptor impurities or defects like the SiN or $\text{V}_{\text{Ga}}\text{-O}$ complexes. Figure 6.23d, e indicates that two kinds of emissions were generated from the core, suggesting the uniform distribution of dopants with small variations. From Fig. 6.23f, the DAP emission was quenched at the corners of the

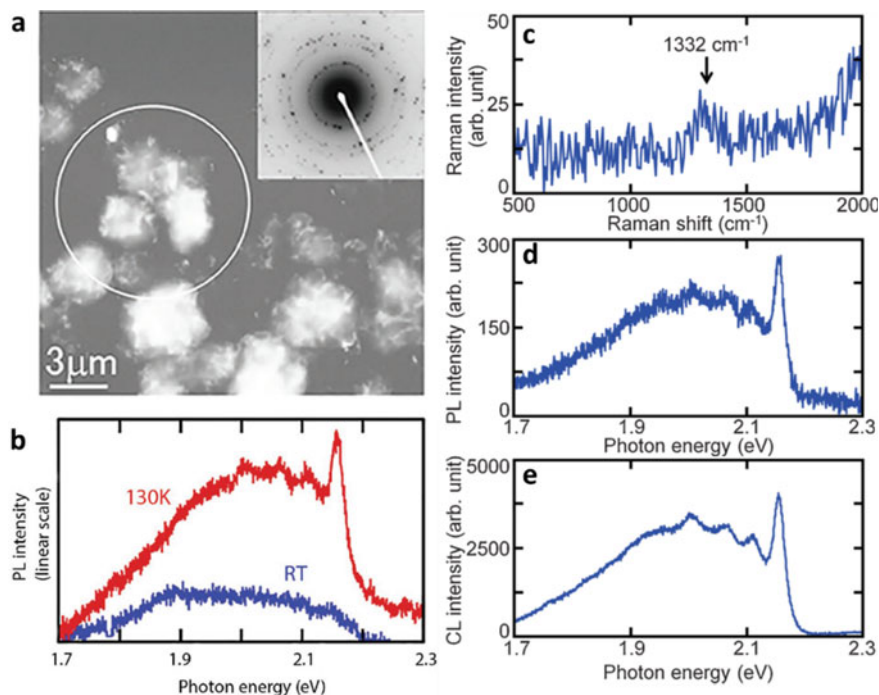


Fig. 6.22 **a** A TEM image and **b** the corresponding PL spectrum taken from the area of a diamond film in **a** (reproduced with permission from Ref. [21], Copyright 2014, Elsevier) **c** Raman, **d** PL, and **e** CL spectra taken from the same area of a CVD-grown diamond film (about 500 nm thick) (reproduced with permission from Ref. [20], Copyright 2012, The Japan Society of Applied Physics)

nanowire, which may result from piezoelectric and spontaneous polarization in the shell.

Besides nanowires, the high spatial resolution of STEM-CL also enables the ability to observe InGaN/GaN quantum wells (QWs) in LED devices. The reduced quantum confined Stark effect in InGaN/GaN QWs LEDs was reported using such a technique. Figure 6.24 shows six spectral features related to QWs1-6. The CL spatial resolution is much smaller than the diffusion length of the carriers (~ 100 nm for GaN, InGaN) that limits the overall resolution, and the improved CL spatial resolution can be attributed to the carrier's quantum confinement. Similar work on GaN quantum disks and red quantum dots have also been studied [64, 65].

Through the combination of EELS and CL measurements by A. Losquin et al. (Fig. 6.25a), nanometric-scale extinction and scattering phenomena were unveiled [61]. From Fig. 6.25 b, the EELS spectrum has a significant blue shift with respect to the CL spectrum. Analogous shifts and broadening have been recorded on different specimens, which lead to the association of the phenomena of extinction and scattering. The calculations of EELS and CL spectra in Fig. 6.25c show that EELS signal corresponds to extinction, while CL signal corresponds to scattering, between which

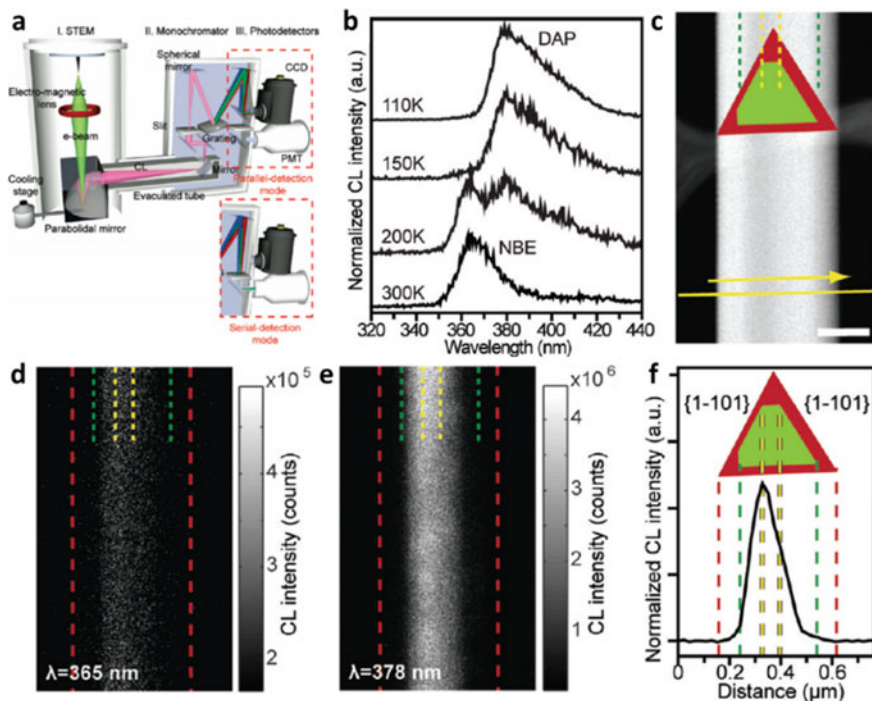


Fig. 6.23 **a** A schematic diagram of a type of CL-STEM apparatus. **b–f** Structural and optical properties of an individual GaN/AlGaN core-shell (CS) nanowire. **b** Normalized CL spectra obtained at different temperatures. **c** Dark-field STEM image of a CS nanowire structure. **d, e** Monochromatic CL images taken at 365 nm (300 K) and 378 nm (110 K). **f** Normalized CL intensity profile obtained along the yellow line in **c** of the emission at 378 nm (reproduced with permission from Ref. [60], Copyright 2009, American Chemical Society)

there is a blue shift. Similar work on surface plasmon modes of Bi_2Te_3 nanoplates and light-matter interactions of nanoparticles have also been studied by EELS and CL [62, 63].

By using a Gatan Vulcan CL holder, the relationship between the interlayer twist and local light excitation of chiral van der Waals (vdW) nanowires was determined (Fig. 6.26a) [66]. Figure 6.26b, c shows synchronous changes of parameters including FWHM, wavelength, and intensity as a result of the accumulated twist. The changes in the above CL spectra originate from the rotation of the chiral vdW layers or changes in electronic structure of the nanowire. Similar work on luminescence in ZnO nanostructures and nanosized cubic $\text{Y}_2\text{O}_3:\text{Tb}^{3+}$ have also been studied using Gatan Vulcan CL holders [58, 67].

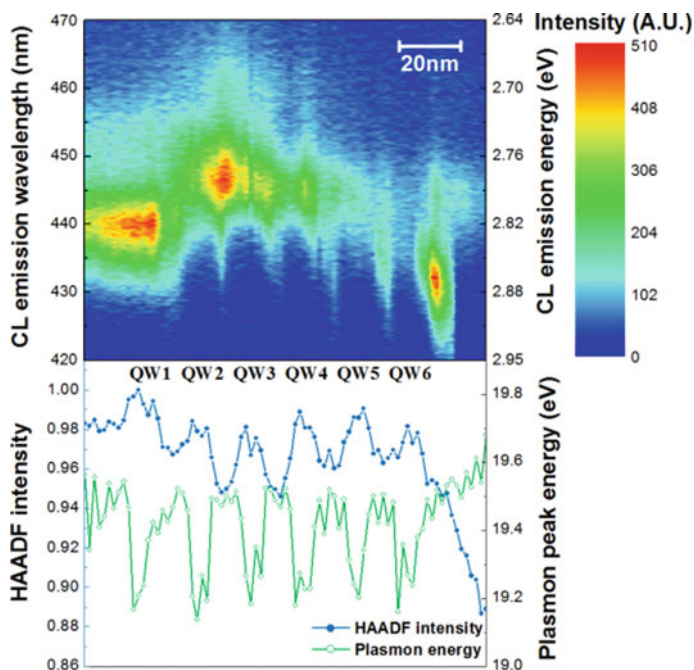


Fig. 6.24 The CL spectral profile, HAADF intensity profile, and plasmon peak energy profile across the InGaN/GaN QWs (reproduced with permission from Ref. [57], Copyright 2015, American Chemical Society)

6.3.3 Photocurrent

Photoelectric conversion is the process of directly converting luminous energy into electric energy through a photovoltaic process. Normal methods to achieve photoelectric conversion include photoelectric devices such as solar cells [68, 69], photodetectors [70, 71], and photodiodes [72]. Semiconductive materials, such as TiO_2 [73], CdS [37, 74], ZnO [27, 28], Si [75], and perovskite [76], are used in diverse photoelectric devices because of their suitable bandgaps and unique electronic, optical, and piezoelectric properties. Measuring the photocurrents of these materials is of great help in studying the factors that affect the photoelectric performance. Based on this, researchers have developed a variety of methods for achieving the measurement of photocurrents inside the TEM, such as introducing optical fibers into the holder, designing MEMS systems, and affixing LEDs on the holder. Some effective work has been carried out through these methods and important results have been gained.

C. Zhang et al. upgraded an optical fiber-compatible TEM holder and carried out a series of work on CdS nanowires [77], CdS/ZnO heterostructures [78], and CdS/p-Si nanowire heterojunctions [37]. A comparative experiment between a CdS nanowire and CdS/ZnO heterostructure on their photoelectric response shows in I - V characteristics measured by sweeping the voltage from -5 to 5 V with a 405 nm

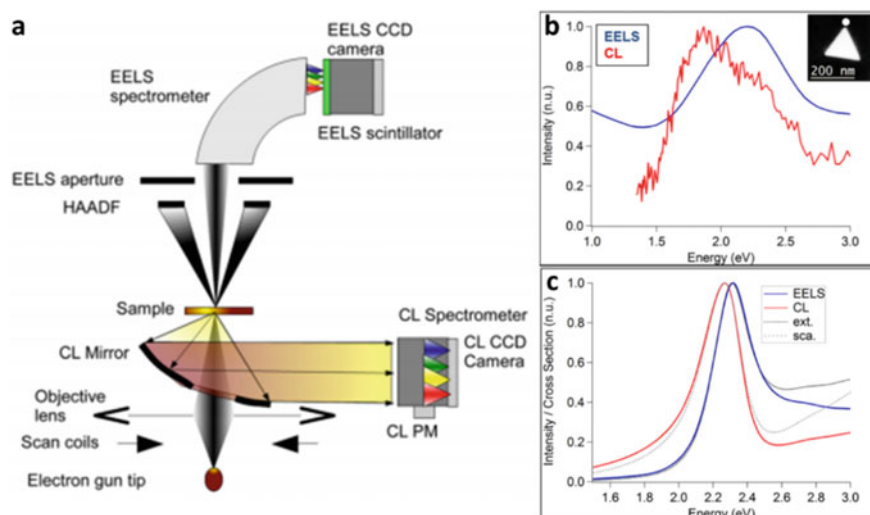


Fig. 6.25 **a** A schematic diagram of a scanning transmission electron microscope (STEM) fitted with homemade EELS and CL systems. **b** EELS and CL spectra obtained at the tip of a gold prism (edge length: 140 nm). **c** Calculated extinction, scattering, EELS, and CL spectra of a small nanoprism (length: 50 nm; thickness: 50 nm) (reproduced with permission from Ref. [61], Copyright 2015, American Chemical Society)

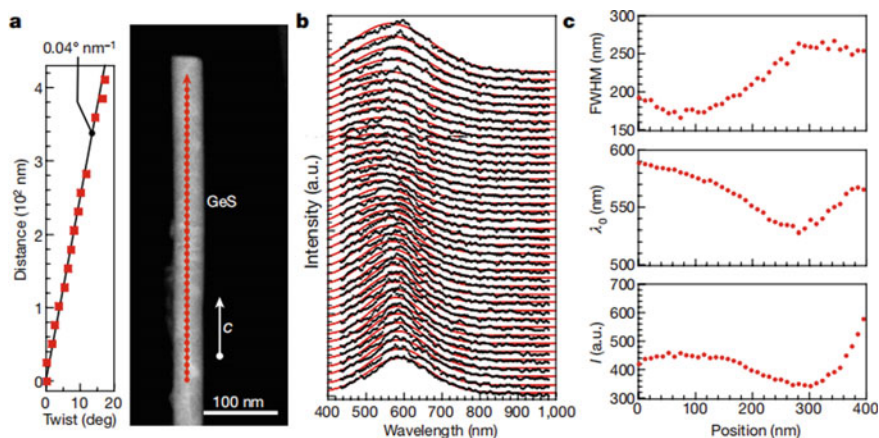


Fig. 6.26 **a** A STEM-HAADF image and a plot of cumulative twist of a GeS nanowire. **b** The CL spectra taken at marked points **a** at room temperature. **c** The FWHM, center wavelength (λ_0), and intensity (I) of the Gaussian fits in **b** (reproduced with permission from Ref. [66], Copyright 2019, Springer Nature)

light on and off, respectively (Fig. 6.27). These indicate the heterostructures show a dramatic photocurrent to dark current ratio and responsivity compared to CdS nanowires. The study on CdS/p-Si nanowire heterojunctions shows a photocurrent saturation effect as well as a good selectivity of light frequencies. Similar work on bending ZnO nanowires have also been studied revealing photocurrent spectra splitting [79], photoconduction, and photoresponse behavior [27, 28] by using an opto-TEM-STM holder with an optical fiber or LED.

Y. Zhu et al. developed a multimodal optical nanoprobe (MON) in cooperation with Nanofactory Instruments AB [80]. The nanoprobe has two channels that pass external light sources (typically 370 nm–2400 nm) to the sample (Fig. 6.28a). These two channels distribute on each side of the sample. In addition to this, two adjustable mirrors help focus input light onto the sample or collect and reflect scattered light from sample to channel for analysis. The MON system also contains a nanomanipulator which can provide fine and coarse motion in three dimensional. Figure 6.28b shows

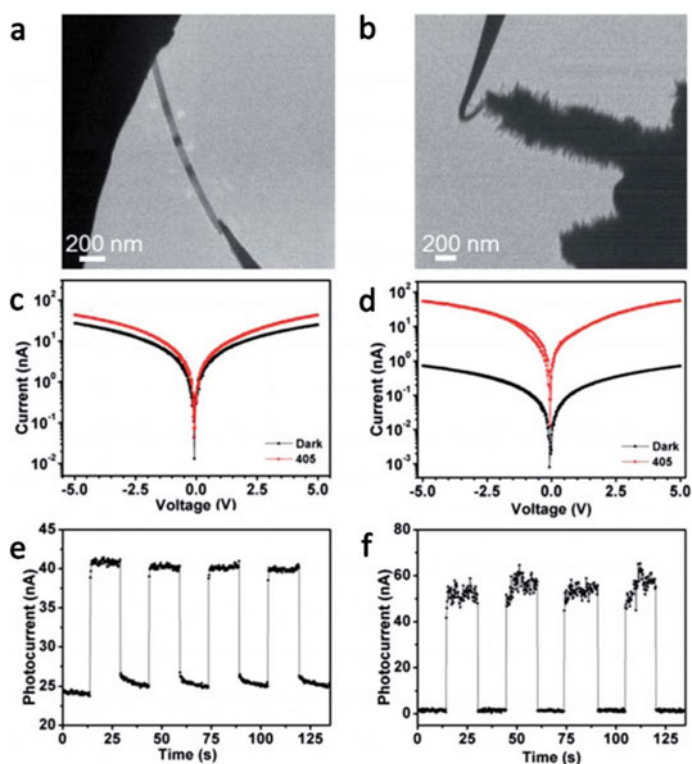


Fig. 6.27 a, b TEM images of an individual CdS nanobelt (a) and an individual CdS/ZnO heterostructure (b). c, d Corresponding photocurrent and dark current of the individual CdS nanobelt and the individual CdS/ZnO heterostructure. e, f Corresponding photocurrent responses of the individual CdS nanobelt photodetector and individual CdS/ZnO heterostructure photodetector (reproduced with permission from Ref. [78], Copyright 2015, IOP Publishing)

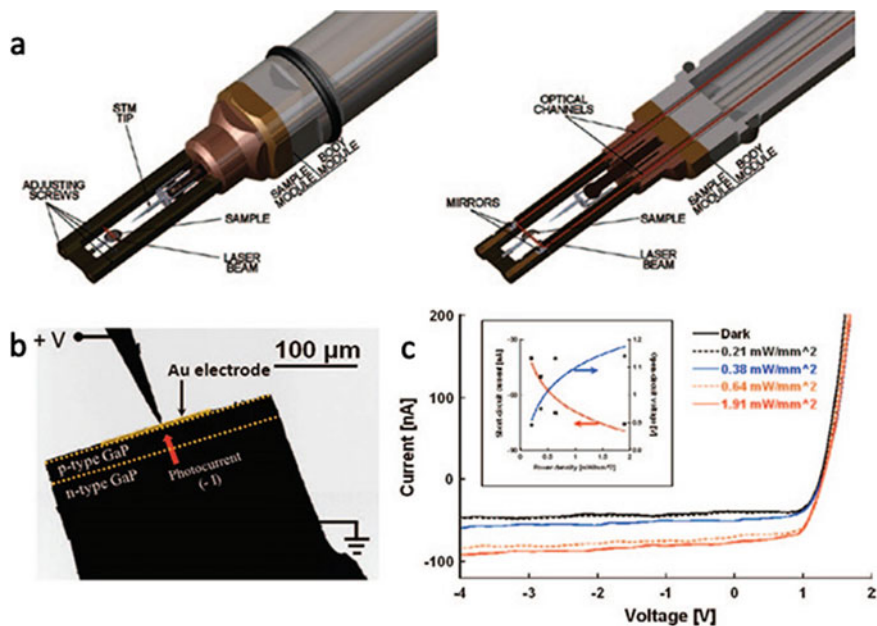


Fig. 6.28 **a** A view of the nanoprobe. **b** TEM image of a commercial LED. **c** Current–voltage (I – V) curve with a 454 nm laser. The inset shows a decrease of I_{sc} and increase of V_{oc} with the power density of the laser (reproduced with permission from Ref. [80], Copyright 2012, Cambridge University Press)

the TEM images of a commercial LED contacted by a movable tungsten probe. Dark current and photocurrent (Fig. 6.28c) were measured with a 454 nm laser. The short-circuit current (I_{sc}) decreases and open-circuit voltage (V_{oc}) increases with the power density of the laser. This MON system can achieve more reliable and accurate photovoltaic measurements.

S. Cai et al. adapted an in situ optoelectrical MEMS system for photoelectrical measurement of a wide range of samples such as one-dimensional (1D) nanowires and FIB-prepared cross-sectional samples (Fig. 6.29) [34]. Figure 6.29c, d shows TEM images of a single 3C-SiC nanowire in Fig. 6.29a and the corresponding selected area electron diffraction (SAED) pattern confirms the crystalline-zinc-blended crystal structure along the $[-110]$ zone axis. Photoconductivity was performed with an external bias ranging from -20 to 20 V where the current increased when the LED switched on. The photocurrent at ± 20 V external bias approximately doubled compared with that in the dark (Fig. 6.29e). The nanowire exhibited simultaneous light-sensing capability where the forward current and photoconductivity increased. By applying a 10-mA forward current square wave, the SiC nanowire at 20-V bias exhibited a fast-current response to the light intensity change (Fig. 6.29f).

Work by H. Dong et al. constructed a single TiO_2 -nanowire/CdSe-QD heterojunction solar cell (QDHSC) within a custom-designed TEM-STM holder to understand

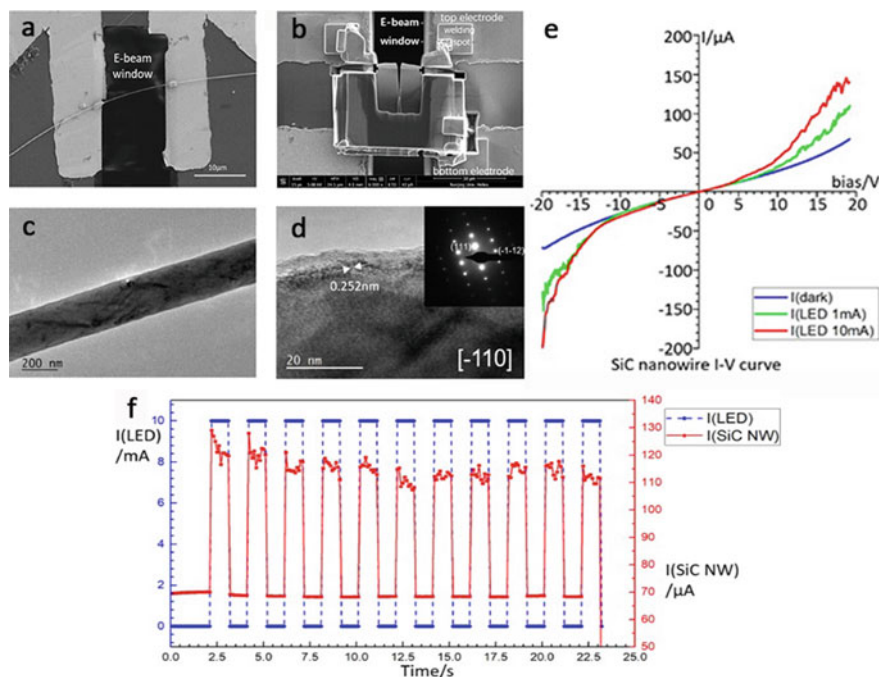


Fig. 6.29 **a** A SiC nanowire welded to both micro-electrodes with Pt deposition and bridging over the viewing window in the middle. **b** A cross-sectional TEM sample was fabricated by FIB system and connected to the MEMS chip. **c** Low-magnification TEM and **d** HRTEM images of SiC nanowires welded on the chip. The corresponding SAED pattern (inset) shows the $[-110]$ zone axis. **e** In situ I-V curve of SiC nanowire with LED ON/OFF measured with electron beam blanked. **f** Photoconductivity measurements of SiC nanowire with 20-V bias voltage using a series of square waves from 1 to 10 mA: forward current to the LED (blue) and photocurrent generated in the nanowire (red) (reproduced with permission from Ref. [34], Copyright 2018, Elsevier)

the effect of interfaces and defects on the photovoltaic performance of QDHSC [30]. This QDHSC consists of an individual TiO_2 nanowire with uniformly coated CdSe QDs and contact electrodes Pt and Cu (Fig. 6.30a, b). The QDHSC is exposed by an LED whose power intensity is 3 mW/cm^2 . The TEM images and fast Fourier transformation pattern reveal the crystal information of the TiO_2 nanowire and CdSe-QD. Then the photocurrent and dark current were measured, and the power conversion efficiency (PCE) of the solar cell was 27.7% with a white light. As shown in Fig. 6.30c–e, direct in situ control over different interface areas (S) was achieved by selecting different nanowire lengths (L) through the movement of the Pt electrode. Simultaneously, a change of photocurrent density occurs with different interfacial areas (Fig. 6.30f). More data were fitted by a modified Shockley–Read–Hall recombination model (Fig. 6.30g). It is noteworthy that photocurrent densities with larger interfacial areas show an inverse trend. In general, a larger interfacial area provides

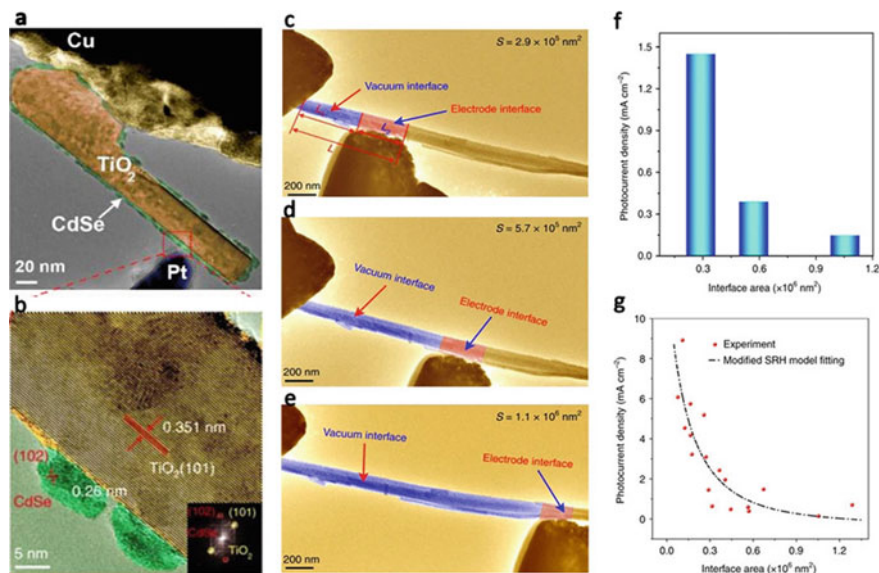


Fig. 6.30 TEM image **a** and HRTEM image **b** of an individual TiO₂ nanowire with CdSe QDs. The inset of **b** is a corresponding FFT pattern. **c–e** TEM images of QDHSC with different interfacial areas (blue and red areas). **f** Histogram of the photocurrent density from the different interface areas in **c–e**. **g** Statistical distribution of the photocurrent density. Fitted data to the modified Shockley–Read–Hall (SRH) model as a function of the interface area (reproduced with permission from Ref. [30], Copyright 2019, Springer Nature)

a larger number of defects, which trap more photoelectrons. Thus, photogenerated carriers suffer a great possibility of being lost during the transport process.

The open-voltage data were fitted as a function of interfacial area using a modified Shockley–Read–Hall model, which indicates the V_{oc} first experiences a sharp increase with S below a value of $3 \times 10^5 \text{ nm}^2$ and levels off with further increase in S (Fig. 6.31a). The increase in V_{oc} is mainly attributed to the decreased current density with increasing interface area. Figure 6.31b shows the statistical distribution of the PCE as a function of the interface area. This provides evidence to elucidate the relationship between the interfaces and the photovoltaic performance and acts as a guideline to optimize the parameters and maximize the efficiency of the corresponding solar cells.

6.4 Future and Opportunities

The fast development of detector and imaging techniques of TEMs has brought more opportunities for material researchers. For example, ultrafast and direct electron cameras greatly improve the efficiency and time resolution of conventional TEMs.

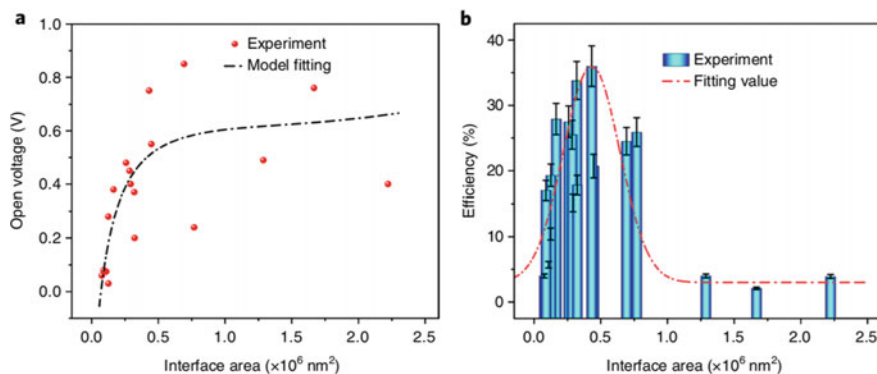


Fig. 6.31 **a** Statistical distribution of the V_{oc} . The fit of the data to the modified Shockley–Read–Hall (SRH) model as a function of interfacial area. **b** Statistical distribution of the PCE as a function of the interfacial area of the QDHSC (reproduced with permission from Ref. [30], Copyright 2019, Springer Nature)

Differential phase contrast (DPC) and four-dimensional STEM (4D-STEM) not only realize functions of traditional STEM, but also provide information like electric field, potential, charge density, and magnetic field [81]. Electron tomography and ptychography have become promising solutions for three-dimensional (3D) structures and light atom characterization with high spatial resolution, respectively. These significant technical improvements will further benefit future applications of in situ optical TEM.

Advanced detectors will stimulate the improvement of both in situ TEM characterizations and in situ facilities. The raising application of ultrafast detectors with time resolution up to $\sim 1 \mu\text{s}$ enables a much more accurate in situ record of structure evolution during reaction processes, which is important for detailed characterization of the photoresponse of photocatalysts and semiconductors. Combined with DPC and 4D-STEM techniques based on ultrafast camera, in situ characterization of light-induced electric field, potential, and charge density evolution is expected to be realized. Direct electron cameras have much better quantum efficiency than traditional cameras, which allows high-quality imaging with extremely low electron dose rates. This can extend the sample adaptability for in situ optical TEM observation such as electron-sensitive metal–organic frameworks (MOF) and covalent organic framework (COF), which have attracted expansive attention as novel catalyst supports and have been utilized for photocatalyst development [82, 83], and may also provide possible solutions for in situ photocurrent measurements of electron-sensitive organic–inorganic hybrid perovskites [84].

Based on the growing quantum efficiency of light detectors, the improvement of in situ PL and CL detection systems will provide better data quality, especially for nanoscale samples, where single-photon detection can be realized one day. High efficiency detection can also help reduce dose rates to avoid electron beam radiation damage and improve acquisition speed for atomically resolved spectroscopy images.

Nevertheless, in situ PL and CL detection in TEM is expected to play more important roles in the development of novel semiconducting materials and devices. In addition, the small-sized, high accuracy light detector will also help the calibration of in situ illumination systems, which is essential for quantitative analysis of sample properties.

The combination of in situ optical measurement and computational reconstruction techniques will bring more details about sample structures and chemical states. Electron tomography can acquire 3D structural information of nanomaterials, and the newly developed 4D electron tomography technique has successfully realized time-resolved 3D spatial resolution [85]. This may realize in situ optical measurements as promising solutions for in situ analysis of active sites and fine 3D structure evolution during photocatalytic reactions. Electron ptychography can achieve better contrast on light atoms [86] and provide more flexibility for the usage of electron signals for image reconstruction simultaneously with EELS acquisition [87]. An unprecedented complete understanding of in situ behaviors can be expected with the continued improvement of both the hardware and software of electron microscopy.

References

1. Zhai T, Li L, Wang X, Fang X, Bando Y, Golberg D (2010) Recent developments in one-dimensional inorganic nanostructures for photodetectors. *Adv Func Mater* 20(24):4233–4248. <https://doi.org/10.1002/adfm.201001259>
2. Jariwala D, Sangwan VK, Lauhon LJ, Marks TJ, Hersam MC (2013) Carbon nanomaterials for electronics, optoelectronics, photovoltaics, and sensing. *Chem Soc Rev* 42(7):2824–2860. <https://doi.org/10.1039/c2cs35335k>
3. Khalid NR, Majid A, Tahir MB, Niaz NA, Khalid S (2017) Carbonaceous-TiO₂ nanomaterials for photocatalytic degradation of pollutants: a review. *Ceram Int* 43(17):14552–14571. <https://doi.org/10.1016/j.ceramint.2017.08.143>
4. Dincer I, Acar C (2015) A review on clean energy solutions for better sustainability. *Int J Energy Res* 39(5):585–606. <https://doi.org/10.1002/er.3329>
5. Li Y, Qian F, Xiang J, Lieber CM (2006) Nanowire electronic and optoelectronic devices. *Mater Today* 9(10):18–27. [https://doi.org/10.1016/S1369-7021\(06\)71650-9](https://doi.org/10.1016/S1369-7021(06)71650-9)
6. Kim Judy S, LaGrange T, Reed Bryan W, Taheri Mitra L, Armstrong Michael R, King Wayne E, Browning Nigel D, Campbell Geoffrey H (2008) Imaging of transient structures using nanosecond in situ TEM. *Science* 321(5895):1472–1475. <https://doi.org/10.1126/science.1161517>
7. Golberg D, Costa PMFJ, Wang M-S, Wei X, Tang D-M, Xu Z, Huang Y, Gautam UK, Liu B, Zeng H, Kawamoto N, Zhi C, Mitome M, Bando Y (2012) Nanomaterial engineering and property studies in a transmission electron microscope. *Adv Mater* 24(2):177–194. <https://doi.org/10.1002/adma.201102579>
8. Ji D, Cai S, Paudel TR, Sun H, Zhang C, Han L, Wei Y, Zang Y, Gu M, Zhang Y, Gao W, Huyan H, Guo W, Wu D, Gu Z, Tsymbal EY, Wang P, Nie Y, Pan X (2019) Freestanding crystalline oxide perovskites down to the monolayer limit. *Nature* 570(7759):87–90. <https://doi.org/10.1038/s41586-019-1255-7>
9. Dou Z, Chen Z, Li N, Yang S, Yu Z, Sun Y, Li Y, Liu B, Luo Q, Ma T, Liao L, Liu Z, Gao P (2019) Atomic mechanism of strong interactions at the graphene/sapphire interface. *Nat Commun* 10(1):5013. <https://doi.org/10.1038/s41467-019-13023-6>

10. Sun Y, Abid AY, Tan C, Ren C, Li M, Li N, Chen P, Li Y, Zhang J, Zhong X, Wang J, Liao M, Liu K, Bai X, Zhou Y, Yu D, Gao P (2019) Subunit cell-level measurement of polarization in an individual polar vortex. *Sci Adv* 5(11):eaav4355. <https://doi.org/10.1126/sciadv.aav4355>
11. Zhu C, Yu M, Zhou J, He Y, Zeng Q, Deng Y, Guo S, Xu M, Shi J, Zhou W, Sun L, Wang L, Hu Z, Zhang Z, Guo W, Liu Z (2020) Strain-driven growth of ultra-long two-dimensional nano-channels. *Nat Commun* 11(1):772. <https://doi.org/10.1038/s41467-020-14521-8>
12. Li W, Zhou J, Cai S, Yu Z, Zhang J, Fang N, Li T, Wu Y, Chen T, Xie X, Ma H, Yan K, Dai N, Wu X, Zhao H, Wang Z, He D, Pan L, Shi Y, Wang P, Chen W, Nagashio K, Duan X, Wang X (2019) Uniform and ultrathin high- κ gate dielectrics for two-dimensional electronic devices. *Nat Electron* 2(12):563–571. <https://doi.org/10.1038/s41928-019-0334-y>
13. Chen Z, Zhang X, Dou Z, Wei T, Liu Z, Qi Y, Ci H, Wang Y, Li Y, Chang H, Yan J, Yang S, Zhang Y, Wang J, Gao P, Li J, Liu Z (2018) High-brightness blue light-emitting diodes enabled by a directly grown graphene buffer layer. *Adv Mater* 30(30):1801608. <https://doi.org/10.1002/adma.201801608>
14. Chen Z, Liu Z, Wei T, Yang S, Dou Z, Wang Y, Ci H, Chang H, Qi Y, Yan J, Wang J, Zhang Y, Gao P, Li J, Liu Z (2019) Improved epitaxy of AlN film for deep-ultraviolet light-emitting diodes enabled by graphene. *Adv Mater* 31(23):1807345. <https://doi.org/10.1002/adma.201807345>
15. Wan S, Zhu Z, Yin K, Su S, Bi H, Xu T, Zhang H, Shi Z, He L, Sun L (2018) A highly skin-conformal and biodegradable graphene-based strain sensor. *Small Methods* 2(10):1700374. <https://doi.org/10.1002/smt.201700374>
16. Golberg D, Zhang C, Xu Z (2014) Cubic lattice nanosheets: thickness-driven light emission. *ACS Nano* 8(7):6516–6519. <https://doi.org/10.1021/nn502999g>
17. Suzuki K, Ichihara M, Takeuchi S, Nakagawa K, Maeda K, Iwanaga H (1984) In situ TEM observation of dislocation motion in II–VI compounds. *Philos Mag A* 49(3):451–461. <https://doi.org/10.1080/01418618408233287>
18. Ohno Y, Takeda S (1995) A new apparatus for in situ photoluminescence spectroscopy in a transmission electron microscope. *Rev Sci Instrum* 66(10):4866–4869. <https://doi.org/10.1063/1.1146166>
19. Ohno Y, Taishi T, Yonenaga I (2009) In situ analysis of optoelectronic properties of dislocations in ZnO in TEM observations. *Phys Status Solidi (a)* 206(8):1904–1911. <https://doi.org/10.1002/pssa.200881466>
20. Ohno Y (2012) Development of an apparatus for in-situ near-field photoexcitation in a transmission electron microscope. *Appl Phys Express* 5(12):125204. <https://doi.org/10.1143/apex.5.125204>
21. Ohno Y, Yonenaga I (2014) In-situ micro and near-field photo-excitation under transmission electron microscopy. *Appl Surf Sci* 302:29–31. <https://doi.org/10.1016/j.apsusc.2013.11.061>
22. Picher M, Mazzucco S, Blankenship S, Sharma R (2015) Vibrational and optical spectroscopies integrated with environmental transmission electron microscopy. *Ultramicroscopy* 150:10–15. <https://doi.org/10.1016/j.ultramic.2014.11.023>
23. Miller BK, Crozier PA (2013) System for in situ UV-visible illumination of environmental transmission electron microscopy samples. *Microsc Microanal* 19(2):461–469. <https://doi.org/10.1017/S1431927612014122>
24. Tanabe T, Muto S, Tohtake S (2002) Development of new TEM specimen holder for cathodoluminescence detection. *J Electron Microsc* 51(5):311–313. <https://doi.org/10.1093/jmicro/51.5.311>
25. Shindo D, Takahashi K, Murakami Y, Yamazaki K, Deguchi S, Suga H, Kondo Y (2009) Development of a multifunctional TEM specimen holder equipped with a piezodriving probe and a laser irradiation port. *J Electron Microsc* 58(4):245–249. <https://doi.org/10.1093/jmicro/dfp018>
26. Cavalca F, Laursen AB, Kardynal BE, Dunin-Borkowski RE, Dahl S, Wagner JB, Hansen TW (2012) In situ transmission electron microscopy of light-induced photocatalytic reactions. *Nanotechnology* 23(7):075705. <https://doi.org/10.1088/0957-4484/23/7/075705>

27. Gao P, Wang ZZ, Liu KH, Xu Z, Wang WL, Bai XD, Wang EG (2009) Photoconducting response on bending of individual ZnO nanowires. *J Mater Chem* 19(7):1002–1005. <https://doi.org/10.1039/b816791e>
28. Yang S, Wang L, Tian X, Xu Z, Wang W, Bai X, Wang E (2012) The piezotronic effect of zinc oxide nanowires studied by in situ TEM. *Adv Mater* 24(34):4676–4682. <https://doi.org/10.1002/adma.201104420>
29. Dong H, Xu T, Sun Z, Zhang Q, Wu X, He L, Xu F, Sun L (2018) Simultaneous atomic-level visualization and high precision photocurrent measurements on photoelectric devices by in situ TEM. *RSC Adv* 8(2):948–953. <https://doi.org/10.1039/c7ra10696c>
30. Dong H, Xu F, Sun Z, Wu X, Zhang Q, Zhai Y, Tan XD, He L, Xu T, Zhang Z, Duan X, Sun L (2019) In situ interface engineering for probing the limit of quantum dot photovoltaic devices. *Nat Nanotechnol* 14(10):950–956. <https://doi.org/10.1038/s41565-019-0526-7>
31. Zhang M, Olson E, Twesten R, Wen J, Allen L, Robertson I, Petrov I (2005) In situ transmission electron microscopy studies enabled by microelectromechanical system technology. *J Mater Res* 20(7):1802–1807. <https://doi.org/10.1557/JMR.2005.0225>
32. Zhu Y, Espinosa HD (2005) An electromechanical material testing system for in situ electron microscopy and applications. *Proc Natl Acad Sci* 102(41):14503–14508. <https://doi.org/10.1073/pnas.0506544102>
33. Haque M, Espinosa H, Lee H (2010) MEMS for in situ testing—handling, actuation, loading, and displacement measurements. *MRS Bull* 35(5):375–381. <https://doi.org/10.1557/mrs2010.570>
34. Cai S, Gu C, Wei Y, Gu M, Pan X, Wang P (2018) Development of in situ optical–electrical MEMS platform for semiconductor characterization. *Ultramicroscopy* 194:57–63. <https://doi.org/10.1016/j.ultramic.2018.07.007>
35. Fernando JFS, Zhang C, Firestein KL, Golberg D (2017) Optical and optoelectronic property analysis of nanomaterials inside transmission electron microscope. *Small* 13(45):1701564. <https://doi.org/10.1002/smll.201701564>
36. Zhang L, Miller BK, Crozier PA (2013) Atomic level in situ observation of surface amorphization in anatase nanocrystals during light irradiation in water vapor. *Nano Lett* 13(2):679–684. <https://doi.org/10.1021/nl304333h>
37. Zhang C, Xu Z, Tian W, Tang D-M, Wang X, Bando Y, Fukata N, Golberg D (2015) In situ fabrication and optoelectronic analysis of axial CdS/p-Si nanowire heterojunctions in a high-resolution transmission electron microscope. *Nanotechnology* 26(15):154001. <https://doi.org/10.1088/0957-4484/26/15/154001>
38. Miller DR, Williams RE, Akbar SA, Morris PA, McComb DW (2017) STEM-cathodoluminescence of SnO₂ nanowires and powders. *Sens Actuators B Chem* 240:193–203. <https://doi.org/10.1016/j.snb.2016.08.145>
39. Vadai M, Angell DK, Hayee F, Sytwu K, Dionne JA (2018) In-situ observation of plasmon-controlled photocatalytic dehydrogenation of individual palladium nanoparticles. *Nat Commun* 9(1):4658. <https://doi.org/10.1038/s41467-018-07108-x>
40. Huang JY, Zhong L, Wang CM, Sullivan JP, Xu W, Zhang LQ, Mao SX, Hudak NS, Liu XH, Subramanian A, Fan H, Qi L, Kushima A, Li J (2010) In situ observation of the electrochemical lithiation of a single SnO₂ nanowire electrode. *Science* 330(6010):1515–1520. <https://doi.org/10.1126/science.1195628>
41. Yang Y, Gao P, Gaba S, Chang T, Pan X, Lu W (2012) Observation of conducting filament growth in nanoscale resistive memories. *Nat Commun* 3(1):732. <https://doi.org/10.1038/ncomms1737>
42. Liu Q, Sun J, Lv H, Long S, Yin K, Wan N, Li Y, Sun L, Liu M (2012) Real-time observation on dynamic growth/dissolution of conductive filaments in oxide-electrolyte-based ReRAM. *Adv Mater* 24(14):1844–1849. <https://doi.org/10.1002/adma.201104104>
43. Sun J, He L, Lo Y-C, Xu T, Bi H, Sun L, Zhang Z, Mao SX, Li J (2014) Liquid-like pseudoelasticity of sub-10-nm crystalline silver particles. *Nat Mater* 13(11):1007–1012. <https://doi.org/10.1038/nmat4105>

44. Costa PMFJ, Golberg D, Shen G, Mitome M, Bando Y (2008) ZnO low-dimensional structures: electrical properties measured inside a transmission electron microscope. *J Mater Sci* 43(4):1460–1470. <https://doi.org/10.1007/s10853-007-2307-1>
45. Grapes MD, LaGrange T, Friedman LH, Reed BW, Campbell GH, Weihs TP, LaVan DA (2014) Combining nanocalorimetry and dynamic transmission electron microscopy for in situ characterization of materials processes under rapid heating and cooling. *Rev Sci Instrum* 85(8):084902. <https://doi.org/10.1063/1.4892537>
46. Westenfelder B, Meyer JC, Biskupek J, Algara-Siller G, Lechner LG, Kusterer J, Kaiser U, Krill CE, Kohn E, Scholz F (2011) Graphene-based sample supports for in situ high-resolution TEM electrical investigations. *J Phys D Appl Phys* 44(5):055502. <https://doi.org/10.1088/0022-3727/44/5/055502>
47. Grogan JM, Rotkina L, Bau HH (2011) In situ liquid-cell electron microscopy of colloid aggregation and growth dynamics. *Phys Rev E* 83(6):061405. <https://doi.org/10.1103/PhysRevE.83.061405>
48. van Huis MA, Young NP, Pandraud G, Creemer JF, Vanmaekelbergh D, Kirkland AI, Zandbergen HW (2009) Atomic imaging of phase transitions and morphology transformations in nanocrystals. *Adv Mater* 21(48):4992–4995. <https://doi.org/10.1002/adma.200902561>
49. Allard LF, Bigelow WC, Jose-Yacamán M, Nackashi DP, Damiano J, Mick SE (2009) A new MEMS-based system for ultra-high-resolution imaging at elevated temperatures. *Microsc Res Tech* 72(3):208–215. <https://doi.org/10.1002/jemt.20673>
50. Chen X, Li C, Grätzel M, Kostecki R, Mao SS (2012) Nanomaterials for renewable energy production and storage. *Chem Soc Rev* 41(23):7909–7937. <https://doi.org/10.1039/c2cs35230c>
51. Yoshida K, Yamasaki J, Tanaka N (2004) In situ high-resolution transmission electron microscopy observation of photodecomposition process of poly-hydrocarbons on catalytic TiO₂ films. *Appl Phys Lett* 84(14):2542–2544. <https://doi.org/10.1063/1.1689747>
52. Yoshida K, Nanbara T, Yamasaki J, Tanaka N (2006) Oxygen release and structural changes in TiO₂ films during photocatalytic oxidation. *J Appl Phys* 99(8):084908. <https://doi.org/10.1063/1.2190721>
53. Zhang L, Miller B, Crozier P (2012) In situ analysis of TiO₂ photocatalysts under light exposure in the environmental TEM. *Microsc Microanal* 18(S2):1126–1127. <https://doi.org/10.1017/S1431927612007489>
54. Zhang L, Miller B, Crozier P (2012) CdS sensitized TiO₂ nanorod photocatalysts under light exposure in the environmental TEM. *Microsc Microanal* 18(S2):1298–1299. <https://doi.org/10.1017/S1431927612008343>
55. Yoshida K, Nozaki T, Tanaka N (2007) In-situ high-resolution transmission electron microscopy of liquid phase photocatalytic reaction that uses excited electrons by ionic liquid. *Microsc Microanal* 13(S02):982–983. <https://doi.org/10.1017/S1431927607072534>
56. Cavalca F, Laursen AB, Wagner JB, Damsgaard CD, Chorkendorff I, Hansen TW (2013) Light-induced reduction of cuprous oxide in an environmental transmission electron microscope. *ChemCatChem* 5(9):2667–2672. <https://doi.org/10.1002/cctc.201200887>
57. Griffiths JT, Zhang S, Rouet-Leduc B, Fu WY, Bao A, Zhu D, Wallis DJ, Howkins A, Boyd I, Stowe D, Kappers MJ, Humphreys CJ, Oliver RA (2015) Nanocathodoluminescence reveals mitigation of the Stark shift in InGaN quantum wells by Si doping. *Nano Lett* 15(11):7639–7643. <https://doi.org/10.1021/acs.nanolett.5b03531>
58. White ER, Howkins A, Williams CK, Shaffer MS (2015) Investigating the origin of luminescence in zinc oxide nanostructures with STEM-cathodoluminescence. *Microsc Microanal* 21(S3):1257–1258. <https://doi.org/10.1017/S1431927615007072>
59. Yang S, Tian X, Wang L, Wei J, Qi K, Li X, Xu Z, Wang W, Zhao J, Bai X, Wang E (2014) In-situ optical transmission electron microscope study of exciton phonon replicas in ZnO nanowires by cathodoluminescence. *Appl Phys Lett* 105(7):071901. <https://doi.org/10.1063/1.4893444>
60. Lim SK, Brewster M, Qian F, Li Y, Lieber CM, Gradečak S (2009) Direct correlation between structural and optical properties of III–V nitride nanowire heterostructures with nanoscale resolution. *Nano Lett* 9(11):3940–3944. <https://doi.org/10.1021/nl9025743>

61. Losquin A, Zagonel LF, Myroshnychenko V, Rodríguez-González B, Tencé M, Scarabelli L, Förstner J, Liz-Marzán LM, García de Abajo FJ, Stéphan O, Kociak M (2015) Unveiling nanometer scale extinction and scattering phenomena through combined electron energy loss spectroscopy and cathodoluminescence measurements. *Nano Lett* 15(2):1229–1237. <https://doi.org/10.1021/nl5043775>
62. Ringe E, DeSantis CJ, Collins SM, Duchamp M, Dunin-Borkowski RE, Skrabalak SE, Midgley PA (2015) Resonances of nanoparticles with poor plasmonic metal tips. *Sci Rep* 5(1):17431. <https://doi.org/10.1038/srep17431>
63. Zhao M, Bosman M, Danesh M, Zeng M, Song P, Darma Y, Rusydi A, Lin H, Qiu C-W, Loh KP (2015) Visible surface plasmon modes in single Bi₂Te₃ nanoplate. *Nano Lett* 15(12):8331–8335. <https://doi.org/10.1021/acs.nanolett.5b03966>
64. Williams RE, Carnevale SD, Kent TF, Stowe DJ, Myers RC, McComb DW (2014) Electron energy loss spectroscopy and localized cathodoluminescence characterization of GaN quantum discs. *Microsc Microanal* 20(S3):578–579. <https://doi.org/10.1017/S1431927614004619>
65. Fern GR, Silver J, Coe-Sullivan S (2015) Cathodoluminescence and electron microscopy of red quantum dots used for display applications. *J Soc Inform Display* 23(2):50–55. <https://doi.org/10.1002/jsid.278>
66. Sutter P, Wimer S, Sutter E (2019) Chiral twisted van der Waals nanowires. *Nature* 570(7761):354–357. <https://doi.org/10.1038/s41586-019-1147-x>
67. den Engelsen D, Harris PG, Ireland TG, Fern G, Silver J (2015) Symmetry-related transitions in the photoluminescence and cathodoluminescence spectra of nanosized cubic Y₂O₃:Tb³⁺. *ECS J Solid State Sci Technol* 4(12):R145–R152. <https://doi.org/10.1149/2.0011512jss>
68. Kumar S, Nehra M, Deep A, Kedia D, Dilbaghi N, Kim K-H (2017) Quantum-sized nanomaterials for solar cell applications. *Renew Sustain Energy Rev* 73:821–839. <https://doi.org/10.1016/j.rser.2017.01.172>
69. Zhu L, Wang ZL (2019) Recent progress in Piezo-phototronic effect enhanced solar cells. *Adv Func Mater* 29(41):1808214. <https://doi.org/10.1002/adfm.201808214>
70. Wang X, Tian W, Liao M, Bando Y, Golberg D (2014) Recent advances in solution-processed inorganic nanofilm photodetectors. *Chem Soc Rev* 43(5):1400–1422. <https://doi.org/10.1039/c3cs60348b>
71. Yang T, Zheng Y, Du Z, Liu W, Yang Z, Gao F, Wang L, Chou K-C, Hou X, Yang W (2018) Superior photodetectors based on all-inorganic perovskite CsPbI₃ nanorods with ultrafast response and high stability. *ACS Nano* 12(2):1611–1617. <https://doi.org/10.1021/acsnano.7b08201>
72. Duan X, Huang Y, Cui Y, Wang J, Lieber CM (2001) Indium phosphide nanowires as building blocks for nanoscale electronic and optoelectronic devices. *Nature* 409(6816):66–69. <https://doi.org/10.1038/35051047>
73. Ide Y, Liu F, Zhang J, Kawamoto N, Komaguchi K, Bando Y, Golberg D (2014) Hybridization of Au nanoparticle-loaded TiO₂ with BN nanosheets for efficient solar-driven photocatalysis. *J Mater Chem A* 2(12):4150–4156. <https://doi.org/10.1039/c3ta13769d>
74. Li H, Wang X, Xu J, Zhang Q, Bando Y, Golberg D, Ma Y, Zhai T (2013) One-dimensional CdS nanostructures: a promising candidate for optoelectronics. *Adv Mater* 25(22):3017–3037. <https://doi.org/10.1002/adma.201300244>
75. Wang W, Zhao Q, Laurent K, Leprince-Wang Y, Liao Z-M, Yu D (2012) Nanorainforest solar cells based on multi-junction hierarchical p-Si/n-CdS/n-ZnO nanoheterostructures. *Nanoscale* 4(1):261–268. <https://doi.org/10.1039/c1nr11123j>
76. Yang H, Zhou Y, Yang Y, Yi D, Ye T, Lam TD, Golberg D, Bao B, Yao J, Wang X (2018) Crystal facet engineering induced anisotropic transport of charge carriers in a perovskite. *J Mater Chem C* 6(43):11707–11713. <https://doi.org/10.1039/c8tc04961k>
77. Zhang C, Cretu O, Kvashnin DG, Kawamoto N, Mitome M, Wang X, Bando Y, Sorokin PB, Golberg D (2016) Statistically analyzed photoresponse of elastically bent CdS nanowires probed by light-compatible in situ high-resolution TEM. *Nano Lett* 16(10):6008–6013. <https://doi.org/10.1021/acs.nanolett.6b01614>
78. Zhang C, Tian W, Xu Z, Wang X, Liu J, Li S-L, Tang D-M, Liu D, Liao M, Bando Y, Golberg D (2014) Photosensing performance of branched CdS/ZnO heterostructures as revealed by

- in situ TEM and photodetector tests. *Nanoscale* 6(14):8084–8090. <https://doi.org/10.1039/c4nr00963k>
79. Han X, Wang L, Yue Y, Zhang Z (2015) In situ atomic scale mechanical microscopy discovering the atomistic mechanisms of plasticity in nano-single crystals and grain rotation in polycrystalline metals. *Ultramicroscopy* 151:94–100. <https://doi.org/10.1016/j.ultramicro.2014.11.035>
 80. Zhu Y, Milas M, Han M-G, Rameau J, Sfeir M (2012) Multimodal optical nanoprobe for advanced in-situ electron microscopy. *Microscopy Today* 20(6):32–37. <https://doi.org/10.1017/S1551929512000892>
 81. Ophus C (2019) Four-dimensional scanning transmission electron microscopy (4D-STEM): from scanning nanodiffraction to ptychography and beyond. *Microsc Microanal* 25(3):563–582. <https://doi.org/10.1017/S1431927619000497>
 82. Toyao T, Saito M, Dohshi S, Mochizuki K, Iwata M, Higashimura H, Horiuchi Y, Matsuoka M (2014) Development of a Ru complex-incorporated MOF photocatalyst for hydrogen production under visible-light irradiation. *Chem Commun* 50(51):6779–6781. <https://doi.org/10.1039/c4cc02397h>
 83. Toyao T, Ueno N, Miyahara K, Matsui Y, Kim T-H, Horiuchi Y, Ikeda H, Matsuoka M (2015) Visible-light, photoredox catalyzed, oxidative hydroxylation of arylboronic acids using a metal–organic framework containing tetrakis (carboxyphenyl) porphyrin groups. *Chem Commun* 51(89):16103–16106. <https://doi.org/10.1039/C5CC06163F>
 84. Shi E, Yuan B, Shiring SB, Gao Y, Akriti GY, Su C, Lai M, Yang P, Kong J, Savoie BM, Yu Y, Dou L (2020) Two-dimensional halide perovskite lateral epitaxial heterostructures. *Nature* 580(7805):614–620. <https://doi.org/10.1038/s41586-020-2219-7>
 85. Kwon O-H, Zewail AH (2010) 4D electron tomography. *Science* 328(5986):1668–1673. <https://doi.org/10.1126/science.1190470>
 86. Wang P, Zhang F, Gao S, Zhang M, Kirkland AI (2017) Electron ptychographic diffractive imaging of boron atoms in LaB₆ crystals. *Sci Rep* 7(1):2857. <https://doi.org/10.1038/s41598-017-02778-x>
 87. Song B, Ding Z, Allen CS, Sawada H, Zhang F, Pan X, Warner J, Kirkland AI, Wang P (2018) Hollow electron ptychographic diffractive imaging. *Phys Rev Lett* 121(14):146101. <https://doi.org/10.1103/PhysRevLett.121.146101>

Chapter 7

Magnetism In-Situ TEM



Renchao Che, Yong Peng, and He Tian

7.1 A Brief History of Magnetism In-Situ TEM

The research on magnetic materials has a long history. As early as 2000 BC, humans have discovered and used the natural ferroxide magnets. In current physics, Faraday discovered the electromagnetic induction phenomenon [1], Maxwell unified the electromagnetic theory [2] and Curie proposed the phase transition from the ferromagnetic to paramagnetic phase [3]. Research on magnetism has been gradually deepened. In the 1930s, the quantum mechanics theory has been proposed and the modern magnetism was synchronously largely completed [4]. Up to now, it has been widely accepted that all substances possess magnetic properties. Magnetism can be divided into paramagnetism, diamagnetism, ferromagnetism, antiferromagnetism, and so on [5]. One of the most important is ferromagnetism. Ferromagnetic materials are widely used in many aspects of life, such as motor, watch, hard disk, and magneto-resistive random-access memory (MRAM) [6–9]. Especially in the micro- and nano-scale, ferromagnetic materials play a functional role that other materials cannot replace. Therefore, it requires that ferromagnetic materials must be studied at the micro- and nano-scale, which poses great challenges to the research technology.

A very important characteristic of ferromagnetic materials is the presence of the magnetic domains. Magnetic domain structure refers to the small magnetized

R. Che (✉)

Laboratory of Advanced Materials, Shanghai Key Laboratory of Molecular Catalysis and Innovative Materials, Fudan University, Shanghai 200438, China
e-mail: rcche@fudan.edu.cn

Y. Peng

Key Laboratory of Magnetism and Magnetic Materials of Ministry of Education, School of Physical Science and Technology, Lanzhou University, Lanzhou 730000, China

H. Tian

Center of Electron Microscope, State Key Laboratory of Silicon Material, School of Material Science and Engineering, Zhejiang University, Hangzhou 310027, China

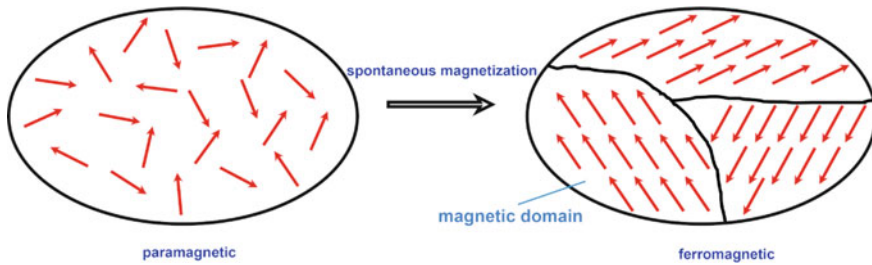


Fig. 7.1 The diagram of spontaneous magnetization and domain structure

regions with different magnetization directions [10]. Through the generation of the domain structure, the magnetostatic energy could be reduced in the spontaneous magnetization process and a stable magnetic structure could be obtained. As shown in Fig. 7.1, the domain structure in ferromagnetic materials contains many regions. Each region contains plenty of atoms. The magnetic moments of these atoms are neatly arranged within the magnetic domain. However, the magnetic moments of atoms in different domains are aligned in different directions. The interface between two neighbor domains is called the domain wall [10]. Most of the ferromagnetic materials have many domain walls. In the demagnetized state, the magnetic moments inside the magnetic domains are different and cancel each other. The sum of the overall moment vectors is nearly zero. So, the stray magnetic field is very tiny and the magnet will not display magnetism to the outside. When the magnet is magnetized, the whole magnet becomes a single domain, and the sum of the magnetic moment vectors is no longer zero. There is an obvious stray magnetic field near the magnet. In the study of ferromagnetic materials, the dynamic evolutions of domain structures and domain walls are essential for practical application and physical mechanisms of magnetics. Many techniques have been used to characterize the structures of magnetic materials.

In the beginning, magnetic powders have been used to study the magnetic domain structures by coating on the surfaces of ferromagnetic materials. This method is called the Bitter map [11]. But only superficial information of samples can be obtained by this method and the spatial resolution is not enough for many magnets, especially for the current development at the micro/nano scale. Later, with the discovery of the magneto-optic effect, the optical microscopes developed on the basis of Kerr effect and Faraday effect were popularized [12]. The spatial resolution of the optical microscope is also limited by the wavelengths of visible light, which only accurately characterize magnetic structures at the scale larger than micrometers [13]. Then, as for the development of the atomic force microscope (AFM) system, magnetic force microscopy (MFM) [14] was invented, but the spatial resolution of the magnetic microscope can only reach the level of tens nanometers, require an extremely smooth surface, moreover, and is extremely time-cost [15]. High-resolution transmission electron microscopy is a very important progress for the development of magnetism at the micro- and nano-scale [16, 17].

This is not a simple extension for the application of TEM. In the column of conventional TEMs, the electron beam is focused by the strong magnetic field of the objective lens [18], which provides the amplification as shown in Fig. 7.2a. Therefore, the sample must be placed in a strong magnetic field. For the ferromagnetic samples, the strong field can completely magnetize them, so it is impossible to observe the magnetic domain structure in the conventional TEMs. At the same time, the sample is also stressed in a strong magnetic field, which may be absorbed to the poles of the objective lens, resulting in a contamination or permanent damage of TEM and the interference of imaging. These factors make the characterization of magnetic materials in TEMs very hard. To solve these problems, the Lorentz transmission electron microscopy (LTEM) was invented, on which scientists tried to observe the magnetic samples without magnetization. The method is to close the objective lens near the sample and uses another lens to magnify the image. The LTEM utilized the Lorentz force of electron passing through the magnetic field in the imaging process. By modifying the defocus distance of the image, the domain walls can be observed. In this way, the observation of the magnetic sample could be achieved [19]. However, the spatial resolution of the LTEM has been obviously decreased in comparison with the traditional TEM image mode because the objective lens is turned off. In the 1980s, this technique was still being popularized and Lorentz TEM accurately revealed the magnetic domain structures of many materials [20]. Globally, Japan, the United States, the United Kingdom, and the Netherlands were the pioneers to develop and study Lorentz TEM. In particular, the JEOL Ltd (Japan), Philips Electronics (Netherlands), Brookhaven National Laboratory (USA), National Institute for Materials Science (Japan), and so on, have made outstanding contributions to the development of Lorentz TEM.

Electron holography is another one of the most important methods to characterize magnetic materials [22]. Gabor proposed the basic principles and experimental

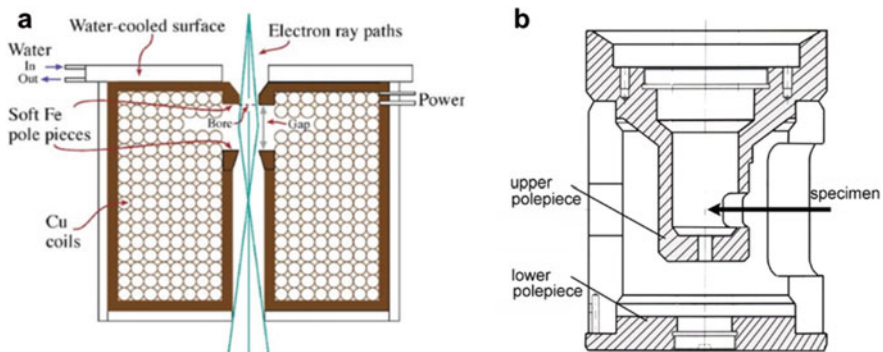


Fig. 7.2 The structure of the objective lens in normal TEM and special-design Lorentz TEM. **a** The objective lens in normal TEM (reproduced with permission from Ref. [18], Copyright 2009, Springer Nature). **b** The objective lens in special-design Lorentz TEM (reproduced with permission from Ref. [21], Copyright 2003, Elsevier)

methods of electronic holography in 1948. Next year, he first proposed the concept of holography in the article “Reconstruction of Wave Fronts in Electron Microscopy”, which includes two processes: one is the acquisition of the interference pattern of the object wave and the reference wave, and the other is the reconstitution of the sample image in the interference pattern [23]. In 1952, Gottfried and co-workers proposed the experimental method of electron biprism, which applied an electric field on both sides of the gold-sprayed glass filament, so as to deflect the passing electron beam and generate an interference pattern. Ten years later, Leith and co-workers successfully reconstructed clear information image with a laser beam with better coherence [24]. In 1986, Lichte coming from the University of Tübingen in Germany used a computer to digitally reproduce electronic holograms to correct spherical aberration. This method achieved a 0.15 nm resolution, providing an ideal method for high-resolution electronic holography [25]. With the increasing use of the field emission electron gun in TEM, electron holography technology is applied in many ways. Electron holography based on the Lorentz TEM can not only qualitatively observe the magnetic domain structure of samples but also quantitatively analyze the magnetic intensity inside the samples and the fine structure of the domain walls. With the improvement of the spatial resolution of TEM, the spatial resolution of Lorentz TEM is also gradually improved. At the beginning of the twenty-first century, JEOL Ltd first brought out a unique technology of placing the samples inside the pole of the objective lens [21] as shown in Fig. 7.2b. The iron coils of the lens will shield the magnetic field generated by the objective lens. Therefore, the magnetic sample can be observed without being magnetized when the objective lens is working. The point spatial resolution of this special designed Lorentz TEM is close to that of high-resolution TEM, which is about 0.15 nm. The spatial resolution of the corresponding electron holography was also increased to nearly 1 nm, which is the highest spatial resolution at that time.

In the 1980s, a new technology to analyze the domain structure in STEM mode was proposed, which is named as the differential phase contrast (DPC) technology [19, 26]. The FEI Company (USA, now Thermo Fisher Scientific) has delivered the commercialization of this technology. It used condenser lens to focus the electron beam on the sample and also closed the objective lens. Therefore, a Lorentz STEM mode could be achieved. Moreover, the annular dark field detector has been divided into several parts and the imaging information received by different parts is individual. Through the processing of the images received by different parts of detector, the domain structure of the magnetic samples could be achieved. The characterization of the magnetic domain structure is not only no longer limited to the bright-field images and dark field images in TEM mode but also extended to the STEM mode. Recently, the spherical aberration correctors are also used in Lorentz TEM and magnetic materials analysis techniques with atomic-scale spatial resolution expected in the near future.

Of course, for the in-situ magnetic experiments, Lorentz TEM technique is just the foundation and platform. With it, how to apply the magnetic field to the sample inside the electron microscope becomes the next challenge that needs to be solved. So far, two typical strategies have been commonly employed to solve this problem.

One is to apply a magnetic field by changing the current of the objective lens [27]. Turning off the objective lens prevents the sample from being magnetized. If the sample needs to be magnetized gradually, the current is injected into the objective lens gradually. Limited by the inherent direction of the magnetic field generated by the objective lens, this method can only apply a magnetic field that is perpendicular to the viewing plane, to the sample which cannot obtain a field parallel to the plane. As for the in-plane anisotropic materials, usually the horizontal component of the magnetic field on the easy axis is usually obtained by tilting the sample, and then the effect of the magnetic field on the domain structure is studied. This can introduce lots of uncertainty. The advantage of this method is that a large magnetic field can be obtained through the objective lens, which can be continuously adjusted from zero field to around 1 T (theoretically 3 T, the maximum magnetic field of objective lens). For the most of the magnetic material, the magnetic field of 1 T is enough to make them saturated. Meanwhile, with respect to the JEOL Lorentz electron microscope, the magnetic field of the objective lens has been completely shielded near the sample. No matter how the current is inside the objective lens changes, the magnetic field cannot be applied to the sample. So this method does not take any effect.

The other method is to modify the sample holder [28]. By attaching an electromagnet to the sample holder, a controllable magnetic field near the sample can be obtained. In this way, a horizontal magnetic field can be applied to the sample, and it facilitates the study of anisotropic samples. But the horizontal magnetic field applied to the sample can significantly deflect the incident electron beam, which means the horizontal field cannot be too big. Otherwise, the electron beam would be totally deflected, and so it cannot be imaged. So far, the horizontal magnetic field that can be applied in TEM is generally less than 1000 Oe, which is quite abundant for the most soft magnetic materials, but not for the half-hard and hard magnetic materials. This magnetic field is far from enough for them.

7.2 Current Technologies of Magnetism In-Situ TEM

This section briefly states the present situations and principles of magnetism in-situ TEM. There are five techniques to observe the magnetic domain structures in TEM: Fresnel mode which obtains domain wall structure by defocusing imaging [29], Foucault mode which obtains domain distribution by dark-field image [30], electron holography [31], DPC technique [32], and the mode magnetic circular dichroism of electron waves which can obtain spin distribution [33]. There are two ways to apply a magnetic field into the samples. One is to apply the magnetic field of the objective lens to the sample. The other is to apply an external magnetic field generated from the in-situ magneto-related sample holder to the sample. The basic principles and applicable scope of these technologies are described below.

7.2.1 *Conventional Imaging Methods in Lorentz TEM*

Fresnel mode [29], also called Lorentz electron microscope defocus mode, is the most commonly used mode for electron microscope observation of magnetic samples. This method is to obtain the domain structure via defocused imaging (Fig. 7.3), which is the most commonly function used in Lorentz electron microscopy [34]. In the conventional TEM bright field, the electron beam is parallel, which directly shines on the sample. Because of the differences of the domain structure inside the sample, the direction and angle of the deflection of the electron beam in different regions which resulted from the Lorentz force between the electron beam and material magnetization are also different after the electron beam passes through the magnetic sample. At this time, change is made at the focal length so that the pictures are imaged at the defocused status, where the bright and dark lines caused by the deflection of the electron beam can be seen. These lines are the distribution of domain walls of the magnetic samples. The magnetization directions of different domains can be obtained by analyzing the defocused state and the contrast of domain walls. By changing the focal length, a series of domain wall images can be obtained. Through linear fitting of defocusing quantity and contrast width of the domain walls, the width of the domain walls can be quantitatively analyzed, and some simple quantitative information can also be obtained. In addition, based on TIE formula [35], the distribution changes of the phase of electron wave after the electron beam passes through the magnetic sample can be obtained by digital reconstruction technology via several pictures with different defocusing quantities, in which the orientation of the magnetic domain structure inside the sample can be accurately analyzed. The advantage of this technique is that the domain walls can be observed in real-time. During the in-situ magnetic experiment, it is very convenient to observe the dynamic behavior of the domain walls. Nevertheless, in the process of defocusing, the spatial resolution of the imaging decreases and too much defocusing may lead to the appearance of the Fresnel interference fringe contrast on the sample, thus disturbing the imaging. According to the results obtained by the TIE technique, only qualitative analysis of domain orientation can be conducted, and it is difficult to accurately analyze the information, such as the magnetization of the sample. Moreover, the TIE technique is greatly affected by the contrast of samples. For monocrystalline or polycrystalline samples, the multiple scattering contrast caused by diffraction easily interferes with the results of TIE. However, the defocused imaging is still the most commonly used method to observe domain walls in LTEM.

Another mode, the Foucault mode [36], is also a traditional method. It uses the principle that after the electron beam passing through the magnetic sample, the diffraction points will split on the diffraction plane (Fig. 7.3). Utilizing the objective aperture to block part of the diffraction points after splitting and imaging part of the electron beam, the bright and dark contrast of different magnetic domain structures can be directly observed. This imaging method is similar to observing the distribution of crystals with different orientations by the dark field image and observing the distribution of different magnetic domains by the splitting diffraction points.

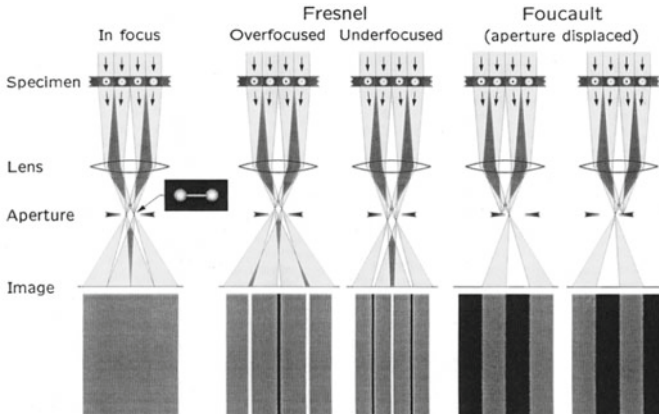


Fig. 7.3 The beam path of different observation methods in LTEM (reproduced with permission from Ref. [34], Copyright 1998, Springer Nature)

However, the Foucault mode has two practical difficulties. The first is the magnetization of the magnetic material that must be strong enough to make the splitting of the diffraction points much clear. If this splitting effect cannot be observed, the Foucault mode cannot be used to observe the magnetic domain. In addition, in order to observe the diffraction image of the sample in TEM, the objective lens must be activated. That is, the ordinary Lorentz electron microscope, which is observed by closing the objective lens, is also difficult to use the Foucault mode for imaging. Only specially modified JEOL Lorentz electron microscope can activate the objective lens without magnetizing the sample, so it is not convenient to observe in this mode.

7.2.2 *Electron Holography Technology*

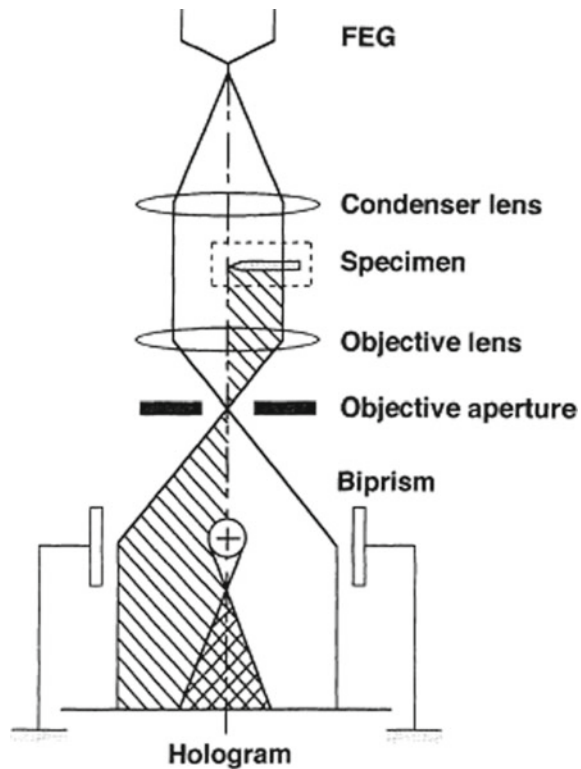
Electron holography is an important technique for analyzing magnetic materials in TEM. Electron holography mainly uses the interference between a beam of reference wave passing through the vacuum and a beam of object wave passing through a magnetic sample. Utilizing the digital reconstruction technique, collecting and analyzing the interference fringes indicate the changes of the electron wave passing through the magnetic sample. Then, the distribution of the magnetic moment in the sample is deduced from the phase changes [37, 38]. The most important feature of electron holography is that it can quantitatively analyze the distribution of magnetization in samples, and accurately estimate the directions of the magnetic moments of domain structure inside the sample, which is important for the analysis of some complex domain structures, such as magnetic Skyrmion [39].

Electron holography requires an attachment of an electron biprism in an electron microscope [40]. The electronic biprism is actually a silica glass filament with a

diameter about $0.35\ \mu\text{m}$. Its surface is plated with a thin layer of gold and connected to the positive pole of DC power supply. It can be adjusted by rotating 270° in the plane of the vertical lens barrel and installed at the location of the selected-area aperture. The holographic glass filament can be loaded with 0–400 V DC voltage, and two grounded metal plates are installed at the same distance on the both sides of the holographic filament, so that two electrostatic fields with opposite electric field directions are formed between the holographic filament and the two metal plates. With this method, there is an annular electric field around the wire. When an electron beam goes through this field, the beam on both sides of the biprism is deflected so that the beams converge and interfere with each other as illustrated by Fig. 7.4.

By regulating the voltage of the electron biprism, the area covered by the interference fringe can be regulated, so that the region of the electronic holographic signal acquisition can also be regulated. Typically, the greater the voltage applied to the electronic biprism, the larger the interference area of the electron beam obtained, and the higher the resolution of the hologram achieved, but the worse the contrast is obtained. However, the principle restricts the analysis area of electron holography to some extent. Only the sample information near the vacuum can be characterized, however, the property of the sample far from the vacuum cannot be estimated. Several years ago, the JEOL further launched an improved electronic holographic

Fig. 7.4 The principle and beam path of electron holography (reproduced with permission from Ref. [40], Copyright 2013, Springer Nature)



technology. By inserting two or three electron biprisms into the optical path of the electron microscope, the electron beam passing through any region can interfere with the electron beam passing through the vacuum. Meanwhile, multiple electron biprisms also help eliminate the Fresnel stripes, which is formed because of the huge defocusing of the electron biprisms when imaging. This makes the analysis of electron holography further improved.

The electronic hologram formulaically contains the intensity information and phase information of the object wave, and the Fourier and inverse Fourier transform can be performed to obtain the phase change of the electronic wave [40]. The change of electron wave passing through an object can be expressed as:

$$q(\vec{r}) = a(\vec{r}) \exp(i\phi(\vec{r})) \quad (7.1)$$

$a(\vec{r})$ and $\phi(\vec{r})$ are amplitude information and phase information, respectively. Due to the existence of the biprism, the object wave and the reference wave are rotated by $-\alpha_h/2$ and $\alpha_h/2$, respectively. Therefore, the wave function of the interference wave is:

$$g_h(\vec{r}) = a(\vec{r}) \exp\left[-\pi i \frac{\alpha_h}{\lambda} x + i\phi(\vec{r})\right] + \exp\left(\pi i \frac{\alpha_h}{\lambda} x\right) \quad (7.2)$$

The first part is the object wave, and the second part is the reference wave. The intensity of electronic holography can be expressed as:

$$I_h(\vec{r}) = |g_h(\vec{r})|^2 = 1 + a^2(\vec{r}) + 2a(\vec{r}) \cos\left(2\pi \frac{\alpha_h}{\lambda} x - \phi(\vec{r})\right) \quad (7.3)$$

Through Fourier transform:

$$\begin{aligned} F(I_h(\vec{r})) &= \delta(\vec{u}) + F\left[a(\vec{r})^2\right] \\ &+ F[a(\vec{r}) \exp(i\phi(\vec{r}))] * \delta\left(\vec{u} + \frac{\alpha_h}{\lambda}\right) \\ &+ F[a(\vec{r}) \exp(-i\phi(\vec{r}))] * \delta\left(\vec{u} - \frac{\alpha_h}{\lambda}\right) \end{aligned} \quad (7.4)$$

The above formula is a complex function, including three parts: centerband, which corresponds to a term related to the Fourier transform center and the background: $\delta(\vec{u}) + F\left[a(\vec{r})^2\right]$; up sideband $F[a(\vec{r}) \exp(i\phi(\vec{r}))] * \delta\left(\vec{u} + \frac{\alpha_h}{\lambda}\right)$; and down sideband $F[a(\vec{r}) \exp(-i\phi(\vec{r}))] * \delta\left(\vec{u} - \frac{\alpha_h}{\lambda}\right)$.

The upper and lower sidebands are conjugates of each other and contain the same information (amplitude and phase). When selecting the upper sideband or the lower sideband to move $\pm \frac{\alpha_h}{\lambda}$ to the center band and perform inverse Fourier transform:

$$F^{-1}\left[F\left[a(\vec{r}) \exp(i\phi(\vec{r}))\right] * \delta\left(\vec{u}\right)\right] = a(\vec{r}) \exp(i\phi(\vec{r})) \quad (7.5)$$

Then the phase change after the electron beam passes through the sample is obtained:

$$\phi(x, y) = \sigma \int \varphi(x, y, z) dz - \frac{e}{\hbar} \oint \vec{A}(x, y, z) \quad (7.6)$$

After amplifying the phase distribution graph by cosine function, some lines with equal phases can be obtained.

Electron holography is a technique for analyzing the electron wave phase. Besides the magnetic field, the electric field, element, thickness, and other factors will affect the change of the electron wave phase. Therefore, many factors must be taken into account in the analysis and processing of data. It also means that the electron holography can be used to not only analyze the magnetic properties of samples, but also estimate the charge distribution, thickness change, and internal potential distribution of samples [41–43]. As an example, Fig. 7.5 shows a cross-sectional sample of CoFeB film, whose hologram was captured by LTEM and the electron phase shift mapping was reconstructed through the hologram. Through the amplification of the phase mapping by cosine function, the black and white fringes are shown in Fig. 7.5c. It is seen that the density of fringes presents the magnetization intensity and the direction of fringes presents the direction of magnetization. Furthermore, the magnetization can be calculated and colored as shown in Fig. 7.5d. The colors present the direction of magnetization and the brightness presents the magnetization intensity. However, it can be easily found that the interface between vacuum and carbon coating is also colored to be pink, which is sure not to be a ferromagnetic material. It demonstrates that the disturbance of electronic signals cannot be simply removed by reconstruction and calculation.

In general, it has been reported that there are two methods in order to extract the information of phase changes of electron waves inside sample caused only by magnetic field. The first one is the reconstruction via the subtraction or sum of the front and back side phase distribution [44]. The phase distribution of the front side is firstly obtained and constructed by an electron hologram. Then, the sample is taken out from the TEM holder and flipped to another side to take electron hologram once again, and reconstruct to get the phase distribution. In these two conditions, the distribution of the phase changes caused by electrical signals cannot be affected by the flip of the sample. On the contrary, the distribution of phase changes caused by the magnetic signal can pick up a completely opposite signal because of chirality. By adding or subtracting the collected phase changes, the phase changes caused by pure magnetic signals and pure electrical signals after the electron beam passes through the sample can be obtained, which can make the quantitative analysis accurate.

The second method is to collect the results of electron holography above and below the Curie temperature of the ferromagnetic materials [41, 45]. Above the Curie temperature, ferromagnetic samples lose ferromagnetism and exhibit paramagnetism. At this state, the electron hologram captures electrical signals completely. While below the Curie temperature, the collected signal is the sum of the magnetic

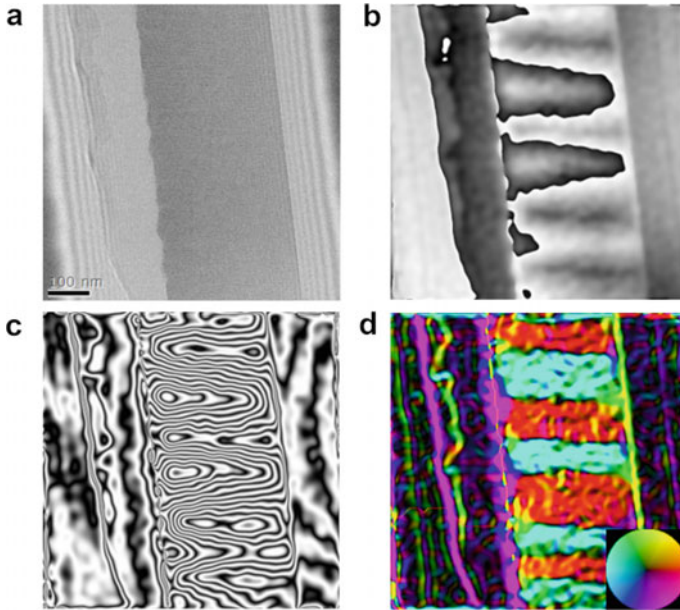


Fig. 7.5 An example of electron holography. **a** The hologram captured by LTEM. **b** The reconstructed phase mapping. **c** The phase mapping amplified by the cosine function. **d** The calculated magnetization mapping

and electrical signals. Thus, by subtracting the two images, a pure magnetic signal can be obtained.

The first method is more suitable for quantitative analysis. However, it is difficult to use if the magnetic field is synchronously applied. At the same time, this method needs to reload the sample by flipping its back-side, which means the two images cannot completely overlap each other. In post-processing, it is difficult for the two images to exactly correspond in position and angle. The second method is more suitable for the in-situ testing of the synchronous application of the magnetic field. But it requires a sample holder that provides in-situ heating function, and the Curie temperature of the sample must be within the temperature range covered by the holder. In fact, this is a combination of various in-situ electron microscopy techniques.

7.2.3 *Differential Phase Technology*

Different from the above three methods, the DPC (differential phase technique) is a STEM-based imaging technique [43, 46, 47]. STEM mode in the Lorentz electron microscope was first realized by using a condenser lens. When it is performed, the objective lenses are closed first of all. Next, the annular dark field image probe of

the modified TEM is divided into four fan segments (now more). Every segment can independently receive scattered electrons and form images. In the STEM mode, the beam is directly focused on the sample, not parallel. The deflection of the magnetic sample to the electron beam becomes more complicated. But in the dark field, because the magnetic sample deflects the electron beam, the electron counting rate received by the four probes is no longer uniform. By differential calculation of the imaging results of the four probes, the Lorentz force occurred between the travel of electron beam and magnetic moments of the magnetic materials can be obtained. Then the distribution of the magnetic moment inside the sample can be calculated (Fig. 7.6). Therefore, in order to obtain an accurate magnetic moment distribution, the key of DPC is to ensure that the signals collected by the four dark field probes must be completely consistent when the electron beam passes through the vacuum.

Compared with electronic holography, DPC has the advantage of obtaining the magnetic structure information of any region in the sample [32]. There is no need to insert multi-stage plug-ins in the optical path of TEM, which is relatively simple. However, it is difficult for the DPC to dynamically carry out the analysis of domain wall movement by exerting a continuous magnetic field to the sample through the objective lens. This is because, when the objective lens applies a magnetic field on the STEM optical path, the electron beam originally focused by the concentrator will not converge on the sample, and the entire light path will be affected by the magnetic field of the objective, which requires complex adjustments to restore. Therefore, every time the magnetic field is changed, it needs to make a complicated adjustment

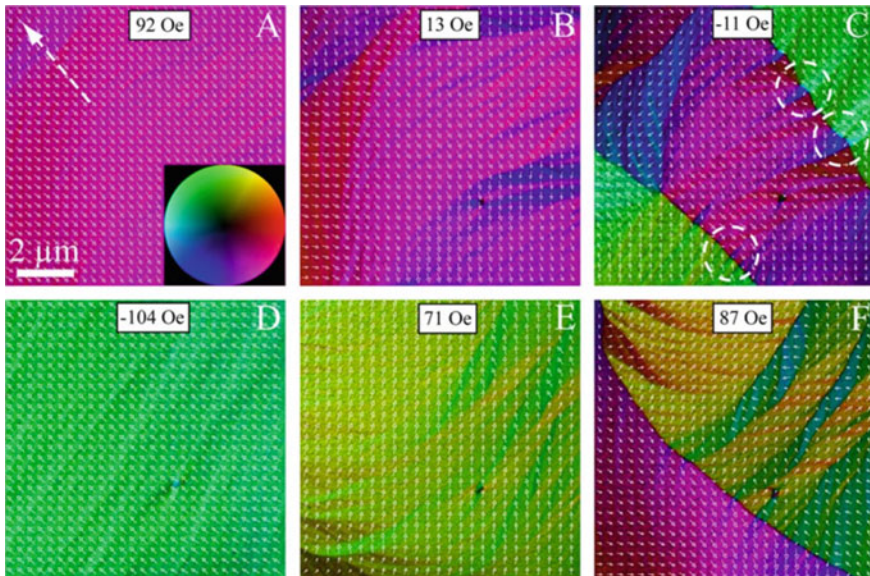


Fig. 7.6 The in-situ domain structure observation of CoFeB/IrMn film by DPC technology (reproduced with permission from Ref. [43], Copyright 2009, Elsevier)

of the light path, which makes the in-situ test very complicated, or maybe impossible. Furthermore, it is also difficult to quantitatively analyze the magnetization of magnetic samples. To some extent, similar to TIE, the DPC can also be affected by crystal orientation, diffraction contrast, and other factors, leading to wrong signals or results.

7.2.4 Energy-Loss Magnetic Chiral Dichroism in TEM

EMCD (Energy-loss Magnetic Chiral Dichroism) is an emerging technique of TEM in recent years [43]. A Belgian research group first invented and improved this technology. The technique is quite similar with the principle of X-ray magnetic circular dichroism in synchrotron radiation [48], but it also combines electron beam diffraction technology, dark field imaging technology, electron energy loss spectrum (EELS) technology [49], electron holography technology, and many other aspects in TEM [50], which is one of the frontiers of the development and research of TEM. The initial EMCD technique is to rotate a magnetic single crystal material to a double-beam diffraction condition. By analyzing its electron wave phase, it can be estimated that, at this time, the phase difference of the electron wave that is in both ends of the perpendicular bisector of the line between the two brightest diffraction points is exactly $\pi/2$. This has the same physical properties as left-handed or right-handed X-rays [48], which is illustrated in Fig. 7.7c. At this time, on utilizing an objective aperture, after collecting the energy loss spectrum of these two parts of electrons passing through the sample, the EMCD signal spectrum of this atom can be obtained by making a difference between the two energy loss spectra, which is shown in Fig. 7.7a. By analyzing the spectral line, the overall situation of the magnetic moments in the sample can be obtained, and the proportion of the spin magnetic moment and orbital magnetic moment in the atomic magnetic moment can be analyzed. It is very important for studying the spin-orbit coupling of the magnetic materials. At present, this technology is still in the process of perfection. In STEM mode, it is the current research frontier that the electron beam passes through an aperture of a specific shape to gain an electron wave with specific phase difference and apply it to EMCD analysis.

7.2.5 Application of Magnetic Field by Objective Lens

Utilizing objective lens is the most commonly used method to apply a magnetic field to samples in situ TEM [51]. By the control of the current flowing through the objective lens, the magnetic field applied by the objective lens on the sample can be precisely controlled. Besides, the advantage of this technique is the ability of applying very high magnetic field to the sample, theoretically the maximum field of objective lens as mentioned above. By changing the direction of the objective

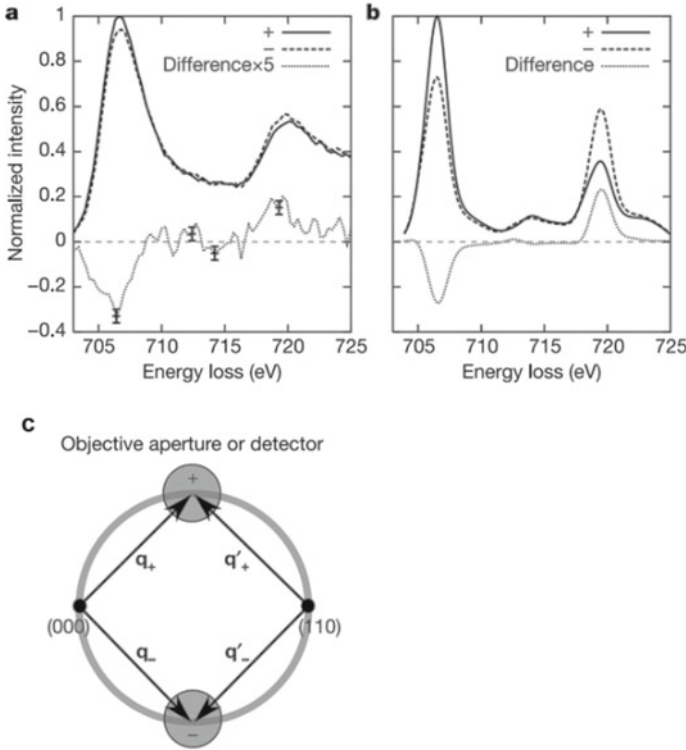


Fig. 7.7 The principle and results of EMCD. **a** The EMCD curves captured in TEM. **b** The XMCD curves captured in synchrotron radiation. **c** The method of capturing the EMCD curves. (reproduced with permission from Ref. [48], Copyright 2006, Springer Nature)

current, it also owns the ability of applying a reverse magnetic field. However, it is noted that after the application of the magnetic field to the sample, the optical path rotates as a whole, and the magnification of the sample changes as well, which is an important problem in the post-processing analysis and must not be ignored.

7.2.6 Application of Magnetic Field by Magnetic Holder

The second method is to apply a magnetic field to the sample by modifying the sample holder [28, 52]. There are various designs for this modification, but overall the purpose is to add a small electromagnet near the sample and further use precision source meter outside the TEM to generate a magnetic field. Figure 7.8 shows an early-stage designed holder for LTEM [53]. In the specially customized LTEM of JEOL, in order to match the in-situ sample holder to analyze the magnetic samples, a two-stage correction coil is intendedly added in the light path of the electron

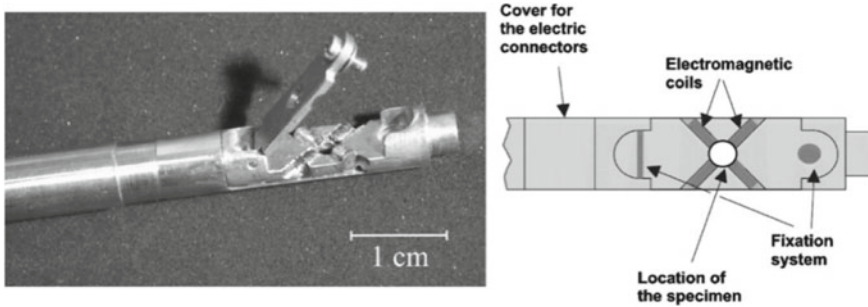


Fig. 7.8 The in-situ magnetical holder designed for Philips CM30 Lorentz TEM (reproduced with permission from Ref. [53], Copyright 2003, Elsevier)

microscope to offset the deflection of the electron beam caused by the electromagnet of holder. Even so, the added horizontal magnetic field typically cannot exceed 1000 Oe. Besides, a too large magnetic field will make the deflection coil uncorrectable. In such a condition, the morphologies of samples under high field will be deformed to a certain level. In the TEM optical path, the alignments of concentrator astigmatism, objective astigmatism, and electron beam voltage center are also affected by the horizontal magnetic field. Therefore, this method is suitable for the study of soft magnetic materials with small coercive force.

7.3 Research on Magnetism In-Situ TEM

In the magnetic field, the explorations of magnetism in-situ TEM have gained great achievements, which include the following aspects: rare earth permanent magnet materials [54], the soft magnetic thin films [55], ferromagnetic exchange coupling systems [56], magnetic micro/nanoparticles [57], magnetic phase change materials [58], magnetic skyrmions [59], and so on. Herein, several aspects are chosen to briefly introduce.

7.3.1 Traditional Magnetic Materials In Situ TEM

The studies on permanent magnets have been a long history [60]. At present, the development of permanent magnets is mainly divided into three generations. The first generation was ferrite materials, such as strontium ferrite, barium ferrite, and so on. Later, in the 1930s, the carbon steel alloy was found to have excellent performance of a permanent magnet. And AlNiCo alloy has become the second generation of permanent magnetic material due to the high Curie temperature and excellent temperature stability. It has been widely used in various aspects including instruments, meters,

electrical appliances, and aerospace, even until now has not been completely replaced [61]. However, in the 1960s, rare earth permanent magnet materials were discovered and the permanent magnet materials entered into the third generation, in which SmCo and NdFeB were representative and gradually became the mainstream. So far, the permanent magnet with the largest magnetic energy integration is still the rare earth permanent magnet material. The development of rare-earth permanent magnet materials also makes rare-earth minerals become important resources with strategic value [62, 63]. In Lorentz electron microscope, the research on rare earth permanent magnet materials is very extensive. At present, due to the rarity of rare earth, the output of Nd, Sm, and other elements is not high, and is difficult to meet the growing demand. In the research of permanent magnet materials, there are several significant development directions. The first is to use rich rare earth elements to replace the original poor rare earth elements, such as, the use of Ce, Dy, and others to replace Nd, which sacrifices a small amount of performance in exchange for a large number of cost reduction [64, 65]. The second is to combine the permanent magnet material with some soft magnetic materials by means of composite of various materials [66]. In other words, the high coercive force of the permanent magnet material is maintained while the high saturation magnetization of the soft magnetic material is retained, so as to increase the magnetic energy product of the composite material. No matter which direction develops, the most important thing in these studies is to explore the mechanism of coercivity of permanent magnet materials, which is for improving coercivity by enhancing the pinning ability of the magnetic moment and magnetic domain structure inside the materials. In situ LTEMs are required to observe and analyze the motion process of the magnetic domain walls. At present, doping in NdFeB nonmagnetic grain boundary phase can effectively improve the coercive force as observed in the TEM (Fig. 7.9) [67]. The nonmagnetic grain boundary phase can effectively block the movement of the magnetic domain wall, reduce the exchange coupling effect between NdFeB grains and improve the energy barrier, which improves the coercivity and BH_{\max} [68, 69]. This kind of research on magnetism in situ TEM not only makes a great contribution to the development of magnetism in science, but also to the engineering and practical applications of Lorentz electron microscopy.

In addition, traditional soft magnetic materials have also been widely studied in the Lorentz electron microscope, such as iron-base alloy materials used in transformers, permalloys, Fe-based and Co-based amorphous alloy materials which gradually emerge in recent years [70–72]. Lorentz electron microscope can clearly observe the rich magnetic domain structures inside soft magnetic materials, especially the fine structures of the magnetic domain walls, such as Bloch line, Bloch point, cross-tie domain, various kinds of magnetic vortex structures, and the motion mechanisms of these structures under the stimulus of the external magnetic field [73–75].

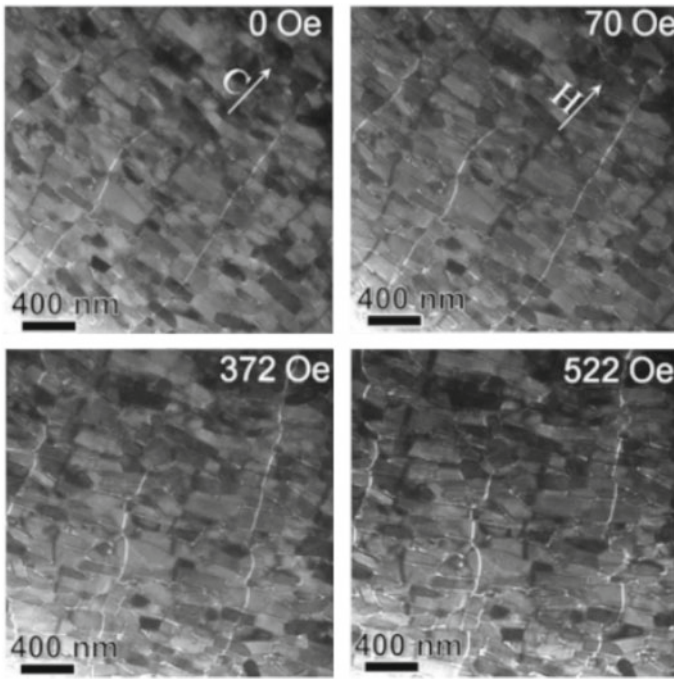


Fig. 7.9 The in-situ domain structure behavior of NdFeB captured by Lorentz TEM (reproduced with permission from Ref. [67], Copyright 2015, Elsevier)

7.3.2 Magnetic Thin Films In Situ TEM

Magnetic thin-film materials are widely used in device applications, especially in the field of spintronics, spin valve structures, tunnel junction structures, and so on, which are realized through multi-layered film composites [76, 77]. The study of magnetic domain structures of magnetic thin films is also an important aspect of magnetism in-situ TEM [78, 79]. In particular, the exchange bias effect caused by ferromagnetic and anti-ferromagnetic interface is the core issue, which is the basis of spintronics and the most important research topic of magnetism in the late twentieth century [80]. However, the mechanism of the exchange bias effect has not been fully understood until now. According to the traditional view, there are uncompensated magnetic moments on the anti-ferromagnetic surface, and these magnetic moments interact with the ferromagnetic materials in exchange coupling, so that the ferromagnetic materials have a unique unidirectional anisotropy in the process of magnetization reversal, that is, the deviation of the hysteresis loop. However, according to the theoretical calculation of the bias field, the bias field is of several orders of magnitude larger than the actual experimental data. Even some anti-ferromagnetic surface magnetic moments under the condition of full compensation still can detect strong exchange bias effects. That is to say, the traditional theory is deficient, which needs to

be further rectified. Lorentz transmission electron microscope and magnetism in-situ TEM play an important role to further improve the understanding of the exchange bias effect [81]. By observing the spin structure of the interface with high resolution and the distribution of the spin structure near the interface after applying the magnetic field in situ TEM, it can be judged that the spin inside the ferromagnetic layer is not affected by the anti-ferromagnetic material and presents a spring structure. This demonstrates that under the stimulus of the external magnetic field the anti-ferromagnetic material in the thin layered film is more likely to be affected by the ferromagnetic material and spin rotation, which has been also been proved by XMLD data [82, 83].

What's more, the Lorentz TEM could directly observe the magnetic domain structure of the bilayer film. As shown in Fig. 7.10, from the dynamic domain structure behavior, it can be easily found that the IrMn layer gives rise to an inhomogeneous strong pinning effect [55]. Only about 1/6 of the AFM interface area provides a strong pinning effect. This work gives the apparent and convincing evidence to understand the pinning mechanism in the FM/AFM exchange bias system (Fig. 7.10).

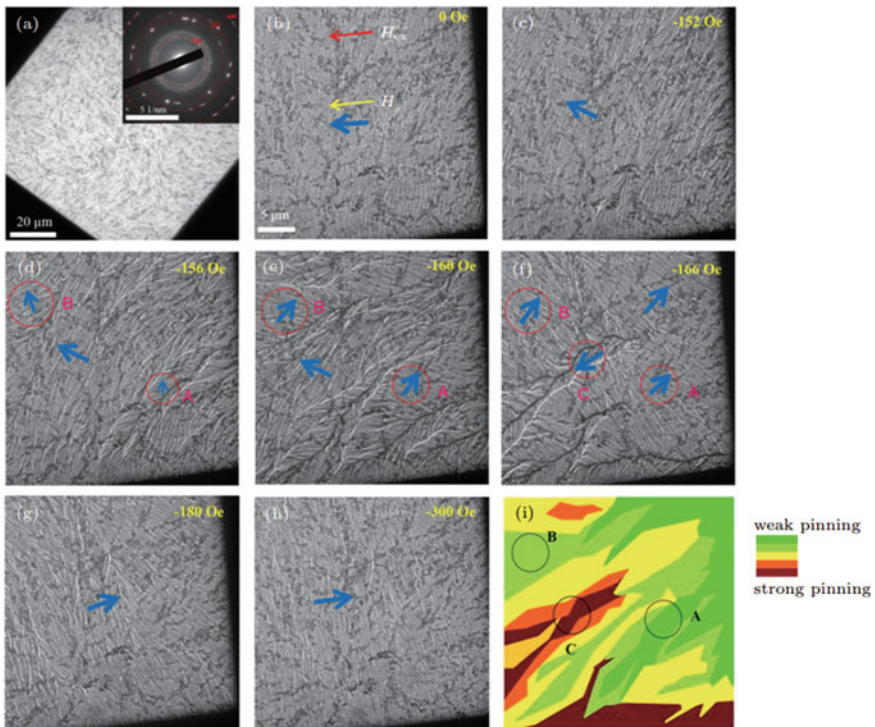


Fig. 7.10 The in-situ domain structure behavior of CoFeB/IrMn bilayer film captured by Lorentz TEM (reproduced with permission from Ref. [55], Copyright 2018, Chinese Physical Society)

7.3.3 Magnetic Nanowires/Particles In Situ TEM

The investigations on magnetic domain structures of magnetic nanowires and magnetic nanoparticles have been a very challenging subject. Most techniques fail to distinguish magnetic moment distributions at the nanoscale. LTEM and high-resolution electronic holography provide important methods. Because the size of the particles is very small, most magnetic particles at the nanoscale are single-domain structures. It is difficult to observe the existence of an obvious magnetic domain wall(s) inside them, which means that Fresnel model and Foucault model cannot accurately observe the magnetic moment distribution of magnetic nanoparticles. Electronic holographic technology with higher resolution is particularly useful and critical in this case. By analyzing the phase of the electron wave, the spin distribution inside the magnetic nanoparticles and the stray field distribution around them can be clearly unveiled (Fig. 7.11), revealing an important technical method for the analysis of the exchange coupling between magnetic nanoparticles.

Especially in the absorbing material, the microwave absorption ability of the composite material can be effectively improved by growing a large number of magnetic particles on the conductive carbon tube [85, 86]. This is because a huge

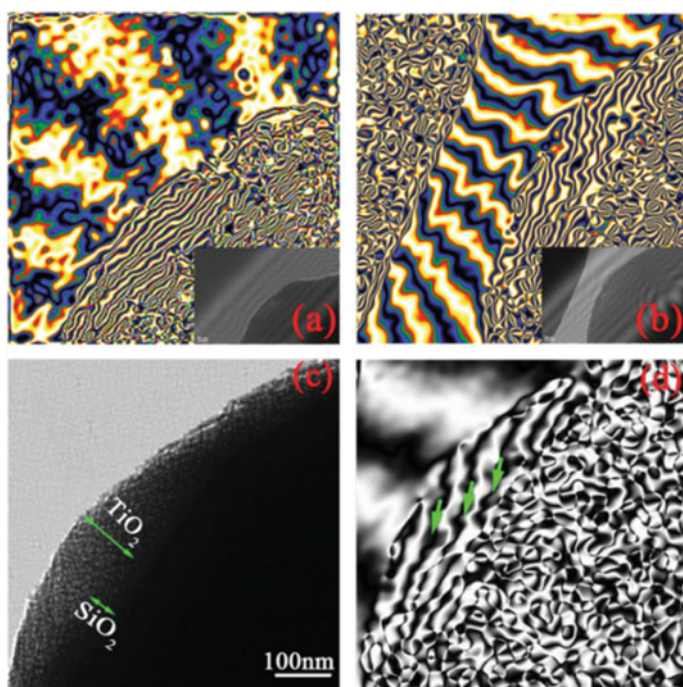


Fig. 7.11 The magnetic stray field of CoNi@SiO₂@TiO₂ nano-particle (reproduced with permission from Ref. [84], Copyright 2015, John Wiley and Sons)

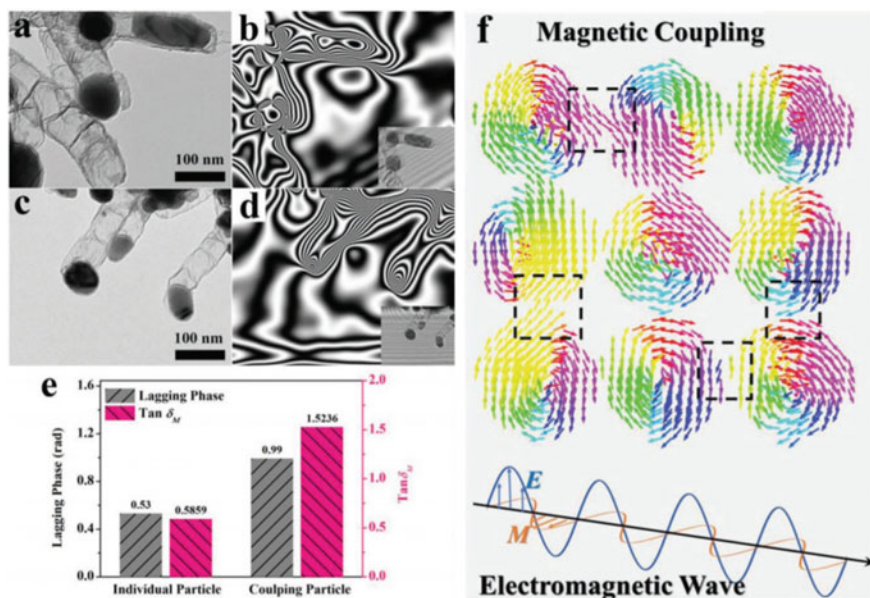


Fig. 7.12 The magnetic coupling network between nano-particles (reproduced with permission from Ref. [85], Copyright 2019, John Wiley and Sons)

magnetic coupling network is formed among the evenly distributed magnetic particles on the carbon tube network. After entering the magnetic coupling network, the electromagnetic wave will be rapidly attenuated and absorbed, and the energy will be converted into internal thermal energy through the vibration of the magnetic moment and completely consumed. LTEM and electron holography can be used to analyze the magnetic coupling network, as demonstrated in Fig. 7.12. This study is significant for the development and design of absorbing materials [87].

As for the nanowires/particles, except for the study on the localized quantitative analysis of magnetization and magnetic induction density distribution, the dynamical study of the magnetization and magnetic induction reversal process can also be further discovered by LTEM and electron holography techniques. As an example of Fig. 7.13, the magnetic induction maps of the NiFe_2O_4 nanowire under different magnetic fields were investigated, in which an external magnetic field was applied by a dedicated magneto-electrical TEM holder [28]. The magnetic field was applied along the easy axis of the shape anisotropy as guided by white arrows and different field strengths were applied. The red arrows represent the direction of in-plane projected magnetic induction inside the nanowire. This work directly visualized that the shape anisotropy dominantly governs the magnetic behaviors of the NiFe_2O_4 nanowire and the magnetization reversal mechanism of the nanowire is in curling rotation mode [28]. These listed examples vividly demonstrate the importance and essentials of magnetism in situ TEM in the intrinsic mechanism explorations of magnetic materials.

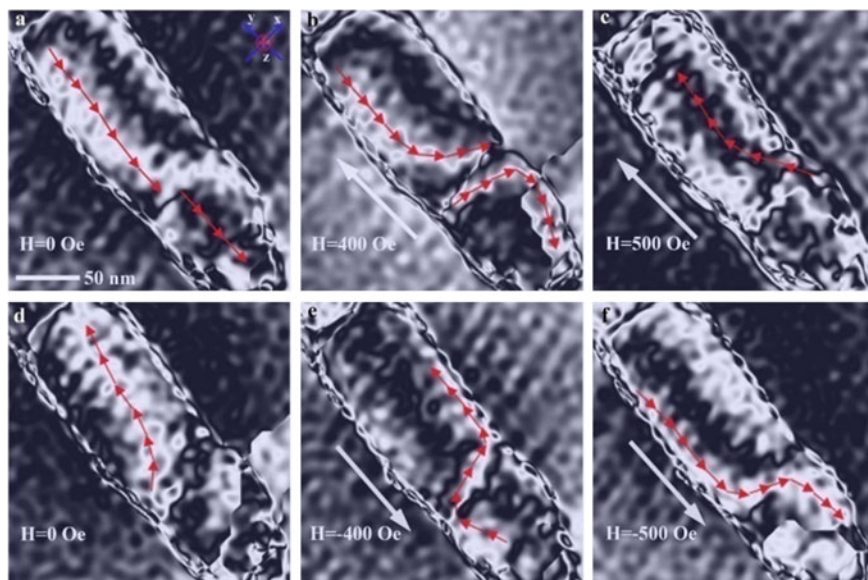


Fig. 7.13 Magnetic induction maps of the NiFe_2O_4 nanowire under different magnetic fields (reproduced with permission from Ref. [28], Copyright 2018, Royal Society of Chemistry)

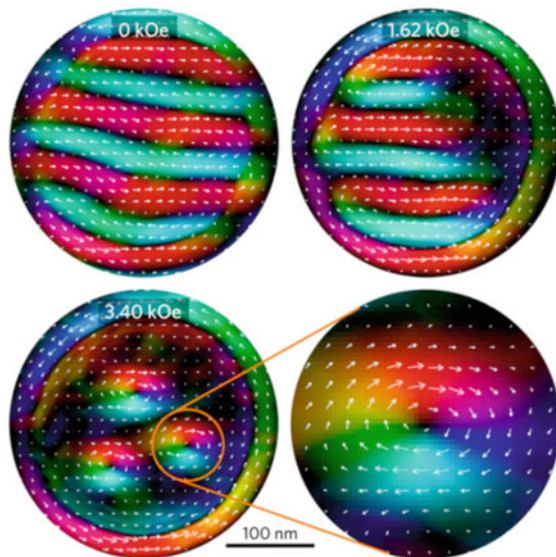
7.3.4 Magnetic Skyrmion In Situ TEM

Magnetic Skyrmion is nanoscale magnetic whirl with nontrivial topology, which is similar to the magnetic vortex [88]. However, the spin texture of Skyrmion is not only continuously changing in the plane but also changing out of the plane. It can be considered as a circular 360° Bloch-type domain wall or circular 360° Néel-type domain wall [89], which corresponds to Bloch-type Skyrmion [90] and Néel-type Skyrmion [91], respectively. These special spin structures result from Dzyaloshinsky–Moriya interaction (DMI) in the materials [92, 93]. After the proposal of race track memory [94], the magnetic Skyrmion is highly applied into future memory devices. The first experimental real-space observation of Skyrmion was carried in the Lorentz TEM by Xiuzhen Yu [95]. In recent a dozen of years, the research of magnetic Skyrmions is one of the hottest topics in the field of condensed matter physics and spintronics [96].

The Skyrmions in FeGe or other pure materials require strict conditions to appear, which include low temperature, appropriate magnetic field, and geometric shape [97]. Unlike other magnetic domain structures, the Skyrmions have unique properties of particles. So, the relationship between morphology of Skyrmions and formation conditions is the key point for the understanding of intrinsic mechanisms and development of practical applications. In virtue of the Lorentz TEM, a lot of relative works have been published. As shown in Fig. 7.14, the spin structure in FeGe is helical without the magnetic field [98]. When the applied field increases, the helical

structure gradually evolves into the Skyrmion structure. The apparent difference between Skyrmion and vortex is the intensity and the direction of magnetic moments inside. The Skyrmion changes both the intensity and vortex but does not change inside moment intensity direction. Therefore, the Lorentz TEM is a powerful technology to study the Skyrmions. The investigations of Skyrmion based on in-situ TEM technology have been widely accepted and become overwhelming. As shown in Fig. 7.15, the magnetic phase transition process of FeGe nanodisk has been investigated from 100 to 270 K [99]. It is found that the packed Skyrmion lattice only appears above about 200 K. The required magnetic field of Skyrmion decreases as the temperature is increasing. It means that the high-density Skyrmions could be achieved near the Curie temperature and the required magnetic field is minimum, which is very critical for their applications. Furthermore, if the angle of the magnetic field changes, the magnetic phase transition process is also changed. Figure 7.15b reveals that when the magnetic field is tilted to about 10° the required magnetic field of the packed Skyrmion lattice will be the minimum. Using this technology, the interaction between individual magnetic skyrmions as well as between skyrmions and edges can be directly evidenced [100], demonstrating the importance of the magnetism in-situ TEM technology.

Fig. 7.14 The evolution process of magnetic Skyrmion by varying the magnetic field (reproduced with permission from Ref. [98], Copyright 2016, National Academy of Sciences, U.S.A.)



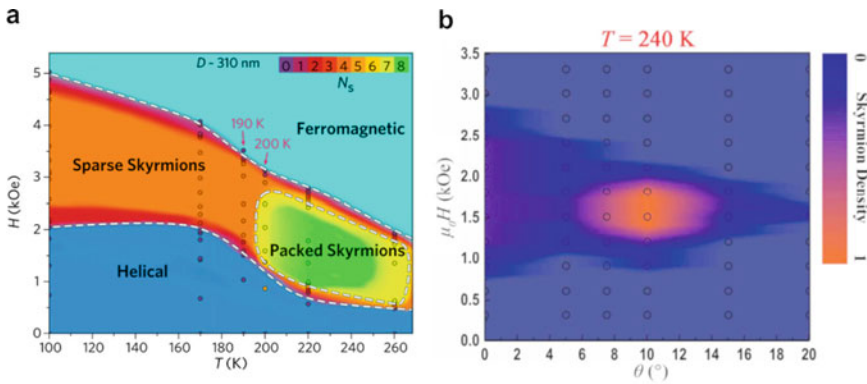


Fig. 7.15 The phase diagrams of FeGe Skyrmions. **a** The H-T phase diagram of FeGe nanodisk (reproduced with permission from Ref. [98], Copyright 2016, National Academy of Sciences, U.S.A.). **b** The tilted angle versus magnetic field phase diagram of FeGe slice (reproduced with permission from Ref. [99], Copyright 2015, American Chemical Society)

7.3.5 Other Magneto-Related Experiments In Situ TEM

Under more circumstances, magnetic materials and devices as functional units are employed to assess their physical behavior under the stimuli of coupling multi-fields [101]. Objective lens in LTEM can primarily realize the load of the magnetic field as one independent variable, whilst in-situ TEM holder can introduce the sample other different field to satisfy the interaction of coupling multi-fields, such as thermal, mechanical, electrical field. Therefore, magnetism in situ TEM under multi-field stimulus can be performed, providing an expanding research ability for the exploration of magnetism science.

Magnetic phase change materials are one group of very important functional materials. Understanding the evolution of magnetic domain in the process of thermomagnetic phase change is of great significance to realize industrial application of these materials. Combined with Lorentz TEM and in-situ heating or cooling holder, the evolution of magnetic domain during thermomagnetic transitions can be seen clearly and intuitively at the micro/nano scale [102, 103]. Generation and control of nanometric magnetic skyrmions have great potential in spintronics applications. Many attempts have been made to current-driven motion of the skyrmions. Combined with Lorentz TEM and in-situ electricity holder, this process can be implemented at a microscopic scale. Figure 7.16 shows the Lorentz TEM images and diagram of a microdevice for the observation of current-driven skyrmion motion [90]. Near-room-temperature motion of skyrmions driven by electrical currents in a microdevice composed of the helimagnet FeGe was demonstrated by this technology [90]. In addition, mechanical control of the motion of skyrmions is also an important approach in spintronics. Combined with the Lorentz TEM and in-situ mechanical holder, this process can also be implemented. Figure 7.17 presents the device structure and observed Lorentz TEM images of the skyrmion crystal before and after uniaxial

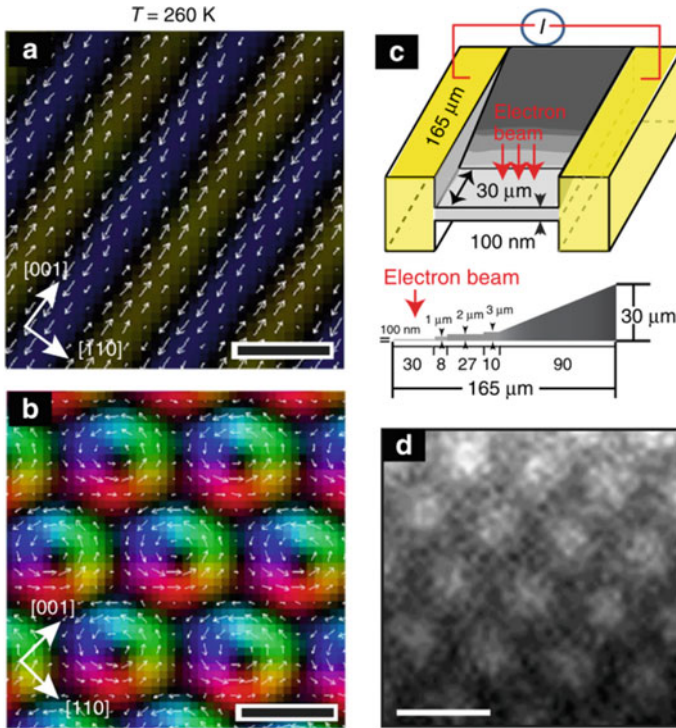


Fig. 7.16 Lorentz TEM images and diagram of a microdevice for the observation of current-driven skyrmion motion (reproduced with permission from Ref. [90], Copyright 2012, Springer Nature)

tensile strain. This study revealed that only 0.3% anisotropic strain can induce very large deformation in magnetic skyrmions, as well as distortion of the skyrmion crystal lattice in the FeGe [104].

Beside the modification of the TEM holder for magneto-related in situ experiments, the Lorentz TEM itself can be modified for the purpose of multi-field stimulus. In order to map the light-induced magnetization changes in the bilayer system, the TEM was modified to allow for in-situ femtosecond laser excitation. Figure 7.18 shows a corresponding result, which was used to study the schematic diagram and optically induced magnetic vortex–network. The author demonstrated the light-induced formation of a magnetic vortex–antivortex texture and analyzed its structural properties by this technology. Meanwhile, this work also provides a general access to a novel magnetic structure on nanometer length scales [105].

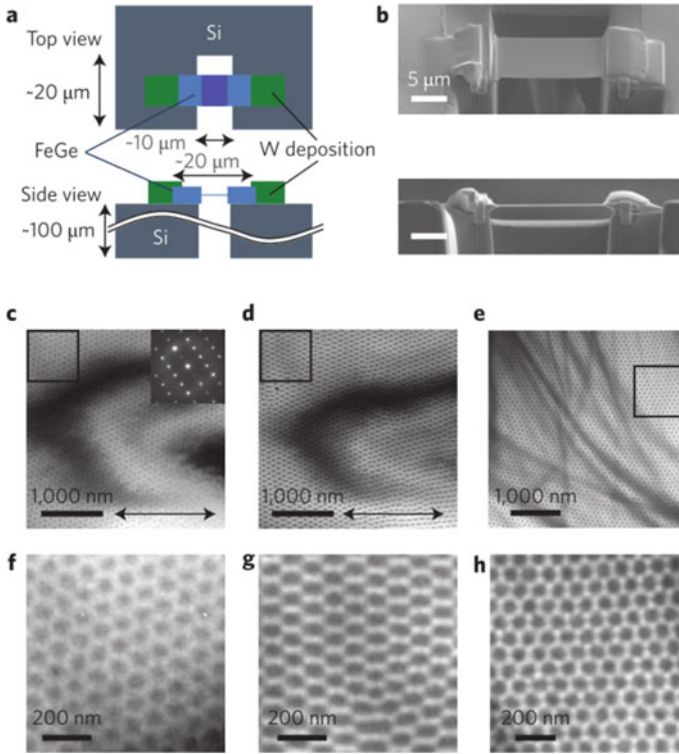


Fig. 7.17 Device structure and observed Lorentz TEM images of the skyrmion before and after uniaxial tensile strain (reproduced with permission from Ref. [104], Copyright 2015, Springer Nature)

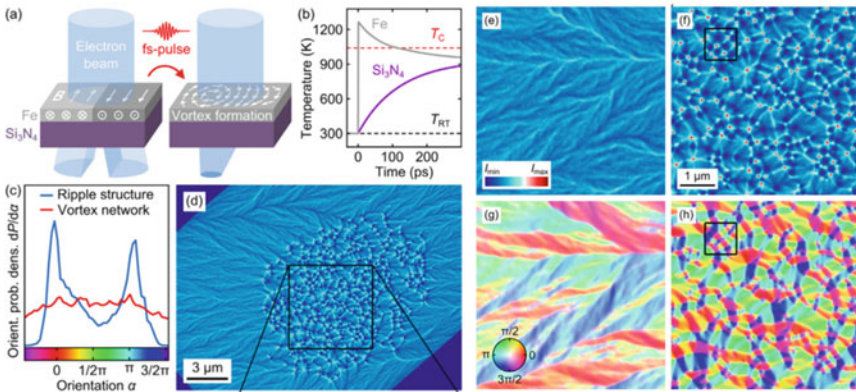


Fig. 7.18 Optically induced magnetic vortex-antivortex network (reproduced with permission from Ref. [105], Copyright 2017, American Physical Society)

7.4 Conclusions and Outlook

The magnetism in-situTEM has played an irreplaceable role in the research of magnetic materials and spintronics. With the continuous progress of TEM technology, it should be an extremely important direction of studying the magnetic mechanisms of magnetic materials and spintronics at the micro/nano scale by TEM or LTEM. There are two main development directions of magnetism in-situ TEM.

The first is a combination of in-situ techniques. At present, with the gradual development and maturity of the in-situ testing techniques of TEM, a more important research trend is to combine various in-situ techniques to form the analysis of materials under the condition of multi-physical field coupling. Especially for functional materials, such as magnetic materials and so on, it is very important for the development of magnetism and the application of magnetic materials to study the transition mechanism of the magnetic domain structure under different temperatures, electric field, and electric current. After the introduction of magnetic random access memory and track memory, the use of current to control the magnetic moment of magnetic materials has become the main research direction of magnetic memory. Various prototype devices based on STT and SOT principles have been proposed and developed. This requires us to conduct a detailed analysis of the working mechanism of the whole process at the micro/nano or even atomic scale, which needs to apply current and magnetic field to the magnetic material at the same time, and even change the temperature of the materials [106]. Only in this way the working state of the simulator can be more real. At present, a lot of work has been done to analyze the magnetic properties of materials by means of multi-physical field coupling in TEM.

Another important development trend is to analyze the magnetic moment distribution of samples at a higher spatial resolution. It is a natural requirement of magnetic research to analyze and study the magnetic moment of atoms in magnetic materials. Especially in the last few years, spintronics has quickly developed and created the discipline of anti-ferromagnetic spintronics. To study anti-ferromagnetic and ferromagnetic materials, it is necessary to analyze the distribution of the magnetic moments of their atoms. So far, this function has not been realized in the transmission electron microscope. However, the rapidly developing EMCD technology is expected to be able to capture atomic resolution EMCD spectra in the next few years, which means that the analysis of atomic resolution magnetic moment distribution can be realized in TEM. In the existing reports, Dr. Xiaoyan Zhong coming from Tsinghua University has achieved the analysis of the magnetic moment of a single atomic plane, and the specific structure of the exchange spring inside the soft and hard magnetic composite material can be observed, which has achieved a good technical breakthrough [107–109]. As for the EMCD technology based on STEM and mask, Professor He Tian coming from Zhejiang University also made a breakthrough. It is expected that in the next 2 or 3 years, EMCD technology with real atomic resolution will be realized. Therefore, further studies on exchange coupling, interface between magnetic materials and heavy metal materials, ferromagnetic materials

and anti-ferromagnetic materials will be conducted in the future, which is of great significance for the development of magnetism science.

References

1. Atherton WA (1980) The history of electromagnetic induction. *Am J Phys* 48(9):781–782. <https://doi.org/10.1119/1.12265>
2. Maxwell JC (1865) VIII. A dynamical theory of the electromagnetic field. *Philos Trans R Soc Lond* 155:459–512. <https://doi.org/10.1098/rstl.1865.0008>
3. Kúrti N, Simon F (1938) LXXIII. Remarks on the “Curie” scale of temperature. *Lond Edinb Dublin Philos Mag J Sci* 26(178):849–854. <https://doi.org/10.1080/14786443808562176>
4. White RM (2007) Quantum theory of magnetism: magnetic properties of materials. In: *Solid-state sciences*, 3 edn. Springer Berlin Heidelberg, Berlin. <https://doi.org/10.1007/978-3-540-69025-2>
5. Myers HP (2009) *Introductory solid state physics*. Taylor & Francis, London. <https://doi.org/10.1201/9781315273303>
6. Rikken RSM, Nolte RJM, Maan JC, van Hest JCM, Wilson DA, Christianen PCM (2014) Manipulation of micro- and nanostructure motion with magnetic fields. *Soft Matter* 10(9):1295–1308. <https://doi.org/10.1039/c3sm52294f>
7. Chappert C, Fert A, Van Dau FN (2009) The emergence of spin electronics in data storage. In: *Nanoscience and technology*. Macmillan Publishers Ltd, UK, pp 147–157. https://doi.org/10.1142/9789814287005_0015
8. Scheunert G, Heinonen O, Hardeman R, Lapicki A, Gubbins M, Bowman RM (2016) A review of high magnetic moment thin films for microscale and nanotechnology applications. *Appl Phys Rev* 3(1):011301. <https://doi.org/10.1063/1.4941311>
9. Yuasa S, Hono K, Hu G, Worledge DC (2018) Materials for spin-transfer-torque magnetoresistive random-access memory. *MRS Bull* 43(5):352–357. <https://doi.org/10.1557/mrs.2018.93>
10. Hubert A, Schäfer R (1998) *Magnetic domains: the analysis of magnetic microstructures*. Springer Berlin Heidelberg, Berlin. <https://doi.org/10.1007/978-3-540-85054-0>
11. Bates LF, Davis PF (1956) ‘Lozenge’ and ‘Tadpole’ domain structures on silicon-iron crystals. *Proc Phys Soc Lond Sect B* 69(11):1109–1111. <https://doi.org/10.1088/0370-1301/69/11/307>
12. Hubert A (1965) Beobachtung und Berechnung von magnetischen Bereichsstrukturen auf Siliziumeisen. *Zeitschrift für angewandte Physik* 18(5–6):474–479
13. Fumagalli P, Rosenberger A, Eggers G, Münnemann A, Held N, Güntherodt G (1998) Quantitative determination of the local Kerr rotation by scanning near-field magneto-optic microscopy. *Appl Phys Lett* 72(22):2803–2805. <https://doi.org/10.1063/1.121463>
14. Rave W, Zueco E, Schäfer R, Hubert A (1998) Observations on high-anisotropy single crystals using a combined Kerr/magnetic force microscope. *J Magn Magn Mater* 177–181:1474–1475. [https://doi.org/10.1016/S0304-8853\(97\)00793-2](https://doi.org/10.1016/S0304-8853(97)00793-2)
15. Chizhik A, Zhukov A, Stupakiewicz A, Maziewski A, Blanco JM, Gonzalez J (2009) Kerr microscopy study of magnetic domain structure changes in amorphous microwires. *IEEE Trans Magn* 45(10):4279–4281. <https://doi.org/10.1109/tmag.2009.2024892>
16. Tsukahara S, Kawakatsu H (1972) Asymmetric 180° domain walls in single crystal iron films. *J Phys Soc Jpn* 32(6):1493–1499. <https://doi.org/10.1143/jpsj.32.1493>
17. Newcomb BA, Giannuzzi LA, Lyons KM, Gulgunje PV, Gupta K, Liu Y, Kamath M, McDonald K, Moon J, Feng B, Peterson GP, Chae HG, Kumar S (2015) High resolution transmission electron microscopy study on polyacrylonitrile/carbon nanotube based carbon fibers and the effect of structure development on the thermal and electrical conductivities. *Carbon* 93:502–514. <https://doi.org/10.1016/j.carbon.2015.05.037>

18. Williams DB, Carter CB (2009) *Transmission electron microscopy: a textbook for materials science*, 2nd edn. Springer Science & Business Media, New York. <https://doi.org/10.1007/978-0-387-76501-3>
19. Chapman JN, McFadyen IR, McVitie S (1990) Modified differential phase contrast Lorentz microscopy for improved imaging of magnetic structures. *IEEE Trans Magn* 26(5):1506–1511. <https://doi.org/10.1109/20.104427>
20. Chapman JN, Waddell EM, Batson PE, Ferrier RP (1979) The Fresnel mode of Lorentz microscopy using a scanning transmission electron microscope. *Ultramicroscopy* 4(3):283–292. [https://doi.org/10.1016/S0304-3991\(79\)80038-8](https://doi.org/10.1016/S0304-3991(79)80038-8)
21. Shindo D, Park Y-G, Murakami Y, Gao Y, Kanekiyo H, Hirotsawa S (2003) Electron holography of Nd–Fe–B nanocomposite magnets. *Scr Mater* 48(7):851–856. [https://doi.org/10.1016/S1359-6462\(02\)00601-2](https://doi.org/10.1016/S1359-6462(02)00601-2)
22. Dunin-Borkowski RE, Kasama T, Harrison RJ (2015) Electron holography of nanostructured materials. In: *Nanocharacterisation*. The Royal Society of Chemistry, pp 158–210. <https://doi.org/10.1039/9781782621867-00158>
23. Gabor D (1948) A new microscopic principle. *Nature* 161(4098):777–778. <https://doi.org/10.1038/161777a0>
24. Leith EN, Upatnieks J (1965) Photography by laser. *Sci Am* 212(6):24–35. <https://doi.org/10.1038/scientificamerican0665-24>
25. Lichte H (1986) Electron holography approaching atomic resolution. *Ultramicroscopy* 20(3):293–304. [https://doi.org/10.1016/0304-3991\(86\)90193-2](https://doi.org/10.1016/0304-3991(86)90193-2)
26. Dekkers N, De Lang H (1974) Differential phase contrast in a STEM. *Optik* 41(4):452–456
27. Zhang S, Zhang J, Wen Y, Chudnovsky EM, Zhang X (2018) Creation of a thermally assisted skyrmion lattice in Pt/Co/Ta multilayer films. *Appl Phys Lett* 113(19):192403. <https://doi.org/10.1063/1.5053983>
28. Zhang J, Zhu S, Li H, Zhu L, Hu Y, Xia W, Zhang X, Peng Y, Fu J (2018) Direct observation of dynamical magnetization reversal process governed by shape anisotropy in single NiFe₂O₄ nanowire. *Nanoscale* 10(21):10123–10129. <https://doi.org/10.1039/c8nr01393d>
29. Chapman JN (1984) The investigation of magnetic domain structures in thin foils by electron microscopy. *J Phys D Appl Phys* 17(4):623–647. <https://doi.org/10.1088/0022-3727/17/4/003>
30. Daykin A, Petford-Long A (1995) Quantitative mapping of the magnetic induction distribution using Foucault images formed in a transmission electron microscope. *Ultramicroscopy* 58(3–4):365–380. [https://doi.org/10.1016/0304-3991\(95\)00008-0](https://doi.org/10.1016/0304-3991(95)00008-0)
31. Shindo D, Murakami Y (2008) Electron holography of magnetic materials. *J Phys D Appl Phys* 41(18):183002. <https://doi.org/10.1088/0022-3727/41/18/183002>
32. Chapman J, Ploessl R, Donnet D (1992) Differential phase contrast microscopy of magnetic materials. *Ultramicroscopy* 47(4):331–338. [https://doi.org/10.1016/0304-3991\(92\)90162-D](https://doi.org/10.1016/0304-3991(92)90162-D)
33. Chen CT, Idzerda YU, Lin HJ, Smith NV, Meigs G, Chaban E, Ho GH, Pellegrin E, Sette F (1995) Experimental confirmation of the X-Ray magnetic circular dichroism sum rules for iron and cobalt. *Phys Rev Lett* 75(1):152–155. <https://doi.org/10.1103/PhysRevLett.75.152>
34. Hubert A, Schäfer R (2008) Domain observation techniques. In: *Magnetic domains*. Springer, Berlin, pp 11–97. https://doi.org/10.1007/978-3-540-85054-0_2
35. Zuo C, Chen Q, Asundi A (2014) Boundary-artifact-free phase retrieval with the transport of intensity equation: fast solution with use of discrete cosine transform. *Opt Expr* 22(8):9220–9244. <https://doi.org/10.1364/oe.22.009220>
36. Johnston AB, Chapman JN (1995) The development of coherent Foucault imaging to investigate magnetic microstructure. *J Microsc* 179(2):119–128. <https://doi.org/10.1111/j.1365-2818.1995.tb03621.x>
37. Lichte H, Lehmann M (2007) Electron holography—basics and applications. *Rep Prog Phys* 71(1):016102. <https://doi.org/10.1088/0034-4885/71/1/016102>
38. Midgley PA, Dunin-Borkowski RE (2009) Electron tomography and holography in materials science. *Nat Mater* 8(4):271–280. <https://doi.org/10.1038/nmat2406>
39. Park HS, Yu X, Aizawa S, Tanigaki T, Akashi T, Takahashi Y, Matsuda T, Kanazawa N, Onose Y, Shindo D, Tonomura A, Tokura Y (2014) Observation of the magnetic flux and

- three-dimensional structure of skyrmion lattices by electron holography. *Nat Nanotechnol* 9(5):337–342. <https://doi.org/10.1038/nnano.2014.52>
40. Shindo D, Oikawa T (2013) Peripheral instruments and techniques for analytical electron microscopy. In: *Analytical electron microscopy for materials science*. Springer, Tokyo, pp 103–136. https://doi.org/10.1007/978-4-431-66988-3_5
 41. Song D, Li Z-A, Caron J, Kovács A, Tian H, Jin C, Du H, Tian M, Li J, Zhu J, Dunin-Borkowski RE (2018) Quantification of magnetic surface and edge states in an FeGe nanostripe by off-axis electron holography. *Phys Rev Lett* 120(16):167204. <https://doi.org/10.1103/PhysRevLett.120.167204>
 42. Hu S, Pei K, Wang B, Xia W, Yang H, Zhan Q, Li X, Liu X, Li R-W (2018) Direct imaging of cross-sectional magnetization reversal in an exchange-biased CoFeB/IrMn bilayer. *Phys Rev B* 97(5):054422. <https://doi.org/10.1103/PhysRevB.97.054422>
 43. Masseurboeuf A, Gatel C, Bayle-Guillemaud P, Lamy Y, Viala B (2009) The use of Lorentz microscopy for the determination of magnetic reversal mechanism of exchange-biased Co₃₀Fe₇₀/NiMn bilayer. *J Magn Magn Mater* 321(19):3080–3083. <https://doi.org/10.1016/j.jmmm.2009.05.011>
 44. Dunin-Borkowski RE, McCartney MR, Kardynal B, Parkin SSP, Scheinfein MR, Smith DJ (2000) Off-axis electron holography of patterned magnetic nanostructures. *J Microsc* 200(3):187–205. <https://doi.org/10.1046/j.1365-2818.2000.00753.x>
 45. Almeida Trevor P, Muxworthy Adrian R, Kovács A, Williams W, Brown Paul D, Dunin-Borkowski RE (2016) Direct visualization of the thermomagnetic behavior of pseudo-single-domain magnetite particles. *Sci Adv* 2(4):e1501801. <https://doi.org/10.1126/sciadv.1501801>
 46. Matsumoto T, So Y-G, Kohno Y, Sawada H, Ikuhara Y, Shibata N (2016) Direct observation of $\Sigma 7$ domain boundary core structure in magnetic skyrmion lattice. *Sci Adv* 2(2):e1501280. <https://doi.org/10.1126/sciadv.1501280>
 47. Matsumoto T, So Y-G, Kohno Y, Ikuhara Y, Shibata N (2018) Stable magnetic skyrmion states at room temperature confined to corrals of artificial surface pits fabricated by a focused electron beam. *Nano Lett* 18(2):754–762. <https://doi.org/10.1021/acs.nanolett.7b03967>
 48. Schattschneider P, Rubino S, Hébert C, Rusz J, Kuneš J, Novák P, Carlino E, Fabriziooli M, Panaccione G, Rossi G (2006) Detection of magnetic circular dichroism using a transmission electron microscope. *Nature* 441(7092):486–488. <https://doi.org/10.1038/nature04778>
 49. Schattschneider P, Hébert C, Rubino S, Stöger-Pollach M, Rusz J, Novák P (2008) Magnetic circular dichroism in EELS: towards 10 nm resolution. *Ultramicroscopy* 108(5):433–438. <https://doi.org/10.1016/j.ultramic.2007.07.002>
 50. Lidbaum H, Rusz J, Liebig A, Hjörvarsson B, Oppeneer PM, Coronel E, Eriksson O, Leifer K (2009) Quantitative magnetic information from reciprocal space maps in transmission electron microscopy. *Phys Rev Lett* 102(3):037201. <https://doi.org/10.1103/PhysRevLett.102.037201>
 51. Yu ACC, Petford-Long A, Miyazaki T (2001) Direct observation of domain structure and magnetization reversal of magnetic thin films using Lorentz transmission electron microscopy. *Jpn J Appl Phys* 40(Part 1, No. 8):4891–4896. <https://doi.org/10.1143/jjap.40.4891>
 52. Sugawara A, Shimakura T, Nishihara H, Akashi T, Takahashi Y, Moriya N, Sugaya M (2019) A 0.5-T pure-in-plane-field magnetizing holder for in-situ Lorentz microscopy. *Ultramicroscopy* 197:105–111. <https://doi.org/10.1016/j.ultramic.2018.11.012>
 53. Uhlig T, Heumann M, Zweck J (2003) Development of a specimen holder for in situ generation of pure in-plane magnetic fields in a transmission electron microscope. *Ultramicroscopy* 94(3):193–196. [https://doi.org/10.1016/S0304-3991\(02\)00264-4](https://doi.org/10.1016/S0304-3991(02)00264-4)
 54. Jin J, Yan M, Liu Y, Peng B, Bai G (2019) Attaining high magnetic performance in as-sintered multi-main-phase Nd-La-Ce-Fe-B magnets: toward skipping the post-sinter annealing treatment. *Acta Mater* 169:248–259. <https://doi.org/10.1016/j.actamat.2019.03.005>
 55. Pei K, Xia W-X, Wang B-M, Wen X-C, Sheng P, Liu J-P, Liu X-C, Li R-W (2018) Investigation of magnetization reversal process in pinned CoFeB thin film by in-situ Lorentz TEM. *Chin Phys B* 27(4):047502. <https://doi.org/10.1088/1674-1056/27/4/047502>
 56. Zweck J, Zimmermann T, Schuhrke T (1997) TEM imaging and evaluation of magnetic structures in Co/Cu multilayers. *Ultramicroscopy* 67(1–4):153–162. [https://doi.org/10.1016/S0304-3991\(96\)00107-6](https://doi.org/10.1016/S0304-3991(96)00107-6)

57. Dunin-Borkowski RE, Kasama T, Wei A, Tripp SL, Hýtch MJ, Snoeck E, Harrison RJ, Putnis A (2004) Off-axis electron holography of magnetic nanowires and chains, rings, and planar arrays of magnetic nanoparticles. *Microsc Res Tech* 64(5–6):390–402. <https://doi.org/10.1002/jemt.20098>
58. Graef MD, Willard MA, McHenry ME, Yimei Z (2001) In-situ Lorentz TEM cooling study of magnetic domain configurations in Ni₂MnGa. *IEEE Trans Magn* 37(4):2663–2665. <https://doi.org/10.1109/20.951267>
59. Romming N, Hanneken C, Menzel M, Bickel Jessica E, Wolter B, von Bergmann K, Kubetzka A, Wiesendanger R (2013) Writing and deleting single magnetic skyrmions. *Science* 341(6146):636–639. <https://doi.org/10.1126/science.1240573>
60. Kramer MJ, McCallum RW, Anderson IA, Constantinides S (2012) Prospects for non-rare earth permanent magnets for traction motors and generators. *JOM* 64(7):752–763. <https://doi.org/10.1007/s11837-012-0351-z>
61. Zhou L, Miller MK, Lu P, Ke L, Skomski R, Dillon H, Xing Q, Palasyuk A, McCartney M, Smith D (2014) Architecture and magnetism of alnico. *Acta Mater* 74:224–233. <https://doi.org/10.1016/j.actamat.2014.04.044>
62. Fastenau RHJ, van Loenen EJ (1996) Applications of rare earth permanent magnets. *J Magn Magn Mater* 157–158:1–6. [https://doi.org/10.1016/0304-8853\(95\)01279-6](https://doi.org/10.1016/0304-8853(95)01279-6)
63. Minowa T (2008) Rare earth magnets: conservation of energy and the environment. *Resour Geol* 58(4):414–422. <https://doi.org/10.1111/j.1751-3928.2008.00073.x>
64. Zeng X, Zhang J, Si M, Cao D, Deng X, Ma H, Lan Q, Xue D, Zhang X, Tao K, Peng Y (2019) Direct imaging of dopant sites in rare-earth element-doped permanent magnet and correlated magnetism origin. *Nanoscale* 11(10):4385–4393. <https://doi.org/10.1039/c8nr09922g>
65. Srinivasamurthy KM, Angadi VJ, Kubrin SP, Matteppanavar S, Sarychev DA, Rudraswamy B (2019) Effect of Ce₃₊ ion on structural and hyperfine interaction studies of Co_{0.5}Ni_{0.5}Fe_{2-x}Ce_xO₄ ferrites: useful for permanent magnet applications. *J Supercond Nov Magn* 32(3):693–704. <https://doi.org/10.1007/s10948-018-4752-2>
66. López-Ortega A, Estrader M, Salazar-Alvarez G, Roca AG, Nogués J (2015) Applications of exchange coupled bi-magnetic hard/soft and soft/hard magnetic core/shell nanoparticles. *Phys Rep* 553:1–32. <https://doi.org/10.1016/j.physrep.2014.09.007>
67. Liu J, Sepehri-Amin H, Ohkubo T, Hioki K, Hattori A, Schrefl T, Hono K (2015) Grain size dependence of coercivity of hot-deformed Nd–Fe–B anisotropic magnets. *Acta Mater* 82:336–343. <https://doi.org/10.1016/j.actamat.2014.09.021>
68. Gao RW, Zhang DH, Li W, Li XM, Zhang JC (2000) Hard magnetic property and $\delta M(H)$ plot for sintered NdFeB magnet. *J Magn Magn Mater* 208(3):239–243. [https://doi.org/10.1016/S0304-8853\(99\)00562-4](https://doi.org/10.1016/S0304-8853(99)00562-4)
69. Gao RW, Feng WC, Liu HQ, Wang B, Chen W, Han GB, Zhang P, Li H, Li W, Guo YQ, Pan W, Li XM, Zhu MG, Li X (2003) Exchange-coupling interaction, effective anisotropy and coercivity in nanocomposite permanent materials. *J Appl Phys* 94(1):664–668. <https://doi.org/10.1063/1.1581380>
70. Inoue M, Tomita T, Naruse M, Akase Z, Murakami Y, Shindo D (2005) Development of a magnetizing stage for in situ observations with electron holography and Lorentz microscopy. *J Electron Microsc* 54(6):509–513. <https://doi.org/10.1093/jmicro/dfi068>
71. Akase Z, Aizawa S, Shindo D, Sharma P, Makino A (2015) In-situ Lorentz microscopy of Fe₈₅Si₂B₈P₄Cu₁ nanocrystalline soft magnetic alloys. *J Magn Magn Mater* 375:10–14. <https://doi.org/10.1016/j.jmmm.2014.08.101>
72. De Hosson JTM, Chechenin NG, Alesm D-H, Vystavel T, Kooi BJ, Chezan AR, Boerma DO (2002) Ultrasoft magnetic films investigated with Lorentz transmission electron microscopy and electron holography. *Microsc Microanal* 8(4):274–287. <https://doi.org/10.1017/s1431927602020214>
73. Che RC, Liang CY, He X, Liu HH, Duan XF (2011) Characterization of magnetic domain walls using electron magnetic chiral dichroism. *Sci Technol Adv Mater* 12(2):025004. <https://doi.org/10.1088/1468-6996/12/2/025004>

74. Catalan G, Seidel J, Ramesh R, Scott JF (2012) Domain wall nanoelectronics. *Rev Mod Phys* 84(1):119–156. <https://doi.org/10.1103/RevModPhys.84.119>
75. Herranen T, Laurson L (2017) Bloch-line dynamics within moving domain walls in 3D ferromagnets. *Phys Rev B* 96(14):144422. <https://doi.org/10.1103/PhysRevB.96.144422>
76. Wang X, Liao Y, Zhang D, Wen T, Zhong Z (2018) A review of Fe₃O₄ thin films: synthesis, modification and applications. *J Mater Sci Technol* 34(8):1259–1272. <https://doi.org/10.1016/j.jmst.2018.01.011>
77. Shin HW, Ahn Y, Son JY (2019) Multiferroic properties and enhanced leakage current characteristics of polycrystalline Bi₂MnFeO₆ thin films grown on glass substrates. *Thin Solid Films* 692:137655. <https://doi.org/10.1016/j.tsf.2019.137655>
78. Peng L, Zhang Y, He M, Ding B, Wang W, Tian H, Li J, Wang S, Cai J, Wu G, Liu JP, Kramer MJ, Shen B-G (2017) Generation of high-density biskyrmions by electric current. *npj Quant Mater* 2(1):30. <https://doi.org/10.1038/s41535-017-0034-7>
79. Almeida TP, McGrouther D, Pivak Y, Perez Garza HH, Temple R, Massey J, Marrows CH, McVitie S (2017) Preparation of high-quality planar FeRh thin films for in situ TEM investigations. *J Phys Conf Ser* 903:012022. <https://doi.org/10.1088/1742-6596/903/1/012022>
80. Zhu L, Deng X, Hu Y, Liu J, Ma H, Zhang J, Fu J, He S, Wang J, Wang B, Xue D, Peng Y (2018) Atomic-scale imaging of the ferrimagnetic/diamagnetic interface in Au-Fe₃O₄ nanodimers and correlated exchange-bias origin. *Nanoscale* 10(45):21499–21508. <https://doi.org/10.1039/c8nr07642a>
81. Gaul A, Emmrich D, Ueltzhöffer T, Huckfeldt H, Doğanay H, Hackl J, Khan MI, Gottlob DM, Hartmann G, Beyer A (2018) Size limits of magnetic-domain engineering in continuous in-plane exchange-bias prototype films. *Beilstein J Nanotechnol* 9(1):2968–2979. <https://doi.org/10.3762/bjnano.9.276>
82. Tan A, Li J, Jenkins CA, Arenholz E, Scholl A, Hwang C, Qiu ZQ (2012) Exchange bias in epitaxially grown CoO/MgO/Fe/Ag(001). *Phys Rev B* 86(6):064406. <https://doi.org/10.1103/PhysRevB.86.064406>
83. Wu J, Park JS, Kim W, Arenholz E, Liberati M, Scholl A, Wu YZ, Hwang C, Qiu ZQ (2010) Direct measurement of rotatable and frozen CoO spins in exchange bias system of CoO/Fe/Ag(001). *Phys Rev Lett* 104(21):217204. <https://doi.org/10.1103/PhysRevLett.104.217204>
84. Liu Q, Cao Q, Bi H, Liang C, Yuan K, She W, Yang Y, Che R (2016) CoNi@SiO₂@TiO₂ and CoNi@Air@TiO₂ microspheres with strong wideband microwave absorption. *Adv Mater* 28(3):486–490. <https://doi.org/10.1002/adma.201503149>
85. Wu Z, Pei K, Xing L, Yu X, You W, Che R (2019) Enhanced microwave absorption performance from magnetic coupling of magnetic nanoparticles suspended within hierarchically tubular composite. *Adv Funct Mater* 29(28):1901448. <https://doi.org/10.1002/adfm.201901448>
86. Li X, Wang L, You W, Xing L, Yu X, Li Y, Che R (2019) Morphology-controlled synthesis and excellent microwave absorption performance of ZnCo₂O₄ nanostructures via a self-assembly process of flake units. *Nanoscale* 11(6):2694–2702. <https://doi.org/10.1039/c8nr08601j>
87. Wang L, Li X, Li Q, Yu X, Zhao Y, Zhang J, Wang M, Che R (2019) Oriented polarization tuning broadband absorption from flexible hierarchical ZnO arrays vertically supported on carbon cloth. *Small* 15(18):1900900. <https://doi.org/10.1002/smll.201900900>
88. Mühlbauer S, Binz B, Jonietz F, Pfleiderer C, Rosch A, Neubauer A, Georgii R, Böni P (2009) Skyrmion lattice in a chiral magnet. *Science* 323(5916):915–919. <https://doi.org/10.1126/science.1166767>
89. Mruczkiewicz M, Krawczyk M, Guslienko KY (2017) Spin excitation spectrum in a magnetic nanodot with continuous transitions between the vortex, Bloch-type skyrmion, and Néel-type skyrmion states. *Phys Rev B* 95(9):094414. <https://doi.org/10.1103/PhysRevB.95.094414>
90. Yu XZ, Kanazawa N, Zhang WZ, Nagai T, Hara T, Kimoto K, Matsui Y, Onose Y, Tokura Y (2012) Skyrmion flow near room temperature in an ultralow current density. *Nat Commun* 3(1):988. <https://doi.org/10.1038/ncomms1990>

91. Kézsmárki I, Bordács S, Milde P, Neuber E, Eng LM, White JS, Rønnow HM, Dewhurst CD, Mochizuki M, Yanai K, Nakamura H, Ehlers D, Tsurkan V, Loidl A (2015) Néel-type skyrmion lattice with confined orientation in the polar magnetic semiconductor GaV₄S₈. *Nat Mater* 14(11):1116–1122. <https://doi.org/10.1038/nmat4402>
92. Dzyaloshinsky I (1958) A thermodynamic theory of “weak” ferromagnetism of antiferromagnetics. *J Phys Chem Solids* 4(4):241–255. [https://doi.org/10.1016/0022-3697\(58\)90076-3](https://doi.org/10.1016/0022-3697(58)90076-3)
93. Moriya T (1960) Anisotropic superexchange interaction and weak ferromagnetism. *Phys Rev* 120(1):91–98. <https://doi.org/10.1103/PhysRev.120.91>
94. Parkin SSP, Hayashi M, Thomas L (2008) Magnetic domain-wall racetrack memory. *Science* 320(5873):190–194. <https://doi.org/10.1126/science.1145799>
95. Tonomura A, Yu X, Yanagisawa K, Matsuda T, Onose Y, Kanazawa N, Park HS, Tokura Y (2012) Real-space observation of skyrmion lattice in helimagnet MnSi thin samples. *Nano Lett* 12(3):1673–1677. <https://doi.org/10.1021/nl300073m>
96. Pollard SD, Garlow JA, Yu J, Wang Z, Zhu Y, Yang H (2017) Observation of stable Néel skyrmions in cobalt/palladium multilayers with Lorentz transmission electron microscopy. *Nat Commun* 8(1):14761. <https://doi.org/10.1038/ncomms14761>
97. Du H, Che R, Kong L, Zhao X, Jin C, Wang C, Yang J, Ning W, Li R, Jin C, Chen X, Zang J, Zhang Y, Tian M (2015) Edge-mediated skyrmion chain and its collective dynamics in a confined geometry. *Nat Commun* 6(1):8504. <https://doi.org/10.1038/ncomms9504>
98. Zhao X, Jin C, Wang C, Du H, Zang J, Tian M, Che R, Zhang Y (2016) Direct imaging of magnetic field-driven transitions of skyrmion cluster states in FeGe nanodisks. *Proc Natl Acad Sci* 113(18):4918. <https://doi.org/10.1073/pnas.1600197113>
99. Wang C, Du H, Zhao X, Jin C, Tian M, Zhang Y, Che R (2017) Enhanced stability of the magnetic skyrmion lattice phase under a tilted magnetic field in a two-dimensional chiral magnet. *Nano Lett* 17(5):2921–2927. <https://doi.org/10.1021/acs.nanolett.7b00135>
100. Du H, Zhao X, Rybakov FN, Borisov AB, Wang S, Tang J, Jin C, Wang C, Wei W, Kiselev NS, Zhang Y, Che R, Blügel S, Tian M (2018) Interaction of individual skyrmions in a nanostructured cubic chiral magnet. *Phys Rev Lett* 120(19):197203. <https://doi.org/10.1103/PhysRevLett.120.197203>
101. Han B, Gao Y-Y, Zhang Y-L, Liu Y-Q, Ma Z-C, Guo Q, Zhu L, Chen Q-D, Sun H-B (2020) Multi-field-coupling energy conversion for flexible manipulation of graphene-based soft robots. *Nano Energy* 71:104578. <https://doi.org/10.1016/j.nanoen.2020.104578>
102. Karim A, Guan C, Chen B, Li Y, Zhang J, Zhu L, Deng X, Hu Y, Bi K, Li H, Peng Y, Li L (2020) Dynamic observation of Joule heating-induced structural and domain transformation in smart shape-memory alloy. *Acta Mater* 186:223–228. <https://doi.org/10.1016/j.actamat.2020.01.006>
103. Venkateswaran SP, Nuhfer NT, De Graef M (2007) Magnetic domain memory in multiferroic Ni₂MnGa. *Acta Mater* 55(16):5419–5427. <https://doi.org/10.1016/j.actamat.2007.05.055>
104. Shibata K, Iwasaki J, Kanazawa N, Aizawa S, Tanigaki T, Shirai M, Nakajima T, Kubota M, Kawasaki M, Park HS, Shindo D, Nagaosa N, Tokura Y (2015) Large anisotropic deformation of skyrmions in strained crystal. *Nat Nanotechnol* 10(7):589–592. <https://doi.org/10.1038/nnano.2015.113>
105. Eggebrecht T, Möller M, Gatzmann JG, Rubiano da Silva N, Feist A, Martens U, Ulrichs H, Münzenberg M, Ropers C, Schäfer S (2017) Light-induced metastable magnetic texture uncovered by in situ Lorentz microscopy. *Phys Rev Lett* 118(9):097203. <https://doi.org/10.1103/PhysRevLett.118.097203>
106. Zhao X, Wang S, Wang C, Che R (2018) Thermal effects on current-related skyrmion formation in a nanobelt. *Appl Phys Lett* 112(21):212403. <https://doi.org/10.1063/1.5031474>
107. Wang ZQ, Zhong XY, Yu R, Cheng ZY, Zhu J (2013) Quantitative experimental determination of site-specific magnetic structures by transmitted electrons. *Nat Commun* 4(1):1395. <https://doi.org/10.1038/ncomms2323>
108. Wang ZC, Zhong XY, Jin L, Chen XF, Moritomo Y, Mayer J (2017) Effects of dynamic diffraction conditions on magnetic parameter determination in a double perovskite Sr₂FeMoO₆ using

- electron energy-loss magnetic chiral dichroism. *Ultramicroscopy* 176:212–217. <https://doi.org/10.1016/j.ultramic.2016.12.024>
109. Song D-S, Wang Z-Q, Zhong X-Y, Zhu J (2018) Quantitative measurement of magnetic parameters by electron magnetic chiral dichroism. *Chin Phys B* 27(5):056801. <https://doi.org/10.1088/1674-1056/27/5/056801>

Chapter 8

In-Situ Liquid Cell TEM



Chao Zhu, Wen Wang, Honggang Liao, and Litao Sun

8.1 A Brief History of In-Situ Liquid Cell TEM

In nature, water covers 71% surface of the earth and also exists as a vapor state in the air, playing an important role in most reactive processes, renovation of environment, as well as the evolution of life. Identically in industry or laboratory, an enormous amount of chemical, biological, biochemical, and electrochemical reactions require the participation of liquid solvent. However, the lack of effective experimental methods prevents in-depth exploration of liquid involved reactions. We know the beginning and end, but we can only speculate how it happens. Until recently, the great improvement of liquid cell techniques based on TEM successfully realizes truly seeing reactions in liquid, opening a new avenue for detailed and insightful investigations of dynamic signatures in a liquid environment.

The idea of imaging materials in liquid using TEM can be dated back to 1935 [1]. Marton proposed two methods to restrict or control the liquid solutions around specimens in the electron microscope. The first is to seal the liquid between two electron transparent windows to isolate from the vacuum environment. The second is to place pairs of apertures to construct an open environmental chamber. Afterwards, several attempts about the development of liquid environment TEM (ETEM) techniques have been demonstrated [2–4]. Despite some progress, the following

C. Zhu · W. Wang · L. Sun (✉)

Key Lab of MEMS of Ministry of Education, SEU-FEI Nano-Pico Center, Southeast University, Nanjing 210096, P. R. China
e-mail: slt@seu.edu.cn

W. Wang

School of Mechanics and Safety Engineering, Zhengzhou University, Zhengzhou 450001, P. R. China

H. Liao

State Key Lab of Physical Chemistry of Solid Surfaces, College of Chemistry and Chemical Engineering, Xiamen University, Xiamen 361005, P. R. China

two factors lead to the significant increasing of experimental difficulties, seriously restricting the application of these techniques in some fields:

The small amount and short duration of liquids in a vacuum environment for “opened” cell (sample directly contact with the column environment of TEM) ETEM [5].

The poor resolution due to the thick window layer for “closed” cell (sample is sealed or isolated from the column environment by plastic windows) ETEM.

Until recently, TEM studies of liquid samples step into an eruption period, benefiting from the microfabrication technology and the usage of Si_xN_y thin films. In 2003, the first Si_xN_y -based liquid cell was developed to investigate the growth dynamic of Cu nano-clusters [6]. The cell was assembled by one lower silicon wafer with 80 nm Si_xN_y as the viewing window and an upper wafer possessing the same window as well as two reservoirs. Au electrodes were deposited onto the lower wafer and additional electrodes stretched into the reservoirs with the help of top glass spacers for the electrochemical experiment. After the penetration of 1 μm (the thickness of SiO_2 spacer between two wafers) liquid and 160 nm Si_xN_y by electrons, a resolution of ~ 5 nm was finally achieved. In 2008, a similar liquid cell with epoxy as the spacer was also designed for imaging of living bio-reactions [7], but the resolution was not much improved. In 2009, by using In as the spacer (200 nm) and thinner Si_xN_y (25 nm) membrane, the sub-nanometer resolution during in-situ observation of Pt nanoparticle growth trajectories was realized [8]. Then in 2014, further reduction of both In (100 nm) spacer and viewing window (10 nm) eventually contributed to an atomic resolution in the silicon wafer liquid cell [9].

Along with the development of Si_xN_y liquid cell, other membranes have also been applied in the construction of different liquid cells. In 2012, two pieces of monolayer graphene were used to encapsulate a nano-sized liquid droplet and then transferred to TEM for the investigation of Pt nanocrystal growth inside the droplet [10]. Due to the single-atomic layer structure of graphene, direct imaging of crystal lattice was easily obtained even under 80 kV operation voltage. In 2018, amorphous carbon films were proved to be another excellent viewing widow for in-situ observation of the growth process of Au nanoparticles [11]. This carbon film liquid cell exhibited the robust feature under 300 keV electron irradiation, while maintaining the atomic resolution. In 2019, a hybrid liquid cell consisted of graphene and MoS_2 was invented [12]. The monolayer MoS_2 served not only as the substrate but also as the membrane window, enabling the exploration of van der Waals epitaxial relationship between Pt nanoparticles and MoS_2 .

Although liquid cell TEM techniques have provided a good platform for the investigation of liquid–solid reactions, the research system is still very limited because the reaction is always triggered by the incident electron beam in static/sealed environment, which is quite different from the real reaction in the macro-level experiment. On considering this, flow cell then becomes an efficient solution, duplicating the real reaction into the micro-level. In 2009, the first microfluidic flow cell was reported for the time-evolving imaging of whole cells under a constant liquid flow [13]. In their design, microspheres were adopted as the spacer between two silicon chips with

silicon nitride windows, leaving a liquid flow channel. During the experiment, the liquid was supplied by a fluid specimen holder to form a continuous liquid flow. In 2014, by using a dual flow liquid cell, two different reaction solutions got mixed at viewing regions, leading to the visualization of CaCO_3 nucleation [14]. The advantage of this dual flow cell was the isolation of the reaction solutions before the in-situ experiment, allowing the capture of the very initial nucleation stage.

Recent years, in order to exploit the application of liquid cell in more research directions, multiple external fields have been introduced into this technique, on the basis of the fundamental structure. For instance, metal electrodes were deposited onto the silicon chips to apply an electrical bias for the study of electrochemical growth [6] or lithium ion battery [15]. In addition, metal electrodes deposited on the membrane windows could also be used to deliver sufficient heat to the liquid, resulting in bubble formation [16]. UV illumination was successfully introduced into a liquid cell through an optical fiber to initiate the photocatalytic reaction of TiO_2 in water, which was in-situ imaged [17]. As a matter of fact, there is great potential to incorporate more functions into this technique, since the liquid cell owns a high degree of flexibility for self-design and modification. And certainly, the successful integration of electrical, heating, optical fields or other functions with the liquid cell will attract intense interest of scientists among various domains.

8.2 Current In-Situ Liquid Cell TEM Technologies

As discussed in Sect. 8.1, both “opened” and “closed” cells have been invented for liquid samples in TEM. However, the special design of cell, holder, or even TEM column largely limits the widespread usage of the “opened” type. In comparison, the “closed” cell that requires the absolute isolation of liquid, shows some advantages in the compatibility with ordinary TEM holders and the simplicity for daily operation. More importantly, the “closed” cell allows sufficient liquid to stay in the normal pressure environment, which is the prerequisite for long-time steady in-situ observation. Therefore, in this section, we will focus on the “closed” cell techniques. Several different “closed” liquid cells have been developed, and all of them consist of electron transparent membranes to seal the liquid. As a result, a high quality membrane has now become the crux of a liquid cell, requiring that the membrane must find the balance between two competing rivals: thinness and robustness.

In the following sections, we will first discuss the static liquid cell based on the categories of membrane materials. The specific construction and fabrication process will be included for each type. Then, we will describe the flow cell, a combined setup of cell chips and holders, ensuring the mixture of various solutions during observation. Finally, we will highlight the integration of multi-fields into liquid cell systems, including electric, thermal and optical fields.

8.2.1 Static Liquid Cell

A static liquid cell usually means there is no external liquid flow passing through the cell. This provides a high tolerance for cell design and membranes. Theoretically, any sealed space may become a cell if the liquid can be capsulated, and of course, the container should also be thin enough for electron penetration, for example, a nano-sized metal cavity [18] or a nanotube. While in practical experiments, thin film materials with macro-size are commonly used as the membranes to capsulate liquid, typically Si_xN_y , graphene, amorphous carbon film and hybrid membranes. Other membrane techniques such as SiO_2 that has been almost replaced by Si_xN_y and polyimide that is used in liquid cell SEM will not be discussed in this section.

Si_xN_y Liquid Cell

Amorphous Si_xN_y is the most popular material for cell membranes, on the basis of the following features: (1) It is compatible with the microfabrication technology of silicon chips. Considering the commercial production and the combination of other techniques, Si_xN_y is the best choice, allowing us to control the membrane thickness and also to self-design peculiar structures for different purposes through wafer-scale fabrication. (2) It is robust enough against large bulging. Low stress Si_xN_y (stoichiometric ratio ranging from 3:4 to 2:1) thin films deposited by the low pressure chemical vapor deposition (LPCVD) method have proved to be a robust membrane for liquid capsulation, and at the same time maintains electron transparency for the viewing window [19].

The microfabrication process of a standard Si_xN_y liquid cell containing reservoirs is shown in Fig. 8.1a. Cells are usually fabricated using 100–200 μm silicon wafers instead of traditional 400 μm ones because the reduced thickness is more favorable for the cell mounting with holders. Low stress Si_xN_y membrane (e.g. 20–200 nm) is firstly grown among the whole silicon wafer through the LPCVD method. Lithography patterning and reactive ion etching (RIE) is then used to remove the patterned Si_xN_y membrane. The viewing windows and reservoirs (reservoirs are optional structures depending on needs) are produced by 30 wt% KOH wet etching at 70–80 °C to remove the silicon. The membrane of viewing windows is kept intact and that of reservoirs can be physically destroyed for later liquid injection. After wet etching, a spacer layer is coated onto the side of the bottom piece, which creates space for a liquid layer. However, the real thickness of a liquid layer is determined by not only the spacer but also the local bulging. Finally, the top and bottom pieces could be assembled into a whole liquid cell.

Assembling and alignment of chips are also important processes before *in-situ* experiments. If a liquid cell is prepared for the common holder usage, there are two efficient assembling constructions: (1) Self-bonded construction. Usually, the windows of two pieces are manually aligned and then bonded together with deposited indium (100–200 nm) at 120 °C for 1 h, where indium is used as both the spacer and binder as shown in Fig. 8.1b. This assembling method ensures a fixed spacer for every single cell but sometimes shows the difficulties in window alignment and liquid

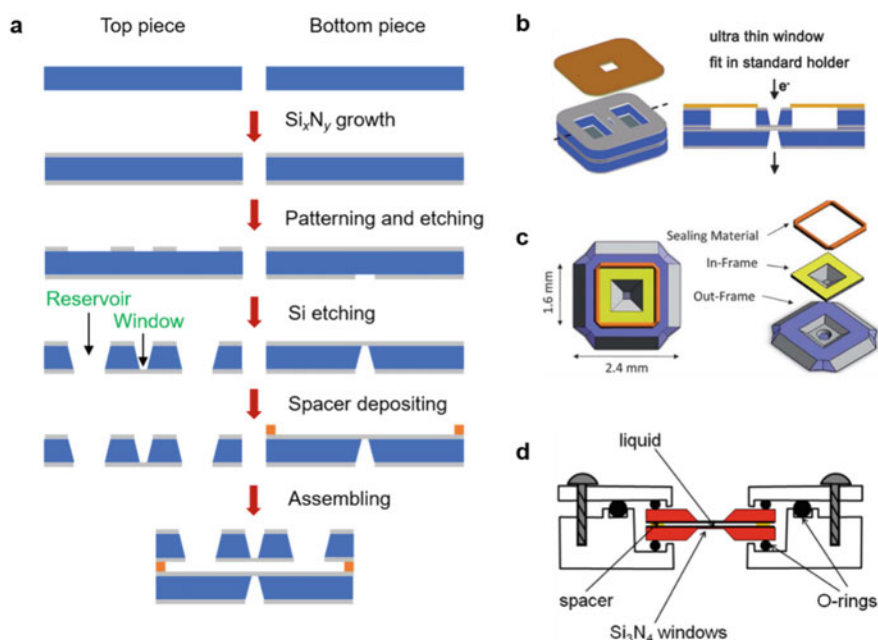


Fig. 8.1 **a** Microfabrication of a liquid cell chip, including Si_xN_y growth, patterning and etching of Si_xN_y membrane, Si etching, spacer deposition and assembling process. **b** A self-bonded liquid cell (reproduced with permission from Ref. [4], Copyright 2013, Royal Society of Chemistry). **c** A self-aligned liquid cell (reprinted with permission from Ref. [20], Copyright 2012, Royal Society of Chemistry). **d** An O-ring sealed liquid cell (reprinted with permission from Ref. [21], Copyright 2012, Springer Nature)

loading. (2) Self-aligned construction. In this method, two structurally complementary chips can be assembled through the surface tension of liquid droplets, where the in-frame is precisely embedded into the out-frame and their windows are self-aligned [20, 21] as shown in Fig. 8.1c. After self-alignment, the cell is then sealed via vacuum grease or epoxy. This structure guarantees easy alignment but has the disadvantage in spacer decreasing.

If a liquid cell is prepared for the specialized holder, the O-ring assembling is the most straightforward approach. Figure 8.1d displays a cross-section structure of an O-ring sealed liquid cell, where two O-rings clamp the top and bottom chips together with metal or oxide as the spacer [21]. Elastic O-rings will tightly compress the chips while avoiding damage under certain pressure. In order to prevent contact between liquid and vacuum environment, a third O-ring and screws are utilized to form a complete liquid cell setup. This kind of O-ring sealed liquid cells is widely adopted by commercial manufacturers, generally accompanied with supporting holders. Of course, the special design of these holders is favorable for the viewing window alignment of the corresponding chips.

Liquid loading is another challenge for a successful experiment. Before loading, chips are usually treated with plasma cleaning to increase the hydrophilicity of the Si_xN_y surface. For the liquid cell with reservoirs (Fig. 8.1b), a tiny volume (~ 100 nL) of liquid is injected into one reservoir with the assistance of a syringe and Teflon nanotube, and then the capillary force can draw the liquid into another reservoir, so that the spacer between the viewing windows is eventually filled with the solution. For the liquid cell without reservoirs (Fig. 8.1c, d), the solution (~ 1 μL) is directly dropped onto the out-frame/bottom chip, followed by the capping of in-frame/top chip, and sealed with epoxy/O-rings.

Carbon Film Liquid Cell

Carbon films have been chosen as the viewing window of liquid cells which can be further divided into two types: (1) graphene liquid cell; (2) amorphous carbon film liquid cell. Despite the difference in the fabrication process, they have some similarities as discussed below.

Discovering a true electron transparent viewing window to prevent the loss of resolution is always an ultimate goal for liquid cell techniques. With the emergency of two-dimensional (2D) materials, graphene has attracted much attention as an excellent membrane material due to the unique monoatomic layer structure. It has nearly no scattering effect for electron beams, good conductivity for the avoidance of charge accumulation, and possesses considerable mechanical strength, making it an ideal view window material for the liquid cell. The polymer-free transfer method of graphene [22] is crucial for the fabrication of a liquid cell, as shown in Fig. 8.2a. A gold TEM grid with amorphous holey carbon film is first placed on the monolayer graphene grown on Cu foil, followed by the dropping of isopropanol (IPA) onto their surface. During the evaporation of IPA, graphene gradually adheres to the carbon film via surface tension. Then Cu foil is etched by FeCl_3 aqueous solution to obtain a TEM grid with graphene suspended on the holes of the carbon film. The next step is to place two such grids facing in the opposite directions and wet them with the sample solution. The extra solution is then suctioned away. After drying naturally, these two graphene layers will capsule small liquid pockets (several to hundreds of nanometers) between them due to the strong van der Waals force. Finally, the top grid is removed before transferring the graphene liquid cell to a TEM, in which the capsulated liquid pockets are utilized for in-situ imaging.

Despite that the application of amorphous carbon films as the window membrane is prior to graphene, it was mainly adopted for ETEM and biological samples [23], resulting in a poor resolution. Recently, inspired by the success of the graphene liquid cell, the amorphous carbon film is also used for liquid capsulation, as presented in Fig. 8.2b. The fabrication process is much easier than that of the graphene liquid cell. A droplet of the sample solution is sandwiched by two ordinary TEM grids with the carbon film face to face. Then, the grids naturally dry and adhere with each other via van der Waals interaction to form a liquid cell. Similarly, some liquid pockets generate between amorphous carbon films. In comparison with the graphene liquid cell, the amorphous carbon film liquid cell has thicker membrane (graphene: 0.34 nm; carbon film: ~ 15 nm), but still ensures atomic spatial resolution. This is because the

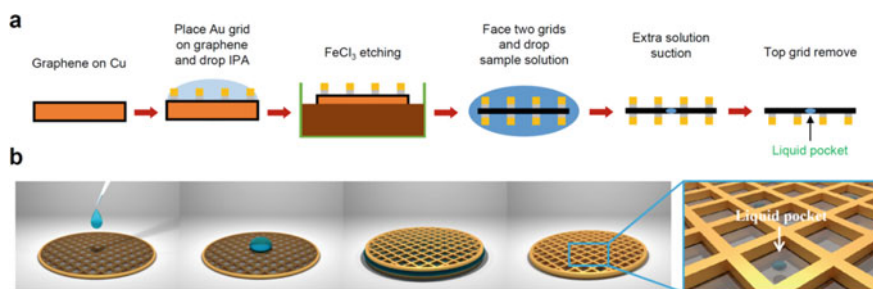


Fig. 8.2 **a** Fabrication procedure of a graphene liquid cell. **b** Preparation of an amorphous carbon film liquid cell (reprinted with permission from Ref. [11], Copyright 2018, Springer Nature)

carbon film can stand a high electron dose under 300 kV, while the best voltage for graphene is 80 or 100 kV because of its vulnerability to electron irradiation.

There are some advantages of the carbon film liquid cell. First of all, it owns low cost and facile fabrication process, especially for the amorphous carbon film liquid cell. Secondly, this kind of liquid cell is based on ordinary grids, which can be mounted into any common TEM holder. Last but most importantly, it provides high resolution information for the investigation of materials at the atomic level.

Hybrid Liquid Cell

Some hybrid liquid cells have also been developed for specific purposes. Among these liquid cells, graphene also plays a critical role in the formation of diverse cell structures, largely ascribed to the easy fabrication and transfer property of this material.

The structure of a Si_xN_y -graphene liquid cell is shown in Fig. 8.3a. The Si_xN_y microchip with a Si_xN_y window first serves as the substrate to cultivate a eukaryotic cell. After the labeling, a graphene sheet is transferred and positioned onto the eukaryotic cell [24]. In this case, the flat Si_xN_y window is used to grow organics, while the flexible graphene provides the tightly coating, leading to good sealing and resolution.

Besides Si_xN_y , other materials such as 2D transition metal dichalcogenides (TMDs) can also act as the substrate to form a MoS_2 -graphene liquid cell (Fig. 8.3b). The fabrication process of this liquid cell resembles that of the graphene liquid cell, except for the different transfer methods of MoS_2 . This structure offers a van der Waals epitaxial relationship between MoS_2 and metal crystals grown on it, so that the formation kinetics affected by substrate could be studied [12].

The combination of layered hexagonal boron nitride (*h*-BN) and graphene brings about an upgraded structure of the graphene liquid cell, the *h*-BN-graphene liquid cell (Fig. 8.3c). To fabricate such liquid cells, several circular holes are created onto an exfoliated thin *h*-BN crystal by lithographical ion etching. After surface cleaning, a graphene sheet is transferred to the top of the *h*-BN. Then the *h*-BN + graphene is further transferred to cover another graphene sheet, meanwhile being submerged in the sample solution. After drying, some solution is sealed in the cylindrical holes

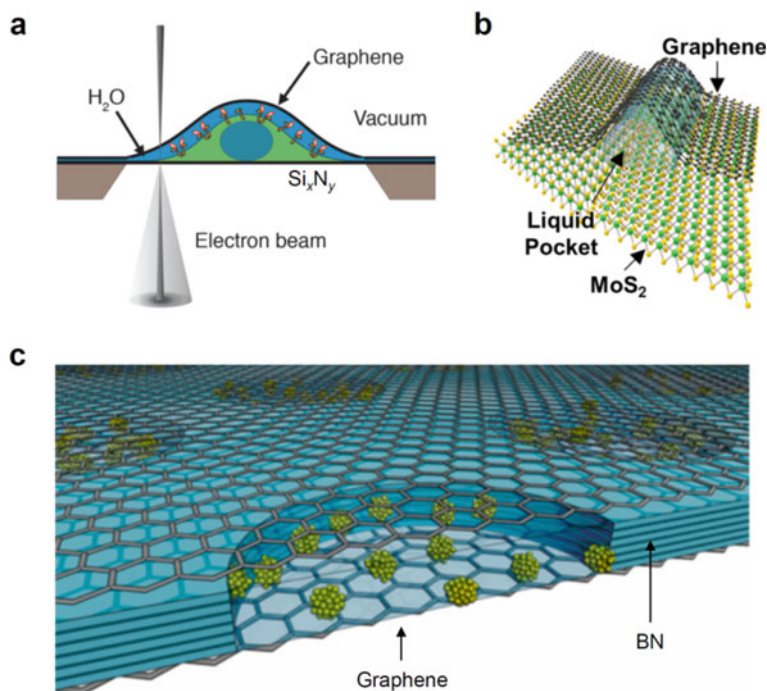


Fig. 8.3 **a** Si_xN_y -graphene liquid cell (reprinted with permission from Ref. [24], Copyright 2017, American Chemical Society). **b** MoS_2 -graphene liquid cell (reprinted with permission from Ref. [12], Copyright 2019, American Chemical Society). **c** h -BN-graphene liquid cell (reprinted with permission from Ref. [25], Copyright 2018, American Chemical Society)

[25]. Apparently, this h -BN-graphene liquid cell ensures very uniform liquid thickness when compared with the liquid pocket of graphene liquid cell. In addition, the thickness of the layered h -BN can be easily tuned from several nanometers to micrometers, indicating a broader application in various fields.

8.2.2 Flow Cell

Now, most of the atomic resolution investigations are realized in static liquid cells, since the static solution allows a thin liquid layer and stable imaging. However, chemical reactions inside a static liquid cell are usually initiated by electron beams, which highly restrict the diversity of the research system. To overcome this deficiency, the capability of the liquid flow is introduced, enabling more *in-situ* experiments including the physical motion of the nanocrystals under flow, the changing of solution during observation, the mixing of different reaction solutions, etc. In this section, we will describe the principle of the flow cell.

The liquid flow function is achieved in Si chips through the microfabrication technology. The fundamental structure of a flow cell is exactly the same as that of the static one, but an extra channel is necessary for liquid flow [26]. The inlet and outlet vias on the top chip are separated at two sides of the middle viewing window, and they connect with O-rings to prevent leakage. The solution can pass through the spacer from the vias, or from the side of chips in other kinds of the flow cell [13]. The whole flow cell is placed into a groove of the specimen holder with some excess room around the chip as the buffer region. During the experiment, the flowing liquid, controlled by the external setup, first goes into the buffer region and then enters the channel to fill up the spacer between the membranes.

The mixing of the reaction solution requires a dual flow cell [14]. As shown in Fig. 8.4, different solutions are injected by two independent tubes equipped inside the holder. The solutions get mixed when arriving at the buffer region, and shortly the mixed solution reaches the chips and passes across the flow channel. Although the occurrence of the liquid mixture at viewing windows cannot be accomplished in the present configuration, it indeed offers valuable information for solution–solution reaction.

Besides the above flow mode, this cell also effectively minimizes the bubble formation, which frequently happens in static liquid cells. But the major issue is the variation of the fluid layer thickness over the experimental course.

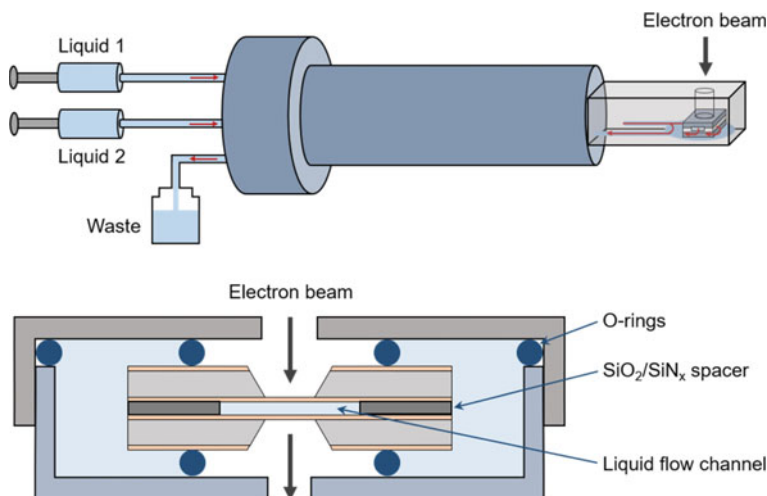


Fig. 8.4 The configuration of a dual flow cell and the corresponding setup of the flow holder

8.2.3 Introduction of Multi-Fields to Liquid Cell

The introduction of external fields into TEM is vital to explore the dynamic process of materials in a deliberate way. The “feedbacks” of materials to a variety of “inputs”, such as electrical signal, heating and cooling, strain, light irradiation, etc., have been systematically studied in vacuum and some environments [27]. Now, in the same way, the emergency of liquid cell techniques is prompting the combination of multiple fields with the liquid environment for in-situ TEM research.

Electrical field is first introduced into the liquid cell. As described in Sect. 8.2.1, the spacer on the bottom chip is created by the patterned deposition. Analogously, a polycrystalline Au electrode can be deposited on the viewing window of the chip [6], and connected to an external electrode (Fig. 8.5a). The reference and counter electrodes are separately placed in the two reservoirs with a part outside. As a result, three electrodes contact the liquid and meanwhile connect to the electrochemical measurement system through the wires embedded in the holder. With the introduction of the electrical signal during the experiment, reactions that occur at the working electrode are imaged through the window. In recent commercial products, this structure has been optimized, where all the three electrodes are coated on the bottom chip and connect to a current source and measurement equipment via metal clamps fixed at the tip of the holder.

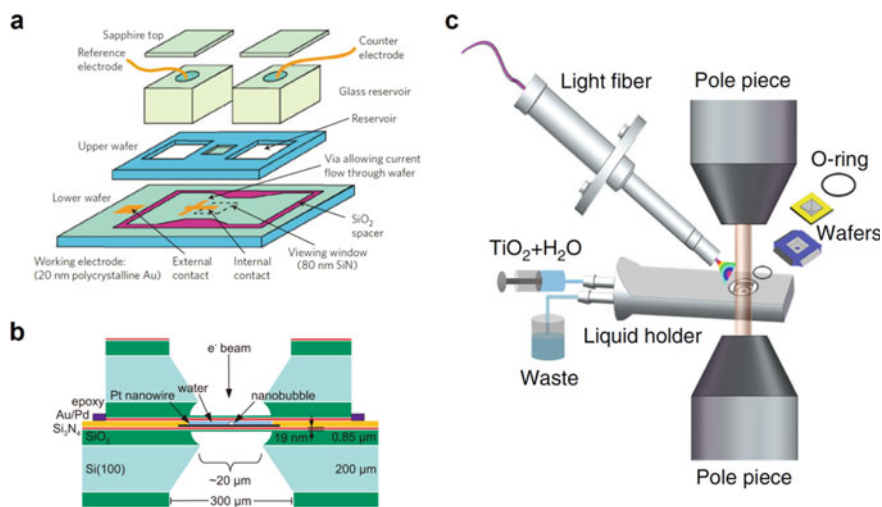


Fig. 8.5 **a** The schematic of an electrochemical liquid cell (reprinted with permission from Ref. [6], Copyright 2003, Springer Nature). **b** The structure of a heating liquid cell (reproduced with permission from Ref. [16], Copyright 2011, The Japan Society of Applied Physics). **c** The setup of a UV light integrated liquid cell (reprinted with permission from Ref. [17], Copyright 2018, Springer Nature)

The most popular strategies for temperature change in in-situ experiments are Joule heating (temperature increasing) and conduction of thermal fluid (both temperature increasing and decreasing). These approaches are now transplanted to liquid cell TEM for the study of temperature-dependent phenomena. A Joule heating method is depicted in Fig. 8.5b. In the fabrication process, a thin Pt wire is deposited across the window of the bottom chip using e-beam lithography, and connected to large metal pads extended to the edges of the chip [16]. This Pt wire serves as the heating source, allowing the direct contact of the liquid to it. The thermal fluid strategy has been employed to a non-electrode liquid cell [28], which is put into a small furnace built inside the holder tip with the size capable of a standard 3 mm sample. It is also notable that the heating experiments of a liquid cell should be carefully carried out, because the imaging quality and sealing property will be seriously affected by the evaporation of the liquid, the bubble generation, and the local fluctuation due to thermal gradients, that are not problematic for a vacuum based in-situ heating experiment.

The optical source has been applied to the liquid cell TEM until very recently [17], as schematically illustrated in Fig. 8.5c. The UV light with the wavelength range from 254 to 450 nm is introduced to the liquid cell by an optical fiber for the in-situ observation of catalyst evolution during the photocatalysis reaction. In this structure, a balanced position of the optical fiber is of great importance. The fiber cannot block the electron beam and must keep the appropriate incident angle due to the groove of the chips, and at the same time the gap of the pole piece should also be taken into account.

8.3 Research Based on In-Situ Liquid Cell TEM

With the booming development of electron microscopy and modern liquid cell techniques, many liquid-related phenomena and reactions can be directly imaged in real time, which is hard to accomplish in old experimental methods. Scientists from different domains are utilizing this technique to study various topics they concern. In this section, we will focus on the discussion about the research of liquid cell TEM in material science, the most successful application among these domains. Physical motion in liquid and chemical behaviors including growth, nucleation, etching, electrochemical and photocatalytic reactions will be the main content. Finally, we will also give a brief description of the life science research using liquid cell TEM.

8.3.1 *Physical Motion*

The physical motion of nanomaterials or bubbles is the most commonly observed behavior in liquid. It does not require a very thin window membrane or special imaging techniques, only if the material and liquid have apparent mass-thickness

contrast difference. Hence, the motion trajectories can be easily obtained for the investigation of physical dynamics of nanomaterials in liquid.

One critical purpose to study the motion dynamics of nanomaterials is the better prediction of their behavior so that researchers can build novel architectures using these nanomaterials as building blocks. By using the electron beam, it was found that the movement of nanoparticles can be precisely manipulated in a liquid cell [29]. As shown in Fig. 8.6a, Au nanoparticles sit on the viewing window membrane if the beam is off, whereas when the electron beam is turned on and focused on a nanoparticle, this nanoparticle is then trapped inside it. With the movement of the beam, the nanoparticle exactly follows beam trajectories due to a piconewton trapping force. In addition, the manipulation of multiple nanoparticles including motion and assembling could also be achieved in the same manner.

Self-assembled colloidal nanoparticles have shown great potential in energy and photo-electronic applications, so the fundamental mechanism of self-assembly is important for the guidance and establishment of such devices. This assembly process was successfully observed using liquid cell techniques [30]. As the solvent evaporates under the electron beam, the motion of the liquid front drags the nanoparticles and aggregates them into a dense disordered phase. Then, the local fluctuations instead

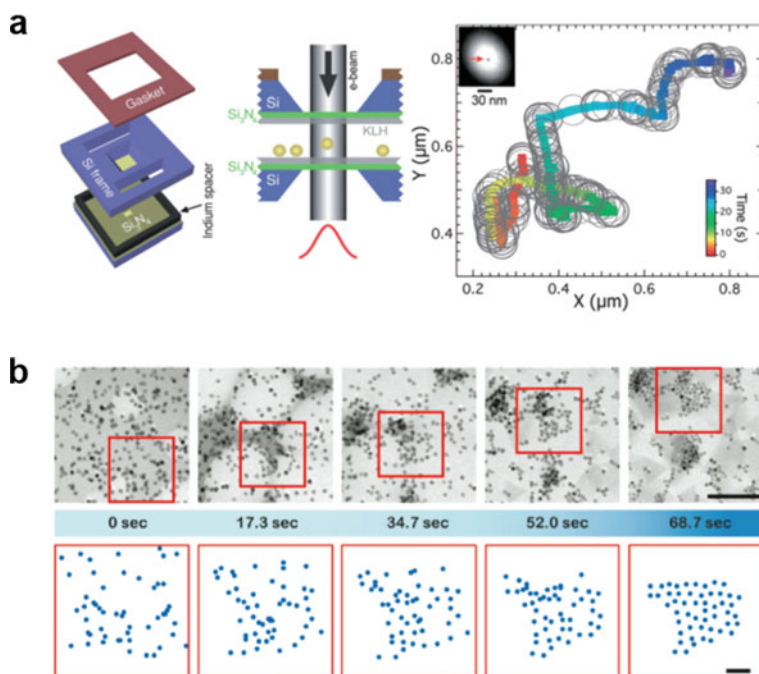


Fig. 8.6 **a** Manipulation of the motion of a Au nanoparticle inside liquid by the incident electron beam (reprinted with permission from Ref. [29], Copyright 2012, American Chemical Society). **b** The formation course of nanoparticle Pt superlattice structure. The scale bar is 100 nm (reprinted with permission from Ref. [30], Copyright 2012, American Chemical Society)

of Brownian motion drive them to form an ordered two-dimensional superlattice, as illustrated in Fig. 8.6b. After the self-assembly event, the superlattice domain can continue to grow through the addition of nearby nanoparticles due to the capillary force. This multiple-stage assembly mechanism is in good agreement with the lattice gas simulation results.

The fast intrinsic dynamics of the physical motion of nanoparticles in liquid have also been revealed. In recent literature [31], two ultrafast laser systems were applied to *in-situ* liquid cell microscope: one was for the generation of ultrafast electron pulse, and the other one was used to initiate the motion of particle dimer, leading to the imaging of the transient rotation dynamics in the nanosecond scale. When the two nanoparticles have similar size, the rotation obeys the traditionally diffusive mode, where the mean square angular displacement shows a linear relationship with time. If the dimer shape asymmetry slightly increases, the rotation then becomes a superdiffusive mode due to the anisotropic random impulsive torques. With further increase of the shape asymmetry, the dimer displays a ballistic rotation because of the unidirectional random impulsive torques.

Other studies about the motion of nanomaterials in liquid, which actuated by electron beams, surface charges, local environment fluctuations, liquid flow, etc., have also been reported. The movement of cobalt oxide nanoparticles and the formation of nanoparticle rings driven by the gradient force of the curved surface of nanodroplets are observed [32]. The 3D configuration and motion of DNA-Au nanoconjugates in an aqueous solution have been revealed through the reconstruction of 2D projected images [33]. Under the condition of flowing fluid, different motion types of Au nanorods have been captured [34].

8.3.2 Nucleation

Besides physical motion, the chemical reactions of nanomaterials attract more attention. The typical synthesis pathway of nanomaterials can be roughly divided into three distinct stages: nucleation from atoms, evolution of nuclei into seeds, and growth of seeds into nanocrystals [35]. However, our study of these processes is still far from the understanding in atomic perspective or even structure details. Especially among those chemical reactions in liquid, nucleation process is the most difficult one to clarify due to the short reaction time and small nuclei size. Recently, liquid cell TEM has been demonstrated to provide opportunities for understanding nuclei mechanisms by capturing the earliest nucleation stage with high spatial and temporal resolution.

The debate of whether the final, stable phase can nucleate directly from solution or through a multistep, multiphase evolution has been lasting for more than a century. Using a dual inlet liquid cell TEM, the careful nucleation pathways of CaCO_3 were imaged through mixing two precursor salt solutions to create a supersaturated solution [14]. Although the atomic *in-situ* observation has not been achieved in this work, the morphology evolution combined with diffraction of CaCO_3 nuclei during each stage provides substantial structural information to make the nature of nucleation

appear real, as shown in Fig. 8.7a. It is found that the amorphous calcium carbonate (ACC) and crystalline phases including vaterite, aragonite, and calcite of CaCO_3 can directly nucleate from the solution and grow to large particles, indicating the direct nucleation pathway. The transformation from ACC to the vaterite and aragonite phase is also observed, but an anticipated ACC to calcite transformation does not exist. In addition, a crystal to crystal transformation of aragonite to calcite is captured if these two phases appear in close contact. All these results suggest the existence of multiple nucleation pathways during the formation of CaCO_3 , which contains the direct generation from solution and indirect transformation from amorphous or anhydrous crystalline phases.

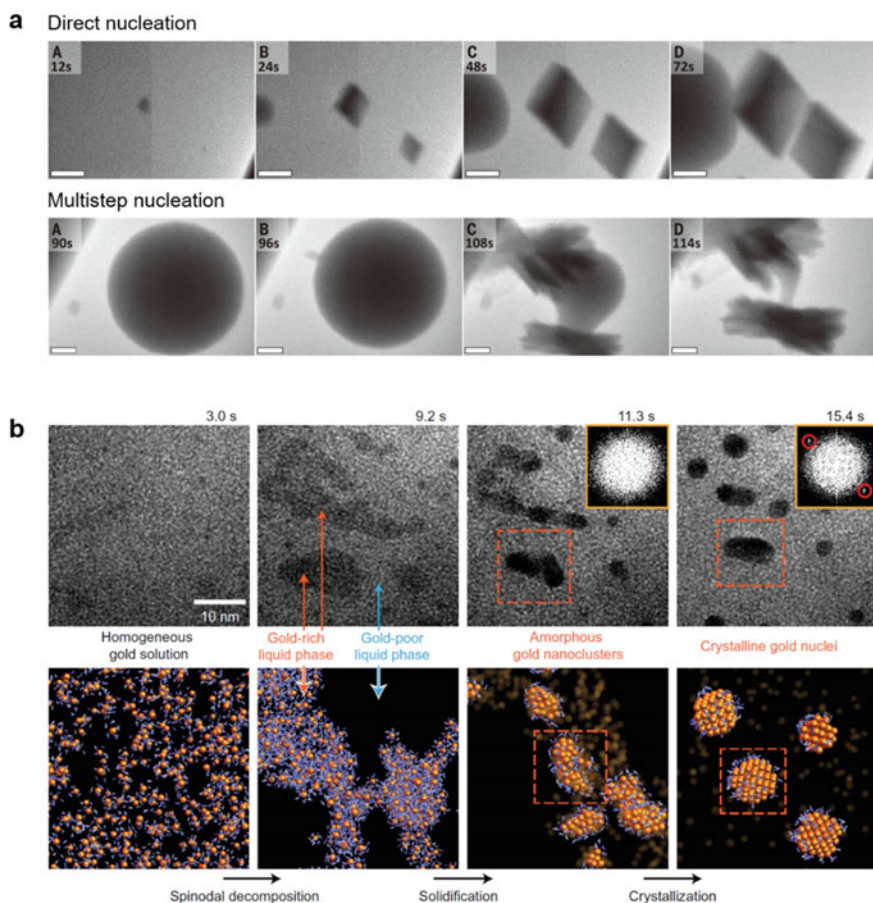


Fig. 8.7 **a** Direct nucleation of ACC and vaterite CaCO_3 phase from the solution, as well as the multistep nucleation from previously nucleated ACC to aragonite phase. Scale bar is 500 nm (reproduced with permission from Ref. [14], Copyright 2014, The American Association for the Advancement of Science). **b** Three-step nucleation pathway for gold nanoclusters in solution (reprinted with permission from Ref. [36], Copyright 2016, Springer Nature)

The complex nucleation process of CaCO_3 may be attributed to the ternary composition, so how about the nucleation of mono-element materials? This question was answered in the recent investigation of the in-situ observation of Au and Ag nucleation pathways [36]. Only one kind of nucleation process accomplished in three distinct steps has been revealed, as presented in Fig. 8.7b. A spinodal decomposition is noticed at the early nucleation stage, where the solution demixes into Au-poor and Au-rich phases. The second step is the formation of an amorphous phase from the Au-rich region. Eventually, amorphous nanoclusters undergo crystallization to form the stable face-centered-cubic (fcc) Au nuclei. This three-step course also applies to Ag nucleation, implying the universality for mono-element noble-metal nanoparticles. The elaborate data processing and ab initio calculation illustrate that the strong coupling of Au atoms and metastable Au complexes should be responsible for these multi-step nucleation pathways.

The in-situ probing of nucleation using liquid cell TEM is becoming a hot topic for the understanding of some fundamental phase transition questions. By adding a matrix of polymer polystyrene sulphonate (PSS) into the reaction solution, it is evidenced that the formed Ca-PSS globules play a key role in the generation of metastable ACC, which is an important phase in CaCO_3 nucleation [37]. Besides the solid state materials, the gas nucleation has also been visualized. It has been reported that the gas bubbles nucleate inside the iron hydroxide during the phase transformation of solids, and then migrate driven by the lattice strain [38]. In spite of these progresses, a thorough understanding of the nucleation process remains with further efforts along with the assistance of liquid cell TEM techniques.

8.3.3 Growth

After nucleation, the nanomaterials grow into different structures, morphologies, and sizes depending on the reaction conditions. The growth of the nanomaterials is most studied in liquid cell TEM experiments, because this process is easy to induce and control as compared to other chemical behaviors. Various stimuli can be used to initiate the nanomaterial growth such as electron beam irradiation, heat, and electrodeposition. The time scale of growth ranges from seconds to hours and can be adjusted by experimental parameters, enabling the real-time record of detailed information. In the following part, we mainly discuss the growth trajectories and mechanisms of nanomaterials. Many important behaviors and phenomena that have not been previously reported are imaged during the in-situ TEM study of nanomaterial growth.

Before the first observation of growth trajectories using liquid cell TEM, the nanoparticle growth through monomer attachment or Ostwald Ripening (OR) is the classical and most acceptable mechanism. However, the coalescence growth, questioned for a long time, is considered resulting in the production of nanoparticles of various sizes which should be avoided to achieve monodisperse nanoparticles.

However, the direct imaging of individual Pt nanocrystal growth presents two simultaneous growth trajectories: monomer attachment from solution and coalescence of two particles [8], as shown in Fig. 8.8a. The Pt nanocrystal grown through monomer attachment gradually increases the size and maintains the spherical morphology. In comparison, the nanocrystal grown through coalescence shows a different pathway. After the coalescence event, the nanocrystal size increases abruptly and reshapes from irregular to spherical morphology eventually. The combination of these two growth trajectories leads to a spontaneous narrowing of size distribution. It is also found that the evolution of mean particle size shows a similar trend of the diffusion-controlled OR process, in spite of different growth mechanisms. This work confirms coalescence as an alternative growth pathway, which should also play an important role in a wide range of nanocrystal synthesis. Later, more experiments reveal the existence of multiple mechanisms co-existed during the nanoparticle growth and their role in different growth stages [39, 40].

Considering that the shape of nanocrystals strongly influences the performance applications, the morphology evolution during monomer attachment growing this is critical for the shape engineering of nanocrystals. According to the Wulff construction, the high energy facets grow faster than the low energy facets, eventually leading to an equilibrium shape with low energy facets exposed. However, recent liquid cell

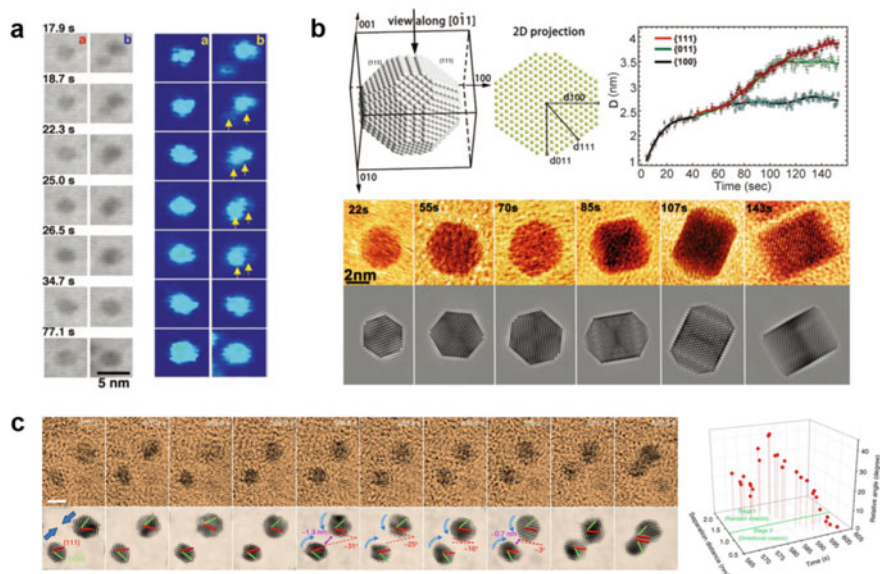


Fig. 8.8 **a** The growth of Pt nanocrystals through monomer attachment and coalescence (reproduced with permission from Ref. [8], Copyright 2009, The American Association for the Advancement of Science). **b** The facet-dependent growth of single Pt nanocube (reprinted with permission from Ref. [9], Copyright 2014, The American Association for the Advancement of Science). **c** The OA growth trajectories of Au nanoparticles (reprinted with permission from Ref. [11], Copyright 2018, Springer Nature)

observations of Pt nanocube growth showed a different perspective [9]. Initially, a truncated octahedron nanocrystal grows in all three main facets, i.e. {100}, {110}, and {111}, and these facets have a similar growth rate until the {100} facets stop growth at a constant size. Afterward, the {110} and {111} facets continue to grow for a while with the same growth rate. Then the growth of {110} facets stops before that of {111} facets because they reach the edge limitation of the cube. Finally, only the {111} facets grow to fill the corners of the cube (Fig. 8.8b). This observation contradicts the Wuff rule about the surface energy minimization. To address this question, the theoretical calculation is performed and reveals that the selective facet arrested shape evolution should be the consequence of the different mobility of surface ligands on different facets.

If the coalescence of nanoparticles occurs at a specific facet, this process is an oriented attachment (OA) growth. OA growth has attracted much attention since it is found to be responsible for the anisotropic development of nanomaterials. Nevertheless, the kinetics and driving force of OA growth are still under debate. Through tracking the OA trajectories of Au nanoparticles, it was demonstrated that the capping ligands play a key role in controlling OA growth [11]. As shown in Fig. 8.8c, when separate at a long distance, particle pairs rotate randomly in liquid, suggesting their free motion. As the particles get closer to about 1.3 nm, their surface ligands interact with each other and result in a directional rotation until they share the same {111} orientation. At this moment, the distance between the particle pair decreases to 0.7 nm, exactly the same as the single layer thickness of surface ligands. The simultaneous expulsion of the ligands then occurs to make their surface jump to contact. The first principle calculations confirm that the weak ligand binding ability on {111} surfaces is the dominant reason for the preferential attachment growth. This ligand driving mechanism should also be applied to other solution based growth systems even when there are no organic ligands, cause the water molecules can also adsorb on particle surfaces to create a hydration force [41].

The growth of nanostructures with complex shapes or different compositions has also been studied. For example, the Au–Pd core–shell nanoparticles, considered as the promising hetero-structure for enhanced catalytic activity, were chosen as a case to demonstrate the seed mediated growth [42]. As shown in Fig. 8.9a, the morphology of the core–shell nanoparticle is very sensitive to the size of Au cores. A uniform deposition of Pd shell is observed on small spherical Au seed particles (5 nm), and this shell can extend to a large thickness. The shell growth on larger Au particles (10 nm, 30 nm) goes in a different way, where Pd preferentially deposits on low-coordination sites like corners and asperities. This non-uniform deposition turns the core–shell particles into a flower-like or dendritic chain morphology. A diffusion limited mechanism of hydrated electrons is then proposed to interpret the related growth process.

Hollow nanoparticles are another attractive structure due to the special void space, which potentially enables drug delivery, energy storage, gas sensing, and so on. The investigation of Bi₂O₃ hollow nanoparticle formation through Kirkendall effect was carried out by using liquid cell TEM [43]. A typical Kirkendall process is shown in Fig. 8.9b. Firstly, a thin Bi₂O₃ layer forms on the Bi nanoparticle surface, resulting

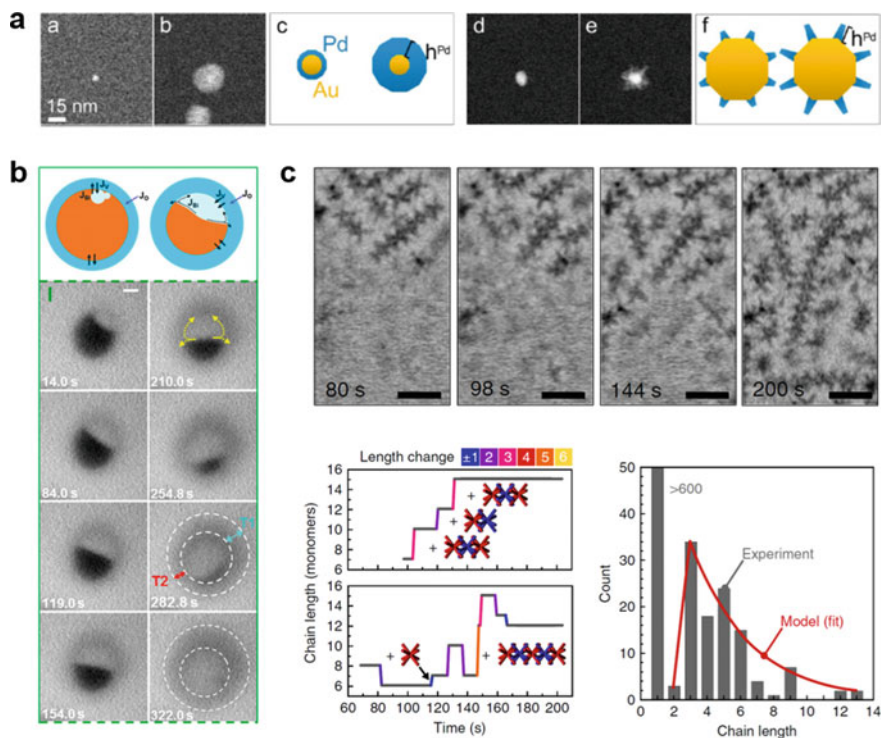


Fig. 8.9 **a** The growth of Au–Pd core–shell nanoparticles with different morphologies (reprinted with permission from Ref. [42], Copyright 2013, American Chemical Society). **b** The formation process of a hollow Bi_2O_3 nanoparticle by Kirkendall effect. Scale bar is 20 nm (reprinted with permission from Ref. [43], Copyright 2013, American Chemical Society). **c** The statistics of the growth dynamics of CdSe/CdS octapod based linear chains. Scale bar is 200 nm (reprinted with permission from Ref. [44], Copyright 2016, Springer Nature)

in a core–shell structure. Subsequently, voids appear at the core/shell interface and become larger by the continuous cost of Bi. At the same time, the Bi_2O_3 shell grew thicker and thicker due to the oxidation of the Bi core. Eventually, a hollow nanoparticle s formed with a non-uniform Bi_2O_3 shell. It is also observed that Bi can also directly diffuse through the shell and get oxidized to form a hollow particle, indicating the rich diffusion pathways during Kirkendall hollowing process.

Construction of functional materials via self-assembled growth of nanocrystals into hierarchical structures is a widespread strategy, but its dynamics with respect to various driving factors remain a question. Using CdSe/CdS octapods as the basic units, the growth mechanism of linear chain superstructures was elucidated [44]. During the growth, octapods orderly interlock with each other to form a stable 1D chain, probably guided by the dynamic fluctuations and the incorporation of organics. As presented in Fig. 8.9c, a statistical mechanics model is then established to describe

the role of van der Waals interactions and entropic forces, from which the strength of inter-particle interaction can be determined.

Nanomaterials growth from liquid environment is a quite complicated process, involving only not the solid state products but also the surrounding chemical solution. So far, the most efficient experimental method to uncover this process is the liquid cell TEM, which offers direct insight into the evolution of morphologies and structures, as well as their relations with external stimuli. Besides the growth trajectories and dynamics mentioned above, many other growth pathways of nanomaterials have also been reported, such as the growth of metal–organic nanotubes [45], nanorods [46], 2D dendritic nanostructures [47], spinel ferrite [48], bonding growth [49], aggregative growth [40], and so on.

8.3.4 Etching

Oxidative etching or corrosion is a common phenomenon no matter in nature, lab, or industry. It refers to the oxidation of zero-valent atoms into an ionic state by oxidizing species in water or solutions. In some cases, etching has a negative influence on the stability of structure and composition of materials, which should be prevented. While in other cases, etching is a valid method to realize materials design and construction. Therefore, a full understanding of the etching mechanism is very essential for the application of materials, especial on a small scale. Recent research efforts mainly focus on metals, metallic oxides, and alloys because these corrosion-sensitive materials exhibit excellent properties in many fields. In this part, we will introduce the progress and challenges in the chemical etching of nanostructures using liquid cell TEM.

In a liquid cell, the electron beam can be used to directly cause growth and motion of samples, as discussed above. Besides these effects, the electron irradiation can indirectly participate in the chemical etching reaction through the generation of oxidizing species in water. It has been reported that these produced oxidizing agents, for example, OH^\bullet , HO_2^\bullet , O , and H_2O_2 , facilitate the etching of Pd nanocrystals [50]. It is found that halogen ions Br^- also play an important role in this oxidative etching, where Pd atoms on the nanocrystal surface are captured by Br^- and transferred into solution in the form of $[\text{PdBr}_4]^{2-}$ (Fig. 8.10a). Moreover, a cubic to round shape transformation is observed during etching, suggesting the preferential etching of edge atoms with more dangling bonds. In spite of these phenomena, the electron beam induced chemical etching is actually very complicated due to the plentiful generated species and limited ion diffusion space.

The etching kinetics are not only dependent on the reaction solution, but also on the structure of nanoparticles. Different corrosion pathways were revealed in core–shell Pd@Pt nanoparticles in the same solution environment [51]. As for the perfect nanoparticles, the etching starts at the corner of internal Pd cores, and then extends to the central part, eventually forming a hollow Pt cage, as illustrated in Fig. 8.10b. When the Pd@Pt cubes have defects, the etching initiates at the defect

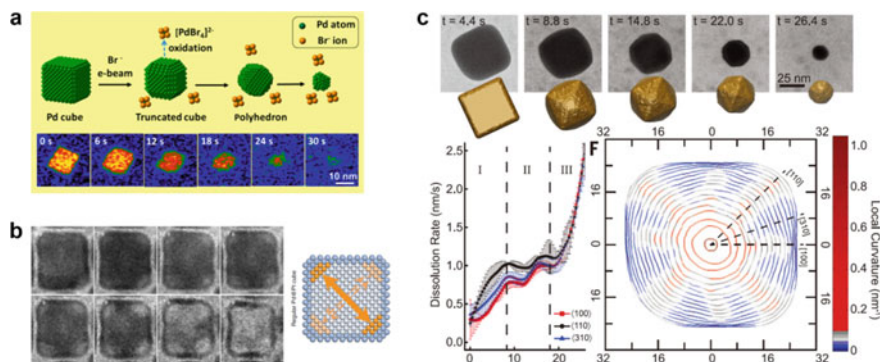


Fig. 8.10 **a** The oxidative etching of Pd nanocrystals with the assistance of Br⁻ ions (reprinted with permission from Ref. [50], Copyright 2014, American Chemical Society). **b** The asymmetrical corrosion of core-shell Pd@Pt nanoparticles. Scale bar is 5 nm (reprinted with permission from Ref. [51], Copyright 2018, Springer Nature). **c** The observation of nonequilibrium Au nanocrystals during etching process (reprinted with permission from Ref. [52], Copyright 2016, The American Association for the Advancement of Science)

areas regardless of their locations, finally leading to a large void. These two cases arise from different etching kinetics: the former is a galvanic process and the latter is a halogen-induced process, which is confirmed from the etching rates and ex-situ characterizations.

In order to create a controllable system for in-situ TEM study of etching dynamics, some etchants are utilized to ensure a uniform solution environment. In such an environment, the nonequilibrium Au nanocrystal state was imaged and quantitatively analyzed during the etching course in FeCl₃ solution [52]. When the FeCl₃ concentration is low, the nanocrystal maintains an equilibrium state with the shape obeying the Wulff construction. In contrast at a high concentration, the competitive etching and restructuring rates lead to a short-lived nonequilibrium state. This metastable state can be clearly recognized through the altering of facet dissolution rates and the formation of the tetrahexahedron intermediate, as shown in Fig. 8.10c. The Monte Carlo simulations also confirm that the tetrahexahedron nanocrystal is a general intermediate structure for fcc metals under a wide range of experimental environments.

Besides metal and bimetallic nanoparticles, etching kinetics of metal films, metal oxides, metal chalcogenides, semiconductors, and carbon nanotubes are also investigated [53–56]. Some other methods like electrochemical etching have also been used in liquid cell TEM to study the industrial corrosion problems.

8.3.5 *Electrochemistry*

As we discussed in Sect. 8.2, with the introduction of metal electrodes onto the chips during the cleanroom fabrication process, external electrical signals can be directly applied to the liquid cell for electrochemical experiments. The working electrode where dominant reactions usually occur is deposited on the viewing window for imaging, and some other electrodes are used for the measurement of feedback signals. The advantage of studying electrochemistry reactions in TEM is that it allows researchers to monitor the relationship between structure information and electrochemical data in real time, which cannot be achieved by other methods.

In the first demonstration of silicon nitride liquid cell techniques, electrical biasing was already incorporated to study the electrochemical deposition of Cu [6], which was a successful method adopted in industrial integrated circuits. By applying a galvanostatic biasing of 5 and 50 mA/cm², the nucleation and growth of Cu clusters are visualized. The nucleation sites of Cu on Au electrodes do not show a preference, but display a homogeneous characteristic instead. After nucleation, the subsequent time-resolved growth of Cu clusters is recorded and the size evolution of some individual clusters is fitted versus time, as shown in Fig. 8.11a. Within the early growth stage (0~2 s), the experimental data of growth kinetics fit well with the Faraday's law, indicating the surface-reaction limited growth mode. However, after ~2 s, a slower growth rate is noticed because the depletion of ions results in the diffusion-limited growth mode at this stage. This work sheds light on the growth mechanism of Cu clusters at the solid-liquid interface, and most importantly opens a venue for the investigation of electrochemical phenomena at the nanoscale or even atomic level. From then on, more and more electrochemical systems have been studied by using liquid cell microscopy techniques.

Electrochemical experiments usually come with electroanalytical techniques to elucidate the scientific issues such as the performance and charge transport mechanism. Therefore, quantitative electrochemical measurements are needed in liquid cell TEM to establish a reliable relationship between the observed dynamics and the corresponding electrochemical data. With the assistance of the improved fabrication techniques of chips and optimized geometry of electrodes, the quantitative measurements were first performed in a flow electrochemical cell [57]. Figure 8.11b shows cyclic voltammetry and impedance spectroscopy nyquist plots of the redox couple [Fe(CN)₆]^{3-/4-}-based system. Under the constant electrolyte flow rate of 2 μL/min, serial scan rates and potentials are used in cyclic voltammetry and impedance spectroscopy to evaluate the redox process and electron/charge/mass transport, respectively. The diffusion coefficients extracted from the measured data well agree with the wide-accepted values in other reports, suggesting the validation of this quantitative electrochemical application.

Energy related systems such as lithium ion batteries have also become a hot electrochemical topic by using liquid cell TEM techniques. Through the direct imaging of the reaction area during the charge and discharge process, some mechanisms of electrochemical events that occur at electrode-electrolyte surface are revealed at the

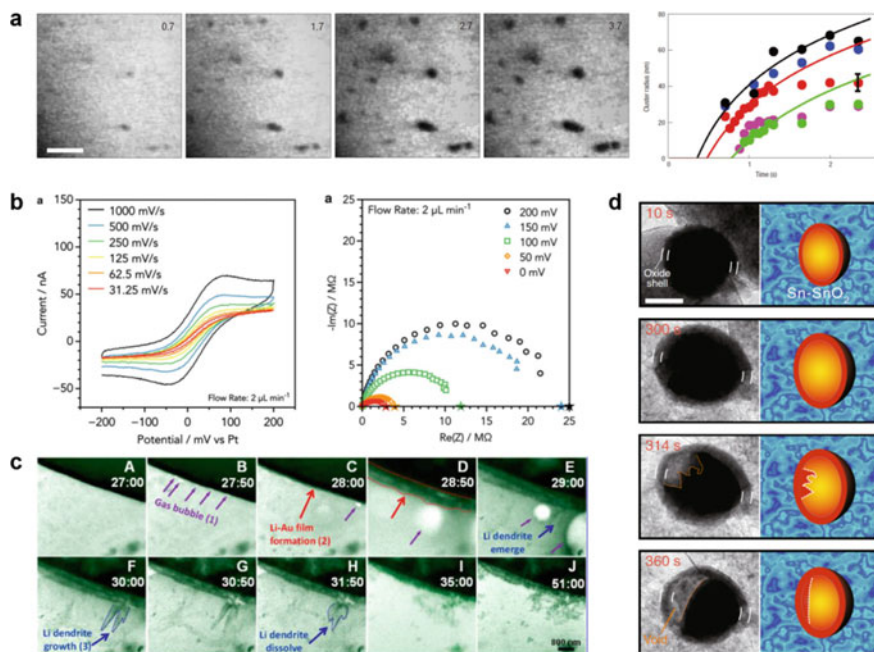


Fig. 8.11 **a** The nucleation and growth of Cu clusters during electrodeposition process. Scale bar is 500 nm (reprinted with permission from Ref. [6], Copyright 2003, Springer Nature). **b** Quantitative electrochemical measurements (cyclic voltammetry and impedance spectroscopy nyquistplots) of $[\text{Fe}(\text{CN})_6]^-$ based electrolyte using liquid cell devices (reprinted with permission from Ref. [57], Copyright 2014, Cambridge University Press). **c** The evolution of Au electrodes during lithiation and delithiation courses (reprinted with permission from Ref. [15], Copyright 2014, American Chemical Society). **d** The morphology deformation of a Sn-SnO₂ core-shell nanoparticle during lithiation under stress. Scale bar is 100 nm (reprinted with permission from Ref. [58], Copyright 2019, Springer Nature)

nanometer scale. As shown in Fig. 8.11c, the in-situ charge and discharge experiment was performed in the commercial $\text{LiPF}_6/\text{EC}/\text{DEC}$ electrolyte [15]. Some bubbles were generated in the early reaction, followed by the formation of a thin Li-Au alloyed layer. With the further increase of the Li-Au layer, drastic decomposition of $\text{LiPF}_6/\text{EC}/\text{DEC}$ initiates the nucleation and rapid growth of Li dendrites. When a reverse sweep voltage is applied, the Li dendrites begin to dissolve and disappear eventually, while the Li-Au alloyed layer remains with thickness reduced. In addition, the formation of the solid-electrolyte interface layer is also observed in this experiment, which is critical for the understanding of the battery stability.

Recently, the stress effect during electrochemical reactions was demonstrated by using in-situ graphene liquid cell TEM [58]. It is found that the stress-related lithiation behavior of Sn-SnO₂ core-shell nanoparticles usually leads to the special morphology evolution, as illustrated in Fig. 8.11d. The nanoparticle undergoes a volume expansion upon initial lithiation, and then shows an oscillation of its size. The

continuous lithiation gives rise to the shrinkage of the nanoparticle spontaneously, accompanied with Kirkendall voids emerging inside the core area, finally resulting in a half-void and half-meniscus structure. This unique evolution of nanoparticle morphology is attributed to the induced mechanical stress and the corresponding uniformity of Li composition among the core–shell structure, implying a huge potential for the stress engineering of Li distribution in lithium ion batteries.

Liquid cell TEM has shown the significant advantages in the in-situ visualization of various electrochemical systems. Some other critical problems about solid–liquid interfaces [59], localized corrosion [60] and energy storage techniques [61] have also been successfully investigated. In the future, this method will certainly attract more and more attention to the research of electrochemical kinetics.

8.3.6 Photocatalysis

The observation of photocatalysis reaction at the solution/catalyst interface is of great importance to the understanding of the catalyst efficiency and activity. Although there have been some literature about the investigation of photocatalysis reaction in nanoscale by using scanning tunneling microscopy (STM) and ETEM techniques, only very limited liquid could exist and be in contact with the catalyst, which fails to reflect the actual reaction environment in the laboratory or industry. Now the liquid cell TEM has provided a great opportunity to study the photocatalysis pathway in real time.

The first in-situ photocatalysis demonstration using liquid cell TEM focused on the water splitting reaction of the most well-known anatase TiO_2 catalyst [17]. Under UV (wavelength from 254 to 450 nm) illumination, a 3.2 nm surface shell appears on TiO_2 after 12 h exposure, followed by the generation of gas bubbles after 18 h exposure, as shown in Fig. 8.12a. The structure analysis, electron energy loss spectroscopy (EELS), and theoretical calculation confirm that the subsurface diffusion of photo-generated water protons that leads to the formation of the metastable surface shell containing Ti^{3+} , which facilitates hydrogen generation due to the effective reduction of the energy barrier. When combining anatase TiO_2 with Pt as the co-catalyst, the self-hydrogenated TiO_2 is still observed, indicating that the formation of the shell is a universal behavior and plays a vital role in the water splitting process.

In addition to the real photocatalysis reaction, the pseudo-photocatalytic behavior stimulated by electron beams instead of the light source has also been studied in liquid cells [62]. Figure 8.12b shows the image sequences of the water splitting phenomena at rutile TiO_2 surface, where the hydrogen evolution occurs preferentially on $\{110\}$ facet rather than other facets. Further investigation reveals that the lower work function of electron removing on $\{110\}$ facet should be responsible for this facet-dependent bubble generation behavior. Although the oxygen evolution is not observed, this reaction is expected to occur on $\{111\}$ and $\{001\}$ facets.

The utilization of the liquid cell to explore photocatalysis in reactions is a new direction among the in-situ TEM techniques, and so far only very limited reports

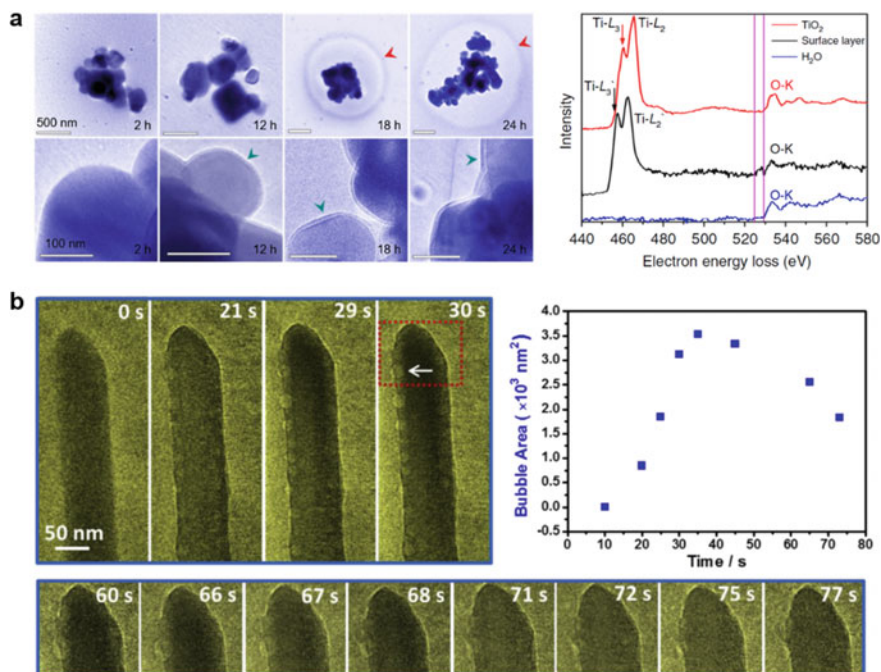


Fig. 8.12 **a** The formation of nanobubble and surface shell during the photocatalytic water splitting reaction of anatase TiO₂ nanoparticles (reprinted with permission from Ref. [17], Copyright 2018, Springer Nature). **b** The facet-dependent production of gas bubble in the pseudo-photocatalytic behavior of TiO₂ nanorods (reprinted with permission from Ref. [62], Copyright 2019, Elsevier)

have been published. However, this field will definitely receive much attention and attract more researchers, because it will provide important insight into the issues of clean renewable energy.

8.3.7 Life Science

Liquid cell TEM technique achieves great success not only in material science but also in life science. It offers several advantages compared to the widely used cryo-TEM when applied in biological samples and soft materials, such as higher imaging contrast and easier sample preparation procedure. Most importantly, the vitrification of cryo-samples inevitably results in the altering of the native state, which can be largely avoided in liquid cell TEM due to the damage resistance of some viewing windows.

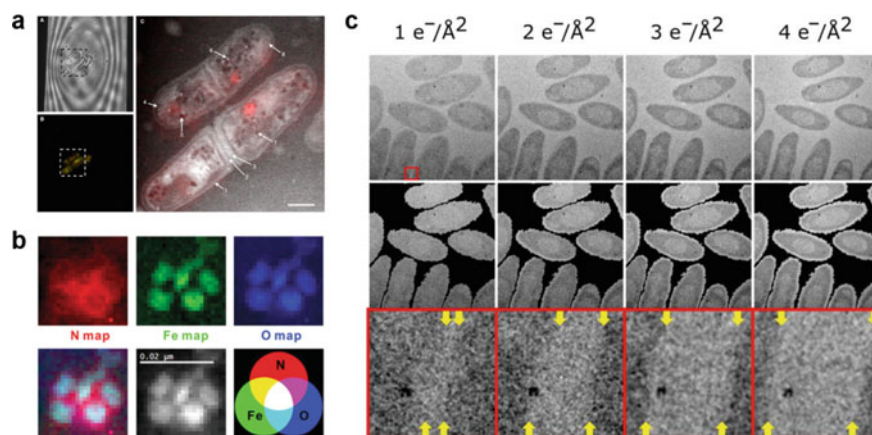


Fig. 8.13 **a** The direct liquid cell STEM imaging of wild-type *S. pombe* yeast cells. Scale bar is 2 μm (reprinted with permission from Ref. [63], Copyright 2011, Elsevier). **b** EELS mapping of ferritin molecules sealed in graphene liquid cell (reprinted with permission from Ref. [64], Copyright, John Wiley and Sons). **c** The cumulative electron effect on *C. metallidurans* biological cells inside liquid cells (reproduced with permission from Ref. [65], Copyright 2018, The American Association for the Advancement of Science)

The visualization of live cells by using liquid cell STEM was first demonstrated on yeast cells [63]. As shown in Fig. 8.13a, a maximal 32 ± 8 nm spatial resolution can be achieved inside a 4 μm liquid layer, much better than that of the traditional light microscopy. The cell is still alive at the initial period of STEM imaging, allowing the identification of some structural features, such as cell wall, primary septum, secondary septum, cell membrane invagination, lipid droplet, peroxisome, and unclassified vesicle.

Besides the imaging, energy spectroscopy analysis is also compatible with biological samples. The nanoscale EELS mapping was carried out on ferritin molecules [64], as shown in Fig. 8.13b. The protein shell containing N and O, and ferritin core containing Fe can be clearly distinguished from the mapping results. The capability of combing imaging with spectroscopy enables us to detect both the structure and chemical bonding information of biological samples.

The interaction of electron irradiation and biological samples is a severe side-effect for the in-situ liquid cell TEM imaging. This effect was studied through the accumulation of electrons on biological cells [65], as shown in Fig. 8.13c. It is found that the cumulative electron flux of 1 to 4 e⁻/Å² is enough to cause the shrinking of *C. metallidurans* cells, implying the structural breaking of the intact organism. This investigation provides valuable evidence for the role of electron irradiation history in liquid cell TEM when dealing with biological samples.

Many other biological species including bacteria [66] and viruses [67] have also been studied using liquid cell TEM. We expect that, in the future, this technique will become an important complement to cryo-TEM for the deeply scientific exploration in life science.

8.4 Conclusions and Outlook

From the static liquid cell to flow cell and then to multi-field cell, every advance in liquid cell techniques has brought with it tremendous possibilities for the exploration of new frontiers in material science, chemistry, physics, and life science. More and more scientists are using liquid cell TEM to probe the fundamentals in liquid environments that are not reachable by previous techniques. The real time imaging at the nanoscale or even atomic level allows the interpretation of the connection between material structure and external stimuli. Various types of liquid cells can satisfy the different needs from many fields. Energy spectroscopy (EDX and EELS) is also compatible with the techniques, which provides broader information about composition and chemical bonding beyond image and structure. Based on the above facts, a wide range of physical dynamics, chemical reactions, and biomaterial behaviors like motion, nucleation, growth, etching, electrochemistry, photocatalysis, etc. have been reported. All these accomplishments indicate an exciting future for liquid cell TEM.

However, liquid cell techniques still need substantial improvement. First of all, there is a lot of room to find the best balance among the thickness, flatness and firmness of the viewing window. This may require an optimized design of the liquid cell structure and a better choice for membrane composition. Secondly, a sophisticated sample preparation method should be established. In the present condition, liquid loading is a big problem because the amount of liquid cannot be well controlled and the thickness of the liquid layer may dramatically vary for each test, which limits the experimental repeatability. Thirdly, more extreme stimuli and external fields should be introduced to the liquid. The purpose of in-situ liquid cell observation is to scale down the lab reaction into the microscopy, in order to know what happens at the nanoscale. But many solution reactions are initiated by electron beams or simple mixing inside the liquid cell, quite different from the lab situation, where hot injection, stirring, and high temperature may be used. Fourthly, the side-effects of the electron beam should be well understood and alleviated. When the electron beam penetrates the liquid solution, it can easily interact with the liquid molecules to generate some species. This process may seriously affect the solution environment or materials inside. By solving these problems, the liquid cell techniques are expected to achieve further success in future research.

References

1. Marton L (1935) La microscopie electronique des objets biologiques. Académie Royale de Belgique: Bulletin de la Classe des Sciences 21:553–564
2. Abrams IM, McBain JW (1944) A closed cell for electron microscopy. *J Appl Phys* 15(8):607–609. <https://doi.org/10.1063/1.1707475>
3. Swift JA, Brown AC (1970) An environmental cell for the examination of wet biological specimens at atmospheric pressure by transmission scanning electron microscopy. *J Phys E: Sci Instrum* 3(11):924–926. <https://doi.org/10.1088/0022-3735/3/11/426>

4. Liao H-G, Niu K, Zheng H (2013) Observation of growth of metal nanoparticles. *Chem Commun* 49(100):11720–11727. <https://doi.org/10.1039/c3cc47473a>
5. Gai PL (2002) Development of wet environmental TEM (Wet-ETEM) for in situ studies of liquid-catalyst reactions on the nanoscale. *Microsc Microanal* 8(1):21–28. <https://doi.org/10.1017/S143192760201005X>
6. Williamson MJ, Tromp RM, Vereecken PM, Hull R, Ross FM (2003) Dynamic microscopy of nanoscale cluster growth at the solid-liquid interface. *Nat Mater* 2(8):532–536. <https://doi.org/10.1038/nmat944>
7. Liu K-L, Wu C-C, Huang Y-J, Peng H-L, Chang H-Y, Chang P, Hsu L, Yew T-R (2008) Novel microchip for in situ TEM imaging of living organisms and bio-reactions in aqueous conditions. *Lab Chip* 8(11):1915–1921. <https://doi.org/10.1039/b804986f>
8. Zheng H, Smith RK, Jun Y-w, Kisielowski C, Dahmen U, Alivisatos AP (2009) Observation of single colloidal platinum nanocrystal growth trajectories. *Science* 324(5932):1309–1312. <https://doi.org/10.1126/science.1172104>
9. Liao H-G, Zherebetsky D, Xin H, Czarnik C, Ercius P, Elmlund H, Pan M, Wang L-W, Zheng H (2014) Facet development during platinum nanocube growth. *Science* 345(6199):916–919. <https://doi.org/10.1126/science.1253149>
10. Yuk JM, Park J, Ercius P, Kim K, Hellebusch DJ, Crommie MF, Lee JY, Zettl A, Alivisatos AP (2012) High-resolution EM of colloidal nanocrystal growth using graphene liquid cells. *Science* 336(6077):61–64. <https://doi.org/10.1126/science.1217654>
11. Zhu C, Liang S, Song E, Zhou Y, Wang W, Shan F, Shi Y, Hao C, Yin K, Zhang T, Liu J, Zheng H, Sun L (2018) In-situ liquid cell transmission electron microscopy investigation on oriented attachment of gold nanoparticles. *Nat Commun* 9(1):421. <https://doi.org/10.1038/s41467-018-02925-6>
12. Yang J, Choi MK, Sheng Y, Jung J, Bustillo K, Chen T, Lee S-W, Ercius P, Kim JH, Warner JH, Chan EM, Zheng H (2019) MoS₂ liquid cell electron microscopy through clean and fast polymer-free MoS₂ transfer. *Nano Lett* 19(3):1788–1795. <https://doi.org/10.1021/acs.nanolett.8b04821>
13. de Jonge N, Peckys DB, Kremers GJ, Piston DW (2009) Electron microscopy of whole cells in liquid with nanometer resolution. *Proc Natl Acad Sci* 106(7):2159–2164. <https://doi.org/10.1073/pnas.0809567106>
14. Nielsen MH, Aloni S, De Yoreo JJ (2014) In situ TEM imaging of CaCO₃ nucleation reveals coexistence of direct and indirect pathways. *Science* 345(6201):1158–1162. <https://doi.org/10.1126/science.1254051>
15. Zeng Z, Liang W-I, Liao H-G, Xin HL, Chu Y-H, Zheng H (2014) Visualization of electrode-electrolyte interfaces in LiPF₆/EC/DEC electrolyte for lithium ion batteries via in situ TEM. *Nano Lett* 14(4):1745–1750. <https://doi.org/10.1021/nl403922u>
16. White ER, Mecklenburg M, Singer SB, Aloni S, Regan BC (2011) Imaging nanobubbles in water with scanning transmission electron microscopy. *Appl Phys Express* 4(5):055201. <https://doi.org/10.1143/apex.4.055201>
17. Lu Y, Yin W-J, Peng K-L, Wang K, Hu Q, Selloni A, Chen F-R, Liu L-M, Sui M-L (2018) Self-hydrogenated shell promoting photocatalytic H₂ evolution on anatase TiO₂. *Nat Commun* 9(1):2752. <https://doi.org/10.1038/s41467-018-05144-1>
18. Donnelly SE, Birtcher RC, Allen CW, Morrison I, Furuya K, Song M, Mitsuishi K, Dahmen U (2002) Ordering in a fluid inert gas confined by flat surfaces. *Science* 296(5567):507. <https://doi.org/10.1126/science.1068521>
19. Zheng H, Claridge SA, Minor AM, Alivisatos AP, Dahmen U (2009) Nanocrystal diffusion in a liquid thin film observed by in situ transmission electron microscopy. *Nano Lett* 9(6):2460–2465. <https://doi.org/10.1021/nl9012369>
20. Huang T-W, Liu S-Y, Chuang Y-J, Hsieh H-Y, Tsai C-Y, Huang Y-T, Mirsaidov U, Matsudaira P, Tseng F-G, Chang C-S, Chen F-R (2012) Self-aligned wet-cell for hydrated microbiology observation in TEM. *Lab Chip* 12(2):340–347. <https://doi.org/10.1039/c1lc20647h>
21. Chen X, Wen J (2012) In situ wet-cell TEM observation of gold nanoparticle motion in an aqueous solution. *Nanoscale Res Lett* 7(1):598. <https://doi.org/10.1186/1556-276x-7-598>

22. Regan W, Alem N, Alemán B, Geng B, Girit Ç, Maserati L, Wang F, Crommie M, Zettl A (2010) A direct transfer of layer-area graphene. *Appl Phys Lett* 96(11):113102. <https://doi.org/10.1063/1.3337091>
23. Daulton TL, Little BJ, Lowe K, Jones-Meehan J (2001) In situ environmental cell–transmission electron microscopy study of microbial reduction of chromium (VI) using electron energy loss spectroscopy. *Microsc Microanal* 7(6):470–485. <https://doi.org/10.1007/S10005-001-0021-3>
24. Dahmke IN, Verch A, Hermannsdörfer J, Peckys DB, Weatherup RS, Hofmann S, de Jonge N (2017) Graphene liquid enclosure for single-molecule analysis of membrane proteins in whole cells using electron microscopy. *ACS Nano* 11(11):11108–11117. <https://doi.org/10.1021/acs.nano.7b05258>
25. Kelly DJ, Zhou M, Clark N, Hamer MJ, Lewis EA, Rakowski AM, Haigh SJ, Gorbachev RV (2018) Nanometer resolution elemental mapping in graphene-based TEM liquid cells. *Nano Lett* 18(2):1168–1174. <https://doi.org/10.1021/acs.nanolett.7b04713>
26. Grogan JM (2011) The nanoaquarium: a nanofluidic platform for in situ transmission electron microscopy in liquid media. University of Pennsylvania
27. Carter CB, Williams DB (2016) Transmission electron microscopy: Diffraction, imaging, and spectrometry, 3rd edn. Springer Science+Business Media, New York. <https://doi.org/10.1007/978-3-319-26651-0>
28. Xin HL, Zheng H (2012) In situ observation of oscillatory growth of bismuth nanoparticles. *Nano Lett* 12(3):1470–1474. <https://doi.org/10.1021/nl2041854>
29. Zheng H, Mirsaidov UM, Wang L-W, Matsudaira P (2012) Electron beam manipulation of nanoparticles. *Nano Lett* 12(11):5644–5648. <https://doi.org/10.1021/nl302788g>
30. Park J, Zheng H, Lee WC, Geissler PL, Rabani E, Alivisatos AP (2012) Direct observation of nanoparticle superlattice formation by using liquid cell transmission electron microscopy. *ACS Nano* 6(3):2078–2085. <https://doi.org/10.1021/nn203837m>
31. Fu X, Chen B, Tang J, Hassan MT, Zewail AH (2017) Imaging rotational dynamics of nanoparticles in liquid by 4D electron microscopy. *Science* 355(6324):494–498. <https://doi.org/10.1126/science.aah3582>
32. Zhou Y, Powers AS, Zhang X, Xu T, Bustillo K, Sun L, Zheng H (2017) Growth and assembly of cobalt oxide nanoparticle rings at liquid nanodroplets with solid junction. *Nanoscale* 9(37):13915–13921. <https://doi.org/10.1039/c7nr04554a>
33. Chen Q, Smith JM, Park J, Kim K, Ho D, Rasool HI, Zettl A, Alivisatos AP (2013) 3D motion of DNA–Au nanoconjugates in graphene liquid cell electron microscopy. *Nano Lett* 13(9):4556–4561. <https://doi.org/10.1021/nl402694n>
34. Mueller C, Harb M, Dwyer JR, Miller RJD (2013) Nanofluidic cells with controlled pathlength and liquid flow for rapid, high-resolution in situ imaging with electrons. *J Phys Chem Lett* 4(14):2339–2347. <https://doi.org/10.1021/jz401067k>
35. Xia Y, Xiong Y, Lim B, Skrabalak SE (2009) Shape-controlled synthesis of metal nanocrystals: simple chemistry meets complex physics? *Angew Chem Int Ed* 48(1):60–103. <https://doi.org/10.1002/anie.200802248>
36. Loh ND, Sen S, Bosman M, Tan SF, Zhong J, Nijhuis CA, Král P, Matsudaira P, Mirsaidov U (2017) Multistep nucleation of nanocrystals in aqueous solution. *Nat Chem* 9(1):77–82. <https://doi.org/10.1038/nchem.2618>
37. Smeets PJM, Cho KR, Kempen RGE, Sommerdijk NAJM, De Yoreo JJ (2015) Calcium carbonate nucleation driven by ion binding in a biomimetic matrix revealed by in situ electron microscopy. *Nat Mater* 14(4):394–399. <https://doi.org/10.1038/nmat4193>
38. Niu K, Frolov T, Xin HL, Wang J, Asta M, Zheng H (2015) Bubble nucleation and migration in a lead–iron hydr(oxide) core–shell nanoparticle. *Proc Natl Acad Sci* 112(42):12928–12932. <https://doi.org/10.1073/pnas.1510342112>
39. Liu Y, Tai K, Dillon SJ (2013) Growth kinetics and morphological evolution of ZnO precipitated from solution. *Chem Mater* 25(15):2927–2933. <https://doi.org/10.1021/cm303522z>
40. Woehl TJ, Park C, Evans JE, Arslan I, Ristenpart WD, Browning ND (2014) Direct observation of aggregative nanoparticle growth: kinetic modeling of the size distribution and growth rate. *Nano Lett* 14(1):373–378. <https://doi.org/10.1021/nl4043328>

41. Anand U, Lu J, Loh D, Aabdin Z, Mirsaidov U (2016) Hydration layer-mediated pairwise interaction of nanoparticles. *Nano Lett* 16(1):786–790. <https://doi.org/10.1021/acs.nanolett.5b04808>
42. Jungjohann KL, Bliznakov S, Sutter PW, Stach EA, Sutter EA (2013) In situ liquid cell electron microscopy of the solution growth of au–pd core-shell nanostructures. *Nano Lett* 13(6):2964–2970. <https://doi.org/10.1021/nl4014277>
43. Niu K-Y, Park J, Zheng H, Alivisatos AP (2013) Revealing bismuth oxide hollow nanoparticle formation by the Kirkendall effect. *Nano Lett* 13(11):5715–5719. <https://doi.org/10.1021/nl4035362>
44. Sutter E, Sutter P, Tkachenko AV, Krahn R, de Graaf J, Arciniegas M, Manna L (2016) In situ microscopy of the self-assembly of branched nanocrystals in solution. *Nat Commun* 7(1):11213. <https://doi.org/10.1038/ncomms11213>
45. Vailonis KM, Gnanasekaran K, Powers XB, Gianneschi NC, Jenkins DM (2019) Elucidating the growth of metal-organic nanotubes combining isoreticular synthesis with liquid-cell transmission electron microscopy. *J Am Chem Soc* 141(26):10177–10182. <https://doi.org/10.1021/jacs.9b04586>
46. Liao H-G, Cui L, Whitelam S, Zheng H (2012) Real-time imaging of Pt₃Fe nanorod growth in solution. *Science* 336(6084):1011–1014. <https://doi.org/10.1126/science.1219185>
47. Zhu G, Jiang Y, Lin F, Zhang H, Jin C, Yuan J, Yang D, Zhang Z (2014) In situ study of the growth of two-dimensional palladium dendritic nanostructures using liquid-cell electron microscopy. *Chem Commun* 50(67):9447–9450. <https://doi.org/10.1039/c4cc03500c>
48. Liang W-I, Zhang X, Bustillo K, Chiu C-H, Wu W-W, Xu J, Chu Y-H, Zheng H (2015) In situ study of spinel ferrite nanocrystal growth using liquid cell transmission electron microscopy. *Chem Mater* 27(23):8146–8152. <https://doi.org/10.1021/acs.chemmater.5b03930>
49. Aabdin Z, Lu J, Zhu X, Anand U, Loh ND, Su H, Mirsaidov U (2014) Bonding pathways of gold nanocrystals in solution. *Nano Lett* 14(11):6639–6643. <https://doi.org/10.1021/nl5032919>
50. Jiang Y, Zhu G, Lin F, Zhang H, Jin C, Yuan J, Yang D, Zhang Z (2014) In situ study of oxidative etching of palladium nanocrystals by liquid cell electron microscopy. *Nano Lett* 14(7):3761–3765. <https://doi.org/10.1021/nl500670q>
51. Shan H, Gao W, Xiong Y, Shi F, Yan Y, Ma Y, Shang W, Tao P, Song C, Deng T, Zhang H, Yang D, Pan X, Wu J (2018) Nanoscale kinetics of asymmetrical corrosion in core-shell nanoparticles. *Nat Commun* 9(1):1011. <https://doi.org/10.1038/s41467-018-03372-z>
52. Ye X, Jones MR, Frechette LB, Chen Q, Powers AS, Ercius P, Dunn G, Rotskoff GM, Nguyen SC, Adiga VP, Zettl A, Rabani E, Geissler PL, Alivisatos AP (2016) Single-particle mapping of nonequilibrium nanocrystal transformations. *Science* 354(6314):874–877. <https://doi.org/10.1126/science.aah4434>
53. Lu Y, Geng J, Wang K, Zhang W, Ding W, Zhang Z, Xie S, Dai H, Chen F-R, Sui M (2017) Modifying surface chemistry of metal oxides for boosting dissolution kinetics in water by liquid cell electron microscopy. *ACS Nano* 11(8):8018–8025. <https://doi.org/10.1021/acsnano.7b02656>
54. Fan K, Zou H, Lu Y, Chen H, Li F, Liu J, Sun L, Tong L, Toney MF, Sui M, Yu J (2018) Direct observation of structural evolution of metal chalcogenide in electrocatalytic water oxidation. *ACS Nano* 12(12):12369–12379. <https://doi.org/10.1021/acsnano.8b06312>
55. Sun M, Li X, Tang Z, Wei X, Chen Q (2018) Constant-rate dissolution of InAs nanowires in radiolytic water observed by in situ liquid cell TEM. *Nanoscale* 10(42):19733–19741. <https://doi.org/10.1039/c8nr04096f>
56. Wang H, Liu Z, Liu H, Guan L, Cao X, Zhang Z, Huang Y, Jin C (2019) Probing the degradation of carbon nanotubes in aqueous solution by liquid cell transmission electron microscopy. *Carbon* 148:481–486. <https://doi.org/10.1016/j.carbon.2019.04.008>
57. Unocic RR, Sacci RL, Brown GM, Veith GM, Dudney NJ, More KL, Walden FS, Gardiner DS, Damiano J, Nackashi DP (2014) Quantitative electrochemical measurements using in situ ec-S/TEM devices. *Microsc Microanal* 20(2):452–461. <https://doi.org/10.1017/S1431927614000166>

58. Seo HK, Park JY, Chang JH, Dae KS, Noh M-S, Kim S-S, Kang C-Y, Zhao K, Kim S, Yuk JM (2019) Strong stress-composition coupling in lithium alloy nanoparticles. *Nat Commun* 10(1):3428. <https://doi.org/10.1038/s41467-019-11361-z>
59. Chen X, Noh KW, Wen JG, Dillon SJ (2012) In situ electrochemical wet cell transmission electron microscopy characterization of solid–liquid interactions between Ni and aqueous NiCl₂. *Acta Mater* 60(1):192–198. <https://doi.org/10.1016/j.actamat.2011.09.047>
60. Chee SW, Pratt SH, Hattar K, Duquette D, Ross FM, Hull R (2015) Studying localized corrosion using liquid cell transmission electron microscopy. *Chem Commun* 51(1):168–171. <https://doi.org/10.1039/c4cc06443g>
61. Mehdi BL, Qian J, Nasybulin E, Park C, Welch DA, Faller R, Mehta H, Henderson WA, Xu W, Wang CM, Evans JE, Liu J, Zhang JG, Mueller KT, Browning ND (2015) Observation and quantification of nanoscale processes in lithium batteries by operando electrochemical (S)TEM. *Nano Lett* 15(3):2168–2173. <https://doi.org/10.1021/acs.nanolett.5b00175>
62. Yin Z-W, Betzler SB, Sheng T, Zhang Q, Peng X, Shangguan J, Bustillo KC, Li J-T, Sun S-G, Zheng H (2019) Visualization of facet-dependent pseudo-photocatalytic behavior of TiO₂ nanorods for water splitting using in situ liquid cell TEM. *Nano Energy* 62:507–512. <https://doi.org/10.1016/j.nanoen.2019.05.068>
63. Peckys Diana B, Mazur P, Gould Kathleen L, de Jonge N (2011) Fully hydrated yeast cells imaged with electron microscopy. *Biophys J* 100(10):2522–2529. <https://doi.org/10.1016/j.bpj.2011.03.045>
64. Wang C, Qiao Q, Shokuhfar T, Klie RF (2014) High-resolution electron microscopy and spectroscopy of ferritin in biocompatible graphene liquid cells and graphene sandwiches. *Adv Mater* 26(21):3410–3414. <https://doi.org/10.1002/adma.201306069>
65. Moser TH, Mehta H, Park C, Kelly RT, Shokuhfar T, Evans JE (2018) The role of electron irradiation history in liquid cell transmission electron microscopy. *Sci Adv* 4(4):eaq1202. <https://doi.org/10.1126/sciadv.aaq1202>
66. Mohanty N, Fahrenholtz M, Nagaraja A, Boyle D, Berry V (2011) Impermeable graphenic encasement of bacteria. *Nano Lett* 11(3):1270–1275. <https://doi.org/10.1021/nl104292k>
67. Cameron Varano A, Rahimi A, Dukes MJ, Poelzing SM, McDonald S, Kelly DF (2015) Visualizing virus particle mobility in liquid at the nanoscale. *Chem Commun* 51(90):16176–16179. <https://doi.org/10.1039/c5cc05744b>

Chapter 9

In-Situ Gas Transmission Electron Microscopy



Ke Fang, Wentao Yuan, Jakob B. Wagner, Ze Zhang, and Yong Wang

9.1 A History of In Situ Gas TEM

Since the pioneers of transmission electron microscope (TEM) laid the foundation of electron microscopy in 1932 [1, 2], the exploration and development of the TEM apparatus itself and various accessories are being constantly carried out.

In the early stages of development, due to the low magnification and unsatisfying resolution of the TEM, high spatial resolution and sensitivity are the main pursuits of modifications to the microscope. Among the affecting factors, the degree of vacuum is an important and accessible factor to improve the resolution. The scattering of electrons by gas molecules on the electron pathway can influence the coherency of the electron beam (e-beam), which can further affect (degrade) the intensity, resolution, and contrast of imaging. Therefore, the tendency to develop the microscope with high vacuum as much as possible prevailed in the early decades. Special attention was paid to optimizing the specimen chamber, because changing the specimen each time could run the risk of vacuum breaking.

However, the specimen characterized in such a high vacuum environment may not represent the structure or status of it under realistic operating conditions, especially for some gas-sensitive materials or special atomic structures that only existed in a gaseous environment. In addition, the dynamic information of structural and compositional evolution of materials in real environment is missing in these vacuum characterizations, though it is of great significance to understand many physical and chemical processes. This dilemma stimulated the development of environmental

K. Fang · W. Yuan · Z. Zhang · Y. Wang (✉)
Center of Electron Microscopy and State Key Laboratory of Silicon Materials, School of
Materials Science and Engineering, Zhejiang University, Hangzhou 310027, China
e-mail: yongwang@zju.edu.cn

J. B. Wagner
DTU Nanolab, Technical University of Denmark, 2800 Kgs. Lyngby, Denmark

TEM techniques, which emphasize simulating realistic gaseous conditions during real-time observation of the specimen.

Actually, the thought of introducing gas into the TEM emerged almost as early as the birth of TEM. The controllable gaseous environment was firstly proposed by Marton in 1935, including two approaches which could accomplish the gas confinement in the close vicinity of the specimen while maintaining the high vacuum in other essential parts of TEM. The first approach is realized by modifying the objective pole pieces, placing pairs of apertures above and below the specimen to confine the gas around the specimen chamber in 1942 [3]; the second approach is creating a sealed (closed) gas cell with electron-transparent windows placed above and below the specimen, which could withstand the pressure difference between the inside and the outside of the cell in 1944 [4].

These two approaches have been subsequently employed in tremendous designs of TEM in the following decades. Both approaches developed well independently and established their special structures and own complete systems, with the amount of applications, respectively. The first method is generally called “opened type” or “aperture”, and another one is named “closed type” or “window”.

At the early stage of development, several researchers carried out TEM observation in reactions by using the residual gases in the microscope column [5, 6]. This method, obviously, suffered from shortcomings including low maximum pressure ($\sim 10^{-3}$ Torr) and uncontrollable gas composition, so that a variety of chemical reactions may occur. To solve these problems, a means of providing an atmosphere of known composition and stable pressure around the specimen is desired.

In 1958, Ito and Hiziya [7] modified the specimen chamber of an ordinary TEM to directly observe the specimen in a chemical reaction at varied temperatures (room temperature to 1000 °C) in gas atmospheres. The gas distance that electrons passed through in that device was 2 cm, and the gas pressure was limited by suppressing the gas diffusion to the column through doubled diaphragms and a separated pump. Image quality was not worse in the range (10^{-4} to 1 mm of Hg) of the gas pressure used if the gas of light elements such as air or hydrogen was employed. In 1962, Heide [8, 9] exhibited another solution of the closed type. The specimen chamber was formed by two specimen grids with the flat surfaces facing each other and kept apart at the desired distance by pieces of thin metal foil. Meanwhile, the grids were covered with a supporting film of low contrast, which had to withstand the gas pressure difference from vacuum (10^{-6} Torr) to 760 Torr.

The available gas pressure in aperture mode was lifted in the following years. In 1968 [10], Hashimoto attained the gas pressure of 300 Torr through modification of TEM, based on the design in which the heating capability up to 1000 °C was achieved [7, 11]. The phrase “controlled atmosphere electron microscopy” (CAEM) was put forward by Baker et al. in the 1970s [12], to describe the technique which enables one to study reactions between gases and solids at very high magnifications, while they were taking place under realistic conditions of temperature, gas, and pressure. The key design idea of CAEM was to create a high-pressure environment in the specimen region while maintaining very low pressure in the rest of the microscope [12]. The pressure in a sealed cell, which was designed by Fujita et al. [13], and exceeded one

atmospheric pressure in 1976. The cell consisted of three films that could be filled with gas or liquid on a 3MV-class electron microscope. It could be used for the study of both biological and physical subjects at high pressure (close to two atmospheres).

The importance of differential pumping gradually emerged with the higher desire for controllable pressure in aperture mode. In 1972, Baker and Harris [14] incorporated the gas reaction stage designed by Hashimoto [10, 11] onto a high-resolution TEM. The specimen chamber was evacuated by a three-stage diffusion pump which was backed by a rotary pump. Differential pumping was exploited in Rodríguez's work [15] in 1990 as well as Lee's modification [16] in 1991. With five apertures and four turbomolecular pumps employed, 0.41 nm of the point-to-point resolution was achieved in 9.3 kPa of H₂ gas for hours. In 1997, Boyes [17] introduced two pairs of apertures above and below the specimen, which were mounted inside the bores of the objective pole pieces rather than between them as in previous designs. The designed custom set of pole pieces for the first stage of differential pumping allowed unrestricted use of regular sample holders in lenses with much lower aberration coefficients. Meanwhile, the apertures restricted the higher angle of diffraction, but useful data can be recorded and provided for convergent beam diffraction pattern analysis with a STEM probe.

In the 2000s, Boyes' design was adapted by TEM manufacturer Philips Electron Optics (acquired by FEI Company in 1997, and FEI was acquired by ThermoFisher in 2017), with further development in electron source and different objective pole piece gaps.

The next significant progress was the introduction of microelectromechanical systems (MEMS) technology [18–21] in the window approach. A MEMS-based nanoreactor was invented for the atomic-resolution ETEM study of nanostructured materials under ambient pressures and elevated temperatures. Creemer et al. [18] miniaturized the gas volume and heater into a sealed system, which allows the observation of nanocrystal growth and mobility on a sub-second time scale with a spatial resolution of 0.18 nm, during heating to 500 °C and exposure to 1.2 bar of H₂. This technique has a more rapid thermal response and smaller specimen drift compared with the furnace-based heater. Since then, MEMS becomes the main trend in the development of the window approach. Of course, the usage of MEMS already expanded to aperture mode spontaneously with the development and maturity of technology itself.

9.2 In Situ Gas TEM Technologies

Since Marton's proposal about two approaches which could accomplish the gaseous environment in TEM, great efforts have been devoted to studying and developing both methods in the following decades.

9.2.1 Aperture (Opened) Approach

Aperture approach is modifying the specimen chamber by placing pairs of apertures between or inside [17] the objective pole pieces to confine the gas leakage, and differentially evacuate individual vacuum stages of the microscope column. The position, number, and size of apertures are essential and influential factors which balance the conflict between the passage of electrons and the airtightness of the specimen chamber. The complete system would incorporate the differential pumping system as well, to avoid a gas leak and maintain the high vacuum in the other essential segments of the TEM.

There are no additional membranes, which are made of amorphous material on windows to degrade the resolution completely, meaning that the images are only derived from the specimen itself and gas molecules (disperse uniformly). Meanwhile, the modification of the specimen chamber has little effect on the specimen holder, which means that the normal holders used in a regular TEM are also compatible with the ETEM. In particular, the use of standard TEM specimen holders supports various sample geometries and allows additional (in situ) functionality, such as tomography, optical studies (of photocatalysts), and mechanical testing (of metals). Furthermore, the specimen preparation of aperture mode is also much easier and more convenient than the window mode, given the fact that the completion of a perfectly sealed cell requires several critical processes which should be paid enough attention to. The disadvantages of aperture mode are also obvious. It can't be used for liquid–solid interactions, and another distinct shortcoming is the maximum gas pressure limited to the size of the apertures, the power of the differential pumping system, and a much thicker gas layer compared with window mode. Actually, the controllable gas pressure in the aperture mode is still lower than the window mode nowadays.

Owing to its robustness and compatibility with specimen types as well as flexibility in experimental conditions [22], the aperture mode was preferred in the early developing period of the gaseous environment.

The aperture environmental cell was constructed by Ito [7]. In the same year, Hashimoto [11, 23] also modified an electron microscope with three lenses to observe the metal-oxide crystal growth on the surface of metal filament (tungsten) under heating and a gaseous environment. The metallic tungsten wire was heated from 700 °C to its melting point (nearly 3000 °C) in a vacuum of 10^{-2} mm Hg (1.33 Pa). In 1968, Hashimoto [10] improved the design of the specimen stage and elevated the acceptable gas pressure to 300 Torr. The specimen was placed on a film covering the hole in the platinum ribbon and heated by an electric current sent through the ribbon (Fig. 9.1b). The gas was supplied around the specimen through a pipe and overflowed into the vacuum of the microscope column through the two platinum apertures on either side of the ribbon. The overflowed gas from the specimen chamber was pumped out separately from the evacuation system of the main column, and the specimen stage can be taken out from the vacuum of electron microscope column through an air lock system without breaking down the vacuum. These efforts led to the

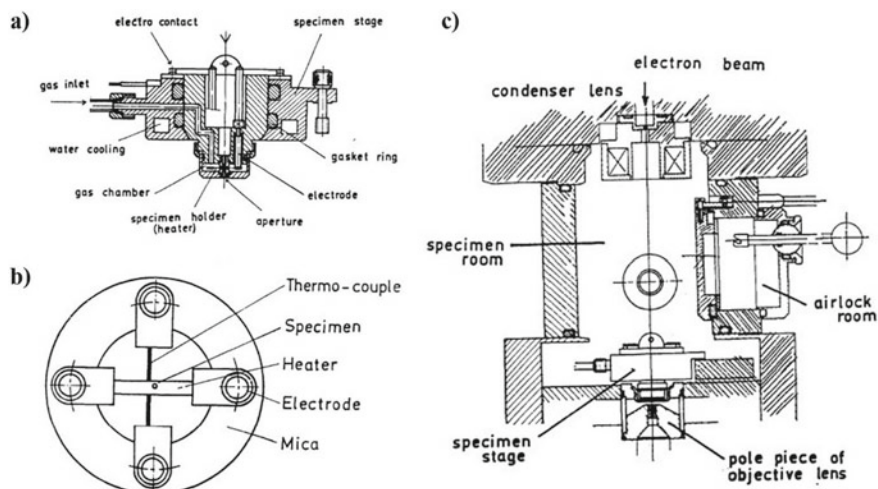


Fig. 9.1 a Cross-section of gas reaction specimen chamber. b Specimen holder. c Cross-section of the electron microscope column in which gas reaction chamber is installed (reproduced with permission from Ref. [10], Copyright 1968, The Physical Society of Japan and The Japan Society of Applied Physics)

production of a commercial gas reaction stage, and the image resolution achievable was 5–10 nm with an air pressure of 40 kPa (300 Torr).

In the same year, Fryer [24] investigated the oxidation of graphite catalyzed by palladium by heating the specimen to 500 °C using a Siemens Elmiskop I electron microscope with a heating stage in a vacuum of 10^{-5} Torr, then let in dry air passing over the specimen by means of special attachment. The behavior was watched and recorded on photographic plates and on videotape by means of closed-circuit television.

Mills and Moodie designed and constructed an electron microscope stage which combined operation at high resolution with various facilities including free movement, tilting, heating and cooling, anticontamination, and gas injection in 1968 [25] as well. A curved silver capillary whose tip engaged in the sleeve of an injector was mounted on the specimen platform and extended inside the capsule to within 5 mm of the specimen cup. The column pumps, working through the capillary, satisfy a rate adequate for the evacuation of the line between the taps and the valves, and for adjustment of the pressure in the fixed volume.

Although the differential pumping system was not employed in Mill's experiment, the importance and necessity of it displayed gradually, especially catering to the higher gas pressure demand during research.

In 1972, Baker and Harris incorporated a modified gas reaction stage (JEOLCO JEM AGI attachment, commercially available, designed by Hashimoto [10, 11]) onto a JEM 7A "high-resolution" electron microscope. The specimen chamber was evacuated by a three-stage diffusion pump backed by a rotary pump. The attachment

omitted the second aperture used in Hashimoto's design in order to retain the diffraction facility, but with some sacrifice to the maximum attainable gas pressure (up to 30 kPa instead of 40 kPa). Of course, the maximum operating pressure in the cell was dependent upon the area of the aperture, the pumping speed of the auxiliary pump, and the molecular diameter of the gas.

Lee and coworkers [16] employed the aperture-limited, differential pump type in their experiment as well in 1991. A pole piece was designed for a JEOL 4000 that has a gap of 14 mm compared to 4–6 mm in the high-resolution pole pieces. Five apertures were used, with two primary apertures of them located in the body of the cell, two secondary apertures located in the pole piece, and a final aperture located in the lower section of the condenser lens stack. The gap between the principal apertures was reduced to 4.3 mm and a tilt of $\pm 30^\circ$ can still be obtained from two perpendicular observing directions using this scheme. Another spotlight of the design was the release of restrictions on high-angle diffraction. For an accelerating voltage of 400 keV, the maximum diffraction angle that can be observed corresponds to 1.4° . Four Seiko-Seiki turbomolecular pumps were employed to accomplish the differential pumping (1) between the principal and secondary apertures, (2) in the volume surrounding the pole piece, (3) between the upper secondary aperture and the condenser stack aperture. With this arrangement, the environmental cell can support 20 kPa (150 Torr) of H_2 for short periods of time (minutes) or 9.3 kPa (70 Torr) of H_2 gas for several hours.

In 1997, Boyes and Gai [17] made a breakthrough in the position of apertures on a Philips CM30T TEM/STEM (scanning TEM) system. They introduced two pairs of apertures above and below the specimen, which were mounted inside the bores of the objective pole pieces rather than between them as in previous designs (Fig. 9.2). This approach allowed unrestricted use of regular sample holders in a relatively narrow gap lens ($S = 9$ mm) with much lower aberration coefficients ($C_s = C_c = 2$ mm) than have been possible with previous environmental cell designs. Such design is dedicated to the environmental cell (ECELL, or gas reaction cell), and the controlled environment ECELL volume is the regular sample chamber of the microscope. It was separated from the rest of the column by the apertures in each pole piece and by the addition of a gate valve, which was normally kept closed, in the line to the regular ion getter pump (IGP) at the rear of the column. Pumping ports have been added to the column between the ECELL apertures located in upper objective lens (OL) polepiece and lower OL polepiece, respectively, for the first stage of differential pumping. Then a second stage of pumping between the condenser aperture and upper OL polepiece, and between lower OL polepiece and selected area apertures was accomplished in the modified column liner tubes. The maximum allowable pressure of this apparatus was 50 mbar. In addition, due to the desire for maximum gas pressure attainable, the apertures were normally small enough to restrain gas leakage, which block the high-angle scattered electrons simultaneously, limiting annular dark-field STEM (ADF-STEM) imaging. Here, the relatively large apertures in the cell provided useful angles of diffraction in TEM mode, and for convergent beam diffraction pattern analysis with a STEM probe. The design of the ECELL is outstanding and developed continuously in the following years with the improving capability and expanding research fields

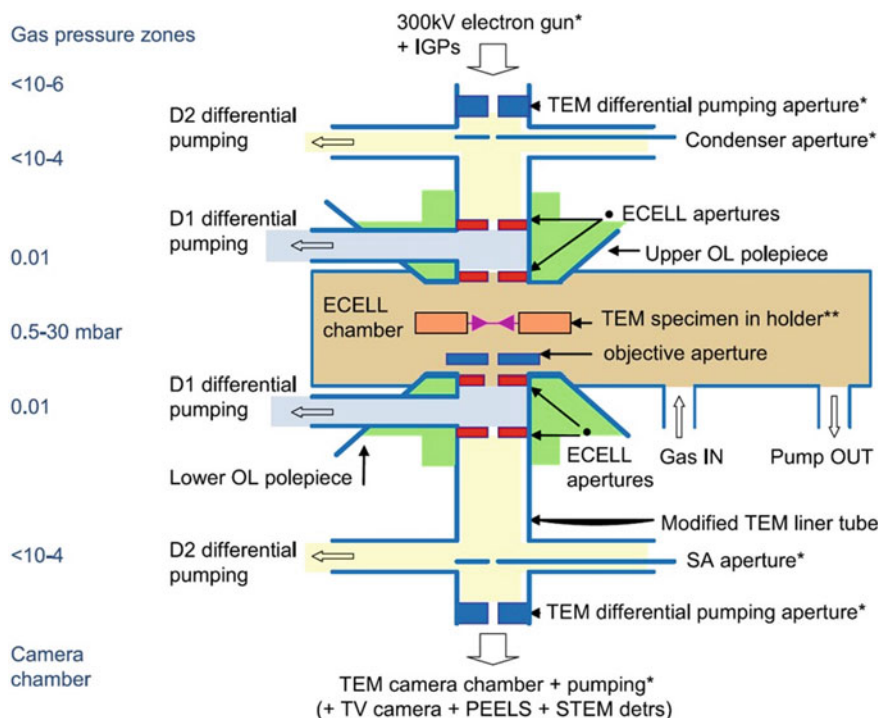


Fig. 9.2 Schematic of the basic geometry of the aperture system from Boyes and Gai (reproduced from Ref. [26], copyright 2014, Elsevier Masson SAS)

[26–30]. And in 2013 [28], they introduced the modification of double aberration-corrected (2AC) JEOL 2200 FS FEG TEM/STEM to provide both ETEM, and for the first time environmental STEM (ESTEM), with full functionalities. These include introducing controlled conditions of the gas environment and high temperature with uncompromised high angle annular dark field (HAADF) Z-contrast ESTEM imaging, low background ESTEM EDS (energy-dispersive X-ray spectroscopy) microanalysis, AC ESTEM EELS (electron energy-loss spectroscopy), and wide-angle electron diffraction analyses of nanoparticle structures and wider crystallography.

An inventive gas-providing method with a specialized holder was proposed by Kamino et al. [31] in 2005. The side-entry specimen holder consisting of a heating element and a gas injection nozzle could be attached to a conventional TEM without any modification. A spirally wound fine wire of tungsten with a diameter of 25 μm was used as a heating element (Fig. 9.3a), which was heated by a direct electric current via a power supply unit equipped with batteries. Since a firewire of tungsten was used as the heating element, the application is limited to particles with a diameter of several micrometer or smaller. Definitely, the design provided the capability of high-resolution TEM imaging at very high temperatures. A gas injection nozzle with an inner diameter of 0.5 mm was built near the heating element at a distance

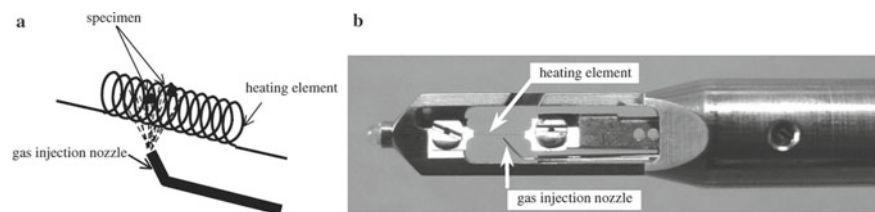


Fig. 9.3 Schematic diagram (a) and an external view (b) of the gas injection/specimen heating holder (reprinted with permission from Ref. [31], Copyright 2006, Oxford University Press)

of ~ 1 mm. The experiment was manipulated in a Hitachi H-9500 and a Hitachi-9000NAR, which were ETEM actually (the microscopes have fixed apertures with a diameter of 0.3 mm between the first and second condenser lenses, without any added aperture between the specimen chamber and the electron gun chamber). The pressure of the electron gun chamber was kept in the middle of 10^{-5} Pa even after the pressure of the specimen chamber reached the middle of 10^{-2} Pa at the gas-flow rate of ~ 7 ml \cdot min $^{-1}$. This pressure in the electron gun chamber was sufficient for working with the LaB $_6$ cathode. In other words, the observation of chemical reactions in a gaseous atmosphere in the range of 10^{-2} Pa can be carried out in a conventional TEM equipped with a LaB $_6$ cathode without any modifications of the column and/or the pumping systems. In fact, the holder allowed observation of TEM images of the gas-reacted specimen at temperatures of 1300 K in the $\sim 2 \times 10^{-2}$ Pa gaseous environment at atomic resolution.

In the 2000s, the design of Boyes and his coworkers was adapted by TEM manufacturer Philips Electron Optics, with further development in electron source and different objective pole piece gaps. Later versions of the in situ ETEM instrument, (which include the CM 200–300 series, and Titan) have been installed in laboratories around the world.

The ETEM installed at the Center for Electron Nanoscopy in the Technical University of Denmark (DTU Cen) [32] is a typical example based on the collaboration of Boys, Gai and Philips. Multilevel turbomolecular and ion getter pumps were equipped successively to sustain high vacuum around the electron source. As shown in Fig. 9.4a, each pumping stage is separated by additional apertures that result in pressure drops, approximately three orders of magnitude lower per aperture, from a pressure of ~ 1500 Pa in the sample region to below 10^{-6} Pa in the field emission gun region. The microscope can be operated in two primary modes, including conventional operation (low pressure) which is pumped using the standard ion getter pumps, and ETEM mode whose pumping pathway is through three turbomolecular pump valves. Furthermore, an image C_s corrector and a monochromated electron source are both employed to improve the spatial resolution and energy resolution, respectively. When the microscope is operated at an acceleration voltage of 300 kV, the measured energy spread could be better than 200 meV (in high vacuum) with the monochromator, and the point resolution could be brought down to below 0.1 nm with the C_s corrector.

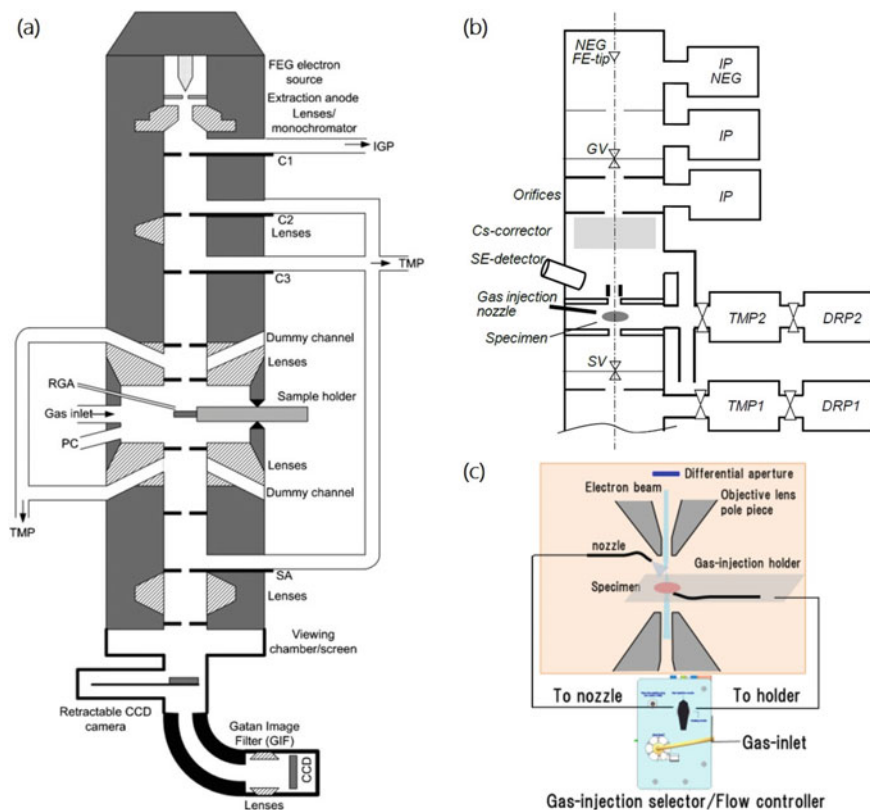


Fig. 9.4 **a** Schematic diagram of differentially pumped TEM column (FEG, field emission gun; IGP, ion getter pump; TMP, turbomolecular pump; RGA, residual gas analyzer; PC, plasma cleaner; C1, first condenser aperture; SA, selected area aperture) (reproduced with permission from Ref. [32], Copyright 2010, Taylor and Francis). **b** A schematic diagram of differential pumping system suitable for environmental (S)TEM imaging (reproduced with permission from Ref. [33], Copyright 2019, Cambridge University Press). **c** A schematic diagram of gas injection system suitable for environmental (S)TEM imaging (reproduced with permission from Ref. [34], Copyright 2019, Cambridge University Press)

The ETEM series in FEI developed in the following years, and the up-to-date model is called “Themis ETEM”, which can be combined with optional image C_s corrector, Thermo Scientific™ X-FEG module, and monochromator technology to further extend it to meet the high standards in atomic-resolution STEM imaging and spectroscopy expected from Themis TEM technology. The Themis ETEM features an innovative differentially pumped objective lens, uniquely designed for the ETEM platform. This lens design enables all the same features from a standard Themis S/TEM, such as window-free imaging and compatibility with Themis TEM heating holders for easy sample insertion, while also allowing ample chamber space for a full double-tilt capability to support 3D tomography. Gas inlets allow safely adding

of inert and reactive gases to the chamber. Gas pressures in ETEM experiments can be accurately preset from 10^{-3} Pa up to 2,000 Pa (for N_2). Furthermore, The Themis ETEM is equipped with a mass spectrometer to determine the gas composition in either the gas inlet system or the specimen area. A built-in plasma cleaner allows for the cleaning of the specimen area after using a gas.

In 2018, the analytical 200 kV cold field emission TEM (HF5000, Hitachi High-Technologies) equipped with an in house designed probe-forming aberration corrector was introduced and the imaging performance of the environmental real-time STEM was reported by Hitachi Company [33, 34]. Figure 9.4b shows the schematic diagram of the differential pumping system of HF5000 suitable for environmental (S)TEM imaging. An orifice is added between the gun valve and specimen chamber for enhancement of the differential pumping system. The HF5000 can have two gas injection nozzles, one is attached to the specimen chamber and the other is in a filament-heating holder. The gas can be chosen independently (Fig. 9.4c). Gas flow is limited to one nozzle at a time and can be controlled. Maximum allowable flow rate is 3.5 sccm and the calibrated local pressure around the specimen is 10 Pa at the maximum flow. At an accelerating voltage of 200 kV, the TEM resolution (lattice) is 0.102 nm, while the STEM resolution is 78 pm. In addition to retaining key features of previous instruments, such as the automatic correction function and the symmetry-dual Silicon Drift Detector, the HF5000 could simultaneously obtain a secondary electron image with rich high-resolution surface morphology information at the atomic scale besides DF/BF live images. The HF5000 key feature of in situ STEM is a live scanning acquisition (25 frames/s) that allows real-time observation and video recording of dynamic atomic-scale reactions (structure change and elemental diffusion). Meanwhile, the chip-based sample holder is developed using MEMS technology by Norcada and Hitachi High-Technologies Canada. Maximum heating temperature of this holder is 1100 °C and the minimum controllable temperature increment is 1 °C. Heating up speed from room temperature (RT) to 1000 °C is as fast as a few seconds. In other words, HF5000 almost aggregates and fuses core technologies perfected in the development of Hitachi's HF series of TEMs.

9.2.2 Window (Closed) Approach

The window approach is creating a sealed cell which contains the specimen, with electron-transparent windows which could withstand the atmospheric pressure between the inside and the outside of the cell.

The feature of this mode is the airtightness of the cell, which enjoys conspicuous advantages. Firstly, the whole volume and the specimen itself are confined by the electron-transparent windows, which could sustain higher gas pressure with the development of window material. The length of gas–electron interaction is much shorter compared with the aperture mode (normally several microns), so as to improve the acceptable gas pressure. The atomic resolution can be achieved under one atmosphere or higher (~ 4.5 bar) [18–20, 35–37] nowadays. Secondly, a window-friendly

cell specimen holder is compatible with different TEMs without any modification to the microscope itself. And the cost of purchasing or modifying a specimen holder is much smaller compared with a differential pumped ETEM. Furthermore, the sealed cell could contain liquid or wet samples, which is the unique advantage of the window mode. Finally, due to the lack of additional apertures which restrict the leakage and diffusion of gases, wide-angle electron diffraction and HAADF imaging could be operated (definitely, HAADF could be implemented in the aperture mode at present).

Unavoidable drawbacks are obvious as well. The unique airtightness is a superiority and a risk simultaneously. The possibility of the fracture of the windows or leakage of the gas during experiments would deteriorate the high vacuum of the column and electron source. Meanwhile, the airtightness results in the complexity and difficulty of the sample loading operation, especially under the demand of maintaining the centering and coupling of top and bottom cell windows. Thirdly, even though the window materials were selected carefully and fabricated finely to sustain the amorphism and homogeneity, the electron-transparent windows still interact with the electrons, resulting in the scattering information superimposed on the image obtained. Furthermore, the scattering effect that results from the amorphous windows is not neglectable, especially since the thickness would influence the quality of imaging immensely. Another easily neglected problem is the contamination from the specimen, which will evaporate/sublimate and condensate on the top window, hindering the observation. Finally, the existence of windows hindered the acquisition of EDS signals as well (it is realizable using specifically designed cells nowadays and is already commercialized, e.g. DENSsolution and Protochips), and local sample loading area and windows confined the observation view, normally much smaller than conventional TEM. Generally, samples could only tilt in one direction with the limitation of the geometrical shape of nanoreactors, which influenced the observation of specific directions.

The materials of the electron-transparent window are essential in the development of the window mode, and they must satisfy the following requirements: (1) be electron-transparent, which is the vital factor; (2) have sufficient strength to resist the pressure difference inside and outside the cell; (3) scatter weakly and non-oriented to preserve the diffraction information of the specimen. The atomic number of the element contained in the window is usually small since a larger atomic mass exacerbates the scattered effect. Initially, the windowed cells were constructed from metal (e.g. Cu/Ni) grids, O-rings, and thin films [8, 38, 39]. Gradually the amorphous material (carbon, polyimide, silicon nitride, silicon dioxide, and alumina) have been used as windows [39].

An enclosed cell to protect the specimen from the high vacuum and electron bombardment was devised by Abrams and McBain in 1944 [4]. The plastic windows scarcely interacted with electrons, and they were liquid-tight and vapor-tight and easily withstand a difference of one atmosphere pressure between the inside of the cell and the remainder of the electron microscope.

In 1962, Heide's experiment [8, 9] exhibited a successful sealed cell of variable gas pressure. The specimen chamber was formed by two specimen grids with the flat surfaces facing each other and kept apart at the desired distance by pieces of thin

metal foil. Both grids were covered with a supporting film of low contrast, which has to withstand the air or gas pressure (760 Torr) over the central openings, meanwhile one of them served as a supporting film for the specimen. The gas was injected through a tube placed in the opening of the column.

So far, the specimen supporting method was placing the specimen on the grid or the supporting film served as the window, which resulted in the difficulty in heating, and the gaseous environment was confined by the single gas line which is incapable of continuous flowing gas.

Escaig and Sella made an important integration of the heater and gas support system in 1969. Twin gas lines in their holder supported the continuous circulation of gas while the temperature of the specimen varied. The windowed cell consisted of triple layers of carbon, nitrocellulose, and silica (facing the specimen), and maintained a gap of approximately 1 mm between window and specimen, which was successfully employed for in situ oxidation of copper, tungsten, and titanium.

In the late 1960s and 1970s, the development of high-voltage (1 meV) electron microscopes with the stronger penetrating power of electrons led to enclosed gas reaction cells with thicker, stronger windows. Fujita [13] designed a new sealed cell with a twin gas line for a 3 MV-class electron microscope. Metal meshes which supported the cell films were chosen from vapor-deposited aluminum, SiO_x , and carbon film depending on the purpose. The sealed gas cell can be pressurized up to 195 kPa (1471 Torr) by circulating gas or liquid into the capsule. Meanwhile, the specimen can be heated to 1000 °C or even higher through direct electrization of Ni-mesh or the specimen itself, and cooled with a liquid nitrogen tank.

Images of the crystal lattice of ceria were recorded under flowing nitrogen gas at 20 Torr in 1989 by Parkinson [38]. The key features were that the gas was contained between very thin (ca 5–10 nm), evaporated carbon windows, and the path length of the beam was kept small (10–50 μm). The cell was able to support a pressure difference of circa one atmosphere with a high flow rate (up to 50 ml/min). This was the first time that such high resolution had been achieved under conditions not far from those typical of in situ use (medium voltage, 400 kV). From then on, structural information contains chemical significance became discernible, while the technique began to offer real hope of carrying out fundamental dynamic studies of the activation, reaction, and passivation of gas/solid systems close to the atomic level.

In the following two decades, similar techniques [36, 37, 40–42] were developed in the area of film material and simplification of structure. In 2005, Komatsu [40] used a window whose base is a commercially available copper mesh grid with double-layer polyvinyl-formvar/carbon thin films formed by vapor deposition (Fig. 9.5a). Onto this base, additional layers of nylon and amorphous carbon were evaporated to improve both mechanical strength and heat resistance, and the cell pressure could be increased to $\sim 1.3 \times 10^4$ Pa. In Giorgio's experiment [41], the cell was closed by two copper disks where seven holes have been drilled, which were pre-covered by ~ 10 nm amorphous carbon films, located inside the cell (Fig. 9.5b). The sample (powder) was deposited on the heating wire made of W–Re, which was isolated from the grids by an insulator ceramic. The electrical connections for the heating wire and both tubes for gas circulation were included in the sample holder. The Viton

O-rings provided the sealing of the cell toward the vacuum of the TEM column. In 2009, Kawasaki et al. [42] developed a simplified E-cell, thanks to the successful development of remarkably tough thin carbon films as the window material. These films, with a thickness of <10 nm, were found to withstand pressure difference >2 atm. The E-cell at the tip of the specimen holder connected two stainless pipes from the other side of the holder, allowing gases to pass in and out (Fig. 9.5c). In 2010, de Jonge [37] constructed a cell to record the STEM images of gold NPs at atmospheric pressure through a 0.36 mm thick mixture of CO, O₂, and He. A sample compartment filled with gas at atmospheric pressure was enclosed between two silicon microchips supported by electron-transparent SiN windows. The microchips were separated by a spacer and sealed with epoxy. Images are obtained by scanning a focused e-beam over NPs attached to the top window and detecting elastically scattered transmitted electrons. In this drawing, gas entry and exit were not shown, and the dimensions and angles were not to scale (Fig. 9.5d). In 2011, Yaguchi [36] developed a new windowed environmental cell holder based on his work 6 years ago, which allows ETEM study of nanomaterials at a maximum temperature of 1500 °C in the gaseous environment at the atmospheric pressure. Figure 9.5e shows the external views of the equipment, and the schematic (Fig. 9.5f) exhibits positions of windows, heating element, gas tubes, and a micropressure gauge. The side-entry type was employed as well with a built-in specimen-heating element of a spiral-shaped fine tungsten wire, which allows heating of specimens up to 1500 °C. Gas pressure inside the environmental cell can be continuously varied from 10⁻⁵ Pa to atmospheric pressure while TEM image observation of the specimen is carried out. This design was commercialized by Hitachi in the following years.

Besides the pressure, the heating process was also another challenge impeding the high-quality TEM images. For conventional windowed gas cells based on metal grids, the two metal grids form a metal “furnace”, into which a ceramic encasing a heating filament is placed [43]. The disadvantages, as followings, of this design are obvious, and greatly affected the observation of the specimen: (1) The grids not only sealed the cell, but also served as the heating device for the specimen, and easily expand and retract during the heating and cooling process. It's one of the major reasons for sample drift, which will typically be several tens of micrometers. Actually, the sample drift during heating/cooling has been a major challenge that disturbed the researchers for a long time; (2) The metal wires, which played the role of heating, always couldn't sustain the high and stable heating rate, and sometimes it's still difficult to find and maintain the balance of a stable temperature between the metal wire heating and flowing of the gases.

Until the end of the 2010s, a microelectromechanical system based on closed cells emerged [18–21, 39, 44–46], which utilized the MEMS technology to produce the chips used as cell windows. The MEMS-based nanoreactor employed in the TEM was proposed by Creemer et al. [18]. The nanoreactor (Fig. 9.6a) consists of two facing dies made with thin film technology on a silicon substrate. Each die has a central hole of 1 mm² that is covered by a 1.2 mm thick membrane of SiN_x while the small ovaloids are only carpeted by a 10 nm thin film (Fig. 9.6c). The opposing membranes form the top and bottom of a shallow gas-flow channel. The

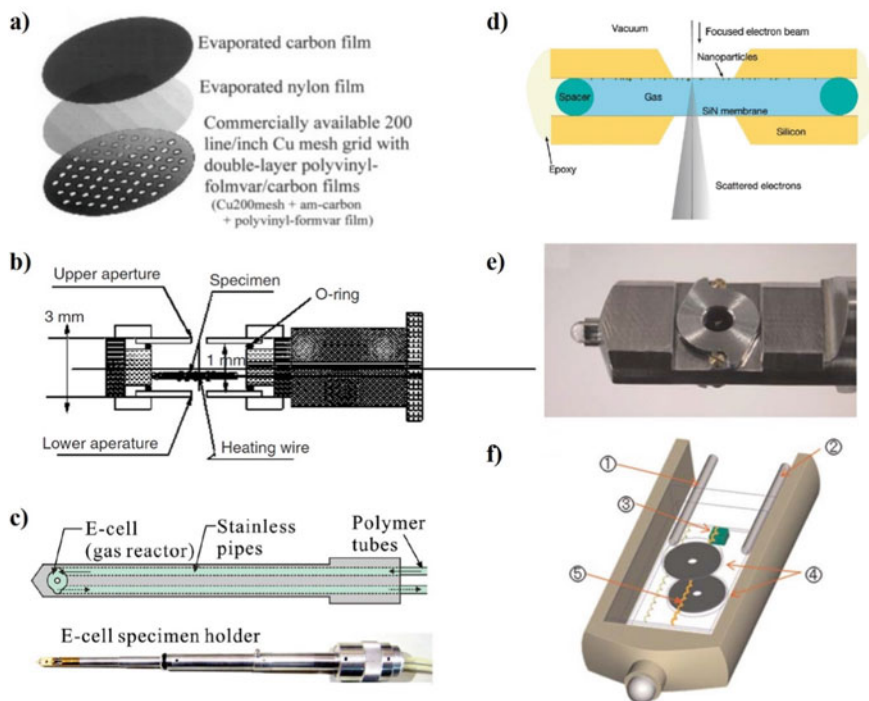


Fig. 9.5 **a** Newly improved multi-layer amorphous film window (reproduced with permission from Ref. [40], Copyright 2005, Oxford University Press). **b** E-cell heating holder in profile view (reproduced with permission from Ref. [41], Copyright 2006, Elsevier). **c** Schematic drawing and photograph of the E-cell specimen holder (reproduced with permission from Ref. [42], Copyright 2009, AIP Publishing). **d** Schematic of the flow system for atmospheric pressure scanning transmission electron microscopy (STEM) (reproduced with permission from Ref. [37], Copyright 2010, American Chemical Society). **e** External view of the windowed environmental cell holder. **f** Position of windows, heating element, gas tubes, and a micropressure gauge (1. gas outlet tube; 2. gas inlet tube; 3. micropressure gauge; 4. windows; 5. heating element) (reproduced with permission from Ref. [36], Copyright 2011, Oxford University Press)

minimum height of the channel is 4 mm, determined by disk-shaped spacers (SiO_2) integrated into one of the membranes. This height corresponds to an atomic density along the beam direction of only 0.2×10^3 atoms/ nm^2 at 1 bar and RT. The lateral dimensional size (10 μm) and geometric shape (ellipsoid) of ultrathin windows were also carefully selected to satisfy the demanding of pressure difference. In the areas between the windows, the heater is embedded in the form of a spiraled Pt wire (Fig. 9.6c). The MEMS-based technique enabled the integration of the heater into the window membrane, effectively limiting the thermal expansion of the system components and consequently the specimen drift. In the end, the direct observation of samples on a sub-second time scale could reach a spatial resolution of 0.18 nm, during heating to 500 °C and exposure to 1.2 bar of H_2 .

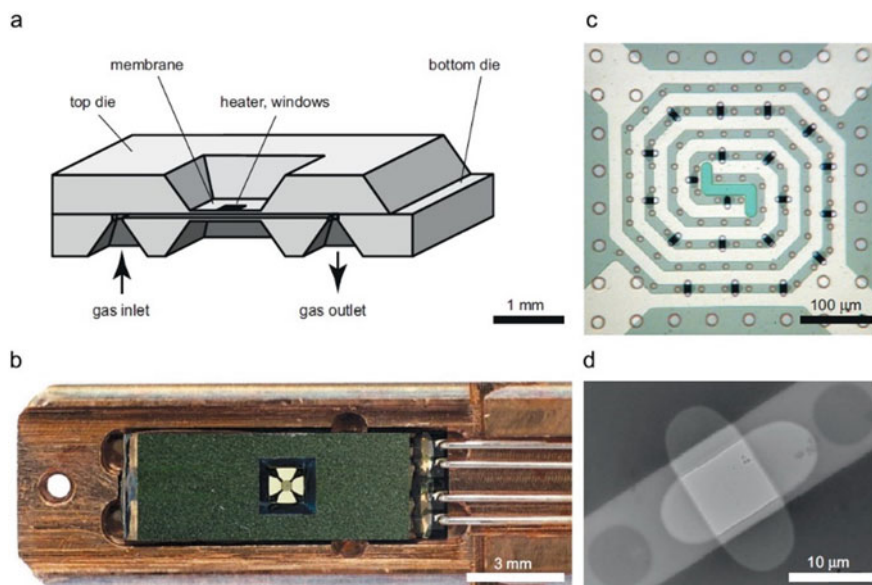


Fig. 9.6 Illustration of the nanoreactor device. **a** Schematic cross-section of the nanoreactor. **b** Optical image of the TEM holder with the integrated nanoreactor and the four electrical probe contacts. **c** Optical close-up of the nanoreactor membrane. The bright spiral is the Pt heater. The small ovaloids are the electron-transparent windows. The circles are the SiO₂ spacers that define the minimum height of the gas channel. **d** A low-magnification TEM image of a pair of superimposed 10 nm thick windows. Their alignment creates a highly electron-transparent (bright) square through which high-resolution TEM imaging can be performed (reproduced with permission from Ref. [18], Copyright 2008, Elsevier)

In 2009, Allard [44] undertook a project with Protochips Inc. (Raleigh, NC) to develop a new MEMS-based device (Aduro™) for in situ heating experiments that provide sub-Å resolution with rapid specimen heating and cooling. The key component of the MEMS devices is a 150 nm thick, 500 μm square, freestanding membrane made from a conductive ceramic that is suspended on a 3-mm Si chip (Fig. 9.7a). In 2012, Allard [20] incorporated the Aduro heating device into a “closed-cell” configuration, and is capable of exposing specimens to gases at pressures up to 1 atm. The atomic resolution performance of the microscope in high-angle annular dark-field and bright-field imaging modes was demonstrated at elevated temperatures and at 1 atm pressure.

In 2011, Creemer et al. [45] improved their MEMS nanoreactor to enable atomic-scale imaging of nanostructured materials under high pressures (14×10^5 Pa, 14 bar) and temperatures (660 °C). They integrated the reactor entirely on a single die, with the use of surface micromachining techniques (Fig. 9.7b), which increased the strength and rigidity of pillars holding together the membranes. The employment of a wafer stepper, resulted in a much better alignment of opposite windows (0.1 μm instead of 2 μm), and improved robustness obviously. In the same year, Yokosawa

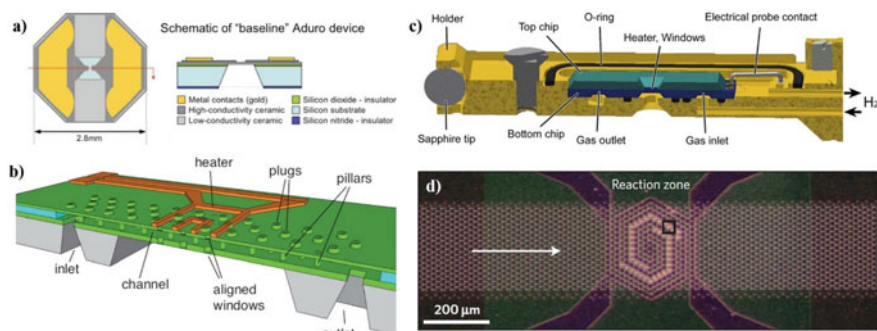


Fig. 9.7 **a** Top and cross-section view schematic of Protochips heater chip, showing composition of the various elements (reproduced with permission from Ref. [44], Copyright 2009, John Wiley and Sons). **b** 3D sketch of the all-in-one nanoreactor (reproduced with permission from Ref. [45], Copyright 2011, IEEE). **c** Schematic diagram of the nanoreactor inserted in the sample holder (reproduced with permission from Ref. [19], Copyright 2012, Elsevier). **d** Light optical micrograph of the nanoreactor with the gas channel and the reaction zone including the heater spiral and electron-transparent windows (reproduced with permission from Ref. [47], Copyright 2014, Springer Nature)

et al. [19] used a modified MEMS-based nanoreactor on the basis of Cremer to observe the (de)hydrogenation of Pd at pressures up to 4.5 bar. Two Si chips with square-shaped 1 μm -thick low stress (silicon-rich) silicon nitride (SiN) membranes, which contain very thin SiN windows (about 20 nm thick), were integrated, and one of the chips (bottom chip) contains a Pt heater and has an inlet and an outlet for the gas. The schematic diagram of the nanoreactor inserted in the sample holder is shown in Fig. 9.7c. Further improvement based on the work of Cremer was exhibited in 2014 [47]. The nanoreactor employed included a unidirectional gas-flow channel (280 μm -wide and 4.5 μm -high), enclosed between two 1 μm -thick SiN_x membranes. At the nanoreactor center (Fig. 9.7d), a Mo thin film resistor enabling heating and temperature measurement of a reaction zone at 1 bar pressure, and 18 nm-thick electron-transparent windows facilitated TEM observation. The reactor shown in Fig. 9.7b, d also has intrinsic drawbacks: as a special one-piece holder, the sample loading has to be done by flushing the sample into the holder with the risk of plugging.

The development of the window approach promoted the commercialization of integrated MEMS cells. And several companies provide unique holders and chips corresponding to TEMs manufactured by different TEM companies nowadays, such as DENSsolutions, Hummingbird, and Protochips. And the holders used for the window approach with additional functions emerge catering to various requirements depending on the experimental purpose.

The in situ heating and gas reaction cell developed by Protochips is called “atmosphere”. The atomic resolution could reach 1.5 Å with the pressure up to 1 atm, and the temperature ranges from RT to 1000 °C. Protochips developed a proprietary silicon carbide membrane heater that can quickly and accurately reach the highest temperatures without the risk of interacting with the sample or participating in catalyst reactions. The design of the Atmosphere holder enables in situ closed-cell EDS

elemental analysis in the TEM. The holder design provides a large line-of-sight solid angle from the sample to the EDS detector, minimizing tilt angle of holder tip and maximizing the count rate.

DENSsolutions also launched a competitive product named as “Climate” system. The atomic resolution could be better than 100 pm (1 Å, depending on microscope configuration) with 2000 mbar (~2 atm) pressure (Climate). The temperature ranges from RT to 1000 °C as well. 4-point probe heating provides the most accurate temperature with 0.01 °C stability even during gas flow, which also allows accurate calorimetry data to be acquired during the experiment. Meanwhile, the Climate G+ system allows direct gas mixing with 3 gas input lines. Using a specially designed and patented mixing valve allows to change the gas composition on the fly and to vary rates with an accuracy of 0.1%. With the defined gas channel and minimal gas volume inside the nanoreactor, the gas environment of the sample can be changed within seconds. The EDS and EELS compatibility is also satisfying. Furthermore, the integration with the optional dedicated DENSsolutions gas analyzer allows full dynamic correlation of the structural and chemical data. Gas analyzation and calorimetry data can also be produced by the Climate system if required, so that it enables to define the optimum experiment conditions before going to the TEM.

No matter which approach (aperture/window) the actual experiment employed, or no matter how complicated the system was designed, the interior process reaction that happened in the CATEM could be clearly simplified as in Fig. 9.8 [48]. On this basis, researchers developed various applications in tremendous fields.

9.3 Research Based on In Situ Gas TEM

CATEM has been successfully applied in a variety of research fields. The following application fields will be discussed in this section: reshaping of nanomaterials; redox of nanomaterials; surface reconstruction and segregation; growth of low-dimensional nanomaterials; the catalysts (dynamic observation of catalytic reactions; sintering and dispersion; photocatalysts).

These applications expressed the advances and unique characterization adequately in TEM capabilities embodying imaging and spectroscopy of materials in gaseous environments.

9.3.1 *Reshaping of Nanomaterials*

Generally, many properties (e.g. optical, magnetic, and electronic) of nanomaterials mainly depend on their shape, size, composition, and surface structure. In particular, the reshaping of the nanomaterial is intuitive and obvious in various gaseous environments, and could significantly influence the properties. Therefore, to in situ observe

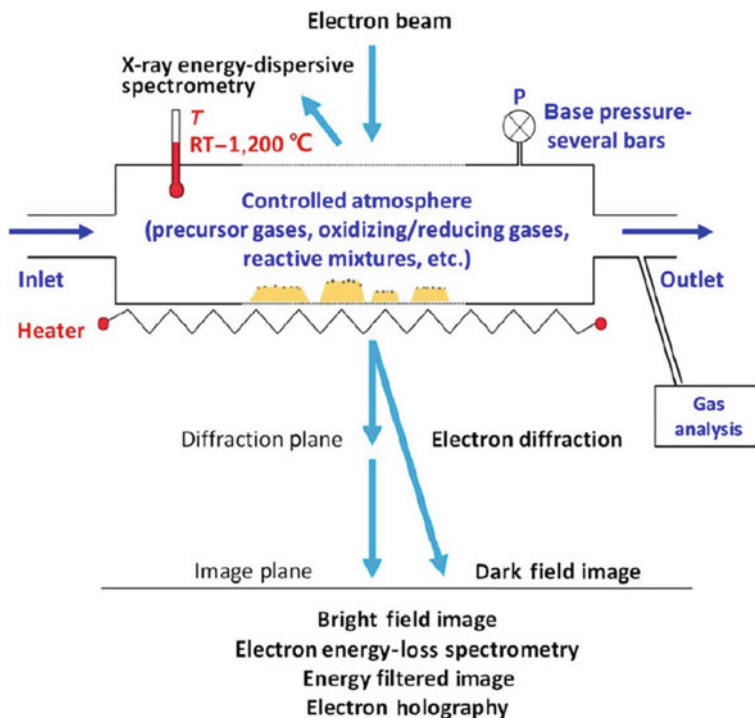


Fig. 9.8 Schematic of the CATEM technique and analytical methods (reproduced with permission from Ref. [48], Copyright 2018, Springer Nature)

and characterize the morphology evolution under operational conditions is of great significance to establish the structure–reactivity relationship of nanomaterials.

In 2002, Hansen and his coworkers [49] observed the copper (Cu) nanocrystals underwent reversible shape changes in response to the changes in the gaseous environment. Cu nanocrystals (NCs) with diameters of 3–6 nm were dispersed on ZnO and Si supports, and the interaction relationship between crystals and surfaces was studied. With the environmental change from more oxidizing conditions (mixed gas of H₂O and H₂) to more reducing conditions (CO and H₂), the Cu NCs changed to a more spherical (Fig. 9.9a) and a disklike structure (Fig. 9.9e), respectively. The authors attributed the reason to the different driving forces, respectively, water adsorption on the different Cu facets for the former and the change of Cu/ZnO interface energy (not the relative Cu surface energies) caused by the addition of CO for the latter. Supplementary experiments testified the conclusion: the shape transformations (to more spherical) were found to be reversible with the gas changes (H₂–H₂/H₂O–H₂) for both ZnO-supported (Fig. 9.9g–i) and silica-supported Cu NCs, which indicated the influence of H₂O, while the transformations (to more disklike, H₂–H₂/CO) were not observed for silica-supported Cu NCs, and the reason focused on the interface between NCs and the support.

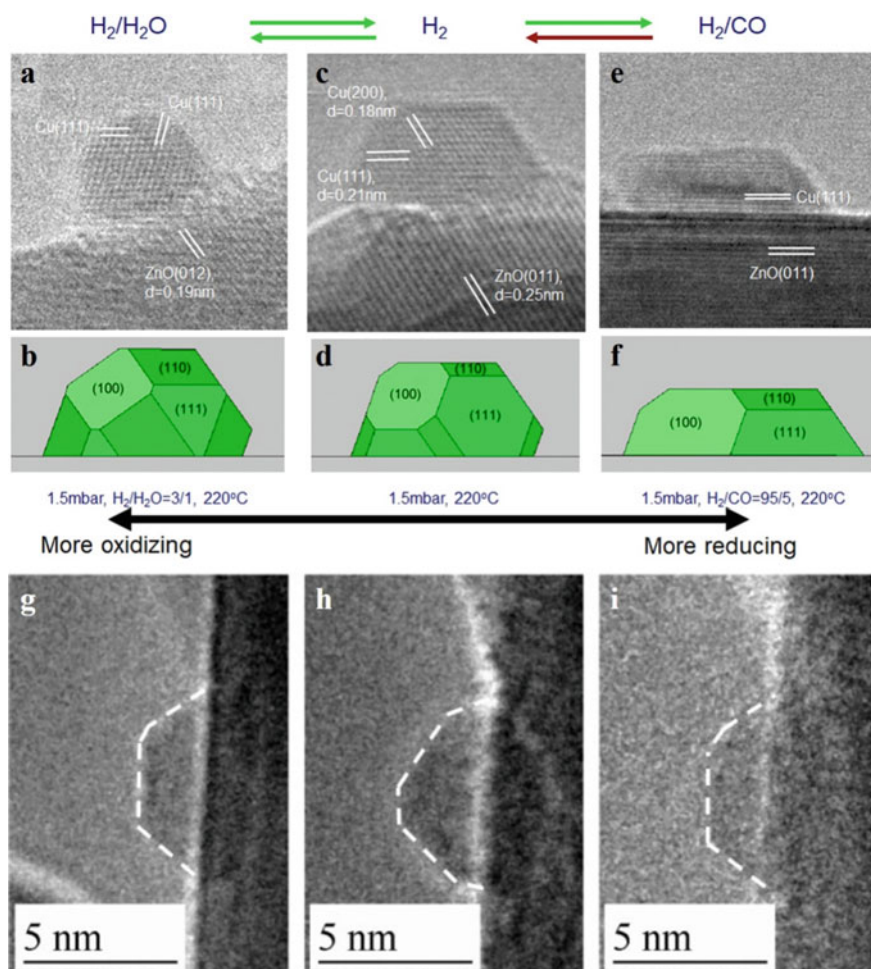


Fig. 9.9 In situ TEM images of a Cu/ZnO catalyst in various gas environments together with the corresponding Wulff constructions of the Cu nanocrystals. **a** 1.5 mbar of H_2 : H_2O = 3:1 at 220 °C. **c** 1.5 mbar of H_2 at 220 °C. **e** 5 mbar of H_2 : CO = 11:1 at 220 °C. **g** 1.5 mbar of H_2 at 220 °C. **h** 1.5 mbar of H_2 : H_2O = 3:1 at 220 °C. **i** 1.5 mbar of H_2 (reproduced with permission from Ref. [49], Copyright 2002, The American Association for the Advancement of Science)

Reversible shape transformations of faceted Pt NPs during oxidation–reduction cycles were in situ observed by Cabié et al. [50] using ETEM in 2010. The sample holder employed in the present study was closed by two carbon windows, which allows a pressure lower than 10 mbar and a temperature varying between RT and 350 °C. The Pt NPs were square in vacuum observed along the [001] direction, with truncations by (111) facets at the eight corners. Their shape was still close to cubes exposed by (100) surfaces mostly and truncated (111) surfaces at the corners in 3 mbar of O_2 . Along with the evacuation of O_2 and introduction of H_2 , the (111)

surfaces expanded and the (100) surfaces diminished until the shape was close to a cuboctahedron. Finally, when it was reverted to O₂, the Pt NPs recovered to cubic shape mainly exposed by (001) facets. The authors believed that the adsorption of gases on different surfaces took effect in the morphological change.

Uchiyama and coworkers systematically investigated the morphology changes of gold NPs (GNP) supported on CeO₂ during CO oxidation in 2011 [51]. In CO oxidation environment (1 vol% CO, 21 vol% O₂, 78 vol% N₂) at 1 mbar pressure, the GNP appeared to be faceted and enclosed by the {111} and {100} facets. Then the GNP became rounded in pure O₂ gas and faceted in both inactive N₂ gas at 1 mbar and in vacuum, while the GNPs supported on crystalline TiC remained polyhedral in all of the gas environments including pure O₂ gas, which indicated that the Au–CeO₂ interface played an important role in the catalytic activity. This in situ observation also suggested that CO molecules stabilized the major {111} and {100} facets of GNPs, while oxygen atoms adsorbed on not only the major {111} and {100} facets but also the minority {110} facet of GNPs. A morphology diagram was obtained, which showed the morphology of GNP in different environments.

It should be noted that most prior work was limited to low pressure, which was significantly different from realistic operating conditions. In this regard, the in situ study under conditions that more closer to realistic operating conditions is highly desired. The dynamic morphological evolution of palladium–copper (PdCu) nanocrystal (NC) with atmospheric pressure hydrogen was studied at the atomic scale by Jiang et al. [52] in 2016. The chemically synthesized monodisperse PdCu NCs (Pd/Cu ratio is 1:1) were spherical. Then the PdCu NCs on a SiN chip were loaded into a sealed gas reactor and exposed to 1 bar H₂, as Fig. 9.10a shows (along [111] axis). When annealed at 600 K, the spherical PdCu NC started to rotate and showed smoother surfaces, as indicated by the blue dashed line in Fig. 9.10b. Subsequently, accompanied by roll-over and rotation, the NC exhibited four flat surfaces (Fig. 9.10c) and finally became a truncated cube with distinct {001} and {011} facets (Fig. 9.10d). The surface energy of PdCu was calculated by density functional theory (DFT), which indicated the truncated morphology was induced by the order change of the surface energies with hydrogen adsorption. The morphology PdCu was obtained based on Wulff construction (Fig. 9.10k, l) considering hydrogen adsorption, which showed perfect consistency with the experimental images (Fig. 9.10i, j), both from the [100] and [111] zone axes. Furthermore, the PdCu NCs retained the as-synthesized shape (round) when heating in vacuum (10⁻⁷ bar) at 600 K in control group, which suggested adsorbed hydrogen-promoting surface diffusion.

Shape evolutions of different metal NPs [53, 54] are commonly believed to happen in reducing or oxidizing gas under high pressure. However, in 2018, Zhang et al. [55] observed an unexpected refacetting process of Pd NP under N₂, which was considered as an inert gas, with atmospheric pressure. As shown in Fig. 9.11a, c, the initial morphologies of two Pd NPs after annealing in air at 200 °C were rounded shapes with curved corners. Surprisingly, the NPs underwent obvious refacetting processes after being exposed to 1 bar N₂ gas at the same temperature (Fig. 9.11b, d), with flat facets and truncated cuboids appearing. The atomic-scale TEM images (Fig. 9.11e–h) showed that a notable increase in the fraction of Pd {110} surfaces

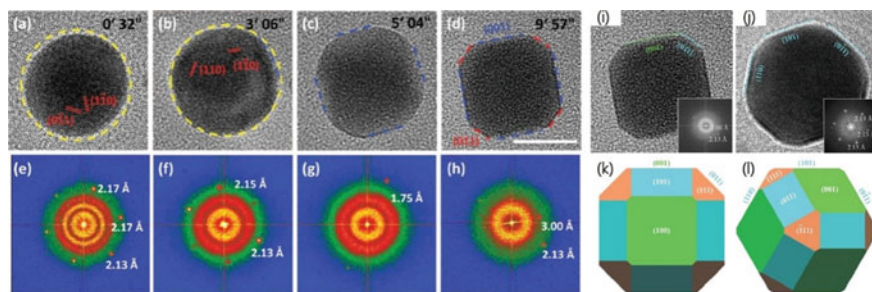


Fig. 9.10 a–d Lattice-resolved TEM images and the corresponding FFT patterns showing the morphological evolution of the PdCu NC when exposed to H₂ at 1 bar and with heating at 600 K. Scale bar: 10 nm. TEM images and Wulff constructions of the PdCu NCs projected from specific directions: i and k [100]; j and l [111] (reproduced with permission from Ref. [52], Copyright 2016, John Wiley and Sons)

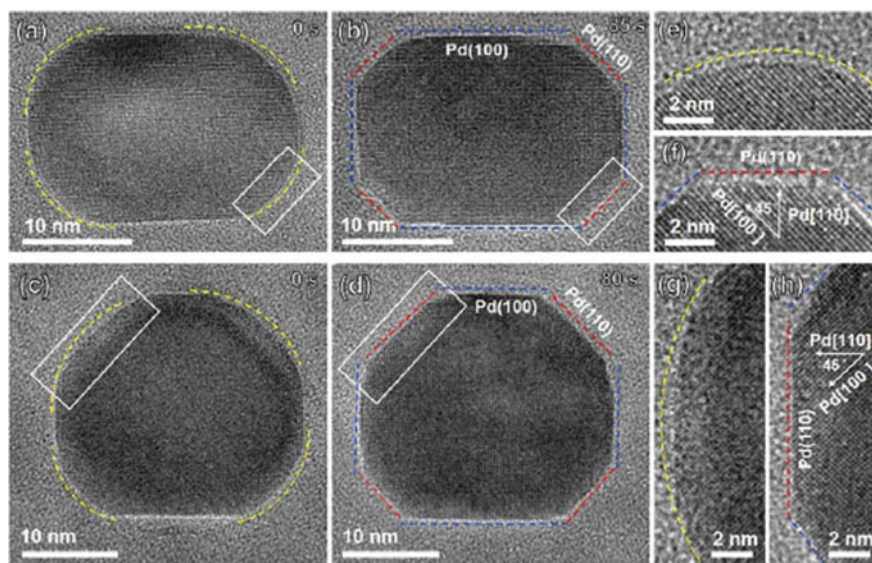


Fig. 9.11 Time-resolved TEM images of the dynamic refacetting of two Pd NPs under 1 bar N₂ at 200 °C (a–d). The TEM images showed that the NPs changed from rounded shapes to truncated cuboids (e–h). The atomic-scale images of the indicated parts of (a–d) (reproduced with permission from Ref. [55], Copyright 2018, Royal Society of Chemistry)

occurred in N₂ at atmospheric pressure at 200 °C. The remarkable refacetting of Pd NPs was ascribed to the stabilization of the {110} facets by N₂ adsorption by DFT calculations. In comparison, similar experiments under 1 bar Ar pressure were performed, and no refacetting phenomenon was observed at any temperature. The results suggested that N₂ was not always an inert gas in high-level pressure, and it should be very careful when using N₂ as an inert gas in the pretreatment.

A minireview was published in 2019 by Zhu et al. [56], which combined the in situ environmental transmission electron microscopy experiments and the newly developed multiscale structure reconstruction (MSR) model to study the equilibrium shapes of metal NPs in various reactive environments at atmospheric pressure. The MSR model consists of three parts: the Wulff construction, adsorption isotherms [57], and DFT calculation. The authors corrected the surface tension of a clean surface γ_{hkl} to be the interface tension γ_{hkl}^{int} (Eq. (9.1)), where $\theta(T, P)$ is the coverage of the gas molecules on the $[hkl]$ surface depending on the temperature and gas pressure, E_{ads} refers to the adsorption energy, and A_{at} is the surface area per atom of the $[hkl]$ surface:

$$\gamma_{hkl}^{int} = \gamma_{hkl} + \frac{\theta(T, P)E_{ads}}{A_{at}} \quad (9.1)$$

The equilibrium shape of metal NPs can be constructed at a given temperature and pressure using the derived interface tension. The MSR model achieved great success in reproducing representative experimental results [58, 59], which could be extended to the situations of mixed-gas environments [60]. It was also employed in the works mentioned hereinbefore [52–55]:

$$\gamma_{c-s}^E = \gamma_A - E_{adh} - \frac{\theta^B E_{ads}^B}{A_{at}^B} \quad (9.2)$$

For a supported NP, the contact-surface tension between the metal NP and the support should be considered, according to the Wulff–Kaischew theorem [61]. With gas adsorption, the contact-surface tension can be evaluated by Eq. (9.2), where γ_A is the surface tension of the metal surface in contact with the substrate, E_{adh} is the adhesion energy between the metal and the support, θ^B is the gas coverage on the support, E_{ads}^B is the adsorption energy of the gas on the support, and A_{at}^B is the surface area of the support.

The combination of in situ experiments and theoretical modeling shows that the effect of the environment on the shape of NPs can be predicted quantitatively and efficiently using the MSR model, which facilitated the relationship understanding between the reshaping of the NPs and its catalytic properties in real reaction, further offering possibilities to control the reactivity by real-time regulation of the reaction conditions.

9.3.2 Redox of Nanomaterials

As early as 1958, Ito and Hizaya [7] employed a modified TEM (aperture mode) to investigate the oxidation of Aluminum (Al) thin film and the reduction of oxide copper film/whisker. They obtained the electron microscopic image and diffraction pattern before and after the reaction, which indicated the occurrence of oxidation and

reduction. In the following decades, similar in situ redox experiments were performed on other materials such as graphite [24], metals (Fe, Cu, and Ni) [62], and special chemical compound $((\text{NH}_4)_6\text{MO}_7\text{O}_{24}\cdot 4\text{H}_2\text{O})$ [10].

With the employment of a new window material which increased resolution and contrast in high-voltage electron microscopy, Komatsu and Mori [40] observed the oxidation of copper, reduction of copper oxides, and the growth process of CuO whiskers on a thick (50 μm) Cu film. As shown in Fig. 9.12a–e, a small amount of copper oxide (Cu_2O) was formed in the initial stage. Then oxygen gas was introduced into the initially evacuated cell (10^{-2} Pa) to 1.3×10^3 Pa and the specimen was gradually heated to 470 K. Upon heating in oxygen, Cu_2O nucleated on the film surface. As the temperature increased, Cu was oxidized to Cu_2O and then completely transformed to fine CuO particles (~ 10 nm in diameter, in 670 K). And the average grain size increased at 770 K. The reduction of CuO in hydrogen is shown in Fig. 9.12f–h. The same CuO area was reheated after cooling down to RT, and the CuO was completely reduced to Cu at 670 K. The growth of CuO whiskers (Fig. 9.12i–n) in 4×10^3 Pa of oxygen was also recorded using the same apparatus, which is discussed in Sect. 9.3.4.2 Semiconductor/Metal-Oxide 1D Nanomaterials. In general, the research about the oxidation of Cu started to focus on the microscopic domain. However, due to the limitation of the apparatus, the structural evolution at atomic resolution could not be acquired still.

In 2016, with ESTEM, Boyes and Gai [30] observed the nucleation of the Cu_2O by tracking the oxidation process with real-time HAADF imaging (Fig. 9.13a). The oxidation was proved to be a pressure- and temperature-dependent procedure, since the reaction occurred more quickly at higher pressures (2, 5, and 10 Pa) or temperatures (300–500 $^\circ\text{C}$). The reduction process was also recorded in a similar way (Fig. 9.13c). The Cu formed as a protruding island off the NP at first (with a dewetting angle, Fig. 9.13b), then the interface length increased and the protrusion lessened with increasing temperature, finally the reduction went to completion and the NP recovered to a single Cu metal NP. The high-resolution dynamic HAADF-ESTEM images indicated that the (111) spacing of Cu and the (111) spacing of Cu_2O were related to each other with parallel epitaxy between two phases, and a 7×6 or a 6×5 lattice matching relationships existed due to an 18% discrepancy in lattice constant.

Besides typical Cu, other metal NPs were also researched. In 2012, Jeangros et al. [66, 67] studied the redox of nickel particles in ETEM. Images, diffraction patterns, and EELS were acquired to monitor the structural and chemical evolution of the system during the reaction. The structural models that describe NiO reduction and Ni oxidation were also proposed based on the ETEM observation.

The redox usually occurred rapidly on the time scale of second to millisecond, which promoted the development of time-resolved quantitative characterization techniques. In 2018, an approach has been developed that integrated time-resolved in situ electron diffraction and an atmospheric gas cell system, allowing quantitative structural information characterization under ambient pressure with millisecond time resolution. Yu et al. [68] employed this technique in studying the ultrafast oxidation kinetics of Ni NPs at 600 $^\circ\text{C}$ with a total pressure of 1000 mbar.

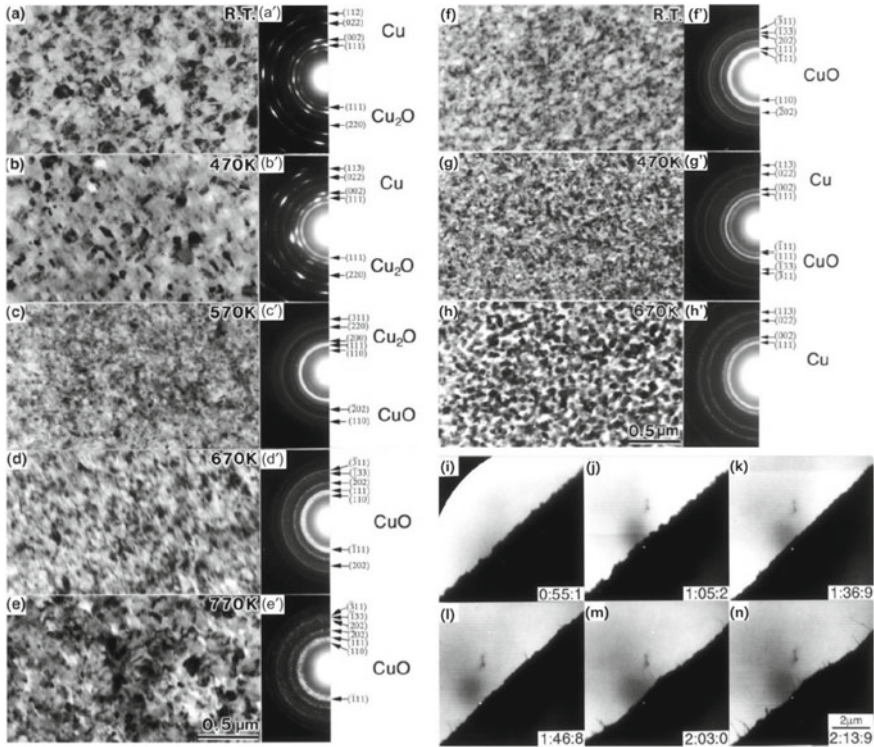


Fig. 9.12 a–e Successive stages of the oxide growth on a 100 nm-thick copper thin film between RT and ~770 K under 1.3×10^3 Pa of oxygen; a’–e’ the corresponding selected area electron diffractions (SAEDs). f–h successive stages of reduction of copper oxide (CuO) between RT and ~670 K under 1.3×10^3 Pa of hydrogen; f’–h’ the corresponding SAEDs. i–n Successive stages of growth of a copper oxide layer (Cu₂O) and CuO whiskers under 4×10^3 Pa of oxygen (reproduced with permission from Ref. [40], Copyright 2005, Oxford University Press)

In contrast to the well accepted Wagner and Mott Cabrera models (diffusion-dominated), the oxidation of Ni nanoparticles is linear at the initial stage (<0.5 s), and follows the Avrami Erofeev model ($n=1.12$) at the following stage, which indicates the oxidation of Ni nanoparticles is a nucleation and growth dominated process.

The presence of water vapor, intentional or unavoidable, is crucial to many materials applications. Phenomenologically, water vapor has been noted to accelerate the oxidation of metals and alloys. However, the atomistic mechanisms behind such oxidation remain elusive. Luo et al. [69] studied the oxidation mechanisms of the single crystalline Ni-10at%Cr alloy in water. As shown in Fig. 9.14, during the growth of NiO on the surface, there were vacancy clusters (white dashed circles) formed by incorporating both Ni and O vacancies, which would migrate, increase in size and annihilate. They revealed that protons derived from water dissociation could occupy interstitial positions in the oxide lattice, consequently lowering vacancy formation

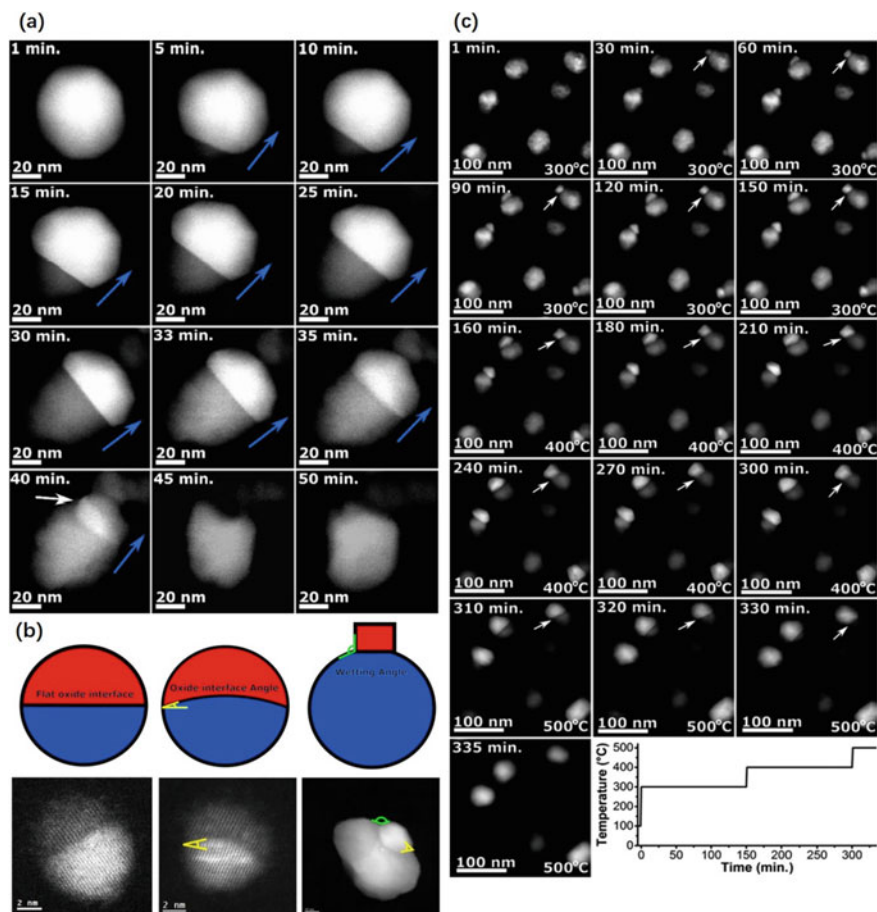


Fig. 9.13 **a** In situ oxidation of Cu carried out at 500 °C in 2 Pa oxygen. The blue arrow indicates the direction in which the interface moved. **b** A schematic of how the interface angles and wetting angles were defined and measured, and examples of the different cases taken from oxidation on the left and center, and from the reduction on the right (from SI). **c** In situ reduction of Cu_2O in 2 Pa hydrogen over the course of 335 min. In the lower right-hand corner, the temperature profile of the reaction is shown (reproduced with permission from Ref. [30], Copyright 2017, American Chemical Society)

energy and decreasing the diffusion barrier of both cations and anions, which led to enhanced oxidation in moist environments at elevated temperatures.

The oxidation of organic materials was also observed in detail. The oxidation of carbon nanotubes (CNTs) at the high resolution of an aberration-corrected environmental TEM (ETEM) was directly studied by Koh and coworkers [63] in 2013. Contrary to the previous thought that CNT oxidation triggered at the end of the tube due to high energy at the cap [64, 65], they observed the outer wall was oxidized and removed first (Fig. 9.15). The blue arrow in Fig. 9.15b started to “peel” away and

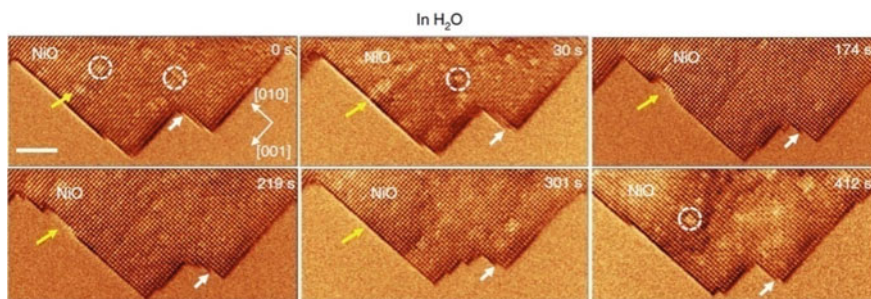


Fig. 9.14 ETEM images showing the growth of an initial NiO crystal on the surface of Ni–Cr alloy in 1×10^{-6} mbar H₂O at 350 °C (reproduced with permission from Ref. [69], Copyright 2018, Springer Nature)

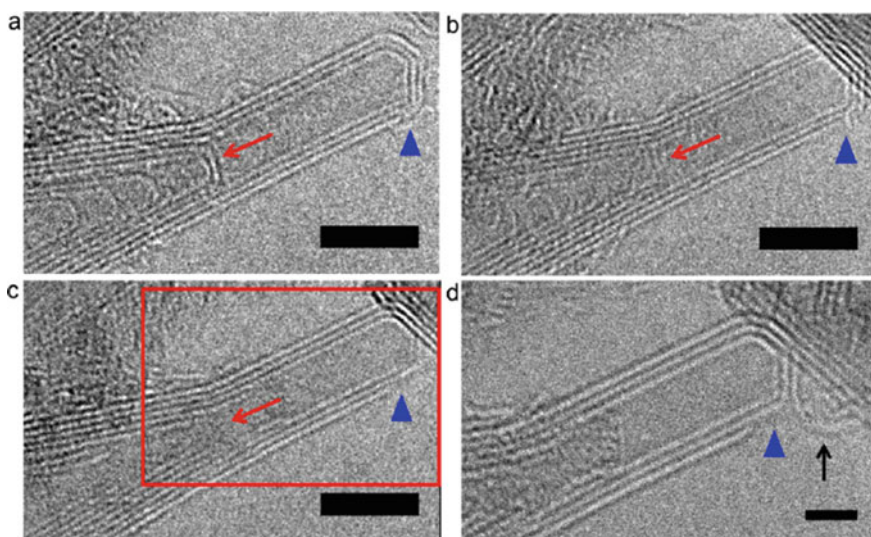


Fig. 9.15 Observations at the ending cap of a CNT during oxidation. The inner walls and outer wall of the nanotube at 300 °C **a** were removed after 1.5 mbar oxidation for 15 min at 300 °C (red arrow and blue triangle). **b** More etching was observed after the same nanotube was oxidized for 15 min with 1.5 mbar oxygen at 400 °C. **c** The inset of **(c)** is shown in **(d)**, where one can see the outermost wall being removed and dangling (black arrow) after oxidation at 400 °C. Scale bars in **(a–c)** and **d** represent 5 and 2 nm, respectively (reproduced with permission from Ref. [63], Copyright 2013, American Chemical Society)

detached more upon further oxidation at 400 °C, while the wall remained attached to the nanotube cap (black arrow in Fig. 9.15d). Furthermore, on occasion, they observed that the interior wall was oxidized first (red arrow in Fig. 9.15b–c), which was ascribed to oxygen infiltrating into the hollow nanotube through an open end or cracks in the tube.

Besides conventional redox of NPs [70] and alloy, sometimes metal NPs could react with gas which is commonly considered inactive, then form a protective layer restraining possible corrosion. Wang and her coworkers [71] turned a native Mg alloy surface into an anti-corrosion coating in excited CO_2 . As known the native surface film on Mg formed in air mainly consists of $\text{Mg}(\text{OH})_2$ and MgO , which is porous and unprotective. By reacting with excited CO_2 (activated by e-beam irradiation), researchers fabricated a smooth, compact MgCO_3 protective layer (Fig. 9.16) on the Mg alloy surface. A Mg micropillar was fabricated by focused ion beam, which was then exposed to air for 30 min to form a native oxide surface film firstly. After exposure to air for 30 min, a surface oxide layer with a thickness of about 8 nm was formed (Fig. 9.16b). Then it was reacted with the e-beam excited CO_2^* , producing a compact MgCO_3 protective layer on the pillar's surface without any extra heating. Selected area electron diffraction (SAED) and electron energy loss spectroscopy (EELS) analysis were performed to identify the composition of the final reaction product (Fig. 9.16f, g), which confirmed the presence of both crystalline MgCO_3 and MgO . Subsequent immersion tests in an aqueous environment were performed to examine the corrosion resistance of the as-grown MgCO_3 films. The results demonstrated that the MgCO_3 was effective in preventing the Mg metal from deionized water corrosion.

The observation of nanomaterials with oxidizing, reducing, and inactive atmospheres with the employment of ETEM was an important and extensively studied area. With the development of techniques and accessories, detailed information about structure and composition which is critically needed but hidden deeply could be obtained.

9.3.3 Surface Reconstruction and Segregation

The surface structural change of nanomaterials is another important research field, which attracted tremendous attention in recent years especially with the breakthrough of spatial resolution of ETEM. The surface atoms would occupy a higher proportion for NPs with small sizes, and further influence or even decide the character and property of materials.

Yoshida and coworkers [72] examined a catalyst which is composed of GNPs supported on CeO_2 by a 300 keV aberration-corrected ETEM. Observing along Au [110] zone axis at the under-focus condition, a surface reconstruction of the Au/ CeO_2 powder catalyst was acquired on the {100} surface in reaction environments. As shown in the enlarged images in Fig. 9.17a, the {100} facets remained unreconstructed in vacuum, and the distance of 0.20 nm between the topmost and the second topmost {100} surface layers was the same as the interplanar distance of the {200} planes in crystalline bulk gold. The average distance of the adjoining Au atomic columns on the topmost surface layer was the same as the corresponding distance in a {100} plane in crystalline bulk gold. Under a typical reaction environment (1 volume% CO in air at 45 Pa at RT), as shown in Fig. 9.17b, the Au atomic columns on

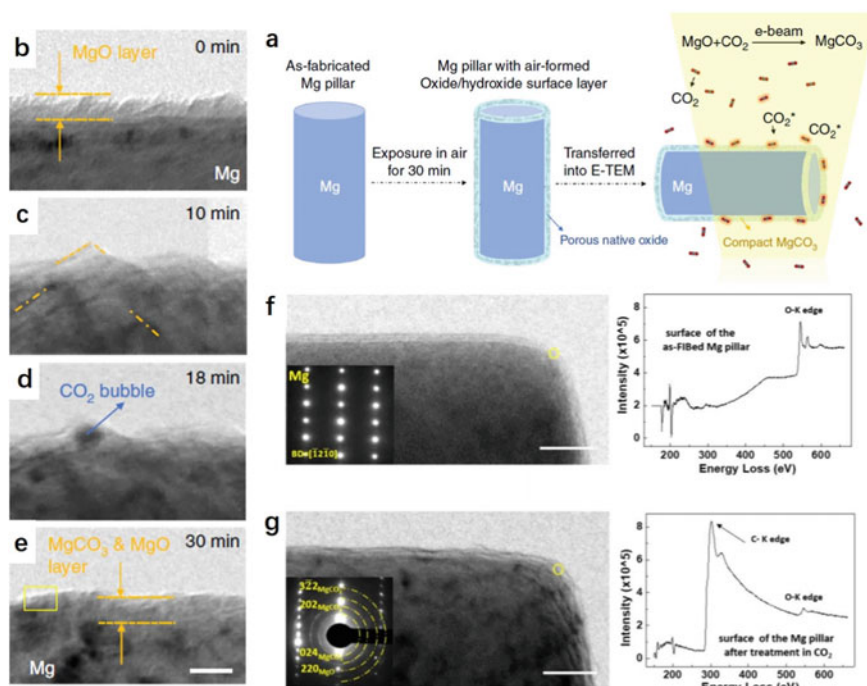


Fig. 9.16 **a** Schematic diagram showing how to transform the native surface to MgCO_3 . **b–e** Surface evolution of a FIB-fabricated Mg pillar during the exposure in 2 Pa CO_2 and e-beam irradiation. TEM images showed transformation process of the native oxide layer to the compact nanocrystalline MgCO_3 and MgO layer. **f** Diffraction pattern of the as-FIBed Mg pillar with an amorphous MgO layer and the EELS spectrum of the surface zone in the yellow circle. **g** Extra diffraction rings from the newly formed film after treatment in CO_2 showed the existence of nanocrystalline MgO and MgCO_3 . Obvious C-K edge can be seen in the corresponding EELS spectrum (reproduced with permission from Ref. [71], Copyright 2018, Springer Nature)

the topmost and second topmost $\{100\}$ layers shifted. Both the average distance of the adjoining Au atomic columns and the interplanar distance changed to 0.25 nm. The reconstructed surface Au atomic columns correspond well to those of the Au $\{100\}$ -hex reconstructed surface. In this reconstructed surface, the Au atoms on the topmost surface layer formed an undulating hexagonal lattice, whereas those on the second layer formed a normal square lattice with slight distortion. The researchers performed the ab initio electronic calculations with regard to CO adsorption on the Au $\{100\}$ -hex reconstructed surface, and the simulation image based on an energetically favorable model for CO adsorption fit well with the observed image. Therefore, it was deduced that the Au atoms on the topmost layer have unusual bonding configurations with the second surface layer, which sustained the high-density adsorption of CO molecules on the reconstructed surface. The methodology demonstrated in this study has opened an experimental route toward the elucidation of GNP catalytic mechanisms by direct observations of metal atoms and gas species at the particle-support periphery.

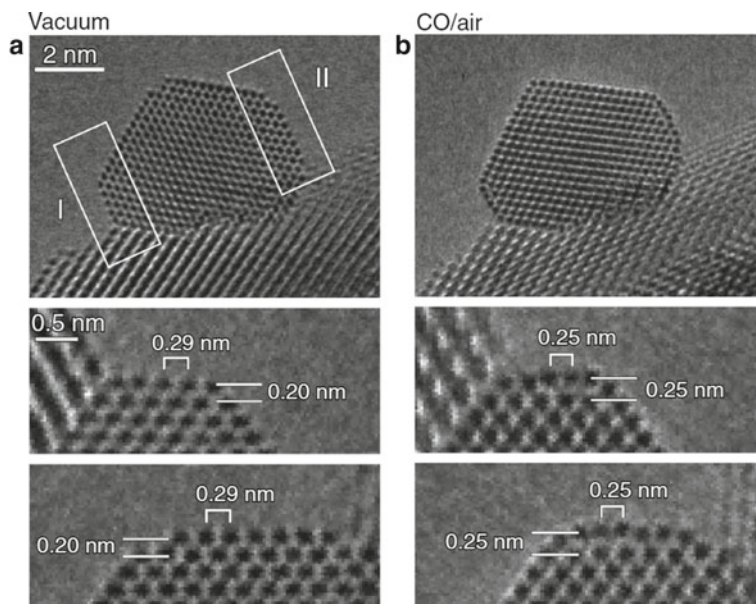


Fig. 9.17 Au{100}-hex reconstructed surface under catalytic conditions. GNP supported on CeO₂ in **a** a vacuum and **b** a reaction environment (1 vol% CO in air gas mixture at 45 Pa at RT). Two {100} facets were present in the rectangular regions indicated by I and II in (a) (reproduced with permission from Ref. [72], Copyright 2012, The American Association for the Advancement of Science)

Besides NPs, reconstruction often occurred on the exposed cleaved surface of the crystal as well, which shows different physical and chemical properties with respect to the bulk-truncated ones. A typical instance is the surface reconstruction of TiO₂ (001) surface. Generally speaking, the intrinsic structure of some specific oxides is sensitive to the e-beam and easily destroyed, which precludes direct observations in TEM. Using ETEM, Yuan et al. [73] acquired real-time information on the formation and evolution of the (1 × 4) reconstructed TiO₂ (001) surface in oxygen which protects the fragile surface reconstruction. Figure 9.18 displayed the formation process of the reconstruction at 500 °C in an oxygen environment (5 × 10⁻² Pa). At the beginning, adsorbed layers (mixture of amorphous organics and TiO_x species) covered the (001) surface (Fig. 9.18a, set as t = 0 s). After a few seconds, amorphous layers were gradually removed (Fig. 9.18b, t = 34.9 s) in oxygen with e-beam irradiation, and a crystalline layer appeared on the (001) surface, corresponding to adsorbed Ti or TiO_x species. After 56.2 s (Fig. 9.18c), adsorbed species began to exhibit non-uniform contrast; at t = 257.8 s (Fig. 9.18d), adsorbed species finally formed the 4 × periodicity, which remained stable during the following reaction. This evolution was also reflected in the intensity profiles for the outmost two surface layers (Fig. 9.18e–f). These results also confirmed that the (1 × 4) reconstruction

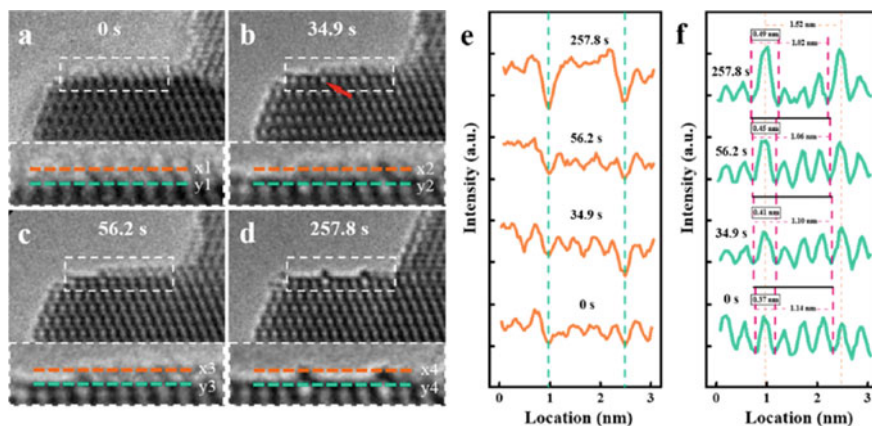


Fig. 9.18 Tracking the formation process of the (1×4) reconstruction, viewed from $[010]$ direction. **a–d** Sequential HRTEM images of the anatase TiO_2 (001) surface during the reconstruction, acquired at 0, 34.9, 56.2, and 257.8 s. The enlarged images of the dotted rectangles are shown in the lower panels of **(a–d)**, respectively. **e, f** Intensity profiles along the dashed lines in the lower panels of **(a–d)** (matching colors). The orange and green lines were acquired from the reconstructed layer and top-surface layer, respectively (reproduced with permission from Ref. [73], Copyright 2016, American Chemical Society)

could occur on the nanometer-sized TiO_2 crystal surface, which had been an open question since it was only observed on the surface of micron-sized single crystals.

CeO_2 is another widely used catalyst and catalyst support both at the laboratory scale and in industry, due to its ability to release or store oxygen atoms from the environment by altering its valence state ($3+/4+$) to compensate anionic vacancies in the Ce cationic lattice. However, the temporal evolution of reactive surfaces of CeO_2 under a gaseous environment was still ambiguous, which hampered the understanding of its catalytic mechanism. Bugnet et al. [74] visualized and quantified the mobility of Ce atoms at $\{100\}$ surfaces in high vacuum (HV), O_2 , and CO_2 atmosphere via ETEM. As shown in Fig. 9.19a, the contrast at oxygen atomic positions (indicated by arrows) increased from HV to O_2 and CO_2 environments, and the intensity variation of the most external Ce atomic layer decreased accordingly. Especially with the introduction of O_2 into the TEM chamber, O columns terminated (001) surface as a saturated state, because the oxygen supply compensated the e-beam-induced oxygen loss. This O-terminated surface in turn limited the mobility of the underlying Ce atoms. When CO_2 was introduced into the chamber, the surface mobility was completely stopped, and dark dots corresponding to the positions of oxygen atoms (Fig. 9.19a, bottom) had a greater contrast than that in oxygen (Fig. 9.19a, O_2), which was attributed to carbonates from adsorbed CO_2 . Quantitative analysis of atomic intensities at $\{100\}$ surfaces (Fig. 9.19b) demonstrated a high mobility of Ce atoms under HV. The mobility was lower under the O_2 atmosphere and nearly stopped in the CO_2 environment.

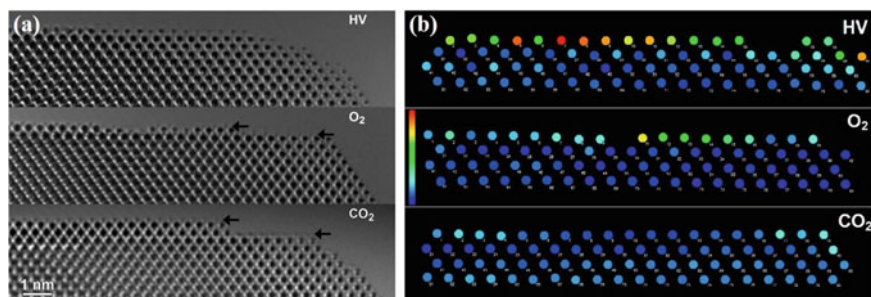


Fig. 9.19 **a** Two-second average of 50 frames from recorded video showing the edge-on (001) surface of a nanocube in the [110] orientation under high vacuum at 5×10^{-6} mbar, 5×10^{-2} mbar O₂, and 5×10^{-2} mbar CO₂ (respectively from top to bottom). **b** Quantitative analysis of Ce mobility at {100} surfaces. Variation of the standard deviation of atomic column intensities of a ceria nanocube viewed along the [110] direction under high vacuum at 5×10^{-6} mbar, 5×10^{-2} mbar O₂, and 2.6×10^{-2} mbar CO₂ (respectively from top to bottom). Each dot images a single atomic column position, and its color indicates the variation of intensity over 420 images recorded at 25 fps on a normalized scale (Blue, low variation; red, high variation). Missing columns correspond to positions where columns fully disappear within the time frame spanned by the 420 frames (approximately 17 s) (reproduced with permission from Ref. [74], Copyright 2017, American Chemical Society)

Generally, the reconstruction emerged on the surfaces of metal-oxide more easily, especially when exposed to the reductive atmosphere, the loss of oxygen atoms would influence the surface stoichiometry so as to rearrange the atomic structure and relationship to some extent. Of course, the intrinsic property of oxide, the environmental gas, the temperature, and the e-beam, all take effect on the loss extent of oxygen atoms, which result in different surface structures in the end.

Besides reconstruction, atomic-scale chemical segregation was also observed using ETEM. Dai et al. [75, 76] studied the oxygen-driven element segregation process in a Pt₃Co fuel cell-cathode catalyst under atmospheric pressures. Platinum-metal (Pt-M, M = Fe, Co, Ni, etc.) NPs were considered as a promising alternative to traditional Pt NPs as the oxygen reduction reaction (ORR) catalyst in polymer electrolyte membrane fuel cells. However, there were still some unsolved crucial questions, such as the element segregation mechanism during high-temperature annealing in pure oxygen. In situ TEM at atmospheric pressure provided valuable data to derive the corresponding mechanism.

The Pt₃Co/C powder sample (a commercial ORR catalyst) [75] was pretreated to create equilibrium-shaped NPs with a random distribution of Pt and Co. Then the sample was heated from RT to 350 °C in 760 Torr of pure oxygen. Figure 9.20a showed a twinned Pt₃Co NP after oxygen annealing for more than 10 min. One or two additional atomic layer(s) with a lower contrast formed on the {111} surfaces in the false-colored BF-STEM images. By comparing the marked green and black distance as #1 and #6, it is obvious that the segregated layers have a larger lattice spacing than the inner part. Meanwhile, the concrete data about the length of the side and intersection angle (Fig. 9.20b) are in excellent agreement with the Co sublattice

unit cell (Fig. 9.20c) in the structure of CoO. By checking more than 20 Pt₃Co NPs, outermost CoO layers are always found on {111}, but not on {100} surfaces, without exception, clearly revealing that facet-dependent oxidation is taking place on the Pt₃Co NPs. In comparison, additional atoms were attached on the top {100} surface (yellow arrow in Fig. 9.20f), until a new layer (#14) formed completely at the time $t = 32$ s (Fig. 9.20g). Because the contrast of the newly formed top layer (#14) is similar to the previous outermost layer #13, it indicated that the atoms newly attached on the {100} surface are closer to pure Pt. Therefore, the authors presumed that Pt atoms possess higher mobility in an oxygen environment, which tend to take place on the {100} Pt₃Co surfaces to result in structural fluctuations. In contrast, the CoO layers on the {111} surfaces blocked exposure of underlying Pt to the oxygen environment, and stopped the possible diffusion and reconstruction. The contrast difference of the additional atoms and high spatial resolution of the STEM images played an important role in distinguishing the attached atoms on different surfaces. The outstanding capability in characterizing structure and composition at microscopic domain of ETEM is obviously proved.

Recently, Zhang et al. [77] reported reversible segregation and alloy of Ni–Au bimetallic NPs during CO₂ hydrogenation. An ETEM was employed for the in situ observation in the reaction atmosphere (9 ± 0.1 mbar, 25% CO₂/75% H₂). As shown in Fig. 9.21, the core–shell nanoparticle was maintained with a darker Au–rich shell at 450 °C. When the temperature reached 600 °C, the catalysts showed the highest catalytic activity and the Au shell dissolved into the Ni matrix and vanished, forming a mixed NiAu alloy. When the catalysts cooled to 400 °C, the Au shell reappeared, recovering the Ni@Au core–shell structure. The phase evolution was further revealed via in situ electron diffraction seen in Fig. 9.21d that a broadened diffraction peak which corresponded to the NiAu alloy phase emerged between the Au(220) and

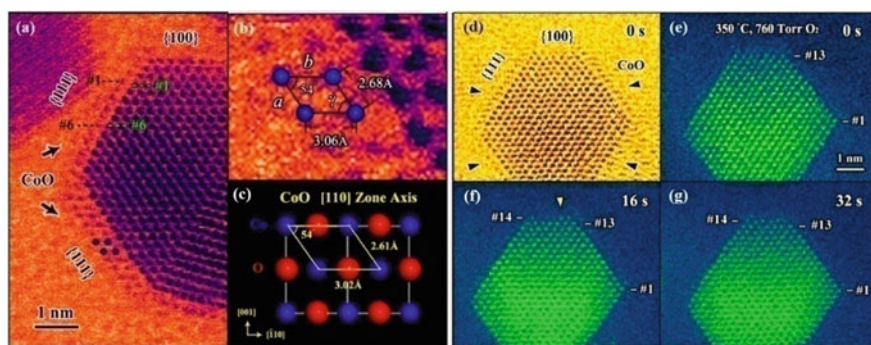


Fig. 9.20 In situ observation on the {111} and {100} surfaces of Pt₃Co NPs in an oxidizing environment. **a–b** False-colored BF-STEM images illustrating the periodical unit cell of the oxide layer on {111} Pt₃Co surfaces. **c** Projection of a CoO model along the (110) zone axis. Blue and red spheres represent Co and O atoms, respectively. **d–g** Sequential STEM images showing the additional Pt layer growth on the {100} surface of the oxidized Pt₃Co NP (reproduced with permission from Ref. [75], Copyright 2017, American Chemical Society)

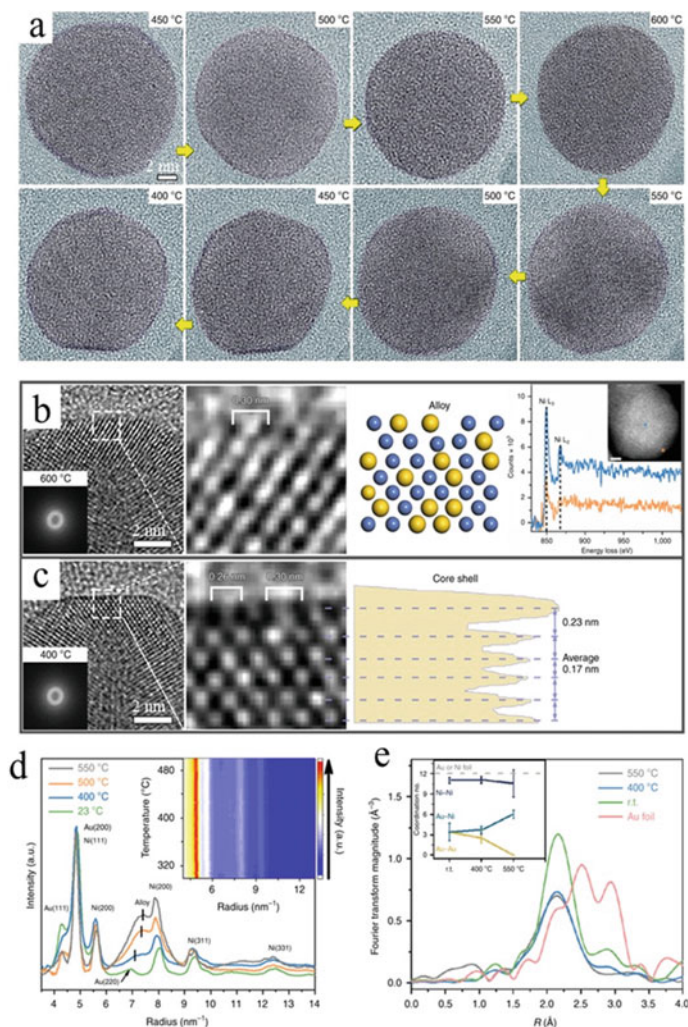


Fig. 9.21 The reversible structural transition of NiAu NPs during the CO₂ hydrogenation reaction. **a** In situ TEM images showing the alloying and dealloying evolution of an individual NiAu particle in the reaction atmosphere (9 ± 0.1 mbar, 25% CO₂/75% H₂). **b, c** Surface atom arrangement of a NiAu nanoparticle reconstructed from the full alloy (600 °C) (**b**) to the Ni@Au core-shell (400 °C) (**c**); the four parts from left to right in **b** show the high-resolution TEM (with a Thon ring inset), the corresponding enlargement of the surface area, schematic structure, and point analysis of the EELS (with a HAADF inset); the three parts from left to right in **c** show the HRTEM image (with a Thon ring inset), the corresponding enlargement of the surface area, and phase contrast profile. **d** Intensity profiles from the integration of diffraction rings of SAED patterns during the reaction. The inset shows 2D profiles stacking along with reaction temperature. **e** In situ EXAFS of the Au L₃ edge and coordination number changes (inset) of the Au–Au, Au–Ni, and Ni–Ni pairs at room temperature, 400 and 550 °C. a.u., arbitrary units (reproduced with permission from Ref. [77], Copyright 2020, Springer Nature)

Ni(220) peaks above 400 °C. If we just investigate the catalysts before and after the catalytic reaction, the Au shell could be thought to be the active site since the NiAu alloy only appeared during the reaction. Combining with other in situ spectroscopies and DFT calculations, the authors thought that the surface Ni atoms offered the active sites for the hydrogenation of CO₂ and the surface Au atoms contributed to the selective production of CO. This result gave a universal insight into designing a polynary metal catalyst with reversible structure responding to the environment and reminded us again that the importance of in situ observing the dynamic evolution of catalysts as the ex situ results may lead to a confusing conclusion.

Besides the compositional variations, segregation is usually accompanied by misfit strain and the formation of dislocations in the subsurface region via a surface diffusion and trapping process. Actually, two decades ago, it has been shown that the presence of hydrogen in solution enhanced the dislocation velocity in face-centered cubic, body-centered cubic, and hexagonal close-packed materials. Ferreira [78] proposed that solute hydrogen reduced the elastic interactions between dislocations and elastic centers which act as barriers. Using dynamic, atomic-scale resolution in situ HRTEM and theory modeling, Zhou et al. [79] demonstrated the Au surface segregation in the Cu(Au) solid solution, and focused on the misfit dislocations and its migration and climb facilitated by the segregation. This observed coupling between segregation and dislocation formation has wide relevance, as the partitioning of alloying elements (or impurities) occurs in most multi-component materials under a suitable environmental.

9.3.4 Growth of Low-Dimensional Nanomaterials

The introduction of gas into the TEM facilitated the development of another area which focused on the nucleation and growth of low-dimensional nanomaterials, especially 1D nanowires and nanotubes, which usually enjoy unique and unexpected properties due to quantum confinement effects and the absence of defects. Besides their high surface-to-volume ratios, morphology and crystallography also play important roles in manipulating properties. Therefore, the technique of synthesis of ideal or satisfactory 1D nanomaterials is the basis of further research in extraordinary properties and various applications.

There is no doubt that the traditional ex situ information obtained after the synthesis couldn't reflect the real-time structural change information during the growing process, which is critical to optimize the synthesis process. ETEM enables the in situ observation during synthesis, and thus direct atomic resolution images in growing processes and kinetic change (morphology, crystallography, defect structure, and chemical composition) could be obtained. It lays the foundation for the understanding of mechanism and improvement of synthesis technology.

For chemical vapor deposition (CVD), there exist three commonly accepted growth mechanisms of low-dimensional nanomaterials as vapor-liquid-solid (VLS), vapor-solid-solid (VSS) and catalyst-free growth [48], and all of them have been

observed directly in ETEM [80]. As an ideal cold-wall nanoreactor for CVD, the energy needed to decompose the precursor molecules can be provided either by the e-beam or by thermally heating the substrate.

9.3.4.1 Nanostructure (Island/Dot)

The effect of e-beam on the nucleation and growth of nanostructures is nonnegligible, especially when the temperature was taken into account in synthesis. Electron-beam-induced decomposition (EBID) techniques were extensively used to fabricate periodic arrays of metal/semiconductors. The process involves introducing organometallic source vapor (precursor vapor) into the microscope column and irradiating the target area of the substrate with a focused e-beam.

In 2001, Jiang and coworkers [81] investigated the detailed parameters, such as deposition temperature, source compound, organometallic partial pressure, and electron dose, of EBID to fabricate periodic and aperiodic nanostructures and nanodevices. Metallocene compound, nickelocene ($\text{Ni}(\text{C}_2\text{H}_5)_2$), was used as an organometallic source and the deposits with edge sharpness under 4 nm had been fabricated, despite the quantity of the deposited material being too small for XPS to detect.

Mitsubishi [82] employed a 200 kV TEM equipped with a gas introduction system satisfying a gaseous flux of $2 \times 10^{-4} \text{ Pa L s}^{-1}$ to fabricate nanometer-sized W dots with a diameter of less than 5 nm in 2003. The precursor employed for the W deposition was tungsten hexacarbonyl [$\text{W}(\text{CO})_6$], and the depositions were performed at RT. As shown in Fig. 9.22a, c and b, d, the bright-field TEM and HAADF-STEM images showed the W nanodots deposited on the Si substrate, and the time periods for the large and small dots were about 1.5 and 0.5 s. The depositions were made for 10 s at two regions with different substrate thicknesses. The result showed that the deposition size at the thicker substrate region was only slightly larger, which indicated that the method can also be applied to the bulk substrate used in practical applications.

The deposition of GaN quantum dot arrays with uniform size onto a SiO_x substrate was done using a nanolithography technique in 2004 by Crozier [83] as well. The nanolithography technique is based on a combination of sub-nanometer electron-beam-induced chemical vapor deposition and single-source molecular hydride chemistries. A completely inorganic and highly reactive gaseous perdeuterated gallium azide (D_2GaN_3) was utilized as a hydride source, dissociated exothermically under electron irradiation, resulting in the formation of stoichiometric GaN, with byproducts of volatile D_2 and N_2 . The nanolithography and characterization were conducted in a Tecnai ETEM, which is fitted with an environmental cell and essentially operates as a cold-wall CVD reactor. Figure 9.22e, f showed a periodic array of uniform GaN dots grown by exposing the substrate to a precursor pressure of $\sim 30 \times 10^{-5}$ Torr, evacuating the microscope for 5 min and then depositing a series of dots (the deposition time per dot was 0.5 s). The dots were highly uniform, and displayed an average full width at half-maximum (FWHM) of ~ 4 nm and a base

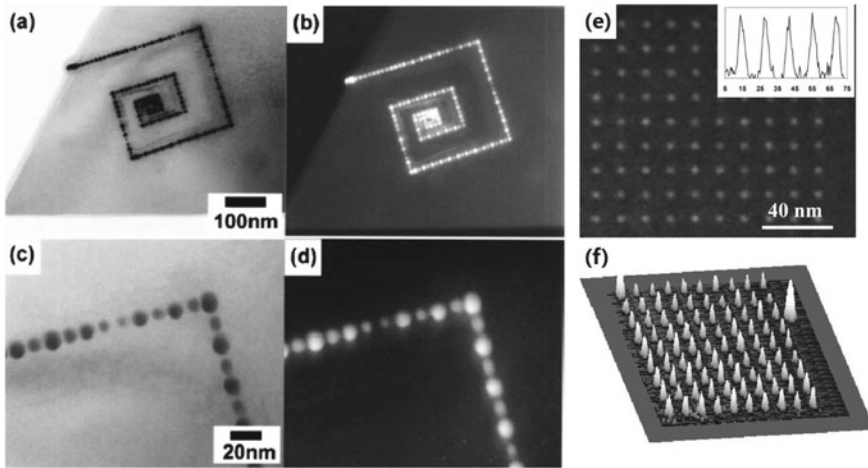


Fig. 9.22 **a** TEM bright-field and **b** HAADF-STEM image of W nanodots deposited on Si. The bright contrast indicates a concentration of the heavy element, W. **c** The BF and **d** HAADF-STEM images, in which well-defined nanodots are clearly seen, and are magnifications of the upper right corner of **(a)** and **(b)**, respectively (reproduced with permission from Ref. [82], Copyright 2003, AIP Publishing). **e** Z-contrast image of 2D periodic array of GaN dots. Inset shows line profiles through the Z-contrast images, showing a FWHM of 4 nm. **f** Surface plot of array of dots showing the height of dots derived from the ADF image intensity. Average dot height is 5 nm (reproduced with permission from Ref. [83], Copyright 2004, AIP Publishing)

width of ~ 9 nm. The diameter of dots was considerably larger than the used e-beam, indicating that the dot size was controlled by the spatial distribution of secondary electrons leaving the substrate surface. In 2005, employing the same device, van Dorp et al. [84] wrote dots with an average FWHM of 1.0 nm, in an array with a spacing of 4.0 nm, further improving the resolution limit of the EBID approach. These experiments demonstrated that EBID is a promising technique for high-resolution resistless lithography, and the ETEM allowed the entire growth process to be observed and controlled in real time as the container and reactor.

9.3.4.2 Semiconductor/Metal-Oxide 1D Nanomaterials

Semiconductor nanowires have important applications in electronic devices, information storage, microelectromechanical systems, and photovoltaics. For many applications, it is essential to control the structure, orientation, and location of the nanowires, and the factors that determine the growth rate, orientation, and epitaxial relationship with the substrate are therefore of key importance [85].

Since the VLS mechanism was proposed by Wagner et al. [86] in 1964, it was extensively studied and verified in the following decades. The characteristic feature of this mechanism is the liquid eutectic mediating the mass transport from the vapor to the solid interface. In 2000, the first real-time observation of semiconductor

nanowire growth in an in situ high-temperature TEM unambiguously confirmed the VLS crystal growth mechanism at the nanoscale. Yang and Wu dispersed a small amount of micrometer-sized Ge particles on TEM grids together with solution-made monodispersed Au nanoclusters. In their experiments, they used a conventional TEM without environmental equipment. Therefore, the nucleation and growth were dependent on the Ge evaporation at 900 °C, from a solid Ge source (a thin layer of Ge/C coating). Three well-defined stages have been clearly identified during the process: (I) metal alloying (Ge and Au), (II) crystal nucleation, and (III) axial growth, as shown in Fig. 9.23a [87].

Employed a UHV-TEM equipped with facilities for introducing the reactive gas disilane (Si_2H_6), Kim et al. systematically studied the first and second stages of Si nanowires growth in the Si–Au system, including the size effect [88] during the phase transition and kinetics of individual nucleation [89]. Figure 9.23b–g showed the images of the transition from two-phase Au + AuSi to single-phase AuSi. The

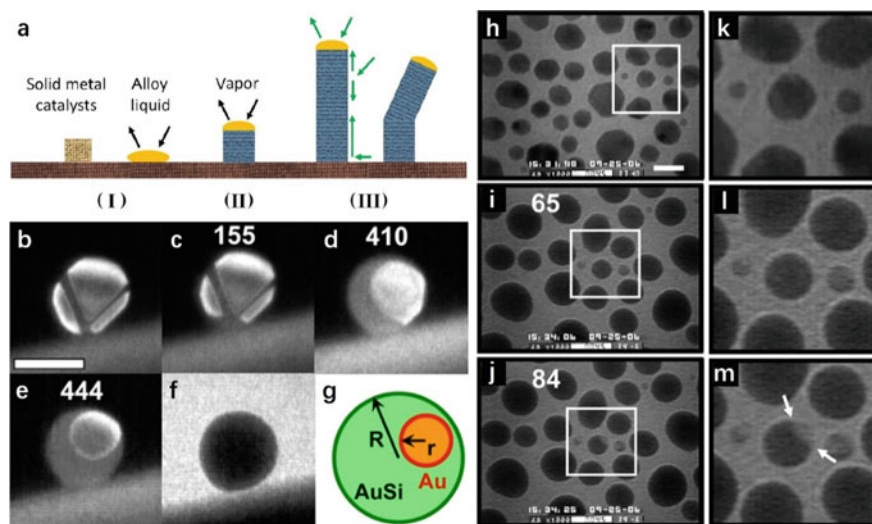


Fig. 9.23 **a** Schematic illustration of VLS nanowire growth mechanism including three stages (I) alloying, (II) nucleation, and (III) axial growth (reproduced with permission from Ref. [48], Copyright 2017, Springer Nature). **b–e** Dark-field images in side view during the solid-to-liquid transformation. **f** Bright-field image showing the droplet after the transformation is complete. **g** Idealized schematic of the inferred geometry (reproduced with permission from Ref. [88], Copyright 2009, American Physical Society). **h–j** Bright-field images extracted from a video obtained during nucleation of Si from polycrystalline Au clusters. **h** Image acquired before opening the leak valve, showing polycrystalline Au particles, as indicated by their faceted shapes and by the interparticle variations in their brightfield contrast. **i** Image acquired after 65 s, showing the formation of the liquid AuSi alloy as reflected by the rounded shapes in projection and the disappearance of crystalline contrast. **j** Image acquired after 84 s, showing the appearance of a Si nucleus with lighter contrast at the edge of one AuSi droplet. (**k–m**) Enlarged images of the boxed regions of (**h–j**), respectively. Arrows in (**m**) indicate the interface between liquid AuSi and solid Si (reproduced with permission from Ref. [89], Copyright 2008, The American Association for the Advancement of Science)

first four frames were recorded at an orientation where the crystalline Au provides bright contrast, and the Au particle appeared to consist of a single crystal with multiple twins (visible as dark bands). Figure 9.23f shows the liquid droplet that remained after the crystal had disappeared (bright field), and the idealized schematic of the inferred geometry is illustrated in (g). Similarly, a series of images obtained when introducing the reactive gas disilane to a heated sample illustrated the initial transformation of polycrystalline Au islands (Fig. 9.23h) into eutectic droplets of AuSi (i), followed by the appearance of Si nuclei (j). The Si nucleation occurred at the edge of the droplet, which suggests that this is the energetically favorable location that minimizes the nucleation barrier.

Ross and coworkers further systematically [90–93] studied steady-state growth of Si and Ge nanowires, considering growth kinetics, sidewall structure, and the phase (liquid or solid) and stability of the catalyst at the nanowire tip. In Si nanowire growth (Fig. 9.24a), the VLS mechanism has a characteristic appearance in the TEM. The droplet, with an amorphous structure and curved surface, rests on the tip of the nanowire. Meanwhile, the droplet/nanowire interface is generally planar, and appears to be composed of Si(111) planes, whatever the growth direction of the nanowire. The dependence of growth rate on pressure, temperature, and particularly nanowire diameter was also observed and recorded in this system, to deduce the growth kinetics of Si nanowires. They suggested that the rate-limiting step was the thermally activated, Au-catalyzed dissociative adsorption of disilane, and that dissociation takes place directly on the catalyst droplet, with no contribution due to adsorption and diffusion from elsewhere. This result was fully consistent with the VLS model, in which the droplet surface was taken to be a preferential site for the adsorption of the growth species [91].

Besides classical Si and Ge nanowires, the VLS mechanism was also verified in other materials, such as GaN [96] and InAs [97]. Growing III–V GaP nanowires in an ETEM, Chou et al. [98] measured the local kinetics in situ as each atomic plane was added at the catalyst–nanowire growth interface by the VLS process. They found that the growth rate was very sensitive to perturbations using a high V/III ratio, and such sensitivity was absent when growing at a low V/III ratio, creating a highly regular regime that may be optimal for the growth of complex materials. The relationship between local growth kinetics and atomic structure provides insights into understanding the growth mechanism and the requirements for the most precise control over growth.

In the case of Ge nanowires are catalyzed by Au, in situ studies found that nanowires can grow below the eutectic temperature with either liquid or solid catalysts, and the state of the catalyst only depends on the thermal history. The second pathway was called the VSS mechanism. Kodambaka et al. [94] unveiled the phenomenon clearly in 2007. As illustrated in Fig. 9.24b–c, (b) shows a Ge wire at three successive times during VLS growth and the catalyst persisted liquid state (smooth round shape). After cooling the specimen to solidify the catalysts and then reheating to the original temperature, the nanowire growth continued with solid catalyst (Fig. 9.24c, faceted surface). Measurements made on several wires showed that VSS growth was 10–100 times slower than VLS growth even at the same gaseous

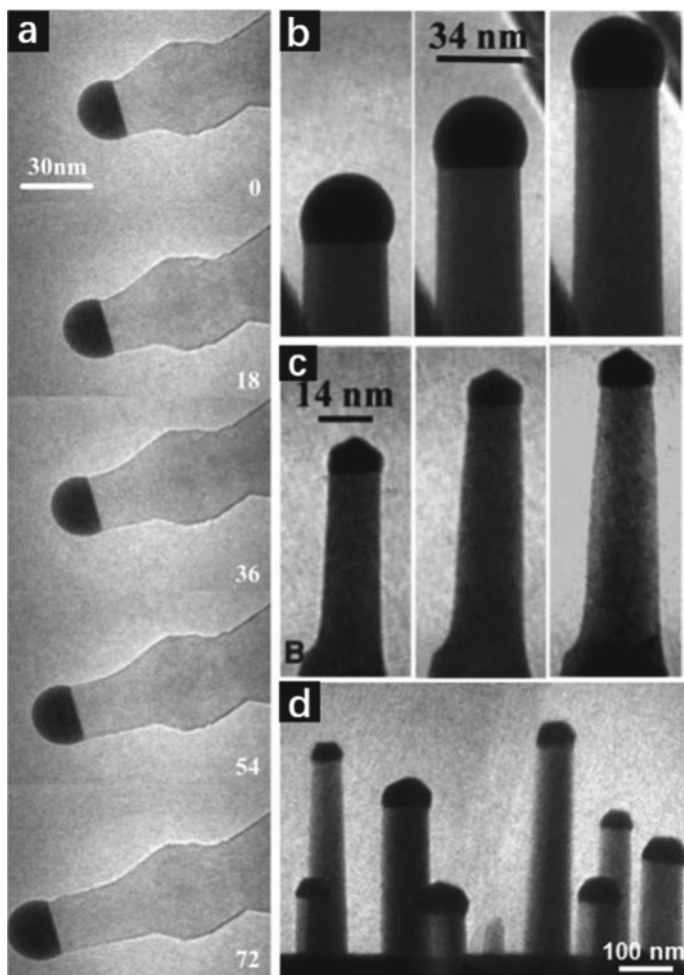


Fig. 9.24 **a** Sequence of images recorded during the growth of a 26 nm diameter Si nanowire, with the time shown in seconds since the first image. Bright-field imaging conditions were used so that Si appears medium gray and the droplet (AuAuSi) is a dark semicircle (reproduced with permission from Ref. [91], Copyright 2010, IOP Publishing). **b** Ge nanowire growth from an AuGe liquid droplet. **c** Ge nanowire growth from solid Au prepared as follows: at constant pressure, the specimen was cooled to solidify the droplets and then returned to the same temperature as (**b**), where the catalysts remained solid due to hysteresis (reproduced with permission from Ref. [94], Copyright 2007, The American Association for the Advancement of Science). **d** Si nanowire growth in the VSS modes (AgAu_2 at 556 °C and 1×10^{-5} Torr disilane) (reproduced with permission from Ref. [95], Copyright 2012, American Chemical Society)

pressure and temperature, presumably as a result of weaker surface reactivity and/or lower diffusivity through the solid. The principal cause of VLS growth below eutectic temperature excluded the Gibbs–Thomson effect or any direct effect of small size, and finally was identified as the inhibition to nucleation of solid clusters caused by high Ge supersaturation in the droplet. VSS mechanism and similar phenomena were also demonstrated in Si/Ge nanowires growth catalyzed by other catalysts [95, 99–101] (Fig. 9.24d).

Besides the common and extensively accepted VLS and VSS growth mechanism, there existed some research [40, 102–106] focused on the catalyst-free pathway, especially for metal-oxide nanowire growth in the presence of oxygen. No external catalysts or solvents were directly used during the growth process, and the nanowires were directly grown on the metal surface through a reaction with oxygen, which was named as vapor–solid (VS) mechanism.

Actually, as early as 1955 [102], Sears's experiment demonstrated the vapor–solid process in the growth of mercury whiskers. In 2001, Pan et al. [103] deemed that their nanobelts of semiconducting oxides were also governed by VS mechanism because the only source material used was pure oxide powders.

Another possible mechanism explained nanowire growth is accomplished via the incorporation of O from vapor and metal ions through diffusion along the defects, such as twin boundaries, stacking faults, and surfaces, from the substrate to the nanowire tip [40, 48]. As Fig. 9.12i–n shows, the successive stages of growth of copper oxide whiskers in 4×10^3 Pa of oxygen were recorded. At the beginning of the heating (estimated to ~ 670 K), an oxide film with non-uniform thickness was formed on the copper surface, and consequently the shape of the edge became jagged (Fig. 9.12i–j). After about 40 s, the oxide layer stabilized and the edge became smoother (Fig. 9.12k). Gradually, whiskers started to grow on the oxide layer (Fig. 9.12l–n), and two kinds of whiskers were identified in these micrographs: (i) thick and short and (ii) thin and long. The analysis of grown whiskers suggested that copper atoms easily diffuse along the lattice defects in CuO, and upon reaching the whisker tip, react with the ambient oxygen there. Tokunaga et al. [105] also studied the growth and structure of tungsten oxide nanorods using ETEM. They concluded that it was dominated by the solid diffusion mechanism: cracks occurred in the surface of the natural tungsten oxide layer when the tungsten was heated, after which tungsten diffused through the cracks of natural tungsten oxide layer from the tungsten wire to form a highly crystalline prominence. In 2015, Zhang et al. [104] demonstrated the layer-by-layer growth kinetics statistics in the growth of tungsten oxide nanowires with ETEM.

In 2014, Rackauskas et al. [106] observed the synthesized CuO nanowires in an ETEM by oxidation of pure metallic Cu in the presence of 3.2–7 mbar of O₂ in the temperature range of 350–475 °C. They also confirmed the occurrence of the copper diffusion (along the grain boundaries of the oxide layers and to the nanowire tip). Meanwhile, collecting kinetics of the growth, they concluded that nanowire growth should be described as the layer-by-layer formation process, in which nucleation of a new layer is the growth limiting stage, rather than the copper diffusion (along the grain boundaries of the oxide layers and to the nanowire tip).

Based on the growth of semiconductor nanowires, simple nanoscale devices were fabricated and observed over their complete lifecycle from creation to failure with additional electrical measurements. Kallesøe et al. [107] used the VLS method to grow Si nanowires as devices bridged between Si cantilevers. They characterized the formation of the contact between the nanowire and the cantilever, measured the electrical properties and high current failure characteristics of the resulting bridge devices, and related these to the structure. Probably the growth of nanowires in ETEM could be controlled more accurately so as to fabricate more complex structures or special devices in the future.

9.3.4.3 Carbon 1D Nanomaterials

As early as 1971, Baker and Harris [108] had already used the modified controlled atmosphere electron microscope to observe gas reaction, including the investigation of filamentous carbon formation from acetylene, catalyzed by nickel, iron, and cobalt. In spite of the resolution limit, early studies already focused on morphological changes and growing rates, from which kinetic parameters and activation energy could be obtained, so as to help put forward the growth mechanism.

Since carbon nanotubes (CNTs) were discovered in 1991 by Iijima [109], various applications, especially in displays or in X-ray tubes for medical applications, were developed in the following years. These applications require strict control of the diameter, length, and number of walls (such as multi-wall CNTs for field emitters, and single-walled CNTs for transistors) and the chirality. However, it's difficult to monitor and control the nucleation and growth of CNTs during traditional high-temperature arc-discharge and laser ablation processes. By contrast, CVD is an increasingly important and steady method, especially when ETEM was used as a cold-wall nanoreactor. With the development of accessories and techniques, the ETEM offers an excellent opportunity to satisfy the demand for in situ observation of CNTs growth.

In 2004, there were two groups [110, 111] that completed direct imaging of CNT nucleation and growth process at reaction temperature using ETEM. Helveg et al. [110] presented in situ TEM observations of the formation of carbon nanofibers (including nanotubes) from methane decomposition over supported nickel nanocrystals. The consecutive TEM images of the main equilibrium shape transformed into a highly elongated shape were demonstrated in Fig. 9.25. The formation of more graphene sheets whose basal (002) planes were parallel to the Ni surface was attributed to the elongation of the Ni particle, and it could be concluded that the reshaping of the Ni nanocluster assisted in the alignment of graphene layers into a tubular structure. Specifically, the nucleation and growth of graphene layers were found to be assisted by a dynamic formation and restructuring of mono-atomic step edges at the nickel surface (in Fig. 9.25b–g).

Sharma and Iqbal [111] reported the in situ observation of carbon filaments and CNTs as well with the employment of ETEM. They used two different catalyst systems (Ni–SiO₂ and Co, Mo–MgO) in two flowing precursors, propylene

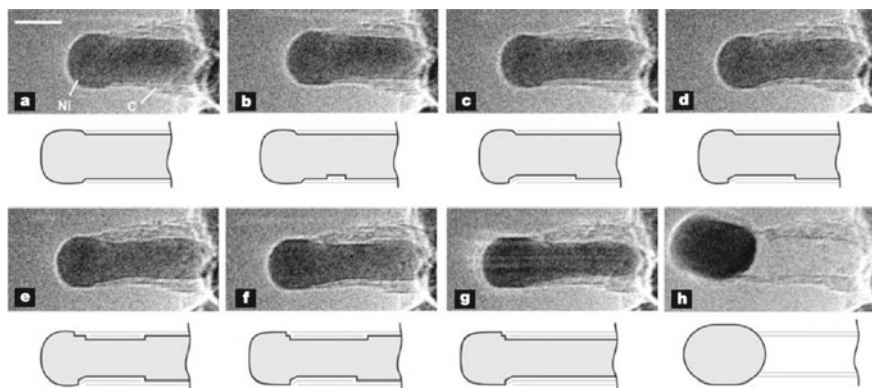


Fig. 9.25 Image sequence of a growing carbon nanofiber. Images a–h illustrated the elongation/contraction process. Drawings were included to guide the eye in locating the positions of mono-atomic Ni step edges at the C–Ni interface. The images were acquired in situ with $\text{CH}_4:\text{H}_2 = 1:1$ at a total pressure of 2.1 mbar with the sample heated to 536 °C (reproduced with permission from Ref. [110], Copyright 2004, Springer Nature)

(99.9999%) and welder’s grade acetylene, respectively. Filamentous growth was observed when propylene was leaked over Ni–SiO₂ at 400 °C while acetylene, on the other hand, provided the growth of a well-defined nanotube structure. Furthermore, the growth of multi-wall nanotubes (MWNTs) favored at 450 °C, and compared with single- and double-walled CNTs were observed to form predominantly at higher temperatures (700–800 °C).

In the following years, Sharma and coworkers continuously studied the CNTs’ growth under diverse reaction conditions, and they concluded that the growth rate and morphology of the formed nanotubes depended on the synthesis conditions (i.e. temperature and pressure) [80, 101, 112, 113]. For example, catalyzed by Ni–SiO₂ with narrow particle size distributions (1.5–3.0 nm), at an average rate of 35–40 nm s^{−1} under 20–100 mTorr of gas pressures at 480 °C, serpentine-shaped or zigzag multi-wall carbon nanotubes grew, while at an average growth rate of 6–9 nm s^{−1} at pressure <10 mTorr at the same temperature, straight single-wall carbon nanotubes with nearly uniform diameters (~3.5 nm) formed [112]. Furthermore, the plausible growth mechanism for small-diameter CNTs was also put forward, and shown in Fig. 9.26a–e. The model assumed that nanotubes grow preferentially along <111> direction on certain crystallographic Ni planes (the most active {110}, in (a)), then the particle rotated, or melted and re-crystallized (b), which would stop the growth of the tube momentarily until a new set of active {110} surfaces resume the growth. Epitaxial lattice-matching of the Ni {110} plane to the graphene lattice of the nanotube could induce the Ni particle to re-orient itself so that the Ni {111} aligns with the nanotube axis. The new growth direction would be controlled by the angle between two sets of 110 surfaces (i.e. 110 and 101, 60°). By incorporating 5-ring/7-ring pairs into the graphene lattice, the particle could continue to grow as a fully 3-coordinated seamless tube (c). If the 5-ring/7-ring defect pairs were at low

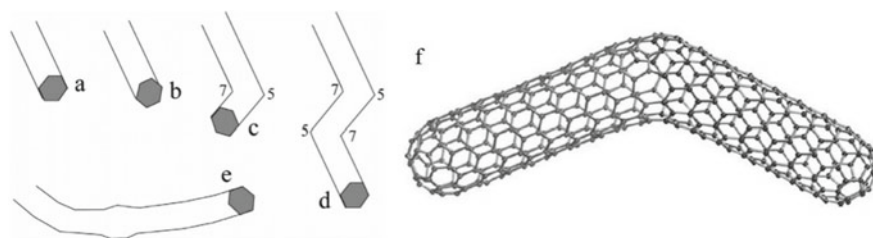


Fig. 9.26 a–e Sketches showing a plausible growth mechanism for small-diameter CNTs. f A hypothetical bend in a SWCNT model induced by three 5-ring/7-ring pairs (reproduced with permission from Ref. [112], Copyright 2005, Oxford University Press)

densities, the nanotube segments were straight, punctuated by 60° and 120° bends (d), while they could appear to be continuously curved and of irregular diameter with high densities of defects (e). Figure 9.26f showed a model of such a bend in a SWCNT in detail. The two nanotubes can be merged seamlessly, with fully 3-coordinated carbon atoms, by introducing equal number of 5-rings and 7-rings so that the overall polyhedral curvature of the nanotube does not change. In this model, 3 such 5-ring/7-ring pairs were introduced. The distribution shown here was not unique; many different variants that supported such a bend were possible.

In another article [113], Sharma and coworkers concluded that straight, single-wall, carbon nanotubes tend to form at high temperatures and low pressures while bent, zigzag, multi-wall carbon nanotubes form at lower temperatures and higher pressures. It's also perceived that high nucleation and growth rates would reduce the time/or energy required for annealing 5- and 7-ring defects. Furthermore, the overall activity of Ni catalyst particles, i.e. the number of particles active for tube formation, was improved by the addition of a small amount (below 0.2 mol fraction) of Au [114].

Yoshida and Takeda also made intensive and detailed studies on the growth of CNTs. In 2005, they outlined a theory of image information in an ETEM and applied the theory to simulating HRTEM images of SWNT in source gases of ethanol at the actual growth condition [115]. The ETEM observation of the swinging and rotational growth of CNTs in 2007 provided an explanation of the suspended growth mechanism [116]. In 2008, the nucleation and growth process of CNTs catalyzed by NP catalysts of fluctuating crystalline Fe carbide in CVD with C_2H_2 was acquired with ETEM [117]. 1 nm thick Fe (99.999%) was deposited on the thin SiO_2 surface layer of silicon substrates by vacuum evaporation. Then the substrates were set in an FEI Tecnai F20 equipped with an environmental cell, and heated to $600^\circ C$ in a vacuum, and subsequently, a mixture of $C_2H_2:H_2 = 1:1$ was introduced into the ETEM (10 Pa). Figure 9.27 shows the root growth process of a SWNT from an Fe carbide NP catalyst viewed nearly normal to the growth direction. In NP catalyst, various kinds of lattice images appeared and faded out, while all of them were identified as the iron–carbide structure (cementite, Fe_3C). The lattice image shown in Fig. 9.27a–d continued for 1–2 s, 1–2 s, 1–2 s, and 7 s, respectively. The phenomenon was accounted for by

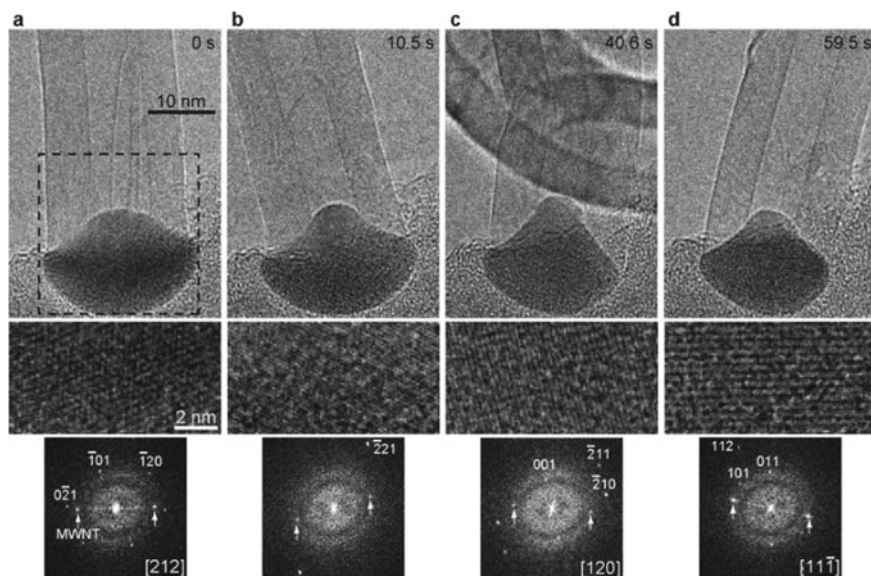


Fig. 9.27 a–d Growth process of a MWNT from an Fe carbide NP catalyst viewed nearly normal to the growth direction. Enlarged images and Fourier transforms of the dotted square regions in images are shown below, which indicated that phase of catalyst was Fe_3C (reproduced with permission from Ref. [117], Copyright 2008, American Chemical Society)

a change in crystal orientation without physically rotating the whole NP since it remained at nearly the same position and deformed only slightly. In conclusion, the NP catalysts were deemed as fluctuated crystalline cementite, Fe_3C .

Besides CNT, the formation of different allotropes of carbon on the nanoscale (e.g. graphene layers [118]) was also studied extensively with the employment of ETEM. There is no doubt that the ETEM has the indispensable advantage in observing the dynamics of catalyzed nanostructure growth, which provided the possibilities for understanding the mechanism and promoting the synthesis technology. Furthermore, it's common that the catalyst would cause some dynamic change during the catalyza-tion (e.g. in Yoshida's experiment, the NP catalyst Fe_3C already deformed slightly), which would be discussed in the next section.

9.3.5 The Catalyza-tion

Heterogeneous catalysis plays an essential role in modern industrial manufacturing. Over 85% of commercial chemicals in the industry are catalytically produced, mostly via gas-involved processes [48]. Traditional heterogeneous catalysts consist of metal NPs, which are supported on specific oxide substrates (even specific crystallographic planes). Since the catalytic activity varied with the atomic arrangement on the surface

of metal NPs, the interfaces between particles and substrate, the surficial status of the substrate (oxidation/reduction/doping), it's of great importance to study the structure and composition of catalyst at the atomic scale. Meanwhile, the catalytic reactions usually occur in an atmospheric environment, which means that the catalysts are likely demonstrating different characteristics and properties in traditional TEM under high vacuum. Therefore, the emergence of ETEM could satisfy the requirement of observation in detail at the atomic scale by maintaining the catalyst under active status in the reaction atmosphere [119].

9.3.5.1 Dynamic Observation of Catalytic Reactions

The catalytic performance of metal catalysts is determined by their structures [120], e.g. size, morphology, composition, crystal structure, metal–support interactions, and so on, while recent studies suggested that the structure of metal catalysts would dynamically change during reaction conditions [121], and their statuses in reaction could be dramatically different from the original/final ones [122, 123]. Therefore, real-time studying the metal catalysts is well expected to give insight into the underlying mechanism and to help further improve the properties of metal catalysts.

The nucleation and growth of CNT is a typical catalytic process, and the catalyst would undergo some dynamic changes in both morphology and composition during the whole growth. For example, the Fe_3C catalyst deformed during the reaction (Fig. 9.27). Similarly, in the work of Hofmann et al. [124], the catalyst particle showed a periodical morphology change, from its initial equilibrium shape into a highly elongated shape during carbon nanofibers nucleation. As shown in Fig. 9.28, the Ni particle elongated and then suddenly contracted into a rounder shape. Typically, the substrate anchorage was overcome during the first contraction and the catalyst crystal lifted off the substrate, resulting in a tip growth mode.

The composition change of the catalyst was also reported. Mazzucco et al. [125] observed and recorded the whole deactivation process of Fe catalyst NP in ETEM, and found that the Fe catalyst transformed into two distinct carbide phases, cementite

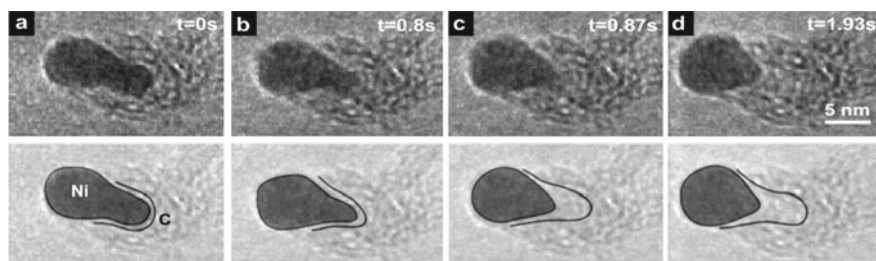


Fig. 9.28 a–d ETEM image sequence showing a growing CNT in 3:1 $\text{NH}_3:\text{C}_2\text{H}_2$ at 1.3 mbar and 480 °C. The Ni particle elongated and then suddenly contracted into a rounder shape (reproduced with permission from Ref. [124], Copyright 2007, American Chemical Society)

(Fe₃C) and Hägg (Fe₅C₂) under CNT growth conditions. Moreover, the carbon-rich Hägg carbide was inactive for the competitive process in contrast to the less carbon-rich cementite phase.

As a classical catalyst which is highly active for low-temperature CO oxidation and water–gas shift reaction, Au/CeO₂ is studied at the atomic scale to improve and stabilize the catalytic property. Since the interfacial perimeters between metal NPs and oxide substrate probably tip the scale for the catalysis, the structural collapse and reconstruction of the gold–ceria interfacial perimeters under various reaction conditions attracted extensive attention. Using ETEM, Ta et al. [127] directly observed the structural changes of the Au NPs and the interfacial structure (Au/CeO₂) under oxidizing and reducing (reactive) atmospheres at 573 K. As shown in Fig. 9.29a, a truncated octahedral Au particle (size: ~3 nm) directly contacted to ceria without any transition layers (Au{111}–CeO₂{111}), and the Au–CeO₂ interfaces retained their original configuration without appreciable variation in shape and size under an oxidizing gas environment (10 vol% O₂/N₂). When the same particle was exposed to a reducing and reactive environment (42 vol% CO/6 vol% O₂/N₂), the Au–CeO₂ interfaces reconstructed with the appearance of disordered CeO₂ layers adjacent to the gold particle as shown in Fig. 9.29b, which even increased in thickness over time. The chemical nature of the newly formed ceria layers was identified as CeO_{1.714}, which was partially reduced and probably resulted in the electronic state change of the gold atoms at the perimeter of the gold–ceria interface. Therefore, the authors proposed an anchoring mechanism as Fig. 9.29d shows, the faceted Au NP was constructed of four different domains with different functions.

Based on the observation of reversible changes in NPs, the oscillatory CO oxidation behaviors catalyzed by Pt NPs were reported with the employment of a nanoreactor, time-resolved HRTEM, mass spectrometry, and calorimetry in 2014 [47]. The technologies of MEMS and a unidirectional gas-flow channel with a reaction zone satisfied the in situ time-resolved observations of the periodic refacetting of the Pt NPs at 1 bar pressure and elevated temperatures. As shown in Fig. 9.30a, mass spectrometry demonstrated periodic oscillations of O₂ and CO pressures in anti-phase, and similar variations are shown in the CO₂ pressure. Meanwhile, to keep the nanoreactor temperature constant, the heater power would be reduced (Fig. 9.30b), which was at least 3 orders of magnitude faster than the time scale of reaction oscillations, to compensate the exothermic reaction heat. Finally, the Pt NPs near the reaction zone exit switched between a more spherical and a more faceted morphology (Fig. 9.30c, d). Specifically, as the CO conversion increased rapidly, Pt NPs immediately started a gradual transformation from a more spherical shape toward a more faceted shape (Fig. 9.30d I–III). On the decrease in the CO conversion, the NP transformed back to the more spherical shape (Fig. 9.30d IV) and retained that shape until the CO conversion rose steeply again. Thus, the individual NPs near the exit from the reaction zone could undergo oscillatory and reversible shape changes with a temporal frequency matching the oscillations in reaction power, indicating that the oscillatory CO conversion and the dynamic shape change of the Pt NPs were coupled.

Besides the dynamic observation of the catalyst, the oxide substrate was also studied because it usually interacts with the NPs under specific environments. The

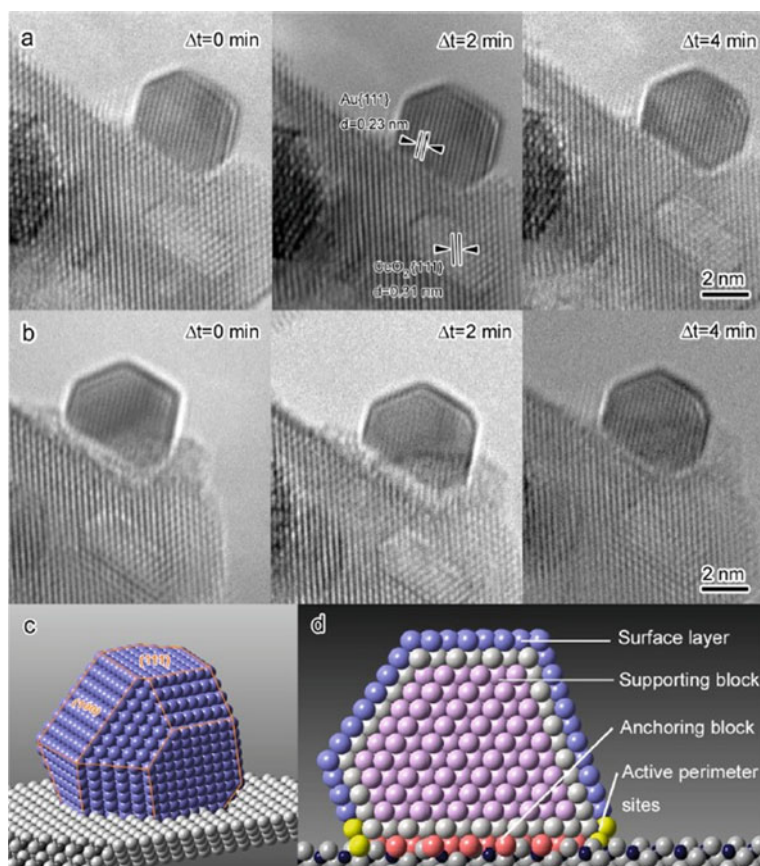


Fig. 9.29 ETEM images of the Au-673 catalyst (the selected Au NP) under oxidizing and reducing atmospheres at 573 K. **a, b** A truncated octahedral Au particle of ~ 3 nm size under a 10 vol% O_2/N_2 environment (**a**) and a 42 vol% CO/6 vol% O_2/N_2 atmosphere (**b**). **c** Schematic depicting a typical gold NP enclosed by {111} and {100} planes. **d** Atomic scheme of a gold NP anchoring onto a CeO₂ nanorod, illustrating the functions of different domains (reproduced with permission from Ref. [127], Copyright 2012, American Chemical Society)

reconstruction of gold–ceria interfaces in Fig. 9.29b was one manifestation, and another typical and obvious phenomenon was strong metal–support interactions (SMSI) (More details referred to SMSI could be found in [194]). As early as 1978, Tauster [128] had already explored the possibility of strong interactions between group VIII metals and supports containing titanium cations, and proposed the SMSI which was associated with the formation of bonds between the metal and titanium cations or titanium atoms. The definition of SMSI [129, 130] was later extended to include interactions between an active metallic component and any support materials that exhibit similar phenomena to that observed by Tauster. Generally speaking, the phrase was used for catalyst systems consisting of active metal particles on reducible

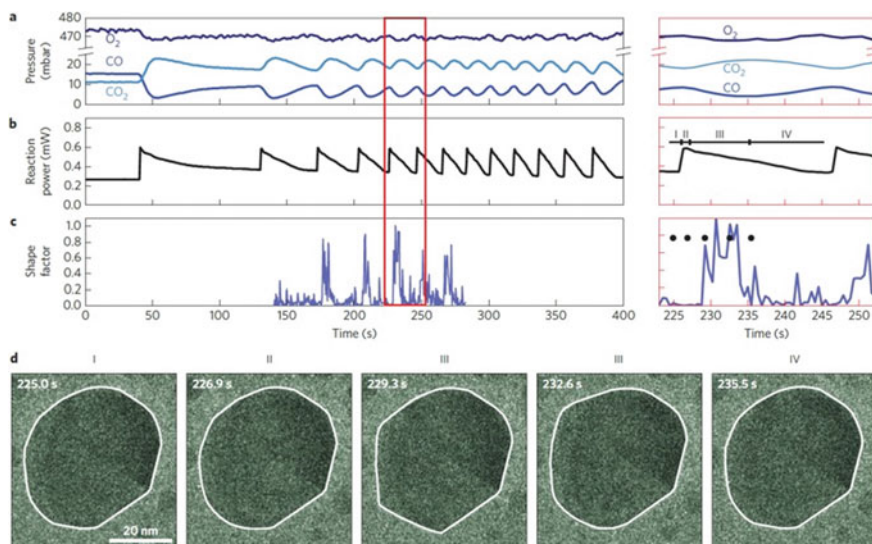


Fig. 9.30 Correlation of oscillatory CO oxidation reaction data with the projected morphology of a Pt NP (Supplementary Movie 1). The gas entering the reaction zone is 1.0 bar of CO:O₂:He at 3%:42%:55% and nanoreactor temperature is 659 K. **a–c** Mass spectrometry of the CO, O₂, and CO₂ pressures (**a**), reaction power (**b**), and shape factor (**c**) for the Pt NP in **d** as a function of time. The shape factor corresponds to the relative difference in the area from the best elliptical fit in image I in **d** (Ref. [4]). The morphology factor is zero for the more spherical shape and deviates for more faceted particles. Part of the reaction oscillation data is highlighted by the red rectangle. **d** Time-resolved TEM images of a Pt NP at the gas exit of the reaction zone (reproduced with permission from Ref. [47], Copyright 2014, Springer Nature)

support [131], because the interaction under reducing conditions can induce an electronic effect (charge transfer between support and metal particles), changing the chemisorption capacity of the active phase, and/or preventing the interaction between the gas molecules and the metal surface due to newly formed surface layer.

In 1997, Boyes and Gai [17] had observed the phenomena of catalyst deactivation caused by SMSI in an environmental high-resolution electron microscope (EHREM) at the atomic scale. Owing to the modification of apertures mounted inside the bores of the objective pole pieces rather than between them, the aberration coefficients could low down to 2 mm. Multi-directional resolution of atomic lattice planes with spacings in the range 0.34 (graphitic carbon)-0.23 nm (gold islands with (111) lattice) was routine. Figure 9.31a shows EHREM of finely dispersed Pt/TiO₂. In situ dynamic catalyst activation in hydrogen at 300 °C is shown in Fig. 9.31b. Growth of an amorphous Ti-rich overlayer or coating, with a composition close to slightly anion-deficient TiO₂ was observed (indicated at C, determined by EDX) on the surface of the same particle at 450 °C in Fig. 9.31c. In addition, there emerged some nm-scale single crystal clusters of Pt metal (arrowed) near the observed particle, and they were not in an epitaxial relationship with the substrate and not encapsulated by titania overlayers during the early development.

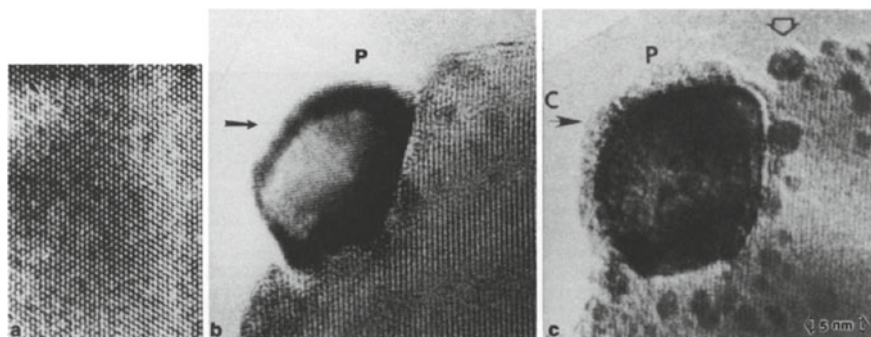


Fig. 9.31 **a** EHREM of finely dispersed Pt/TiO₂ prepared by impregnation of TiO₂ with Pt solution. **b** In situ dynamic catalyst activation in hydrogen imaged at 300 °C. The 0.23 nm (111) lattice spacings were clearly resolved in the Pt metal particle (P). **c** The same particle of Pt (P) imaged at 450 °C, also in H₂ (reproduced with permission from Ref. [17], Copyright 1997, Elsevier)

In 2016, Zhang et al. [132] described the atomic migration of a palladium/titania (Pd/TiO₂) system, by combining ESTEM and DFT calculations, which visualized the formation of the overlayers at the atomic scale under atmospheric pressure and high temperature. As Fig. 9.32a shows, an amorphous layer started to form on the particles under reducing conditions (H₂(5 vol%)/Ar at 1 atm) at 250 °C, arguably through the diffusion of reduced TiO_x species from the support to the particle surface, starting from the metal–support boundary (arrow). When the temperature was increased to 500 °C under the same conditions, the amorphous layer crystallized to form a bilayer that was almost epitaxial with the Pd(111) plane (Fig. 9.32b and higher magnification images in C, D). The lattice spacing was ~ 2.9 Å for the lower layer and 3.0 Å for the top layer, and the overlayer followed ABCABC stacking of the underneath Pd along [111] direction. The comparison between ABF (Fig. 9.32c) and HAADF (Fig. 9.32d), where the image contrast is the opposite and brightness in the latter case is proportional to atomic number, confirmed that the surface layer was composed of a material with lower atomic number than Pd.

Generally speaking, common SMSI overlayers as mentioned before are crystalline, while there exists special case in which environmental gas participated in the formation of end product, and resulted in amorphous overlayer. Matsubu et al. [133] proposed adsorbate-mediated SMSI (A-SMSI) encapsulation state that formed with the treatment of TiO₂-supported Rh NPs in CO₂-H₂ (CO₂-rich) environments at temperatures of 150–300 °C. According to the conditions known to form the traditional SMSI state, a crystalline bilayer of TiO_x quickly formed as a conformal coating on large crystalline Rh particles, with Ti exclusively in the Ti³⁺ oxidation state (Fig. 9.33a). In contrast, after 20CO₂: 2H₂ treatment for three hours at 250 °C, an amorphous overlayer on Rh was observed to form (Fig. 9.33b). In situ electron energy-loss spectroscopy (EELS) measurements with a 1.0–1.5 Å spot size focused at various locations on the overlayer directly proved that Ti existing in a combination of Ti³⁺ ($\sim 30\%$) and Ti⁴⁺ ($\sim 70\%$) oxidation states in the amorphous overlayer.

Fig. 9.32 Formation of the TiO_x overlayer on Pd nanocrystal in Pd/TiO_2 . Sequential in situ observations, under reducing conditions (H_2 (5 vol%)/Ar at 1 atm) of the Pd/TiO_2 sample at 250 °C (a), then 500 °C for 10 min (b); c, d are higher magnification ABF and HAADF images, respectively, of a section of part (b) showing the TiO_x double layer (reproduced with permission from Ref. [132], Copyright 2016, American Chemical Society)

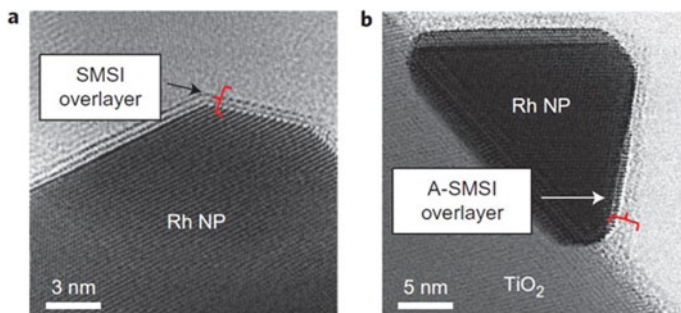
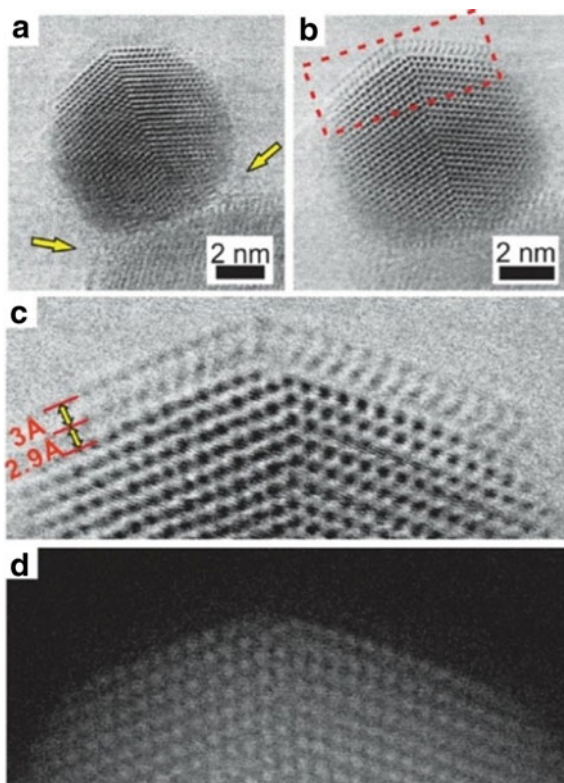


Fig. 9.33 In situ STEM images of Rh/TiO_2 after treatment in 5% H_2 and 95% N_2 at 550 °C for 10 min (a), which induced the formation of a TiO_x SMSI crystalline bilayer, containing exclusively Ti^{3+} , and after treatment in $20\text{CO}_2:2\text{H}_2$ at 250 °C for 3 h (b), which caused the formation of an amorphous A-SMSI overlayer, containing a mixture of Ti^{3+} and Ti^{4+} (reproduced with permission from Ref. [133], Copyright 2017, Springer Nature)

Differences in Ti oxidation state for the traditional SMSI and A-SMSI overlayers were hypothesized to result from the presence of HCO_x in the A-SMSI overlayer

and to be related to the unique reactivity and stability of the A-SMSI overlayer in humid CO₂-reduction conditions.

Besides the common surface structure fluctuation and reshaping of nanomaterials in catalyzation, there exist some extremely subtle structural changes during the real-time catalytic process. To reveal the structure–activity relationship, the most direct method is to directly observe the catalytic reaction occurring on the catalyst surface at the atomic level. In 2020, Yuan et al. [134] visualized the gas molecules that adsorb and react dynamically at the specific structure with the employment of spherical aberration-corrected ETEM. Normally, the spatial distribution of active sites on the catalyst surface is disordered, and the molecules adsorbed on the sites do not offer sufficient contrast for TEM identification. To solve this issue, they came up with a strategy to construct a highly ordered active row to enhance the image contrast. They took advantage of the highly ordered four-coordinated Ti(Ti_{4c}) rows on the anatase TiO₂ (1 × 4)-(001) surface to facilitate enhanced contrast of adsorbing molecules along the row direction and allow real-time monitoring of H₂O species dissociating. As shown in Fig. 9.34a, the reconstructed TiO₂ (1 × 4)-(001) surface was obtained after heating in O₂, in which the protruding black dots represent the Ti_{4c} rows. Then O₂ gas was evacuated and H₂O vapor was introduced (Fig. 9.34b). With the raising H₂O pressure, two additional small protrusions were observed at the top of the Ti_{4c} rows, and became clearly visible (in Fig. 9.34d). Combined with in situ Fourier transform infrared spectroscopy (FTIR) and density functional theory (DFT), the researchers attributed the twin protrusions to the adsorbed water species, which was composed of two different hydroxyl species. Since TiO₂ can catalyze the water gas shift reaction (H₂O + CO → H₂ + CO₂) at elevated temperatures, the researchers introduced CO into the ETEM column after the formation of twin protrusions. They found that the twin-protrusion structure changed dynamically between blur and clearness (Fig. 9.34e, f), which indicated that the adsorbed hydroxyls were reacting with CO molecules, and the Ti_{4c} sites are the reaction sites.

Another challenging and unexpected interface structure change was explored in 2021 by Yuan et al. as well [135]. Supported nanoparticles are widely used as catalysts for heterogeneous reactions, and the active sites in many reactions are located at the perimeter interface (PI), which is generally considered to be rigid. However, by employing the aberration-corrected ETEM (same as the former apparatus), they found that Au nanoparticles could rotate reversibly on the TiO₂ (001) surface in different gas environments. Furthermore, by controlling the external oxidative/reductive gaseous environments and temperature, the researchers realized the in situ manipulation of the atomic configuration of the active Au–TiO₂ interface. In brief, a perfect epitaxial relationship was found at the interface between the Au NP and the TiO₂ (001) interface at high oxygen pressure (Fig. 9.34g, i), while the Au NP rotated by a small angle along the axis perpendicular to the TiO₂ (001) surface with the introduction of CO ($V_{O_2} : V_{CO} = 1:2$) (Fig. 9.34h, j). The rotation was so subtle that the whole process couldn't be observed and monitored without the possibility and convenience provided by the ETEM. This result suggests that real-time design of the catalytic interface in operating conditions may be possible.

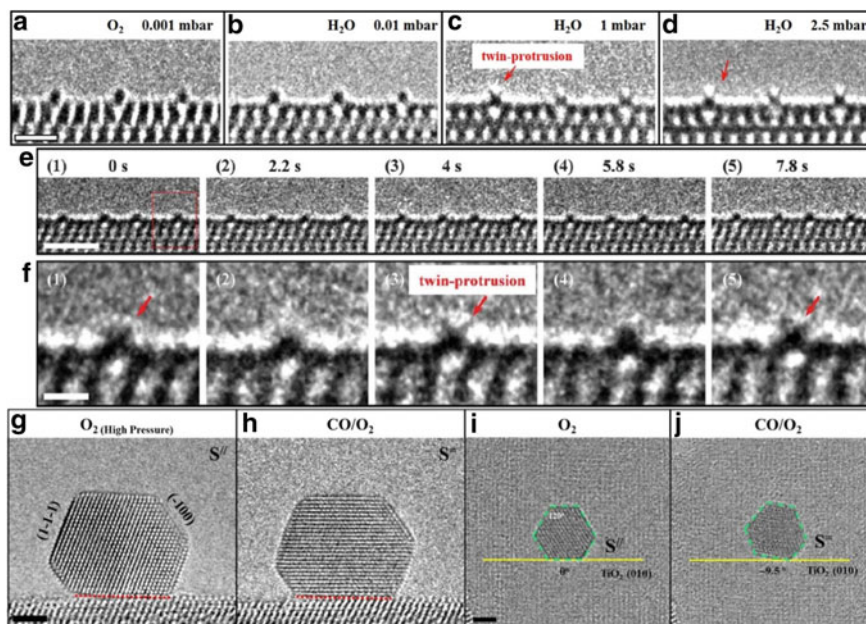


Fig. 9.34 **a–d** Aberration-corrected in situ ETEM images show the same area of TiO_2 (001) surface at 700 °C under oxygen [**a** 0.001 mbar] and water vapor [**b** 0.01 mbar; **c** 1 mbar; **d** 2.5 mbar] conditions, scale bar, 1 nm; **e** Sequential ETEM images acquired in the mixed gas environment (1:1 ratio of CO and H_2O vapor; gas pressure: 5 mbar; temperature: 700 °C), viewed from the [010] direction. Scale bar, 2 nm. **f** Enlarged ETEM images show the dynamic structural evolution of the Ti row outlined by the dotted rectangle in (**e**). Scale bar, 0.5 nm (reproduced with permission from Ref. [134], Copyright 2020, The American Association for the Advancement of Science). **g** and **h** Aberration-corrected in situ ETEM images of a Au NP supported on a TiO_2 (001) surface in **g** a high-pressure oxygen (6.5 mbar) environment, and **h** a CO oxidation (total pressure: 4.4 mbar, $V_{\text{CO}}: V_{\text{O}_2} = 1:2$) environment, scale bar, 2 nm; **i** and **j** Aberration-corrected in situ ETEM images show the structural evolution of the Au– TiO_2 (001) nanocatalyst from an oxygen environment [**i** 5 mbar] to a reactive environment [**j** 500 °C, 5 mbar, $V_{\text{O}_2}: V_{\text{CO}} = 1:2$], scale bar, 2 nm (reproduced with permission from Ref. [135], Copyright 2021, The American Association for the Advancement of Science)

9.3.5.2 Sintering and Dispersion

Catalyst deactivation was a major concern in many industrial processes, besides SMSI in a specific gaseous environment; sintering was another typical reason which could account for it. The active sites are usually related to the surface area or the specific size, while sintering always result in the decrease of the surface area and changing the size of the catalyst particles. Furthermore, the sintering of supported NP catalysts occurs in various applications, ranging from high-temperature automotive exhaust emission controls to low-temperature fuel cells, made it an urgent demand to stabilize the catalyst distribution, lifting the commercial value. ETEM could provide direct

evidence about size/distribution/morphology of NPs, further the dynamic evolution of these information under gaseous environment.

There are two widely accepted sintering mechanisms [130, 136–138]: (a) Ostwald ripening (OR) [139], in which the larger particles grow at the expense of small ones, by the diffusion of atoms/clusters due to a difference in chemical potential depending on NP size/surface curvature; (b) Particle migration and coalescence (PMC) [140], in which the independent particles migrated on the substrate surface in a Brownian-like motion and coalesce to other encountered particles. Both mechanisms may co-exist during a real catalytic reaction, and the dominant one is determined by reaction conditions and catalyst characteristics, e.g. loading amount, and weak metal–support interaction (MSI) facilitate the PMC process while strong MSI avails the OR process.

As early as 1974, Baker et al. [141] has observed particle mobility on a graphite surface in a gaseous environment with their modified TEM. In 2004, Liu et al. [142, 143] studied the sintering of palladium NPs on Al_2O_3 during the catalyst regeneration process. Fresh Pd particle catalyst was located on the Al_2O_3 surface and sintering occurred in 500 mTorr of steam at 700 °C, via traditional ripening (OR) and coalescence (PMC) mechanisms. As shown in Fig. 9.35a–c, particles marked 1 gradually shrunk in size and finally disappeared, while particles marked 2 coalesced into one. As for the used catalyst, which deactivated apparently due to the coverage of a complex mixture of unsaturated aliphatic hydrocarbons (HC in Fig. 9.35d), Pd particles moved through the hydrocarbon, leaving light contrast tracks in their wake (black arrow in Fig. 9.35e) in 500 mTorr of steam at 350 °C. In this process, the Pd particles catalyzed the gasification of green oil residue, meanwhile the exothermic nature of the reaction raised the temperature and facilitated the coalescence of Pd particles even at much lower temperatures.

In 2012, Hansen et al. [138] proposed that the sintering process could be divided into three phases via reviewing and analyzing recent in situ observations (Fig. 9.36). Phase I involved rapid loss in catalyst activity (or surface area), phase II was where sintering slows down, and phase III was where the catalyst may reach a stable performance. The experimental data suggested that, in phase I, very little PMC was observed while the disappearance of the smallest particles (OR) was probably responsible for the obvious declining activity. In phase II, sintering slowed down since the small particles already disappeared, and during this stage both OR and PMC could be observed. In phase III, the particles had grown large and been very stable. In this phase, particle migration slowed down, and some other parasitic phenomena, such as support restructuring, turned out to be important or influential, especially at high temperatures. Considering several technical and chemical improvements related to changes in the composition of the NPs or changes in support surface structure, morphology, and chemistry, they endorsed the viewpoint proposed by Moulijn et al. [144], which the movement of atoms holds more weight accounting for the sintering mechanism.

As a model system for automotive exhaust abatement, Pt NPs dispersed on a planar, amorphous Al_2O_3 support were monitored during the exposure to 10 mbar air at 650 °C under in situ TEM by Simonsen et al. in 2010 [145]. Time-resolved image series unequivocally revealed that the sintering of Pt NPs was mediated by

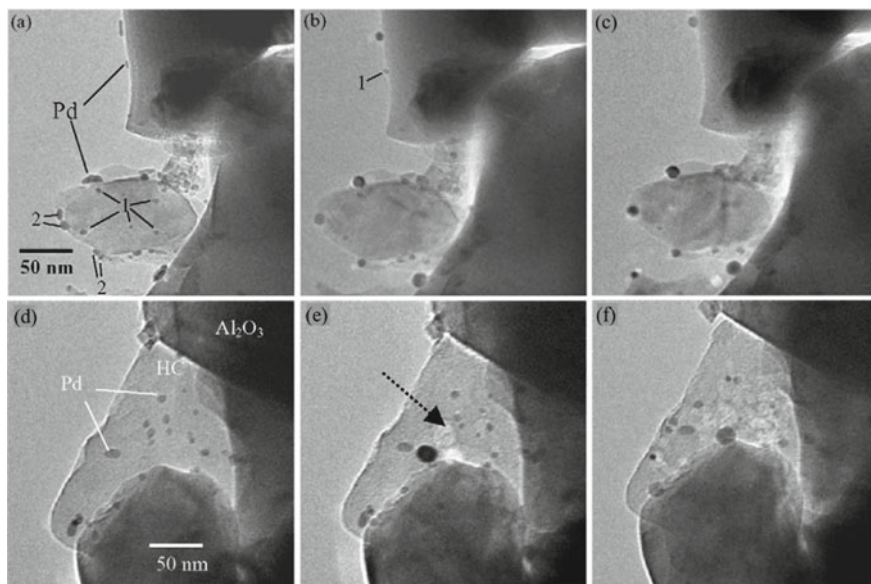


Fig. 9.35 a–c Fresh Pd/Al₂O₃ catalyst a in the as-received condition (RT); after heating in 500 mTorr steam at 700 °C for b 1 h; c 3 h. d–f Used Pd/Al₂O₃ catalyst heating in 500 mTorr steam at 350 °C for d 0 h, e 1 h, f 2 h (reproduced with permission from Ref. [142], Copyright 2005, Elsevier)

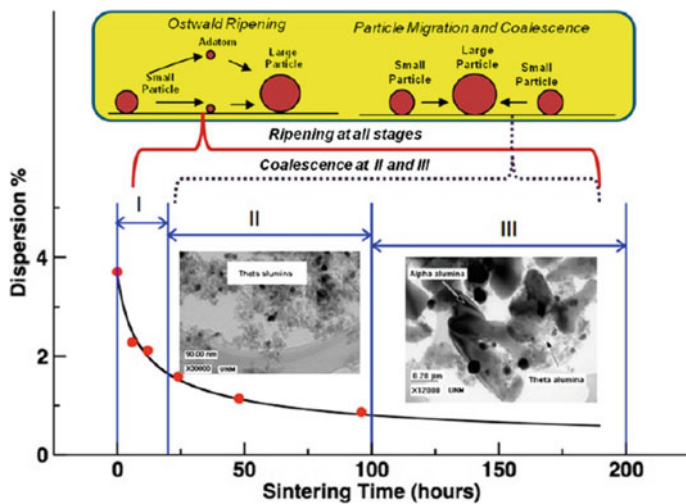


Fig. 9.36 The sintering process could be divided into three phases according to the change of the catalyst activity, and OR could happen during all three phases while PMC mainly occurred during phases II and III (reproduced with permission from Ref. [138], Copyright 2013, American Chemical Society)

an Ostwald ripening process. Benavidez and coworkers [146] performed an ETEM study of Pd/carbon and Pt/SiO₂ under high temperatures as well. Anomalous growth patterns were detected wherein some particles grew much larger than others, and they were not caused by random migration and coalescence of particles. The dominant process leading to particle growth was OR, the same as the former research.

Impressive advances had been realized by in situ TEM in several supported catalyst systems, while most of them still focused on determining the dominating sintering mechanism by statistical analysis of particle size evolution from the top view, whose dynamics would respond to environmental and support change. Yuan et al. [147] obtained the atomic-scale information of the interface between metal and support from a side view with the combination of AC-STEM and ETEM. The researchers loaded Au NPs on two typical anatase supports, well-defined Au–TiO₂ (101) and Au–TiO₂ (001), through impregnation and in situ annealing methods. As shown in Fig. 9.37a, the typical HAADF-STEM image viewed along TiO₂ [010] direction exhibited a round-shape Au NP with a small contacting interface, and an incoherent relationship between the NP and support. In contrast, a preferential contacting relationship that Au–TiO₂ (001) interface shared the plane with Au (111) was observed in Fig. 9.37b, with a relatively larger interface. Then the samples were heated to 500 °C in an oxygen environment (5×10^{-2} Pa). The Au NPs on the Au–TiO₂ (001) surfaces were stable, which was confirmed from both the top view (Fig. 9.37c, d) and the side view (Fig. 9.37e, f) even after several thousand seconds. Though the minimum distance of two particles was less than 0.46 nm, almost all of the particles were firmly attached to the support and kept unchanged. Strong interaction between Au NPs and TiO₂ (001) surfaces was obvious. During the sintering of Au–TiO₂ (101) catalysts, both PMC and OR processes were observed, as Fig. 9.37g–j shows. The seven particles were labeled from 1 to 7, respectively, then with time going by, initially connected particles 4 and 5 started to coalesce with the diminution of adjacent particle 6. The tendency developed steadily until one large particle was left at the cost of the disappearance of particle 6. It should be noted that the contacting area is still small, indicating a weak interfacial interaction. This work emphasized the facet-dependent sintering behaviors, proposing a feasible method of choosing a suitable support to prevent sintering.

In 2009, Amama et al. [148] demonstrated that the Ostwald ripening behavior of Fe catalyst films deposited on thin alumina supporting layers was a function of thermal annealing in H₂ and H₂/H₂O. The introduction of H₂O to the catalysis of CNT was proposed by Iijima's group as long ago as 2004 [149], as a prospective agent against amorphous carbon coating, to enhance the activity and lifetime of the catalysts. Amama considered that the addition of H₂O inhibited OR through the ability of oxygen and hydroxyl species to reduce diffusion or migration rates of catalyst atoms from one catalyst to another across the sample substrate, on the basis of the ex situ experiment.

Besides the sintering behaviors of tiny clusters (<1 nm) and NPs (<3 nm), the dispersion of a single atom was also recorded using TEM/ETEM/ESTEM. Atomically dispersed catalyst species was reported by Iwasawa et al. [150] as early as 1999 with the usage of EXAFS. In 2011, Zhang et al. [151] proposed the concept,

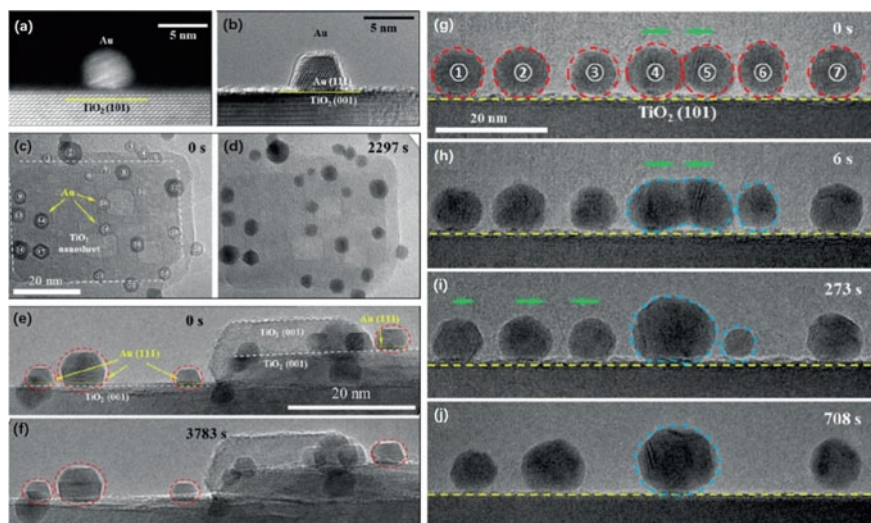


Fig. 9.37 **a** The HAADF-STEM image shows the typical interface between Au NP and TiO_2 (101) surface. **b** The TEM image shows the typical interface between Au NP and TiO_2 (001) surface. **c–f** The serial TEM images show the sintering behavior of Au NPs on the TiO_2 (001) surface, both from top view (**c** and **d**) and side view (**e** and **f**). The red dashed circles show the initial states of the Au NPs. **g–j** The serial ETEM images show the sintering behavior of Au NPs on the TiO_2 (101) surface. The red and blue dashed circles show the initial and changed states of the Au NPs. The green arrows show the moving direction of the Au NPs (reproduced with permission from Ref. [147], Copyright 2018, John Wiley and Sons)

a single-atom catalyst (SAC) that consists of only isolated single atoms anchored to the surface. Normally, the isolated single atoms still possess chemical bonds with surfaces or exist charge transfer. Actually, the SAC inspires an approach to optimize the thermal stability of the catalysts and attracted extensive attention in just a few years [152–155]. In 2012, Yoshida et al. [156] studied dynamic behaviors of Pt single atoms on amorphous carbon without gaseous introduction. And then they characterized Pt/amorphous carbon (Pt/a-carbon) electrode catalysts in different atmospheres [157], such as hydrogen and air, and a conventional high vacuum of 10^{-5} Pa. The real-time visualization of atomic behaviors during crystal growth, such as coalescence and surface reconstruction, were acquired with AC-ETEM. Boyes et al. [28] focused on the same area. They demonstrated the dynamic ESTEM imaging of single atoms detected “loose” on the carbon support in 0.02 mbar hydrogen gas at 25, 400, and 500 °C. With the advanced in situ ETEM techniques, the SACs and their dynamics during catalysis could be captured [158, 159].

In most experiments, SACs were stabilized by diverse defects, which limited the fabrication and development of high-metal-loading and thermally stable SACs. In 2019, Lang et al. [160] developed the method that isolated Pt atoms can be stabilized through a strong covalent metal–support interaction, which utilizes the crucial oxide reducibility of support. Firstly, a 1.8 wt% Pt/ FeO_x catalyst was prepared (denoted as

Pt₁/FeO_x), and subsequently calcined at 800 °C in air for 5 h (denoted as Pt₁/FeO_x-C800). AC-HAADF-STEM was used to compare the nature of Pt species between two materials. As Fig. 9.38a, b and c, d shows, there only existed isolated Pt atoms dispersed on the support, and there were no Pt nanoclusters or NPs observed even though the sample had experienced 800 °C calcination. Following is the designed in situ ETEM experiment. Colloidal Pt NPs were supported on Fe₂O₃ at a 1 wt% loading (denoted as 1Pt/Fe₂O₃-NP). Prior to calcination, about 300 Pt particles with an average particle size of about 3 nm were visible across a randomly picked Fe₂O₃ support (Fig. 9.38e, f). After heating to 800 °C under a flow of 1 bar O₂ for 20 min, the total number of Pt NPs decreased to ~200, since many of the 2–3 nm Pt NPs shrank/or disappeared entirely (Fig. 9.38g, h). Therefore, the researchers proposed that the Fe₂O₃ support could facilitate the dispersion of Pt NPs and transform into isolated Pt atoms by high-temperature calcination. Three factors which played crucial roles in the dispersion were concluded as high temperature to promote Pt mobility; the presence of molecular O₂ to partially oxidize the surface of Pt NPs, thereby enabling vaporization of (mobile) PtO₂; and a strong interaction between support and surface Pt atoms.

The isolated atoms sometimes could coalesce under a specific gaseous environment, or even possess cycles of coalescing to NPs and dissolving back to single atoms. Dai et al. [161] demonstrated the cyclical precipitation–dissolution of Rh NPs in response to redox cycling of the ambient gas. These dynamic evolutions must be studied with the employment of in situ ETEM or gas-cell system to monitor the whole process, or else we could only obtain the ex situ information of the catalyst

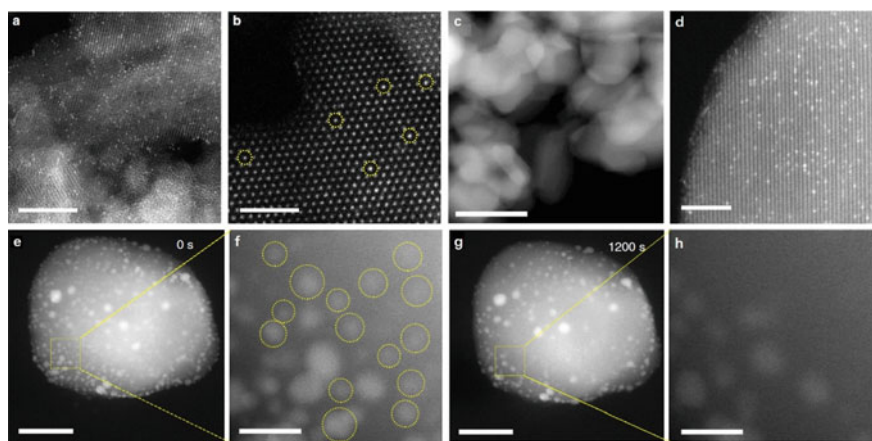


Fig. 9.38 a, b AC-HAADF-STEM images of Pt₁/FeO_x and c, d Pt₁/FeO_x-C800, highlighting atomically dispersed Pt (circled in b). 5 nm scale bar for panel a, 2 nm scale bars for b, d, and 100 nm scale bar for c. e–f HAADF-STEM images of 1Pt/Fe₂O₃-NP before, and g–h after in situ calcination at 800 °C under 1 bar flowing O₂ for 20 min: the yellow squares in panels e and g show the same sample area. A 50 nm scale bars in e and g and 10 nm scale bars in f and h (reproduced with permission from Ref. [160], Copyright 2018, Springer Nature)

which easily caused a misunderstanding due to the change of gaseous environment and temperature, and the real catalytic factors or components could not be revealed anymore.

9.3.5.3 Photocatalysis

As an important catalytic process widely used in sustainable energy development, photocatalysis attracted tremendous attention. Considering the outstanding ability of ETEM for real-time observation, introducing light in the ETEM would facilitate the understanding of the photocatalytic mechanism at the atomic scale.

Two mainstream methods allow the introduction of light irradiation into the ETEM nowadays, modifying the specimen holder or the TEM column.

Generally, the modifications of the TEM column have been done using traditional optics [162] (reflective surfaces, lenses, ellipsoidal and/or mirrors, etc.) or optical fibers [163–167]. Actually, as early as 1984, Suzuki et al. [163] had used optical fiber to direct 514.5 nm light from a 4 W Ar-ion laser into the specimen chamber to study dislocation motion in II–VI compounds. In 2004, Yoshida et al. [164] employed the same design to study the photodecomposition process of poly-hydrocarbons on TiO₂ catalyst films. The intensity of the light was measured to be 10 mW/cm² ($\lambda = 360$ nm) on the sample plane. This system enabled researchers to change wavelength and intensity by changing the light source easily. With UV light, they observed the decomposition phenomenon of the organic materials, which was considered to be a distinct photocatalytic process catalyzed by TiO₂ thin films.

Miller and Crozier [165–167] devised a system for in situ illuminating a sample with visible and UV light inside a TEM with the employment of optical fiber as well. The fiber enters the ETEM in a direction perpendicular to the sample rod, and has no physical contact with the sample holder. This configuration allows for movement, tilting, heating, and cooling of the sample with little impact on the optical fiber. They balanced various considerations and showed no notable detrimental effect on the microscope performance while illuminating the sample with over 1 W/cm² of broadband UV and visible light. Zhang [168] employed the system in the same year to investigate the surface structure of anatase nanocrystals under the conditions of photocatalytic splitting of water (Fig. 9.39a). When the titania was exposed to light and water vapor, the initially crystalline surface converted to an amorphous phase with 1–2 monolayers thick (Fig. 9.39b, c).

The method based on traditional optics evolved slightly slower. In 1995, Ohno and Takeda [162] developed an apparatus of the side-entry type that enabled laser beam introduction using a reflection mirror, optical window, and lens with the modification of a JEOL 2000EX TEM. Thus, the specimen could be illuminated simultaneously by both electron and laser beams.

Picher et al. [169] proposed another approach which used a parabolic mirror to focus the light from an external source and simultaneously collect the sample response in 2014. A free-space, broadband (wavelength $\lambda > 200$ nm), high-efficiency (1.5 sr) light delivery and collection system is employed, which is independent of

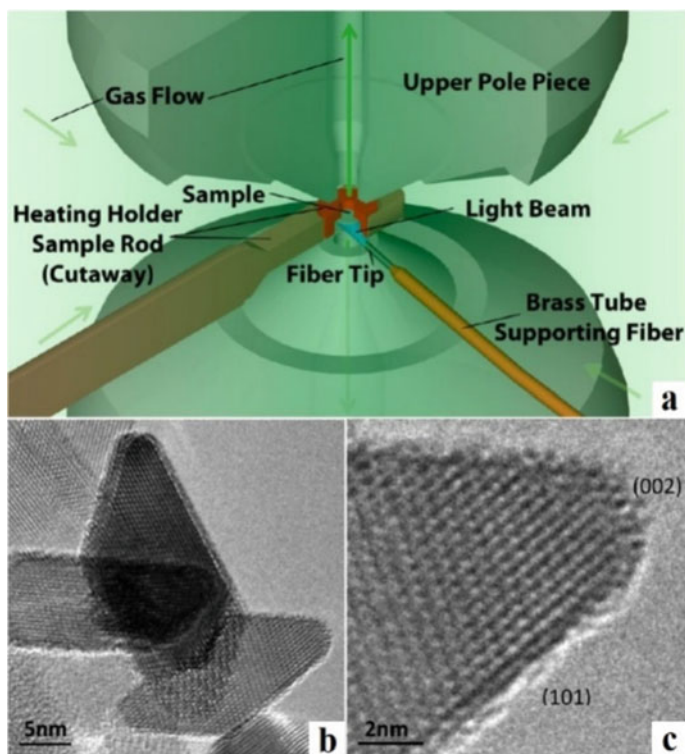


Fig. 9.39 **a** Schematic diagram on in situ TEM showing gases flowing into the sample chamber from an external mixing tank, and exiting through differential pumping apertures in objective lens pole pieces. The temperature is controlled with a heating holder. Light illumination is provided by an optical fiber which is supported by a brass tube perpendicular to the sample rod; the fiber tip is cut at an angle to direct the light onto the sample. **b** Fresh anatase particles after 40 h in H_2O gas at 150°C , light exposure 12 h; **c** magnified images of the (101) and (002) surfaces after illumination. The image was taken in 20 s including adjusting the focus (reproduced with permission from Ref. [168], Copyright 2013, American Chemical Society)

the TEM sample holder. The insertion of a parabolic mirror between the sample holder and the lower objective pole piece of the ESTEM satisfied the delivery and collection of light. Light reaches the parabolic mirror along a free-space beam path through a viewport on a hollow rod into the vacuum system, then be focused on the sample. At the same time, due to the collection of light information of the parabola itself, multiple types of spectroscopy analyses could be integrated into the system, such as Raman spectroscopy. Therefore, it allows the simultaneous collection of microscale spectroscopy data and nanoscale ESTEM images to complement atomic-scale information with a large-scale picture of the structure and kinetics, mitigating the need for two separate in situ measurements. This rod-mirror assembly replaces the objective aperture holder, and both of them are easily interchangeable.

In general, the introduction of light by both optical fiber through a separate port in TEM and employing various mirrors based on traditional optics involves the modification of the microscope, which limited the use of the current system to a single specific microscope while maintaining holder flexibility. Oppositely, the holder-based designs could be used in different microscopes.

Shindo et al. [170] modified double-probe piezo-driving specimen holder by introducing a laser irradiation port in one of two arms. As a result, the new specimen holder consists of a piezo-driving probe and a laser irradiation port, both of which can be 3-dimensionally controlled by using piezoelectric elements and micrometers. While the piezo-driving probe interacts with the specimen set in the holder in several ways, the laser beam causes photo-induced phenomena to occur.

Cavalca [171, 172] followed the same modifying idea of the specimen holder, and developed two novel types of holders that enable in situ illumination: lens-based holder design and fiber-based holder design. The former design comprises a standard TEM specimen holder with a customized tip, whose custom parts can be adapted easily to other holder shafts. The fiber-based design was constructed using a feed-through equipped with single or multiple multi-mode optical fibers, which might be highly desirable for a study of the optical properties of nanomaterials in the future. Cavalca performed the photo-induced degradation of cuprous oxide (Cu_2O) experiment using both TEM holder designs, and yielded the same result. Water vapor was leaked into the specimen chamber to a steady-state pressure of ~ 3 mbar and the sample was exposed to light with $\lambda = 405$ nm and a power density of 6 W cm^{-2} for various time periods. The column was then evacuated to 10^{-6} mbar for 5 h in order to reduce the water vapor before the specimen was exposed to the e-beam. This procedure excluded the influences induced by e-beam. The morphology of particles evolved considerably, with change in lattice spacing (electron diffraction patterns) and oxidation state (electron energy loss spectroscopy). A more detailed and complete analysis of the reduction reaction was finished in 2013 [172].

9.4 Conclusions and Outlook

Over the past decades, the introduction of gases in the TEM truly changed the traditional *post mortem* characterization limited to the vacuum environment. With the developing accessory technologies (such as aberration corrector and microelectromechanical system) and continuously updated design of the TEM, the research boundary expanded gradually and steadily, ranging from structural characterization to atomic-scale activity and property of materials. Accordingly, the various, demanding and stricter restrictions in different exploring fields promoted the improvements in accessory technologies and design.

There is no doubt that there exist universal and concurrent pursuits in almost all TEM research areas, while specific and unique requirements emerged during special experiments. In general, the requirements could be classified as follows.

9.4.1 *Spatial and Temporal Resolution*

With the incorporation of a monochromator and aberration corrector (probe/image), the spatial and energy resolution in commercially available ETEM already reached the criterion that satisfied many applications. For example, the Themis ETEM (ThermoFisher), which is combined with image C_s corrector, Thermo Scientific X-FEG module, and monochromator technology, could reach the TEM point resolution of 0.12 nm, while the system energy resolution could minimize to 0.25 eV, with the N_2 pressure <0.5 mbar. As for the window approach, advancing processing technology for the generation of ultrathin windows could minimize the scattering of electrons, further improving the spatial resolution. Among ultrathin graphene, graphene oxide, and boron nitride membrane as specimen supports for TEM developed in recent years, graphene membrane stands out with an atomic thickness of only one carbon atom used in a liquid cell.

However, the spatial resolution would decline to some extent on account of the scattering of gas molecules doubtless, which is influenced by the pressure and variety of gas as well. Meanwhile, the maximum pressure reported in the literature published is 5 bar (window mode), which is still far below some real reaction conditions. Therefore, the balance between gas pressure and spatial resolution still should be paid enough attention to keep, no matter what kind of methods are employed, e.g. improvement of aperture design.

Another more serious obstacle laid on the temporal resolution due to the demand for the observation across a range of time scale, especially for ultrafast time scale. The employment of ETEM in in situ experiments is usually prepared for monitoring and recording the whole dynamic reaction process, which probably happened in several milliseconds or even nanoseconds. The vital emphasis is the data collection or recording media, which is confined to the electron dose, detection quantum efficiency (DQE) of the camera, and information processability of the computer.

At present, in terms of recording attachment, the temporal and spatial resolution are contradictory performances. Available technologies usually satisfied one of them to sacrifice another one, for example, image acquisition systems allow high spatial resolution (<0.1 nm) images with low temporal resolution (0.033–0.2 s range) or low resolution (a few nanometers in single shot mode) with high temporal resolution [173]. The compromise between them restricts the applications in observing numerous quick chemical reactions.

One of the solutions to the dilemma is the direct electron camera, which is based on complementary metal-oxide semiconductor (CMOS) technology. As the indirect electron detection method, conventional charge-coupled device (CCD) cameras with a capability of 20 frames per second (fps) [174] would have to convert high-energy electrons to photons firstly, which encumbered the response speed. The direct electron camera omits the essential fluorescent coating in CCD, improving the electron collection efficiency a lot. The fps with correspondingly high DQEs of readout rates reached 10^3 (such as Gatan K3, 1500 frames per second at 5760×4092 pixels can be achieved) magnitude. The highly improved temporal resolution provided new

possibilities in in situ experiments, while it's still inadequate in observing transient nucleation events or intermediates during chemical reactions.

Regardless of the camera, another radical method is ultrafast TEM, in the time scale up to femtosecond/nanosecond theoretically. Two principal approaches have emerged in recent decades: the stroboscopic ultrafast electron microscope (4-dimensional ultrafast electron microscope, 4D UEM) [175–177] and the nanosecond-time-resolved single-shot instrument (Dynamic Transmission Electron Microscope, DTEM) [178].

4D UEM has expanded the depth and breadth in different application fields, including photon-induced near-field EM [179], diffraction patterns [180], EELS [181], tomography [182], cryo-EM [183], Lorentz imaging [184], imaging in liquid [185], etc. Using this method, temporal, and spatial resolution can be maintained at the optimum levels, but the fact that the specimen must be laser-pumped millions of times means that the process being studied must be perfectly reversible—the sample must recover from the excited state back to the ground state between shots. This limitation allows 4D UEM to study the perfectly reversible chemical and materials processes, but is unavailable to many of the structural phase transformations and the nucleation, growth and mobility of dislocations, voids, and even complex nanostructures [178]. In this regard, 4D UEM may not be appropriate for investigating catalytic reactions.

As for DTEM, since all the information is obtained in a single specimen drive event, this technique is able to measure irreversible and unique material events that could not be studied by the stroboscopic approach. However, the limitation of this method is that space-charge effects in the beam can lead to degradation in resolution, and the essential high current will limit the overall temporal and spatial resolution of the instrument as well [186–189].

The stroboscopic and single-shot approaches to high-time-resolution in situ TEM are complementary, based on similar physical principles but in different regimes, and occupy specific superiorities, respectively. Limited to the electron–electron interactions and the brightness of the electron source, the spatial and temporal resolutions of the single-shot technique are in the nanometer and nanosecond scale, compared with the sub-picosecond time scale of the stroboscopic approach [189]. The stroboscopic approach is restricted to highly reversible processes, and limited by the emittance which determines the spatial coherence obtainable in a given spot size, which affects contrast and resolution. The detailed interpretation could be consulted in Chap. 10, 4D Ultrafast TEM.

9.4.2 Multiple Stimuli and Characterization Techniques

There is no doubt that researchers always endeavor for observation of the most realistic status of the specimen under various conditions, simulating the actual performance in operating conditions. The ETEM possesses extraordinary prospects in the visualization of dynamic changes in morphology, structure, and chemistry of

materials at the atomic scale, especially when it is employed with external stimuli (strain/heating/cooling/electrical biasing/lighting).

Considering the varying stimuli probably induce different manifestations of the specimen, it would naturally take the other common characterization methods into the incorporation of ETEM. A combination of in situ ETEM and other characterization techniques, e.g. gas chromatography, quadrupole mass spectroscopy, in situ spectroscopy (infrared/ultraviolet-visible near-infrared/Raman spectroscopy), in situ XRD, in situ nuclear magnetic resonance (NMR) spectroscopy, and in situ XPS, in situ XAS, would be the fast-growing and fascinating area in the future.

It is clear that spectroscopy was paid a lot of attention, for its outstanding complementary ability to ETEM: (1) the ETEM focused on changes in a small area while the spectroscopy could give a whole overview of the sample to ensure the local effects are representative, or elucidate the specific situation happened actually; (2) the ETEM could observe the morphologic and structural changes, but is slightly weaker in chemical component analysis (EDS and EELS focus on subtle information), which is exactly the superiority of spectroscopy. Definitely, the spatial and temporal resolution of the spectroscopy is another challenge for the synchronous acquisition of information with the TEM images.

As for electron-beam-sensitive materials, the solution which could degrade the electron beam irradiation damage is the pursuit of researchers all the time. Clearly, the diffraction mode is the most common method which satisfies real-time dynamic crystallographic characterization of structure with much lower electron dose interacted with a specimen. Nowadays, no matter whether in ETEM or in a gas-cell holder, the diffraction capability is reserved well and is employed to characterize the beam-sensitive specimen still.

However, since the diffraction methods provided the average results over materials, another technique named as integrated differential phase contrast (iDPC) STEM [190, 191] emerged and developed well in recent years. The iDPC-STEM enabled the linear imaging of the projected electrostatic potential in a lattice, and the resulting contrast is nearly proportional to the atomic number Z instead of its square in the high angle annular dark field (HAADF) STEM, greatly improving the capacity of light-element imaging. Intriguingly, the iDPC technique allowed the researchers [192] to image the adsorbed molecules with a high resolution and signal-to-noise ratio under an ultra-low beam current. The lower damage allows continuous images of the same area so that the temporal changes of structures could be investigated, especially in studying various porous catalysts [193] and inside hydrocarbon pools.

Furthermore, the introduction of gas in TEM sometimes could compensate the electron irradiation damage for specific materials in continuous characterization, e.g. Yuan et al. [73] introduced the protection gas (O_2) in the ETEM chamber to compensate the lost oxygen atoms in TiO_2 , considering the surface structures can be easily damaged by the electron beam. By analogy, the specific gas which could facilitate the repair of the irradiation damage for electron-sensitive materials, especially the oxides, satisfies the requirement of real-time dynamic continuous characterization at

the atomic scale in TEM. In other words, the introduction of gas weakened the influence imposed on the specimen by the electron beam to some extent, which provided a possible solution for the characterization of electron-beam-sensitive materials.

9.4.3 Accurate Process Control

It has been a focused problem for a long time since the TEM was invented and would be a continuous problem in the following development: the accurate manipulation of the specimen and external stimuli, including sample position (avoidance of sample drift), uniformity, temperature (enough high/low temperature, and fast real-time rate of temperature change), and gas flux.

The more complex the system designed and the more equipment involved, it would be more difficult to obtain the accurate parameters or control the whole reactor/system accurately, especially when they interacted and influenced themselves. The external stimuli aggravated the situation, especially when the extreme environment is considered to realize in the TEM, e.g. corrosive gaseous environment and multi-stimuli incorporated holder. Definitely, there are some efforts directed to mitigate the problem but a universally available solution is still to be realized.

The electron beam irradiation is also a vital question for TEM characterization. It should be seriously considered, especially for electron-beam-sensitive materials, such as zeolites and metal–organic frameworks. The approach, which would entirely eliminate the influence of the electron beam, or rational model established to deduce and evaluate the influential extent imposed on the specimen by the electron beam, is the pursuit of the researchers.

References

1. Knoll M, Ruska E (1932) Beitrag zur geometrischen Elektronenoptik. I. *Annalen der Physik* 404(5):607–640. <https://doi.org/10.1002/andp.19324040506>
2. Knoll M, Ruska E (1932) Das Elektronenmikroskop. *Z Phys* 79(9):699. <https://doi.org/10.1007/bf01330526>
3. Ruska E (1942) Beitrag zur übermikroskopischen Abbildung bei höheren Drucken. *Kolloid-Zeitschrift* 100(2):212–219. <https://doi.org/10.1007/bf01519549>
4. Abrams IM, McBain JW (1944) A closed cell for electron microscopy. *J Appl Phys* 15(8):607–609. <https://doi.org/10.1063/1.1707475>
5. Bailey JE (1963) On the oxidation of thin films of zirconium. *J Nucl Mater* 8(2):259–262. [https://doi.org/10.1016/0022-3115\(63\)90042-4](https://doi.org/10.1016/0022-3115(63)90042-4)
6. De Jonghe LC, Thomas G (1971) High voltage electron microscopy studies of phase transformations in cobalt ferrites. *Mater Sci Eng* 8(5):259–274. [https://doi.org/10.1016/0025-5416\(71\)90092-9](https://doi.org/10.1016/0025-5416(71)90092-9)
7. Ito T, Hiziyi K (1958) A specimen reaction device for the electron microscope and its applications. *J Electron Microsc* 6(1):4–8. <https://doi.org/10.1093/oxfordjournals.jmicro.a051252>

8. Heide HG (1962) Electron microscopic observation of specimens under controlled gas pressure. *J Cell Biol* 13(1):147–152. <https://doi.org/10.1083/jcb.13.1.147>
9. Heide HG (1960) Elektronenmikroskopie von Objekten unter Atmosphärendruck oder unter Drucken, welche ihre Austrocknung verhindern. *Naturwissenschaften* 47(14):313–317. <https://doi.org/10.1007/bf00628703>
10. Hashimoto H, Naiki T, Eto T, Fujiwara K (1968) High temperature gas reaction specimen chamber for an electron microscope. *Jpn J Appl Phys* 7(8):946–952. <https://doi.org/10.1143/jjap.7.946>
11. Hashimoto H, Tanaka K, Yoda E (1958) A specimen treating device at high temperature for the electron microscope. *J Electron Microsc* 6(1):8–11. <https://doi.org/10.1093/oxfordjournals.jmicro.a051258>
12. Baker RTK (1979) In situ electron microscopy studies of catalyst particle behavior. *Catal Rev* 19(2):161–209. <https://doi.org/10.1080/03602457908068055>
13. Fujita H, Komatsu M, Ishikawa I (1976) A universal environmental cell for a 3MV-class electron microscope and its applications to metallurgical subjects. *Jpn J Appl Phys* 15(11):2221–2228. <https://doi.org/10.1143/jjap.15.2221>
14. Baker RTK, Harris PS (1972) Controlled atmosphere electron microscopy. *J Phys E: Sci Instrum* 5(8):793–797. <https://doi.org/10.1088/0022-3735/5/8/024>
15. Rodríguez NM, Oh SG, Downs WB, Pattabiraman P, Baker RTK (1990) An atomic oxygen environmental cell for a transmission electron microscope. *Rev Sci Instrum* 61(7):1863–1868. <https://doi.org/10.1063/1.1141109>
16. Lee TC, Dewald DK, Eades JA, Robertson IM, Birnbaum HK (1991) An environmental cell transmission electron microscope. *Rev Sci Instrum* 62(6):1438–1444. <https://doi.org/10.1063/1.1142464>
17. Boyes ED, Gai PL (1997) Environmental high resolution electron microscopy and applications to chemical science. *Ultramicroscopy* 67(1):219–232. [https://doi.org/10.1016/S0304-3991\(96\)00099-X](https://doi.org/10.1016/S0304-3991(96)00099-X)
18. Creemer JF, Helveg S, Hoveling GH, Ullmann S, Molenbroek AM, Sarro PM, Zandbergen HW (2008) Atomic-scale electron microscopy at ambient pressure. *Ultramicroscopy* 108(9):993–998. <https://doi.org/10.1016/j.ultramic.2008.04.014>
19. Yokosawa T, Alan T, Pandraud G, Dam B, Zandbergen H (2012) In-situ TEM on (de)hydrogenation of Pd at 0.5–4.5 bar hydrogen pressure and 20–400 °C. *Ultramicroscopy* 112(1):47–52. <https://doi.org/10.1016/j.ultramic.2011.10.010>
20. Allard LF, Overbury SH, Bigelow WC, Katz MB, Nackashi DP, Damiano J (2012) Novel MEMS-based gas-cell/heating specimen holder provides advanced imaging capabilities for in situ reaction studies. *Microsc Microanal* 18(4):656–666. <https://doi.org/10.1017/S1431927612001249>
21. Alsem D, Salmon N, Unocic R, Veith G, More K (2012) In-situ liquid and gas transmission electron microscopy of nano-scale materials. *Microsc Microanal* 18(S2):1158–1159. <https://doi.org/10.1017/S1431927612007647>
22. Jinschek JR (2014) Advances in the environmental transmission electron microscope (ETEM) for nanoscale in situ studies of gas–solid interactions. *Chem Commun* 50(21):2696–2706. <https://doi.org/10.1039/c3cc49092k>
23. Hashimoto H, Tanaka K, Yoda E, Araki H (1958) Bundle structure of needle crystal of tungsten oxide. *Acta Metall* 6(8):557–559. [https://doi.org/10.1016/0001-6160\(58\)90178-0](https://doi.org/10.1016/0001-6160(58)90178-0)
24. Fryer JR (1968) Oxidation of graphite catalysed by palladium. *Nature* 220(5172):1121–1122. <https://doi.org/10.1038/2201121b0>
25. Mills JC, Moodie AF (1968) Multipurpose high resolution stage for the electron microscope. *Rev Sci Instrum* 39(7):962–969. <https://doi.org/10.1063/1.1683578>
26. Boyes ED, Gai PL (2014) Visualising reacting single atoms under controlled conditions: advances in atomic resolution in situ environmental (scanning) transmission electron microscopy (E(S)TEM). *C R Phys* 15(2):200–213. <https://doi.org/10.1016/j.crhy.2014.01.002>
27. Gai PL, Boyes ED (2009) Advances in atomic resolution in situ environmental transmission electron microscopy and 1 Å aberration corrected in situ electron microscopy. *Microsc Res Tech* 72(3):153–164. <https://doi.org/10.1002/jemt.20668>

28. Boyes ED, Ward MR, Lari L, Gai PL (2013) ESTEM imaging of single atoms under controlled temperature and gas environment conditions in catalyst reaction studies. *Ann Phys* 525(6):423–429. <https://doi.org/10.1002/andp.201300068>
29. Boyes ED, Gai PL (2014) Aberration corrected environmental STEM (AC ESTEM) for dynamic in-situ gas reaction studies of nanoparticle catalysts. *J Phys: Conf Ser* 522:012004. <https://doi.org/10.1088/1742-6596/522/1/012004>
30. LaGrow AP, Ward MR, Lloyd DC, Gai PL, Boyes ED (2017) Visualizing the Cu/Cu₂O interface transition in nanoparticles with environmental scanning transmission electron microscopy. *J Am Chem Soc* 139(1):179–185. <https://doi.org/10.1021/jacs.6b08842>
31. Kamino T, Yaguchi T, Konno M, Watabe A, Marukawa T, Mima T, Kuroda K, Saka H, Arai S, Makino H, Suzuki Y, Kishita K (2006) Development of a gas injection/specimen heating holder for use with transmission electron microscope. *J Electron Microsc* 54(6):497–503. <https://doi.org/10.1093/jmicro/dfi071>
32. Hansen TW, Wagner JB, Dunin-Borkowski RE (2010) Aberration corrected and monochromated environmental transmission electron microscopy: challenges and prospects for materials science. *Mater Sci Technol* 26(11):1338–1344. <https://doi.org/10.1179/026708310x12756557336355>
33. Shirai M, Hanawa A, Kikuchi H, Inada H, Matsumoto H (2019) In-situ observation of catalytic reaction in gas atmosphere using an aberration corrected STEM. *Microsc Microanal* 25(S2):1526–1527. <https://doi.org/10.1017/S1431927619008365>
34. Hanawa A, Kubo Y, Kikuchi H, Nakamura K, Shirai M, Inada H, Matsumoto H, Kawasaki M (2019) Evaluation of high-resolution STEM imaging advancement under gas-environment with open window MEMS holder and gas injection system. *Microsc Microanal* 25(S2):694–695. <https://doi.org/10.1017/S1431927619004203>
35. Hansen TW, Wagner JB (2014) Catalysts under controlled atmospheres in the transmission electron microscope. *ACS Catal* 4(6):1673–1685. <https://doi.org/10.1021/cs401148d>
36. Yaguchi T, Suzuki M, Watabe A, Nagakubo Y, Ueda K, Kamino T (2011) Development of a high temperature–atmospheric pressure environmental cell for high-resolution TEM. *J Electron Microsc* 60(3):217–225. <https://doi.org/10.1093/jmicro/dfr011>
37. de Jonge N, Bigelow WC, Veith GM (2010) Atmospheric pressure scanning transmission electron microscopy. *Nano Lett* 10(3):1028–1031. <https://doi.org/10.1021/nl904254g>
38. Parkinson GM (1989) High resolution, in-situ controlled atmosphere transmission electron microscopy (CATEM) of heterogeneous catalysts. *Catal Lett* 2(5):303–307. <https://doi.org/10.1007/bf00770228>
39. Creemer JF, Helveg S, Kooyman PJ, Molenbroek AM, Zandbergen HW, Sarro PM (2010) A MEMS reactor for atomic-scale microscopy of nanomaterials under industrially relevant conditions. *J Microelectromech Syst* 19(2):254–264. <https://doi.org/10.1109/jmems.2010.2041190>
40. Komatsu M, Mori H (2005) In situ HVEM study on copper oxidation using an improved environmental cell. *J Electron Microsc* 54(2):99–107. <https://doi.org/10.1093/jmicro/dfi032>
41. Giorgio S, Sao Joao S, Nitsche S, Chaudanson D, Sitja G, Henry CR (2006) Environmental electron microscopy (ETEM) for catalysts with a closed E-cell with carbon windows. *Ultramicroscopy* 106(6):503–507. <https://doi.org/10.1016/j.ultramic.2006.01.006>
42. Kawasaki T, Ueda K, Ichihashi M, Tanji T (2009) Improvement of windowed type environmental-cell transmission electron microscope for in situ observation of gas-solid interactions. *Rev Sci Instrum* 80(11):113701. <https://doi.org/10.1063/1.3250862>
43. Wu F, Yao N (2015) Advances in windowed gas cells for in-situ TEM studies. *Nano Energy* 13:735–756. <https://doi.org/10.1016/j.nanoen.2015.03.015>
44. Allard LF, Bigelow WC, Jose-Yacamán M, Nackashi DP, Damiano J, Mick SE (2009) A new MEMS-based system for ultra-high-resolution imaging at elevated temperatures. *Microsc Res Tech* 72(3):208–215. <https://doi.org/10.1002/jemt.20673>
45. Creemer JF, Santagata F, Morana B, Mele L, Alan T, Iervolino E, Pandraud G, Sarro PM (2011) An all-in-one nanoreactor for high-resolution microscopy on nanomaterials at high pressures. In: 2011 IEEE 24th International conference on micro electro mechanical systems, 23–27 Jan 2011, pp 1103–1106. <https://doi.org/10.1109/memsys.2011.5734622>

46. Xin HL, Niu K, Alsem DH, Zheng H (2013) In situ TEM study of catalytic nanoparticle reactions in atmospheric pressure gas environment. *Microsc Microanal* 19(6):1558–1568. <https://doi.org/10.1017/s1431927613013433>
47. Vendelbo SB, Elkjær CF, Falsig H, Puspitasari I, Dona P, Mele L, Morana B, Nelissen BJ, van Rijn R, Creemer JF, Kooyman PJ, Helveg S (2014) Visualization of oscillatory behaviour of Pt nanoparticles catalysing CO oxidation. *Nat Mater* 13(9):884–890. <https://doi.org/10.1038/nmat4033>
48. Jiang Y, Zhang Z, Yuan W, Zhang X, Wang Y, Zhang Z (2018) Recent advances in gas-involved in situ studies via transmission electron microscopy. *Nano Res* 11(1):42–67. <https://doi.org/10.1007/s12274-017-1645-9>
49. Hansen PL, Wagner JB, Helveg S, Rostrup-Nielsen JR, Clausen BS, Topsøe H (2002) Atom-resolved imaging of dynamic shape changes in supported copper nanocrystals. *Science* 295(5562):2053–2055. <https://doi.org/10.1126/science.1069325>
50. Cabié M, Giorgio S, Henry CR, Axet MR, Philippot K, Chaudret B (2010) Direct observation of the reversible changes of the morphology of Pt nanoparticles under gas environment. *J Phys Chem C* 114(5):2160–2163. <https://doi.org/10.1021/jp906721g>
51. Uchiyama T, Yoshida H, Kuwauchi Y, Ichikawa S, Shimada S, Haruta M, Takeda S (2011) Systematic morphology changes of gold nanoparticles supported on CeO₂ during CO oxidation. *Angew Chem Int Ed* 50(43):10157–10160. <https://doi.org/10.1002/anie.201102487>
52. Jiang Y, Li H, Wu Z, Ye W, Zhang H, Wang Y, Sun C, Zhang Z (2016) In situ observation of hydrogen-induced surface faceting for palladium-copper nanocrystals at atmospheric pressure. *Angew Chem Int Ed* 55(40):12427–12430. <https://doi.org/10.1002/anie.201605956>
53. Zhang X, Meng J, Zhu B, Yu J, Zou S, Zhang Z, Gao Y, Wang Y (2017) In situ TEM studies of the shape evolution of Pd nanocrystals under oxygen and hydrogen environments at atmospheric pressure. *Chem Commun* 53(99):13213–13216. <https://doi.org/10.1039/c7cc07649e>
54. Chmielewski A, Meng J, Zhu B, Gao Y, Guesmi H, Prunier H, Alloyeau D, Wang G, Louis C, Delannoy L, Afanasiev P, Ricolleau C, Nelayah J (2019) Reshaping dynamics of gold nanoparticles under H₂ and O₂ at atmospheric pressure. *ACS Nano* 13(2):2024–2033. <https://doi.org/10.1021/acsnano.8b08530>
55. Zhang X, Meng J, Zhu B, Yuan W, Yang H, Zhang Z, Gao Y, Wang Y (2018) Unexpected refaceting of palladium nanoparticles under atmospheric N₂ conditions. *Chem Commun* 54(62):8587–8590. <https://doi.org/10.1039/c8cc04574g>
56. Zhu B, Meng J, Yuan W, Zhang X, Yang H, Wang Y, Gao Y (2020) Reshaping of metal nanoparticles under reaction conditions. *Angew Chem Int Ed* 59(6):2171–2180. <https://doi.org/10.1002/anie.201906799>
57. Langmuir I (1918) The adsorption of gases on plane surfaces of glass, mica and platinum. *J Am Chem Soc* 40(9):1361–1403. <https://doi.org/10.1021/ja02242a004>
58. Zhu B, Xu Z, Wang C, Gao Y (2016) Shape evolution of metal nanoparticles in water vapor environment. *Nano Lett* 16(4):2628–2632. <https://doi.org/10.1021/acs.nanolett.6b00254>
59. Zhu B, Meng J, Gao Y (2017) Equilibrium shape of metal nanoparticles under reactive gas conditions. *J Phys Chem C* 121(10):5629–5634. <https://doi.org/10.1021/acs.jpcc.6b13021>
60. Meng J, Zhu B, Gao Y (2018) Shape evolution of metal nanoparticles in binary gas environment. *J Phys Chem C* 122(11):6144–6150. <https://doi.org/10.1021/acs.jpcc.8b00052>
61. Henry CR (2005) Morphology of supported nanoparticles. *Prog Surf Sci* 80(3):92–116. <https://doi.org/10.1016/j.progsurf.2005.09.004>
62. Gallegos EJ (1964) Gas reactor for hot stage transmission electron microscopy. *Rev Sci Instrum* 35(9):1123–1124. <https://doi.org/10.1063/1.1718978>
63. Koh AL, Gidcumb E, Zhou O, Sinclair R (2013) Observations of carbon nanotube oxidation in an aberration-corrected environmental transmission electron microscope. *ACS Nano* 7(3):2566–2572. <https://doi.org/10.1021/nn305949h>
64. Ajayan PM, Ebbesen TW, Ichihashi T, Iijima S, Tanigaki K, Hiura H (1993) Opening carbon nanotubes with oxygen and implications for filling. *Nature* 362(6420):522–525. <https://doi.org/10.1038/362522a0>

65. Tsang SC, Harris PJF, Green MLH (1993) Thinning and opening of carbon nanotubes by oxidation using carbon dioxide. *Nature* 362(6420):520–522. <https://doi.org/10.1038/362520a0>
66. Jeangros Q, Hansen TW, Wagner JB, Damsgaard CD, Dunin-Borkowski RE, Hébert C, Van Herle J, Hessler-Wyser A (2013) Reduction of nickel oxide particles by hydrogen studied in an environmental TEM. *J Mater Sci* 48(7):2893–2907. <https://doi.org/10.1007/s10853-012-7001-2>
67. Jeangros Q, Hansen TW, Wagner JB, Dunin-Borkowski RE, Hébert C, Van Herle J, Hessler-Wyser A (2014) Oxidation mechanism of nickel particles studied in an environmental transmission electron microscope. *Acta Mater* 67:362–372. <https://doi.org/10.1016/j.actamat.2013.12.035>
68. Yu J, Yuan W, Yang H, Xu Q, Wang Y, Zhang Z (2018) Fast gas-solid reaction kinetics of nanoparticles unveiled by millisecond in situ electron diffraction at ambient pressure. *Angew Chem Int Ed* 57(35):11344–11348. <https://doi.org/10.1002/anie.201806541>
69. Luo L, Su M, Yan P, Zou L, Schreiber DK, Baer DR, Zhu Z, Zhou G, Wang Y, Bruemmer SM, Xu Z, Wang C (2018) Atomic origins of water-vapour-promoted alloy oxidation. *Nat Mater* 17(6):514–518. <https://doi.org/10.1038/s41563-018-0078-5>
70. Huang X, Jones T, Fedorov A, Farra R, Copéret C, Schlögl R, Willinger M-G (2021) Phase coexistence and structural dynamics of redox metal catalysts revealed by operando TEM. *Adv Mater* 33(31):2101772. <https://doi.org/10.1002/adma.202101772>
71. Wang Y, Liu B, Xia Z, Zhang X, Miao Y, Yang N, Yang B, Zhang L, Kuang W, Li J, Ma E, Shan Z (2018) Turning a native or corroded Mg alloy surface into an anti-corrosion coating in excited CO₂. *Nat Commun* 9(1):4058. <https://doi.org/10.1038/s41467-018-06433-5>
72. Yoshida H, Kuwauchi Y, Jinschek Joerg R, Sun K, Tanaka S, Kohyama M, Shimada S, Haruta M, Takeda S (2012) Visualizing gas molecules interacting with supported nanoparticulate catalysts at reaction conditions. *Science* 335(6066):317–319. <https://doi.org/10.1126/science.1213194>
73. Yuan W, Wang Y, Li H, Wu H, Zhang Z, Selloni A, Sun C (2016) Real-time observation of reconstruction dynamics on TiO₂(001) surface under oxygen via an environmental transmission electron microscope. *Nano Lett* 16(1):132–137. <https://doi.org/10.1021/acs.nanolett.5b03277>
74. Bugnet M, Overbury SH, Wu ZL, Epicier T (2017) Direct visualization and control of atomic mobility at 100 surfaces of ceria in the environmental transmission electron microscope. *Nano Lett* 17(12):7652–7658. <https://doi.org/10.1021/acs.nanolett.7b03680>
75. Dai S, Hou Y, Onoue M, Zhang S, Gao W, Yan X, Graham GW, Wu R, Pan X (2017) Revealing surface elemental composition and dynamic processes involved in facet-dependent oxidation of Pt₃Co nanoparticles via in situ transmission electron microscopy. *Nano Lett* 17(8):4683–4688. <https://doi.org/10.1021/acs.nanolett.7b01325>
76. Dai S, You Y, Zhang S, Cai W, Xu M, Xie L, Wu R, Graham GW, Pan X (2017) In situ atomic-scale observation of oxygen-driven core-shell formation in Pt₃Co nanoparticles. *Nat Commun* 8(1):204. <https://doi.org/10.1038/s41467-017-00161-y>
77. Zhang X, Han S, Zhu B, Zhang G, Li X, Gao Y, Wu Z, Yang B, Liu Y, Baaziz W, Ersen O, Gu M, Miller JT, Liu W (2020) Reversible loss of core-shell structure for Ni–Au bimetallic nanoparticles during CO₂ hydrogenation. *Nat Catal* 3(4):411–417. <https://doi.org/10.1038/s41929-020-0440-2>
78. Ferreira PJ, Robertson IM, Birnbaum HK (1998) Hydrogen effects on the interaction between dislocations. *Acta Mater* 46(5):1749–1757. [https://doi.org/10.1016/S1359-6454\(97\)00349-2](https://doi.org/10.1016/S1359-6454(97)00349-2)
79. Zou L, Yang C, Lei Y, Zakharov D, Wiezorek JMK, Su D, Yin Q, Li J, Liu Z, Stach EA, Yang JC, Qi L, Wang G, Zhou G (2018) Dislocation nucleation facilitated by atomic segregation. *Nat Mater* 17(1):56–63. <https://doi.org/10.1038/nmat5034>
80. Sharma R (2005) An environmental transmission electron microscope for in situ synthesis and characterization of nanomaterials. *J Mater Res* 20(7):1695–1707. <https://doi.org/10.1557/jmr.2005.0241>

81. Jiang H, Borca CN, Xu B, Robertson BW (2001) Fabrication of 2- and 3-dimensional nanostructures. *Int J Mod Phys B* 15(24–25):3207–3213. <https://doi.org/10.1142/s02179792010749x>
82. Mitsuishi K, Shimojo M, Han M, Furuya K (2003) Electron-beam-induced deposition using a subnanometer-sized probe of high-energy electrons. *Appl Phys Lett* 83(10):2064–2066. <https://doi.org/10.1063/1.1611274>
83. Crozier PA, Tolle J, Kouvetakis J, Ritter C (2004) Synthesis of uniform GaN quantum dot arrays via electron nanolithography of D2GaN3. *Appl Phys Lett* 84(18):3441–3443. <https://doi.org/10.1063/1.1736314>
84. van Dorp WF, van Someren B, Hagen CW, Kruit P, Crozier PA (2005) Approaching the resolution limit of nanometer-scale electron beam-induced deposition. *Nano Lett* 5(7):1303–1307. <https://doi.org/10.1021/nl050522i>
85. Gai PL, Sharma R, Ross FM (2008) Environmental (S)TEM studies of gas–liquid–solid interactions under reaction conditions. *MRS Bull* 33(2):107–114. <https://doi.org/10.1557/mrs2008.23>
86. Wagner RS, Ellis WC (1964) Vapor-liquid-solid mechanism of single crystal growth. *Appl Phys Lett* 4(5):89–90. <https://doi.org/10.1063/1.1753975>
87. Wu Y, Yang P (2001) Direct observation of vapor–liquid–solid nanowire growth. *J Am Chem Soc* 123(13):3165–3166. <https://doi.org/10.1021/ja0059084>
88. Kim BJ, Tersoff J, Wen CY, Reuter MC, Stach EA, Ross FM (2009) Determination of size effects during the phase transition of a nanoscale Au-Si eutectic. *Phys Rev Lett* 103(15):155701. <https://doi.org/10.1103/PhysRevLett.103.155701>
89. Kim BJ, Tersoff J, Kodambaka S, Reuter MC, Stach EA, Ross FM (2008) Kinetics of individual nucleation events observed in nanoscale vapor-liquid-solid growth. *Science* 322(5904):1070–1073. <https://doi.org/10.1126/science.1163494>
90. Hannon JB, Kodambaka S, Ross FM, Tromp RM (2006) The influence of the surface migration of gold on the growth of silicon nanowires. *Nature* 440(7080):69–71. <https://doi.org/10.1038/nature04574>
91. Ross FM (2010) Controlling nanowire structures through real time growth studies. *Rep Prog Phys* 73(11):114501. <https://doi.org/10.1088/0034-4885/73/11/114501>
92. Ross FM, Wen CY, Kodambaka S, Wacaser BA, Reuter MC, Stach EA (2010) The growth and characterization of Si and Ge nanowires grown from reactive metal catalysts. *Phil Mag* 90(35–36):4769–4778. <https://doi.org/10.1080/14786435.2010.527713>
93. Ross FM, Tersoff J, Reuter MC (2005) Sawtooth faceting in silicon nanowires. *Phys Rev Lett* 95(14):146104. <https://doi.org/10.1103/PhysRevLett.95.146104>
94. Kodambaka S, Tersoff J, Reuter MC, Ross FM (2007) Germanium nanowire growth below the eutectic temperature. *Science* 316(5825):729–732. <https://doi.org/10.1126/science.1139105>
95. Chou Y-C, Wen C-Y, Reuter MC, Su D, Stach EA, Ross FM (2012) Controlling the growth of Si/Ge nanowires and heterojunctions using silver-gold alloy catalysts. *ACS Nano* 6(7):6407–6415. <https://doi.org/10.1021/nm301978x>
96. Gamalski AD, Tersoff J, Stach EA (2016) Atomic resolution in situ imaging of a double-bilayer multistep growth mode in gallium nitride nanowires. *Nano Lett* 16(4):2283–2288. <https://doi.org/10.1021/acs.nanolett.5b04650>
97. Lenrick F, Ek M, Deppert K, Samuelson L, Reine Wallenberg L (2014) Straight and kinked InAs nanowire growth observed in situ by transmission electron microscopy. *Nano Res* 7(8):1188–1194. <https://doi.org/10.1007/s12274-014-0481-4>
98. Chou YC, Hillerich K, Tersoff J, Reuter MC, Dick KA, Ross FM (2014) Atomic-scale variability and control of III-V nanowire growth kinetics. *Science* 343(6168):281–284. <https://doi.org/10.1126/science.1244623>
99. Wen CY, Reuter MC, Bruley J, Tersoff J, Kodambaka S, Stach EA, Ross FM (2009) Formation of compositionally abrupt axial heterojunctions in silicon-germanium nanowires. *Science* 326(5957):1247–1250. <https://doi.org/10.1126/science.1178606>
100. Wen CY, Reuter MC, Tersoff J, Stach EA, Ross FM (2010) Structure, growth kinetics, and ledge flow during vapor–solid–solid growth of copper-catalyzed silicon nanowires. *Nano Lett* 10(2):514–519. <https://doi.org/10.1021/nl903362y>

101. Hofmann S, Sharma R, Wirth CT, Cervantes-Sodi F, Ducati C, Kasama T, Dunin-Borkowski RE, Drucker J, Bennett P, Robertson J (2008) Ledge-flow-controlled catalyst interface dynamics during Si nanowire growth. *Nat Mater* 7(5):372–375. <https://doi.org/10.1038/nmat2140>
102. Sears GW (1955) A growth mechanism for mercury whiskers. *Acta Metall* 3(4):361–366. [https://doi.org/10.1016/0001-6160\(55\)90041-9](https://doi.org/10.1016/0001-6160(55)90041-9)
103. Pan ZW, Dai ZR, Wang ZL (2001) Nanobelts of semiconducting oxides. *Science* 291(5510):1947–1949. <https://doi.org/10.1126/science.1058120>
104. Zhang Z, Wang Y, Li H, Yuan W, Zhang X, Sun C, Zhang Z (2016) Atomic-scale observation of vapor-solid nanowire growth via oscillatory mass transport. *ACS Nano* 10(1):763–769. <https://doi.org/10.1021/acsnano.5b05851>
105. Tokunaga T, Kawamoto T, Tanaka K, Nakamura N, Hayashi Y, Sasaki K, Kuroda K, Yamamoto T (2012) Growth and structure analysis of tungsten oxide nanorods using environmental TEM. *Nanoscale Res Lett* 7(1):85. <https://doi.org/10.1186/1556-276x-7-85>
106. Rackauskas S, Jiang H, Wagner JB, Shandakov SD, Hansen TW, Kauppinen EI, Nasibulin AG (2014) In situ study of noncatalytic metal oxide nanowire growth. *Nano Lett* 14(10):5810–5813. <https://doi.org/10.1021/nl502687s>
107. Kallesøe C, Wen C-Y, Booth TJ, Hansen O, Bøggild P, Ross FM, Mølhav K (2012) In situ TEM creation and electrical characterization of nanowire devices. *Nano Lett* 12(6):2965–2970. <https://doi.org/10.1021/nl300704u>
108. Baker RTK, Feates FS, Harris PS (1972) Continuous electron microscopic observation of carbonaceous deposits formed on graphite and silica surfaces. *Carbon* 10(1):93–96. [https://doi.org/10.1016/0008-6223\(72\)90014-0](https://doi.org/10.1016/0008-6223(72)90014-0)
109. Iijima S (1991) Helical microtubules of graphitic carbon. *Nature* 354(6348):56–58. <https://doi.org/10.1038/354056a0>
110. Helveg S, López-Cartes C, Sehested J, Hansen PL, Clausen BS, Rostrup-Nielsen JR, Abild-Pedersen F, Nørskov JK (2004) Atomic-scale imaging of carbon nanofibre growth. *Nature* 427(6973):426–429. <https://doi.org/10.1038/nature02278>
111. Sharma R, Iqbal Z (2004) In situ observations of carbon nanotube formation using environmental transmission electron microscopy. *Appl Phys Lett* 84(6):990–992. <https://doi.org/10.1063/1.1646465>
112. Sharma R, Rez P, Treacy MMJ, Stuart SJ (2005) In situ observation of the growth mechanisms of carbon nanotubes under diverse reaction conditions. *J Electron Microsc* 54(3):231–237. <https://doi.org/10.1093/jmicro/dfi037>
113. Sharma R, Rez P, Brown M, Du G, Treacy MMJ (2007) Dynamic observations of the effect of pressure and temperature conditions on the selective synthesis of carbon nanotubes. *Nanotechnology* 18(12):125602. <https://doi.org/10.1088/0957-4484/18/12/125602>
114. Sharma R, Chee S-W, Herzing A, Miranda R, Rez P (2011) Evaluation of the role of Au in improving catalytic activity of Ni nanoparticles for the formation of one-dimensional carbon nanostructures. *Nano Lett* 11(6):2464–2471. <https://doi.org/10.1021/nl2009026>
115. Yoshida H, Takeda S (2005) Image formation in a transmission electron microscope equipped with an environmental cell: single-walled carbon nanotubes in source gases. *Phys Rev B* 72(19):195428. <https://doi.org/10.1103/PhysRevB.72.195428>
116. Yoshida H, Uchiyama T, Takeda S (2007) Environmental transmission electron microscopy observations of swinging and rotational growth of carbon nanotubes. *Jpn J Appl Phys* 46(37):L917–L919. <https://doi.org/10.1143/jjap.46.1917>
117. Yoshida H, Takeda S, Uchiyama T, Kohno H, Homma Y (2008) Atomic-scale in-situ observation of carbon nanotube growth from solid state iron carbide nanoparticles. *Nano Lett* 8(7):2082–2086. <https://doi.org/10.1021/nl080452q>
118. Peng Z, Somodi F, Helveg S, Kisielowski C, Specht P, Bell AT (2012) High-resolution in situ and ex situ TEM studies on graphene formation and growth on Pt nanoparticles. *J Catal* 286:22–29. <https://doi.org/10.1016/j.jcat.2011.10.008>
119. Wu J, Shan H, Chen W, Gu X, Tao P, Song C, Shang W, Deng T (2016) In situ environmental TEM in imaging gas and liquid phase chemical reactions for materials research. *Adv Mater* 28(44):9686–9712. <https://doi.org/10.1002/adma.201602519>

120. Haruta M (1997) Size- and support-dependency in the catalysis of gold. *Catal Today* 36(1):153–166. [https://doi.org/10.1016/S0920-5861\(96\)00208-8](https://doi.org/10.1016/S0920-5861(96)00208-8)
121. He Y, Liu J-C, Luo L, Wang Y-G, Zhu J, Du Y, Li J, Mao SX, Wang C (2018) Size-dependent dynamic structures of supported gold nanoparticles in CO oxidation reaction condition. *Proc Natl Acad Sci* 115(30):7700. <https://doi.org/10.1073/pnas.1800262115>
122. Tao F, Crozier PA (2016) Atomic-scale observations of catalyst structures under reaction conditions and during catalysis. *Chem Rev* 116(6):3487–3539. <https://doi.org/10.1021/cr5002657>
123. Zhang S, Nguyen L, Zhu Y, Zhan S, Tsung C-K, Tao F (2013) In-situ studies of nanocatalysis. *Acc Chem Res* 46(8):1731–1739. <https://doi.org/10.1021/ar300245g>
124. Hofmann S, Sharma R, Ducati C, Du G, Mattevi C, Cepek C, Cantoro M, Pisana S, Parvez A, Cervantes-Sodi F, Ferrari AC, Dunin-Borkowski R, Lizzit S, Petaccia L, Goldoni A, Robertson J (2007) In situ observations of catalyst dynamics during surface-bound carbon nanotube nucleation. *Nano Lett* 7(3):602–608. <https://doi.org/10.1021/ml0624824>
125. Mazzucco S, Wang Y, Tanase M, Picher M, Li K, Wu Z, Irle S, Sharma R (2014) Direct evidence of active and inactive phases of Fe catalyst nanoparticles for carbon nanotube formation. *J Catal* 319:54–60. <https://doi.org/10.1016/j.jcat.2014.07.023>
126. Zhou Y, Jin C, Li Y, Shen W (2018) Dynamic behavior of metal nanoparticles for catalysis. *Nano Today* 20:101–120. <https://doi.org/10.1016/j.nantod.2018.04.005>
127. Ta N, Liu J, Chenna S, Crozier PA, Li Y, Chen A, Shen W (2012) Stabilized gold nanoparticles on ceria nanorods by strong interfacial anchoring. *J Am Chem Soc* 134(51):20585–20588. <https://doi.org/10.1021/ja310341j>
128. Tauster SJ, Fung SC, Garten RL (1978) Strong metal-support interactions. Group 8 noble metals supported on titanium dioxide. *J Am Chem Soc* 100(1):170–175. <https://doi.org/10.1021/ja00469a029>
129. Haller GL, Resasco DE (1989) Metal–support interaction: group VIII metals and reducible oxides. In: Eley DD, Pines H, Weisz PB (eds) *Advances in catalysis*, vol 36. Academic Press, pp 173–235. [https://doi.org/10.1016/S0360-0564\(08\)60018-8](https://doi.org/10.1016/S0360-0564(08)60018-8)
130. Liu J (2011) Advanced electron microscopy of metal-support interactions in supported metal catalysts. *ChemCatChem* 3(6):934–948. <https://doi.org/10.1002/cctc.201100090>
131. Su DS, Zhang B, Schlögl R (2015) Electron microscopy of solid catalysts—transforming from a challenge to a toolbox. *Chem Rev* 115(8):2818–2882. <https://doi.org/10.1021/cr500084c>
132. Zhang S, Plessow PN, Willis JJ, Dai S, Xu M, Graham GW, Cargnello M, Abild-Pedersen F, Pan X (2016) Dynamical observation and detailed description of catalysts under strong metal-support interaction. *Nano Lett* 16(7):4528–4534. <https://doi.org/10.1021/acs.nanolett.6b01769>
133. Matsubu JC, Zhang S, DeRita L, Marinkovic NS, Chen JG, Graham GW, Pan X, Christopher P (2017) Adsorbate-mediated strong metal–support interactions in oxide-supported Rh catalysts. *Nat Chem* 9(2):120–127. <https://doi.org/10.1038/nchem.2607>
134. Yuan W, Zhu B, Li X-Y, Hansen Thomas W, Ou Y, Fang K, Yang H, Zhang Z, Wagner Jakob B, Gao Y, Wang Y (2020) Visualizing H₂O molecules reacting at TiO₂ active sites with transmission electron microscopy. *Science* 367(6476):428–430. <https://doi.org/10.1126/science.aay2474>
135. Yuan W, Zhu B, Fang K, Li X-Y, Hansen Thomas W, Ou Y, Yang H, Wagner Jakob B, Gao Y, Wang Y, Zhang Z (2021) In situ manipulation of the active Au-TiO₂ interface with atomic precision during CO oxidation. *Science* 371(6528):517–521. <https://doi.org/10.1126/science.abe3558>
136. Wanke SE, Flynn PC (1975) The sintering of supported metal catalysts. *Catal Rev* 12(1):93–135. <https://doi.org/10.1080/01614947508067523>
137. Granqvist CG, Buhrman RA (1976) Size distributions for supported metal catalysts: coalescence growth versus Ostwald ripening. *J Catal* 42(3):477–479. [https://doi.org/10.1016/0021-9517\(76\)90125-1](https://doi.org/10.1016/0021-9517(76)90125-1)
138. Hansen TW, DeLaRiva AT, Challa SR, Datsy AK (2013) Sintering of catalytic nanoparticles: particle migration or Ostwald ripening? *Acc Chem Res* 46(8):1720–1730. <https://doi.org/10.1021/ar3002427>

139. Wynblatt P, Gjostein NA (1976) Particle growth in model supported metal catalysts—I. Theory. *Acta Metall* 24(12):1165–1174. [https://doi.org/10.1016/0001-6160\(76\)90034-1](https://doi.org/10.1016/0001-6160(76)90034-1)
140. Granqvist CG, Buhrman RA (1975) Statistical model for coalescence of islands in discontinuous films. *Appl Phys Lett* 27(12):693–694. <https://doi.org/10.1063/1.88342>
141. Baker RTK, Harris PS, Thomas RB (1974) Direct observation of particle mobility on a surface in a gaseous environment. *Surf Sci* 46(1):311–316. [https://doi.org/10.1016/0039-6028\(74\)90259-3](https://doi.org/10.1016/0039-6028(74)90259-3)
142. Liu RJ, Crozier PA, Smith CM, Hucul DA, Blackson J, Salaita G (2005) Metal sintering mechanisms and regeneration of palladium/alumina hydrogenation catalysts. *Appl Catal A* 282(1):111–121. <https://doi.org/10.1016/j.apcata.2004.12.015>
143. Liu R-J, Crozier PA, Smith CM, Hucul DA, Blackson J, Salaita G (2004) In situ electron microscopy studies of the sintering of palladium nanoparticles on alumina during catalyst regeneration processes. *Microsc Microanal* 10(1):77–85. <https://doi.org/10.1017/s1431927604040188>
144. Moulijn JA, van Diepen AE, Kapteijn F (2001) Catalyst deactivation: is it predictable?: what to do? *Appl Catal A* 212(1):3–16. [https://doi.org/10.1016/S0926-860X\(00\)00842-5](https://doi.org/10.1016/S0926-860X(00)00842-5)
145. Simonsen SB, Chorkendorff I, Dahl S, Skoglundh M, Sehested J, Helveg S (2010) Direct observations of oxygen-induced platinum nanoparticle ripening studied by in situ TEM. *J Am Chem Soc* 132(23):7968–7975. <https://doi.org/10.1021/ja910094r>
146. Benavidez AD, Kovarik L, Genc A, Agrawal N, Larsson EM, Hansen TW, Karim AM, Datye AK (2012) Environmental transmission electron microscopy study of the origins of anomalous particle size distributions in supported metal catalysts. *ACS Catal* 2(11):2349–2356. <https://doi.org/10.1021/cs3005117>
147. Yuan W, Zhang D, Ou Y, Fang K, Zhu B, Yang H, Hansen TW, Wagner JB, Zhang Z, Gao Y (2018) Direct in situ TEM visualization and insight into the facet-dependent sintering behaviors of gold on TiO₂. *Angew Chem* 130(51):17069–17073. <https://doi.org/10.1002/ange.201811933>
148. Amama PB, Pint CL, McJilton L, Kim SM, Stach EA, Murray PT, Hauge RH, Maruyama B (2009) Role of water in super growth of single-walled carbon nanotube carpets. *Nano Lett* 9(1):44–49. <https://doi.org/10.1021/nl801876h>
149. Hata K, Futaba Don N, Mizuno K, Namai T, Yumura M, Iijima S (2004) Water-assisted highly efficient synthesis of impurity-free single-walled carbon nanotubes. *Science* 306(5700):1362–1364. <https://doi.org/10.1126/science.1104962>
150. Asakura K, Nagahiro H, Ichikuni N, Iwasawa Y (1999) Structure and catalytic combustion activity of atomically dispersed Pt species at MgO surface. *Appl Catal A* 188(1):313–324. [https://doi.org/10.1016/S0926-860X\(99\)00247-1](https://doi.org/10.1016/S0926-860X(99)00247-1)
151. Qiao B, Wang A, Yang X, Allard LF, Jiang Z, Cui Y, Liu J, Li J, Zhang T (2011) Single-atom catalysis of CO oxidation using Pt1/FeOx. *Nat Chem* 3(8):634–641. <https://doi.org/10.1038/nchem.1095>
152. Jones J, Xiong H, DeLaRiva AT, Peterson Eric J, Pham H, Challa Sivakumar R, Qi G, Oh S, Wiebenga Michelle H, Pereira Hernández Xavier I, Wang Y, Datye Abhaya K (2016) Thermally stable single-atom platinum-on-ceria catalysts via atom trapping. *Science* 353(6295):150–154. <https://doi.org/10.1126/science.aaf8800>
153. Gänzler AM, Casapu M, Vernoux P, Loricant S, Cadete Santos Aires FJ, Epicier T, Betz B, Hoyer R, Grunwaldt J-D (2017) Tuning the structure of platinum particles on ceria in situ for enhancing the catalytic performance of exhaust gas catalysts. *Angew Chem Int Ed* 56(42):13078–13082. <https://doi.org/10.1002/anie.201707842>
154. Yang X-F, Wang A, Qiao B, Li J, Liu J, Zhang T (2013) Single-atom catalysts: a new frontier in heterogeneous catalysis. *Acc Chem Res* 46(8):1740–1748. <https://doi.org/10.1021/ar300361m>
155. Yao Y, Huang Z, Xie P, Wu L, Ma L, Li T, Pang Z, Jiao M, Liang Z, Gao J, He Y, Kline DJ, Zachariah MR, Wang C, Lu J, Wu T, Li T, Wang C, Shahbazian-Yassar R, Hu L (2019) High temperature shockwave stabilized single atoms. *Nat Nanotechnol* 14(9):851–857. <https://doi.org/10.1038/s41565-019-0518-7>

156. Yoshida K, Bright A, Tanaka N (2012) Direct observation of the initial process of Ostwald ripening using spherical aberration-corrected transmission electron microscopy. *J Electron Microsc* 61(2):99–103. <https://doi.org/10.1093/jmicro/dfp100>
157. Yoshida K, Xudong Z, Bright AN, Saitoh K, Tanaka N (2013) Dynamic environmental transmission electron microscopy observation of platinum electrode catalyst deactivation in a proton-exchange-membrane fuel cell. *Nanotechnology* 24(6):065705. <https://doi.org/10.1088/0957-4484/24/6/065705>
158. DeRita L, Resasco J, Dai S, Boubnov A, Thang HV, Hoffman AS, Ro I, Graham GW, Bare SR, Pacchioni G, Pan X, Christopher P (2019) Structural evolution of atomically dispersed Pt catalysts dictates reactivity. *Nat Mater* 18(7):746–751. <https://doi.org/10.1038/s41563-019-0349-9>
159. Wei S, Li A, Liu J-C, Li Z, Chen W, Gong Y, Zhang Q, Cheong W-C, Wang Y, Zheng L, Xiao H, Chen C, Wang D, Peng Q, Gu L, Han X, Li J, Li Y (2018) Direct observation of noble metal nanoparticles transforming to thermally stable single atoms. *Nat Nanotechnol* 13(9):856–861. <https://doi.org/10.1038/s41565-018-0197-9>
160. Lang R, Xi W, Liu J-C, Cui Y-T, Li T, Lee AF, Chen F, Chen Y, Li L, Li L, Lin J, Miao S, Liu X, Wang A-Q, Wang X, Luo J, Qiao B, Li J, Zhang T (2019) Non defect-stabilized thermally stable single-atom catalyst. *Nat Commun* 10(1):234. <https://doi.org/10.1038/s41467-018-08136-3>
161. Dai S, Zhang S, Katz MB, Graham GW, Pan X (2017) In situ observation of Rh-CaTiO₃ catalysts during reduction and oxidation treatments by transmission electron microscopy. *ACS Catal* 7(3):1579–1582. <https://doi.org/10.1021/acscatal.6b03604>
162. Ohno Y, Takeda S (1995) A new apparatus for in situ photoluminescence spectroscopy in a transmission electron microscope. *Rev Sci Instrum* 66(10):4866–4869. <https://doi.org/10.1063/1.1146166>
163. Suzuki K, Ichihara M, Takeuchi S, Nakagawa K, Maeda K, Iwanaga H (1984) In situ TEM observation of dislocation motion in II–VI compounds. *Philos Mag A* 49(3):451–461. <https://doi.org/10.1080/01418618408233287>
164. Yoshida K, Yamasaki J, Tanaka N (2004) In situ high-resolution transmission electron microscopy observation of photodecomposition process of poly-hydrocarbons on catalytic TiO₂ films. *Appl Phys Lett* 84(14):2542–2544. <https://doi.org/10.1063/1.1689747>
165. Miller B, Crozier P (2011) Visible and UV irradiation of ETEM samples for in-situ studies of photocatalysts. *Microsc Microanal* 17(S2):472–473. <https://doi.org/10.1017/s1431927611003230>
166. Miller B, Crozier PA (2012) In situ visible and UV illumination of ETEM samples. *Microsc Microanal* 18(S2):1074–1075. <https://doi.org/10.1017/s1431927612007222>
167. Miller BK, Crozier PA (2013) System for in situ UV-visible illumination of environmental transmission electron microscopy samples. *Microsc Microanal* 19(2):461–469. <https://doi.org/10.1017/s1431927612014122>
168. Zhang L, Miller BK, Crozier PA (2013) atomic level in situ observation of surface amorphization in anatase nanocrystals during light irradiation in water vapor. *Nano Lett* 13(2):679–684. <https://doi.org/10.1021/nl304333h>
169. Picher M, Mazzucco S, Blankenship S, Sharma R (2015) Vibrational and optical spectroscopies integrated with environmental transmission electron microscopy. *Ultramicroscopy* 150:10–15. <https://doi.org/10.1016/j.ultramic.2014.11.023>
170. Shindo D, Takahashi K, Murakami Y, Yamazaki K, Deguchi S, Suga H, Kondo Y (2009) Development of a multifunctional TEM specimen holder equipped with a piezodriving probe and a laser irradiation port. *J Electron Microsc* 58(4):245–249. <https://doi.org/10.1093/jmicro/dfp018>
171. Cavalca F, Laursen AB, Kardynal BE, Dunin-Borkowski RE, Dahl S, Wagner JB, Hansen TW (2012) In situtransmission electron microscopy of light-induced photocatalytic reactions. *Nanotechnology* 23(7):075705. <https://doi.org/10.1088/0957-4484/23/7/075705>
172. Cavalca F, Laursen AB, Wagner JB, Damsgaard CD, Chorkendorff I, Hansen TW (2013) Light-induced reduction of cuprous oxide in an environmental transmission electron microscope. *ChemCatChem* 5(9):2667–2672. <https://doi.org/10.1002/cctc.201200887>

173. Taheri ML, Stach EA, Arslan I, Crozier PA, Kabius BC, LaGrange T, Minor AM, Takeda S, Tanase M, Wagner JB, Sharma R (2016) Current status and future directions for in situ transmission electron microscopy. *Ultramicroscopy* 170:86–95. <https://doi.org/10.1016/j.ultramicro.2016.08.007>
174. Faruqi AR, McMullan G (2011) Electronic detectors for electron microscopy. *Q Rev Biophys* 44(3):357–390. <https://doi.org/10.1017/s0033583511000035>
175. Lobastov VA, Srinivasan R, Zewail AH (2005) Four-dimensional ultrafast electron microscopy. *Proc Natl Acad Sci USA* 102(20):7069. <https://doi.org/10.1073/pnas.0502607102>
176. Zewail AH (2006) 4D ultrafast electron diffraction, crystallography, and microscopy. *Annu Rev Phys Chem* 57(1):65–103. <https://doi.org/10.1146/annurev.physchem.57.032905.104748>
177. Zewail AH (2010) Four-dimensional electron microscopy. *Science* 328(5975):187–193. <https://doi.org/10.1126/science.1166135>
178. LaGrange T, Reed BW, Santala MK, McKeown JT, Kulovits A, Wiezorek JMK, Nikolova L, Rosei F, Siwick BJ, Campbell GH (2012) Approaches for ultrafast imaging of transient materials processes in the transmission electron microscope. *Micron* 43(11):1108–1120. <https://doi.org/10.1016/j.micron.2012.04.010>
179. Barwick B, Flannigan DJ, Zewail AH (2009) Photon-induced near-field electron microscopy. *Nature* 462(7275):902–906. <https://doi.org/10.1038/nature08662>
180. Baum P, Yang D-S, Zewail Ahmed H (2007) 4D visualization of transitional structures in phase transformations by electron diffraction. *Science* 318(5851):788–792. <https://doi.org/10.1126/science.1147724>
181. Carbone F, Kwon O-H, Zewail Ahmed H (2009) Dynamics of chemical bonding mapped by energy-resolved 4D electron microscopy. *Science* 325(5937):181–184. <https://doi.org/10.1126/science.1175005>
182. Kwon O-H, Zewail Ahmed H (2010) 4D electron tomography. *Science* 328(5986):1668–1673. <https://doi.org/10.1126/science.1190470>
183. Fitzpatrick AWP, Lorenz UJ, Vanacore GM, Zewail AH (2013) 4D Cryo-electron microscopy of proteins. *J Am Chem Soc* 135(51):19123–19126. <https://doi.org/10.1021/ja4115055>
184. Fu X, Pollard Shawn D, Chen B, Yoo B-K, Yang H, Zhu Y (2018) Optical manipulation of magnetic vortices visualized in situ by Lorentz electron microscopy. *Sci Adv* 4(7):eaat3077. <https://doi.org/10.1126/sciadv.aat3077>
185. Fu X, Chen B, Tang J, Hassan Mohammed T, Zewail Ahmed H (2017) Imaging rotational dynamics of nanoparticles in liquid by 4D electron microscopy. *Science* 355(6324):494–498. <https://doi.org/10.1126/science.aah3582>
186. Armstrong MR, Boyden K, Browning ND, Campbell GH, Colvin JD, DeHope WJ, Frank AM, Gibson DJ, Hartemann F, Kim JS, King WE, LaGrange TB, Pyke BJ, Reed BW, Shuttlesworth RM, Stuart BC, Torralva BR (2007) Practical considerations for high spatial and temporal resolution dynamic transmission electron microscopy. *Ultramicroscopy* 107(4):356–367. <https://doi.org/10.1016/j.ultramicro.2006.09.005>
187. King WE, Campbell GH, Frank A, Reed B, Schmerge JF, Siwick BJ, Stuart BC, Weber PM (2005) Ultrafast electron microscopy in materials science, biology, and chemistry. *J Appl Phys* 97(11):111101. <https://doi.org/10.1063/1.1927699>
188. LaGrange T, Armstrong MR, Boyden K, Brown CG, Campbell GH, Colvin JD, DeHope WJ, Frank AM, Gibson DJ, Hartemann FV, Kim JS, King WE, Pyke BJ, Reed BW, Shirk MD, Shuttlesworth RM, Stuart BC, Torralva BR, Browning ND (2006) Single-shot dynamic transmission electron microscopy. *Appl Phys Lett* 89(4):044105. <https://doi.org/10.1063/1.2236263>
189. Reed BW, Armstrong MR, Browning ND, Campbell GH, Evans JE, LaGrange T, Masiel DJ (2009) The evolution of ultrafast electron microscope instrumentation. *Microsc Microanal* 15(4):272–281. <https://doi.org/10.1017/s1431927609090394>
190. Lazić I, Bosch EGT, Lazar S (2016) Phase contrast STEM for thin samples: Integrated differential phase contrast. *Ultramicroscopy* 160:265–280. <https://doi.org/10.1016/j.ultramicro.2015.10.011>

191. Yücelen E, Lazić I, Bosch EGT (2018) Phase contrast scanning transmission electron microscopy imaging of light and heavy atoms at the limit of contrast and resolution. *Sci Rep* 8(1):2676. <https://doi.org/10.1038/s41598-018-20377-2>
192. Shen B, Chen X, Cai D, Xiong H, Liu X, Meng C, Han Y, Wei F (2020) Atomic spatial and temporal imaging of local structures and light elements inside zeolite frameworks. *Adv Mater* 32(4):1906103. <https://doi.org/10.1002/adma.201906103>
193. Liu L, Wang N, Zhu C, Liu X, Zhu Y, Guo P, Alfilil L, Dong X, Zhang D, Han Y (2020) Direct imaging of atomically dispersed molybdenum that enables location of aluminum in the framework of zeolite ZSM-5. *Angew Chem Int Ed* 59(2):819–825. <https://doi.org/10.1002/anie.201909834>
194. The significant role of the atomic surface structure of support in strong metal-support interaction. <https://doi.org/10.1002/chem.202104519>

Chapter 10

4D Ultrafast TEM



Bin Chen, Jianming Cao, and Dongping Zhong

10.1 A Brief History of 4D Ultrafast TEM

Material and biological structures transform at different time scales through transition states on complex energy landscapes. The global shape in nuclear-coordinate space reflects the possible conformations (entropy) and interactions (enthalpy) that lead to the changes. Though time-averaged structural determination is important, the static structures cannot elucidate the nonequilibrium dynamics that may govern the functions. In the early days, for example, the visualization of intermediate structural changes caused by chemical reactions in 3D space was impossible because of their transient nature on the time scale of a picosecond or less. These intermediate structures are “dark” because they undergo radiationless transitions through reactive/nonreactive channels. Therefore, only ultrafast dynamical studies in 4D space and time can resolve the complexity of the pathways and structures that are involved, which uncover the true nature of the landscapes.

Normally the term “ultrashort” refers to pulses with a temporal duration of a few tens of femtoseconds, but in a broad sense any pulse lasting less than a few picoseconds can be regarded ultrafast. Over a century of developments in science and technology (Fig. 10.1), it has become possible in the past three decades to observe the dynamics from seconds down to femtoseconds range [1, 2], the scale

B. Chen (✉) · J. Cao · D. Zhong
Center for Ultrafast Science and Technology, Shanghai Jiao Tong University, Shanghai 200240, China
e-mail: cbcce@sjtu.edu.cn

J. Cao
Physics Department and National High Magnetic Field Laboratory, Florida State University, Tallahassee, FL 32310, USA

D. Zhong
Department of Physics, Department of Chemistry and Biochemistry, Programs of Biophysics, Chemical Physics, and Biochemistry, The Ohio State University, Columbus, OH 43210, USA

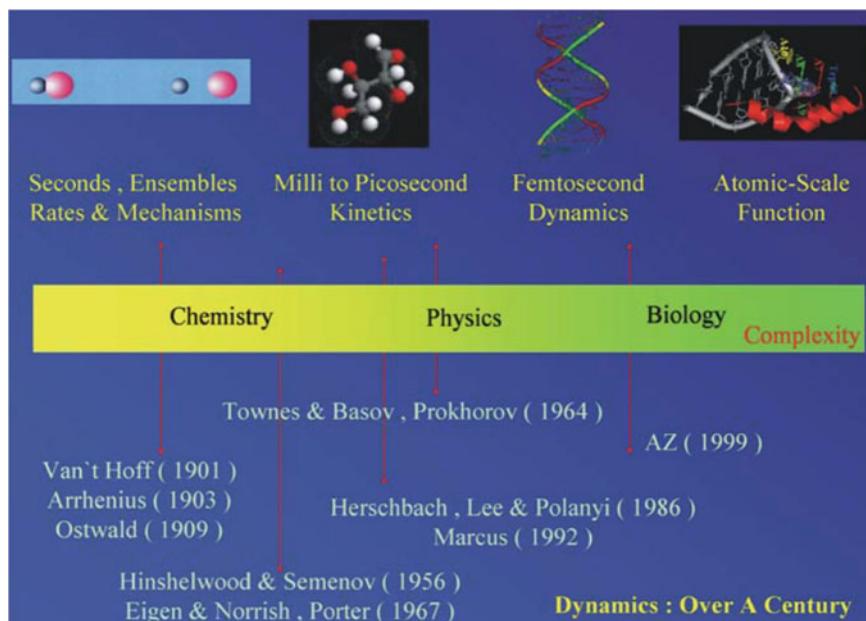


Fig. 10.1 Historical developments in the courses of kinetics and dynamics, from seconds toward the femtosecond atomic scale as cited by Nobel prizes (reproduced with permission from Ref. [1], Copyright 2006, Annual Reviews, Inc)

of vibrational periods. The coherent nuclear motions on such time scales describe a fundamental transition, from ensemble-rate kinetics to single-molecule-trajectory dynamics. In the past 30 years, the field of ultrafast phenomena has moved ahead in a breathtaking fashion, which is partly due to the development of new laser-based as well as accelerator-based sources of ultrashort pulses of light and electrons. The historical development of ultrafast technologies then follows a sequence of ultrafast laser spectroscopy, ultrafast electron diffraction and electron microscopy.

The first laser was obtained by using a synthetic ruby crystal in 1960 (Theodore Maiman). Shortly after that, the generation of shorter laser pulses came out: nanoseconds by Q-switching (Robert W. Hellwarth 1961) and picoseconds (Anthony J. DeMaria 1966) by mode-locking. Sub-picosecond pulses from dye lasers were achieved in 1974 [3] by Chuck V. Shank and then a 6 fs pulse was realized in 1987 [4]. With the discovery of femtosecond pulse generation from solid-state Ti-sapphire lasers by Wilson Sibbett in 1991 [5], dye lasers were quickly replaced and femtosecond pulse generation became a standard laboratory tool. Thanks to the development of such short laser pulses, the studies of ultrafast dynamics were achieved by using the “pump–probe” scheme. Generally, a pump pulse excites the system to be studied, while a second probe pulse measures the response of the system to the excitation. The landmark “pump–probe” experiment was carried out

by Abraham and Lemoine in 1899 [6], demonstrating the importance of synchronization between the pump and probe pulses. They used an electrical pulse to produce a spark for activating a Kerr shutter. Light from the spark was collimated through the Kerr cell and through a variable path for setting delay times. The rotation of the analyzer indicated the presence/disappearance of birefringence in the cell, reflecting the electrical/optical response behavior.

Using the “pump–probe” scheme, ultrafast spectroscopy has been developing rapidly and expanding the knowledge base of fundamental chemical and physical processes. Some representative works in the late 1960s and 1970s included the photo-physical rates of internal conversion and biological studies by Peter Rentzep [7, 8], the first ps study of chemical reactions (and orientational relaxations) in solutions by Ken Eisensthal [9], the direct measurement of the rates of intersystem crossing by Robin Hochstrasser [10] and the novel approach for measurement of ps vibrational relaxations (in the ground state of molecules) in liquids by Wolfgang Kaiser and colleagues [11]. By using femtosecond spectroscopy, direct observation of the elementary bond breakage in ICN and the subsequent transient species $I\cdots CN^{*\ddagger}$ was realized by Zewail and colleagues in 1987 [12]. His group then extended this femtosecond technique to the studies of biological systems (e.g., proteins and DNAs) [13].

The above research activities used ultrashort pulses for optical studies of light–matter interaction with the efforts to access events occurring on an elementary time scale. The spectral range of ultrashort pulses has been extended to the short wavelength range such as the soft and hard X-ray domains. The development of X-ray-based and electron-based diffraction techniques has allowed the determination of structural information, delivering an impressive degree of insight into phenomena both within atoms and between atoms. Because the electrons scatter off all atoms and atom–atom pairs of the samples in electron diffraction, the electron probe is sensitive to all species in its path and can thus disclose structures that spectroscopy may be blind to (the optical probe in spectroscopy is tuned to specific transitions). In addition, the advantages of electron-based techniques are that the cross-section for electron scattering is about six orders of magnitude larger than that of X-ray scattering, and electrons can be also focused to obtain images in a microscope. On the basis of the above considerations, progress has been extensively made in developing and advancing electron-based methodologies.

One of the common electron-based techniques in ultrafast fields is ultrafast electron diffraction (UED). The UED technique uses properly timed sequences of ultrafast pulses, namely a laser pulse to initiate the dynamic changes and an electron pulse to probe the ensuing structural changes in the sample. The resulting electron diffraction patterns are then recorded on a camera. Each time-resolved diffraction pattern is then inverted to reveal the sample structure that gives birth to the pattern at that specific time delay. Early in 1982, Mourou and Williamson used a modified streak camera to record diffraction from thin Al films in a transmission mode with ~ 100 ps pulses [14]; subsequently in 1984, 20 ps electron pulses were produced to investigate the melting of Al films before and after the laser irradiation [15]. Elsayed-Ali and colleagues succeeded in using 200 ps electron pulses to study surface melting by

reflection high-energy electron diffraction in 1988 [16]. In 1991, Zewail proposed to replace the “spectroscopic probes” of femtochemistry with ultrashort electron pulses for studying the nature of transient structures and the trajectories of chemical reactions on the femtosecond time scale [17]. A year later, they succeeded in acquiring diffraction patterns with ~ 10 ps electron pulses [18]. Through technical and theoretical advancement, they further developed the UED apparatus from the first generation (UED-1) to the fourth generation (UED-4) [19–22], with the temporal resolution from the initial picosecond down to the femtosecond range (~ 300 fs). The UED-4, also called ultrafast electron crystallography, has both reflection and transmission modes, allowing to record the temporal evolution of chemical reactions at the atomic-scale spatial resolution and the femtosecond time resolution [21, 22].

UED, in principle, is the diffraction technique that reveals the transient structural information at the atomic length scale in reciprocal space. In the case of biological and nanoscopic materials with characteristic length scales ranging from sub-nanometers up to micrometers in real space, microscopy techniques possess unique advantages. Optical microscopy has allowed us to visualize dynamic events occurring *in vitro*, but its spatial resolution is limited to the optical wavelengths employed, typically ~ 200 – 800 nm. Transmission electron microscopy (TEM) has long been a powerful technique in many areas of research, allowing for sub-nanometer spatial resolution but lacking ultrafast temporal resolution. The ultimate techniques would be the effective combination of both the spatial resolution of electron microscopy and the temporal resolution capability of optical methods. As known, the first transmission electron microscope was invented in 1931, and then the instrumental development has tended toward ultimate spatial resolution. In fact, the spatial resolution of TEMs is limited not by the wavelength of the incident electrons but rather by the performance of the magnetic objective lens. In 1995, Maximilian Haider designed the practical spherical aberration correcting lens systems, enabling breakthrough improvements in the TEM spatial resolution [23]. Since then, scanning TEM (STEM) systems with aberration correcting lenses have achieved sub-Å spatial resolution in real space [24, 25]. Recently, the 300 kV STEM with sub-0.5 Å resolution has been reported [26], allowing individual single atoms to be routinely imaged by these commercial microscopes.

The other direction of development in TEM systems is pursuing ultrafast temporal resolution. In the standard TEM mentioned above, the temporal resolution is generally in the millisecond range, being limited by the charge-coupled device (CCD) detector. In 1999, Bostanjoglo and colleagues modified the standard TEM, and achieved the spatiotemporal resolution at ~ 200 nm and ~ 10 ns, which was called high-speed TEM [27, 28]. They utilized a single giant pulse with $\sim 10^8$ electrons, and such electron pulses with several to several tens of nanoseconds duration were photoelectrically generated by the Q-switched cathode-driving laser. By applying a decreasing staircase voltage across the capacitor, the image-shifting capacitor was used to produce successive frames by displacing the image on the detector between the illuminating electron pulses. A frame grabber card supplied a clock signal, which was fed to a dedicated circuit that produced a synchronized clock with trigger pulses for the photocathode driving laser, the specimen-treating laser, the beam blanker

and the frame-shifting circuit after the required delay times. Note that the electron pulses with a large number of electrons, which were used here to study laser-induced melting in metals, had a detrimental effect on achieving ultrashort pulse imaging. Moreover, because the time window for imaging in the experiments was nanoseconds, the uncertainty in spatial resolution due to noise statistics was on the order of micrometers.

With the accumulation of numerous UED works in the 1990s, Zewail pioneered the development of 4D ultrafast TEM in 2004 [29, 30], which was different from the one used in the work of Bostanjoglo. Determining transient structures on the ultrafast time scale requires not only the marriage of ultrafast probing techniques with diffraction capability, but also the development of new concepts for reaching simultaneously the ultrafast temporal resolution and the atomic spatial resolution. The conceptual framework of the approach is that the evolving transient structures are determined when properly timed frame referencing is made before and during the changes. Upon initiation of the specimen by ultrashort pump laser pulses, a series of electron pulses are used to probe the changes with well-defined time delays through an optical delay stage or a digital delay generator. A series of images or diffraction patterns recorded at a number of delay times provide direct insight into the temporal evolution of the structural changes. The progress in 4D ultrafast electron microscopy (UEM) studies has been from the integration of the generation of ultrashort coherent electron packets with fs laser pulses, the in situ pulse sequencing and clocking, and the frame-reference method for data processing—all of which give unprecedented levels of sensitivity and spatiotemporal resolution to perform the experiments for determining structural dynamics.

UEM provides the ability to image complex structures with a spatial resolution similar to TEM, but as snapshots acquired with ultrafast electron packets derived from a train of fs pulses. The temporal resolution is independent of the response of the CCD camera, and it is determined by the duration of the pump laser pulses, electron pulses and the jitter. The space-charge effect in the electron pulses will give rise to temporal broadening. In order to reach the fs resolution, the strict requirement for proper electron focusing in real-space imaging is challenging. The central concept is to use single-electron packets, which excludes the space-charge effect between electrons. The paradigm has been achieved using timed, coherent and space-charge-free single-electron packets for imaging material structures and biological cells in the past 15 years, with the spatiotemporal resolutions of several hundreds of femtoseconds and several angstroms. It should be pointed out that increasing the number of electrons in the pulse would allow for single-pulse imaging, which is suited for studying irreversible processes that result in permanent changes. With the advancement of 4D UEM, the different domains of electron microscopy have been made possible: ultrafast real-space imaging, diffraction and electron-energy-loss spectroscopy. During the course of such developments, Zewail family members have been continuing their efforts in this field [31–36]. In addition, several other groups also built the UEM apparatuses in the past years. LaGrange and colleagues in Lawrence Livermore National Laboratory constructed a single-shot dynamic TEM (2006), with a spatial resolution of ~20 nm and temporal resolution of ~30 ns [37]. Li in Institute of Physics

(China) designed the 4D UEM (2015) with the capability of achieving ~ 0.5 nm and 1 ps spatiotemporal resolution [38]. Recently, more groups have been starting UEM projects and/or planning to join this field.

Last but not the least, after the invention of 4D ultrafast TEM, Zewail and colleagues took a step forward to design 4D scanning UEM (SUEM) in 2010 [39, 40]. Compared to the 4D UEM, SUEM uses secondary electrons for imaging, which is suitable to study the morphological, chemical and physical dynamics of surfaces. SUEM possesses the following advantages: (1) the specimen preparation is simple and thick specimens can be examined, which is an attractive feature in many studies; (2) the capabilities of SUEM equipping with low-voltage-imaging and favorable heat dissipation due to thick samples significantly reduce the radiation damage by electrons and/or heating laser; (3) SUEM collects the signal from the secondary electrons, enabling the unique investigation of ultrafast carrier dynamics.

On the basis of the above historical perspective, Fig. 10.2 briefly summarizes the developments of ultrafast techniques using electron probes [20, 30, 39]. All these are accompanied by advancements and improvements in conceptual designs, theoretical models and technical methodology, which are indispensable for the fundamental understanding of ultrashort phenomena. Armed with these ultrafast techniques, a variety of complex systems including the gas and condensed phases, surfaces and interfaces have been extensively studied with their temporal evolution dynamics. In this chapter, we will focus on the application of 4D ultrafast TEM in the studies of material and biological systems.

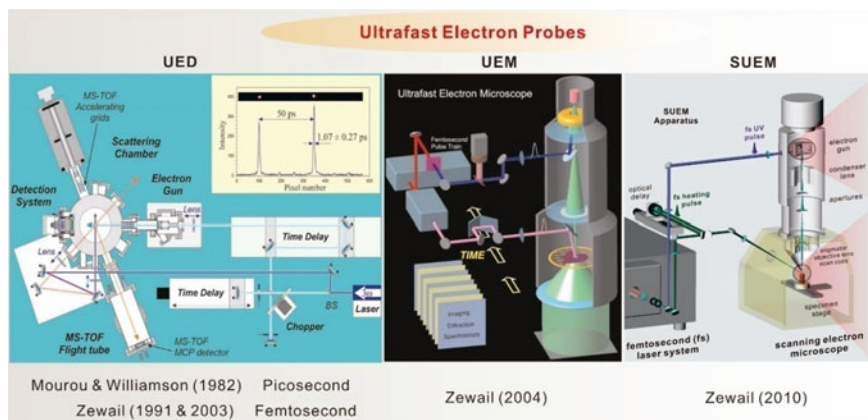


Fig. 10.2 Developments of ultrafast electron probes, such as UED, UEM and SUEM. The date given is the year for that pioneered development (UED, reproduced with permission from Ref. [20], Copyright 2001, The American Association for the Advancement of Science; UEM, reproduced with permission from Ref. [30], Copyright 2005, National Academy of Sciences, U. S. A.; SUEM, reproduced with permission from Ref. [39], Copyright 2010, National Academy of Sciences, U. S. A.)

10.2 4D Ultrafast Electron Imaging in Space and Time

The 4D ultrafast electron imaging is realized through the pump–probe scheme. The design of 4D UEM is shown in Fig. 10.3, which outlines the interfacing of a femtosecond/nanosecond optical system with a standard TEM (top panel). Upon the initiation of changes by either heating the specimen or through electronic excitation by the laser pump pulses, an electron pulse generated by the photoelectric effect is used to probe the specimen with a well-defined time delay. Generally, green laser (pump) pulses at ~ 520 nm are used to pump the sample, whereas ultraviolet laser pulses at around 260 nm are directed to the photocathode to generate electron (probe) pulses. The photoelectrons in each pulse for probing are then accelerated. A series of time-framed snapshots of the image, the diffraction pattern or the electron energy loss spectroscopy (EELS) data recorded at a number of delay times provides a movie, showing the temporal evolution of the changes. For femtosecond or picosecond dynamics, the femtosecond laser system (duration of several tens to several hundred femtoseconds) is used, whereas the nanosecond laser system (duration of ~ 10 ns) is employed for dynamics occurring on longer time scales. The timing between the pump pulse and the probe pulse is controlled by changing the delay time between the two through an optical delay stage (for femtosecond system) or a digital delay generator (for nanosecond system). In this scheme, the temporal resolution is not limited to the response of the CCD camera, but is rather controlled by the convolution among the pump pulse duration, the probe pulse duration and the jitter. 4D UEM can operate in either stroboscopic (for reversible processes) or single-pulse mode (for irreversible dynamics). For the stroboscopic experiments, the repetition rate is normally set at 1 kHz or higher, ensuring the full recovery of the dynamical process. In the case of the single-pulse mode, an entire image is acquired with only one incident laser pump pulse followed by one electron probe pulse (contains $\sim 10^5$ – 10^7 or more electrons). Recently, the single-pulse methodology can be extended to the advanced one called “movie mode”, where up to 16 electron pulses probe the sequence of changes at 16 different delay times (16 frames at every turn) after the excitation of the specimen.

The methodology of 4D UEM involves the use of pulsed beams whose essential characteristics are briefly introduced below (bottom panel) [41]. In the UEM column, propagation is determined by the initial conditions of the electron wave packet and the distributions from pulse to pulse. For the pump–probe scheme, there are two types of parameters in a train of single electrons: those describing the single electrons as quantum objects, and those associated with the statistics of the many pulses forming images or diffraction patterns. The central electron energy E_0 determines the de Broglie wavelength λ_0 , essential for atomic-scale resolution, while the central speed v_0 determines how much time the pulses spend in free space before the sample. The bandwidth ΔE is a consequence of the photoemission process on the femtosecond scale, which would cause temporal broadening. Therefore, in the single-electron regime a match between the laser’s photon energy and the cathode material’s work

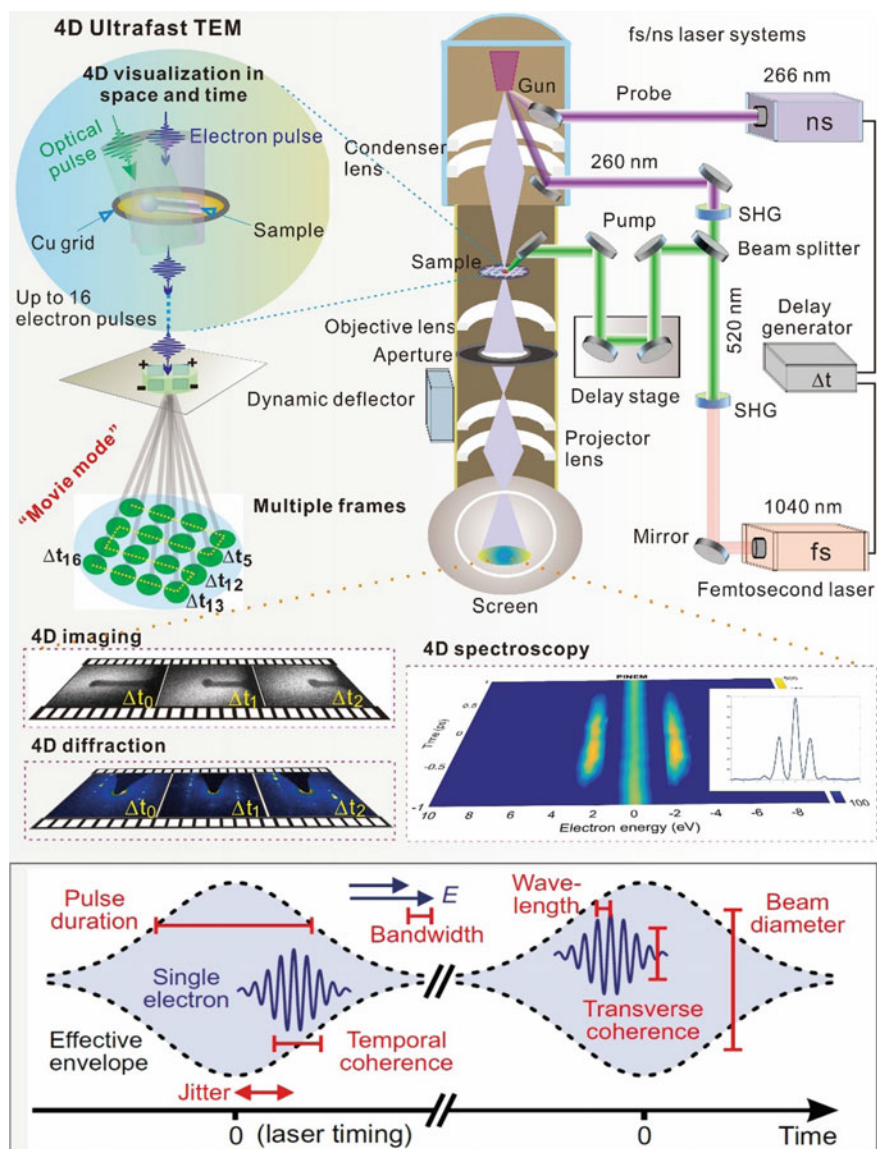


Fig. 10.3 (Top) Schematic diagram of 4D ultrafast TEM. The green laser pulse enables the sample changes to be measured by the delayed electron pulse at a given time delay. The different information associated with the changes is obtained through 4D imaging, diffraction or spectroscopy. (Bottom) Essential parameters for single-electron pulses (reproduced with permission from Ref. [41], Copyright 2013, Elsevier)

function is important to reduce the electron pulses' velocity spreads in both longitudinal and transverse directions [42]. For the flat femtosecond cathodes, an effective $\Delta E \approx 0.1\text{--}0.3$ eV was determined experimentally [42]. After acceleration to typical 30–300 keV, the degree of monochromaticity, $\Delta E/E_0$, is in the range of 10^{-5} to 10^{-6} , which is as good as that of the standard electron microscopes but with femtosecond pulses.

Coherence is the essential concept in 4D UEM, determining the ability to resolve complex structures. The transverse coherence ξ_{\perp} determines the ability of single electrons to diffract from atoms that are far apart, which is a decisive factor for the spatial resolution of complex materials. In order to obtain a full and direct resolution of all atoms and their motion, the molecular nanostructure or unit cell in a crystal should be entirely covered by a coherent electron wave so that the important information would not be lost. Written in terms of transverse momentum spread, one obtains the transverse coherence [41, 42],

$$\xi_{\perp} = \hbar / \sigma_{p\perp} \quad (10.1)$$

where the transverse momentum spread $\sigma_{p\perp}$ and the beam radius σ_{\perp} originate from the limited emittance at the source and are affected by the imaging system. The lateral velocity spread of single electrons, $\sigma_{p\perp}/m_e$, from flat surfaces could be in the range of 6–140 km/s [42, 43]. For multi-electron beams, the transverse coherence was estimated at 2–3 nm for beams with $\sigma_{\perp} \approx 150\text{--}200$ μm [44, 45], and for single electrons it was shown to reach 20 nm for a beam with $\sigma_{\perp} < 100$ μm [43].

The longitudinal coherence time ξ_t and the coherence length ξ_{\parallel} describe the ability of electron waves to interfere in time and in the propagation direction. While this is almost irrelevant for diffraction [46], it becomes important if electron pulses are compressed in time or if energies are measured in a time-resolved experiment. Applying the uncertainty relation in the time–energy domain, one can obtain the following equations [41]:

$$\xi_t \geq \hbar / \sigma_E \quad (10.2)$$

$$\xi_{\parallel} = v_0 \xi_t \quad (10.3)$$

$$\xi_{\parallel} \geq v_{\parallel} \hbar / \sigma_E \quad (10.4)$$

where σ_E is the energy spread of the beam, and $\sigma_E \approx \Delta E / \sqrt{8 \ln 2}$. Under good conditions, the single-electron pulses have $E_0 = 200$ keV, $\Delta E \approx 0.2$ eV, $\sigma_E \approx 0.085$ eV and $v_{\parallel} \approx 0.7c$ (speed of light). These values predict a longitudinal coherence length of $\xi_{\parallel} \approx 1.5$ μm .

After acquiring the original UEM data, it is challenging to retrieve the information for obtaining the temporal changes in comparison to the procedures conducted in

the normal TEM. The recorded data normally contain contributions from both incoherent and coherent scatterings. A key advance in accessing the very small changes embedded in the large background signal has been the application of the frame-reference method [1, 2]. The method consists of timing the electron pulses before or after the laser pulses so as to establish a reference signal (frame). The reference frame usually refers to the ground-state structure obtained at negative time. At different time delays, this methodology then allows obtaining the difference of each time-resolved evolving structure (normally at positive time) subtracted from the selected reference signal. With this treatment, the frame-reference method has the following advantages. On the one hand, the large unwanted background signal is a common contribution to all the original data, which can be practically eliminated in the difference. On the other hand, any intrinsic systematic error of the detection system will effectively be eliminated or greatly reduced by the difference. Therefore, the significance of transient structure contribution is dramatically enhanced in the frame-reference patterns.

10.3 Research Based on 4D Ultrafast TEM

In this section, we review the research reports on the phenomena of material and biological systems by using the 4D ultrafast TEM. The potential of UEM has been demonstrated by obtaining images, diffraction patterns and electron energy-loss spectra of materials and biological cells whose ultrafast dynamics are classified into reversible (stroboscopic mode) and irreversible (single-pulse mode) processes. The scope of such applications has been introduced with the subjects shown below.

10.3.1 Phase Transitions

Phase transition refers to a change from one state to another without a change in chemical composition. Generally, phase transitions are classified according to the Ehrenfest classification. The order of a phase transition is defined as the order of the lowest order derivative, which changes discontinuously at the phase boundary. There are many types of phase transitions, e.g., the first-order transition including the melting, evaporation and crystallization/condensation, and the second-order transition containing the paramagnetism–ferromagnetism and conducting–superconducting change.

With the high spatiotemporal resolution of 4D UEM, the studies of imaging and diffraction for the metal–insulator phase transition in vanadium dioxide (VO_2) are demonstrated [47, 48]. The images and diffraction patterns were obtained when the VO_2 films were driven through the transition by the heating laser pulses, as shown in Fig. 10.4. In general, the laser power required to induce phase transitions is a function of the light absorption ability (“heating”) and the thermal conductivity (“cooling”) of

a material. The material VO_2 undergoes the phase transition from a low-temperature monoclinic (M) phase to a high-temperature tetragonal rutile (R) phase at $\sim 67^\circ\text{C}$ [49]. For the samples with a thickness of ~ 200 nm, an average laser power of ~ 1 mW was sufficient to induce such phase transition. The UEM micrographs presented drastic changes after the phase transition (top left and middle). In the case of the diffraction patterns, the M and R phases share most of the diffraction peaks except several characteristic peaks of A ($10\bar{1}$), B (101) and C ($30\bar{1}$) for the monoclinic M phase (top right and bottom left). The occurrence of such distinct peaks was due to the broken symmetry upon laser illumination, which was used for probing the structural dynamics. The transient response of the diffraction peak amplitude shows the increase in the fraction of the monoclinic structure when maintaining the average laser power (indicated by the arrow in Inset, bottom right). From the fit, a rise time of 3.1 ± 0.1 ps indicates the increase in the contribution from the monoclinic structure at the temperature around the middle of the phase change. Optical reflectivity studies of the M-R transition in the ~ 50 nm-thick VO_2 have indicated that the transition occurs in 100 fs [50]. However, when the sample thickness was increased to ~ 200 nm, the rise time of 2.9 ps was observed, which was in close agreement with the 3.1 ps reported in the UEM study.

Figure 10.5 shows the spatiotemporal visualization of the spin transition in the spin crossover (SCO) nanoparticles (NPs) of the metal-organic $\text{Fe}(\text{pyrazine})\text{Pt}(\text{CN})_4$ [51]. SCO generally occurs in metal complexes wherein the spin state of the complex changes. Owing to external stimuli such as light irradiation, a variation of temperature, magnetic field and pressure, the change of the spin state is a transition from a low spin (LS) ground-state electron configuration to a high spin (HS) one of the metal's d atomic orbitals, or vice versa. The SCO phenomenon represents a prototype example of cooperative phase transition in solids. In the $\text{Fe}(\text{pyrazine})\text{Pt}(\text{CN})_4$ system, the SCO process involves a rearrangement of electrons in the t_{2g} and e_g orbitals of the Fe atom, giving rise to a diamagnetic LS state at low temperatures and a paramagnetic HS state at elevated temperatures with the elongated Fe-N bonds (top left). The metal-ligand bond distance elongates by 0.2 \AA for the Fe-N SCO systems due to the population of antibonding transition-metal e_g orbitals in the HS state [52]. As a result, the flexible 3D molecular structure of the $\text{Fe}(\text{pyrazine})\text{Pt}(\text{CN})_4$ accommodates an anisotropic unit-cell volume expansion of 13% [53].

The structural dynamics that accompany the phase transition of the individual NPs are visualized in both real and reciprocal space. The specimen in equilibrium was kept at 90 K, at which the majority of the SCO centers were in the LS state. At -300 ns before the heating laser pulse, the bend contours were observed, which might result from the warping of the NP (top right). At positive times after laser excitation, dramatic changes in image contrast were seen. The initially localized intensity spread until it almost spanned the entire NP at around 50 ns, but at later times, e.g., 400 ns, the localized feature partially reformed. The homogenization of the image intensity shortly after excitation and the concomitant increase of the diffracted intensity indicate that additional lattice planes rotate into the Bragg condition when the NP undergoes SCO with a large volume expansion. These dynamics directly map the local lattice motion when the strained NP in the LS state releases the stress upon

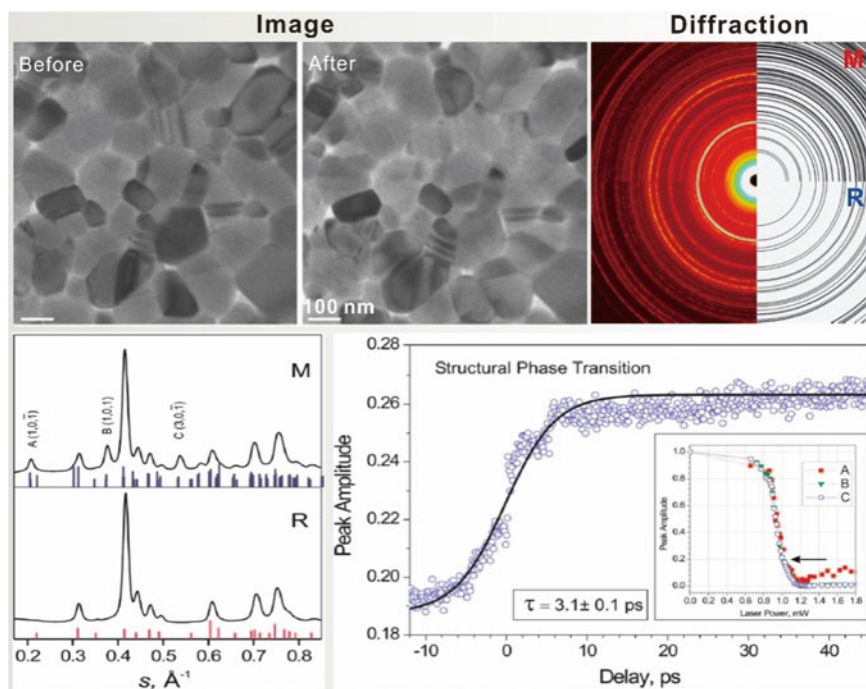


Fig. 10.4 (Top) UEM images and diffraction patterns of VO₂ before and after the phase transition. (Bottom left) The diffraction peaks of the M and R phases. (Bottom right) The temporal evolution of the peak amplitude (reproduced with permission from Ref. [47], Copyright 2006, National Academy of Sciences, U. S. A.)

laser excitation into the structurally relaxed HS state, as schematically illustrated (bottom left).

The real-space NP expansion dynamics along the two principal axes of the NP are plotted for different time delays, which directly visualizes the difference in molecular size between the two electronic spin states (bottom middle). This shows a clear spatiotemporal anisotropy in the a, b plane, namely 0.8% and 1.9% along directions 1 and 2, respectively, suggesting an appreciable friction force at the interface that hinders the motion of the NP parallel to the substrate [54]. The trends are correlated with the time-dependent diffraction dynamics (bottom right). From the diffraction patterns, the Bragg peak separations and intensities would be obtained by Gaussian peak fitting as a function of time delays. Upon laser excitation, the (110) diffraction peaks abruptly (<15 ns) moved closer to each other, while at later times they partially recovered within 230 ± 26 ns. The maximum contraction appeared at ~ 50 ns, corresponding to a unit-cell expansion of 1.7% (or 0.12 Å) in the a, b crystal plane. It suggests $\sim 75\%$ of LS \rightarrow HS conversion in the NP when a small (<0.2%) counteracting thermal lattice contraction was considered over the observed temperature range.

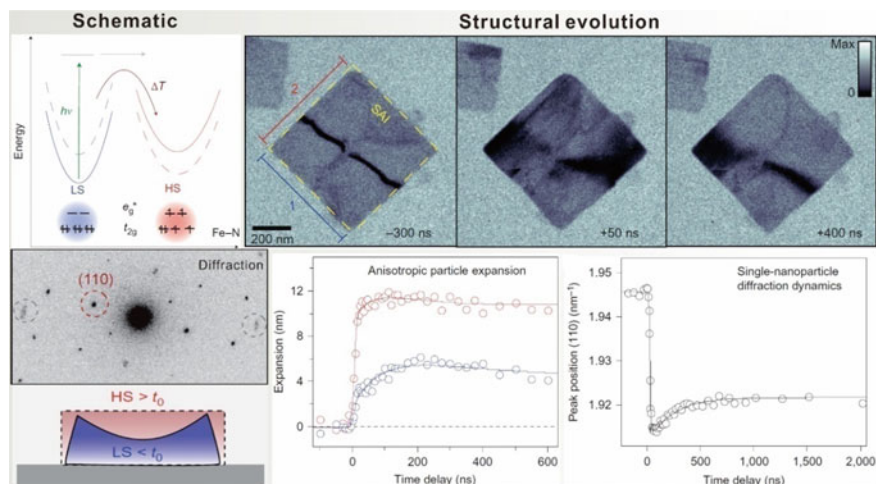


Fig. 10.5 (Top left) Induced by a temperature jump, the SCO involves a rearrangement of electrons in the orbitals of the Fe atom, resulting in the LS and HS configuration, respectively. (Top right) UEM images of the NPs taken at three different delay times. The changes in the image contrasts were observed after the laser excitation. (Bottom left) The diffraction pattern of the NP used for dynamics studies. The schematics show the morphological dynamics related to the SCO. (Bottom middle) The expansion dynamics along the two axes (marked 1 and 2 in the top right figure) of the NP. (Bottom right) The temporal evolution of the (110) peak position. (reproduced with permission from Ref. [51], Copyright 2013, Springer Nature)

Recently, the charge-density wave (CDW) phase transition has been observed in 1 T-TaSe₂ between a commensurate phase and an incommensurate phase [55]. The CDW with inherent modulation of electron density and associated periodic lattice distortion is a typical cooperative phenomenon arising from strong coupling between electron and phonon in quasi-1D (or 2D) metallic materials, which often competes and/or coexists with other ordered states (e.g., superconductivity). In the CDW phase transition, the hot electrons were generated by heating laser pulses, inducing the CDW melting. The energy was transferred from the electronic system to phonons at a time scale of around 300–500 fs. It then relaxed through further electron–phonon and phonon–phonon pathways, leading to lattice heating. The results suggest that the photo-induced CDW transition in 1 T-TaSe₂ is thermally driven, with a recovery time of (3 ± 1) ps from the incommensurate phase to the commensurate phase.

10.3.2 Oscillation Behavior

With the rapid development of novel nanoscale devices, many investigations of nanostructures have emerged due to their unique electrical, optical and mechanical properties that can be used in a wide variety of electronic, optoelectronic and

electromechanical applications [56, 57]. To realize the integration of nanostructures into functional nanodevices, the mechanical behavior (e.g., Young's modulus) of such nanostructures needs to be addressed. 4D UEM has been demonstrated to be a unique technique for nondestructively studying the mechanical properties of nanostructures [58–61]. Graphite was chosen for the demonstration because of its unique anisotropic electromechanical properties of high strength, and electrical/thermal conductivity along the 2D graphene sheets, in which the atoms of each sheet are covalently bonded in a honeycomb lattice. Figure 10.6 shows the visualization of vibrations of mechanical drumming in the single-crystalline graphite film on the nanosecond and microsecond time scale [59]. The stress was induced impulsively by a ns heating pulse, while the motions of the sample were observed in real space using the stroboscopic electron pulses (top left). Visual changes were seen in the contrast fringes which change their location in the images as time elapsed. To more clearly display the temporal evolution, difference images referencing the $-1 \mu\text{s}$ frame were constructed (top right). In the difference images, the regions in white or black indicate locations of surface morphology change, while gray regions are areas with no contrast change with respect to the reference frame. Note that the image changes here were fully reproducible, retracing the identical evolution after each heating pulse. Therefore, the reversal of contrast with time directly images the oscillatory behavior of the drumming.

The quantitative cross-correlation values between the image at each measured time point and the reference image are plotted against the delay times ranging from ten ns to hundreds of μs (middle panel). Upon impulsive laser heating in the $\sim 5 \mu\text{s}$ range (regime I), the image cross-correlation changed considerably in a “chaotic” manner. After $\sim 10 \mu\text{s}$, however, the cross-correlation changes started to exhibit periodicity (regime II), and at a longer time, a well-defined resonance oscillation appeared (regime III, bottom left), indicating that the motion of the nanofilm finally collapsed into a global resonance. It should be pointed out that the shape of the cross-correlation dynamics was robust at the laser fluencies ranging from ~ 2 to 10 mJ/cm^2 . The resonance modes are highlighted by taking the fast Fourier transform (FFT) of the image cross-correlation during the time of $0\text{--}100 \mu\text{s}$ (bottom right). The FFT presents several peaks at different frequencies. Various local mechanical modes at early time damped out and one global mode around 1 MHz survived. After fitting to a Lorentzian, the peak yielded a resonant frequency of 1.08 MHz. This dominant peak was the fundamental vibration mode of the plate in graphite. Note that the one at 2.13 MHz is attributed to the overtone of 1.08 MHz because of the truncated nature of the cross-correlation.

A square mechanical resonator clamped at three edges has a fundamental resonance mode of f_0 that is given by

$$f_0 = A \frac{d}{L^2} \left[\frac{Y}{(1 - \nu^2)\rho} \right]^{1/2} + f(T) \quad (10.5)$$

where Y is Young's modulus, ρ the mass density, ν Poisson's ratio, L the dimension of a grid square, d the thickness of the graphite. A is a constant of 1.103 and $f(T)$

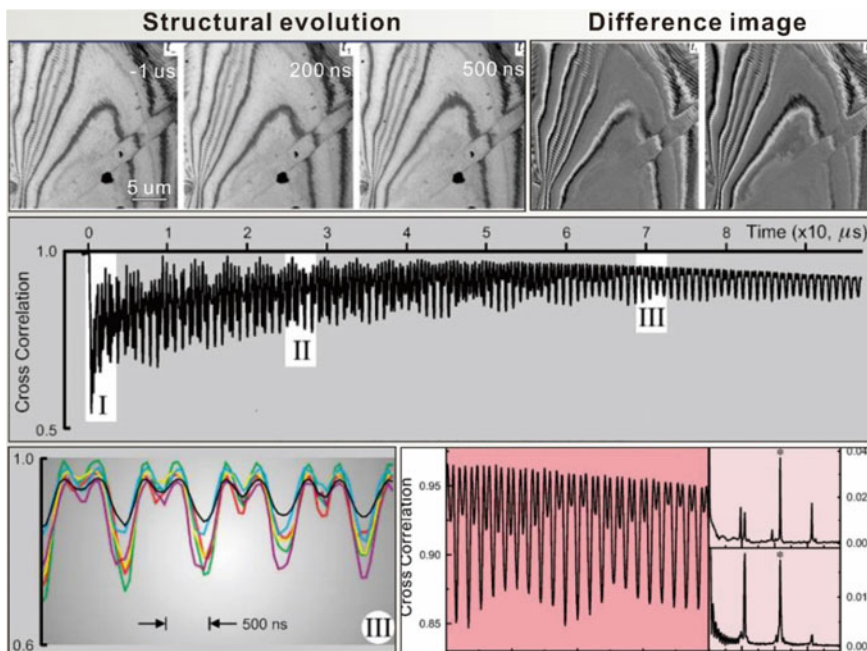


Fig. 10.6 (Top left) UEM images recorded at different delay times, displaying the structural evolution of the graphite. (Top right) Difference images with respect to the reference image taken at $-1 \mu\text{s}$. (Middle panel) Temporal evolution of the image cross-correlation. It was classified into three regimes, from the chaotic to the global resonance behavior. (Bottom left) The zoomed-in image cross-correlation at the regime III. (Bottom right) Resonance dynamics and the corresponding FFTs (time range of 0–100 μs and 60–100 μs , respectively) of the graphite. (reproduced with permission from Ref. [59], Copyright 2008, American Chemical Society)

due to tension is taken to be zero in this case [62]. Substituting the values of $d = 75 \text{ nm}$, $\rho = 2260 \text{ kg/m}^3$, $\nu = 0.16$ and $L = 40 \mu\text{m}$ into Eq. (10.5), Young's modulus of the graphite obtained from the observed resonance frequency was estimated to be 1.0 TPa. This value was in good agreement with the in-plane average value of 1.02 TPa, obtained using the common stress–strain measurements [63].

In addition to the mechanical drumming resonance, direct visualization of the acoustic-phonon dynamics and acoustic vibrations [64–66], and spatiotemporal evolution of coherent elastic strain waves [67] have also been demonstrated using 4D UEM in recent years.

10.3.3 Electron–Phonon Coupling

As introduced in the historical development, UED is a powerful technique for investigating electron–phonon coupling behavior in materials. Equipped with a diffraction

methodology similar to that in UED, 4D UEM not only provides such capability, but also has the flexibility to disclose the coupling mechanisms in the local selected area of interest [58, 68]. Figure 10.7 presents an example of using 4D UEM to study the electron–phonon coupling in the gold films [58]. The real-space imaging (left panel) shows the time-dependent morphology, while the reciprocal diffraction (middle panel) provides structural changes on the ultrashort time scale. In the initial sample before the clocking pulse, some bend contours were observed in the image (-84 ps). After the heating pulse at positive times (e.g., 66 ps), the bend contours moved because of the tilting of the local crystal lattice caused by the deformation. The insets are the difference images obtained when referencing the -84 ps frame for $t = 66$ ps and 151 ps, respectively. The characteristic features in the difference images are on the nanometer scale, which reflect the local dynamics of deformations. The transient structural evolutions were supported by the changes in the diffraction patterns (middle panel), e.g., the two frames at a negative time and at $+50$ ns. Additional Bragg spots were visible in the latter, which were due to the bulging of the film upon the laser heating at longer times. Knowing the film surface was normal to the $[100]$ zone axis, the diffraction patterns were properly indexed according to the face-centered cubic structure of Au. The additional spots were reflections from the $\{113\}$ and $\{133\}$ planes whose interplanar spacings were measured to be 1.248 and 0.951 Å, respectively.

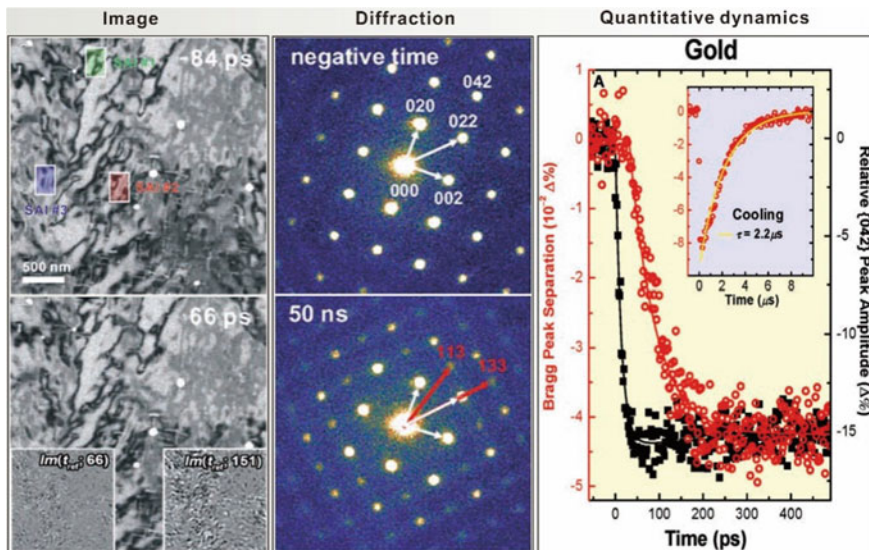


Fig. 10.7 (Left panel) UEM images of the gold film taken at different delay times. The insets are the difference images referencing the -84 ps frame. (Middle panel) Time-resolved diffraction patterns. (Right panel) The time dependence of the Bragg peak separation and the $\{042\}$ peak amplitude (reproduced with permission from Ref. [58], Copyright 2008, The American Association for the Advancement of Science)

The transient amplitude of {042} diffraction peaks drops significantly with the delay times (right panel). The rise time was obtained to be 12.9 ps from the exponential fitting. The atomic-scale motions caused by the heating pulse lead to structural and morphological changes, resulting in the variation of the diffraction intensities. In the case of metals, the lattice temperature is generally acquired after a significant increase in electron temperature. Because the Au film was nanoscale in thickness, the initial temperature was essentially uniform across the atomic layers and the heat would dissipate laterally. From the electron and lattice heat capacity constants of $C_1 = 70$ and $C_2 = 2.5 \times 10^6$ J/(m³·K), and the electron–phonon coupling of $g = 2 \times 10^{16}$ W/(m³·K), the initial heating time was estimated to be ~10 ps for the electron temperature of ~2500 K, in good agreement with the observed rise time of 12.9 ps. Owing to the confinement effect that limits the ballistic motion of electrons in the specimen, the time scale of heating in the nanoscale material (~10 ps) is longer than that in the bulk sample (~1 ps) [69]. The time constant from the recovery transient in the inset was determined to be 2.2 μs, which was consistent with the calculations of 2D lateral heat transport using the thermal conductivity of 3.17 W/(cm·K) at 300 K, and laser spot diameter and fluence of 60 μm and 7 mJ/cm².

The change in average separation of all diffraction peaks observed in the [100] zone axis is delayed by 31 ps with a rise time of 60 ps (right panel). The delay in the onset of separation change is similar to the time scale for the amplitude of the 042 peak to reach its plateau value of 15% reduction. Upon the pump laser heating, the lattice was hot up to 30 ps, and the lattice temperature was estimated to be 420 K according to the calculated Debye–Waller factor for structural changes. Because of the macroscopic lattice constraint, the atomic stress would not lead to changes in lateral separations within ~30 ps. As time elapsed, the structural constraint would be relieved, which could be disclosed from the morphology warping change being correlated with atomic displacements in the structure. Indeed, the time scale of the initial image contrast change is comparable to that of plane separations in diffraction (60–90 ps). The change of the average peak separation (0.043%) in Au results in a lateral lattice constant change of 0.17 pm. When this change was applied to the thickness, the stress over an 11-nm sample would give a total expansion of 4.7 pm, reaching the maximum bulging of 1–10 nm that was dependent on the lateral scale.

10.3.4 *Crystal Nucleation and Growth*

Nucleation is the initial process that occurs in the formation of a crystal from a vapor, a liquid or a solution. In this process, a small number of molecules, atoms or ions are arranged in a characteristic pattern of a crystalline solid, forming a site upon which additional particles are deposited as the crystal grows. Subsequently, the growth of a crystal is the process where a pre-existing crystal (nucleus) becomes larger as more molecules or ions add to the positions of the crystal lattice. These elementary steps and the involved dynamics occur on different time scales. A fundamental understanding

of whether crystal formation involves a free-energy surface of one barrier or a two-step process with an intermediate structural state (amorphous or liquid) is important and has been the subject of many studies.

Figure 10.8 shows the direct visualization of the transformation of amorphous TiO_2 nanofilm from the liquid state, passing through the nucleation step, and finally to the ordered crystal phase [70]. Before the laser excitation (top left), the morphology of the film was uniform, and the corresponding diffraction was diffused with characteristics of the amorphous phase. Upon the single-pulsed laser irradiation, clear morphological changes were observed in the image, displaying the grain formation with well-defined diffraction rings. Such behavior indicates that the initial amorphous film was transformed into the liquid state by the laser pulse illumination, and the crystallites were then formed at longer times. In order to reveal such an involved irreversible process, each time the sample was irradiated with a single laser pulse with specific time delays, and the crystallinity was measured from the single-pulse diffraction pattern (bottom left). The diffraction rings at the long times (seconds) suggest that the formed phase after relaxation was the anatase TiO_2 . Therefore, at shorter times (e.g., 1500 ns), the normalized diffraction to the total electron counts would provide the time-dependent ratio of the amorphous-to-anatase phase. The transient diffraction profile at 1500 ns was well fitted using a linear combination of two profiles, namely one at a negative time ($54.7 \pm 4.3\%$) and the other at seconds ($45.3 \pm 4.3\%$).

By employing the same procedure for each transient diffraction frame, the degree of crystallization was plotted with the delay times (right panel). At each given time delay, diffraction data from at least three independent experiments (before, during and after the laser pulse) were obtained and averaged to represent the change (an example shown in the inset). Two robust plateaus for the transformation were seen and the rates of the processes involved at each time delay were obtained from the analytical fitting over the entire time range of 50 μs . Note that the first plateau bridges two distinct rate processes. From the fit, three time constants of 294 ns (α^{-1}), 271 ns (β^{-1}) and 6.72 μs (γ^{-1}), together with the degree of crystallization (η), were quantitatively determined. The structural crystallinity η is 0.45 at the first plateau, and at longer times, reaches its maximum value of 0.9 at the second plateau. It is seen that the slope for reaching the first plateau is less steep than that of the second plateau.

The above phenomena were understood by considering the temperature rise in the TiO_2 film. Knowing the laser fluence and the thermodynamic and optical properties of the material, the temperature after the laser heating was estimated to be 2166 ± 193 K [70], which was consistent with the melting point of TiO_2 (~ 2130 K). Melting of film samples normally occurs on the picosecond time scale [22], and consequently, the quenching of the melt gives rise to recrystallization during cooling down. The crystallization process from the melt may involve a one-step barrier crossing or a two-step nucleation pathway [71, 72]. The observation of two successive S-shape curves for the crystallinity η as a function of time indicates the presence of an intermediate structure on the free-energy surface. In the case of two involved plateaus, the existence of the intermediate plateau is necessary for the nucleation step when the latent heat

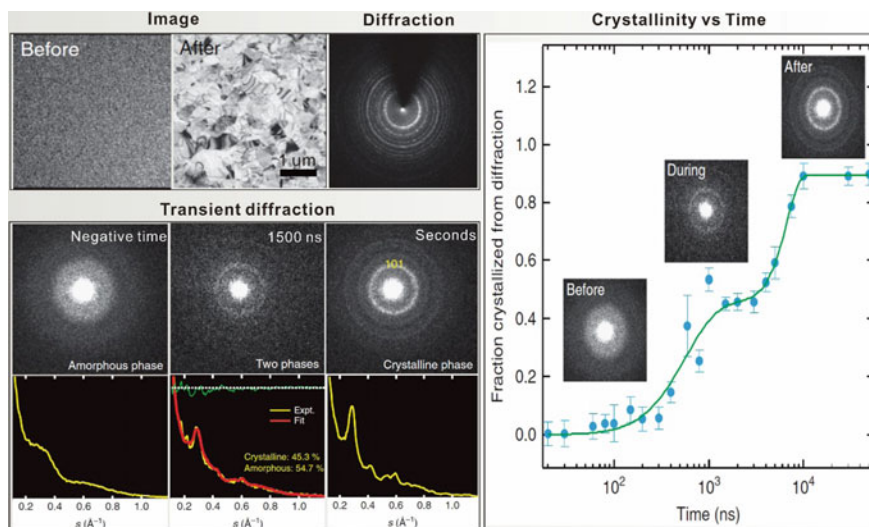


Fig. 10.8 (Top left) UEM images of the TiO₂ film before and after the laser excitation. The diffraction pattern indicated the formation of the polycrystalline anatase TiO₂ after laser heating. (Bottom left) Transient diffraction profiles showing three phases at negative, intermediate and end times. (Right panel) Time-dependent fraction of the crystallized phase obtained from the diffraction intensities. Single-pulse diffraction patterns represent the typical time points before, during and after the process is completed (reproduced with permission from Ref. [70], Copyright 2015, Springer Nature)

and entropy decrease. Up to the first plateau, two rates (α and β) control the formation of the intermediate step: α^{-1} (294 ns) is the time for the process that involves the hot-liquid TiO₂ reaching the isothermal temperature of ~ 2130 K, while the faster β^{-1} (271 ns) defines the nucleation as the latent heat is lowered by the action of the surroundings. The relatively long time ($6.72 \mu\text{s}$ for γ^{-1}) corresponds to the process for crystal formation obtained from the first-to-second plateau. Therefore, single-pulse transient diffraction studies provide the temporal behavior of crystallinity that exhibits the unique two-step dynamics, with the presence of intermediate structure reflecting the precursor of the ordered crystal state.

10.3.5 Reaction Dynamics

Chemical reaction is a process in which one or more substances (reactants) are converted to one or more different substances (products), which plays a central role in different industries and even in our daily life. In general, chemical reactions require a sufficient amount of energy to cause the substances to collide with enough precision and force so that old chemical bonds are broken and new ones are formed. The rates of chemical reactions are associated with chemical kinetics. Figure 10.9 shows the

redox reaction dynamics in the crystalline semiconductor [Cu(TCNQ)] (TCNQ = 7,7,8,8-tetracyanoquinodimethane, $C_{12}H_4N_4$) shocked by the laser pulses [73, 74]. Following this shock with 80 MHz repetition rate, the Cu(TCNQ) crystal fractured and was separated (formation of nanoscale channel) by ~ 140 nm (top left, “off” state). The fractured crystal was used for the irradiation experiments. When the sample was irradiated with laser pulses, the crystal expanded along the long axis and completely closed the gap, namely the two faces of the crystal came into full contact (top middle, “on” state). The gating (closing and opening) of the nanoscale channel (gap) could be repeated by switching between the on and off modes. By measuring the channel opening/closing while varying the number of frames recorded, the time scale of the channel switching was estimated to be less than 10 μ s.

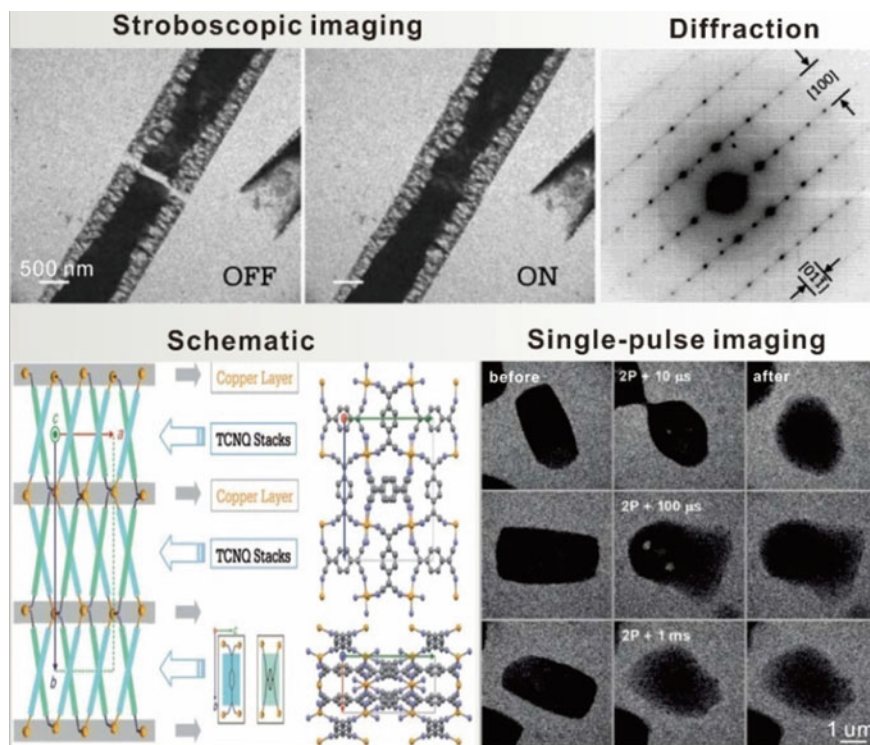
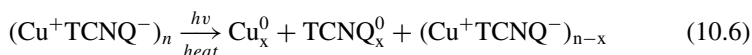


Fig. 10.9 (Top left) UEM images of channel gating in the Cu(TCNQ) crystal. The “OFF” and “ON” correspond to the states without and with pulsed-laser irradiation, respectively. (Top right) Typical diffraction pattern of the crystal obtained along the [011] zone axis. (Bottom left) Schematic of the Cu(TCNQ) molecular structure. The ball-and-stick diagrams in the top and bottom are the structures viewed along the *a* and *b* axes, respectively (reproduced with permission from Ref. [73], Copyright 2007, John Wiley and Sons). (Bottom right) Single-pulse images of the crystal before, at specific time delays (10 μ s, 100 μ s and 1 ms), and several seconds after exposure to laser pulses. (reproduced with permission from Ref. [74], Copyright 2011, American Chemical Society)

The macroscopic gating process was understood from the microscopic structural dynamics. The change in the a axis [100] before the crystal melting obtained from the diffraction data was $\sim 0.2 \text{ \AA}$ (top right). This change in intermolecular planes suggests that for a channel width of 40 nm, the macroscopic effective propagation length is $\sim 2 \text{ }\mu\text{m}$, which agrees well with the length scale of the crystal. Therefore, the gating behavior along the stacking axis [100] indicates the anisotropic characteristics. The forward motion was not caused by equilibrium thermal heating because of the observed lack of expansion in the direction perpendicular to the stacking (the thermal expansion coefficient for $\alpha_{\perp} = 5.8 \times 10^{-5} \text{ K}^{-1}$ is about half of that for $\alpha_{\text{stacking}} = 12 \times 10^{-5}$ [75]). As known, the strong electron acceptor (π acid) TCNQ would undergo a redox reaction with metals such as Cu and Ag at room temperature. In the case of the resulting Cu(TCNQ) crystal, Cu^+ and TCNQ^- form discrete columnar stacks in a face-to-face configuration with a strong overlap in the π system (bottom left). The Cu atoms are bound in a four-coordinate distorted tetrahedral geometry to the N atoms on the cyano groups of the TCNQ molecules. The closing or opening of the nanoscale channel is a modulation of the π -electron interactions of the stacked TCNQ molecules. As shown in Eq. (10.6), the initial crystal is in the $(\text{Cu}^+\text{TCNQ}^-)$ electronic structure before the incoming laser pulses. During the “on” period, the laser excitation creates a mixed-valence structure, which leads to charge transport and to a new lattice expanding along the a stacking direction:



Single-pulse imaging (before, during and after the laser pulses) was used to determine the time scales required for the structural changes and the formation of Cu^0 NPs excited at a wavelength of 671 nm (bottom right) [74]. After one-pulse (1P) excitation, the morphological changes were observed, which were complete within $\sim 100 \text{ ns}$. Note that no noticeable Cu^0 formation was seen, regardless of the time at which the redox reaction was probed. When two-pulse excitation was employed, however, the crystal initially displayed melting, which was evidenced by the formation of the bubbling liquid in less than $10 \text{ }\mu\text{s}$. It was followed by cooling and resolidification. The formation of Cu^0 NPs (dark dots in the images) occurred only after $100 \text{ }\mu\text{s}$, which was complete within 1 ms after the second excitation pulse.

4D UEM is also capable of studying other kinds of reaction dynamics, for example, eutectic reactions. A eutectic reaction is a special chemical/physical reaction involving multiple phases, solid and liquid. A eutectic system refers to a unique thermodynamic entity, which forms a lattice structure with a specific atomic ratio between the constituents at the eutectic temperature that defines the lowest temperature at which the mixed substances become fully molten. Figure 10.10 shows the direct imaging and control of the phase reaction dynamics of a single, as-grown freestanding GaAs nanowire (NW) encapped with a gold NP [76, 77]. The eutectic-related phase reaction processes of the NWs were induced and controlled by a temperature jump triggered by a laser heating pulse, followed by a delayed photo-generated electron packet to probe the spatiotemporal evolution of the nanostructures. In the

stroboscopic approach (top panel), the integrated diffraction intensity was plotted against time for determining the time constant of the nonequilibrium thermodynamics of the NW at a low laser fluence of 3 mJ/cm^2 . Because of the temperature jump initiated by the heating laser pulses, the integrated diffraction intensity displayed a quick decrease after time zero and then a relatively slow recovery of the diffraction intensity. From the fit, the time constant τ for cooling was estimated to be $123 \pm 12 \text{ ns}$.

Guided by the extracted time scale, the transient intermediates of the eutectic-related process of the NWs were imaged by using a single-pulse mode of 4D UEM.

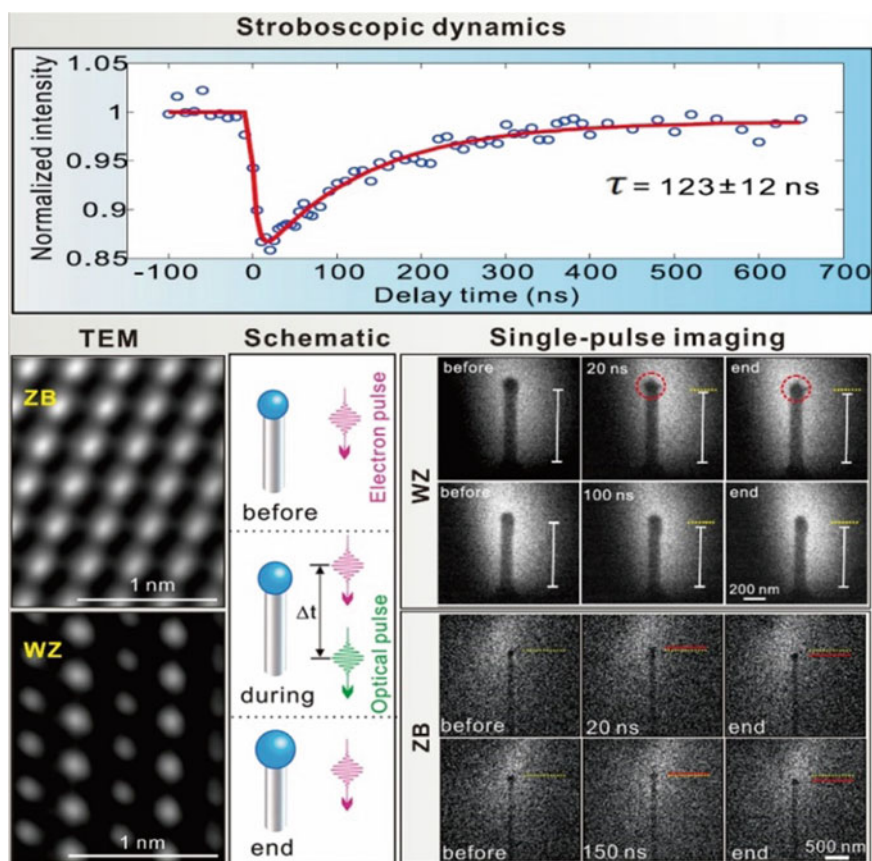


Fig. 10.10 (Top panel) Normalized diffraction intensity as a function of delay time (reproduced with permission from Ref. [76], Copyright 2017, National Academy of Sciences). (Bottom left) High-resolution TEM images of the ZB and WZ GaAs NWs. (Bottom middle) Schematic diagram showing the reaction dynamics studied by single-pulse imaging methodology. (Bottom right) Single-pulsing imaging of the transient structures of the WZ and ZB NWs before, during and after the laser excitation. (reproduced with permission from Ref. [77], Copyright 2019, American Chemical Society)

Two systems of GaAs polytypes, namely cubic zinc-blende (ZB) and hexagonal wurtzite (WZ) structures, were demonstrated here (bottom left). The time sequences of the pump – probe experiments are schematically illustrated in Fig. 10.10, bottom middle. The snapshot with the notation of “before” (initial state) or “end” (final state) was taken when the laser excitation pulse for the sample was blocked, while the image labeling “during” denoted the ongoing dynamics that were captured at a specific time delay with respect to the laser excitation pulse. Four rows in the single-pulse images show the transient states of the NWs after a single optical pulse at different delay times (bottom right). For the WZ NW (first row), a length shrinkage as well as a clear shape change of the top bead (marked with a circle) was observed between the left (“before”) and middle (“20 ns”) images. The bead shape continued its change even after the incident laser pulse was removed (“end”). When observed at 100 ns and at the state after the process ended, however, the length and shape of the NW almost remained unchanged (second row). It indicates that the thermal energy induced by the pump pulse was not sufficient to cause an obviously morphological change of the NW after ~ 100 ns. Further selected-area diffraction studies disclosed that two new phases (AuGa and AuGa₂) were formed at the bead-NW region, which were due to the eutectic reaction, liquid \rightarrow AuGa + AuGa₂. This reaction occurred at 725 K, which was much lower than the melting points of the individual components in the initial materials (Au, 1337 K; GaAs, 1511 K). As a result of such a reaction, the length reduction of the NW was observed.

For the ZB NW (third and fourth rows), there were obvious length reductions of the NW after the whole process had ended. Interestingly, however, the NW length displayed an intermediate increase of ~ 45 nm at 20 ns in comparison to that of the initial NW (“before”). No such transient increase of the NW length was seen when the delay time was longer than ~ 150 ns, suggesting that the process was complete in about 150 ns. This phenomenon was different from that observed in the WZ NWs. The difference could be caused by the favorable material transport along the NW surface. As the temperature exceeded the phase-reaction point, the liquid phase appeared toward a certain distance along the ZB NW as a result of the fast surface transport, leading to the expansion and transient length increase of the ZB NW. Combined with theoretical modeling, the thermodynamic parameters of the newly formed alloy phases, for example, the latent heat and specific heat of AuGa were determined to be 21 kJ/mol and 41 J/(mol K), respectively. It demonstrates that 4D UEM is powerful for quantitatively determining the physical properties of a nanoscale object with a small quantity, especially when not available in bulk counterparts.

10.3.6 Dynamics in Liquids

Liquid cell electron microscopy has attracted significant interest in recent years. It has been possible to image through liquids with nanometer resolution, demonstrating promising applications in NPs growth, electrochemical reactions and imaging of living biological cells [78–80]. Integrated liquid cells into 4D UEM, the temporal

resolution of studying dynamics in liquids has extended to the femtosecond domain. Figure 10.11 shows the rotational dynamics of gold NPs in an aqueous solution [81, 82]. The gold NPs (60–90 nm in diameter) were capped by citrate ligands for stabilization, which were dispersed in an aqueous solution (top left). The solution (~300 nm thick) was sandwiched between two 20-nm-thick, electron/laser-transparent silicon nitride membranes (liquid cell). The precisely timed laser excitation pulse and electron probe pulse arrived at the NPs in the liquid cell through the silicon nitride membrane window. Single-shot/pulse images were then recorded at specific delay times on the same NP to trace its rotational dynamics in the solution. On the long time scale (first row, top right), the rotational motion of the NP dimers (D1, the ratio between the NP diameters is 1:1.1) was acquired by using the continuous electron beam (e-beam) imaging mode. Upon laser excitation, the dimer presented distinct orientations indicated by the red–blue arrow pairs. The direction of the NP rotation would reverse at certain times (arc arrows), displaying the manner of a “random walk”.

The dimer trajectories at different starting times τ_0 and ending times t were extracted to analyze the statistical properties of the rotation angle $\theta(t)$, where the angular displacements of the trajectories were given by $\Delta\theta(t) = \theta(t + \tau_0) - \theta(\tau_0)$. The mean square angular displacement (MSAD) of the NP dimer shows a linear increase in the log–log scale plot (bottom left), which follows a power law of $\langle [\Delta\theta(t)]^2 \rangle \propto t^\alpha$ (the exponent α is associated with the angular displacement distribution). On the basis of Einstein’s theory and the Langevin equation [83], the following equations are described for 2D Brownian rotational motion:

$$\langle [\Delta\theta(t)]^2 \rangle = 2D_r t \quad (\text{diffusive regime}) \quad (10.7)$$

$$\langle [\Delta\theta(t)]^2 \rangle = \omega_{\text{rms}}^2 t^2 \quad (\text{ballistic regime}) \quad (10.8)$$

where D_r is the rotational diffusion coefficient and ω_{rms} the root mean square (RMS) angular velocity. For the D1 dimer with the two NPs of similar size (the diameter ratio of 1:1.1), its MSAD presents the conventional diffusive behavior ($\alpha = 1.11$). By increasing the morphological asymmetry of the NP dimers, the retrieved value of α increases from 1.11 for the D1 dimer to 1.51 for the D2 dimer (the diameter ratio of 1:1.3), and further to 1.95 for the D3 dimer (the diameter ratio of 1:1.5). It suggests that the D2 dimer shows a super diffusive rotation ($1 < \alpha < 2$), while the highly asymmetric D3 dimer exhibits a ballistic rotation ($\alpha \approx 2$). By introducing the asymmetry, a full transition from conventional diffusive rotation to superdiffusive rotation and further to a ballistic rotation was observed.

Single-pulse images were used to disclose the time scale and force for the rotation of the NP dimers. An example of the state at 26 ns is demonstrated in the second row, top right of Fig. 10.11. In comparison to the initial position (“before”), a rotation angle of 12° was observed. At different delays, the rotation angles are 0° , 2° , 12° , 17° , 22° and 29° for 10, 20, 26, 42, 90 and 150 ns, respectively (bottom right). Note that the rotation angles are absolute values here regardless of the rotation direction

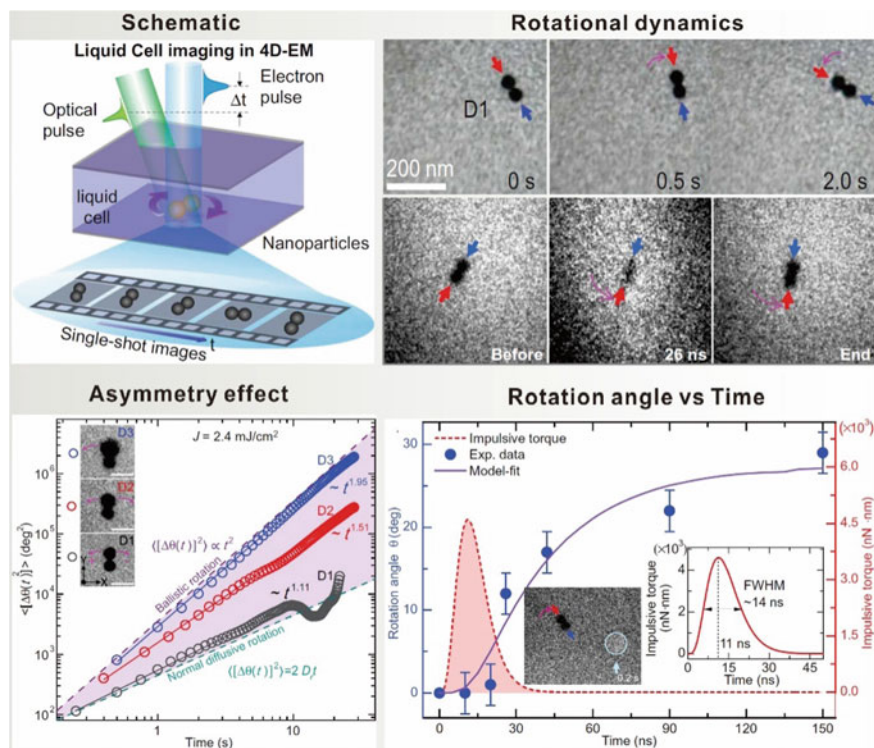


Fig. 10.11 (Top left) Schematic diagram of 4D imaging of NP motions in liquids. (Top right) Rotation dynamics of the Au dimer at the long (upper) and short (bottom) time scale. (Bottom left) The temporal evolution of the MSADs of three kinds of dimers (Inset, scale bar of 100 nm). (Bottom right) Time-dependent rotation angles of the Au dimer. The insets show that the dimer rotation was triggered by the nanobubbles. (reproduced with permission from Ref. [81], Copyright 2017, The American Association for the Advancement of Science)

(clockwise or counterclockwise). The rotation angle only increases to 2° from 10 to 20 ns, but rapidly to 17° at 42 ns, followed by a slow increase. As known, the NPs inside the liquid cell are weakly bound near the substrate surface by the weak electrostatic interaction [84]. Because of the strong optical absorption of gold NPs at 520 nm, the laser pulse heats up the NPs in hundreds of ps, resulting in a nonequilibrium temperature of ~ 900 K at the fluence of 10 mJ/cm^2 . The high nonequilibrium temperature (far above the boiling point ~ 400 K of water) of the NP is sufficient to overcome the latent heat of water and to convert the adjacent water molecules into steam nanobubbles, which is visible near the initial position of the dimer (an example is marked by a circle in the inset of the bottom right figure). Owing to the nonuniform heating caused by the dimer asymmetry, the rapid nucleation, expansion and collapse of the steam nanobubbles near the dimer surface would induce an impulsive force and torque to actuate the rotation and translation of the dimer.

Combined model simulations and experimental results indicate that the impulsive torque from the photo-induced nanobubbles has a peak value of 4.6×10^3 nN·nm and a duration of ~ 14 ns, respectively (bottom right, inset). Because of the large impulsive torques, the rotational diffusion coefficient ($4.68 \text{ rad}^2/\text{s}$) of the dimer is nearly four orders of magnitude larger than that of the colloidal nanorods without laser pulse excitation [85]. As the asymmetry of the dimer increases, the random impulsive torques have a much higher probability in one direction than that in the opposite one. Beyond a certain critical point, the impulsive torques are unidirectional for the asymmetric D3 dimer, indicating that the photo-induced nanobubbles occur at the nearly identical position of the dimer for triggering the ballistic rotation.

4D UEM also permits to study a wide range of nanofluidic phenomena in individual nanotubes. With a temperature jump induced by a single laser pulse, the melting of the lead core in a ZnO nanotube is visualized in situ [86]. The core reaches a temperature of several hundred degrees above the melting point, then cools on a time scale of ~ 200 ns. The laser-induced pressure jump induces the fission of a small lead column, the explosion of a droplet or even the rupture of the tube wall. The temporal changes of the expansion dynamics of the lead column would enable studies of the viscous friction involved in the flow of liquid within the nanotube.

10.3.7 4D Electron Tomography

Electron tomography, as a means to reconstruct 3D objects from a series of 2D projections, provides 3D information on material and biological structures including those of nanostructures, viruses, bacteria and cells. Historically, the initial advances in the reconstruction of 3D biostructures were traced to the 1960s [87, 88]. With the recent development of 4D electron tomography by integrating the fourth dimension, the different time frames of tomograms constitute a movie of the object in motion. It enables the studies of nonequilibrium structures and transient processes, which makes use of the full space–time range with the nanometer–femtosecond spatiotemporal resolution. Figure 10.12 demonstrates the different modes of motion in a bracelet-like carbon nanotube [89]. In the schematic representation of the approach, an arrangement of sample tilt is configured to enable the recording of various 2D projections of an object at a given time (top left). Specifically, the frames are taken for each degree of tilt with various delay times (top right). The 2D projections at different angles are then constructed into a 3D tomogram at a well-defined time, t_i^α , where i denotes a given time step and α is the tilt angle. Each 3D tomogram at the given delay time t_i represents a 4D frame.

The evolutions of 4D tomograms of the carbon nanotube for two representative tilt angles were observed at early times (bottom left) and at long times (bottom right), respectively. The tomograms were constructed from ~ 4000 projections for a whole series of tilt angles and time steps, displaying the temporal evolution of the 3D morphological and mechanical motions. At early times (bottom left), the volumes in black show the original state of the nanotube while those in beige display the

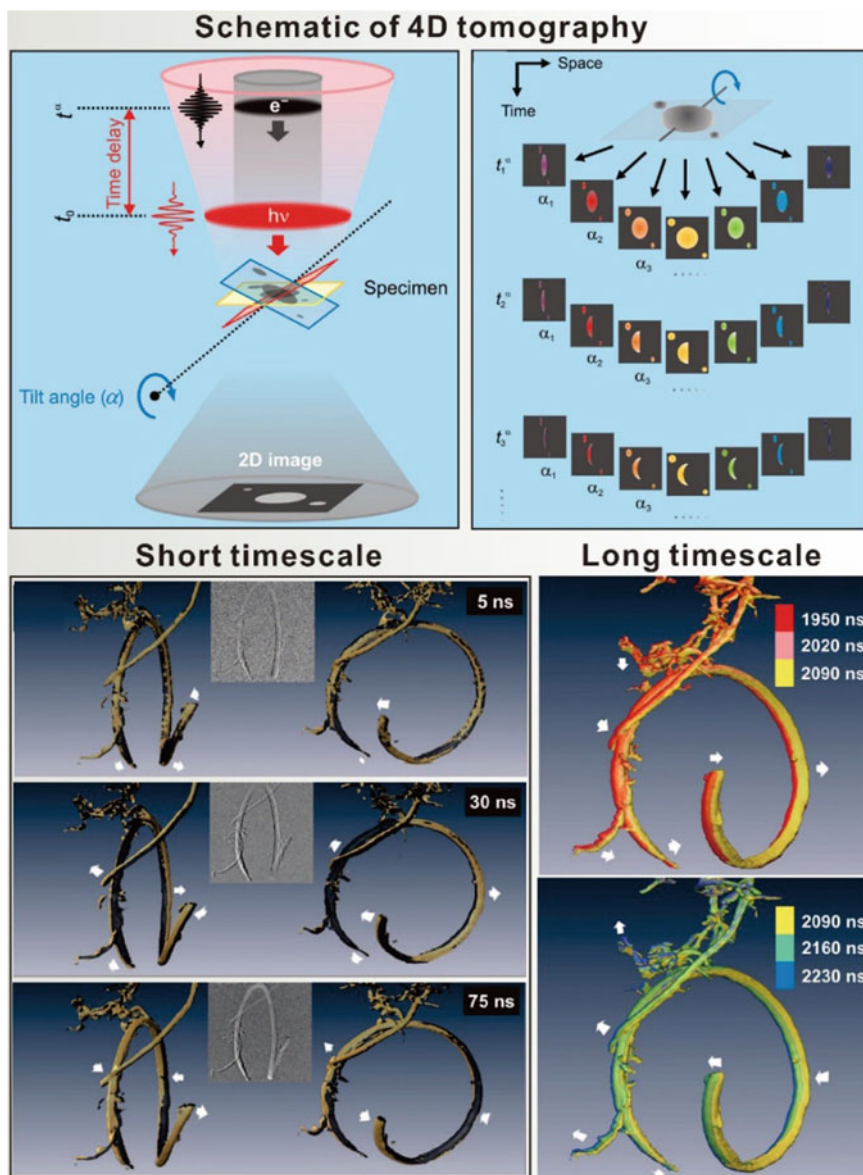


Fig. 10.12 (Top panel) Schematic diagram of 4D electron tomography. (Bottom left) Representative 3D images of the carbon nanotubes at early time delays. The gray images in the insets describe the original configuration of the nanotube. (Bottom right) The time-dependent structures visualized at longer times. (reproduced with permission from Ref. [89], Copyright 2010, The American Association for the Advancement of Science)

new configuration displaced from the original position. As time elapsed, the bracelet began to move after the heating pulse. Specifically, at 5 ns, the two ends of the ring started to move. The bending motion of the ring was observed at 30 ns, namely the two ends moved in the same direction while the middle part of the ring displaced oppositely. This bent-ring configuration nearly restored the structure to its original volume density of the ring at ~ 75 ns. At long times (bottom right), the bracelet resonated on a slower time scale. As seen from 3D changes in the volume density, the bracelet wiggled with displacement in the same direction from 1950 to 2090 ns. However, the direction of motion was reversed in the next 140 ns, which indicated that the resonance motion was a wiggling of the whole ring around the anchored position.

Similar to the oscillation behavior shown in the 2D case, resonance frequencies of motions in the complex structures after laser-driven impulsive heating can be also obtained by the FFT analysis. The restoring period of ~ 70 ns corresponds to a well-defined resonance frequency 13.5 MHz obtained in the analysis. On the assumption of a beam undergoing bending motions in an open ring, Young's modulus of the carbon nanotubes was estimated to be 61 GPa. This value is in the range reported for carbon nanotubes, from ~ 1 TPa for diameters of < 10 nm to ~ 100 GPa for larger diameters [90, 91].

10.3.8 PINEM

Over the past years, optical near-field microscopies have enabled spatial resolutions beyond the diffraction limit, but would not provide the atomic-scale imaging capabilities of TEM. Given the nature of interactions between electrons and photons through nanostructures, it is possible to achieve imaging of evanescent electromagnetic fields with a train of electron pulses. Photon-induced near-field electron microscopy (PINEM) is such a technique in EELS of 4D UEM to produce and then image evanescent electromagnetic fields on the surfaces of nanostructures with the spatiotemporal resolution of femtosecond, nanometer and below. Figure 10.13 shows the PINEM spectra and images of an individual carbon nanotube irradiated with the intense femtosecond laser pulse [92]. Two separate spectra are displayed for comparison (top left), namely the $t = -2$ ps spectrum obtained when the electron probe pulse arrived before the laser pump pulse, and the $t = 0$ fs spectrum recorded when the electron and photon pulses were configured for maximum overlap. For the $t = -2$ ps one, besides the zero-loss peak (ZLP) only the π and $\pi + \sigma$ plasmon peaks are observed at 6 and 25 eV, respectively [93]. As known, an electron cannot absorb a quantum of electromagnetic energy in free space because of the lack of energy-momentum conservation. However, with the presence of a third body, e.g., a nanotube here, the $t = 0$ fs spectrum consists of discrete peaks of decreasing intensity on both the lower- and higher-energy side of the ZLP. A magnified view of the spectrum (inset) reveals that these discrete peaks occur at integer multiples of 2.4 eV ($\hbar\omega$) due to the interaction of the 200 keV ultrafast electron packet with the 2.4 eV

femtosecond photon pulse. It suggests from the spectra that electrons of the ultrafast packets can absorb more than eight photons during the interaction with the carbon nanotube. The large influence of the photon-induced near-field effect would cause a substantial decrease in the ZLP intensity at the maximum overlap.

A typical carbon nanotube with a diameter of ~ 140 nm was used for demonstrating the PINEM imaging capability (top right). By energy-filtering the ZLP when selecting only the electrons that gained quanta of photon energy (10 eV total width), the

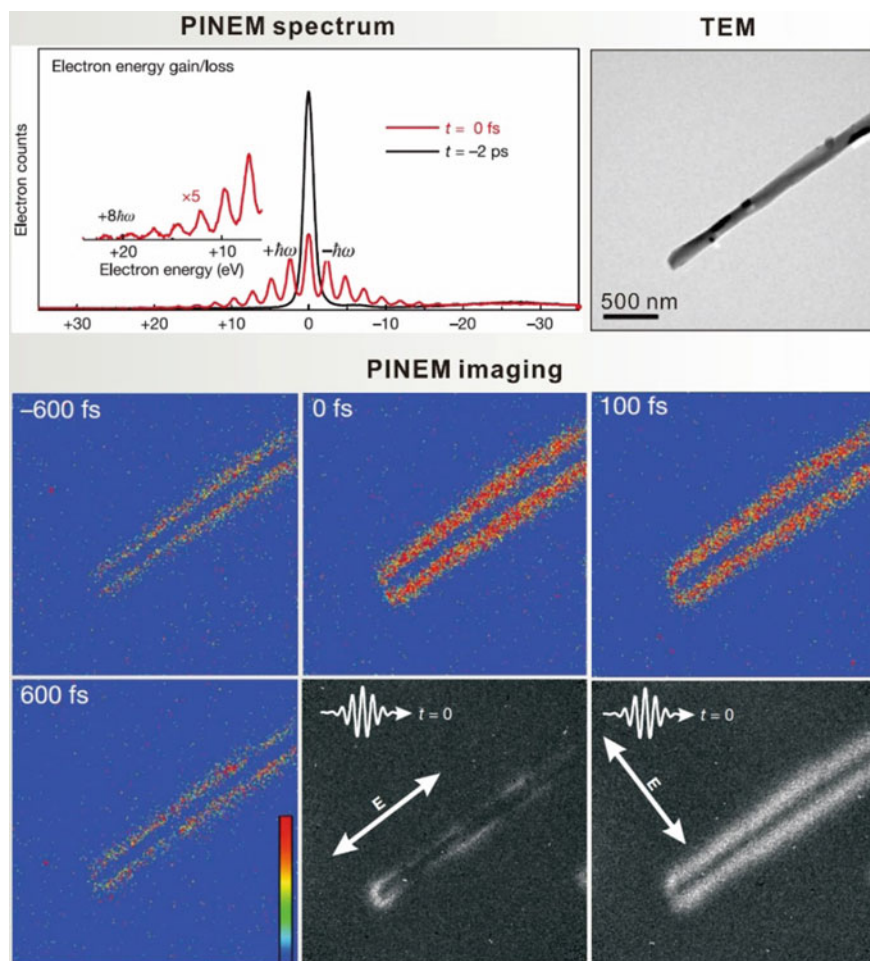


Fig. 10.13 (Top left) Electron energy spectra of the carbon nanotube irradiated with a fs laser pulse at two different time delays. (Top right) A typical TEM image of the carbon nanotube used for the PINEM imaging. (Bottom panel) PINEM images of the carbon nanotube taken at different delay times. Image counts were seen at the local vicinity of the nanotube surface, with the maximum observed at time zero. (reproduced with permission from Ref. [92], Copyright 2009, Springer Nature)

evanescent electric field was visualized in real-space images of the nanostructure by varying the arrival time of the electron packet relative to the clocking laser pulse (bottom panel). It is seen that the image counts only occur within the local vicinity of the nanotube surface. As the temporal overlap increases from negative to positive times, the image counts due to the evanescent optical field first increases and then reaches a maximum at $t = 0$ (maximum overlap), which decreases to almost zero at $t = 600$ fs. Temporally, the rise time of the evanescent field is revealed to be less than one picosecond, and spatially the sequence of images shows that such a field extends at the interface to ~ 50 nm into vacuum on either side of the nanotube. This length scale is consistent with theoretical considerations of optically excited plasmons [94].

The spatial distribution of the PINEM images is dependent on the polarization of the femtosecond pulse relative to the orientation of the carbon nanotube. As the laser pulse encounters the nanostructure ($t = 0$), it produces near-field excitations, causing the surface field to oscillate with the electric field (E-field) of the laser [95]. Since the nanotube diameter (~ 140 nm) is much less than ($d < \lambda$) the wavelength of the laser used (519 nm), the field is confined by the dimensions of the nanotube, which then sets up an oscillating dipole in the structure. The PINEM images obtained at $t = 0$ with the E-field of the femtosecond laser pulse polarized either parallel or perpendicular to the long axis of the carbon nanotube display striking changes: for the parallel case, a spatial enhancement of the evanescent field is observed on the nanotube tips, whereas for the other polarization, the enhancement of two sides of the nanotube is seen. The intensity of the evanescent field extends beyond the structure of the nanotube and falls off exponentially with distance from the surface [94]. This example demonstrates that the evanescent fields effectively mediate the interaction between the 200 keV electron in UEM and the 2.4 eV photons in the femtosecond excitation pulse within less than 1 ps.

Using the PINEM technique, it enables the visualization and control of the plasmon-related dynamics in materials systems [96–98], and the dynamics of surface structural changes in biological cells [99–101]. In addition, on the basis of the PINEM concepts, many attempts have been devoted to 4D UEM for improving its energy resolution from ~ 1.2 eV down to ~ 0.6 eV [102] and even to ~ 20 meV [103], and to increase its temporal resolution to ~ 30 fs [104, 105]. By this, the potential for applications in direct visualization of phenomena related to plasmonics, photonics and biosystems with high space–time–energy resolutions would be further explored.

10.3.9 Ultrafast EELS

EELS in TEM is a powerful technique for providing a wealth of information including chemical composition and bonding, valence state and spin state. When EELS is integrated into 4D UEM with high resolution in space–time–energy domains, the dynamics of chemical bonding in nanoscale graphite (energy range of 0–300 eV) and oxidation state in α -Fe₂O₃ (energy range of 500–1000 eV) under laser excitation have been revealed [106–108]. As known, the cross-section for inelastic scattering

decays with increasing energy loss in a power-law dependence of AE^{-r} , where A is a constant, E the energy loss and r the inverse power law exponent [109]. Therefore, it becomes more challenging to effectively detect the core-loss edge because of the dramatically weaker signals caused by the high energy loss E . Generally, the $2p \rightarrow 3d$ transitions in transition metals are located in the core-loss range, which are essential in the determination of oxidation state and chemical environment for understanding the relevant photocatalytic processes. Figure 10.14 demonstrates the in situ studies of the temporal change of the valence state of iron in $\alpha\text{-Fe}_2\text{O}_3$ (bandgap of ~ 2.1 eV) by ultrafast EELS in the core-loss range [108]. The monocrystalline $\alpha\text{-Fe}_2\text{O}_3$ particles, indicated from the diffraction pattern, have a feather-like shape with the thickness of ~ 40 nm for all the branches (top panel, left and middle). The Fe L-edge core-loss EELS corresponds to the excitation of an Fe $2p$ core electron in $\alpha\text{-Fe}_2\text{O}_3$ to an unoccupied $3d$ orbital with an energy loss of over 700 eV (top panel, right). Note that the position and shape of the L-edge peak are extremely sensitive to the Fe oxidation state.

The temporal evolution of the Fe L-edge EELS in $\alpha\text{-Fe}_2\text{O}_3$ was probed by femtosecond electron pulses after optical excitations ($\lambda = 519$ nm; fluence of 12 mJ/cm²). The PINEM-electron unaffected spectrum (negative time at -2.5 ps) is relatively sharp and high in intensity (middle panel, left). However, the experimentally observed Fe L_3 -edge at 0.15 ps shows the broadening effect, which is larger than the simulation of the pure PINEM-electron-induced broadening effect (blue curve). It implies that the PINEM-electrons cannot take full responsibility for the total broadening. The full width at half-maximum (FWHM) of the experimentally observed overall Fe L_3 -edges as a function of time was then compared with that of the simulated one (convolution of the intrinsic Fe L_3 -edge before photoexcitation with the time-varying ZLP). A maximum broadening of ~ 1.8 eV (from 6.5 to 8.3 eV) was observed, while no noticeable temporal change of the peak position was detected (middle panel, middle). With the PINEM-electron effect removed, the inherent dynamics of the FWHM of the Fe L_3 -edge is illustrated (middle panel, right). After the initial fast rise, the FWHM of the Fe L_3 -edge recovers within ~ 3 ps. For the peak position, the energy of the Fe L_3 -edge was reported to shift from ~ 707.8 eV for Fe^{2+} in FeO to ~ 709.5 eV for Fe^{3+} in Fe_2O_3 [110]. Therefore, the results of the maximum broadening of ~ 1.8 eV as well as no detectable peak shift did not support the idea that the direct ligand to metal ($\text{O } 2p \rightarrow \text{Fe } 3d$) charge transfer transition dominated the 519 nm photoexcitation of Fe_2O_3 . It suggests that the Fe $3d$ to Fe $3d$ charge transfer may dominate, and that the shift of the Fe L_3 -edge induced by the photo-generated Fe^{2+} is offset by the same amount of Fe^{4+} created (canceling of the peak shift), leading to the broadening of the Fe L_3 -edge.

The ultrafast EELS results indicate that two photo-induced electron transfer processes might account for the generation of $\text{Fe}^{2+} - \text{Fe}^{4+}$ pairs after the 519 nm laser excitation (bottom panel). In the case of pair excitation, two magnetically coupled Fe^{3+} cations are simultaneously excited to the ${}^4\text{T}_1({}^4\text{G})$ state from the ${}^6\text{A}_1$ ground state by the 519 nm laser pulse. Electron transfers from one Fe^{3+} cation to the other then occur by superexchange or hopping via the bridge oxygen anions. Alternatively, the $3d-3d$ transition would take place only in a single cation of the pair. The energy

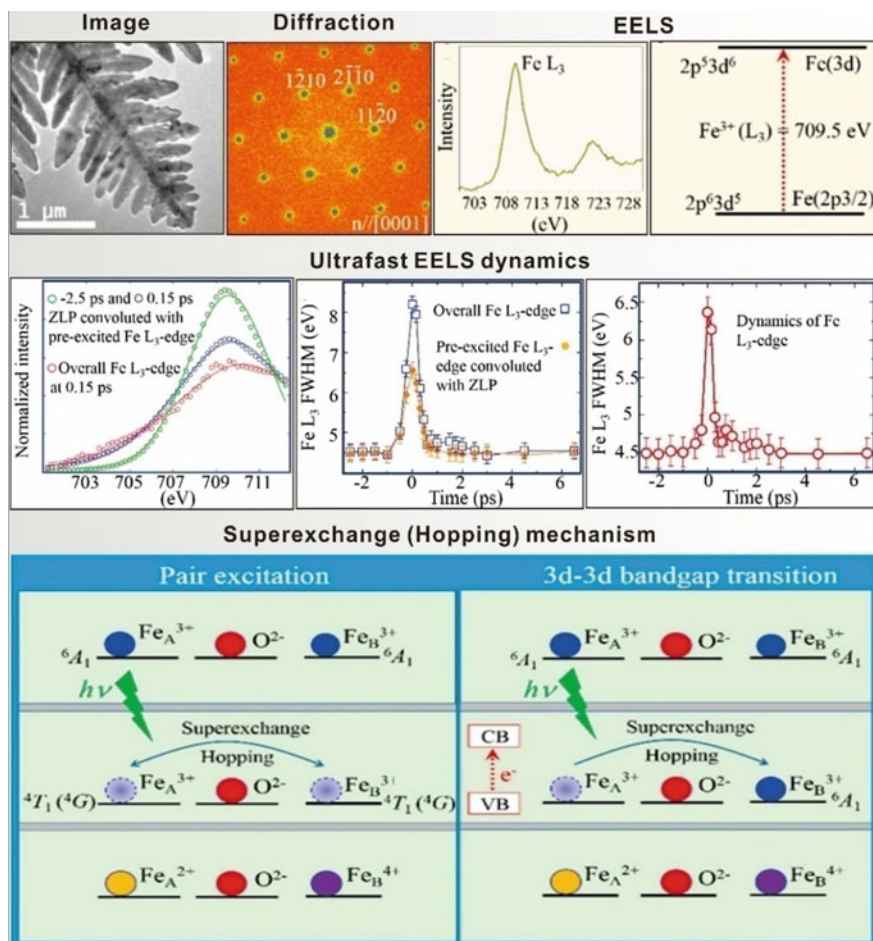


Fig. 10.14 (Top panel) Image, diffraction pattern and EELS of the feather-like $\alpha\text{-Fe}_2\text{O}_3$ crystal. (Middle panel) Comparison of the Fe L_3 -edge with and without PINEM-electron effect (left); Time-dependent FWHM of the overall Fe L_3 -edge and the Fe L_3 -edge before laser excitation (middle); The intrinsic FWHM dynamics of the Fe L_3 -edge (right). (Bottom panel) Schematics of the two possible electron transfer processes between a pair of neighboring Fe^{3+} cations under 519 nm laser illumination. (reproduced with permission from Ref. [108], Copyright 2017, American Chemical Society)

of the pump photons is high enough to excite electrons from the valence band to the conduction band. The excited electrons transfer to the other Fe^{3+} cation via the superexchange or hopping mechanism, resulting in the formation of $\text{Fe}^{2+}-\text{Fe}^{4+}$ pairs [111]. The dynamical studies reveal that the photo-generated $\text{Fe}^{2+}-\text{Fe}^{4+}$ pairs would fully recombine in ~ 3 ps.

10.3.10 Biological Dynamics

Following years of the development and improvement of cryo-electron microscopy (Cryo-EM), structural biology is entering a new and exciting age. With the integration of the fourth dimension, time, into Cryo-EM, a fundamental understanding of the relationship among structure, dynamics and function would be established for the molecular mechanisms in biological systems. Figure 10.15 presents the direct visualization of the movements of the constituent protein molecules in insulin amyloid fibrils, a prototypical biomacromolecule [112]. The fibrils were lying on the lacey carbon grids. The images and diffraction patterns of a network of amyloid fibrils were taken at room temperature (300 K), cryogenic temperature (118 K, absence of vitreous ice) and 118 K with vitreous ice, respectively (left and middle panel). Amyloid fibrils have a characteristic “cross- β ” structure that is composed of paired hydrogen-bonded β -sheets running parallel to the long axis of the fibrils. The regular interstrand spacing gives rise to a distinctive 0.48 nm cross- β reflection in electron diffraction. Note that two broad rings at 0.37 nm and 0.21 nm were related to the presence of vitreous ice except the characteristic 0.48 nm amyloid ring.

The dynamics of the amyloid fibrils under native-like conditions (embedded in glassy ice) were initiated by a heating laser pulse, which were then recorded by the time series of frames displaying the structural dynamics of the fibrils in the hydrated environment (top right). In general, many protein stuff are poor in absorbing visible light. To efficiently transfer heat into the fibrils for triggering the dynamics, a small amyloidophilic dye molecule (Congo red) was bound to the outer surface of the fibrils (the dye did not perturb the cross- β structure). Because of a temperature jump caused by the heating laser, the stretching of the β -sheets was determined by calculating the change in radius of the 0.48 nm diffraction rings. For the fibrils at room temperature, an immediate expansion was observed as the laser pulse illuminated the sample (bottom right). The relative expansion is $(4.0 \pm 0.2) \times 10^{-3}$, corresponding to 1.9 ± 0.1 pm. Since the heating is uniform, the expansion along the long axis of the fibril can be considered to be a stretching of ~ 1 pm ($\approx 1.9/2$ pm) in opposite directions. When the temperature of the fibrils was lowered to 118 K via liquid nitrogen cooling, an increased expansion $(7.4 \pm 0.3) \times 10^{-3}$ of the hydrogen-bonded β -sheets was seen, which corresponded to a total expansion of 3.5 ± 0.1 pm (or $3.5/2 = 1.8$ pm in opposite directions). This behavior might be caused by an increased absorption cross-section of the dye at low temperatures [113]. Another contributing factor may be due to a decrease in the heat capacity of the fibrils at low temperatures [114].

When the fibrils were embedded in the vitreous ice at 118 K, an increased expansion of the hydrogen-bonded β -sheets was observed upon laser excitation with a relative expansion of $(11.3 \pm 1.2) \times 10^{-3}$, corresponding to a movement of 5.4 ± 0.6 pm (or $5.4/2 = 2.7$ pm in opposite directions). This increased expansion by almost a factor of 2 compared to that measured at 118 K in the absence of glassy ice can be rationalized by considering that amyloid fibrils are mainly stabilized by a network of inter-backbone hydrogen bonds. From experiment and computation, the strength of a hydrogen bond in vacuum is ~ 4.8 kcal/mol which is reduced to

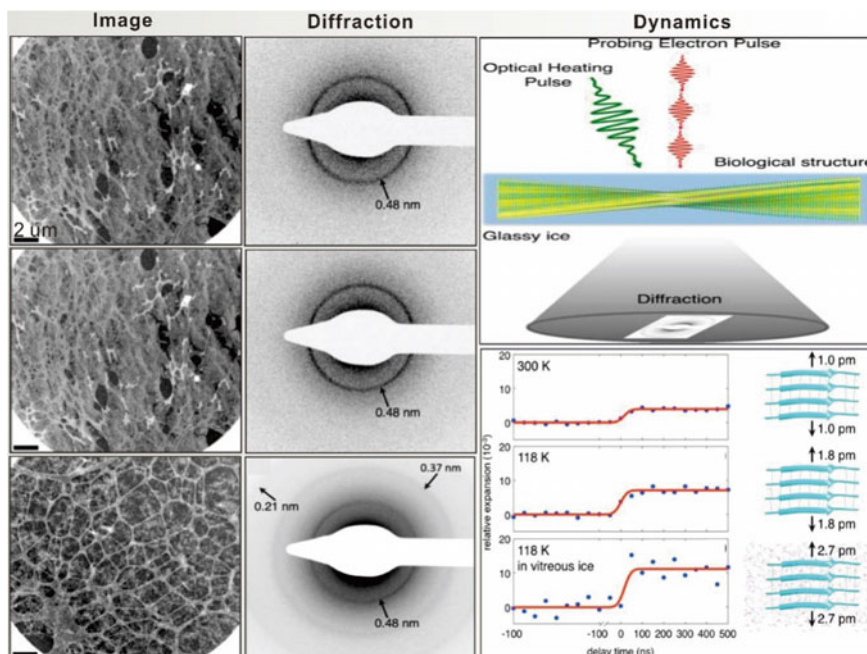


Fig. 10.15 (Left panel) UEM images of the amyloid fibrils taken at 300 K, 118 K and 118 K with vitreous ice covering the sample. (Middle panel) The diffraction patterns of the samples corresponding to the images shown in the left panel. (Right panel) Schematic diagram of the ultrafast studies in the amyloid sample (top); expansion dynamics of the amyloid fibrils at three different conditions (bottom). An increased expansion was observed at low temperatures, especially when the fibrils were hydrated in vitreous water. (reproduced with permission from Ref. [112], Copyright 2013, American Chemical Society)

~ 1.5 kcal/mol in the presence of water [115, 116]. Therefore, the increased expansion of the β -sheets following the T-jump is due to the weakening of the fibrils' hydrogen-bonding network in the aqueous environment, making the fibrils more stretchable.

4D UEM has been demonstrated to nondestructively determine the mechanical Young's moduli in materials systems. In a similar approach, it has recently been extended to the realm of biological structures. Vibrational oscillations of the DNA structures [117] and amyloid-like microcrystals [118] are excited through a short burst of laser pulses, while the mechanical motions are probed with electron pulses to obtain the frequencies and amplitudes of the oscillations so that Young's moduli of the involved biological structures could be determined. This time-resolved approach enables in situ visualization of the biomechanics and the nanoscale mechanics studies of macromolecules and biological networks.

10.3.11 Instrumental Development

High resolution is always one of the key essentials that are pursued in the electron microscopy field. Because 4D UEM is modified from the standard TEM, the increase of spatial resolution largely relies on the work from main TEM companies, like FEI and JEOL. Scientists from various research laboratories then focus on the interference parts between the TEM and ultrafast laser systems, devoting to improving the temporal resolution. In regard to the temporal resolution, short electron pulses are central to time-resolved atomic-scale diffraction and electron microscopy. However, the broadening of electron pulse duration usually occurs as a result of dispersion during propagation and the space-charge effect. Therefore, electron pulse compression is indispensable for reaching subphonon or electronic time scales [119]. The compression requires deceleration and acceleration of the electron when arriving before or after the mean electron arrival time, respectively. The compression techniques include microwave compression [119], beam blanking [120], ponderomotive bunching [121], photon-gating [104] and terahertz field compression [34, 122], which make the electron pulse duration reach the few-femtosecond regime or even better.

The commonly used microwave technology generally suffers from appreciable phase shift, and laser-microwave synchronization below 10 fs becomes challenging [123, 124]. In contrast, pulsed terahertz fields can be generated in a much more controlled way from the coherent nonlinear polarization of matter [125]. Terahertz control fields derived from a single ultrafast laser via nonlinear optics give rise to near-perfect (potentially sub-femtosecond) temporal synchronization, which is ideally suited for controlling electron pulses. Figure 10.16 shows the conceptual design and the results of the electron pulse compression by using the terahertz field approach [34, 122]. Femtosecond electron pulses are generated by pulsed-laser photoemission (left panel). The electron wave packets are then compressed in time by a terahertz field. A magnetic lens widens the beam for passage through the sample with close-to-zero divergence, while an objective magnetic lens magnifies the structure onto the screen for observation. The electron pulse compression is schematically displayed in the top right panel. The ~ 1 ps laser pulses drive two optical rectification stages for generating few-cycle terahertz pulses. The electron pulses with about one electron per pulse are generated through the excitation of a gold thin-film photocathode by the same laser source. The optical rectification stages produce near-single-cycle pulses at 0.3 THz with pulse energies up to 40 nJ and field strengths up to $\sim 10^6$ V/m, which are then used to control the electron pulse's momentum, energy and duration.

The butterfly-shaped metal resonators are used to mediate the interaction between the electrons and the terahertz fields. The terahertz electric field is enhanced in the plane of the resonators and confined to subwavelength dimensions so that energy and momentum conservation during the electron-photon interaction is satisfied [126]. Electrons passing through the resonators experience a net change in momentum which corresponds to the integral of the Lorentz force along their trajectories. The change varies sinusoidally as a function of the arrival time of the electron in the terahertz field. The first terahertz control stage uses a tilted resonator, providing force

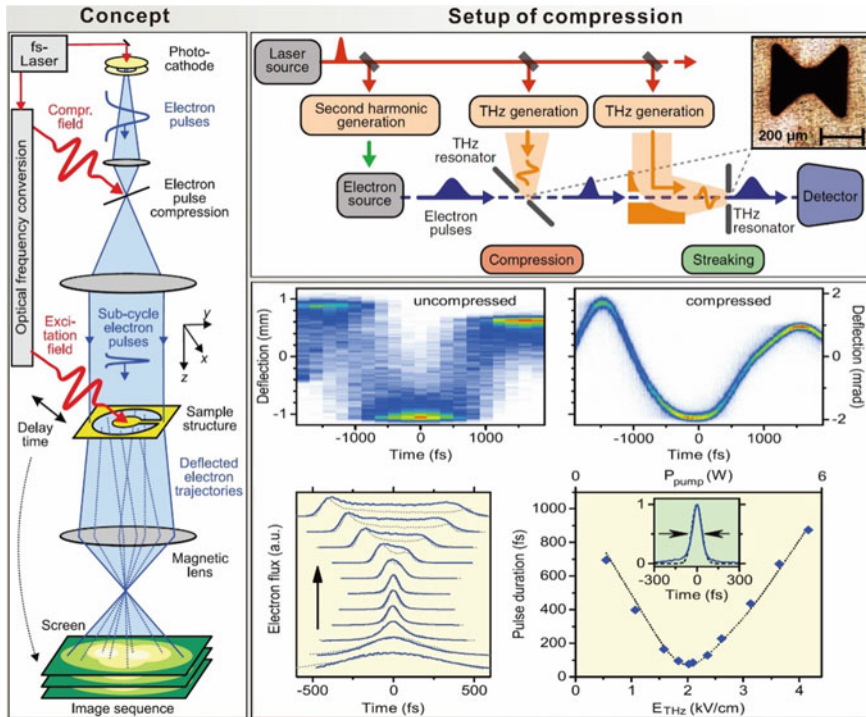


Fig. 10.16 (Left panel) Conceptual design of the electron pulse compression (reproduced with permission from Ref. [34], Copyright 2016, The American Association for the Advancement of Science). (Top right) Experimental setup of the compression. The first THz field provides force for temporal compression while the second one is used for temporal characterization. (Bottom right) Streaking deflectograms showing the comparison before and after the electron pulse compression. The pulse duration first decreases and then increases with the compression strength, reaching the shortest one at 75 fs. (reproduced with permission from Ref. [122], Copyright 2016, The American Association for the Advancement of Science)

components longitudinal to the electron beam for temporal compression. The second terahertz control stage (normal to the beam) offers a delay-dependent deflection (streaking) for temporal characterization. Since the electron pulse from the source (<1 ps) is shorter than the half cycle of the terahertz field, such a field imposes a uniform time-dependent force on the electron wave packet in all dimensions. The force causes acceleration and/or compression in the first stage and streaking in the second stage. Consequently, the pulsed electron beam is entirely under the effective control of the laser system and its optical fields.

The time-dependent fields enable compression of the electron pulse substantially below its initial duration. The effective strength of the compression stage is determined by the energy imposed on the electrons in the forward direction with changing delay time, g_E , which is proportional to the incoming terahertz peak field strength divided by the cycle period. After the compression, the electron pulse becomes shorter

during its propagation, reaching a minimum duration at a distance [122]:

$$f_c = m_e(\gamma\beta c)^3/g_E \quad (10.9)$$

where m_e is the electron mass, c the speed of light, β the ratio of the electron speed to the speed of light and $\gamma = 1/\sqrt{1 - \beta^2}$. When the localized terahertz fields reach $\sim 10^6$ V/m, it is sufficient to yield a g_E of 50 eV/ps, offering a convenient temporal focus at a distance of tens of centimeters from the compression stage [122].

Streaking deflectograms with and without terahertz field compression are shown for comparison (bottom right). A pronounced sharpening of the trace is observed in the vertical (streaking) direction, suggesting a substantial compression of the electron pulses. The evolution of measured electron temporal profile with a varying compression strength g_E shows that the electron pulse first shortens to a minimum duration and then lengthens. As the electron pulse was overcompressed by a sinusoidal field, a double-peaked shape appeared [127]. The tendency was also seen from the curve of the electron pulse durations as a function of the terahertz-field strength and average power of the driving laser. The shortest pulse has a FWHM duration of 75 fs (inset), which is a factor of 12 shorter than the original one (930 fs). This achieved electron pulse is shorter than the half period of many fundamental phonon modes and molecular vibrations.

Recently, much shorter pulses, namely isolated attosecond electron pulses, have potentially been generated via single-electron wave packet compression [119] or ponderomotive effects [121]. It has been demonstrated that attosecond electron pulse trains [127] have been realized in an electron microscope [33]. Besides the pursuit of a short electron pulse, another direction of development is to achieve high coherence and brightness of the electron beam. Such a UEM has been realized through the modification from a field-emission TEM [128, 129], with the capabilities of micrometer-scale coherence, sub-picosecond pulse durations and energy widths of ~ 0.65 eV.

10.4 Conclusions and Outlook

4D UEM, integrating the domains of space, energy and time in structural dynamics, has explored the potential for applications in the quantitative determination of the transient structures and/or states in material and biological systems. This methodology permits high-resolution real-space imaging, reciprocal-space diffraction and spectroscopy on the scales of sub-nanometer, sub-picosecond and sub-eV (or even meV). In this chapter, after the introduction of the historical development of 4D UEM, we described the conceptual framework of the design and the basic principle of the methodology. We highlighted prototypical cases of materials dynamics including phase transitions, mechanical oscillations, electron–phonon coupling, reaction and nucleation dynamics, plasmon-related dynamics and biological dynamics in different environments, and the present status of the instrumental developments.

The multifunctional 4D UEM with the high spatiotemporal resolution has enabled the explosion of applications in various systems from nanoscale to mesoscale. Such trends will keep moving forward in future research. From a perspective in material systems, manipulation and engineering of transient states of matter through external fields or environments could be a strategy for further extending the realm of 4D UEM. In strongly correlated materials, charge, spin, orbital and lattice degrees of freedom result in competing complex interactions. Using terahertz fields, subtle modulation of the lattice structure would induce substantial changes in the magnetic and electronic properties [130]. The normal laser-pump and electron-probe scheme could be replaced by the strategy of an electric-field pump [131] with the electron pulses as the probe. In multiferroics, this allows recording real-time domain switching processes induced by an electric field, leading to the improvement and manipulation of the novel electronic/magnetic properties. As known, the systems to be studied are normally located inside the UEM chamber with the vacuum condition. Recently, the realization of 4D imaging in liquids [81] offers a window for studying dynamics in native environments. Such development opens up the exploration of 4D environmental imaging, such as in the fields of solution phase synthesis, catalytic reactions in liquid and gas environments, microfluidics and NP/drug delivery in liquids. As for the biological systems, structural biology has been the leading revolution in this century because of the development of cryo-EM. The future direction would be the studies of the dynamical processes of complex biological structures in native environments by using 4D imaging and diffraction with cryogenic or liquid-cell configuration. It would allow recording of conformational intermediates in action with high spatiotemporal resolution, for example, protein folding process in native conditions so that the underlying mechanisms regulating biological functions could be revealed [132].

From the technological point of view, the issues involved in further developing UEM include the coherence of the source, electron pulse duration, stability, detection sensitivity and the number of electrons per pulse in single-pulse methodology. One strategy would be the field-emission-based UEM technology that could increase the coherence of the electron beam and also reduce its energy spread. It will foster an enhanced energy resolution in the stroboscopic experiments, especially for PINEM-related studies [128, 129]. To shorten the electron pulse duration, single-electron coherent packets can be employed to remove the space-charge problem, while electron compression technologies further reduce the dispersion effect during propagation. This would lead to the generation of attosecond electron pulses. The application of attosecond electron pulse trains ultimately allows electron microscopy to enter the realm of attosecond science, which would record dynamic changes of electron-related phenomena in complex systems. Additional strategies would include the extension of single-frame acquisition to multi-frame recording (movie mode) at every turn, the use of direct detection cameras to increase the signal-to-noise ratio, and the modifications from the cryo-EM or aberration-corrected TEM to the advanced UEMs. With those strategies, it is anticipated that new and/or improved functionality of 4D UEM would become practically accessible for the incoming studies of protein conformational dynamics and irreversible chemical reaction dynamics.

References

1. Zewail AH (2006) 4D ultrafast electron diffraction, crystallography, and microscopy. *Annu Rev Phys Chem* 57(1):65–103. <https://doi.org/10.1146/annurev.physchem.57.032905.104748>
2. Zewail AH, Thomas JM (2009) 4D electron microscopy: imaging in space and time. Imperial College Press, London. <https://doi.org/10.1142/P641>
3. Shank CV, Ippen EP (1974) Subpicosecond kilowatt pulses from a mode-locked cw dye laser. *Appl Phys Lett* 24(8):373–375. <https://doi.org/10.1063/1.1655222>
4. Fork RL, Brito Cruz CH, Becker PC, Shank CV (1987) Compression of optical pulses to six femtoseconds by using cubic phase compensation. *Opt Lett* 12(7):483–485. <https://doi.org/10.1364/ol.12.000483>
5. Spence DE, Kean PN, Sibbett W (1991) 60-fsec pulse generation from a self-mode-locked Ti:sapphire laser. *Opt Lett* 16(1):42–44. <https://doi.org/10.1364/ol.16.000042>
6. Abraham H, Lemoine J (1899) Disparition instantanée du phénomène de Kerr. *Comptes Rendus de l'Académie des Sciences* 129:206–208
7. Rentzepis PM (1968) Direct measurements of radiationless transitions in liquids. *Chem Phys Lett* 2(2):117–120. [https://doi.org/10.1016/0009-2614\(68\)80066-1](https://doi.org/10.1016/0009-2614(68)80066-1)
8. Kaufmann KJ, Rentzepis PM (1975) Picosecond spectroscopy in chemistry and biology. *Acc Chem Res* 8(12):407–412. <https://doi.org/10.1021/ar50096a003>
9. Chuang TJ, Hoffman GW, Eisenthal KB (1974) Picosecond studies of the cage effect and collision induced predissociation of iodine in liquids. *Chem Phys Lett* 25(2):201–205. [https://doi.org/10.1016/0009-2614\(74\)89117-7](https://doi.org/10.1016/0009-2614(74)89117-7)
10. Hochstrasser RM, Lutz H, Scott GW (1974) The dynamics of populating the lowest triplet state of benzophenone following singlet excitation. *Chem Phys Lett* 24(2):162–167. [https://doi.org/10.1016/0009-2614\(74\)85424-2](https://doi.org/10.1016/0009-2614(74)85424-2)
11. von der Linde D, Laubereau A, Kaiser W (1971) Molecular vibrations in liquids: direct measurement of the molecular dephasing time; determination of the shape of picosecond light pulses. *Phys Rev Lett* 26(16):954–957. <https://doi.org/10.1103/PhysRevLett.26.954>
12. Dantus M, Rosker MJ, Zewail AH (1987) Real-time femtosecond probing of “transition states” in chemical reactions. *J Chem Phys* 87(4):2395–2397. <https://doi.org/10.1063/1.453122>
13. Zhong D, Douhal A, Zewail AH (2000) Femtosecond studies of protein–ligand hydrophobic binding and dynamics: human serum albumin. *Proc Natl Acad Sci* 97(26):14056–14061. <https://doi.org/10.1073/pnas.250491297>
14. Mourou G, Williamson S (1982) Picosecond electron diffraction. *Appl Phys Lett* 41(1):44–45. <https://doi.org/10.1063/1.93316>
15. Williamson S, Mourou G, Li JCM (1984) Time-resolved laser-induced phase transformation in aluminum. *Phys Rev Lett* 52(26):2364–2367. <https://doi.org/10.1103/PhysRevLett.52.2364>
16. Elsayed-Ali HE, Mourou GA (1988) Picosecond reflection high-energy electron diffraction. *Appl Phys Lett* 52(2):103–104. <https://doi.org/10.1063/1.99063>
17. Williamson JC, Zewail AH (1991) Structural femtochemistry: experimental methodology. *Proc Natl Acad Sci* 88(11):5021–5025. <https://doi.org/10.1073/pnas.88.11.5021>
18. Williamson JC, Dantus M, Kim SB, Zewail AH (1992) Ultrafast diffraction and molecular structure. *Chem Phys Lett* 196(6):529–534. [https://doi.org/10.1016/0009-2614\(92\)85988-M](https://doi.org/10.1016/0009-2614(92)85988-M)
19. Williamson JC, Cao J, Ihee H, Frey H, Zewail AH (1997) Clocking transient chemical changes by ultrafast electron diffraction. *Nature* 386(6621):159–162. <https://doi.org/10.1038/386159a0>
20. Ihee H, Lobastov VA, Gomez UM, Goodson BM, Srinivasan R, Ruan C-Y, Zewail AH (2001) Direct imaging of transient molecular structures with ultrafast diffraction. *Science* 291(5503):458–462. <https://doi.org/10.1126/science.291.5503.458>
21. Lobastov VA, Srinivasan R, Vigliotti F, Ruan C-Y, Feenstra JS, Chen S, Park ST, Xu S, Zewail AH (2004) Ultrafast electron diffraction. In: Krausz F, Korn G, Corkum P, Walmsley I (eds) *Ultrafast optics IV*. Springer, New York, pp 419–435. https://doi.org/10.1007/978-0-387-34756-1_54

22. Ruan C-Y, Vigliotti F, Lobastov VA, Chen S, Zewail AH (2004) Ultrafast electron crystallography: transient structures of molecules, surfaces, and phase transitions. *Proc Natl Acad Sci USA* 101(5):1123–1128. <https://doi.org/10.1073/pnas.0307302101>
23. Haider M, Braunshausen G, Schwan E (1995) Correction of the spherical aberration of a 200 kV TEM by means of a hexapole-corrector. *Optik* 99(4):167–179
24. Krivanek OL, Dellby N, Lupini AR (1999) Towards sub-Å electron beams. *Ultramicroscopy* 78(1):1–11. [https://doi.org/10.1016/S0304-3991\(99\)00013-3](https://doi.org/10.1016/S0304-3991(99)00013-3)
25. Batson PE, Dellby N, Krivanek OL (2002) Sub-ångstrom resolution using aberration corrected electron optics. *Nature* 418(6898):617–620. <https://doi.org/10.1038/nature00972>
26. Morishita S, Ishikawa R, Kohno Y, Sawada H, Shibata N, Ikuhara Y (2018) Attainment of 40.5 pm spatial resolution using 300 kV scanning transmission electron microscope equipped with fifth-order aberration corrector. *Microscopy* 67(1):46–50. <https://doi.org/10.1093/jmicro/dfx122>
27. Bostanjoglo O, Elschner R, Mao Z, Nink T, Weingärtner M (2000) Nanosecond electron microscopes. *Ultramicroscopy* 81(3):141–147. [https://doi.org/10.1016/S0304-3991\(99\)00180-1](https://doi.org/10.1016/S0304-3991(99)00180-1)
28. Dömer H, Bostanjoglo O (2003) High-speed transmission electron microscope. *Rev Sci Instrum* 74(10):4369–4372. <https://doi.org/10.1063/1.1611612>
29. Zewail AH (2005) Diffraction, crystallography and microscopy beyond three dimensions: structural dynamics in space and time. *Philos Trans Roy Soc A: Math Phys Eng Sci* 363(1827):315–329. <https://doi.org/10.1098/rsta.2004.1513>
30. Lobastov VA, Srinivasan R, Zewail AH (2005) Four-dimensional ultrafast electron microscopy. *Proc Natl Acad Sci* 102(20):7069–7073. <https://doi.org/10.1073/pnas.0502607102>
31. Piazza L, Cottet M, Carbone F, Masiel D, LaGrange T (2012) Principles and implementation of an ultrafast transmission electron microscope. *Microsc Microanal* 18(S2):600–601. <https://doi.org/10.1017/S1431927612004850>
32. Plemmons DA, Suri PK, Flannigan DJ (2015) Probing structural and electronic dynamics with ultrafast electron microscopy. *Chem Mater* 27(9):3178–3192. <https://doi.org/10.1021/acs.chemmater.5b00433>
33. Feist A, Echterkamp KE, Schauss J, Yalunin SV, Schäfer S, Ropers C (2015) Quantum coherent optical phase modulation in an ultrafast transmission electron microscope. *Nature* 521(7551):200–203. <https://doi.org/10.1038/nature14463>
34. Ryabov A, Baum P (2016) Electron microscopy of electromagnetic waveforms. *Science* 353(6297):374–377. <https://doi.org/10.1126/science.aaf8589>
35. Lee YM, Kim YJ, Kim Y-J, Kwon O-H (2017) Ultrafast electron microscopy integrated with a direct electron detection camera. *Struct Dyn* 4(4):044023. <https://doi.org/10.1063/1.4983226>
36. Voss JM, Olshin PK, Charbonnier R, Drabbels M, Lorenz UJ (2019) In situ observation of coulomb fission of individual plasmonic nanoparticles. *ACS Nano* 13(11):12445–12451. <https://doi.org/10.1021/acsnano.9b06664>
37. LaGrange T, Armstrong MR, Boyden K, Brown CG, Campbell GH, Colvin JD, DeHope WJ, Frank AM, Gibson DJ, Hartemann FV, Kim JS, King WE, Pyke BJ, Reed BW, Shirk MD, Shuttlesworth RM, Stuart BC, Torralva BR, Browning ND (2006) Single-shot dynamic transmission electron microscopy. *Appl Phys Lett* 89(4):044105. <https://doi.org/10.1063/1.2236263>
38. Cao G, Sun S, Li Z, Tian H, Yang H, Li J (2015) Clocking the anisotropic lattice dynamics of multi-walled carbon nanotubes by four-dimensional ultrafast transmission electron microscopy. *Sci Rep* 5(1):8404. <https://doi.org/10.1038/srep08404>
39. Yang D-S, Mohammed OF, Zewail AH (2010) Scanning ultrafast electron microscopy. *Proc Natl Acad Sci* 107(34):14993–14998. <https://doi.org/10.1073/pnas.1009321107>
40. Mohammed OF, Yang D-S, Pal SK, Zewail AH (2011) 4D scanning ultrafast electron microscopy: visualization of materials surface dynamics. *J Am Chem Soc* 133(20):7708–7711. <https://doi.org/10.1021/ja2031322>

41. Baum P (2013) On the physics of ultrashort single-electron pulses for time-resolved microscopy and diffraction. *Chem Phys* 423:55–61. <https://doi.org/10.1016/j.chemphys.2013.06.012>
42. Aidelsburger M, Kirchner FO, Krausz F, Baum P (2010) Single-electron pulses for ultrafast diffraction. *Proc Natl Acad Sci* 107(46):19714–19719. <https://doi.org/10.1073/pnas.1010165107>
43. Kirchner FO, Lahme S, Krausz F, Baum P (2013) Coherence of femtosecond single electrons exceeds biomolecular dimensions. *New J Phys* 15(6):063021. <https://doi.org/10.1088/1367-2630/15/6/063021>
44. Gahlmann A, Tae Park S, Zewail AH (2008) Ultrashort electron pulses for diffraction, crystallography and microscopy: theoretical and experimental resolutions. *Phys Chem Chem Phys* 10(20):2894–2909. <https://doi.org/10.1039/b802136h>
45. van Oudheusden T, de Jong EF, van der Geer SB, Root WPEMO, Luiten OJ, Siwick BJ (2007) Electron source concept for single-shot sub-100 fs electron diffraction in the 100 keV range. *J Appl Phys* 102(9):093501. <https://doi.org/10.1063/1.2801027>
46. Michalik AM, Sherman EY, Sipe JE (2008) Theory of ultrafast electron diffraction: the role of the electron bunch properties. *J Appl Phys* 104(5):054905. <https://doi.org/10.1063/1.2973157>
47. Grinolds MS, Lobastov VA, Weissenrieder J, Zewail AH (2006) Four-dimensional ultrafast electron microscopy of phase transitions. *Proc Natl Acad Sci* 103(49):18427–18431. <https://doi.org/10.1073/pnas.0609233103>
48. Lobastov VA, Weissenrieder J, Tang J, Zewail AH (2007) Ultrafast electron microscopy (UEM): four-dimensional imaging and diffraction of nanostructures during phase transitions. *Nano Lett* 7(9):2552–2558. <https://doi.org/10.1021/nl071341e>
49. Morin FJ (1959) Oxides which show a metal-to-insulator transition at the Neel temperature. *Phys Rev Lett* 3(1):34–36. <https://doi.org/10.1103/PhysRevLett.3.34>
50. Cavalleri A, Chong HHW, Fourmaux S, Glover TE, Heimann PA, Kieffer JC, Mun BS, Padmore HA, Schoenlein RW (2004) Picosecond soft x-ray absorption measurement of the photoinduced insulator-to-metal transition in VO₂. *Phys Rev B* 69(15):153106. <https://doi.org/10.1103/PhysRevB.69.153106>
51. van der Veen RM, Kwon O-H, Tissot A, Hauser A, Zewail AH (2013) Single-nanoparticle phase transitions visualized by four-dimensional electron microscopy. *Nat Chem* 5(5):395–402. <https://doi.org/10.1038/nchem.1622>
52. Gawelda W, Pham V-T, Benfatto M, Zaushitsyn Y, Kaiser M, Grolimund D, Johnson SL, Abela R, Hauser A, Bressler C, Chergui M (2007) Structural determination of a short-lived excited iron(II) complex by picosecond x-ray absorption spectroscopy. *Phys Rev Lett* 98(5):057401. <https://doi.org/10.1103/PhysRevLett.98.057401>
53. Cobo S, Ostrovskii D, Bonhommeau S, Vendier L, Molnár G, Salmon L, Tanaka K, Bousseksou A (2008) Single-laser-shot-induced complete bidirectional spin transition at room temperature in single crystals of (FeII(pyrazine)(Pt(CN)4)). *J Am Chem Soc* 130(28):9019–9024. <https://doi.org/10.1021/ja800878f>
54. Flannigan DJ, Park ST, Zewail AH (2010) Nanofriction visualized in space and time by 4D electron microscopy. *Nano Lett* 10(11):4767–4773. <https://doi.org/10.1021/nl103589p>
55. Sun S, Wei L, Li Z, Cao G, Liu Y, Lu WJ, Sun YP, Tian H, Yang H, Li J (2015) Direct observation of an optically induced charge density wave transition in 1T-TaSe₂. *Phys Rev B* 92(22):224303. <https://doi.org/10.1103/PhysRevB.92.224303>
56. Tian B, Zheng X, Kempa TJ, Fang Y, Yu N, Yu G, Huang J, Lieber CM (2007) Coaxial silicon nanowires as solar cells and nanoelectronic power sources. *Nature* 449(7164):885–889. <https://doi.org/10.1038/nature06181>
57. Chen B, Wang J, Gao Q, Chen Y, Liao X, Lu C, Tan HH, Mai Y-W, Zou J, Ringer SP, Gao H, Jagadish C (2013) Strengthening brittle semiconductor nanowires through stacking faults: insights from in situ mechanical testing. *Nano Lett* 13(9):4369–4373. <https://doi.org/10.1021/nl402180k>

58. Barwick B, Park HS, Kwon O-H, Baskin JS, Zewail AH (2008) 4D imaging of transient structures and morphologies in ultrafast electron microscopy. *Science* 322(5905):1227–1231. <https://doi.org/10.1126/science.1164000>
59. Kwon O-H, Barwick B, Park HS, Baskin JS, Zewail AH (2008) Nanoscale mechanical drumming visualized by 4D electron microscopy. *Nano Lett* 8(11):3557–3562. <https://doi.org/10.1021/nl8029866>
60. Flannigan DJ, Samartzis PC, Yurtsever A, Zewail AH (2009) Nanomechanical motions of cantilevers: direct imaging in real space and time with 4D electron microscopy. *Nano Lett* 9(2):875–881. <https://doi.org/10.1021/nl803770e>
61. Baskin JS, Park HS, Zewail AH (2011) Nanomusical systems visualized and controlled in 4D electron microscopy. *Nano Lett* 11(5):2183–2191. <https://doi.org/10.1021/nl200930a>
62. Wilson JF, Henry JK, Clark RL (2000) Measured free vibrations of partially clamped, square plates. *J Sound Vib* 231(5):1311–1320. <https://doi.org/10.1006/jsvi.1999.2732>
63. Blakslee OL, Proctor DG, Seldin EJ, Spence GB, Weng T (1970) Elastic constants of compression-annealed pyrolytic graphite. *J Appl Phys* 41(8):3373–3382. <https://doi.org/10.1063/1.1659428>
64. Cremons DR, Plemmons DA, Flannigan DJ (2016) Femtosecond electron imaging of defect-modulated phonon dynamics. *Nat Commun* 7(1):11230. <https://doi.org/10.1038/ncomms11230>
65. Valley DT, Ferry VE, Flannigan DJ (2016) Imaging intra- and interparticle acousto-plasmonic vibrational dynamics with ultrafast electron microscopy. *Nano Lett* 16(11):7302–7308. <https://doi.org/10.1021/acs.nanolett.6b03975>
66. Kim Y-J, Jung H, Han SW, Kwon O-H (2019) Ultrafast electron microscopy visualizes acoustic vibrations of plasmonic nanorods at the interfaces. *Matter* 1(2):481–495. <https://doi.org/10.1016/j.matt.2019.03.004>
67. McKenna AJ, Eliason JK, Flannigan DJ (2017) Spatiotemporal evolution of coherent elastic strain waves in a single MoS₂ flake. *Nano Lett* 17(6):3952–3958. <https://doi.org/10.1021/acs.nanolett.7b01565>
68. Park ST, Flannigan DJ, Zewail AH (2012) 4D electron microscopy visualization of anisotropic atomic motions in carbon nanotubes. *J Am Chem Soc* 134(22):9146–9149. <https://doi.org/10.1021/ja304042r>
69. Hohlfeld J, Wellershoff SS, Güdde J, Conrad U, Jähnke V, Matthias E (2000) Electron and lattice dynamics following optical excitation of metals. *Chem Phys* 251(1):237–258. [https://doi.org/10.1016/S0301-0104\(99\)00330-4](https://doi.org/10.1016/S0301-0104(99)00330-4)
70. Yoo B-K, Kwon O-H, Liu H, Tang J, Zewail AH (2015) Observing in space and time the ephemeral nucleation of liquid-to-crystal phase transitions. *Nat Commun* 6(1):8639. <https://doi.org/10.1038/ncomms9639>
71. Kemsley J (2015) Illuminating crystal nucleation. *Chem Eng News* 93(2):28–29. <https://doi.org/10.1021/cen-09302-scitech1>
72. Nielsen MH, Aloni S, De Yoreo JJ (2014) In situ TEM imaging of CaCO₃ nucleation reveals coexistence of direct and indirect pathways. *Science* 345(6201):1158–1162. <https://doi.org/10.1126/science.1254051>
73. Flannigan DJ, Lobastov VA, Zewail AH (2007) Controlled nanoscale mechanical phenomena discovered with ultrafast electron microscopy. *Angew Chem Int Ed* 46(48):9206–9210. <https://doi.org/10.1002/anie.200704147>
74. Park ST, Flannigan DJ, Zewail AH (2011) Irreversible chemical reactions visualized in space and time with 4D electron microscopy. *J Am Chem Soc* 133(6):1730–1733. <https://doi.org/10.1021/ja110952k>
75. van Smaalen S, de Boer JL, Haas C, Kommandeur J (1985) Anisotropic thermal expansion in crystals with stacks of planar molecules, such as tetracyanoquinodimethanide (TCNQ) salts. *Phys Rev B* 31(6):3496–3503. <https://doi.org/10.1103/PhysRevB.31.3496>
76. Chen B, Fu X, Tang J, Lysevych M, Tan HH, Jagadish C, Zewail AH (2017) Dynamics and control of gold-encapped gallium arsenide nanowires imaged by 4D electron microscopy. *Proc Natl Acad Sci* 114(49):12876–12881. <https://doi.org/10.1073/pnas.1708761114>

77. Chen B, Fu X, Lysevych M, Tan HH, Jagadish C (2019) Four-dimensional probing of phase-reaction dynamics in Au/GaAs nanowires. *Nano Lett* 19(2):781–786. <https://doi.org/10.1021/acs.nanolett.8b03870>
78. Liao H-G, Cui L, Whitelam S, Zheng H (2012) Real-time imaging of Pt₃Fe nanorod growth in solution. *Science* 336(6084):1011–1014. <https://doi.org/10.1126/science.1219185>
79. de Jonge N, Ross FM (2011) Electron microscopy of specimens in liquid. *Nat Nanotechnol* 6(11):695–704. <https://doi.org/10.1038/nnano.2011.161>
80. Jonge N, Peckys DB, Kremers GJ, Piston DW (2009) Electron microscopy of whole cells in liquid with nanometer resolution. *Proc Natl Acad Sci* 106(7):2159–2164. <https://doi.org/10.1073/pnas.0809567106>
81. Fu X, Chen B, Tang J, Hassan MT, Zewail AH (2017) Imaging rotational dynamics of nanoparticles in liquid by 4D electron microscopy. *Science* 355(6324):494–498. <https://doi.org/10.1126/science.aah3582>
82. Fu X, Chen B, Tang J, Zewail AH (2017) Photoinduced nanobubble-driven superfast diffusion of nanoparticles imaged by 4D electron microscopy. *Sci Adv* 3(8):e1701160. <https://doi.org/10.1126/sciadv.1701160>
83. Li T, Kheifets S, Medellin D, Raizen MG (2010) Measurement of the instantaneous velocity of a Brownian particle. *Science* 328(5986):1673–1675. <https://doi.org/10.1126/science.1189403>
84. Zheng H, Claridge SA, Minor AM, Alivisatos AP, Dahmen U (2009) Nanocrystal diffusion in a liquid thin film observed by in situ transmission electron microscopy. *Nano Lett* 9(6):2460–2465. <https://doi.org/10.1021/nl9012369>
85. Hong L, Anthony SM, Granick S (2006) Rotation in suspension of a rod-shaped colloid. *Langmuir* 22(17):7128–7131. <https://doi.org/10.1021/la061169e>
86. Lorenz UJ, Zewail AH (2014) Observing liquid flow in nanotubes by 4D electron microscopy. *Science* 344(6191):1496–1500. <https://doi.org/10.1126/science.1253618>
87. De Rosier DJ, Klug A (1968) Reconstruction of three dimensional structures from electron micrographs. *Nature* 217(5124):130–134. <https://doi.org/10.1038/217130a0>
88. Hart RG (1968) Electron microscopy of unstained biological material: the polytropic montage. *Science* 159(3822):1464. <https://doi.org/10.1126/science.159.3822.1464>
89. Kwon O-H, Zewail AH (2010) 4D electron tomography. *Science* 328(5986):1668–1673. <https://doi.org/10.1126/science.1190470>
90. Poncharal P, Wang ZL, Ugarte D, de Heer WA (1999) Electrostatic deflections and electromechanical resonances of carbon nanotubes. *Science* 283(5407):1513–1516. <https://doi.org/10.1126/science.283.5407.1513>
91. Wei X-L, Liu Y, Chen Q, Wang M-S, Peng L-M (2008) The very-low shear modulus of multi-walled carbon nanotubes determined simultaneously with the axial young's modulus via in situ experiments. *Adv Func Mater* 18(10):1555–1562. <https://doi.org/10.1002/adfm.200701105>
92. Barwick B, Flannigan DJ, Zewail AH (2009) Photon-induced near-field electron microscopy. *Nature* 462(7275):902–906. <https://doi.org/10.1038/nature08662>
93. Dravid VP, Lin X, Wang Y, Wang XK, Yee A, Ketterson JB, Chang RPH (1993) Buckytubes and derivatives: their growth and implications for buckyball formation. *Science* 259(5101):1601–1604. <https://doi.org/10.1126/science.259.5101.1601>
94. Kawata S, Inouye Y, Verma P (2009) Plasmonics for near-field nano-imaging and superlensing. *Nat Photonics* 3(7):388–394. <https://doi.org/10.1038/nphoton.2009.111>
95. Kim S, Jin J, Kim Y-J, Park I-Y, Kim Y, Kim S-W (2008) High-harmonic generation by resonant plasmon field enhancement. *Nature* 453(7196):757–760. <https://doi.org/10.1038/nature07012>
96. Yurtsever A, van der Veen RM, Zewail AH (2012) Subparticle ultrafast spectrum imaging in 4D electron microscopy. *Science* 335(6064):59–64. <https://doi.org/10.1126/science.1213504>
97. Piazza L, Lummen TTA, Quiñonez E, Murooka Y, Reed BW, Barwick B, Carbone F (2015) Simultaneous observation of the quantization and the interference pattern of a plasmonic near-field. *Nat Commun* 6(1):6407. <https://doi.org/10.1038/ncomms7407>

98. Vanacore GM, Berruto G, Madan I, Pomarico E, Biagioni P, Lamb RJ, McGrouther D, Reinhardt O, Kaminer I, Barwick B, Larocque H, Grillo V, Karimi E, García de Abajo FJ, Carbone F (2019) Ultrafast generation and control of an electron vortex beam via chiral plasmonic near fields. *Nat Mater* 18(6):573–579. <https://doi.org/10.1038/s41563-019-0336-1>
99. Flannigan DJ, Barwick B, Zewail AH (2010) Biological imaging with 4D ultrafast electron microscopy. *Proc Natl Acad Sci* 107(22):9933–9937. <https://doi.org/10.1073/pnas.1005653107>
100. Kaplan M, Yoo B-K, Tang J, Karam TE, Liao B, Majumdar D, Baltimore D, Jensen GJ, Zewail AH (2017) Photon-induced near-field electron microscopy of eukaryotic cells. *Angew Chem Int Ed* 56(38):11498–11501. <https://doi.org/10.1002/anie.201706120>
101. Lu Y, Yoo B-K, Ng AHC, Kim J, Yeom S, Tang J, Lin MM, Zewail AH, Heath JR (2019) 4D electron microscopy of T cell activation. *Proc Natl Acad Sci* 116(44):22014–22019. <https://doi.org/10.1073/pnas.1914078116>
102. Liu H, Baskin JS, Zewail AH (2016) Infrared PINEM developed by diffraction in 4D UEM. *Proc Natl Acad Sci* 113(8):2041–2046. <https://doi.org/10.1073/pnas.1600317113>
103. Pomarico E, Madan I, Berruto G, Vanacore GM, Wang K, Kaminer I, García de Abajo FJ, Carbone F (2018) meV resolution in laser-assisted energy-filtered transmission electron microscopy. *ACS Photonics* 5(3):759–764. <https://doi.org/10.1021/acsp Photonics.7b01393>
104. Hassan MT, Liu H, Baskin JS, Zewail AH (2015) Photon gating in four-dimensional ultrafast electron microscopy. *Proc Natl Acad Sci* 112(42):12944–12949. <https://doi.org/10.1073/pnas.1517942112>
105. Hassan MT, Baskin JS, Liao B, Zewail AH (2017) High-temporal-resolution electron microscopy for imaging ultrafast electron dynamics. *Nat Photonics* 11(7):425–430. <https://doi.org/10.1038/nphoton.2017.79>
106. Carbone F, Kwon O-H, Zewail AH (2009) Dynamics of chemical bonding mapped by energy-resolved 4D electron microscopy. *Science* 325(5937):181–184. <https://doi.org/10.1126/science.1175005>
107. van der Veen RM, Penfold TJ, Zewail AH (2015) Ultrafast core-loss spectroscopy in four-dimensional electron microscopy. *Struct Dyn* 2(2):024302. <https://doi.org/10.1063/1.4916897>
108. Su Z, Baskin JS, Zhou W, Thomas JM, Zewail AH (2017) Ultrafast elemental and oxidation-state mapping of hematite by 4D electron microscopy. *J Am Chem Soc* 139(13):4916–4922. <https://doi.org/10.1021/jacs.7b00906>
109. Egerton RF (2011) *Electron energy-loss spectroscopy in the electron microscope*. Springer Science & Business Media, New York
110. Tan H, Verbeeck J, Abakumov A, Van Tendeloo G (2012) Oxidation state and chemical shift investigation in transition metal oxides by EELS. *Ultramicroscopy* 116:24–33. <https://doi.org/10.1016/j.ultramicro.2012.03.002>
111. Natali M, Campagna S, Scandola F (2014) Photoinduced electron transfer across molecular bridges: electron- and hole-transfer superexchange pathways. *Chem Soc Rev* 43(12):4005–4018. <https://doi.org/10.1039/c3cs60463b>
112. Fitzpatrick AWP, Lorenz UJ, Vanacore GM, Zewail AH (2013) 4D cryo-electron microscopy of proteins. *J Am Chem Soc* 135(51):19123–19126. <https://doi.org/10.1021/ja4115055>
113. Rizzo TR, Park YD, Peteanu LA, Levy DH (1986) The electronic spectrum of the amino acid tryptophan in the gas phase. *J Chem Phys* 84(5):2534–2541. <https://doi.org/10.1063/1.450323>
114. Morel B, Varela L, Conejero-Lara F (2010) The thermodynamic stability of amyloid fibrils studied by differential scanning calorimetry. *J Phys Chem B* 114(11):4010–4019. <https://doi.org/10.1021/jp9102993>
115. Fersht AR, Shi J-P, Knill-Jones J, Lowe DM, Wilkinson AJ, Blow DM, Brick P, Carter P, Waye MMY, Winter G (1985) Hydrogen bonding and biological specificity analysed by protein engineering. *Nature* 314(6008):235–238. <https://doi.org/10.1038/314235a0>
116. Sheu S-Y, Yang D-Y, Selzle HL, Schlag EW (2003) Energetics of hydrogen bonds in peptides. *Proc Natl Acad Sci* 100(22):12683–12687. <https://doi.org/10.1073/pnas.2133366100>

117. Lorenz UJ, Zewail AH (2013) Biomechanics of DNA structures visualized by 4D electron microscopy. *Proc Natl Acad Sci* 110(8):2822–2827. <https://doi.org/10.1073/pnas.1300630110>
118. Fitzpatrick AWP, Park ST, Zewail AH (2013) Exceptional rigidity and biomechanics of amyloid revealed by 4D electron microscopy. *Proc Natl Acad Sci* 110(27):10976–10981. <https://doi.org/10.1073/pnas.1309690110>
119. Gliserin A, Walbran M, Krausz F, Baum P (2015) Sub-phonon-period compression of electron pulses for atomic diffraction. *Nat Commun* 6(1):8723. <https://doi.org/10.1038/ncomms9723>
120. Lassise A, Mutsaers P, Luiten O (2012) Compact, low power radio frequency cavity for femtosecond electron microscopy. *Rev Sci Instruments* 83(4):043705. <https://doi.org/10.1063/1.3703314>
121. Wong LJ, Freelon B, Rohwer T, Gedik N, Johnson SG (2015) All-optical three-dimensional electron pulse compression. *New J Phys* 17(1):013051. <https://doi.org/10.1088/1367-2630/17/1/013051>
122. Kealhofer C, Schneider W, Ehberger D, Ryabov A, Krausz F, Baum P (2016) All-optical control and metrology of electron pulses. *Science* 352(6284):429. <https://doi.org/10.1126/science.aae0003>
123. Walbran M, Gliserin A, Jung K, Kim J, Baum P (2015) 5-femtosecond laser-electron synchronization for pump-probe crystallography and diffraction. *Phys Rev Appl* 4(4):044013. <https://doi.org/10.1103/PhysRevApplied.4.044013>
124. Schulz S, Grguraš I, Behrens C, Bromberger H, Costello JT, Czwalinna MK, Felber M, Hoffmann MC, Ilchen M, Liu HY, Mazza T, Meyer M, Pfeiffer S, Prędko P, Schefer S, Schmidt C, Wegner U, Schlarb H, Cavalieri AL (2015) Femtosecond all-optical synchronization of an X-ray free-electron laser. *Nat Commun* 6(1):5938. <https://doi.org/10.1038/ncomms6938>
125. Hoffmann MC, Fülöp JA (2011) Intense ultrashort terahertz pulses: generation and applications. *J Phys D: Appl Phys* 44(8):083001. <https://doi.org/10.1088/0022-3727/44/8/083001>
126. García de Abajo FJ, Kociak M (2008) Electron energy-gain spectroscopy. *New J Phys* 10(7):073035. <https://doi.org/10.1088/1367-2630/10/7/073035>
127. Baum P, Zewail AH (2007) Attosecond electron pulses for 4D diffraction and microscopy. *Proc Natl Acad Sci* 104(47):18409–18414. <https://doi.org/10.1073/pnas.0709019104>
128. Feist A, Bach N, Rubiano da Silva N, Danz T, Möller M, Priebe KE, Domröse T, Gatzmann JG, Rost S, Schauss J, Strauch S, Bormann R, Sivilis M, Schäfer S, Ropers C (2017) Ultrafast transmission electron microscopy using a laser-driven field emitter: femtosecond resolution with a high coherence electron beam. *Ultramicroscopy* 176:63–73. <https://doi.org/10.1016/j.ultramic.2016.12.005>
129. Zhu C, Zheng D, Wang H, Zhang M, Li Z, Sun S, Xu P, Tian H, Li Z, Yang H, Li J (2020) Development of analytical ultrafast transmission electron microscopy based on laser-driven Schottky field emission. *Ultramicroscopy* 209:112887. <https://doi.org/10.1016/j.ultramic.2019.112887>
130. Mankowsky R, Subedi A, Först M, Mariager SO, Chollet M, Lemke HT, Robinson JS, Glowia JM, Miniti MP, Frano A, Fechner M, Spaldin NA, Loew T, Keimer B, Georges A, Cavalleri A (2014) Nonlinear lattice dynamics as a basis for enhanced superconductivity in $\text{YBa}_2\text{Cu}_3\text{O}_{6.5}$. *Nature* 516(7529):71–73. <https://doi.org/10.1038/nature13875>
131. Hekstra DR, White KI, Socolich MA, Henning RW, Šrajcar V, Ranganathan R (2016) Electric-field-stimulated protein mechanics. *Nature* 540(7633):400–405. <https://doi.org/10.1038/nature20571>
132. Zewail AH (2010) Filming the invisible in 4-D. *Sci Am* 303(2):74–81. <https://doi.org/10.1038/scientificamerican0810-74>